# Transactions of the ASME

EDITORIAL STAFF
Editor, J. J. JAKLITSCH, JR.
Production Editor, CORNELIA MONAHAN
Editorial Production Assistant, BETH DARCHI

FLUIDS ENGINEERING DIVISION
Technical Editor
FRANK M. WHITE (1981)
Executive Secretary
L. T. NELSON (1981)
Calendar Editor
M. F. ACKERSON

Associate Editors
Fluid Machinery
H. JAMES HERRING (1981)
BUDUGUR LAKSHMINARAYANA (1982)
Fluid Measurements
BHARATAN R. PATEL (1982)
Fluid Mechanics
CHARLES DALTON (1983)
OWEN M. GRIFFIN (1981)
BRIAN E. LAUNDER (1981)
WILLIAM G. TIEDERMAN (1981)
Fluid Transients
M. HANIF CHAUDHRY (1983)
Polyphase Flow
PAUL H. ROTHE (1983)
ROBERT L. STREET (1981)
Review Articles
KENNETH E. HICKMAN (1981)

FOREIGN CORRESPONDENTS
Europe and Russia
JACQUES CHAUVIN
Europe and Russia
JOHN H. HORLOCK
India and Middle East
ARUN PRASAD
Japan and China
YASUTOSHI SENOO

POLICY BOARD, COMMUNICATIONS
Chairman and Vice-President
I. BERMAN

Members-at-Large
W. J. WARREN
J. E. ORTLOFF
M. J. RABINS
J. W. LOCKE

Policy Board Representiatives
Basic Engineering, FRED LANDIS
General Engineering,
C. F. PHILLIPS
Industry, J. E. ORTLOFF
Power, R. E. REDER
Research, G. P. COOPER
Codes and Stds., L. L. ELDER
Nom. Com. Rep., J. W. LOCKE

Business Staff
345 East 47th St.
New York, N. Y. 10017
(212) 644-7789
Mng. Dir., Publ., J. J. FREY

OFFICERS OF THE ASME
President, CHARLES E. JONES
Deputy Exec. Dir. & Asst. Sec'y, PETER CHIARULLI
Secretary and Treasurer, ROBERT A. BENNETT

The Journal of FLUIDS ENGINEERING (USPS 278-480) is edited and published quarterly at the offices of The American Society of Mechanical Engineers, United Engineering Center, 345 E. 47th St., New York, N. Y. 10017. Cable Address, "Mechaneer," New York. **Second-class** postage paid at New York, **CHANGES OF ADDRESS** must be received at Society headquarters seven weeks before they are to be effective. Please send old label and new address. **PRICES:** To members, $30.00, annually: to nonmembers, $60.00. Single copies, $20.00 each. Add $5.00 for postage to countries outside the United States and Canada. **STATEMENT** from By-Laws. The Society shall not be responsible for statements or opinions advanced in papers or . . . printed in its publications (B7.1, Par. 3).



INDEXED by the Engineering Index, Inc.


# Journal of Fluids Engineering


**Published Quarterly by The American Society of Mechanical Engineers**

VOLUME 103 • NUMBER 1 • MARCH 1981





(Continued on p. 7)

# CONTENTS
## (Continued)



### Announcements and Special Notices

Journal of Fluids Engineering

# Foreign Report

The Secretary of State for Industry in the U.K. set up a Committee of Inquiry into the Engineering Profession in 1977. It was chaired by Sir Monty Finniston, formerly Chairman of the British Steel Corporation, and reported in January 1979. The Committee had a broad charge relating to the engineering profession but an important phrase was included in the terms of reference – the Committee was required to make its review in the light of "the needs of manufacturing industry." Sir Monty placed special emphasis on this rider during the Committee's deliberations – recommendations for the benefit of the profession alone were ruled out of court.

The Committee's analysis of the British economic situation, and the role that engineering should play in a manufacturing nation, has been widely acclaimed in the U.K. But if the diagnosis has been universally accepted, the prescription recommended by the Committee has by no means been so well received [1].

Finniston suggested new arrangements for registration of engineers, with accreditation of both academic courses and industrial training by a new Engineering Authority. This was to be a statutory authority (i.e. state recognized and backed); the state's role in this authority has been opposed tooth and nail by the professional engineering institutions (and the Council of Engineering Institutions (CEI) which maintains a "registration bank" for engineers presently qualifying through these institutions). The Committee saw the new Authority as serving two purposes – firstly the state registration of engineers, and secondly as providing an "engine for change" for the engineering industry.

The new Secretary of State for Industry, Sir Keith Joseph, has indicated that he is prepared to accept the establishment of some kind of authority but it should be chartered rather than statutory. It would thus hold a charter from the Queen, through the Privy Council, which would enable it to award titles, but it would have no other legislative backing and, in particular, no state funding. The Finniston Committee had reported to a Conservative Government with a recommendation for a new "quango" (a quasi-autonomous non-government organization) at a time when the new Government was committed to a major reduction in advisory committees of this kind. It was, therefore, some achievement to get a Conservative Secretary of State to agree that there should be a new "authority" at all, and it was not surprising that he did not agree that it should be statutory.

Fiinniston and his colleagues (myself included) decided against recommending the *licensing* of engineers. Licensing implies that nobody can do a particular engineering job other than a licensed engineer educated and trained for the purpose. However, the Committee did conclude, after studying the systems in many other countries, that there could be some advantages in *registration* – compiling a list of engineers who were educated and trained under a recognized system. It proposed the title of R. Eng. (Registered Engineer) for an engineer who had completed an accredited educational course and accredited training in industry, over a total of about six years (this registration "package" would include the award of a recognized degree of Bachelor of Engineering).

The purpose of the central R.Eng. qualification was to ensure that an integrated formation package would be available for all intending professional engineers. I and my fellows on the Committee wished to see more professional studies of engineering practice introduced into academic courses, woven in with the excellent engineering science that is now taught. We also wished to see training accredited within particular industrial companies. Too many young U.K. graduates have found that their present training ends with their degrees and that there is little organized practical experience offered subsequently by the companies they join.

But in addition Finniston proposed two other streams of "formation," above and below the R.Eng.: the R.Eng. (Dip) for an elite stream of professional engineers, and the R.Eng. (Associate) for engineering technicians. The Committee was strongly criticized for dividing the professional stream into R.Eng. and R.Eng.(Dip). We wished to produce a core of expert engineers trained to the higher standard of R.Eng.(Dip), perhaps some 25 percent of the whole intake, but we have been told since publication of the report that it is educationally unwise to try to separate off such an elite stream after one year in university as we proposed. This is a surprising criticism for MIT has long since shown how it can be done, by selection of its best students to go forward to a Masters degree, skipping the Bachelor degree along the way. But our case for the R.Eng.(Dip) appears to be lost.

Another important point made in the Finniston Report was that U.K. industry should make a major effort to ensure the supply of engineers it requires, by better recognition of its engineers. We recommend that "engineering manpower audits" should be made, that companies should regularly survey that engineering manpower, and that career planning for individual engineers should be undertaken; too often a good engineer does not move up the ladder into management or into advanced engineering supervision. This recommendation for engineering audits has been well received and many companies have acted quickly to implement it.

Well taken also have been Finniston's recommendations for expanding continuing education for graduate engineers. Such education should include up-dating in existing technologies, provision for transfer to new ones and instruction about new legislation and its implications for engineers and engineering industry.

But much wider than these detailed recommendations is the general problem of improving the image of engineering in the U.K. We do not have the tradition of "technik" (a third

culture parallel to arts and science) that exists in Germany and other Continental countries. Our pure science has been strong and recruitment to science has been excellent. But too often the bright young student from high school is attracted into science at the university rather than to an engineering course (which is often regarded as non-mathematical and little above craft level). It is this poor image of engineering that we have to change and it requires a whole new attitude within the U.K. and particularly within our schools. I hope that the Finniston report will go some way towards improving this attitude in our society; but it will not happen overnight.

## Reference

1 "Engineering—Our Future," Report of the Committee of Enquiry into the Engineering Profession, Command .7794, available from H. M. Stationary Office, Hugh Holborn, London, U.K.

**J. H. HORLOCK**

# A Comparison of Two Optical Techniques for Measuring Cavitation Nuclei

**M. L. Billet**
Research Associate,
The Pennsylvania State University,
Applied Research Laboratory,
State College, Pa. 16801

**E. M. Gates**
Assistant Professor,
Department of Mechanical Engineering,
University of Alberta,
Edmonton, Alberta

*Several devices have been developed or adapted to the use of measuring "nucleating sources" in a liquid including acoustic methods, direct observation (e.g. microscopy and holography), single particle counters, light scattering and light extinction. With experience two techniques have become more favored than the others, namely: holography and light scattering. However, with the exception of Peterson et al's study no attempt has been made to simultaneously compare these two techniques under actual test conditions so that some confidence may be gained in deducing the number and type of nuclei from the record produced by either method. The purpose of the present paper is then to report and compare some nuclei populations which were recorded simultaneously by both methods during a series of cavitation inception tests. Measurements of nuclei populations were made in two facilities located at the California Institute of Technology, the Low Turbulence Water Tunnel (LTWT) and the High Speed Water Tunnel (HSWT) which are known to have substantially different nuclei distributions. In each facility nuclei populations were recorded at various combinations of tunnel velocity, pressure and pressure-time histories in an effort to produce different distributions and also to enable one to deduce from the laser scattering results the composition of the nuclei, i.e., solid particulates or bubbles. This deduction could then be checked with the holographic results. Simultaneous nuclei population measurements were recorded in the LTWT, whereas measurements of nuclei in the HSWT were obtained at separate times approximately eleven months apart. Since both methods have different characteristic size detection ranges, they could be compared directly only in the overlapping size range, namely: 10-50 microns diameter. In the LTWT where the populations were recorded simultaneously, there was some good agreement between not only the numbers but also the type of nuclei (mainly gas bubbles). However, the scattering technique indicated somewhat fewer nuclei in most cases. In addition, the scattering technique indicated fewer nuclei in the HSWT than had been previously measured by holography. Although there was some discrepancy between numbers of nuclei, both techniques demonstrated (directly from holography and by inference from the scattering results) that the nuclei were primarily solid particulates rather than gas bubbles.*

## Introduction

It is generally accepted that cavitation inception occurs at nucleation sites which either originate from the model surface or are present in the approaching flow. At one time "surface nuclei" attracted considerable attention (see for example Holl, 1968; Peterson, 1968). While it was shown that under certain circumstances that surface nuclei could exert a controlling influence on inception, it seemed evident on the other hand from the results of the ITTC tests (Lindgren and Johnsson, 1966; Johnson, 1969) that during "normal" cavitation testing freestream nuclei were more important. Hence during the past decade work like that of Silberman and Schiebe (1973), Peterson (1972), and Keller (1972) has been to develop equipment and techniques for determining freestream nuclei populations and attempting to relate them to inception.

Of the many methods applied to nuclei measurements (see Morgan, 1972, for a summary) two optical techniques have become more favored for use in the laboratory environment—light scattering and holography. Although both counters have been used to measure nuclei populations under many different conditions there has been, aside from Peterson et al's (1975) report, no comparison of populations obtained simultaneously with the two counters in the same facility. One of the purposes of the present work was then to carry out such a comparison and here then we shall report the results. In this

Contributed by the Fluids Engineering Division and presented at the International Symposium on Cavitation Inception, Winter Annual Meeting, New York, N. Y., December 5-10, 1980, of THE AMERICAN SOCIETY OF MECHANICAL ENGINEERS. Manuscript received by the Fluids Engineering Division, February 11, 1980.

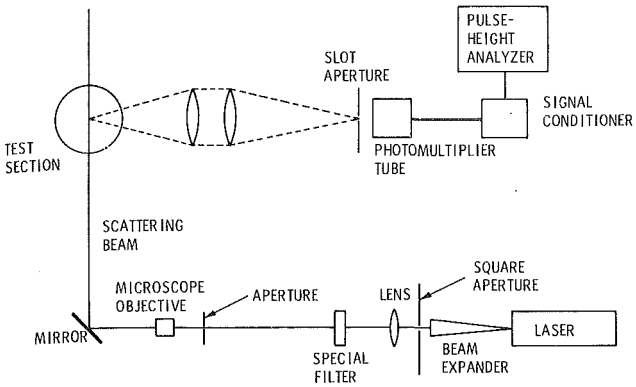


**Fig. 1 Schematic drawing of the light scattering nuclei counter**

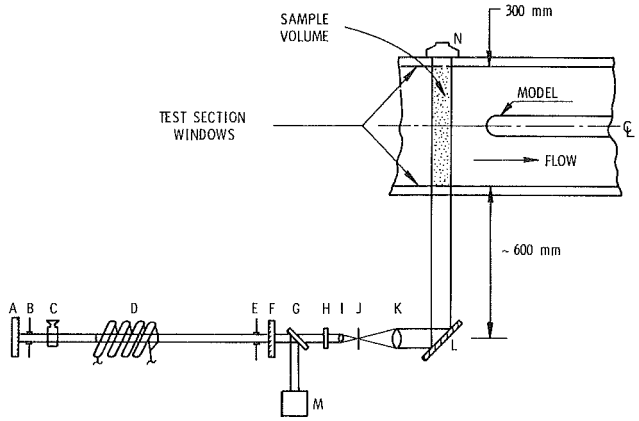


**Fig. 2 Diagram of the homocamera: (*a*) etalon, (*b*) iris, (*c*) dye-quench cell, (*d*) ruby-flash lamp assembly, (*e*) iris, (*f*) dielectric mirror, (*g*) beam splitter, (*h*) neutral density filter, (*i*) beam expander lens, (*j*) 25$\mu$ pinhole, (*k*) collimating lens, (*l*) front surface mirror,(*m*) p.i.n. diode, (*n*) film pack.**

report the terms "nuclei" will refere to particulates and gas bubbles detected by the counters.

## Equipment and Methods

**Water Tunnels.** Measurements of nuclei populations were made in two water tunnels—the Low Turbulence Water Tunnel (LTWT) and the High Speed Water Tunnel (HSWT) both located at the California Institute of Technology. Since both facilities have been described in detail elsewhere (see Knapp et al (1970) for the HSWT and Gates and Acosta (1978) for the LTWT), it will only be noted here that the HSWT has a resorber whereas the LTWT does not. During the tests the air content in the HSWT was approximately 10 ppm and 7 ppm in the LTWT. At these air content levels there were very few macroscopic gas bubbles visible in the HSWT, whereas in the LTWT there were always many bubbles easily discernible in the approaching flow.

**Nuclei Counters.** The light scattering nuclei counter is based on the relationship between the radius of a scattering center (R) and the scattered intensity. The scattered light intensity is not only a function of the radius, but is also dependent on the angle of observation, the polarization angle of the scattered beam, the wavelength of the scattering beam ($\lambda$), and the refractive indices of the various mediums involved. However, Keller (1972) has shown that if the scattered light is collected at an angle of 90 degrees to the scattering beam there is a unique relationship between intensity and a non-dimensional parameter expressed as $2\pi R/\lambda$.

A schematic of the scattering counter is provided in Fig. 1. First, the laser beam is expanded and collimated by a beam expander. A square aperture is used to isolate the central portion of the beam. The square beam is then focused by a long focal length lens. A small focal length lens is positioned after the focal point of the first lens so that a collimated scattering beam will result. The size of the scattering beam is determined by the size of the square aperture and the ratio of the effective focal lengths of the two lenses. Between the two lenses, there is a filter which is used to ensure a scattering beam of constant intensity and an aperture positioned at the focal point to reduce reflections.

The scattered light is collected by a lens and focused by a second lens on a photomultiplier tube. A slot is positioned in front of the photomultiplier tube to restrict the amount of scattered light collected. The size of the slot can be adjusted so that the measuring volume can be varied. The size of the control volume is determined from two considerations, namely, (1) the probability of only one scattering center being in the measuring volume at any time, and (2) the characteristic dimension of the measuring volume should be approximately three times the maximum radius of the scattering center of interest. The scattering volume in the present experiments presented a 0.76 mm × 0.32 mm window to the flow and was 0.76 mm deep.

The output of the photomultiplier tube due to scattered light will be a pulse. This pulse goes through a signal conditioner which filters the high frequencies and adjusts the DC level. The pulse height processor now accepts the conditioned pulse, assesses the size of each detected pulse, and sorts the pulses into selectable categories until a predetermined total number of pulses is achieved. A display then gives the number of pulses in each category and the total amount of counting time. During the present tests the processor was programmed to divide the 0 to 50 micrometer diameter range into 15 size categories. The number of nuclei larger than 50 micrometers were stored in channel 16. The total number of particles counted per sample was 250.

Nuclei distributions were also deduced from holograms of the test fluid. The experimental apparatus and mehtod for this counter is much the same as used by Peterson (1972), Feldberg and Shlemenson (1973), and is described in detail in Gates and Bacon (1978). Essentially it is a two-step image forming process. In the first step, a hologram of a sample volume of the water in the tunnel test section is recorded on a special high resolution film by a "holocamera." In the second step, the developed hologram is reconstructed producing a three dimensional image of the original volume which can be probed at the investigator's leisure. The holocamera and reconstruction system are shown schematically in Figs. 2 and 3, respectively. In the present work a volume 1 cm × 1 cm × 2.5 cm near the center line of the test section was chosen for sampling.

Measurements of nuclei in the HSWT were made separately approximately eleven months apart, whereas the measurements obtained in the LTWT were recorded simultaneously. The physical arrangement of equipment at the LTWT is shown schematically in Fig. 4 and a photograph of the setup is given in Fig. 5. In Fig. 5 the light source (argon laser), the special filters, and lenses of the light scattering counter are seen in the foreground. The conditioned beam is reflected through 90 degrees and enters the test section through the bottom window. On the other side of the test section just ahead of the model can be seen the collecting lens and the photomultiplier tube. Also on the other side of the test section and upstream of the scattering counter can be seen the mirror (see Fig. 2) which reflects the ruby laser pulse through the test section. The holography film holder is not shown.

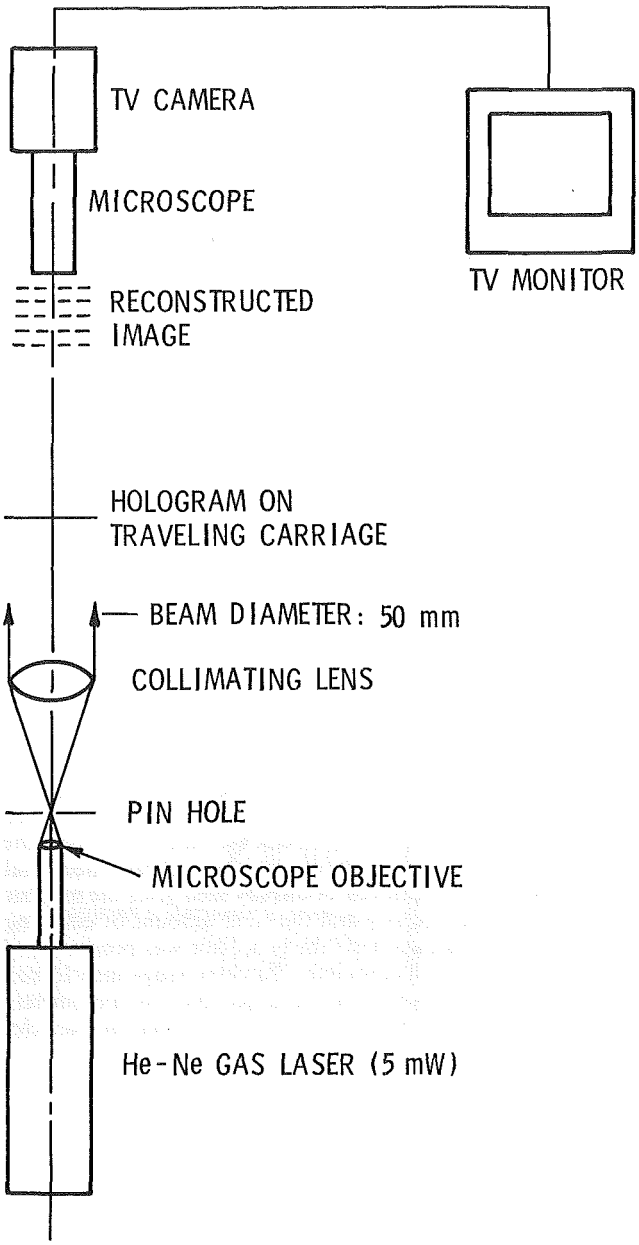


Fig. 3 Arrangement to reconstruct and read the holograms

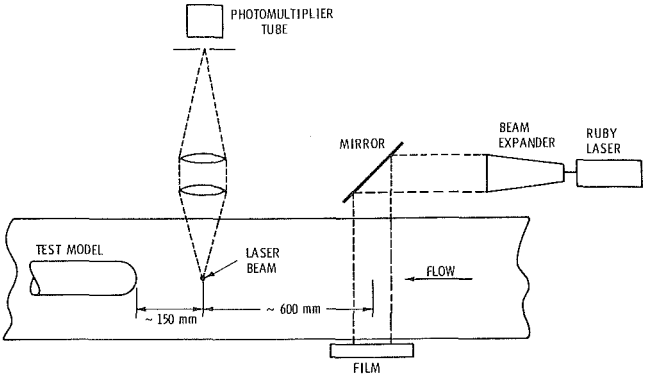


Fig. 4 A schematic drawing of the top view of the arrangment of the nuclei counters at the LTWT

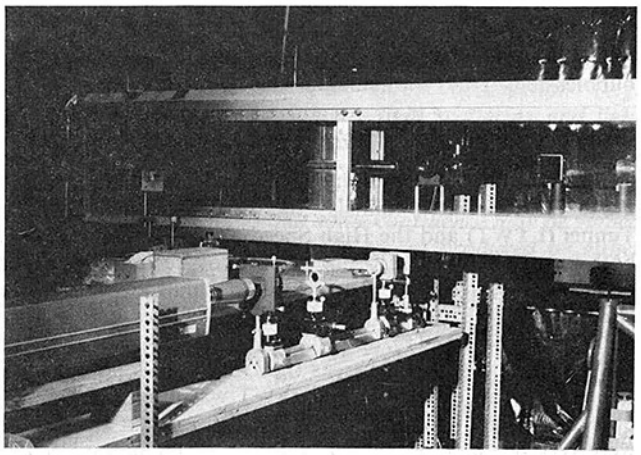

Fig. 5 A photograph of the arrangement of equipment at the LTWT.

## Results

A few of the nuclei populations measured in the HSWT for various conditions of velocity and pressure are presented in Tables 1 and 2. The nuclei populations have also been reduced to a number density function by the following approximation:

$$N\left(\frac{R_1+R_2}{2}\right)=\frac{\text{number of particles with radii between } R_1 \text{ and } R_2}{(R_2-R_1)}$$

and have been plotted versus nuclei radius in Fig. 6. Nuclei populations obtained in the LTWT are summarized in Table 3.

It can readily be seen from the tables that the light scattering counter has recorded substantially fewer nuclei than the holographic counter. Only at a velocity of 14 m/s in the HSWT does the scattering counter measure a population density equal to that of the holography counter. But this agreement is misleading because, as can be seen in Fig. 6, essentially all the particles detected by the scattering counter are less than 10 mocrometers in diameter which is below the detection range of the holographic method. The descrepancy between the populations in the HSWT may be attributable to changing tunnel conditions over the eleven month period between measurements. However, since the counts in the LTWT were obtained simultaneously, the lack of agreement here cannot be explained in this fashion.

**Table 1 Nuclei populations in HSWT measured by holography**

| Cavitation number | Number of nuclei/cubic centimeter |
|---|---|
| 0.23 | 36.0 |
| 0.26 | 60.8 |
| 0.41 | 61.2 |
| 0.43 | 35.6 |
| 0.47 | 66.4 |
| 0.61 | 46.0 |
| 0.73 | 35.6 |

Several aspects of the light scattering counter were examined in an attempt to explain the disagreement between the two counters. The first area given attention was the sampling volume. Recalling that the dimensions of the scattering volume are 0.076 cm × 0.038 xm × 0.076 cm and with 400 particles/cc, it is estimated that the probability of having more than one particle in the volume at anytime is less than one percent. Secondly, if the probability of a 50

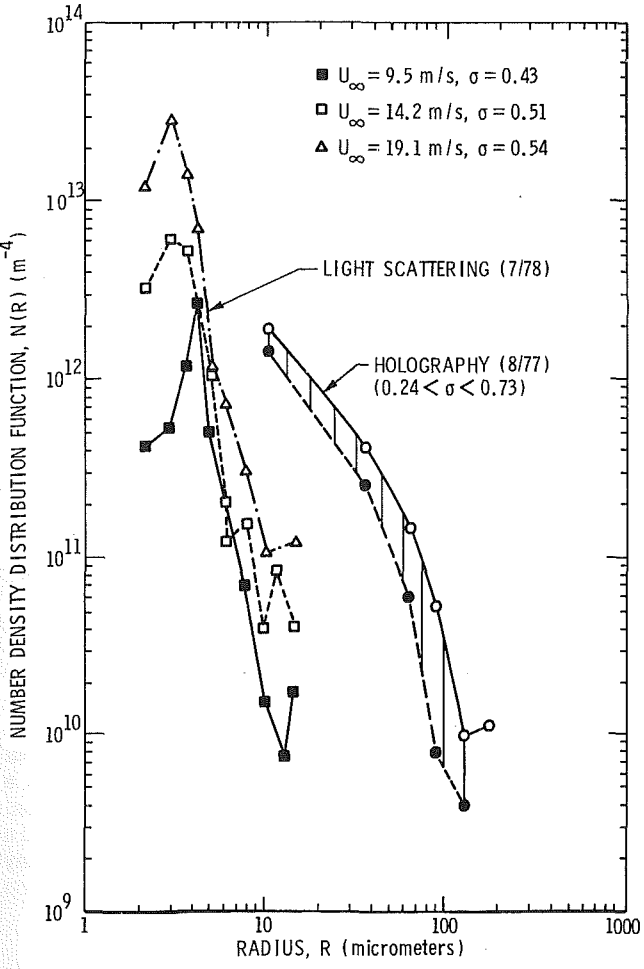


**Fig. 6 Comparison of measurements of nuclei populations obtained in the HSWT**

micrometer diameter particles passing through the sample volume completely within the volume boundaries is estimated a figure of approximately 80 percent is obtained. Hence it appears that negligible error should be introduced into the count through any volume size effects.

**Table 2 Nuclei populations in HSWT measured by light scattering counter**

| Velocity (m/s) | Cavitation number | Number of nuclei/cubic centimeter |
|---|---|---|
| 6.35 | 4.75 | 4.4 |
| 6.33 | 0.96 | 4.0 |
| 9.49 | 2.12 | 6.4 |
| 9.52 | 0.43 | 3.2 |
| 14.27 | 0.94 | 6.2 |
| 14.24 | 0.51 | 15.4 |
| 14.30 | 0.94 | 22.8 |
| 19.13 | 0.66 | 75.0 |
| 19.18 | 0.41 | 50.0 |

The next question considered was the sample size. The processor was programmed to stop counting after 250 particles had been detected. If this sample size is insufficient, two things should be noticed: first, there should be an increasing error with increasing particle size and second, the measured population will not be consistent, i.e., there will be random variations in the count. This particular argument of course only applies to the LTWT results since in the HSWT the nuclei density is only about 50 nuclei/cc. For tests 4 through 10 which were obtained in the LTWT at an average velocity of 6.56 ± 0.3 m/s, an average sampling time of 0.83 ± 0.1 sec and a mean volume of 1.57 ± 0.25 cc was sampled producing an average nuclei density of 162.2 ± 26.8 nuclei/cc. The holographic counter recorded 323 ± 80 nuclei/cc. The light scattering results appear to be reasonably consistent and from Table 3 there does not appear to be any well defined trend in the disagreement between the populations with nuclei size—although there appears to be a substantial increase in error for nuclei between 20-50 micrometers in diameter.

The conclusion of the above paragraph raises the question of sampling from a population which is not uniform across the tunnel test section. That the distribution is not uniform has been deteremined from sampling different sections of the reconstructed hologram. However, the reconstructed portion of the hologram was chosen to be on the center line of the tunnel to ensure that both counters were sampling from the same area of the tunnel cross section. This does not however preclude the question of distribution changing during the sampling time.

The remaining questions concern the detection system of the scattering counter and there are several. One is that the counter was calibrated by using polystyrene spheres of a known size. The question then is are the scattering characteristics of gas bubbles and particulates similar to those of the spheres? If the intensity of the light scattered by a particle or bubble was substantially less than that scattered by a polystyrene sphere of identical size, it is possible that the smaller particles would not be detected and hence the nuclei density measured would be low. The most likely explanation is that the scattering from the irregular shape particles is different than from a spherical shape bubble.

A preliminary study has been conducted after the comparison tests to investigate the influence of dirt particles on measurements obtained by the light scattering method. The system was set up as discussed in the paper and calibrated using polystyrene spheres. Silican carbide particles with a grain size of 45 micrometers diameter were then added to the water in the 30.5 cm water tunnel located at the Applied Research Laboratory of The Pennsylvania State University. Preliminary results show that the particles significantly increased the nuclei density over a large diameter range, and on the average most of the increase appeared in the 5-15 micrometer diameter range.

In the above discussion it has been assumed that the holography results are correct. One tends to take this for granted since the holography technique is based on direct observation of the reconstructed image of the nuclei. For

**Table 3 Comparison of nuclei measurements obtained in the LTWT**

| Test | Number of nuclei/cubic centimeter Nuclei diameter (micrometers) | | | | | | | |
|---|---|---|---|---|---|---|---|---|
| | < 20 | | 20-50 | | > 50 | | Cumulative | |
| number | Holo. | Scat. | Holo. | Scat. | Holo. | Scat. | Holo. | Scat. |
| 16 | 221 | 82 | 39 | 4.6 | 1.2 | 1.0 | 261 | 88 |
| 17 | 290 | 208 | 116 | 4.2 | 3.2 | 0.8 | 409 | 212 |
| 24 | 308 | 126 | 106 | 3.6 | 1.6 | 0.6 | 416 | 128 |
| 25 | 312 | 172 | 81 | 2.8 | 1.6 | - | 394 | 176 |
| 34 | 204 | 166 | 66 | 0.6 | 2.8 | 0.6 | 273 | 168 |
| 35 | 242 | 146 | 64 | 1.6 | 4.4 | - | 310 | 148 |

particles less than 20 micrometers diameter there is some uncertainty because of background noise in the original hologram and in the reconstruction system. To verify that the holograms are examined correctly several were counted independently by at least two people. The results of these separate counts was essentially the same so it is assumed that the error due to the counter is negligible.

The above discussion has addressed the problem of the discrepancy between the two counters regarding the number distribution. Basically the conclusion is that the scattering from dirt particles could explain the disagreement. However, the implication is that the characteristics of the light scattering counter should be investigated more thoroughly.

The remaining pertinent factor regarding the evaluation of nuclei populations is to classify the type of nuclei, i.e., particulate or gas bubble. There is considerable interest in the relative importance of particulates versus bubbles as cavitation nuclei. And while it has been inferred from experiments by Keller (1972), Peterson (1972), Yilmaz, et al. (1976) that particulates may play a major role in inception, other observations by Gates and Acostas (1978) suggest the opposite and by Weitendorf and Keller (1978) suggest, at least, that some particulates apparently do not influence inception. It can be seen then that differentiation between particulates and bubbles is of some controversy. The holographic method is most advantageous here as the nucleus is observed directly and a classification is made based upon shape. The light scattering technique cannot distinguish between particulates and bubbles but some qualitative assessment can be made by attempting to alter the distribution through filtering and/or control of the water pressure-time history.

Some distributions obtained in the HSWT with the scattering counter are given in Figure 6. It was found that for a given test section velocity that the distribution was independent of pressure. If the velocity was increased many small nuclei (< 10 micrometers diameter) and a few large nuclei were produced. Also, if the velocity and pressure were held constant it was observed that the number of small nuclei increased while the number of large nuclei decreased with time. From these observations it was deduced that the nuclei in the HSWT are mainly particulates. And it is believed that they are mainly chips of paint and rust which are continuously being removed from the tunnel walls and being broken up. This conclusion agrees with the holographic results in which so few bubbles were detected that it was not possible to estimate a distribution, i.e., the holography results in Fig. 6 consist entirely of particulates.

In the LTWT it was more difficult to distinguish particulate and nuclei distributions because of limited velocity and pressure control. A comparison of populations measured at a low and a high velocity indicated a doubling of the nuclei density with velocity for nuclei less than 20 micrometers. For a given velocity altering the pressure produced a shifting of the entire distribution either up or down but with no particular relation between the direction of the shift and the direction of the pressure change. (The lack of correlation is believed to be due to pressure-time history effects.) From these observations it could only be deduced that there are a significant number of particulates in the smaller nuclei and the larger nuclei are bubbles. A much more quantitative classification of the nuclei is given in Table 4 where the holography results of Table 3 have been presented again but with the particulate and bubble populations separated. No distinction between particulate and bubble populations for nuclei less than 20 micrometers diameter can be made as the background noise destroys the resolution. From this table it can be seen that nuclei between 20 and 50 micrometers are mainly particulates, between 50-100 micrometers there is approximately an equal number of each and above 100 micrometers diameter the nuclei are believed to be essentially all bubbles.

**Table 4 Particulate and bubble distributions in the LTWT**

| Test Number | Number of nuclei/cubic centimeter nuclei diameter (micrometers) 20-50 Part. | 20-50 Bubbles | 50-100 Part. | 50-100 Bubbles |
|---|---|---|---|---|
| 1 | 82.0 | 0.8 | 8.0 | – |
| 4 | 124.8 | 1.2 | 6.0 | 1.2 |
| 5 | 122.4 | 3.2 | 2.4 | - |
| 6 | 113.6 | 2.4 | 0.4 | 0.8 |
| 7 | 70.0 | 14.4 | – | 2.8 |
| 8 | 69.2 | 10.0 | 1.2 | 1.6 |
| 9 | 104.0 | 6.0 | 0.4 | 4.0 |
| 17 | 98.0 | 17.6 | 0.4 | 2.8 |
| 24 | 92.8 | 12.8 | 0.4 | 1.2 |
| 25 | 70.0 | 10.8 | 0.4 | 1.2 |

## Conclusion

Although all the information from the holographic counter has not yet been reduced, it is clear there exists a significant difference in the number distribution obtained by the two methods. The reasons for this discrepancy are presently unknown and, although it is suspected that the LSC is in error and that the holographic counter is correct, it is not clear at this time that *either* method gives accurate results. What is required is not a direct comparison between the methods, but rather a comparison of each method with a standard i.e. a count of a known particle concentration and size distribution. The discrepancy between the counters must be resolved and a determination of the accuracy of each technique made if any reliable comparison in the performance of various cavitation facilities is to be made.

## Uncertainty Estimates

The data given in the tables were obtained by using the light scattering counter or the holographic counter to measure the nuclei density. The uncertainty of the light scattering counter is estimated to be ±15 percent of the number of nuclei per $cm^3$, and for the holographic counter is estimated at ±5 percent of the number of nuclei per $cm^3$.

## Acknowledgment

The authors are indebted to Professor A. J. Acosta at the California Institute of Technology and to Professor J. W. Holl at The Pennsylvania State University for their suggestions regarding this investigation conducted at the California Institute of Technology. The work was supported in part by the Naval Sea Systems Command Code 63R-31 and by funds from the University of Alberta.

## References

1 Feldberg, L. A., and Shlemenson, K. T., "The Holographic Study of Cavitation Nuclei," Discussion to Proc. IUTAM Symp. on Non-steady Flow of Water at High Speeds, Leningrad, USSR (English version; Moscow 1973) pp. 106-111.

2 Gates, E. M., and Bacon, J., "Determination of Cavitation Nuclei Distributions by Holography," *J. Ship Res.*, Vol. 22, No. 1, Mar. pp. 29-31.

3 Gates, E. M., and Acosta, A. J., "Some Effects of Several Free-Stream Factors on Cavitation Inception on Axisymmetric Bodies," 12th Symposium on Naval Hydrodynamics, Wash., D.C., 1978.

4 Holl, J. W., "Sources of Cavitation Nuclei," Presented at the 15th Amer. Towing Tank Conf., Ottawa, Canada, 1968.

5 Johnsson, C. A., "Cavitation Inception on Head Forms, Further Tests," 12th ITTC, Rome, 1969, pp. 381-392.

6 Keller, A. P., "The Influence of the Cavitation Nucleus Spectrum on Cavitation Inception, Investigated with a Scattered Light Counting Method," ASME *Journal of Basic Eng.*, Dec. 1972, pp. 917-925.

7 Knapp, R. T., Daily, J. W., and Hammitt, F. G., *Cavitation*, McGraw-Hill, New York, 1970.

8 Lindgren, H., and Johnsson, C. A., "Cavitation Inception on Head Forms ITTC Comparative Experiments," Pub. of the Swedish State Shipbuilding Exper. Tank, No. 58. (Also presented at the 11th ITTC, Tokyo, 1966.)

9 Morgan, W. B., "Air Content and Nuclei Measurements," 13th ITTC, Rep. of Cavitation Comm., 1972.

10 Peterson, F. B., "Cavitation Originating at Liquid-Solid Interfaces," NSRDC Rep. 2799, 1968.

11 Peterson, F. B., "Hydrodynamic Cavitation and Some Considerations of the Influence of Free Gas Content," 9th Symp. on Naval Hydro., Paris, 1972.

12 Peterson, F. B., Danel, F., Keller, A., and Lecoffe, Y., "Determination of Bubble and Particulate Spectra and Number Density in a Water Tunnel with Three Optical Techniques," 14th ITTC, 1975.

13 Silberman, E., Schiebe, F., and Mrosla, E., "The Use of Standard Bodies to Measure the Cavitation Strength of Water," St. Anthony Falls Hyd. Lab., Rep. No. 141, Univ. of Minn., 1973.

14 Weitendorf, E. A., and Keller, A. P., "A Determination of the Free Air Content and Velocity in Front of the "Sydney-Express" Propeller in Connection with Pressure Fluctuation Measurements," 12th Symp. on Naval Hydrodynamics, Wash., D.C., 1978.

15 Yilmaz, E., Hammitt, F. G., and Keller, A., "Cavitation Inception Thresholds in Water and Nuclei Spectra by Light-Scattering Technique," *J. Acoust. Soc. Am.*, Vol. 59, No. 2, Feb. 1976, pp. 329–338.

# A Photographic Study of Cavitation in Jet Flow

**J. W. Hoyt**[1]
Mem. ASME

**J. J. Taylor**[2]

Naval Ocean Systems Center,
San Diego, Calif.

*The effect of polymer additives on underwater jet cavitation has been studied using a special camera. Solutions of the drag-reducing additives, polyacrylamide and poly(ethylene oxide), at concentrations of 25 ppm, decreased the cavitation inception index and greatly changed the appearance of the cavitation bubbles. Solutions of the non drag-reducing polymer, Carbopol, produced cavitation bubbles having the same appearance on pure water and did not change the inception index. In pure water, the cavitation appearance resembles ragged groups of small bubbles with the overall impression of sharpness and roughness, but in drag-reducing polymer solutions the bubbles are larger, rounded, and of completely different appearance.*

## Background

The study of cavitation in water has been stimulated by the recent discovery that small amounts (parts per million) of high molecular-weight, long-chain polymers of the type which reduce turbulent fluid friction are also effective in lowering the cavitation inception index (i.e., it becomes more difficult to cause cavitation in a given flow situation). Ellis, Waugh, and Ting [1] showed that cavitation inception on a hemispherical head-form body was greatly reduced by the presence of drag-reducing polymers in the flow. Van der Meulen [2] and Arndt, et al. [3] have confirmed the effect. Van der Meulen and later Gates [4] have shown by flow visualization that the polymer acts to inhibit cavitation on nose shapes by an earlier transition to turbulence, thus suppressing the laminar separation region where cavitation is most likely.

Cavitation in orifice-discharge flows has been shown to be delayed when polymers are present in the flow [5]; propeller cavitation is affected by polymers [6]; and acoustically produced cavitation inception is retarded by the presence of polymers [7,8]. Onset of cavitation in the wake of a cylinder was also inhibited [9] as is cavitation in a vortex [10]. A summary of work on cavitation in polymer solutions has been given by Acosta and Parkin [11].

Cavitation in the shear layer of an underwater jet is profoundly affected by the presence of polymer additives as discussed in [12 and 13]. While the effect of polymers in lowering the cavitation inception index can be rationalized to some extent by considering the viscoelastic properties of polymer solutions [14 and 15], actual observations indicate little difference in growth rate of spark-generated bubbles [16] or gas-bubbles [17] in polymer solutions as compared with water.

However in spite of theoretical analysis (18 and 19) which indicate the bubble collapse rate should be less in polymer solutions than in water, some experimental data [20] show the cavitation erosion rate to be enhanced in polymer solutions, while other data show an opposite effect (21). Underwater jet cutting of metals, which may also be a cavitation effect, is greatly enhanced by polymer addition to the jet fluid [22]. Ting [23] discusses these experiments in view of the polymer relaxation times and polymer solution parameters. The radiated noise from cavitation bubble collapse has been found to be greater in jet cavitation [24] and in cavitation around a rotating disk [25] for polymer solutions compared to water.

The overall appearance of fully developed cavitation is changed by the presence of polymer additives as shown by the photos of Brennen [26] and Hoyt [27]. Ōba [5] has provided somewhat more detailed photos of cavitation events.

The reason for the inhibition of cavitation by polymer solutions is not known at present, and theoretical studies give conflicting results. Thus it is desirable to more precisely visualize the flow during cavitation events in water and in polymer solution flow so as to have a better basis upon which to carry out further studies and evaluations of the effect of polymer solutions on cavitation.

## Experimental

The apparatus consisted of a water nozzle 0.115 inches (2.92 mm) in diameter which discharged into a covered box having optical glass walls approximately 2-1/2 in (7 cm) apart. The box was arranged to provide carefully controlled recirculation of the jet fluid, so the ambient surroundings of the jet were nearly stationary at all times. A slight negative pressure was measured at the top of the box over the jet; this negative pressure was almost exactly balanced by the static head of the fluid at the jet centerline and hence the static pressure at the jet centerline was taken as atmospheric.

The inlet pressure to the nozzle was measured by a calibrated pressure gage, and the water leaving the apparatus was sampled. Air content of the samples was measured by a

[1] Present address: Department of Mechanical, Industrial, and Aerospace Engineering, Rutgers University, Piscataway, N.J. 08854

[2] Presently: Consultant, Santa Barbara, Calif. 93111

Contributed by the Fluids Engineering Division and presented at the Winter Annual Meeting, New York, N.Y., December 2-7, 1979, of THE AMERICAN SOCIETY OF MECHANICAL ENGINEERS. Manuscript received by the Fluids Engineering Division, February 11, 1980.

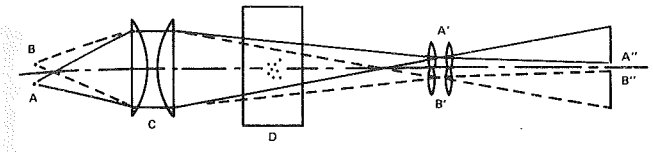


SKETCH OF ILLUMINATION SET-UP FOR DUAL-LENS CAMERA

A, B: ELECTRONIC FLASH UNITS
C: CONDENSER
D: END VIEW OF TANK WITH CAVITATING WATER JET
A', B': CAMERA LENS
A'', B'': FILM PLANE

**Fig. 1 Sketch of illumination set-up for dual-lens camera**

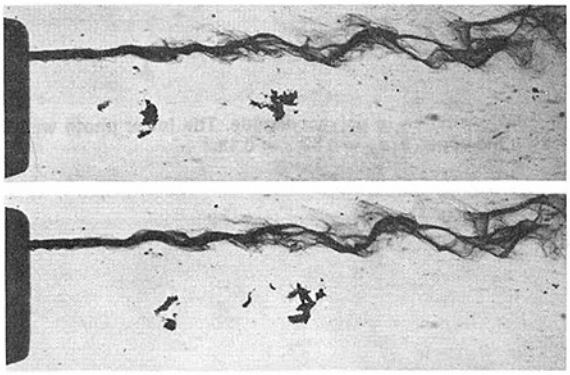

**Fig. 2 Jet cavitation in water (dye streak is in top boundary of the jet). The lower photo was taken 20$\mu$s after the upper. $\alpha/\alpha_s$ = 1.12: $\sigma$ = 0.22.**

van Slyke apparatus, while the polymer content of the samples was estimated with a turbulent-flow rheometer.

The apparatus received fluid from a large pressure tank. Water or polymer solution contained in the tank could be held under vacuum overnight, then re-pressurized, as described in [12], to provide a deaerating effect. The polymer solutions used were 25 ppm solutions of polyacrylamide, poly(ethylene oxide), and Carbopol. These were mixed in a separate tank and were gravity fed into the pressure tank to avoid possible degradation due to pumping. Sources of the polymers were: polyacrylamide, Calgon Corp; poly(ethylene oxide), Union Carbide, Inc, WSR-301; Carbopol 941, B. F. Goodrich Chemical Co.

The most critical part of the apparatus was the camera and lighting equipment, both of which were specially designed for this investigation. The camera used a rotating mirror to provide image-motion compensation of the predominantly axially-moving jet stream, and was fitted with dual lenses which provided two images, separated vertically, on the same film frame. The basic ideas involved in the dual-camera design are cited in [28].

The illumination method used is sketched in Figure 1 and is of the type termed Köhler illumination in microscopy or "trans-illumination" in high-contrast enlargers. As shown in Fig. 1, light from the point source (electronic flash) is imaged by the condensing lens at the diaphragm of the camera lens and thus on the film. The system is very efficient, i.e., there is no lost light and every point on the film sees all the point source and only that. Cavitation bubbles interfere with the light transmission by refracting and reflecting the light so that they appear black in the photos. Flashes from the two flash-heads shown in Fig. 1 can be separated in time, electronically, so that two images with a known time separation are produced on the same film frame. The illumination system is so free from diffused light that the camera body does not need a separator, and there is very little "ghosting" of one image on the other. The electronic flash units are operated at low power because of the high illumination efficiency; the image

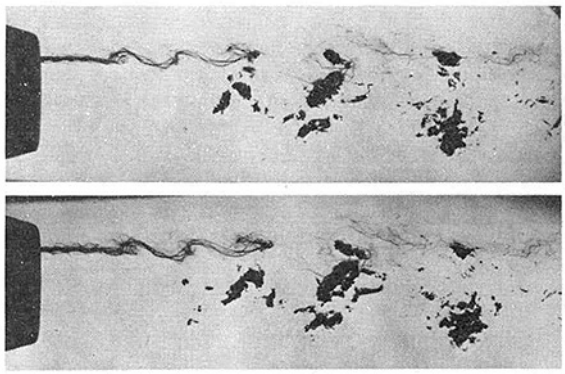

**Fig. 3 Jet cavitation in deaerated water. The lower photo was taken 10$\mu$ sec after the upper. $a/a_s$ = 0.65; $\sigma$ = 0.18.**

duration is thus on the order of 1 to 4$\mu$ s. Verichrome and Plus-X roll film of ASA rating 125 was used.

## Results

Figure 2 shows a typical scene of cavitation events in water having a high air content. The photographs are taken 20$\mu$ sec apart; the upper scene was taken first. Air bubbles in the surrounding water appear in the background; measurements indicate that the air content ratio $\alpha/\alpha_s$ is 1.12, where $\alpha$ is the measured air content of a sample of the water and $\alpha_s$ is the saturated air content for the water temperature according to the International Critical Tables. The cavitation index $\sigma$ is defined as:

$$\sigma = \frac{P - P_v}{\frac{1}{2}\rho v^2}$$

where $P$ = the local pressure around the jet (taken as atmospheric)

$P_v$ = vapor pressure of water at test temperature
$\rho$ = density of water
$v$ = computed jet velocity

For the conditions of Fig. 2, $\sigma$ is 0.22, i.e., well into the cavitation regime, according to the results of [12]. Due to the high air content of the water (above saturation) the cavitation shown here could be termed "gaseous" cavitation, or cavitation based on finite gas bubbles as nuclei. From the flow visualization standpoint, the camera has largely discriminated against the background bubbles, these appearing as dimly lighted streaky objects, while the illumination provides clear and sharp profiles of cavitation bubbles moving with the jet velocity. Note that the cavitation appears to be masses of smaller bubbles with rather sharp and irregular overall contours, and that significant changes in the bubbles have occured in the 20$\mu$ s interval between photographs.

Figure 3 shows cavitation in water having a relatively low air content, $\alpha/\alpha_s$ = 0.65, at a cavitation number of 0.18, with 10$\mu$ s between the photos. One would expect the cavitation to be of the "vaporous" type, i.e., based on infinitesimal discontinuities in the water rather than finite gas bubbles as in Fig. 2. However, the appearance of the cavitation bubble masses is quite similar to those shown earlier. Of special interest in Fig. 3 is the dye streak showing vortex formation at the jet boundary, with cavitation events centered at the regions where vortices are pairing together.

At a sufficiently low cavitation number, the dye streak is not needed to mark the jet boundary since the cavitation pattern provides a good visual indication of the extent of the jet flow. Figure 4 shows extensive cavitation outlining the jet boundaries at a cavitation number of 0.16, in low air-content

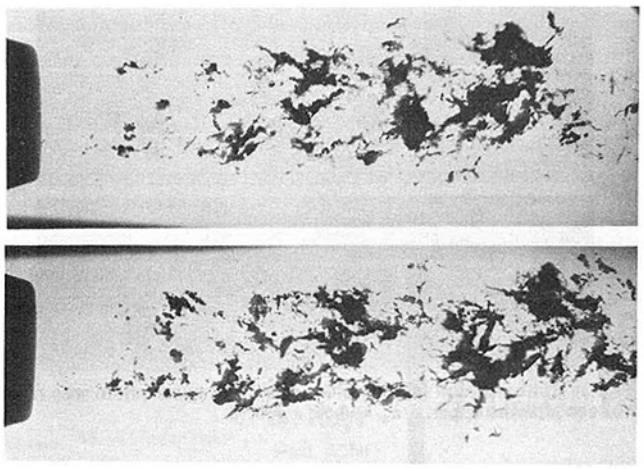

Fig. 4 Extensive cavitation in water jet. $\sigma$ of 0.16. Air content $a/a_s$ = 0.59. Lower photo taken 80$\mu$ sec after the upper.

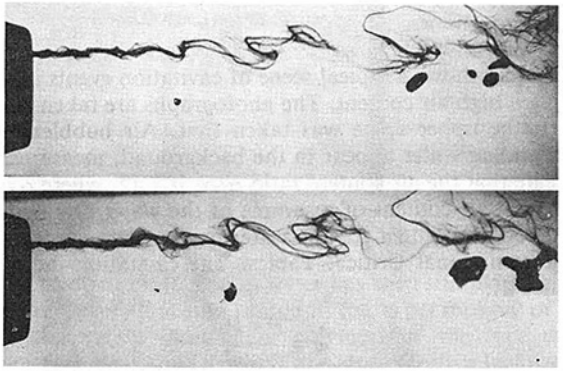

Fig. 5 Jet cavitation in 25 ppm polyacrylamide solution, with 80$\mu$ sec delay in lower photo. $a/a_s$ = 0.82; $\sigma$ = 0.14.

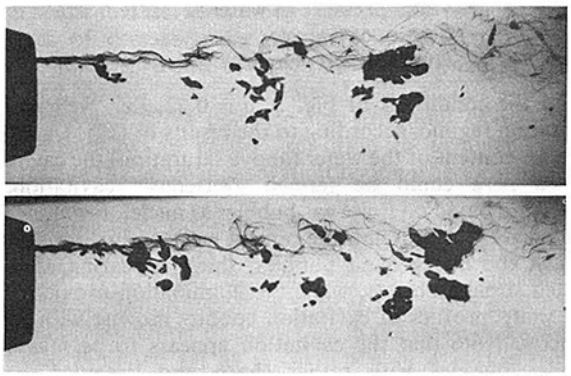

Fig. 6 Jet cavitation in 25 ppm polyacrylamide solution; delay of 80$\mu$ sec between photos. $a/a_s$ = 0.82; $\sigma$ = 0.13.

water, $\alpha/\alpha_s = 0.59$. The cavitation appears to intensify at intervals along the axis of the jet, possibly corresponding to regions of maximum shear at the jet boundary.

Figure 5 shows cavitation in 25 ppm polyacrylamide polymer solution, at air content $\alpha/\alpha_s$ of 0.82 and cavitation number of 0.14. Only sporadic cavitation can be seen at this cavitation number; a considerable inhibition of cavitation is thus evident in polymer solutions as noted in [12]. Of particular interest is the marked change in bubble shape in the polyacrylamide solution; the bubbles appear much larger and smoother than cavitation bubbles in pure water. The same comments apply for Fig. 6, taken at a still lower cavitation number, 0.13. In both Fig. 5 and Fig. 6 the scenes were taken 80$\mu$ sec apart, and considerable changes in bubble shape are

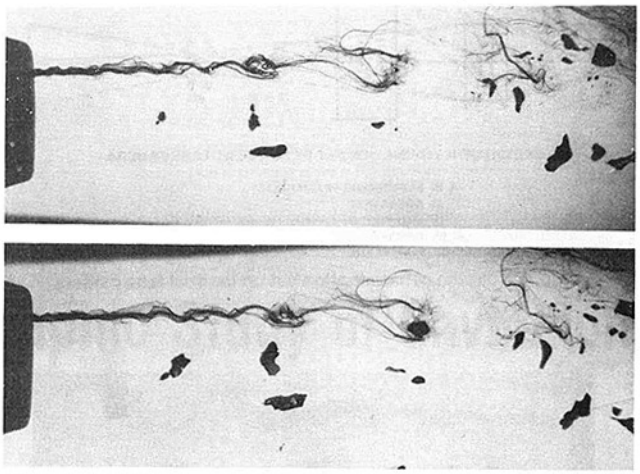

Fig. 7 Jet cavitation in polyacrylamide. The lower photo was taken 20$\mu$ s after the upper. $a/a_s$ = 0.82; $\sigma$ = 0.13.

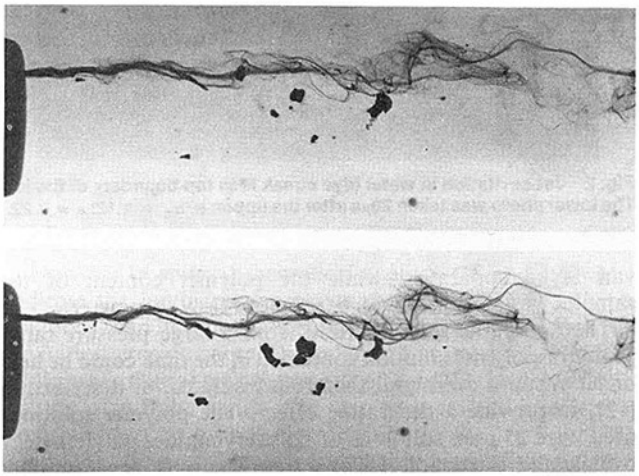

Fig. 8 Jet cavitation in 25 ppm poly(ethylene oxide). Time delay between photos, 28 $\mu$ s. $a/a_s$ = 1.00; $\sigma$ = 0.17.

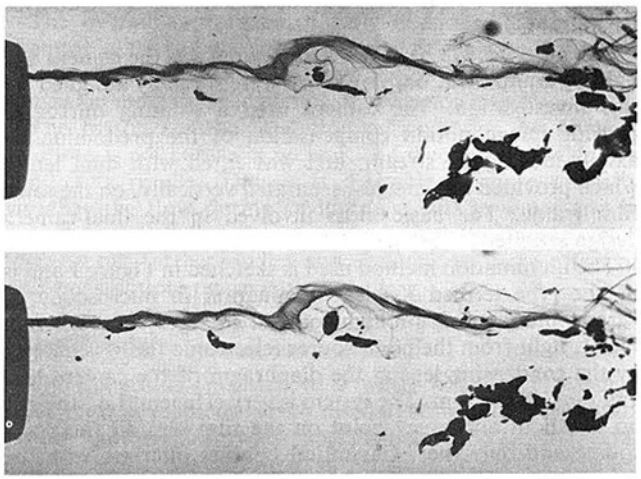

Fig. 9 Jet cavitation in 25 ppm poly(ethylene oxide). Time delay between photos, 28 $\mu$ s. $a/a_s$ = 1.00; $\sigma$ = 0.14

evident in this interval. Figure 7 was taken under the same conditions as Fig. 6, except the time interval between scenes has been reduced to 20$\mu$ s. Large changes in the individual bubble appearance occur within this time interval.

The effect of polymers on bubble size and shape is not

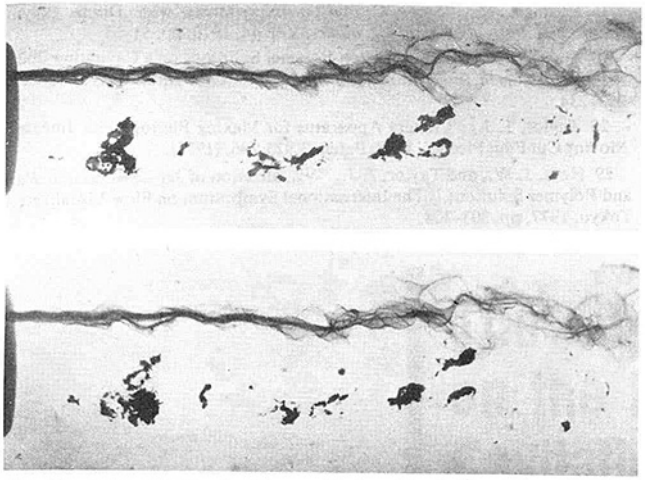

Fig. 10 Jet cavitation in 25 ppm Carbopol solution. Time delay between photographs, 42 $\mu$ s. $a/a_s = 1.02$; $\sigma = 0.21$.

limited to polyacrylamide. Figure 8 shows a 25 ppm poly(ethylene oxide) solution at a $\sigma$ of 0.17, with a delay of 28$\mu$ sec between the two scenes. The bubble size and shape is again distinctly different from the pure water case. The low cavitation number reflects the inhibition of cavitation by the poly(ethylene oxide), since for water at a similar cavitation number, cavitation would be profuse (Fig. 4). At a still lower cavitation number, 0.14, cavitation is more intense in the poly(ethylene oxide), but the characteristic and distinctive cavitation-bubble appearance (Fig. 9) is retained.

The non-drag-reducing polymer, Carbopol, does not change either inception or appearance of the cavitation bubbles compared with water. Figure 10 taken at a $\sigma$ of 0.21, resembles the water data in bubble appearance for a similar cavitation number.

## Discussion

The image-compensation features of the camera and the illumination technique provide a useful flow visualization tool for detailed study of cavitation events. The technique has been especially helpful in pointing out the significant changes in cavitation bubble appearance in drag-reducing polymer solutions as compared with their appearance in pure water [29].

The generally larger bubble size evident in drag-reducing polymer solution cavitation could offer a partial explanation of the higher radiated noise from cavitating polymer solutions [24 and 25] as well as increased erosion [20] compared with water, in that a larger volume is involved as the bubble collapses.

The photographs show that cavitation bubbles produced by both of the drag-reducing polymers (polyacrylamide and poly(ethylene oxide)) are similar in size and general appearance, whereas the nondrag-reducing polymer, Carbopol (carboxy polymethylene) produced cavitation bubbles similar in appearance to pure water. Hence it appears that the generally linear structure typical of drag-reducing polymers plays an important role in the cavitation process.

Cavitation inhibition on head forms due to the presence of polymer has been shown to be associated with earlier transition to turbulence on the head shape with consequent elimination of the laminar separation region where cavitation first occurs. In jet flows, cavitation occurs in low pressure regions associated with high shear, possibly in areas of vortex formation. No transition phenomena are thought to be involved. Thus the polymer molecules, or aggregates of molecules, are interacting with the cavitation bubbles themselves. The picture becomes even more puzzling when it is recalled that the polymer solutions have a lower static surface tension than pure water, which in itself would imply decreased cavitation resistance. A similar situation arises in acoustically induced cavitation where there is no appreciable flow involved, and again the polymer solutions tend to suppress cavitation.

Theoretical studies offer no hint as to larger cavitation bubble size in polymer solutions, and so these photographs may be useful as a basis for further analyses. The photographs confirm that cavitation inception is inhibited in polymer solutions.

Finally, the dual-photo technique shown here permits study of rapidly-occurring events in an inexpensive way, although it is apparent from the photographs that resolution of details of bubble growth and collapse require time scales much shorter than the 10-80$\mu$ intervals used in this work.

## Acknowledgment

This work was carried out at the Naval Ocean Systems Center under Office of Naval Research, U. S. Navy sponsorship.

## References

1 Ellis, A. T., Waugh, J. G., and Ting, R. Y., "Cavitation Suppression and Stress Effects in High-Speed Flows of Water with Dilute Macromolecular Additives," ASME *Journal of Basic Engineering,* Vol. 92, 1970, pp. 459-466.

2 van der Meulen, J. H. J., "Cavitation Suppression by Polymer Injection," *ASME Cavitation and Polyphase Flow Forum,* ASME, New York, 1973, pp. 48-50.

3 Arndt, R. E. A., Billet, M. L., Holl, J. W., and Baker, C. B. "A Note on the Inhibition of Cavitation in Dilute Polymer Solutions" *ASME Cavitation and Polyphase Flow Forum.* ASME New York, 1976, pp. 1-3.

4 Gates, E. M. "The Influences of Freestream Turbulence, Freestream Nuclei Populations, and a Drag-Reducing Polymer on Cavitation Inception on Two Axisymmetric Bodies," PhD. thesis, California Institute of Technology, 1977.

5 Ōba, R., Itō, Y. and Uranishi, K., "Effect of Polymer Additives on Cavitation Development and Noise in Water Flow Through an Orifice," ASME JOURNAL OF FLUIDS ENGINEERING, Vol. 100, 1978 pp. 493-499.

6 Sanders, J. V., Henderson, L. H., and White, R. J. "Effects of Polyethylene-Oxide Solutions on the Performance of a Small Propeller," *Journal of Hydronautics,* Vol. 6, 1973, pp. 124-128.

7 Darner, C. L., "Sonic Cavitation in Water," Naval Research Laboratory Underwater Sound Research Division Report 7131, 1970.

8 Hoyt, J. W. "Cavitation in Polymer Solutions and Fiber Suspensions," *ASME Cavitation and Polyphase Flow Forum,* ASME, New York, 1977, pp. 9-10.

9 Bazin, V. A., Barabanova, Ye.N., and Pokhil'ko, A. F., "Effect of Dilute Aqueous Polymeric Solutions on the Onset of Cavitation on a Cylinder," *Fluid Mechanics — Soviet Research,* Vol. 5, 1976, pp. 79-82.

10 Hoyt, J. W. "Vortex Cavitation in Polymer Solutions," *ASME Cavitation and Polyphase Flow Forum,* ASME New York, 1978, pp. 17-18.

11 Acosta, A. J., and Parkin, B. R., "Cavitation Inception — A Selective Review," *J. Ship Research,* Vol. 19, 1975, pp. 193-205.

12 Hoyt, J. W., "Effect of Polymer Additives on Jet Cavitation". ASME J. FLUIDS ENGINEERING, Vol. 98, 1976, pp. 106-112.

13 Baker, C. B., Holl, J. W. and Arndt, R. E. A. "Influence of Gas Content and Polyethylene Oxide Additive upon Confined Jet Cavitation in Water," *ASME Cavitation and Polyphase Flow Forum,* ASME, New York, 1976, pp. 6-8.

14 Ting, R. Y., "Effects of Viscoelasticity on Cavitation in Drag Reducing Fluids," *The Role of Cavitation in Mechanical Failures,* U.S. Bureau of Standards Special Publication 394, 1974, pp. 100-105.

15 Ting, R. Y., "Viscoelastic Effect of Polymers on Single Bubble Dynamics," *AIChE J.,* Vol. 21, 1975, pp. 810-814.

16 Ellis, A. T. and Ting, R. Y., "Non-Newtonian Effects on Flow-Generated Cavitation and on Cavitation in a Pressure Field," *Fluid Mechanics, Acoustics, and the Design of Turbomachinery.* NASA SP-304, 1974, pp. 403-421.

17 Ting, R. Y. and Ellis, A. T., "Bubble Growth in Dilute Polymer Solutions," *Physics of Fluids,* Vol. 17, 1974, pp. 1461-1462.

18 Folger, H. S. and Goddard, J. D., "Collapse of Spherical Cavities in Viscoelastic Fluids," *Physics of Fluids,* Vol. 13, 1970, pp. 1135-1141.

19 Shima, A., and Tsujino, Y., "The Behavior of Bubbles in Polymer Solutions," *Chemical Engineering Science,* Vol. 31, 1976, pp. 862-869.

20 Ashworth, V., and Proctor, R. P. M., "Cavitation Damage in Dilute Polymer Solutions," *Nature,* Vol. 258, 1975, pp. 64-66.

21 Shapoval, I. F., and Shal'nev, K. K. "Cavitation and Erosion in Aqueous Solutions of Polyacrylamide," *Soviet Physics — Doklady,* Vol. 22, 1977, pp. 635-637.

22 Kudin, A. M., Barenblatt, G. I., Kalashnikov, V.N., Vlasov, S. A., and Belokon, V. S., "Destruction of Metallic Obstacles by a Jet of Dilute Polymer Solution," *Nature Physical Science,* Vol. 245, 1973, pp. 95-96.

23 Ting, R. Y., "Polymer Effects on Microjet Impact and Cavitation Erosion," *Nature,* Vol. 262, 1976, pp. 572-573.

24 Hoyt, J. W., "Effect of Polymer Additives on Jet Cavitation," *Trans 16th American Towing Tank Conference,* Sao Paulo, Brazil, Vol. 1, 1971, pp. 7.0-7.18.

25 Walters, R. R., "Effect of High-Molecular Weight Polymer Additives on the Characteristics of Cavitation," Advanced Technology Center, Inc., Dallas, Texas, Report No. B-94300/2 TR-32, 1972.

26 Brennen, C., "Some Cavitation Experiments with Dilute Polymer Solutions," *Journal of Fluid Mechanics,* Vol. 44, 1970, pp. 51-63.

27 Hoyt, J. W., "Effect of High-Polymer Solutions on a Cavitating Body," *Proceedings, 11th International Towing Tank Conference,* Tokyo, 1966, pp. 233-234.

28 Taylor, J. J., "Camera Apparatus for Making Photographic Images on Moving Cut Film Pieces," U. S. Patent 3,925,796, (1975).

29 Hoyt, J. W., and Taylor, J. J., "Visualization of Jet Cavitation in Water and Polymer Solutions," The International Symposium on Flow Visualization, Tokyo, 1977, pp. 303-308.

# The Effect of Secondary Vorticity on the Inception of Vortex Cavitation

**M. L. Billet**
Research Associate,
Applied Research Laboratory,
The Pennsylvania State University,
State College, Pa. 16801

*Cavitation inception of a vortex is difficult to predict. This is due in a large part to a confusion in the type of cavitation occurring, i.e., vaporous versus nonvaporous cavitation. In addition, the vortex structure is poorly defined in many cases. These two problems are particularly important for the prediction of cavitation inception in a vortex created in the low momentum fluid near the inner wall of a rotor. The purpose of this paper is to present the results of a vortex cavitation investigation which are both experimental and theoretical. A vorticity flow analysis is developed and employed to assess the effect of vorticity on cavitation inception of a vortex. Previous investigations have shown that the minimum pressure coefficient of a vortex depends upon the vorticity associated with the vortex. Employing secondary vorticity equations, the vorticity is calculated in the blade passage. Changes in passage vorticity are used in a simple vortex model to predict trends in cavitation inception of a vortex. Theoretical results indicate that small changes in vorticity distribution near the inner wall of the rotor create rather large differences in the cavitation inception of the vortex. These small changes are primarily due to changes in the secondary vorticity. This secondary vorticity dominates the vortex structure. Comparisons are presented between the predicted and measured cavitation inception and good agreement is shown when the effects of gas on cavitation inception are reduced. Experimental data confirms that secondary vorticity dominates the vortex structure. In addition, experimental cavitation data are presented which show the dramatic influence of a gas on cavitation inception of a vortex.*

## Introduction

Vortex motions in a fluid have long been recognized as sources of low pressure regions where cavitation can occur. The prediction or scaling of cavitation inception for a particular vortex motion is a very difficult problem. Part of this difficulty is due to an insufficient understanding of the flow conditions which result in vortex formation. Additional difficulties are due to a confusion in the type of cavitation occurring, i.e., vaporous versus nonvaporous cavitation.

Vortex motions are produced by the rolling-up of vortex filaments. This process must be clearly understood in order to predict the subsequent behavior of the downstream vortex motion. The initial rolling-up sets the conditions for the long-term growth. While most vortex motions have similar swirl-velocity distributions, they have widely differing axial velocity profiles due mainly to differences in the rolling-up process.

The cavitation that can occur in a vortex motion is important for rotor cavitation performance. The critical cavitation numbers typical of vortex motions are often higher than those associated with any other type of cavitation that can occur on a rotor.

One type of vortex cavitation occurs near the tip of a rotor blade. An extensive amount of work has been done on this particular vortex motion. The structure of a tip vortex has been studied in the aeronautics field for many years. The vortex is formed by the rolling-up of the trailing vortex sheet near the blade tip. McCormick [1, 2] from tests conducted in a water tunnel showed that the minimum pressure coefficient ($C_{p_{min}}$) of a tip vortex depends on the boundary layer thickness on the pressure side of the blade and on the local life. In addition, cavitation inception data were correlated by calculation of the minimum pressure coefficient. McCormick showed for the hydrofoils tested that the cavitation number scales as Reynolds number to a power.

This dependence of cavitation inception—minimum pressure coefficient for a vortex motion on Reynolds number is not new. As an example, Kermeen and Parkin [3] and Arndt [4] have shown that the incipient cavitation number for the wake region of a sharp edged disk is strongly dependent on Reynolds number. An interesting characteristic of these cavitation data is the continual increase in cavitation number with increasing Reynolds number.

Another type of vortex motion is formed in the complicated

Contributed by the Fluids Engineering Division and presented at the International Symposium on Cavitation Inception, Winter Annual Meeting, New York, N.Y., December 5-10, of THE AMERICAN SOCIETY OF MECHANICAL ENGINEERS. Manuscript received by the Fluids Engineering Division, February 11, 1980.

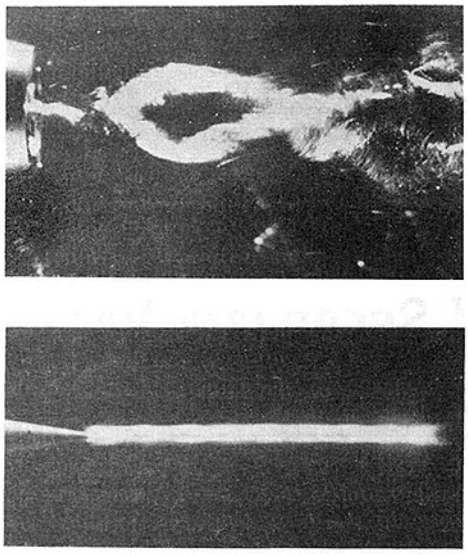

Fig. 1 Vortex cavitation

flow along the inner wall of a rotor. Available experimental data show that cavitation inception for this vortex is also dependent upon Reynolds number. In addition, cavitation inception is dependent on the vorticity in the blade passage.

All rotors operating within a boundary layer have vortex formation along the inner wall. The appearance of this cavitating vortex varies from rotor to rotor, as seen in Fig. 1. Cavitation inception can vary as much as an order of magnitude for small variations in the inlet velocity gradient near the inner wall.

This present investigation was initiated following the analysis of much experimental data on the vortex formed along the inner wall of a rotor. Results indicate that cavitation inception is strongly dependent upon inlet velocity gradient. The objective of this study is to investigate analytically the flow field near the wall and to develop a model which will correlate cavitation inception of the resulting vortex motion.

## Vorticity of the Vortex Motion

It is appropriate to find a simple description of the vortex motion in order to calculate its minimum pressure coefficient. Unfortunately, vortices are composed of a finite number of vortex filaments which induce a swirl velocity and a difficulty arises in specifying this number. In the inner wall region, viscous effects can cause flow separation which will significantly alter the flow field and make any calculation of the vorticity difficult.

The net vorticity in the downstream vortex motion is a combination of the shed vorticity from the blade row and the vorticity in the blade passage. However, some preliminary flow visualization studies showed that the blade passage vorticity controls the early vortex formation. A significant migration of fluid was observed from the pressure surface of one blade to the suction surface of the adjacent blade near the inner wall region. In some cases, there was a rolling-up process in the blade passage. These results were obtained for the case of a thick boundary layer entering a lightly loaded rotor. The rotor was also designed to be unloaded near the blade root.

The blade passage vorticity is due to blade to blade pressure gradients and turning of the flow with entering vorticity and can be calculated from a set of vorticity transport equations. These vorticity transport equations are normally applied along a streamline.

Using the generalized vorticity equations, Lakshminarayana and Horlock [5] derived a set of incompressible vorticity equations valid for a rotor operating with an incoming velocity gradient. The equations were developed along a relative streamline. The resultant equations for incompressible flow are:

## Nomenclature

$a_{b'}$ = distance between neighboring streamlines in $b'$ direction
$b'$ = binormal direction of relative streamline ($\mathbf{b}' = \mathbf{s}' \times \mathbf{n}'$)
$C_p$ = pressure coefficient $\left(C_p = \dfrac{P - P_\infty}{\frac{1}{2}\rho V_\infty^2}\right)$
$C_{p_{\min}}$ = minimum pressure coefficient $\left(C_{p_{\min}} = \dfrac{P_{\min} - P_\infty}{\frac{1}{2}\rho V_\infty^2}\right)$
$L_c$ = vortex core parameter
$n'$ = principle normal direction of relative streamline defined as positive toward center of curvature of the streamline
$P$ = pressure
$P_G$ = gas pressure
$P_{\min}$ = minimum pressure
$P_v$ = vapor pressure
$P_\infty$ = pressure of infinity
$r$ = radius
$r_c$ = vortex core radius
$R_i$ = radius of rotor inner wall
$R_R$ = radius of rotor
$R'$ = radius of curvature of relative streamline
$s'$ = relative streamwise direction (relative flow direction)
$V_\theta$ = tangential velocity
$V_\infty$ = velocity at infinity
$W$ = relative velocity
$\alpha$ = dissolved gas content
$\beta$ = Henry's law constant
$\beta_1$ = flow inlet angle
$\beta_2{}^*$ = flow outlet angle
$\beta_2$ = blade outlet angle
$\Gamma$ = circulation
$\xi$ = relative vorticity
$\nu$ = kinematic viscosity of fluid
$\rho$ = density of fluid
$\sigma$ = cavitation number $\left(\sigma = \dfrac{P_\infty - P_v}{\frac{1}{2}\rho V_\infty^2}\right)$
$\sigma_d$ = desinent cavitation number
$\tau$ = radius of torsion of relative streamline
$\omega_{b'}$ = component of absolute vorticity vector in relative binormal direction
$\omega_{n'}$ = component of absolute vorticity vector in relative normal direction
$\omega_{s'}$ = component of absolute vorticity vector in relative streamwise direction

$$\frac{\partial}{\partial s'}\left(\frac{\omega_{s'}}{W}\right)=\frac{2\omega_{n'}}{WR'}+\frac{2\Omega_{b'}\omega_{n'}}{W^2}$$

$$-\frac{2\Omega_{n'}\omega_{b'}}{W^2}+(\mu/\rho)\mathbf{s}'\cdot\frac{\nabla'^2\xi}{W^2} \quad (1)$$

and

$$\frac{\partial}{\partial n'}[\omega_{n'}W]=\frac{W\omega_{b'}}{\tau}-\frac{W\omega_{n'}}{a_{b'}}\frac{\partial a_{b'}}{\partial s'}+(\mu/\rho)\mathbf{n}'\cdot\nabla'^2\xi, \quad (2)$$

where $s'$, $n'$, $b'$ represent the natural coordinates for the relative flow, $W$ is the relative velocity, $\omega_{s'}$ and $\omega_{n'}$ are absolute vorticity resolved along the relative streamline direction ($\mathbf{s}'$) and the principal normal direction ($\mathbf{n}'$), $\Omega$ is the rotation vector, and $R'$ is the radius of curvature of the relative streamline. In this relative coordinate system indicated by the primes, the streamwise direction ($\mathbf{s}'$) is defined along the flow direction, the principal normal direction ($\mathbf{n}'$) is defined toward the center of curvature of the streamlines, and the bi-normal direction ($\mathbf{b}'$) is defined as $\mathbf{s}' \times \mathbf{n}' = \mathbf{b}'$. Additional definitions are given in the nomenclature and information about flow in the relative coordinate system is given in reference [5].

The equations for secondary vorticity created in the passage, namely, Equations (1) and (2), are extremely difficult to apply because they are nonlinear partial differential equations. Therefore, some simplifying assumptions and specifications of the flow field must be made for any application. The basic flow parameters for this vortex motion are a thick boundary layer entering the rotor and the rotor operating at a flow coefficient less than 0.4.

In order to evaluate the relative importance of the terms that describe the passage vorticity, the vorticity equations were first nondimensionalized. Then an order of magnitude evaluation was applied. The details of this process are given in References [6] and [7].

The resulting normal relative vorticity equation is

$$\frac{\partial}{\partial s'}(\omega_{n'}W)=-\frac{W\omega_{n'}}{a_{b'}}\cdot\frac{\partial a_{b'}}{\partial s'} \quad (3)$$

and the resulting streamwise vorticity equation is

$$\frac{\partial}{\partial s'}\left(\frac{\omega_{s'}}{W}\right)=\frac{2\omega_{n'}}{WR'}+\frac{2\Omega_{b'}\omega_{n'}}{W^2}-\frac{2\Omega_{n'}\omega_{b'}}{W^2}. \quad (4)$$

This simplified normal vorticity equation shows a dependence of the relative component of the normal vorticity on the variation of relative velocity ($W$) along a relative streamline, on the relative component of the absolute inlet normal vorticity ($\omega_{n'}$), and on the flow convergence-divergence in the bi-normal direction ($a_{b'}$). The streamline vorticity equation shows a dependence on the rotor rotation vector ($\Omega$) and on the radius of curvature of the relative streamline ($R'$).

Equations (3) and (4) can be integrated along a relative streamwise direction. The results are

$$\omega_{n'}=\omega_{n'_1}\cdot\frac{W_1 a_{b'_1}}{W a_{b'}} \quad (5)$$

for the normal component and

$$\omega_{s'_2}=W_2\int_1^2\frac{2\omega_{n'}}{WR'}ds'+W_2\int_1^2\frac{2\Omega_{b'}\omega_{n'}}{W^2}ds'$$

$$-W_2\int_1^2\frac{2\Omega_{n'}\omega_{b'}}{W^2}ds'+\omega_{s'}\cdot\frac{W_2}{W_1} \quad (6)$$

for the streamwise component.

The means of which the streamwise component of vorticity is produced in this relative flow are similar to those discussed by many investigators [8, 9] for a stationary vane system. However, it is important to note that additional secondary vorticity is generated when $\Omega \times \mathbf{W}$ has a component in the relative streamwise direction. Rotation has no effect when the absolute vorticity vector lies in the $s'$-$n'$ plane and the rotation ($\Omega$) has no component in the bi-normal direction ($\mathbf{b}'$).

These equations can be used to calculate the vorticity along a relative streamline due to blade to blade effects. All of the quantities in the equations can be determined from the calculation of the mean streamlines. The initial normal component of absolute vorticity ($\omega_{n_1}$) for a streamline can be obtained from the incoming axial velocity profile to the rotor. Application of the vorticity equations depends on the flow procedure used to calculate the streamlines.

The streamlines can be found by using several calculation procedures. In this development, the streamline curvature method of analysis was applied. The fluid is assumed to be incompressible, inviscid, and steady. Because the flow field is axisymmetric, it is necessary to use only two components of velocity, namely, meridional velocity ($V_m$) and tangential velocity ($V_\theta$).

It is important to note that the calculation of the streamlines implies a solution of the direct turbomachinery problem and not the indirect or design turbomachinery problem. For the direct problem, a rotor configuration is specified and the performance for any given initial condition is to be calculated. Thus, the flow outlet angles are specified instead of the tangential velocity ($V_\theta$).

The use of the streamline curvature equations for the calculations of the streamlines allows for vorticity in the flow field. However, it is important to realize that the solution to the flow field does not contain all of the vorticity. In particular, only the circumferential vorticity is totally included. The other components of vorticity contain derivatives with respect to the circumferential direction which are assumed to be zero with an axisymmetric flow analysis. As discussed by Hawthorne and Novak [10], the neglected vorticity terms can be related to the secondary flows that occur in the blade passage.

The secondary flows in this calculation scheme are simply the exit streamwise vorticity minus the inlet streamwise vorticity ($\omega_{s'_2}$-$\omega_{s'_1}$). The effect of this secondary vorticity is to induce secondary velocities which are assumed to occur at the exit plane of the rotor. It is important to note that the normal component of vorticity ($\omega_{n'_2}$) is accounted for in the axisymmetric flow analysis. Thus, only streamwise secondary vorticity calculated as a function of radius influences the flow field.

The circulation of the vortex motion located near the wall region can be related to the blade passage vorticity in this region as

$$\Gamma=2\pi\int_0^{L_c}\omega r dr \quad (7)$$

where $\omega$ is now the blade passage vorticity in the direction of the axis of the resulting vortex motion and $L_c$ is some characteristic dimension of the vortex motion. The minimum pressure is then proportional to the square of the circulation divided by the characteristic dimension and reference velocity. This is

$$C_{p_{\min}}\sim\left(\frac{\Gamma}{L_c V_\infty}\right)^2. \quad (8)$$

For the case of a Rankine combined vortex model, namely, a simple rotational core combined with an irrotational outer flow, the pressure in the vortex can be calculated. For this case, the vortex is axisymmetric with an infinite radius of curvature in the meridional plane and a small gradient of

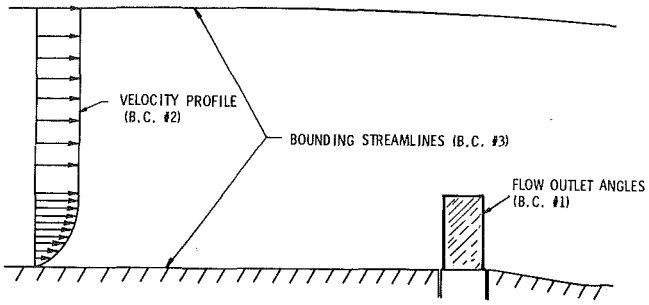


Fig. 2 Schematic of boundary conditions

meridional velocity. The result is

$$C_{p_{\min}} = -2\left(\frac{\Gamma}{2\pi r_c V_\infty}\right)^2. \tag{9}$$

where $\Gamma$ is the circulation of the vortex and $r_c$ is the core radius.

## Application of Theory

The blade passage vorticity was calculated for several basic flow configurations. Each variation in inlet velocity gradient to the rotor at a constant Reynolds number was basic flow configuration. Changes in the inlet velocity gradient were made by adding screens and struts to the body upstream of the rotor. Four of the basic flow configurations are:

Basic Flow No. 1: without upstream struts, without upstream screen, design flow coefficient,
Basic Flow No. 2: without upstream struts, without upstream screen, 0.9 design flow coefficient,
Basic Flow No. 3: without upstream struts, with upstream screen, design flow coefficient,
Basic Flow No. 4: with upstream struts, without upstream screen, design flow coefficient.

These flow configurations were chosen because a series of experiments were conducted in which not only cavitation data were available but also flow field measurements.

Before the passage vorticity could be calculated, the streamlines had to be calculated for each basic flow. This involved a solution of the direct turbomachinery problem using the streamline curvature method. The flow field is assumed to be axisymmetric, inviscid and incompressible. The solution is an iterative one; however, a brief outline will be given.

The streamlines were obtained by using an iterative procedure. The boundary conditions are: (1) the flow outlet angles, (2) the velocity profile far upstream of the rotor plane, and (3) the bounding streamlines of the flow field. The flow outlet angles are obtained from the blade angles of the rotor and a deviation angle. A schematic of the boundary conditions is shown in Fig. 2.

This last boundary condition is the most difficult to define. The open rotor is unique because of the uncertainty of the bounding stream surface of the flow field. The flow field lacks a well-defined boundary, such as the walls of a turbine or compressor. For this reason, the flow field for the open rotor is considered to be a region constrained within a potential flow stream tube. The bounding stream surface of this stream tube is actually located infinitely far from the rotor; however, it is assumed that there is a finite distance beyond which the flow field is relatively unaffected by the presence of the rotor. This distance is assumed to be at less than eight times the rotor radius. This stream surface located by this distance will serve as a flow boundary. In this manner,

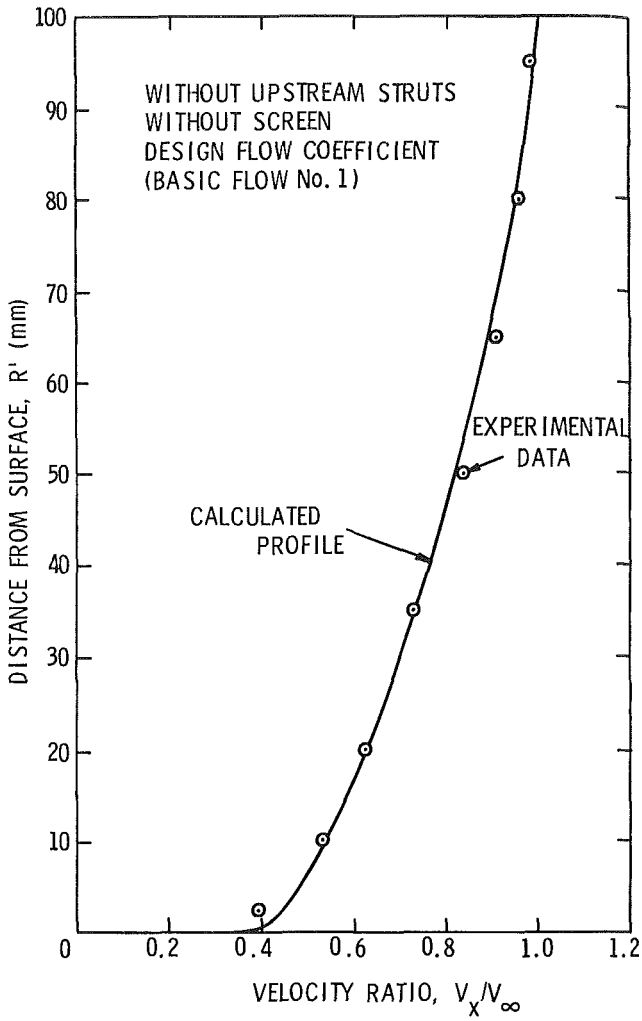


Fig. 3 Rotor inlet velocity comparison for Basic Flow No. 1

the bounding stream tube becomes analogous to the compressor and turbine walls.

The initial conditions (Step 1) to the solution of the direct problem for the streamlines are (1) bounding stream tube and (2) velocity profile in rotor plane without rotor. With this information, the initial streamlines without rotor can be calculated (Step 2). The result of this calculation is the boundary condition of an initial velocity-energy profile at a station far upstream of the rotor plane.

Knowing the blade angles, the first estimate of the flow outlet angles (Step 3) can be calculated. These flow outlet angles depend on the blade angles ($\beta_2$) and deviation angle ($\delta$). The deviation angle correlation developed by Howell [11] is initially applied. This relationship considers only thin blade sections and assumes that each blade section operates near design incidence. As shown in Figure 2, all of the boundary conditions are now known and the flow field can be solved with the rotor included (Step 4).

Once a convergent solution is obtained for the flow field using Howell's deviation rule (Step 4), the axial velocity distributions are known whereby the inlet angles can be estimated in addition to the acceleration through the rotor. Now a second estimate of the flow outlet angles (Step 5) can be made. For this deviation angle, the effects of acceleration ($\Delta\delta'$), blade camber ($\delta_0$), and blade thickness ($\Delta\delta^*$) are calculated separately. For the calculation of the deviation term due to axial acceleration through the rotor, an equation developed by Lakshminarayana [12] is applied. For the

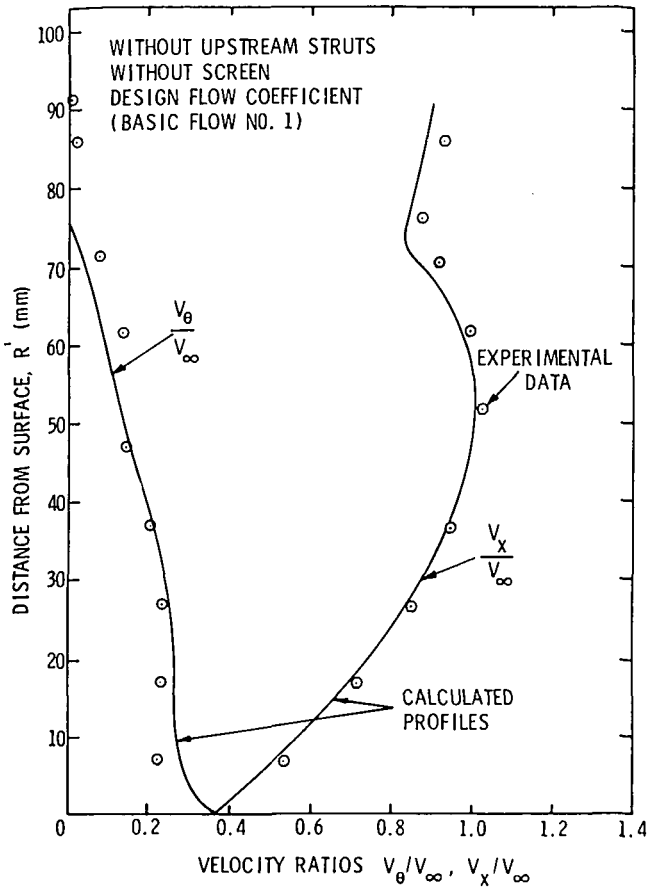


Fig. 4 Rotor outlet velocity comparison for Basic Flow No. 1

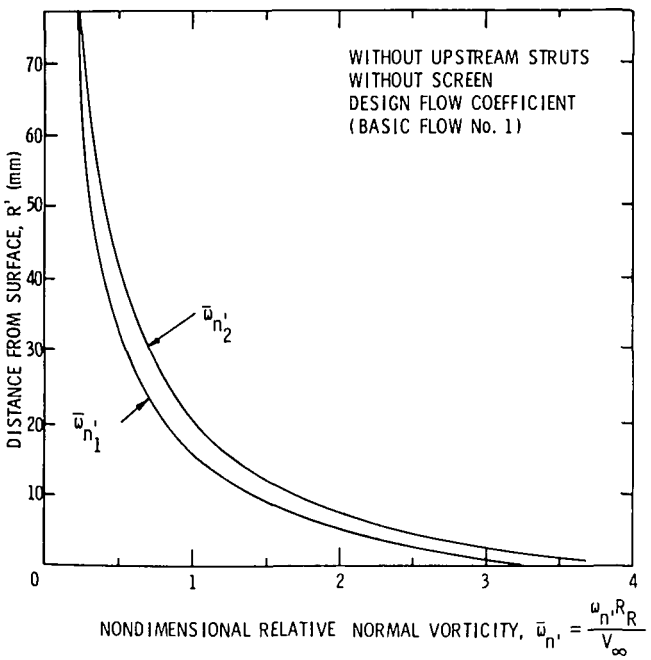


Fig. 5 Relative normal component of absolute vorticity for Basic Flow No. 1

calculation of deviation terms due to camber and thickness effects, the data collected by Lieblein [13] are used. The result is an improved outlet flow angle profile which can be used to again calculate the flow field (Step 6).

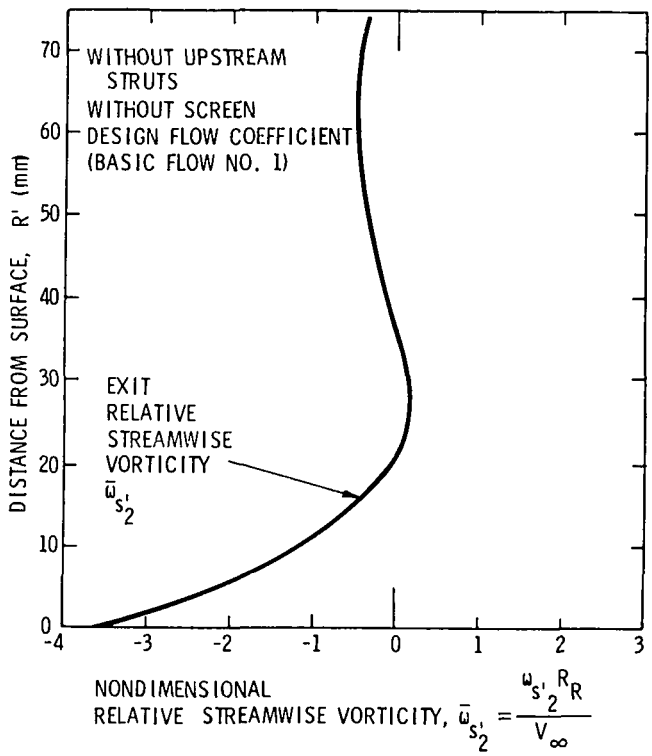


Fig. 6 Relative streamwise component of absolute vorticity for Basic Flow No. 1

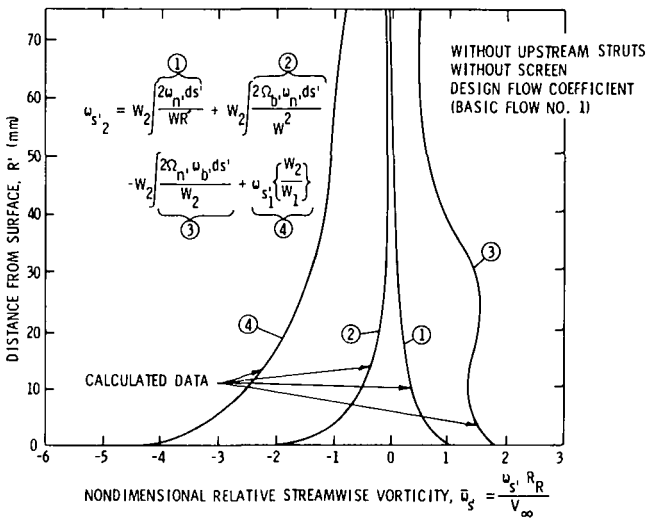


Fig. 7 Terms of the relative streamwise component of absolute vorticity for Basic Flow No. 1

The convergent solution of the flow field (Step 6) gives an estimate of the streamlines. As an example, Fig. 3 and 4 show the calculated flow field and measured data for Basic Flow No. 1.

Equations (5) and (6) were applied along a streamline. The results for the relative component of the normal vorticity ($\omega_{n'}$) are given in Fig. 5. The exit normal vorticity ($\omega_{n'_2}$) is not very different from the inlet normal vorticity ($\omega_{n'_1}$).

The normal vorticity calculations were used in Equation (6) for the calculation of the relative streamwise vorticity. The results for Basic Flow No. 1 are shown in Fig. 6. The exit relative streamwise vorticity ($\omega_{s'_2}$) is very different from the inlet relative streamwise vorticity ($\omega_{s'_1}$).

**Table 1 Vortex circulation and core size calculated flow vorticity data**

| Basic flows | Circulation $\Gamma$ ($cm^2/s$) | Characteristic length $L_c$(cm) | Nondimensional ratio ($\Gamma/L_c V_\infty$) |
|---|---|---|---|
| Basic Flow No. 1 without upstream struts without screen design flow coefficient | −75.10 | 2.06 | −0.080 |
| Basic Flow No. 2 without upstream struts without screen 0.9 design flow coefficient | −53.10 | 1.45 | −0.091 |
| Basic Flow No. 3 without upstream struts with screen design flow coefficient | −70.90 | 2.11 | −0.076 |
| Basic Flow No. 4 with upstream struts without screen design coefficient | −53.48 | 1.14 | −0.102 |

The terms of Equation (6) are shown in Fig. 7. The first term is simply the turning of a normal component of vorticity and is small when compared to the other terms. The second term is also small and is the curvature induced vorticity. The third term is large and is due to rotation-induced vorticity. This result can be anticipated because the rotor operates at a low flow coefficient and hence $\Omega_n{}'$ is large. The last term is simply the stretching of the vorticity by the flow and is large because of the high stagger angles at which the rotor operates.

The secondary passage vorticity is the difference between the inlet and outlet vorticities. The normal secondary vorticity ($\omega_n{}'_2 - \omega_n{}'_1$) is very small and can be neglected. This result has been shown by many secondary flow investigations. The streamwise secondary vorticity is large and positive. This positive vorticity causes an overturning of the flow near the inner wall of this rotor. The vorticity is concentrated near the inner wall which will cause large deviations in the flow angles.

The most interesting result from the calculation of the passage streamwise vorticity is the shape of the exit vorticity curve ($\omega_s{}'_2$). There is a large amount of negative vorticity near the inner wall and very little vorticity in the mid-radius region of the rotor.

A measure of the circulation associated with this passage vorticity was found by integrating the vorticity from the inner wall to the radius where the vorticity changes sign. The equation is

$$\Gamma = 2\pi \int_{R_i}^{R_i + L_c} \omega_s{}'_2 \cos\beta_2{}^* r dr, \tag{10}$$

where r $\cos\beta_2{}^*$ is normal to the vorticity. The calculated circulation is per blade passage.

The vortex parameters for the four basic flow configurations are given in Table 1. Also, the nondimensional ratio ($\Gamma/L_c V_\infty$), which is a measure of the minimum pressure coefficient of a vortex, is given in Table 1.

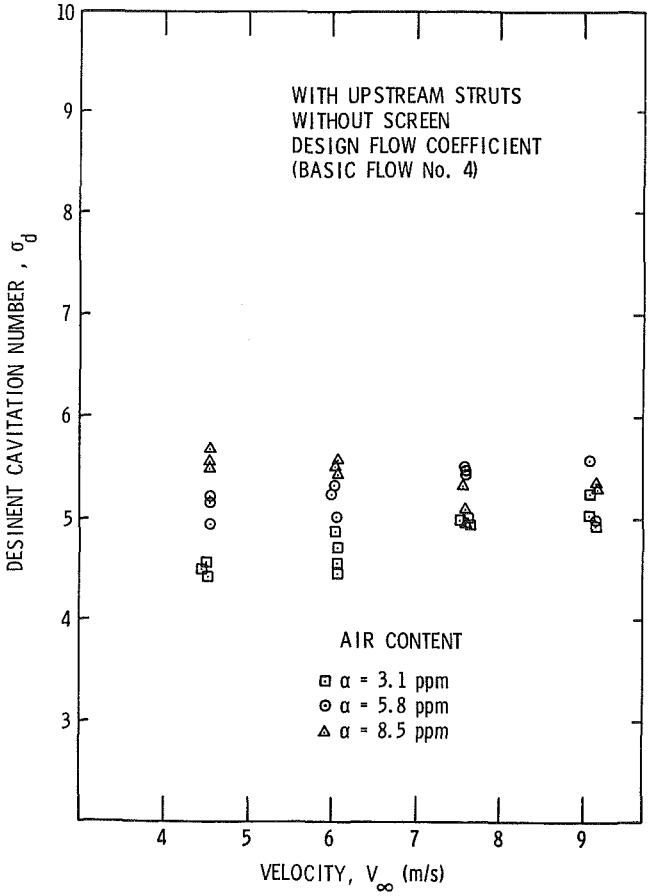


**Fig. 8 Cavitation data - effect of air content (Basic Flow No. 4)**

## Vortex Cavitation Data

An experimental program was conducted in the 1.22 m diameter water tunnel located in the Garfield Thomas Water Tunnel Building of the Applied Research Labortory at The Pennsylvania State University. In this program, cavitation data of the vortex flow were obtained for several basic flow configurations. Flow field measurements near the rotor plane were also made using a LDV system.

In order to maximize the scale of the inlet velocity gradient for measurement, the rotor was located near the end of a large surface. This surface had an unfavorable pressure gradient in front of the rotor plane. Thus, the inlet velocity gradient to the rotor was due in a large part to the boundary layer on a surface. Adding a screen to the surface increased the thickness of the boundary layer entering the rotor. The upstream struts consisted of four struts placed at the 0, 90, 180, and 270 deg points on the surface which made the inlet velocity profile nonaxisymmetric.

Desinent cavitation data were obtained for different inlet velocity profiles to the rotor, i.e., for the various basic flows. In all cases, cavitation in the vortex flow occurred on the end of the cap located downstream of the rotor. The occurrence of the cavitation was sporadic.

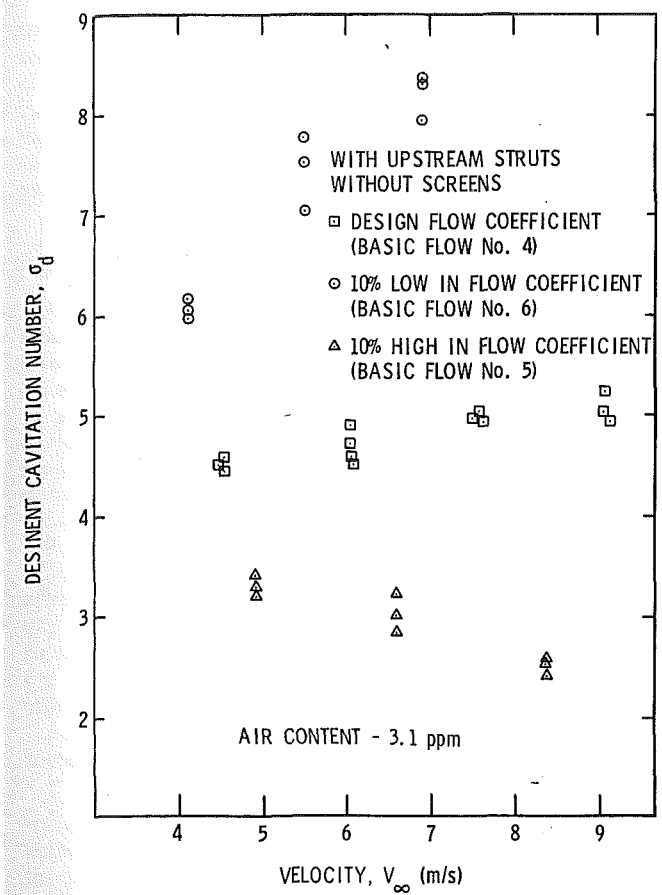


Fig. 9 Cavitation data - effect of flow coefficient (Basic Flow Nos. 4, 5, and 6)

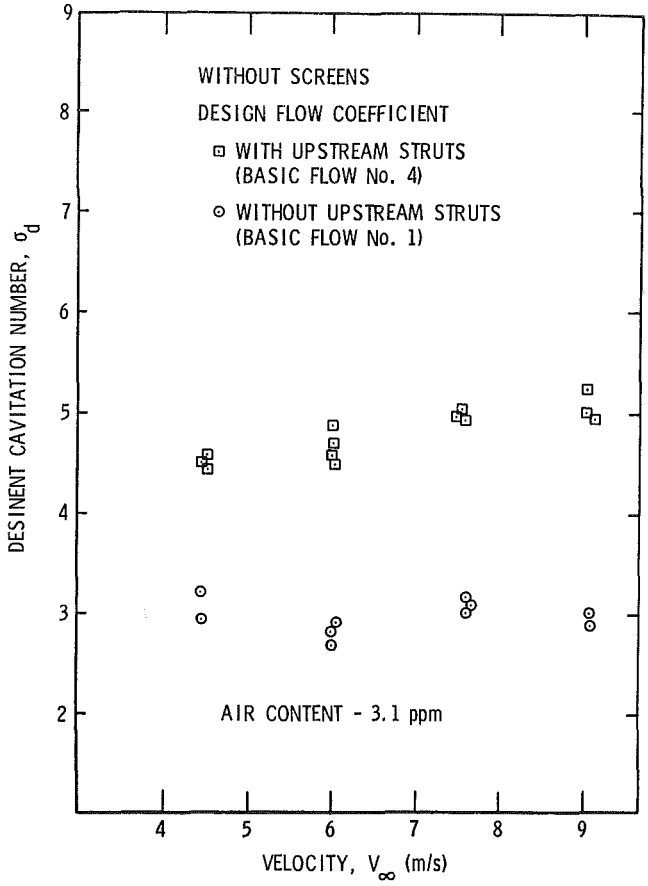


Fig. 10 Cavitation data - effect of struts (Basic Flow Nos. 1 and 4)

The air content was approximately 3.1 ppm for all of the experiments except for one which had a range of air contents. The air content of 3.1 ppm was chosen because gas effects are reduced and the relative saturation level was always much less than unity. The abbreviation ppm denotes moles of air per million moles of water. A more detailed description of the cavitation experiments is given in Reference 14.

Some of the desinent cavitation data are shown in Figs. 8, 9, and 10. The effects of the following factors are displayed: Fig. 8—the effect of air content, Fig. 9—the effect of flow coefficient, and Fig. 10—the effect of upstream struts.

In general, an increase in gas content, the addition of upstream struts, or a 10 percent decrease in flow coefficient causes the cavitation number to increase for a constant Reynolds number. In contrast to these results, the addition of an upstream screen or a 10 percent increase in flow coefficient causes the cavitation number to decrease for a constant Reynolds number.

Figure 8 shows the effect of air content on vortex cavitation and demonstrates the confusion in the type of cavitation of occurring in a vortex flow. By changing the air content level of the water, almost any cavitation number can be obtained. More important is the influence of air content on the change in cavitation number with velocity. At high values of air content, the cavitation number decreases with increasing velocity. At low values of air content, the cavitation number increases with increasing velocity. These trends are in agreement with an equilibrium theory which correlates gas pressure in a bubble with the cavitation number.

In 1960, Holl [15] employing an equilibrium theory which ignored surface tension effects predicted for nonvarporous cavitation that

$$\sigma = -C_p + \frac{P_G}{\frac{1}{2}\rho V_\infty^2}, \tag{11}$$

where $C_p$ is a characteristic pressure coefficient and $P_G$ is a pressure typical of the noncondensable gas in the bubbles. Holl indicated that there was an upper limit to the gas pressure, namely, the equilibrium value given by Henry' law which may be expressed in the form

$$P_{G_{\max}} = \alpha\,\beta, \tag{12}$$

where $\alpha$ is the dissolved gas content and $\beta$ is the Henry's law constant.

Several general implications come from Equation (11). First, the equation predicts that $\sigma$ is a monotonically decreasing function of velocity for constant values of $P_G$ and $C_p$. Second, the equation predicts excessively large values of $\sigma$ at low velocities. These results suggest that if one is to avoid confusing nonvaporous for vaporous cavitation, it is advisable to conduct tests at high velocities and low air content levels. In summary, for many cases of vortex cavitation it is very likely that the cavitation is nonvaporous and its scaling is further complicated.

## Discussion of Results

The vorticity calculated in the blade passage eventually organizes the low momentum fluid near the inner wall into the final vortex flow. This vorticity does dominate the flow field near the inner wall when a rotor is designed to be unloaded in this region as shown by the calculations. In this case, changes in this vorticity will directly influence the resulting minimum pressure of the vortex flow. Therefore, Equation (8) can be written as

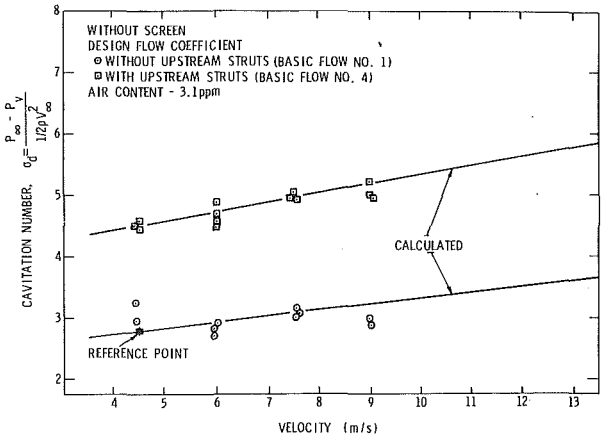


**Fig. 11 Correlation with cavitation data for Basic Flow Nos. 1 and 4**

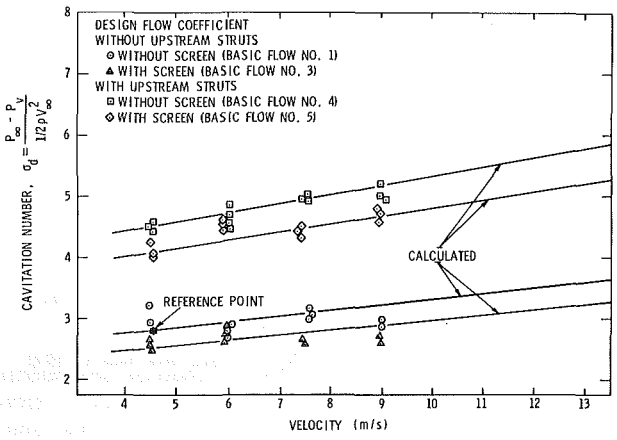


**Fig. 12 Correlation with cavitation data for Basic Flow Nos. 1, 3, 4, and 5**

$$\frac{C_{p_{\min_A}}}{C_{p_{\min_B}}} = \frac{\left(\frac{\Gamma}{L_c V_\infty}\right)_A^2}{\left(\frac{\Gamma}{L_c V_\infty}\right)_B^2} \tag{13}$$

where $\Gamma$ and $L_c$ are the characteristic vortex parameters of the passage streamwise vorticity. The letters $A$ and $B$ refer to different flow states.

In order to relate the $C_{p_{\min}}$ of the vortex flow to the cavitation number, several criteria must apply. First of all, the cavitation data must be free of gas effects as discussed previously. This is to insure that

$$\sigma_d \simeq -C_{p_{\min}} \tag{14}$$

Secondly, the minimum pressure in the final vortex flow must be controlled by the streamwise vorticity associated with the vortex. In addition, variations in inlet velocity gradient must be small enough so as to avoid influencing the mean rotor loading. All of these criteria seem very restrictive; however, most rotors operating within a velocity gradient meet these performance requirements.

A correlation between calculated minimum pressure coefficients and cavitation data can now be made using Equation (13) given a reference point and calculating the effect of Reynolds number on the passage vorticity. A reference point for Basic Flow No. 1 of $\sigma = 2.8$ at a velocity of 4.6 m/sec was chosen. The influence of Reynolds number

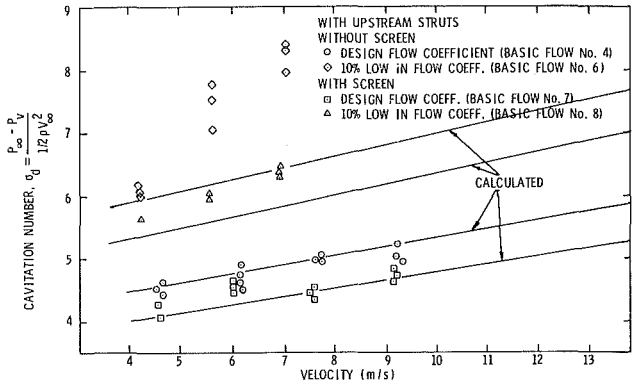


**Fig. 13 Correlation with cavitation data for Basic Flow Nos. 4, 6, 7, and 8**

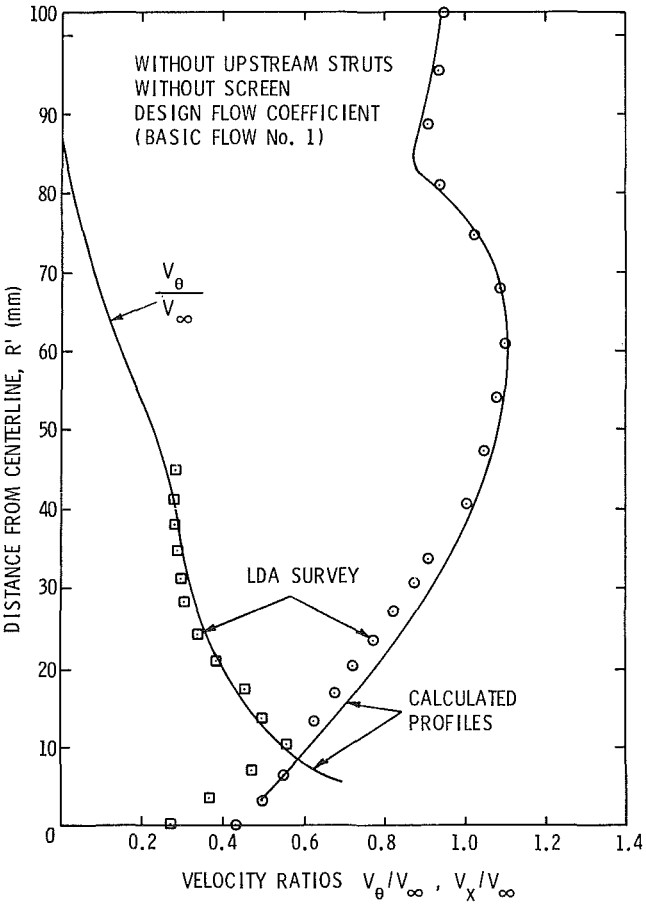


**Fig. 14 Rotor cap velocity comparison including axial velocity variation for Basic Flow No. 1**

on the passage vorticity was calculated by adding another Basic Flow No. 1 at a different reference velocity or Reynolds number.

Now using Equation (13) with a reference point for Basic Flow No. 1, comparisons between cavitation data and a calculated $C_{p_{\min}}$ were made. Some of the correlations are shown in Figs. 11, 12, and 13. Good agreement between theory and measurement was found except for the effect of off-design flow coefficient. Secondary flow theory alone cannot account for this trend. Therefore, these trends must include some additional primary flow effects.

Figure 14 shows a comparison of the velocities measured with the calculated flow field for Basic Flow No. 1 at the end of the rotor cap. This calculated flow field includes the effects

of the additional vorticity generated in the blade passage. The tangential velocity profiles are in very good agreement outside of the vortex core. The structure of the vortex is close to the classical Rankine model. It is important to note that the measured tangential velocity profile did not approach zero on the axis due to measuring difficulties. Finally, the calculated axial velocity profile correlates well with measured data.

## Summary and Conclusions

The critical cavitation number of a vortex flow formed along the inner wall of a rotor operating within a boundary layer has been correlated with the streamwise vorticity calculated in the blade passage. A set of equations were used to calculate the passage vorticity for a lightly loaded rotor having a low hub-to-tip ratio. The streamlines that were needed for the vorticity calculation were estimated using a streamline curvature method to solve equations of motion in the direct turbomachinery problem.

A model of the vortex flow becomes apparent from the analysis. The flow around the rotor cap appears to be like that of several small vortices inside of a larger single vortex. Each one of the smaller vortices is formed within each blade passage. This flow picture explains the vortex flow shown in Fig. 1 and the good agreement between the calculated and measured flow fields.

Some conclusions can be made about cavitation correlations for the vortex flow:

1. The critical cavitation number of the vortex increased with the addition of upstream struts, with increasing Reynolds number, and with a 10 percent reduction in coefficient below the design value.
2. The critical cavitation number of the vortex decreased with the addition of a screen and with a 10 percent increase in flow coefficient above the design value.
3. The calculated effects of Reynolds number, struts, screens, and off-design flow coefficients can be combined to successfully correlate cavitation data for any basic flow considered.
4. The influence of air content on the cavitation number can be large at high air contents and low velocities. Thus to minimize this effect, it is best to conduct tests at low air contents and high velocities.

## Acknowledgment

This investigation was sponsored in part by the Naval Sea Systems Command General Hydromechanics Research Program, Subproject SR 023 01 01, and by the Naval Sea Systems Command, Codes 05H and 63R. The General Hydromechanics Research Program is administered by the David W. Taylor Naval Ship Research and Development Center.

## Uncertainty Estimates

The data shown in Figs. 3, 4, and 14 are for flow field measurements which have an uncertainty of $\pm 2$ percent. The cavitation data presented in Figs. 8, 9, 10, 11, 12, and 13 have an uncertainty of $\pm 5$ percent. Only average data are given for the flow field measurements; however, the uncertainty for the cavitation can be noted on the figures.

## References

1 McCormick, B. W., "A Study of the Minimum Pressure in a Trailing Vortex System," Ph.D. thesis, Dept. of Aerospace Engineering, The Pennsylvania State University, June 1954.

2 McCormick, B. W., "On Cavitation Produced by a Vortex Trailing from a Lifting Surface," ASME *Journal of Basic Engineering*, Sept. 1962, pp. 369-379.

3 Kermeen, R. W., and Parkin, B. R., "Incipient Cavitation and Wake Flow Behind Sharp-Edged Disks," Report 85-4, Hydrodynamics Lab., California Institute of Technology, Aug. 1957.

4 Arndt, R. E. A., "Investigation of the Effects of Dissolved Gas and Free Nuclei on Cavitation and Noise in the Wake of a Sharp Edged Disk," *Procedings of Joint Symposium on Design and Operation of Fluid Machinery*, ASME, Fort Collins, Colo. 12-14 June 1978, pp. 543-556.

5 Lakshminarayana, B., and Horlock, J. H., "Generalized Expressions for Secondary Vorticity Using Intrinsic Coordinates," *J. Fluid Mechanics*, Vol. 59, 1973, pp. 97-115.

6 Billet, M. L., "Secondary-Flow-Related Vortex Cavitation," Ph.D. thesis, Dept. of Aerospace Engineering, The Pennsylvania State University, Nov. 1978.

7 Billet, M. L., "Secondary Flow Vorticity in the Passage of a Rotor," Applied Research Laboratory, Technical Memorandum No. 77-243, Aug. 17, 1977.

8 Hawthorne, W. R., "Secondary Circulation in Fluid Flow," *Proceedings of the Royal Society*, London, England, Series A, Vol. 206, May 1951, p. 374.

9 Lakshminarayana, B. and Horlock, J. H., "Review: Secondary Flows and Losses in Cascades and Axial Turbomachines," *Int. J. Mech. Sci.*, Vol. 5, 1953, p. 257.

10 Hawthorne, W. R., and Novak, R. A., "The Aerodynamics of Turbomachinery," *Ann. Rev. Fluid Mechanics*, Vol. 1, 1969.

11 Horlock, J. H., *Axial Flow Compressors*, R. E. Krieger Company, New York, 1973, pp. 55-60.

12 Lakshminarayana, B., Discussion of Wilson, Mani and Acosta's, "A Note on the Influence of Axial Velocity Ratios on Cascade Performance," NASA SP-304, Part 1, 1974, pp. 127-133.

13 Lieblein, S., "Experimental Flow in Two-Dimensional Cascades," NASA SP-36, 1965, pp. 209-222.

14 Billet, M. L., "Cavitation Results for a Secondary Flow Generated Trailing Vortex," Applied Research Laboratory, Technical Memorandum No. 76-260, Oct. 12, 1976.

15 Holl, J. W., "An Effect of Air Content on the Occurrence of Cavitation," ASME *Journal of Basic Engineering*, Vol. 82, 1960, pp. 941-946.

**V. H. Arakeri**
Formerly Visiting Research Associate at ARL and currently Assistant Professor of Mechanical Engineering at the Indian Institute of Science, Bangalore, India

**J. A. Carroll**
Formerly Graduate Assistant at ARL and currently Test Engineer with McDonnell-Douglas, Long Beach, Calif.

**J. W. Holl**
Professor of Aerospace Engineering at the Applied Research Laboratory (ARL) of the Pennsylvania State University, State College, Pa.

# A Note on the Effect of Short and Long Laminar Separation Bubbles on Desinent Cavitation

*Earlier desinent cavitation studies on a 1/8 caliber ogive by one of the authors (J. W. H.) showed a sudden change in the magnitude of the desinent cavitation number at a critical velocity. In the present work it is shown by means of oil-film flow visualization that below the critical velocity a long laminar separation bubble exists whereas above the critical velocity the laminar separation bubble is short. Thus the desinent cavitation characteristics of a 1/8 caliber ogive are governed by the nature of the viscous flow around the body.*

## Introduction

Normally for a body exhibiting laminar boundary-layer separation one associates the critical velocity with the condition at which the existence of separation is eliminated. However, under certain circumstances a second critical velocity is associated with bodies exhibiting laminar separation. At this critical velocity a dramatic change in the physical structure of the laminar separation bubble takes place which not only alters the length of the separation bubble but also the pressure distribution around the body. A comprehensive review on this subject may be found in an article by Tani [1].

Thus, at least based on the change in the pressure distribution one may expect the cavitation characteristics to be influenced by the aforementioned alteration in the physical structure of the laminar separation bubble. This possibility has already been mentioned by Alexander [2] and more recently by Huang and Peterson [3]. However, no actual experiments on cavitation inception or desinence are referred to by these authors.

In addition, desinent cavitation characteristics of an 1/8 caliber ogive observed by Robertson et al. [4] shown in Figs. 1 and 2 in conjunction with the measured change in pressure distribution with Reynolds number by Rouse and McNown [5] for the same body also strongly suggests that changes in the physical structure of the laminar separation bubble may be governing the desinence characteristics of this particular headform.

Referring to the data in Fig. 1, which was obtained in the 121.92 cm (48-in.) ARL water tunnel, it is seen that the cavitation number increases suddenly as the velocity is increased for the 2.54 cm (1 in.), 5.08 cm (2 in.) and 10.16 cm (4 in.) models. As described in a subsequent section the form of the cavitation changes when $\sigma_d$ increases. Furthermore, in Fig. 1, it is seen that as the model diameter decreases the critical velocity increases. This suggests a Reynolds number dependency which is supported by the graph of $\sigma_d$ versus Reynolds number in Fig. 2.

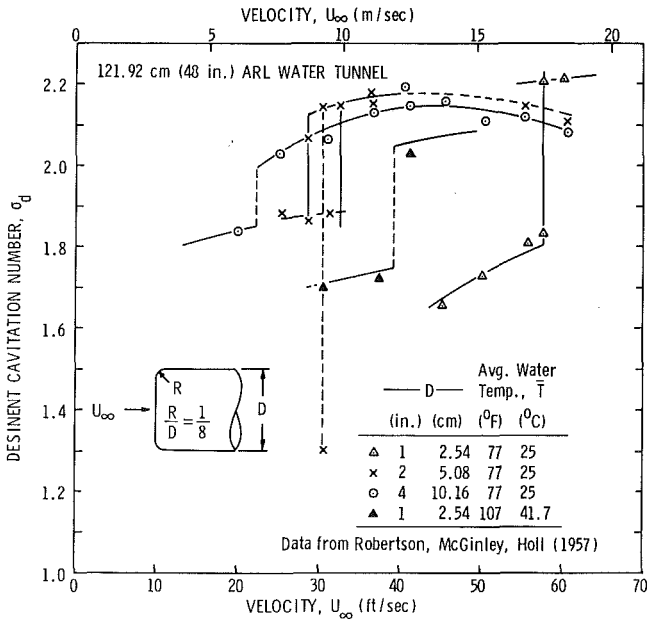


**Fig. 1 Desinent cavitation number versus velocity for 1/8 caliber ogive (Robertson-McGinley-Holl, 1957)**

Thus, it is the purpose of this note to confirm the aforementioned supposition by oil-film flow visualization studies on a 5.08 cm (2 in.), 1/8 caliber ogive used by Robertson, et al. for their desinence studies.

Contributed by the Fluids Engineering Division for publication in the JOURNAL OF FLUIDS ENGINEERING. Manuscript received by the Fluids Engineering Division, August 21, 1979.

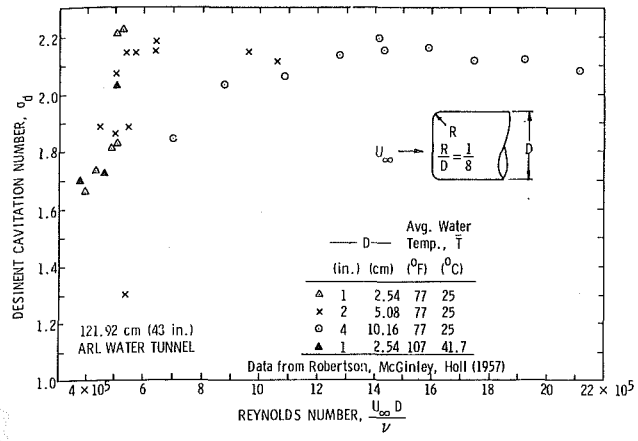


**Fig. 2 Desinent cavitation number versus reynolds number for 1/8 caliber ogive (Robertson-McGinley-Holl, 1957)**

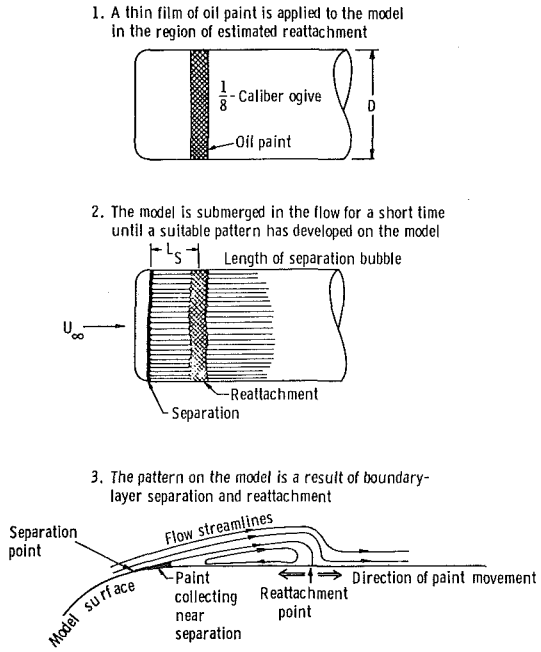


**Fig. 3 Explanation of oil-film flow visualization technique**

## Flow Visualization Studies

The flow investigation was carried out in the 30.48 cm (12 in.) water tunnel of the Applied Research Laboratory. The nominal freestream turbulence level of this facility has been measured to be about 0.5 percent. Since a 5.08 cm (2 in.) body was used in a 30.48 cm (12 in.) test section some blockage effects can be expected.

By trial and error the best medium for oil-film flow visualization was found to be a one-to-one mixture of artist's orange oil based paint and 90 weight lubricating oil. Initially the experiments were carried out by applying a thin coating of the mixture over the entire nose section of the body. Visual observation of the paint movement was made after the test velocity was reached. Several black and white photographs were also taken to note the developments. From these photographs the approximate position of reattachment could be noted. However, a more effective method of locating reattachment was achieved by applying a 1.27 cm (0.5 in.) wide strip of oil-paint mixture at the known approximate location of reattachment. After the test velocity was reached, the oil-paint mixture ahead of reattachment would move upstream in thin fine streaks toward the location of separation, whereas the oil-paint mixture downstream of reattachment would move in thin fine streaks in the direction of the flow. An explanation of this technique is depicted by the sketches in Fig. 3. The sequence of photographs shown in

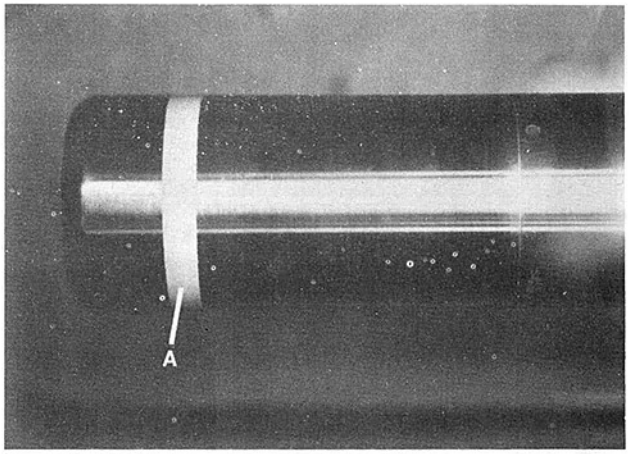


**Fig. 4(a) Oil-paint film on 5.08 cm (2-in.) diameter 1/8 caliber ogive at $U_\infty$ = 0 – Region A – strip of paint at beginning of test**

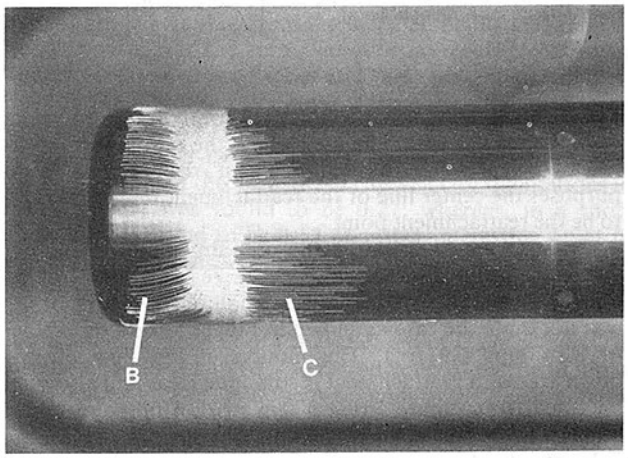


**Fig. 4(b) Oil-paint film on 5.08 cm (2-in.) diameter 1/8 caliber ogive at $U_\infty$ = 6.40 mps (21 fps) 20 seconds after reaching the test velocity – Region B - Upstream Movement of Paint – Region C - Downstream Movement of Paint**

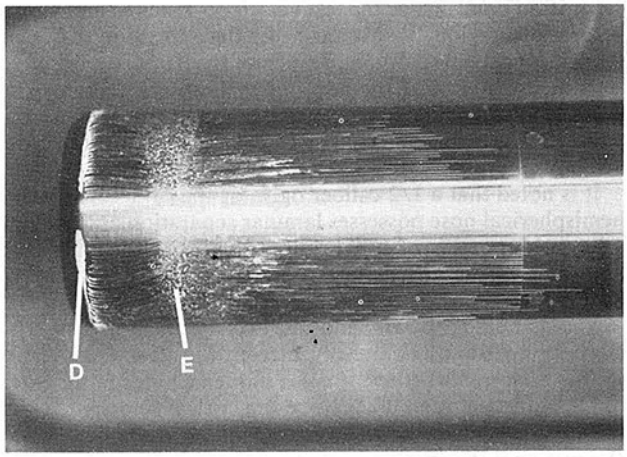


**Fig. 4(c) Oil-paint film on 5.08 cm (2-in.) diameter 1/8 caliber ogive at $U_\infty$ = 6.40 mps (21 fps) 120 seconds after reaching the test velocity – Region D - paint collected near boundary layer separation – Region E - paint remaining in boundary layer reattachment region**

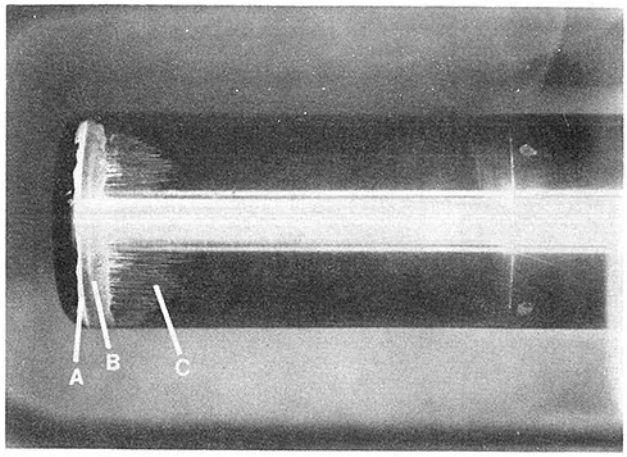


Fig. 5 Oil-paint film on 5.08 cm (2-in.) diameter 1/8 caliber ogive at $U_\infty$ = 8.84 mps (29 fps) 120 seconds after reaching the test velocity – Region A - paint collected near boundary layer separation – Region B - paint remaining in boundary layer reattachment region – Region C - downstream movement of paint

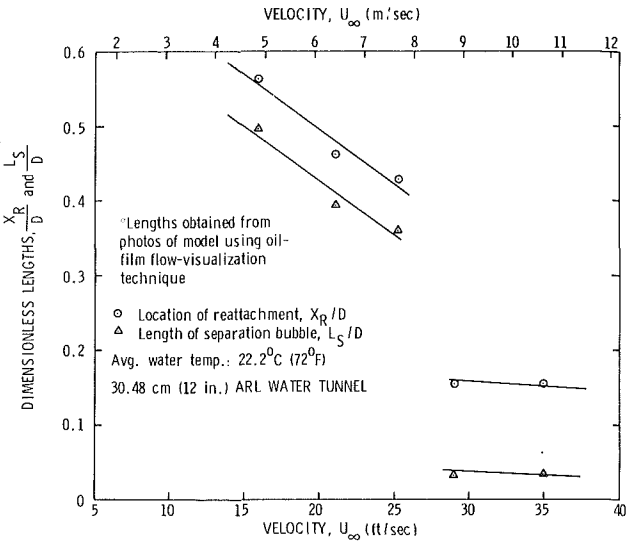


Fig. 6 Location of reattachment and length of separation bubble versus velocity on 5.08 cm (2-in.) diameter 1/8 caliber ogive

Fig. 4 clearly illustrates these developments for a test velocity of 6.40 mps (21 fps). The area where the oil-paint mixture is smeared represents the reattachment region. For present purposes the center line of the reattachment region was taken to be the reattachment point.

The upstream motion of the oil-paint mixture was quite evident at flow velocities with large separated regions. However, at higher velocities with small separated regions this was not quite the case as shown in Figure 5 for a test velocity of 8.84 mps (29 fps). The motion in the flow direction downstream of reattachment is still quite clear and also it may be noted from Figure 5 that a thin strip of oil-paint mixture remains in the reattachment region.

It should be mentioned that in establishing a short separated region at higher velocities, such as that in Fig. 5, the model must first experience a large separated region for a short time at lower velocities until the test velocity is attained. During this time all paint movemement is forward toward the separation point. Once the test velocity is reached and a small separation region is established, the direction of paint movement reverses, although much of the paint remains in the separated region near the point of separation. Therefore less paint is available to move downstream and the formation of paint streaks does not look as well developed as for the lower-velocity case.

It is noted that a 1/2 caliber ogive or the commonly known hemispherical nose possesses laminar separation at least up to a Reynolds number of $10^6$. From the nature of the body shape and the pressure distribution it can be expected that the 1/8 caliber ogive possesses laminar separation at least up to a Reynolds number of $10^6$ and most likely much higher. Thus the only question to be resolved from the flow visualization studies concerns whether or not a sudden change in the extent of laminar separation takes place at a critical velocity.

## Results and Discussion

It is believed that the aforementioned question was resolved from the present tests. The position of reattachment ($x_R/D$) and length of the separation bubble ($L_s/D$) (where $x_R$ is the axial distance from the stagnation point to the reattachment point, $L_S$ is the length of the separation bubble and $D$ is the body diameter) versus velocity are shown in Fig. 6. These data were obtained from photographs of the type shown in Figs. 4 and 5. It is clear that the extent of laminar separation is drastically reduced in the critical velocity range of approximately 7.62 mps (25 fps) to 9.14 mps (30 fps). The data in Fig. 6 also imply that the location of separation shifts downstream by a significant amount for velocities corresponding to a short separation bubble. This observation is consistent with similar findings on aerofoils; for example, as indicated in Fig. 6 of reference [1] the separation location on a Gottingen 801 aerofoil at an angle of attack of 18 deg shifts from $s/c = 0.13$ to $s/c = 0.22$ with an increase in Reynolds number from $4.2 \times 10^4$ to $7.5 \times 10^4$. This shift in the location of separation can presumably be attributed to the drastic alteration in the nature of the pressure distribution which always accompanies transition from a long to a short separation bubble.

By comparing the results of Fig. 6 with those of Fig. 1 it may be noted that the desinent cavitation number for the 5.08 cm (2 in.) diameter model shows a jump in approximately the same velocity range as that found for transition from a long to a short separation bubble. In addition, from Reference [4], photographs of cavitation at desinence show a change in the physical appearance in this critical velocity range. For velocities above the critical velocity range a ring of cavitation bubbles was observed at desinence. In recent years this type of cavitation has been shown to be associated with the reattachment region of a small laminar separated region [6] and is called bubble-ring cavitation. On the other hand, for velocities below the critical velocity range desinent cavitation appears as bubbles along the separated free shear layer similar to cavitation observed on disks [7]. Within the critical velocity range both of the aforementioned types of cavitation may be observed. This is demonstrated by the photographs of Figs. 7(*a*) and 7(*b*) which were obtained by Roberston, McGinley, and Holl [4] at 9.57 mps (31.4 fps) for the 5.08 cm (2-in.) diameter model in the 121.92 cm (48 in.) diameter water tunnel. Thus, with a small laminar separated region, desinent cavitation on a 1/8 caliber ogive may scale in a manner similar to that of a hemispherical nose. Whereas with a long separation bubble, desinent cavitation may scale in a manner similar to that of a zero caliber ogive or disk.

## Final Remarks

From present findings it can be strongly contended that the observed change in the desinent cavitation index at a critical velocity on an 1/8 caliber ogive is associated with the change in the physical structure of the laminar separation bubble.

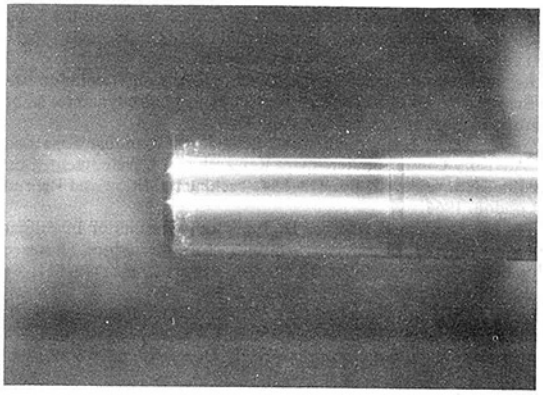

Fig. 7(a) Long bubble desinent cavitation at $U_\infty$ = 9.57 mps (31.4 fps), $\sigma_d$ = 1.49 (Robertson-McGinley-Holl, 1957)

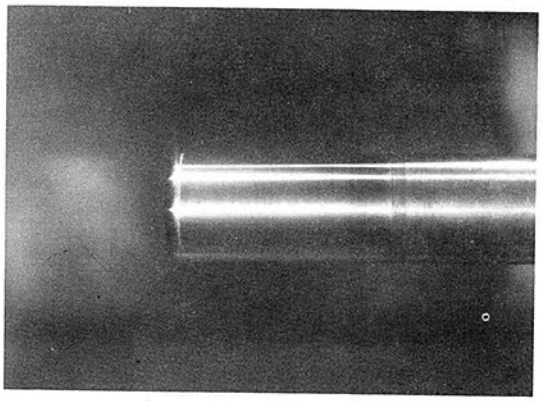

Fig. 7(b) Short bubble desinent cavitation at $U_\infty$ = 9.57 mps (31.4 fps), $\sigma_d$ = 1.90 (Roberston-McGinley-Holl, 1957)

This change as shown in Fig. 6 of reference [1] results in a drastic alternation in the pressure distribution around the body. In particular, the magnitude of the pressure coefficient at separation ($-\bar{C}_{ps}$) is substantially increased as a result of transition from a long to a short bubble. Since, $\sigma_d$ for separated flows has been proposed [3] to be given by the sum of $-\bar{C}_{ps}$ and a pressure coefficient ($C_p'$) based on the fluctuating component of the pressure, we might expect that $\sigma_d$ will be larger for a flow with a short separation bubble than for the case where the bubble is long. However, the exact difference will depend on the relative change in the magnitudes of both $-\bar{C}_{ps}$ and $C_p'$ as a result of transition from a long to a short separation bubble.

Assuming that cavitation occurs when the minimum pressure ($P_{\min}$) equals vapor pressure we can express the cavitation number in the form

$$\sigma_d = \frac{P_\infty - P_{\min}}{1/2\rho U_\infty} . \tag{1}$$

The minimum pressure can be written as

$$P_{\min} = \bar{P}_a - \bar{P}_t + \bar{P}_t - P' \tag{2}$$

where $\bar{P}_a$, $\bar{P}_t$ and $P'$ are the actual mean pressure at the separation point, the theoretical mean pressure at the separation point from perfect fluid theory, and the appropriate turbulent pressure fluctuation below the mean value, respectively. Employing equation (2) in equation (1) yields

$$\sigma_d = -\frac{\bar{P}_t - P_\infty}{1/2\rho U_\infty^2} - \frac{\bar{P}_a - \bar{P}_t}{1/2\rho U_\infty^2} + \frac{P'}{1/2\rho U_\infty^2} \tag{3}$$

or

$$\sigma_d = -\bar{C}_p - \bar{C}_{p-c} + \frac{P'}{1/2\rho U_\infty^2} . \tag{4}$$

We can then write for the short bubble (sb) and long bubble (lb)

$$(\sigma_d)_{sb} - (\sigma_d)_{lb} = -(\bar{C}_{p-c})_{sb} + (\bar{C}_{p-c})_{lb} + \left(\frac{P'}{1/2\rho U_\infty^2}\right)_{sb} - \left(\frac{P'}{1/2\rho U_\infty^2}\right)_{lb} . \tag{5}$$

In equation (5) it may be reasonable to assume that $(\bar{C}_{p-c})_{sb} \cong 0$. However, recent measurements by Holl and Carroll [10] on a hemispherical nose indicate that $(\bar{C}_{p-c})_{sb} \cong 0.07$. From Gaster's (8) findings it may be tempting to estimate $(\bar{C}_{p-c})_{lb}$ to be from about 0.2 to 0.5. However, Gaster investigated only two different pressure profiles and even then $(\bar{C}_{p-c})$ was found to vary. Therefore, the question whether $(\bar{C}_{p-c})_{lb}$ is approximately the same for long separation bubbles on various body shapes is not really resolved. It may be a function of the magnitude of the suction peak which would be dependent on the body shape and the flow angle of attack. We may also note here that from the work of Young and Horton [9] we may expect the turbulent pressure coefficients to be different for the case of short and long separation bubbles. This follows from their finding that the normalized root mean square (rms) velocity fluctuations in a long bubble are significantly higher than in a short bubble. For example, the maximum value of the normalized rms velocity fluctuations in a long bubble was found to be 0.27; whereas, in a short bubble it was found to be 0.12. Another interesting point to note from the work of Young and Horton [9] is that in the case of a long separation bubble, essentially all along the separated free shear layer the normalized rms fluctuations are within about 85 percent of the maximum of 0.27; whereas, in the case of a short bubble, the region covered by fluctuations 85 percent or greater than the maximum of 0.12 is essentially localized in the vicinity of reattachment. It is very likely that the above finding has relevance to the present observations of limited cavitation all along the free shear layer for the case of a long separation bubble (Fig. 7(*a*)); whereas, limited cavitation is localized in the form of a ring of bubbles for the case of a short separation bubble (Fig. 7(*b*)). Referring to Eq. (5), we note that sufficient knowledge concerning $\bar{C}_{p-c}$ for short and long bubbles and turbulent coefficients for both cases is lacking and thus it is difficult to draw any general conclusions. From Fig. 1, it is seen that for the three sizes of ogives tested by Robertson, et al. the difference $(\sigma_d)_{sb} - (\sigma_d)_{lb}$ is 0.8 in one case but in most cases varies between 0.2 and 0.4.

## Experimental Uncertainty

The cavitation data shown in Figs. 1 and 2 were obtained from reference [4] which does not contain a statement concerning experimental uncertainty. The data obtained in this investigation are the length data shown in Fig. 6. The uncertainty in the lengths as measured from the photographs are ± 6 percent and ± 0.6 percent for the short and long bubbles, respectively. The uncertainty in the velocity at 9.14 mps (30 fps), which is near the middle of the test range, was ± 4 percent due to fluctuations in the voltage reading.

## Acknowledgment

The research presented in this paper was conducted in the Fluids Engineering Department (FED) of the Applied Research Laboratory at The Pennsylvania State University. The FED is located in the Garfield Thomas Water Tunnel Building. The research was primarily sponsored by the Naval Sea Systems Command, Code 63R-31, and additional support was given by ARL E and F Grant 6412 monitored by M. T. Piggott.

## References


1 Tani, I., "Low Speed Flows Involving Bubble Separations," *Progress in Aeronautical Science,* Vol., 5, 1964, pp. 70–103.

2 Alexander, A. J., "An Investigation of the Relationship Between Flow Separation and Cavitation," *Proceedings of the Conference on Cavitation,* The Institution of Mechanical Engineers, Heriot Watt University, Edinburgh Scotland, Sept. 3–5, 1974, pp. 1–8.

3 Huang, T. T., and Peterson, F. B., "Influence of Viscous Effects on Model/Full-Scale Cavitation Scaling," *Journal of Ship Research,* Vol. 20, No. 4, Dec. 1976, pp. 215–223.

4 Robertson, J. M., McGinley, J. H., and Holl, J. W., "On Several Laws of Cavitation Scaling," La Houille Blanche, No. 4, Sept. 1957.

5 Rouse, H., and McNown, J. S., "Cavitation and Pressure Distribution-Headforms at Zero Angle of Yaw," Studies in Engineering, Bulletin 32, State University of Iowa, 1948.

6 Arakeri, V. H., and Acosta, A. J., "Viscous Effects in the Inception of Cavitation on Axisymmetric Bodies," ASME JOURNAL OF FLUIDS ENGINEERING, Vol. 95, No. 4, 1974, pp. 519–528.

7 Kermeen, R. W., and Parkin, B. R., "Incipient Cavitation and Wake Flow Behind Sharp-Edged Disks," Report 85-4, Hydrodynamics Laboratory, California Institute of Technology, Aug. 1957.

8 Gaster, M., "The Structure and Behavior of Laminar Separation Bubbles," Advisory Group for Aerospace Research and Development, Conference Proceedings No. 4, Part 2, pp. 813–854, Technical Edition and Reproduction, Ltd., London, 1966.

9 Young, A. D., and Horton, H. P., "Some Results of Investigations of Separation Bubbles," Advisory Group for Aerospace Research and Development, Conference Proceedings No. 4, Part 2, pp. 779–811, Technical Edition and Reproduction, Ltd., London, 1966.

10 Holl, J. W., and Carroll, J. A., "Observations of the Various Types of Limited Cavitation on Axisymmetric Bodies," *Proceedings of the International Symposium on Cavitation Inception,* ASME, Dec. 1979, pp. 87–99.

# ERRATA

**"The Flow Properties of Rooms With Small Ventilation Openings."**
JOURNAL OF FLUIDS ENGINEERING, Vol. 102, Sept. 1980, pp. 316-323, A.D. Gosman, P.V. Nielsen, A. Restivo, and J.H. Whitelaw.

Fig. 3(a): Should be turned 90 deg clockwise.

Page 319, Table 1, note 1
Reads: $\ldots + C_\mu \rho k^{2/} \epsilon$
Should read: $\ldots + C_\mu \rho k^2 / \epsilon$

Page 319, Table 1, note 2
Reads: $C = 1.44$
Should read: $C_1 = 1.44$

Page 320, column 2, line 4 from bottom
Reads: $z = 0.31\, H$
Should read: $z = \pm 0.31\, H$

Page 323, column 1, line 21 from top
Reads: 5 Conclusions
Should read: 6 Conclusions

Page 323, column 2, reference [1]
Reads: Vol. 100, 1968, p. 308
Should read: Vol. 100, 1978, p. 291

# The Third Two-Dimensional Problem of Three-Dimensional Blade Systems of Hydraulic Machines — Part 1 Theoretical Analysis

**P.K. Agarwal**
Reader,
Department of Mechanical Engineering,
M.L.N. Engineering College,
Allahabad, India

**G.V. Viktorov**
Professor and Head,
Department of Hydraulic Machines,
Moscow Power Institute,
Moscow, USSR

*This is the first part of a study of "third" two-dimensional problem of three-dimensional blade systems of hydraulic machines. Proposed herein is a method of obtaining and evaluating the three-dimensional effect on a system of hydraulic machine blades with arbitrary geometry. An analysis method indicating the velocity distributions on surfaces perpendicular to the mean axisymmetric stream surfaces has been formulated to help create a general understanding and awareness of the flow conditions in the runner passage. An application of generalized analytic functions for inviscid, incompressible flow has been made to find out the general solution on an auxiliary plane, transformed conformally from the physical plane. Integral equation systems for the tangential velocity and the velocity potential function have been deduced. Thus, the solution of the three-dimensional flow problem is supplied by two-dimensional computation methods.*

## Introduction

It is widely recognized that the flow in the runner space of a hydraulic machine, in the most general case, is three-dimensional and unsteady in character. An exact solution of such a flow problem is not yet available due to the complexities. Most of the existing methods of runner flow analysis are based on simplifying assumptions, which reduce it to a two-dimensional steady-flow problem. The flow is assumed to be inviscid and incompressible, customary in hydraulic machine flow analysis.

A set of two two-dimensional flow problems is solved as a modern approach to investigate the flow past three-dimensional blade systems of hydraulic machines [1–7]:

(1) the determination of the meridional stream pattern in the meridional section of a runner on the assumption of mean axisymmetric flow, taking into consideration the geometry of blade system and

(2) the determination of the flow around a cascade of airfoils in a part-channel cut out from the bladed space by two meridional stream surfaces of revolution.

The combined solution of these two-dimensional problems gives approximate quasi three-dimensional solution of the three-dimensional problem. For quasi three-dimensional solution the variations in flow parameters in the direction normal to the stream surfaces are ignored in any particular filament assuming the thickness of the filament to be small. In a general case, the velocity component $c_2$, normal to axisymmetric stream surface $q_2$ = const, is present even under ideal fluid condition. As a result, the flow so obtained is unstable in the direction perpendicular to the mean axisymmetric stream surfaces and the condition of dynamic equilibrium of flow in this direction is ensured only on an average. At any point, equilibrium is not guaranteed. Consequently, such an approximate quasi three-dimensional solution consists of an error, which has not been estimated so far.

Generally speaking, the system of two two-dimensional problems is commonly adopted in the design and development of hydraulic machines [1–8]. The proposed idea of the third two-dimensional problem corresponds to the main idea of indicating the three-dimensional flow by the combination of two-dimensional solutions. The degree of accuracy of quasi three-dimensional solution can be attained either by solving the governing flow equations completely, taking into account the transverse velocity component $c_2$ or by considering the third two-dimensional problem for an additional flow on the surfaces of a transverse section of axisymmetric flow.

There have been very few practical, three-dimensional theories which are applicable to such cases as stated above, to the best of author's knowledge, except the method published by Nyiri [9]. Nyiri has given a method for the computation of the stream pattern around a cascade of airfoils in the part-channels influenced by the secondary flow in the cells cut out

Contributed by the Fluids Engineering Division for publication in the JOURNAL OF FLUIDS ENGINEERING. Manuscript received by the Fluids Engineering Division, January 27, 1977.

from the bladed space by surfaces orthogonal to the meridional flow. There are no numerical examples or qualification of the technique, for even hypothetical situations, let alone actual geometries. The present paper intends to put forward a novel approach to describe the effect of three-dimensional flow due to the arbitrary shapes of the mean stream surfaces through blades using analytical means.

The solution of the problem under investigation will help in computing the velocities on the examined surfaces, in evaluating the effectiveness of quasi three-dimensional solution of the three-dimensional problem, in estimating the deviation of the real stream surfaces from the surfaces of rotation of axisymmetric flow and in making necessary corrections to the two two-dimensional flow models, if needed.

## Formulation of the Problem

It is generally assumed that the flow in the runner space develops axisymmetric stream surfaces. The runner space can then be subdivided into a number of fluid filaments bounded by axisymmetric stream surfaces. The flow is assumed to be steady, incompressible and frictionless. The problem of mean axisymmetric flow for thick and finite number of blades has been basically solved [2, 3, 10] and the flow is expressed by the following system of equations:

$$\begin{aligned} \mathbf{C}\times\boldsymbol{\Omega} &= \operatorname{grad} E \\ \operatorname{div}\mathbf{C} &= 0 \end{aligned} \tag{1}$$

where

$$E = gZ+\frac{p}{\rho}+\frac{C^2}{2} \text{ and}$$

$$\boldsymbol{\Omega} = \operatorname{rot}\mathbf{C}$$

Carrying the operation of linear averaging of equations with respect to time and the peripheral coordinate between two blade surfaces, the averaged equations of motion and continuity in the blade system with thick profiles are obtained as follows [10]:

$$\begin{aligned} <\mathbf{C}>\times<\boldsymbol{\Omega}> &= -\mathbf{F}+\operatorname{grad}<E> \\ \operatorname{div}(\epsilon\cdot<\mathbf{C}>) &= 0 \end{aligned} \tag{2}$$

here

$$<\boldsymbol{\Omega}> = <\boldsymbol{\Omega}_0> + <\boldsymbol{\Omega}_*> = \operatorname{rot}<\mathbf{C}>$$

The mass force in equation (2) assumes the value [10]:

$$\mathbf{F} = <\boldsymbol{\Omega}_*>\times<\boldsymbol{\Omega}>$$

meaning thereby that the mass force vector $\mathbf{F}$ acts normal to the averaged relative flow velocity $<\mathbf{W}>$.

In Fig. 1(*a*) is shown in the runner space of a mixed-flow hydraulic machine together with the meridional section lines of the axisymmetric stream surfaces. The chosen orthogonal curvilinear coordinate system $q_1$, $q_2$, $q_3$ with origin 0 is also shown in the figure. The coordinate $q_1$ is along the meridional section of the stream surface, $q_3$ is along the peripheral direction, and $q_2$ is along the normal to $q_1$ and $q_3$, which gives a right-handed coordinate system. While solving the second two-dimensional problem it is assumed that the variation in any flow and cascade parameters along the thickness in case of any particular filament is negligible. The system of equations expressing the flow past the blade cascade on the axisymmetric stream surface $q_2$ = const in the layer of varying thickness will be [2–7]:

$$\begin{aligned} \operatorname{div}\mathbf{C} &= 0, \quad (C_2\equiv 0) \\ \operatorname{rot} q_2\,\mathbf{C} &= 0 \end{aligned} \tag{3}$$

under the condition that vorticity normal to this plane is zero. The solution is obtained under given boundary conditions fulfilling the postulate of Joukowsky-Chapligin [2–7].

On solving the systems of equations (2) and (3) simultaneously, the lines of vortices of averaged flow can be obtained on the surface $q_3$ = const. Further, the solution of the quasi three-dimensional problem gives the flow, the streamlines of which are circular on the surfaces $q_1$ = const and the value of circulation along the circumference of an arbitrary radius on the surface $q_1$ = const is described as [11]:

$$\Gamma^{\circ}(q_2) = 2\pi\cdot H_3\cdot <C>_3(q_2)$$

$$= \Gamma' + 2\pi\cdot\int_{q_2'}^{q_2} R(q_2)\cdot<\Omega>_1(q_2)\cdot H_2\cdot d_{q_2} \tag{4}$$

where

$$<\boldsymbol{\Omega}>_1(q_2) = <\boldsymbol{\Omega}_0>_1(q_2)+<\boldsymbol{\Omega}_*>_1(q_2)$$

$$<\boldsymbol{\Omega}_0>_1 = \frac{1}{H_2\cdot H_3}\cdot\frac{\partial}{\partial q_2}(H_3\cdot<C>_{30})$$

## Nomenclature

$\mathbf{C}$ = flow velocity vector in physical region
$C_1, C_2, C_3$ = velocity components along $q_1$, $q_2$, $q_3$ axes
$C_{n_{23}}$ = velocity component along the normal $n_{23}$ (Fig. 1(*b*))
$D$ = simply connected and bounded region on the surface $q_1$ = const
$D_0$ = inner region of the blade profile (Fig. 2(*b*))
$E$ = total mechanical energy of unit mass
$\mathbf{F}$ = mass force
$H_1, H_2, H_3$ = Lame's coefficients of the coordinate system $q_1$, $q_2$, $q_3$
$h(q_2)$ = relative filament thickness
$L$ = closed boundary of a region $D$
$l$ = length of the boundary contour $L$
$l_0$ = center line of the blade profile
$m$ = number of blades in the runner
$\mathbf{n}$ = a unit normal vector drawn outer to the flow region
$P(\xi,\eta)$ = running point in the region $D$
$Q$ = distribution of sources and sinks on the surface $q_1$ = const
$Q_0$ = discharge through the closed boundary $L$
$q_1, q_2, q_3$ = orthogonal curvilinear coordinates in the physical region
$q_2'$ = $q_2(R')$
$R$ = radial distance from the runner axis = $R(q_2)$
$R_0$ = radial distance between the origin of the coordinate system and the runner axis
$R'$ = hub radius
$s(\rho,\beta)$ and $\sigma(r,\theta)$ = curvilinear coordinates of fixed and running points on the boundary contour $L$
$S_0$ and $\sigma_A$ = arbitrary points on the boundary contour $L$
$\mathbf{u}$ = $\omega\times\mathbf{R}$
$\mathbf{V}$ = vector quantity in the mapped plane
$\bar{V}(Z)$ = conjugate complex velocity in the $Z$ plane

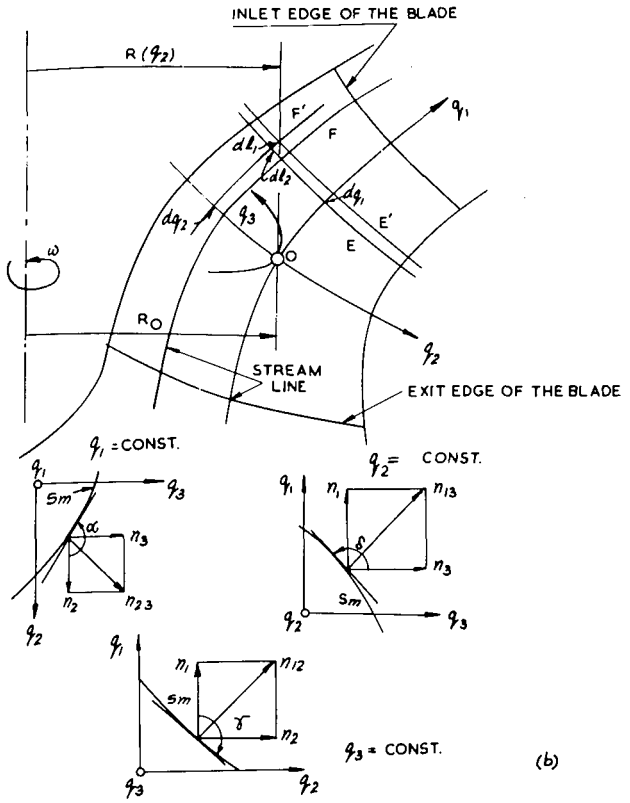


**Fig. 1(a) Meridional projection of the blade system; (b) Sections of the blade skeleton surface with the coordinate surfaces**

$$<\Omega^* >_1 = \frac{1}{H_2 \cdot H_3} \cdot \frac{\partial}{\partial q_2} (H_3 \cdot <C>_3 - H_3 \cdot <C>_{30}) \tag{5}$$

Figure 2 shows the vector field $<\Omega>_{1,2}$ for the averaged flow representing the projection of vector $<\Omega>$ in $q_3 = \text{const}$ plane. Figures 2(*a*) and 2(*b*) correspond to the condition $\partial/\partial q_2 \quad (H_3 \cdot <C>_3) > 0$ and $\partial/\partial q_2 \quad (H_3 \cdot <C>_3) < 0$, respectively, in case of turbines as well as pumps.

Raabe [12,13] has observed the effect of an axial vortex in creating the axial flow asymmetry in axial flow turbomachines with infinitely thin blades under absolute potential flow. It has been shown that the flow deviates considerably from axial symmetry. A similar approach has been made to investigate the influence of an axial vortex on the flow in Francis turbines [13].

As is clear from above, the vortex component along the coordinate $q_1$, which in a general case is not zero, has not been considered in the quasi three-dimensional solution. While investigating the mean axisymmetric flow in the $q_3 = \text{const}$ plane, the effect of the vortex component $<\Omega>_3$ has been taken into account, whereas the vortex component $<\Omega>_2$ is taken into consideration for the flow past the blade cascade on the axisymmetric stream surface $q_2 = \text{const}$ in the layer of variable thickness. Obviously, if $<\Omega>_1 \neq 0$, an additional flow in the limits of the blade system must exist on the surface $q_1 = \text{const.}$, depending on the inception of vorticity in the flow $\Omega_0$, the geometry of blade system and the flow regime.

Further, the flow pattern on the surface of rotation $q_1 = \text{const}$ can be investigated by considering the third two-dimensional flow problem. In the given coordinate system (Fig. 1) the equations of continuity and vorticity will be:

$$Q(q_1, q_2, q_3) = \frac{1}{H_1 \cdot H_2 \cdot H_3} \cdot \left[ \frac{\partial}{\partial q_2} (H_3 \cdot H_1 \cdot \mathbf{C}_2) + \frac{\partial}{\partial q_3} (H_1 \cdot H_2 \cdot \mathbf{C}_3) \right] = -\frac{1}{H_1 \cdot H_2 \cdot H_3} \cdot \frac{\partial}{\partial q_1} (H_2 \cdot H_3 \cdot \mathbf{C}_1) \tag{6}$$

$$\Omega_{01}(q_1, q_2, q_3) = \text{rot}_{q_1} \mathbf{C} = \frac{1}{H_2 \cdot H_3} \cdot \left[ \frac{\partial}{\partial q_2} (H_3 \cdot \mathbf{C}_3) - \frac{\partial}{\partial q_3} (H_2 \cdot \mathbf{C}_2) \right] \tag{7}$$

## Nomenclature (cont.)

$V_\tau$ and $V_n$ = absolute velocity components, tangential and normal to the boundary wall
$\bar{V}_1(Z)$ = conjugate complex velocity in the $Z$ plane defined by equation (33)
$\mathbf{V}_2$ = $\mathbf{V} - \mathbf{V}_1$
$V_{1r}$ and $V_{2r}$ = radial components of velocities $V_1$, $V_2$, respectively
$\mathbf{W}$ = relative flow velocity
$x,y$ = cartesian coordinates in the mapped plane
$Z(x,y)$ = $s$
$\alpha$ = angle between the radial and tangential lines to the blade contour (Fig. 2(*a*))
$\Gamma$ = circulation around the contour $L$
$\Gamma'$ = circulation around $R'$
$\Gamma^\circ$ = circulation around periphery on the surface $q_1 = \text{const}$
$\Omega_0, \Omega_*, \Omega$ = free, forced and cumulative vortices, respectively
$\delta$ = angle between the blade skeleton and the $q_3$ axis
$\lambda$ = $2\pi/m$
$\epsilon$ = coefficient of restriction
$\zeta(\xi,\eta)$ = $\sigma$
$\xi,\eta$ = orthogonal coordinates in the mapped plane
$\Phi$ = complex potential function in the mapped plane
$\varphi$ = velocity potential function
$\Psi$ = stream function in the flow domain
$\omega$ = angular speed of the runner

Subscript

$< >$ = denotes the passage averaged value

Suffix

1 = refers to the values on the surface $q_1 = \text{const}$

Symbols

(//) and (/) = denote the front (according to the direction of motion) and the rear walls of the region $D$

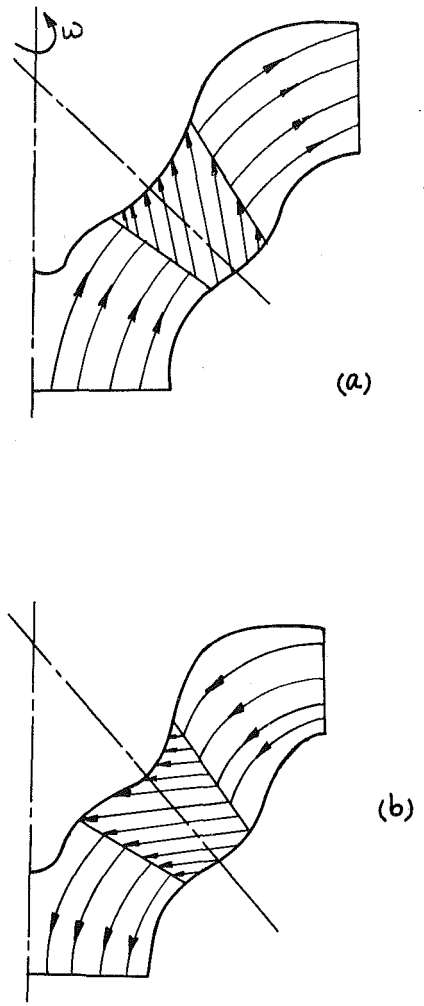


**Fig. 2 Projection of averaged stream surfaces and the line of vortices in $q_3$ = const plane**

where

$$H_1 = \frac{dl_1}{dq_1}; \quad H_2 = \frac{dl_2}{dq_2}; \quad H_3 = \frac{dl_3}{dq_3}$$

are the values of Lame's coefficients. Considering the flow on surface $E$, the projection of which coincides with the coordinate axis $q_2$, we have $dl_2 = dq_2$ and $H_2 = 1$. Obviously

$$H_1 = \mathrm{h}; \quad H_2 = 1; \quad H_3 = \frac{R \cdot d\nu}{R_0 \cdot d\nu} = \frac{R}{R_0}$$

where

$R = R(q_2)$ and $h = h(q_2)$

Besides the governing flow equations (6) and (7) the boundary condition on the blade surface under a nonstalled flow condition originates from the self evident circumstance that the normal component of relative velocity must vanish on the contour $L$ [9]:

$$\mathbf{C} \cdot \mathbf{n} = \mathbf{U} \cdot \mathbf{n} \tag{8}$$

The normal velocity component $C_n$ is zero on the hub and shroud. From equation (8):

$$C_1 \cdot n_1 + C_2 \cdot n_2 + C_3 \cdot n_3 = U \cdot n_3$$

and following Fig. 1 ($b$)

$$\frac{n_1}{n_3} = -\cot\delta \quad ; \quad \frac{n_2}{n_3} = -\tan\alpha$$

Hence

$$C_{n_{23}} = -(U + C_1 \cdot \cot\delta) \cdot \cos\alpha = -C_3 \cdot \cos\alpha \tag{9}$$

The available solution of the quasi three-dimensional problem is utilized to determine the flow pattern on the surface $q_1$ = const. This solution helps in finding out the distribution of velocities $C_1$ and $C_3$ on the boundary and in the flow region on the surface $q_1$ = const and also the distribution of sources $Q$ in domain.

Following Gauss's theorem

$$Q_0 = \int_L C_{n_{23}}(s) \cdot ds = \int\int_D Q(q_2, q_3) H_2 \cdot H_3 \cdot dq_2 \cdot dq_3 \tag{10}$$

The velocity field on the surface $q_1$ = const can, thus, be determined by solving equations (6) and (7) under the boundary condition (9) taking into consideration the influence of a bound vortex component for the main flow.

If the blade is replaced by an equivalent vortex surface of a bound vortex $\gamma_*$, then form the quasi three-dimensional solution, it is possible to find out the intensity of vortices, the geometry of vortex lines and the components $\gamma_{*1}$. The following equality should be fulfilled [11]:

$$\gamma_{*1}'(q_2) + \gamma_{*1}''(q_2) = \lambda \cdot R(q_2) \cdot \langle \Omega_* \rangle_1 (q_2) \tag{11}$$

The bound vortices $\langle \Omega_* \rangle_1$ distributed uniformly along the periphery in the mean axisymmetric flow problem are now concentrated on the contour $l_0^*$ of the blade profile located on surface $q_1$ = const (Fig. 3). For simplified practical solution of the problem the vortices are distributed on the skeleton surface $l_0$, considering it as the center line of the blade profile.

$$\gamma_{*1}(q_2) = \gamma_{*1}'(q_2) + \gamma_{*1}''(q_2) \tag{12}$$

The flow pattern on the surface $q_1$ = const can, therefore, be determined by solving the two-dimensional problem for a periodical system. This system has since been picturized vide equations (6), (7), (9), and (12).

## Transformation of Physical Region Into an Auxiliary Plane

The foregoing equations and the solution of the problem might become somewhat simpler after the transformation of the velocities and the physical region $q_1 = \text{const}$ into an auxiliary plane. This plane $Z(x,y)$ is shown in Fig. 3. It has been obtained by conformally mapping the surfaces $E$ ($q_1 = \text{const}$) orthogonal to mean axisymmetric stream surface. The chosen orthogonal curvilinear coordinate system $S_2$, $S_3$ with origin 0 is also shown in the mapped plane. The coordinate $S_2$ is along the radius and $S_3$ is along the peripheral direction at radius $R_0$.

The transformation should preserve the angle between two directions and the ration of an arc element on $E$ and $Z$

$$\frac{dr}{r \cdot d\theta} = \frac{d_{q2}}{R \cdot d\nu} \tag{13}$$

Assuming that the magnitude of angles along the coordinate axes $q_3$ and $S_3$ is preserved

$$dS_3 = dq_3, \quad \text{or} \quad \gamma_0 \cdot d\theta = R_0 \cdot d\nu \tag{14}$$

From (13) and (14) a formula is obtained

$$r = r_0 \cdot \exp\left[\frac{R_0}{r_0} \cdot \int_0^{q_2} \frac{dq_2}{R(q_2)}\right] \tag{15}$$

connecting the coordinates of curvilinear surface $E$ with the periodical annular domain in the $Z$ plane. As a result of conformal transformation, with the help of function (15), a circular cascade is obtained consisting of m number of profiles

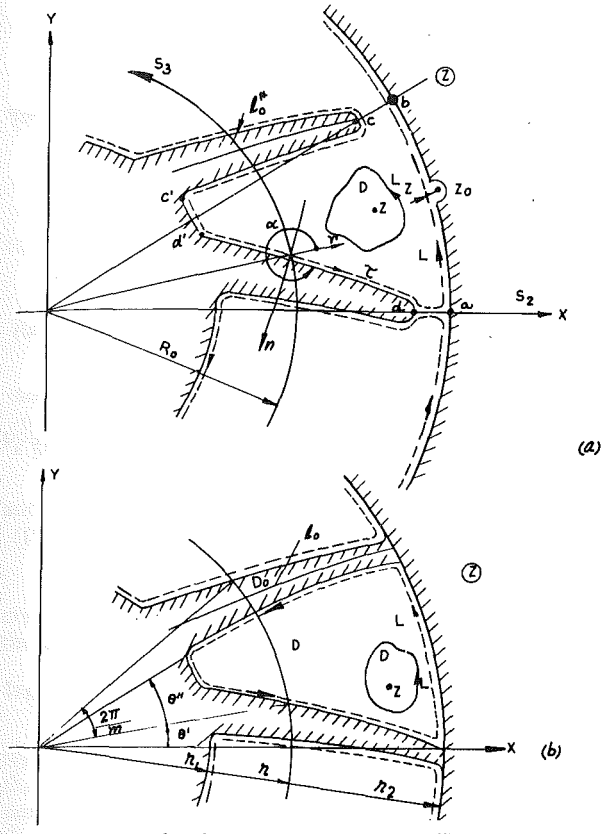


Fig. 3 Mapping of surface $q_1$ = const on an auxiliary plane Z

*(a)* A system in which blades are not bounded by an external rim;
*(b)* A system with the blades in contact with the inner and outer rims

$$m = m_0 \cdot \frac{r_0}{R_0}$$

where

$m_0$ = number of profiles on surface $E$.

To simplify, it can be assumed that

$R_0 = r_0$ and $m = m_0$

which results the function of transformation [3–6, 11]:

$$Z = r \cdot e^{i\theta} = R_0 \cdot \exp\left(\int_0^{q_2} \frac{dq_2}{R(q_2)} + i\theta\right) \tag{16}$$

as a result of which, a periodical domain in the annulus form having periods equal to the number of blades is obtained in the $Z(x,y)$ plane (Fig. 3). Fig. 3$(a)$ depicts the blade system, in which blades are not bounded by an external rim, whereas Fig. 3$(b)$ represents the case with the blades in contact with the inner and outer rims. In other cases the blades may not touch the inner rim at all. Thus, depending upon the type of hydraulic machine and the position of section in the meridional projection, four different types of blade systems are obtained.

The relation between the velocity $C$ in the physical region and the corresponding vector $V$ in the mapped region can be established as:

$$|V| = |C| \cdot \frac{R}{r} \tag{17}$$

As shown by Agarwal [11], the circulation and the discharge at the corresponding elements during transformation does not change and the value of $H_1$ at corresponding points in the physical and mapped regions will remain the same. The system of differential equations describing the flow for a periodical annular domain in the Z plane for $R_0 = 1$ yields the form:

$$\mathrm{div}\mathbf{V} = \left(\frac{R}{r}\right)^2 \cdot Q - V_r \cdot \frac{1}{H_1} \cdot \frac{dH_1}{dr} = q_0(r,\theta) \tag{18}$$

$$\mathrm{rot}\mathbf{V} = \left(\frac{R}{r}\right)^2 \cdot \Omega_{01} = \gamma_0(r,\theta) \tag{19}$$

where the functions $q_0$ and $\gamma_0$ are continuous and finite and div $\mathbf{V} \neq 0$ for the flow in the mapped region.

Corresponding to (17) the normal component of velocity in the $Z$ plane is:

$$V_n = C_{n_{23}} \cdot \frac{R}{r} \tag{20}$$

which can also be expressed by a differential relationship

$$V_n(\sigma) = \frac{1}{H} \cdot \frac{d\psi(\sigma)}{d\sigma}$$

Then

$$\psi(s) + \int_0^s H_1 \cdot V_n(\sigma) \cdot d\sigma \tag{21}$$

Similarly, the distribution of bound vortices $\gamma$ on the blade contour in the $Z$-plane is given as

$$\gamma(r) = \gamma_{*1}(q_2) \cdot \frac{dq_2}{dr} = \gamma_{*1}(q_2) \cdot \frac{R}{r} \tag{22}$$

Thus, the flow pattern on the surface under consideration can be obtained on solving equations (18) and (19) with the known distributions of stream function (21) on the boundary $L$ and the bound vortices (22) on the blade contour.

The system of equations (18) and (19) is a particular case of elliptical type differential equations with variable coefficients and has an unique solution. The solution of such a system of linear differential equations under partial derivatives has been obtained [14, 15] with the help of generalized analytic functions, used widely to solve the hydrodynamical problems of turbomachine blade systems [2–7, 11].

The system of equations (18) and (19) is analogous to the system obtained when solving the direct problem for the blade cascade in the layer of variable thickness [5,6]. Introducing the complex velocity $\mathbf{V}(Z)$ in the $Z$-plane, the following equation is obtained in place of equations (18) and (19):

$$\frac{\partial \bar{V}}{\partial \bar{Z}} = \frac{1}{2} \cdot \left[\mathrm{div}\mathbf{V} - i\,\mathrm{rot}\,\mathbf{V}\right] = \frac{1}{2}(q_0 - i\gamma_0) \tag{23}$$

A general solution of this can be found in the class of generalized analytic functions. Analogous to [2–6], the general expression for velocity has the form:

$$\bar{V}(Z) = \frac{1}{2\pi i} \cdot \int_L \frac{\bar{V}(\zeta) \cdot d\zeta}{\zeta - Z} - \frac{1}{\pi} \iint_D \frac{\partial \bar{V}}{\partial \bar{\zeta}} \cdot \frac{d\xi\, d\eta}{\zeta - Z} \tag{24}$$

The function $\bar{V}(Z)$ is the generalized analytic function giving the solution of equation (23). The general expression for the conjugate complex velocity in the periodical flow domain can be found, similar to [4–6, 11], by deforming the contour $L$ and the domain $D$ (Fig. 3) in the contour

$$\sum_{n=1}^{m} L_n$$

and the domain

$$\sum_{n=1}^{m} D_n,$$

respectively, in a way that the new contour in its limit attains the boundary of the flow region. Thus,

$$\bar{V}(Z) = \frac{1}{2\pi i} \cdot \sum_{n=1}^{m} \int_{L_n} \frac{\bar{V}(\zeta) \cdot d\zeta}{\zeta - Z}$$

$$- \frac{1}{2\pi i} \cdot \sum_{n=1}^{m} \iint_{D_n} (\gamma_0 + i q_0) \frac{d\xi \; d\nu}{(\zeta - Z)} \tag{25}$$

where $L_n$ is the solid boundary of one period of domain and $D_n$ the enclosed area of one period of cascade.

Taking into consideration the periodicity of flow

$$\bar{V}(\zeta) \cdot d\zeta = \bar{V}\left(\zeta \cdot e^{i \cdot \frac{2\pi}{m} \cdot n}\right) \cdot d\left(\zeta \cdot e^{i \cdot \frac{2\pi}{m} \cdot n}\right)$$

equation (25) is written as

$$\bar{V}(Z) = \frac{m Z^{m-1}}{2\pi i} \cdot \int_L \frac{\bar{V}(\zeta) d\zeta}{\zeta^m - Z^m}$$

$$- \frac{m Z^{m-1}}{2\pi i} \cdot \iint_D (\gamma_0 + i q_0) \frac{d\xi \; d\eta}{\zeta^m - Z^m} \tag{26}$$

(For simplicity the indices at $L$ and $D$ are removed).

The double integral in equation (26) converges everywhere in the domain $D$ under the conditions existing for functions $q_0$ and $\gamma_0$. Equation (26) gives the general solution of the system of equations (18) and (19) for periodical flow region.

## Integral Equation for Velocity

The system of differential equations can be solved with the help of numerical methods. The method of integral equations worked out for planar and non-planar blade cascades of hydraulic machines seems to be very effective from the point of view of realization on the computer [3,6,7,11]. Equation (26) can be put in different forms to obtain an integral equation needed for the numerical solution of the problem. In particular, it can be put in a form to obtain the tangential component of velocity on the boundary of the flow region.

The equation is valid for all the points $Z$ lying in the domain except those lying on the boundary contour $L$. When the point $Z = Z_0$ lies on the boundary, the integral expression on the left side of the equation has an infinite discontinuity under $\zeta = Z_0$. Using the Cauchy formula for limiting values of the integral [3,16] when the point $Z_0$ approaches the flow region, and taking into consideration that on $L$

$$\bar{V}(\zeta) \cdot d\zeta = \left[ V_\tau(\sigma) + i \, V_n(\sigma) \right] \cdot d\sigma \tag{27}$$

$$\bar{V}(Z_0) = \left[ V_\tau(s) + i \, V_n(s) \right] \cdot e^{-i\nu}(s) \tag{28}$$

where

$dZ_0$ = $ds \cdot e^{i\nu}$ and $\nu$ = arg $dZ_0$

$\nu$ = angle between the $x$ axis and the tangent drawn at any point s.

the real part of equation (26) is written as:

$$V_\tau(s) + \int_L V_\tau(\sigma) \cdot A(s,\sigma) \cdot d\sigma$$

$$= - \int_L V_n(\sigma) \cdot B(s,\sigma) d\sigma$$

$$+ \iint_D \left[ q_0(P) \cdot B(s,P) + \gamma_0(P) \cdot A(s,P) \right] \cdot d\xi \, d\eta \tag{29}$$

where

$$N(s,\sigma) + iM(s,\sigma) = \frac{1}{\pi} \cdot \ln(\zeta^m - Z_0^m)$$

$$A(s,\sigma) = \frac{dM}{ds}(s,\sigma) \quad ; \quad B(s,\sigma) = \frac{dN}{ds}(s,\sigma) \tag{30}$$

The integral equation (29) does not have a unique solution since the corresponding homogeneous equation has a non-trivial solution. Equation (29) can be cast in a form having a unique solution

$$\Delta V_\tau(s) + \int_L \Delta V_\tau(\sigma) \cdot \Delta A(s, s_0, \sigma) \cdot d\sigma = \Delta b(s) \tag{31}$$

where

$$\Delta V_\tau(s) = V_\tau(s) - V_\tau(s_0); \quad \Delta V_\tau(\sigma) = V_\tau(\sigma) - V_\tau(s_0);$$

$$\Delta b(s) = b(s) - b(s_0); \quad \Delta A(s, s_0, \sigma) = A(s,\sigma) - A(s_0,\sigma)$$

where

$b(s)$ = free term of the equation (29).

The value of $V_\tau(s_0)$ can be found from the subsequent relation

$$\int_L \Delta V_\tau(s) \cdot ds = \Gamma - V_\tau(s_0) \cdot l$$

$$\Gamma = \int_L V_\tau(s) \cdot ds = \iint_D \gamma_0(r,\theta) \cdot d\xi \, d\eta \tag{32}$$

The formulated problem can be solved in two stages. At the first stage the velocity of flow $\bar{V}_1$ in the $Z$ plane is to be determined. This velocity $\bar{V}_1$ has been calculated taking into consideration a vortex $\Gamma'$ at the origin of the coordinate system, vortices $\gamma$ on the profile contour and the sources $q_0$ along with vortices $\gamma_0$ in the flow domain.

$$\bar{V}_1(Z) = \frac{\Gamma'}{2\pi i} \cdot \frac{1}{Z} + \frac{m Z^{m-1}}{2\pi i} \cdot \int_L \frac{\gamma(\sigma) \cdot d\sigma}{Z^m - \zeta^m}$$

$$+ \frac{m Z^{m-1}}{2\pi i} \cdot \iint_D \left[ \gamma_0(P) + i q_{01}(P) \right] \cdot \frac{d\xi \; d\eta}{Z^m - \zeta^m} \tag{33}$$

where

$$q_{01} = \left( \frac{R}{r} \right)^2 \cdot Q - V_{1r} \cdot \frac{1}{H_1} \cdot \frac{dH_1}{dr}$$

From equation (33) the tangential and normal components of velocity, $V_{1\tau}$ and $V_{1n}$, respectively, can be calculated on the contour of the flow region for $Z \to Z_0$, $(Z_0 \leftarrow L)$.

At the second stage, the velocity of flow $\mathbf{V}_2 = \mathbf{V} - \mathbf{V}_1$ on the boundary $L$ of flow region $D$ is to be found from the normal component $V_{2n}$ of this velocity on the boundary $L$.

Corresponding to equation (31)

$$\Delta V_{2\tau}(s) + \int_L \Delta V_{2\tau}(\sigma) \cdot \Delta A(s, s_0, \sigma) \cdot d\sigma = \Delta b_2(s) \tag{34}$$

$$b_2(s) = \int_L \left[ V_{2n}(s) - V_{2n}(\sigma) \right] \cdot B(s,\sigma) d\sigma$$

$$+\iint_D q_{02}(P)\cdot B(s,P)\cdot d\xi\, d\eta \tag{35}$$

where

$$q_{02} = -V_{2r}\cdot\frac{H_1'}{H_1},\quad V_{2n} = V_n - V_{1n} \tag{36}$$

As the circulation of velocity $V_2$ along the contour $L$ is equal to zero, corresponding to (32)

$$V_{2\tau}(s_0) = -\frac{1}{1}\cdot\int_L \Delta V_{2\tau}(s)\cdot ds$$

$$V_{2\tau}(s) = V_{2\tau}(s\tau(s_0)+\Delta V_{2\tau}(s) \tag{37}$$

Thus, after determining $V_\tau$ on $L$ the radial velocity component $V_r$ can be found on the blade contour from

$$V_r = V_\tau\cdot\cos(\nu-\beta) + V_n\cdot\sin(\nu-\beta) \tag{38}$$

and also, the velocity component $c_2$ along $q_2$ axis

$$c_2 = V_r\cdot\frac{r}{R} \tag{39}$$

exposing the flow downwash in the direction perpendicular to the mean stream surfaces of quasi three-dimensional flow.

## Integral Equation for Velocity Potential Function

The method of solution in the case of determining an integral equation for velocity potential function is similar to that followed on the previous chapter. The step-by-step deduction of the solution sought also remains the same. For the sake of completness the relevant steps will be presented.

An integral equation in terms of the velocity potential function $\varphi(Z)$ can be obtained on multiplying the equation of the conjugate complex velocity (26) by $dZ$ and then integrating it with respect to $Z$.

$$\Phi(Z) = \omega + i\Psi = \int \bar{V}(Z)\cdot dZ$$

Thus

$$\Phi(Z) + \frac{1}{2\pi i}\cdot\int_L \bar{V}(\zeta)\cdot\ln(\zeta^m - Z^m)\cdot d\zeta$$

$$= \frac{1}{2\pi i}\cdot\iint_D \left[\gamma_0(\zeta)+iq_0(\zeta)\right]\cdot\ln(\zeta^m - Z^m)\, d\xi\, d\eta + c \tag{40}$$

Integration by parts and further simplification leads to

$$\Phi(Z) + \frac{\Gamma}{2\pi i}\cdot\ln(\zeta_A^m - Z^m) - \frac{1}{2\pi i}\cdot\int_L \frac{\varphi(\zeta)\cdot m\ \zeta^{m-1}}{\zeta^m - Z^m}\cdot d\zeta$$

$$+\frac{1}{2\pi}\cdot\int_L V_n(\sigma)\cdot\ln(\zeta^m - Z^m)\, d\sigma$$

$$= \frac{1}{2\pi i}\cdot\iint_D \left[\gamma_0(\zeta)+iq_0(\zeta)\right]\cdot\ln(\zeta^m - Z^m)\, d\xi d\eta \tag{41}$$

where $\zeta_A$ is an arbitrary point on the boundary contour $L$ and the bypass of the contour starts from this point. The integration constant has been omitted in suceeding treatment.

Using the Cauchy formula for limiting values of the integral [3,16] for $Z\to Z_0$, $(Z_0 - L)$ and making use of relationship (30), similar to (29), the real part of the equation (41) will have the form:

$$\varphi(s) - \int_L \varphi(\sigma)\cdot\frac{dM}{d\sigma}(s,\sigma)\cdot d\sigma$$

$$= -\Gamma\cdot M(s,\sigma_A) - \int_L V_n(\sigma)\cdot N(s,\sigma)\cdot d\sigma$$

$$+\iint_D \left[\gamma_0(\zeta)\cdot M(s,\sigma) + q_0(\zeta)\cdot N(s,\sigma)\right]\cdot r dr d\theta \tag{42}$$

where the kernel of the integral equation $dM/d\sigma$ $(s,\sigma)$ is continuous on the boundary contour $L$.

Integrating the right side single integral by parts, equation (42) transforms to

$$\varphi(s) - \int_L \varphi(\sigma)\cdot dM(s,\sigma) = -\Gamma\cdot M(s,\sigma_A) - Q_0\cdot N(s,\sigma_A)$$

$$-\int\left[\Psi(s)-\Psi(\sigma)\right]\cdot dN(s,\sigma)$$

$$+\iint_D \left[\gamma_0(\zeta)\cdot M(s\sigma) + q_0(\zeta)\cdot N(s,\sigma)\right]\cdot r\, dr\cdot d\theta \tag{43}$$

This integral equation (43) does not have a unique solution. Casting it to a form having a unique solution:

$$\Delta\varphi(s) - \int_L \Delta\varphi(\sigma)\cdot d\Delta M(s,s_0,\sigma) = \Delta b(s)$$

$$\Delta\varphi(s) = \varphi(s) - \varphi(s_0);\quad \Delta\varphi(\sigma) = \varphi(\sigma) - \varphi(s_0);$$

$$\Delta b(s) = b(s) - b(s_0);\quad d\Delta M(s,s_0,\sigma)$$

$$= dM(s,\sigma) - dM(s_0,\sigma) \tag{44}$$

where $b(s)$ = free term of the equation (43).

The imaginary part of the equation (41) will have the form

$$2\Psi(s) = \Gamma\cdot N(s,\sigma_A) - Q_0\cdot M(s,\sigma_A)$$

$$-\int_L \varphi(\sigma)\cdot dN(s,\sigma) + \int_L \Psi\cdot dM(s,\sigma)$$

$$+\iint_D \left[q_0(\zeta)\cdot M(s,\sigma) - \gamma_0(\zeta)\cdot N(s,\sigma)\right]\cdot d\xi\, d\eta \tag{45}$$

giving the stream function distribution $\Psi$ in the region $D$.

The formulated problem will be solved in two stages as done earlier. At the first stage the velocity potential function $\varphi_1(s)$ in the $Z$ plane is to be calculated. Like the previous approach here also we have taken into consideration a vortex $\Gamma'$ at the origin of the coordinate system, vortices $\gamma(\sigma)$ on the profile contour and the sources $q_0$ along with the vortices $\gamma_0$ in the flow domain for calculating $\varphi_1(s)$.

$$\varphi_1(s) = \frac{\beta}{2\pi}\Gamma' + \frac{1}{2}\cdot\int_L \gamma(\sigma)\cdot M(s,\sigma)\cdot d\sigma$$

$$+\frac{1}{2}\cdot\iint_D \left[\gamma_0(P)\cdot M(s,\sigma)\right.$$

$$\left.+q_{01}(P)\cdot N(s,\sigma)\right]\cdot d\xi\cdot d\eta \tag{46}$$

The distribution of stream function under the above-mentioned condition will be

$$\Psi_1(s) = -\frac{\Gamma'}{2\pi}\ln\varphi - \frac{1}{2}\cdot\int_L \left[\gamma(\sigma)-\gamma(s)\right]\cdot N(s,\sigma)\, d\sigma$$

$$-\frac{\gamma(s)}{2}\cdot\int_L N(s,\sigma)\cdot d\sigma$$

$$+\frac{1}{2}\cdot\iint_D\left[q_{01}(P)\cdot M(s,\sigma)\right.$$

$$\left.-\gamma_0(P)\cdot N(s,\sigma)\right]d\xi\,d\eta \tag{47}$$

At the second stage the integral equation for the velocity potential function $\Delta\varphi_2(s)$ on the boundary contour $L$, analogous to (34) will yield the form:

$$\Delta\varphi_2(s)-\int_L\Delta\varphi_2(\sigma)\cdot d\Delta M(s,s_0,\sigma)=\Delta b_2(s) \tag{48}$$

where

$$\begin{aligned}\Delta b_2(s) &= Q_0\cdot\Delta N(s,s_0,\sigma_A)+\int_L\Delta\Psi_2(s_0)\cdot dN(s_0,\sigma)\\ &\quad-\int_L\Delta\Psi_2(s)\cdot dN(s,\sigma)\\ &\quad+\iint_D q_{02}(\zeta)\cdot\Delta N(s,s_0,\sigma)\cdot r dr d\theta\\ \Delta N(s,s_0,\sigma) &= N(s,\sigma)-N(s_0,\sigma);\quad \Delta\Psi_2(s)\\ &= \Psi_2(s)-\Psi_2(\sigma)\end{aligned} \tag{49}$$

Thus, after determining the distribution of function $\Delta\varphi(s)$ on $L$

$$\Delta\varphi(s)=\Delta\varphi_1(s)+\Delta\varphi_2(s) \tag{50}$$

the velocity component, tangential to the boundary wall can be obtained

$$V_\tau(s)=\frac{\partial\Delta\varphi(s)}{\partial s} \tag{51}$$

The stream function $\Psi(s)$ is the sum of functions $\Psi_1(s)$, equation (47), and $\Psi_2(s)$

where

$$2\cdot\Psi_2(s)=-Q_0\cdot M(s,\sigma_A)-\int_L\varphi_2(\sigma)\cdot dN(s,\sigma)$$

$$+\int_L\Psi_2(\sigma)\cdot dM(s,\sigma)+\iint_D q_{02}(\zeta)\cdot M(s,\sigma)\,d\xi\,d\eta \tag{52}$$

For numerical solution of the problem, any one of the two integral equations for velocity or velocity potential function can be chosen and investigated further.

## Investigation and Simplification of Integral Equation for Velocity Potential Function

It has been observed that $dH_1/dr\cdot 1/H_1$ is an extremely small quantity for most hydraulic machines [11]. In the succeeding treatment this quantity is, therefore, being assumed equal to zero. Following equations (33) and (36)

$$\frac{dH_1}{dr}\cdot\frac{1}{H_1}=0;\quad H_1=\text{const};\quad q_{01}=q_0=\left(\frac{R}{r}\right)^2\cdot Q \text{ and } q_{02}=0$$

The instantaneous value of any flow parameter can be considered as the sum of a temporal mean value and a pulsatory component.

$$Q(q_1,q_2,q_3=<Q>(q_1,q_2)+\Delta Q(q_1,q_2,q_3) \tag{53}$$

$$<Q>(q_1,q_2)=\frac{1}{\Delta\theta}\int_{\theta'}^{\theta''}Q(q_1,q_2,q_3)\cdot dq_3$$

$$\theta'\le q_3\le\theta'',\quad \Delta\theta=\theta''-\theta'=\lambda\cdot\epsilon \tag{54}$$

$<Q>(q_1,q_2)$ is the mean value of sources in the limits of the canal width.

$$<Q>=0\quad\text{when}\quad\theta''\le q_3\le\theta'+\lambda$$

Using the Leibnitz rule of differentiation with respect to parameter $q_1$ and making use of equations (6) and (54), equation (53) assumes the form:

$$\frac{\partial}{\partial q_1}(H_2\cdot H_3\cdot\Delta\theta\cdot<C_1>)=\int_{\theta'}^{\theta''}\frac{\partial}{\partial q_1}(H_2\cdot H_3\cdot C_1)\cdot dq_3$$

$$+H_2\cdot H_3\cdot C_1(\theta'')\cdot\frac{\partial\theta''}{\partial q_1}-H_2\cdot H_3\cdot C_1(\theta')\cdot\frac{\partial\theta'}{\partial q_1} \tag{55}$$

The equation of continuity (6) can be rewritten as:

$$<Q>=-\frac{1}{H_1\cdot H_2\cdot H_3}\cdot<\frac{\partial}{\partial q_1}(H_2\cdot H_3\cdot C_1)>$$

Taking (55) into consideration and solving further leads to:

$$\begin{aligned}<Q> &= \frac{1}{H_3\cdot\Delta\theta}\cdot\left[C_1(\theta'')\cdot\cot\delta''-C_1(\theta')\cdot\cot\delta'\right]\\ <Q>(q_2) &= \frac{1}{H_3(q_2)\cdot\Delta\theta(q_2)}\cdot\left[w_3''(q_2)-w_3'(q_2)\right]\\ &= \frac{(C_3''-C_3')}{H_3\cdot\Delta\theta}\end{aligned}$$

Thus, the distribution of sources in the passage canal on surface $q_2$ = const is the difference of peripheral components of absolute or relative velocities at its boundaries.

Sources $\Delta Q$ are dependent on the nonuniform distribution of velocity $C_1$ along the $q_1$ axis. All the existing methods assume that the pulsatory component is negligible and replace the instantaneous value of the flow parameter by its temporal mean value, thus achieving a steady flow [2–7, 10, 11]. Sources $<Q>$ induce circular streamlines in the region $D$. Exclusion of $<Q>$ and $\Delta Q$ will give rise to a change in the velocity field, but will not affect the magnitude of the radial component of velocity, the principal parameter to be investigated. For numerical solution of the problem these sources are, therefore, being neglected from further consideration and the boundary conditions correspondingly changed in the mapped plane.

$$V_n=-<C_3>\cdot\frac{R}{r}\cos\alpha,\quad\psi(r)-\int_{r'}^{r}<C_3>\cdot\frac{R}{r}\cdot dr \tag{56}$$

where

$$<V_u>=<C_3>\cdot\frac{R}{r}=\frac{\Gamma^\circ(r)}{2\pi r\cdot\epsilon}\text{ and }\cos\alpha=\frac{dr}{ds}$$

Analogous to (53) the distribution of vortices in the region $D$ can be represented as:

$$\gamma_0(r,\theta)=<\gamma_0>(r)+\Delta\gamma_0(r,\theta) \tag{57}$$

where

$$<\gamma_0>(r)=\frac{1}{\Delta\theta(r)}\cdot\int_{\theta'(r)}^{\theta''(r)}\gamma_0(r,\theta)\cdot d\theta \tag{58}$$

and

$$\frac{mZ^{m-1}}{2\pi i}\cdot\iint_D<\gamma_0>(P)\frac{d\xi\,d\eta}{Z^m-\zeta^m}$$

$$=\frac{\Gamma_0(r)}{2\pi i\cdot Z}-\frac{mZ^{m-1}}{2\pi i}\cdot\iint_{D_o}<\gamma_0>(P)\frac{d\xi\,d\eta}{Z^m-\zeta^m}$$

where

$$\Gamma_0(r) = 2\pi \cdot \int_{r'}^{r} <\gamma_0>(r) \cdot r \cdot dr \tag{60}$$

Generally speaking, in most of the hydraulic machines slender blades are commonly used in practice. For numerical solution of the problem these vortices, $<\gamma_0>$, distributed in the region $D_0$ can, therefore, be assumed to be concentrated on the center line $l_0$ of the blade profile.

$$\frac{mZ^{m-1}}{2\pi i} \cdot \iint_{D_o} <\gamma_0>(P) \frac{d\xi\, d\eta}{Z^m - \zeta^m} = \frac{mZ^{m-1}}{2\pi i} \cdot \int_{l_0} \frac{\gamma_0^*(r) \cdot dr}{Z^m - \zeta^m} \tag{61}$$

where

$$\gamma_0^*(r) = \lambda \cdot [1 - \epsilon(r)] \cdot <\gamma_0>(r) \cdot r \tag{62}$$

In similar fashion the bound vortices $\gamma(r)$, equation (22), are concentrated on the blade center line $l_0$. Pulsatory sources $\Delta Q$ and vortices $\Delta\gamma_0$ depend upon the nonuniform distribution of velocity fields along the periphery. It has been observed in analogous computation schemes that the nonuniformity of the velocity field is insignificant for optimum and near optimum working regimes [6,7,11]. Besides, the effect of $\Delta Q$ and $\Delta\gamma_0$, the total intensity of which is equal to zero, may be inconsequential on the flow in region $D$. Neglecting terms containing the values $\Delta Q$ and $\Delta\gamma_0$, equations (46) and (47) after simplification assume the form:

$$\varphi_1(s) = \frac{\beta}{2\pi}(\Gamma' + \Gamma_0) + \frac{1}{2} \cdot \int_{l_0} \gamma^*(r) \cdot M(s,r) \cdot dr \tag{63}$$

$$\Psi_1(s) = -\frac{\ln\varphi}{2\pi}(\Gamma' + \Gamma_0) - \frac{1}{2} \cdot \int_{l_0} \gamma^*(r) \cdot N(s,r) \cdot dr \tag{64}$$

where

$$\gamma^*(r) = \gamma'(r) + \gamma''(r) - \gamma_0^*(r) \tag{65}$$

Integral equation (48) reduces to

$$\Delta\varphi_2(s) - \int_L \Delta\varphi_2(\sigma) \cdot d\Delta M(s,s_0,\sigma) = \Delta b_2(s) \tag{66}$$

$$\Delta b_2(s) = \int_L \left[\Psi_2(s_0) - \Psi_2(\sigma)\right] \cdot dN(s_0,\sigma) - \int_L \left[\Psi_2(s) - \Psi_2(\sigma)\right] \cdot dN(s,\sigma) \tag{67}$$

and the stream function (52) after simplification takes the form:

$$\psi_2(s) = \frac{1}{2} \cdot \int_L \psi_2(l) \cdot dM(s,\sigma) - \frac{1}{2} \cdot \int_L \Delta\zeta_2(\sigma) \cdot dN(s,\sigma) \tag{68}$$

Obviously, the distribution of functions $\Delta\varphi_1(s)$ and $\Psi_1(s)$ can be found by knowing the distribution of vortices $\gamma^*(r)$, equation (65), from the quasi three-dimensional solution. Integral equation (66) is solved under the given boundary condition (56) to determine the distribution of function $\Delta\varphi_2(s)$ on the boundary contour $L$. Knowing the distribution of $V_\tau$ on $L$ from equations (50) and (51), the radial velocity component $V_r$ (38) is determined on the blade contour and also, the velocity component $c_2$(39) along the $q_2$ axis.

Hence, the velocity field in the physical plane depends upon the distribution of the normal component of velocity ($C_{n_{23}}$) and the bound vortices $\gamma_{*1}$ on the blade contour, as well as on the distribution of free vortices $\Omega_{01}$ in the flow region.

## Closing Comment

Numerical solution of the integral equation and the analytical results applied in case of actual hydraulic machines will be presented in Part II of this paper.

## References


1 Wu, Chung-Hua, "A General Theory of Three-Dimensional Flow in Subsonic and Supersonic Turbomachines of Axial, Radial and Mixed-Flow Types," Trans. ASME, Vol. 74, 1952, pp. 1363–1379.

2 Stepanoff, G.Y., "Hydrodynamics of Turbomachine Blade Cascades," Fizmatgiz, Moscow, 1962 (In Russian).

3 Viktorov, G.V., *Hydrodynamic Theory of Blade Cascades,* Veeschaya Schkola, Moscow, 1969 (In Russian).

4 Viktorov, G.V., "Solution of Direct Problem of Blade Cascade Theory in Relative Flow System," *Trudi VINI Gidromash,* No. 38, 1968, pp. 97–108 (In Russian).

5 Viktorov, G.V., "Solution of Direct Problem for Blade Cascades on Axisymmetric Stream Surface in the Layer of Variable Thickness," *Trudi VINI Gidromash,* No. 37, 1968, pp. 141–150 (In Russian).

6 Viktorov, G.V., and Vuchkova, I.V., "Calculation of Flow past an Arbitrary Cascade of Profiles on Axisymmetric Stream Surface in the Fluid Filament of Varying Thickness," *Izvestiva Akademi Nauk SSSR,* Mekhanika Zhidkosti i Gaza, No. 5, 1969, pp. 96–102 (In Russian).

7 Raukhman, B.S., "Flow of an Incompressible Fluid past a Cascade of Profiles on Axisymmetric Stream Surface in a Layer of Variable Thickness," *Izvestiva Akademi Nauk SSSR,* Mekhanika Zhidkosti i Gaza, No. 1, Jan. 1971, pp. 83–89 (In Russian).

8 Khan, M.N., Adarsh Swaroop, and Rao, Y.V.N., "Velocity Field Induced by Singularities in a Reaction Turbine Fluid Filament of Varying Thickness Approximated by Hyperbolic Law," ASME JOURNAL OF FLUIDS ENGINEERING, Paper No. 72-WA/FE-33, Mar. 1973, pp. 147–152.

9 Nyiri, A., "Potential Flow around the Blades of Hydraulic Machines," The Second International JSME Symposium on Fluid Machinery and Fluidics, Tokyo, Sept. 1972, pp. 61–70.

10 Topaz, G.I., and Etinberg, I.E., "Equation of Averaged Fluid Motion in Hydraulic Machine Runner," *Katloturbostroenie,* Trudi Tsh. K.T.E., Leningrad, No. 61, 1965, pp. 7–23 (In Russian).

11 Agarwal, P.K., "The Third Two-Dimensional Problem of Three-Dimensional Blade Systems of Hydraulic Machines," Ph.D. thesis, Moscow Power Institute, Moscow, 1976 (In Russian).

12 Raabe, J., "The Relative Vortex as Loss Factor and the Deviation of Stream Surfaces from the Planes of Symmetry in case of an Axial Turbomachine," *Machine Trade,* Vol. 64, No. 3, 1958, pp. 7–13 (In German).

13 Raabe, J., *Hydraulic Machines and Analogues,* Teil I, VDI-Verlag, GMBH, Dusseldorf, 1968 (In German).

14 Bers, L., *Mathematical Problems of Subsonic and Transonic Gas Dynamics,* Fizmatgiz, Moscow, 1961 (In Russian).

15 Vekua, I.N., *Generalized Analytic Functions,* Fizmatgiz, Moscow, 1959 (In Russian).

16 Korn, G.A., and Korn, T.M., *Mathematical Handbook for Scientists and Engineers,* 2nd ed., McGraw-Hill, New York, 1968.

# The Third Two-Dimensional Problem of Three-Dimensional Blade Systems of Hydraulic Machines—Part 2 Analytical Results

**P.K. Agarwal**
Reader,
Department of Mechanical Engineering,
M.L.N. Engineering College,
Allahabad, India

**G.V. Viktorov**
Professor and Head,
Department of Hydraulic Machines,
Moscow Power Institute,
Moscow, USSR

*This is the second part of a study of the "third" two-dimensional problem of three-dimensional blade systems of hydraulic machines. Part I described the formulation of the problem and the proposed method of solution to determine the velocity field on surfaces orthogonal to mean axisymmetric stream surfaces. Part II presents the numerical method of solving the integral equations; a few numerical examples for actual impellers/runners are also given. The results are presented in a series of figures and tables showing the distribution of the velocity component $c_2$ along the blade profile on the surface $q_1$ = const. The purpose of these numerical examples is to demonstrate the method and to help create a general understanding and awareness of the flow conditions existing in the runner passage.*

## Introduction

Part I of this paper consisted of the theoretical analysis of the three-dimensional direct flow problem to obtain and evaluate the effect of three-dimensional flow due to arbitrary shapes of the mean stream surfaces through runner blades. The formulated problem is based on the application of generalized analytic functions. Subsequently, integral equations have also been deduced for velocity and the velocity potential function.

In this part of the study the numerical method of solving the integral equations is given. The results of the proposed algorithm have been obtained for a hypothetical situation to compare the degree of agreement between the proposed solution and Raabe's findings [1]. The method has been applied for a pump and turbine of the diagonal flow type, as well as for the Francis turbine. The results show the variations in flow parameter $c_2$ in directions normal to stream surfaces which are generally ignored in the quasi three-dimensional solution.

## Method of Numerical Solution

The distribution of the velocity component $c_2$ on surfaces $q_1$ = const, orthogonal to mean axisymmetric stream surfaces $q_2$ = const., can be determined by solving the following equations[1]:

$$\zeta_1(s) = \frac{\beta}{2\pi} \bullet (\Gamma < + \Gamma_0) + \frac{1}{2} \bullet \int_{1_0} \gamma^*(r) \bullet M(s,r)\, dr \quad (63)$$

$$\Delta\zeta_2(s) - \int_L \Delta\zeta_2(\sigma) \bullet d\Delta M(s,s_0,\sigma) = \Delta b_2(s) \quad (66)$$

where

$$\Delta b_2(s) = \int_L [\psi_2(s_0) - \psi_2(\sigma)] \bullet dN(s_0,\sigma) - \int_L [\psi_2(s) - \psi_2(\sigma)] \bullet dN(s,\sigma) \quad (67)$$

$$\psi_1(s) = -\frac{\ln\rho}{2\pi}(\Gamma' + \Gamma_0) - \frac{1}{2} \bullet \int_{1_0} \gamma^*(r) \bullet N(s,r)\, dr \quad (64)$$

$$\psi_2(s) = \frac{1}{2} \bullet \int_L \psi_2(\sigma) \bullet dM(s,\sigma) - \frac{1}{2} \bullet \int_L \Delta\zeta_2(\sigma) \bullet dN(s,\sigma) \quad (68)$$

with the boundary conditions:

$$V_n = - < c_3 > \bullet \frac{R}{r} \bullet \cos\alpha, \psi(r) = - \int_{r'}^{r} < c_3 > \bullet \frac{R}{r} \bullet dr \quad (56)$$

[1] Refer to Part I of this paper for previous equations and symbol definitions.

Contributed by the Fluids Engineering Division for publication in the JOURNAL OF FLUIDS ENGINEERING. Manuscript received by the Fluids Engineering Division, January 27, 1977.

Modern techniques of computational mathematics have been used to obtain the numerical solution of the problem. The Krylov-Bogoliubov method [2] has been applied to solve the second-order Fredholm integral equation (66). This equation has been replaced by a system of linear algebraic equations as the kernels of the integral equation are continuous and bounded. The boundary contour $L$ is divided into $n$ small intervals of arbitrary length $\Delta\sigma$. Since the length of these segments is sufficiently small, the function $\Delta\zeta\ (\sigma)$ is determined at the center point of each segment. The values, so obtained, are assumed to be constant throughout the respective lengths. They are also found to be in good agreement with Raabe's results [1]. Thus, the system of linear algebraic equation is

$$\Delta\zeta_2(s_i) - \sum_{j=1}^{2n-1} \Delta\zeta_2(\sigma_j) \bullet [\Delta M(s_i,\sigma_j) - \Delta M(s_1,\sigma_j)] = \Delta b_2(s_i) \tag{69}$$

$i,j = 1,3,5. \ . \ .(2n-1) =$ center point of chosen segments on the boundary contour $L$.

where $\Delta M(s_i,\sigma_j) = M(s_i,\sigma_{j+1}) - M(s_i,\sigma_{j-1})$

$$M(s,\sigma) = \frac{1}{\pi} \arg(\xi^m - Z_0^m)$$

$$= \frac{1}{\pi} \arctan \frac{r^m \bullet \sin m\theta - \rho^m \bullet \sin m\beta}{r^m \bullet \cos m\theta - \rho^m \bullet \cos m\beta}$$

Since the kernel of the integral equation is a continuous function and has a finite value at $s = \sigma$, the coefficients of the system (69) must also render a continuous function on moving along $j$. The coefficients $\Delta M(s_i,\ \sigma_j)$ of the system are computed by separating the continuous branches of the inverse tangent of $M(s_i,\ \sigma_j)$ [3]. The geometrical interpretation of the kernel of the integral equation suggested by Lukashevich has been used here [3].

The free term (67) of the integral equation (66) has a Riemann- Stieltjes integral [2]. It is a continuous curvilinear integral which has been replaced as:

$$\int_L [\psi_2(s_i) - \psi_2(\sigma)] \bullet dN(s_i,\ \sigma)$$

$$= \sum_{j=1}^{2n-1} \int_{\sigma_{j-1}}^{\sigma_{j+1}} [\psi_2(s_i) - \psi_2(\sigma)] \bullet dN(s_i,\sigma) \tag{70}$$

where

$$N(s,\sigma) = \frac{1}{\pi} \ln|\xi^m - Z_0^m|$$

$$= \frac{1}{\pi} \ln\sqrt{r^{2m} - 2r^m \bullet \rho^m \bullet \cos m(\theta-\beta) + \rho^{2m}}$$

For points $\sigma_j \neq s_i$, the trapezoidal formula for approximate computation leads to

$$\int_{\sigma_{j-1}}^{\sigma_{j+1}} [\psi_2(s_i) - \psi_2(\sigma)] \bullet dN(s_i,\sigma)$$

$$= \int_{\sigma_{j-1}}^{\sigma_j} [\psi_2(s_i) - \psi_2(\sigma)] \bullet dN(s_i,\sigma)$$

$$+ \int_{\sigma_j}^{\sigma_{j+1}} [\psi_2(s_i) - \psi_2(\sigma)] \bullet dN(s_i,\sigma)$$

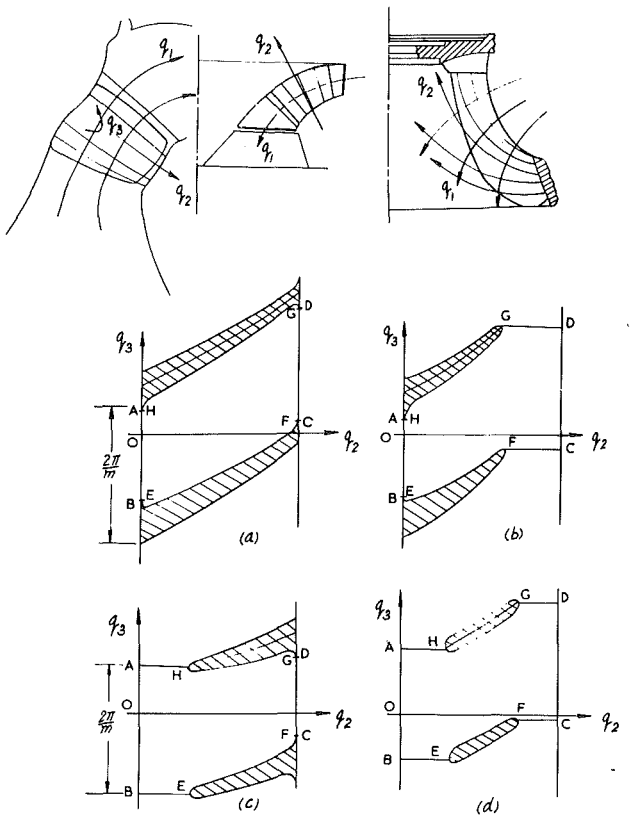


**Fig. 1 Possible variants of sections $q_1$ = const in $q_2$-$q_3$ plane**

$$\int_{\sigma_{j-1}}^{\sigma_j} [\psi_2(s_i) - \psi_2(\sigma)] \bullet dN(s_i,\sigma)$$

$$= \frac{(N_j - N_{j-1})}{2} [2\psi_2(s_i) - \psi_2(\sigma_j) - \pi_2(\sigma_{j-1})]$$

The function $N(s,\sigma)$ has a singularity under $\sigma = s$, since

$$\lim_{\sigma \to s} N(s,\sigma) = \frac{1}{\pi} \bullet \lim_{\xi \to Z_0} \ln|\xi^m - Z_0^m| = \infty$$

However, Lukashevich [3] has shown that integral expression under consideration has a finite limit at the $\sigma_j = s_i$ point.

$$\lim_{\sigma \to s} [\psi_2(s) - \psi_2(\sigma)] \bullet \frac{dN}{d\sigma}(s,\sigma) = -\frac{d\psi_2}{\pi \bullet d\sigma}\Big|_{\sigma_j = s_i}$$

Thus, the integral assumes the following value under $i = j$.

$$\lim_{\sigma \to s} \int_{\sigma_{j-1}}^{\sigma_{j+1}} [\bar{\psi}_2(s_i) - \psi_2(\sigma)] \bullet dN(s_i,\sigma)$$

$$= -\frac{1}{\pi} [\psi_2(\sigma_{j+1}) - \psi_2(\sigma_{j-1})]$$

Knowing the distribution of vortices $\gamma^*(r)$ on the center line of the blade profile under the given geometry of section $q_1$ = const the functions $\zeta_1(s)$ and $\psi_1(s)$ are easily computed. Likewise, the functions $M(s,r)$ and $N(s,r)$ are determined on the boundary contour $L$. However, in this case the location of the points $r$ is along the center line of the blade profile while the points $s$ traverse on the boundary contour $L$.

## Geometry of Flow Field

The solution of the problem is obtained under given geometry of the region and the blade sections on the surface $q_1$ = const. Depending upon the type of runner and the

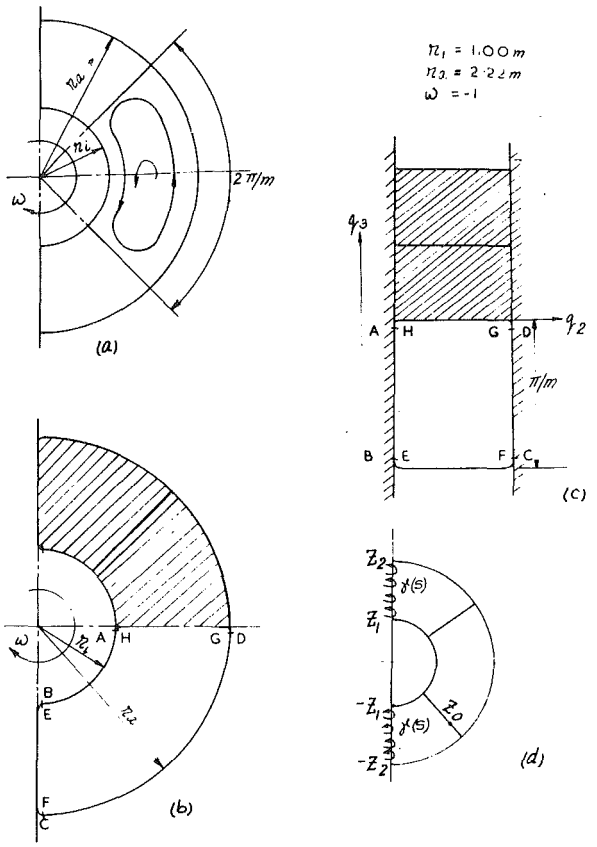


**Fig. 2 Canonical field**

position of section $q_1$ = const in the meridional projection four possible variants exist. Figure 1 shows three types of runners and four types of blade systems in the developed form on coordinated axes $q_2 - q_3$. Figure 1(*a*) represents the case where blades are in contact with the hub and shroud of the runner; Fig. 1(*b*) depicts the system with blades not being in contact with the periphery; Figs. 1(*c*) and 1(*d*) illustrate the cases when blades do not touch the runner hub.

The boundary contour of the flow field is made up of two peripheral arcs AB and CD and two blade lengths EF and GH. Arcs AB and CD refer to the inner and outer rims of the runner, respectively. When the section of the blade profile intersects the hub, the coordinates of the points B, E and A, H correspondingly coincide. Similarly, the coordinates of the points C, F and D, G also coincide when the blade profile intersects the periphery. The direction of movement along the contour L is considered positive if the domain D remains on the left hand side.

## Degree of Accuracy of the Proposed Algorithm

Raabe [1] has deduced equations based on Fourier series to determine the distribution of stream functions in a particular type of flow region. This led to his study of the effect of an axial vortex in creating flow asymmetry for the case of axial flow turbomachines. The distribution of streamlines for the relative flow is shown in this flow region, bounded by two circles and two radial lines (Fig. 2(*a*)). This figure also shows the geometry and the parameters of the canonical flow field. Figure 2(*b*) depicts the region having two blades, each between the two radial lines at an angle $\pi/2$. This has been chosen by the authors to compare Raabe's results with those obtained under the proposed scheme. For the sake of simplicity the domain has been developed on coordinate axes $q_2 - q_3$ (Fig. 2(*c*)). The boundary contour is rounded off at angular points A, B, C, D since it is imperative that the contour of the flow field must be smooth and free of sharp corners.

The computed results have been plotted in Figs. 3 through 6. Figure 3 shows the distribution of the velocity component $c_2$ in the canonical flow region $q_2 - q_3$ under $q_2$ = const. The nature of the velocity distribution on the blade profile is in parabolic form, increasing gradually from the hub, attaining a maximum value in the center of the canal and finally, reaching zero at the periphery. Figures 4 and 5 depict the distribution of streamlines for absolute and relative flows in the region $q_2 - q_3$. In Fig. 6 a comparison is given of results obtained from Raabe's solution and the proposed analysis. These results are shown in the form of a graph for the non-dimensional stream function $\bar{\psi}_0$ for relative flow under $q_3$ = const. It is evident from the figure that the values of $\bar{\psi}_0$ computed by the two methods are quite close to each other. Thus it is confirmed that the proposed theory is in close agreement with that of Raabe.

A check on the degree of accuracy of computation of the functions $\Delta\zeta_1(s)$ and $\psi_1(s)$ due to vortices lying along the center line of the blade profile has been carried out by simple hydrodynamic analysis assuming the uniform vortex distribution $\gamma(s)$ on the blade center line, as shown in Fig. 2(*d*). For the chosen canonical region (Fig. 2(*b*)) the conjugate complex velocity $\bar{V}(Z_0)$ at an arbitrary point $Z_0$ on the boundary contour is as follows:

$$\bar{V}(Z_0) = \frac{\gamma}{2\pi i} \cdot \int_{Z_1}^{Z_2} \frac{dZ}{Z_0 - Z} + \frac{\gamma}{2\pi i} \cdot \int_{-Z_2}^{-Z_1} \frac{dZ}{Z_0 - Z}$$

$$= -\frac{\gamma}{2\pi i} \cdot \ln\left(\frac{Z_0 - Z_2}{Z_0 - Z_1}\right) + \frac{\gamma}{2\pi i} \cdot \ln\left(\frac{Z_0 + Z_2}{Z_0 - Z_1}\right) + c \qquad (71)$$

The complex potential function $\Phi$ can be obtained on integrating the function (71).

$$\Phi = \zeta + i\psi = \frac{\gamma}{2\pi i} \cdot [2(Z_1 - Z_2) + (Z_0 + Z_2) \cdot \ln(Z_0 + Z_2)$$

$$-(Z_0 + Z_1) \cdot \ln(Z_0 + Z_1) -$$

$$-(Z_0 - Z_2) \cdot \ln(Z_0 - Z_2) + (Z_0 - Z_1) \cdot \ln(Z_0 - Z_1)] + c \qquad (72)$$

Simplifying further and separating the real and imaginary parts, the values of velocity potential function and stream function can be determined at point $Z_0$ on the boundary contour. The results so obtained are in fair agreement with the computed results.

Hence, the degree of accuracy of the proposed algorithm and methods of numerical solution seems to be satisfactory for engineering computations.

## Applied Investigation and Results

For investigation purposes three types of runners viz. Diagonal Pump (D-45), Diagonal Turbine (D-60) and Francis Turbine have been chosen (Figs. 7-9). The surfaces $q_1$ = const have been constructed in the meridional plane utilizing the available solution of the quasi three-dimensional problem. For each runner, sections 1,2,3, . . . to be investigated, are arbitrarily selected. The calculations have been made for potential flow at the optimum working regime. In the case of turbines the calculations have even been made for vortex flow with a view to establish a qualitative comparison of secondary flows for potential and vortex flows. Under positive rotational direction of the runner the front wall of the canal is designated as GH and the rear one as EF.

While analyzing the flow, the distribution of functions $\Delta\zeta(\sigma)$, $V_\tau(\sigma)$, $V_n(\sigma)$ and $c_2$ on the boundary contour, as well as the distribution of functions $\psi$ and $c_2$ in the flow field, have been studied [4]. The nature and the form of curves are

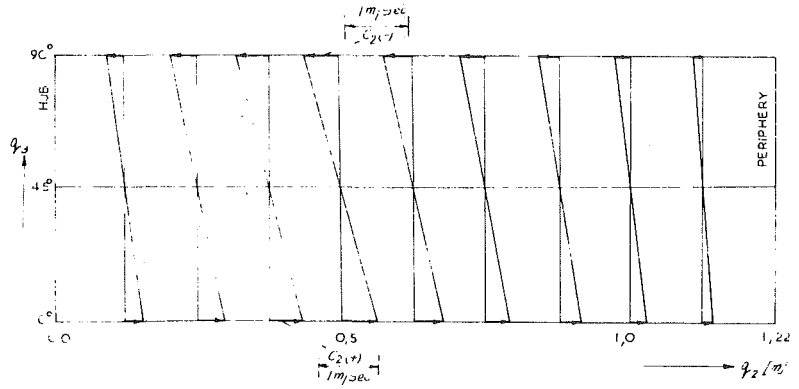


Fig. 3 Distribution of velocity component $c_2$ in the canonical flow field

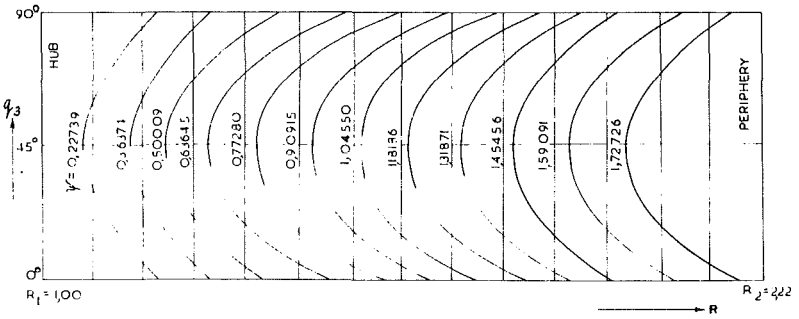


Fig. 4 Distribution of constant streamlines of absolute flow in the canonical region

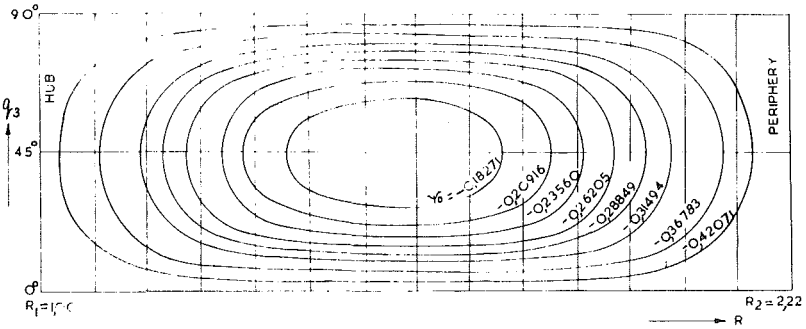


Fig. 5 Distribution of constant streamlines of relative flow in the canonical region

analogous at all the sections. Some of the results are presented here.

Figure 10 shows the distribution of functions $\Delta\zeta\ (\sigma)$, $V_\tau\ (\sigma)$ and $V_n\ (\sigma)$ on the boundary contour for potential and vortex flows. The results shown in the mapped region apply to the Diagonal Turbine, section 1. As observed, the nature of the curves remains the same in two cases but the values are relatively large for vortex flow. The function $V_n\ (\sigma)$ has a positive character on surface GH and negative on EF in view of the positive direction of rotation of runner. The function $\Delta\zeta(\sigma)$ has the same value at the starting and the closing points of the boundary contour giving, thereby, the null varition during the complete traverse of the contour under potential flow. Differentiation of $\Delta\zeta(\sigma)$ with respect to $\sigma$ leads to the distribution of $V_\tau\ (\sigma)$ along the boundary contour with the negative values at the hub to positive at the shroud. The function $V_\tau$ changes abruptly near points A, B, C, D since the flow domain under consideration is a closed one in which points B,E; C,F; D,G and A,H coincide to form a closed flow field. In Fig. 11 is shown the distribution of velocity component $c_2$ in the flow region $q_2 - q_3$ of the Diagonal Pump, section 2. Here $c_2$ attains a zero value roughly in the center of the region and has inverse signs on EF and GH so that the mean value of $c_2$ under $q_2$ = const is nearly zero.

Figures 12 through 16 show the velocity distribution $c_2(q_2)$ at various sections of the chosen runners for potential and vortex flows indicating considerably large velocities for the latter case. At sections near the runner inlet velocities are large for vortex flow as compared to the sections in the vicinity of runner outlet. Tables 1, 2, and 3 give some of the results obtained for the three types of runners. Here the values of the averaged flow parameter $<c_1>$ and the velocity component $c_2$ are given at those points on the surface $q_1$ = const where they are intersected by mean axisymmetric stream surfaces.

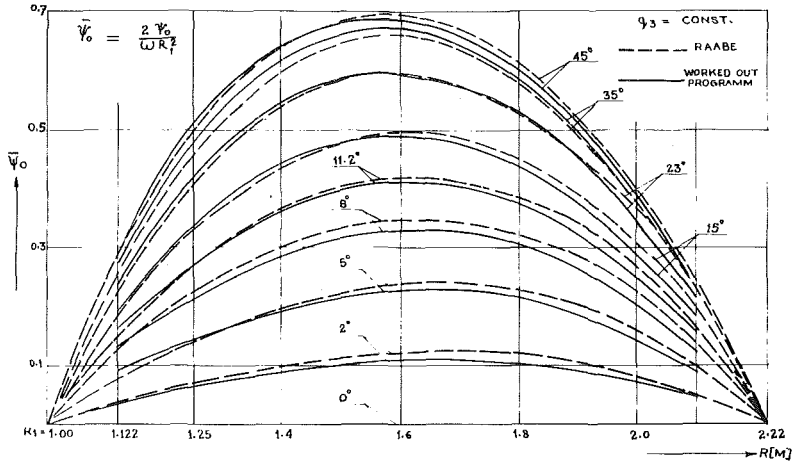


**Fig. 6 Comparison of relative flow stream functions in the canonical region**

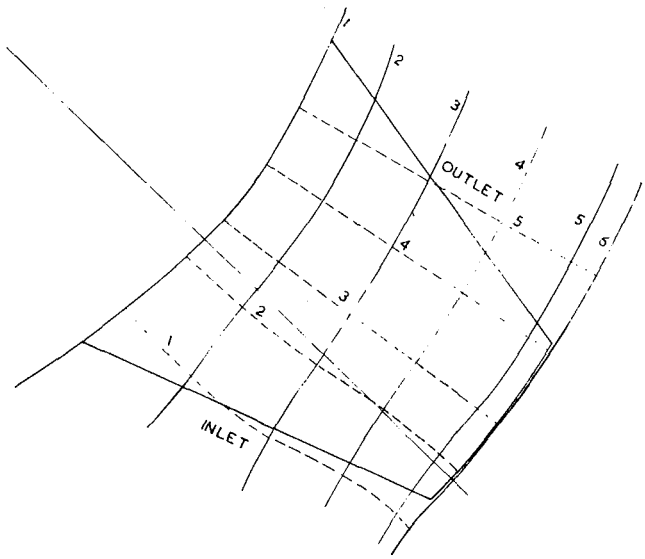


**Fig. 7 Diagonal Pump impeller (D-45): secitons under consideration**

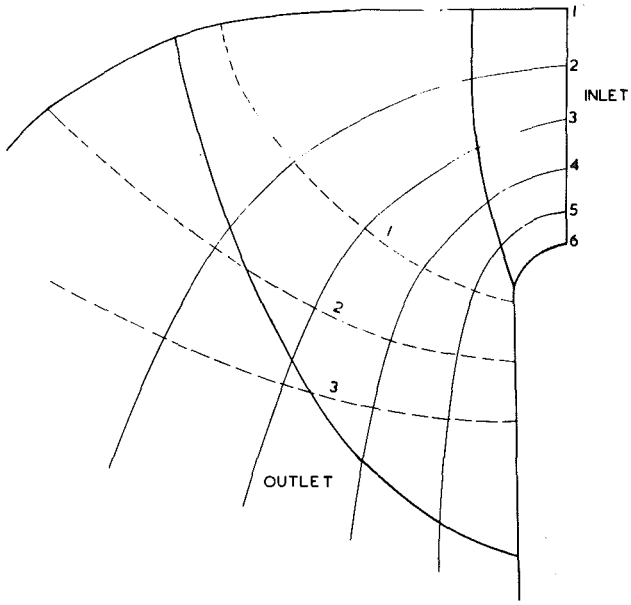


**Fig. 9 Francis Turbine runner: sections $q_1$ = const**

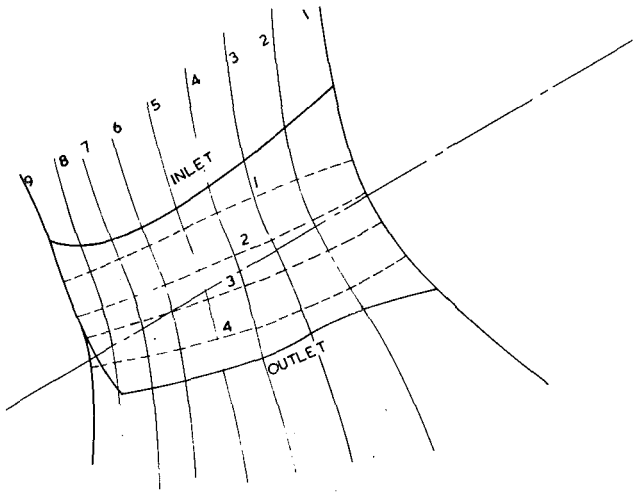


**Fig. 8 Diagonal Turbine runner (D-60): sections under consideration**

It follows from the above results that the values of the velocity component $c_2$ on all observed sections are significant compared to $<c_1>$. The maximum and average values of $c_2/<c_1>$ in the case of the Diagonal Pump are 0.17 and 0.10, respectively. For the Diagonal Turbine and corresponding values are about 0.37 and 0.22 for vortex flow. As observed, $V_n(\sigma)$ is sufficiently large compared to $V_\tau(\sigma)$ in this case, leading to positive values of $c_2$ along both EF and GH surfaces on all streamlines except one (Fig. 15). The axisymmetric stream surfaces will, thus, have a positive inclination for this runner. For potential flow $c_2$ attains its maximum values in the center of the observed sections with a maximum value $\simeq$ 0.15 (Fig. 13). For the Francis Turbine, the maximum and average values for this type of flow are 0.6 and 0.25, respectively (Fig. 14). For vortex flow $c_2$ is nearly equal to $<c_1>$ at a particular place, giving, thereby, the maximum value of $c_2/<c_1> \approx 0.85$ and at the same time the minimum value $\approx 0.12$.

The results confirm that for the selected Diagonal impeller/runner the component $c_2$ has comparatively low values at all observed sections and the change in velocity distribution may not be very significant compared to the one obtained

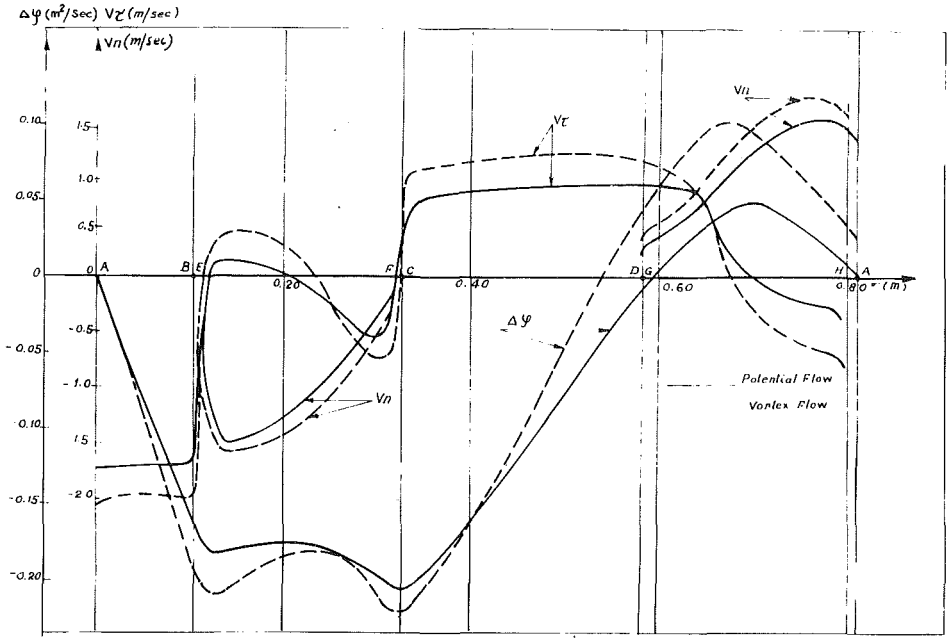


**Fig. 10 Distribution of $\Delta\zeta$ ($\sigma$), $V_\tau$ ($\sigma$), $V_n$ ($\sigma$) in the Z plane: Diagonal turbine runner (D-60), section 1**

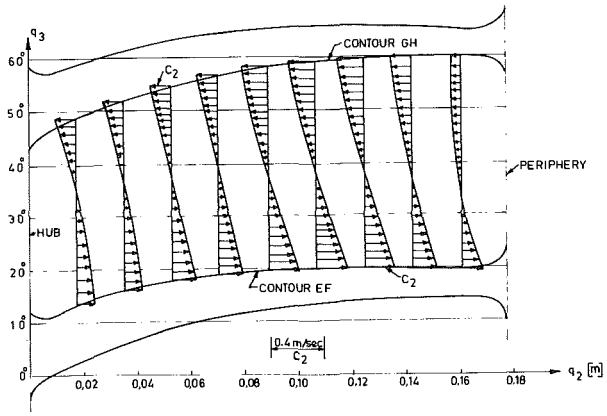


**Fig. 11 Distribution of velocity component $c_2$ in the flow region: Diagonal Flow Pump (D-45), section 2**

**Table 1 Diagonal pump (D-45)**

| Streamline | | 2 | | 3 | | 4 | | 5 | |
|---|---|---|---|---|---|---|---|---|---|
| Velocity m/s | | $<c_1>$ | $c_2$ | $<c_1>$ | $c_2$ | $<c_1>$ | $c_2$ | $<c_1>$ | $c_2$ |
| Section 1 | EF | 1.32 | 0.225 | | | | | | |
| | GH | | −0.190 | | | | | | |
| 2 | EF | 1.365 | 0.126 | 1.350 | 0.210 | 1.370 | 0.225 | 1.360 | 0.140 |
| | GH | | −0.160 | | −0.175 | | −0.175 | | −0.05 |
| 3 | EF | 1.360 | 0.0575 | 1.300 | 0.070 | 1.262 | 0.110 | 1.220 | 0.025 |
| | GH | | −0.0375 | | −0.055 | | −0.105 | | −0.075 |
| 4 | EF | 1.320 | 0.025 | 1.213 | 0.067 | 1.140 | 0.0375 | 1.080 | 0.017 |
| | GH | | −0.015 | | −0.085 | | −0.010 | | −0.050 |
| 5 | EF | 1.260 | 0.100 | 1.150 | 0.025 | | | | |
| | GH | | −0.032 | | −0.050 | | | | |

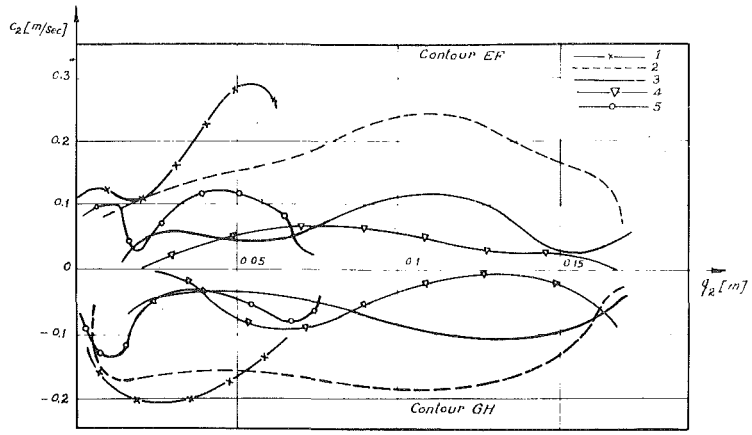


**Fig. 12 Distribution of velocity component $c_2$ on the profile contours: Diagonal Flow Pump (D-45)**

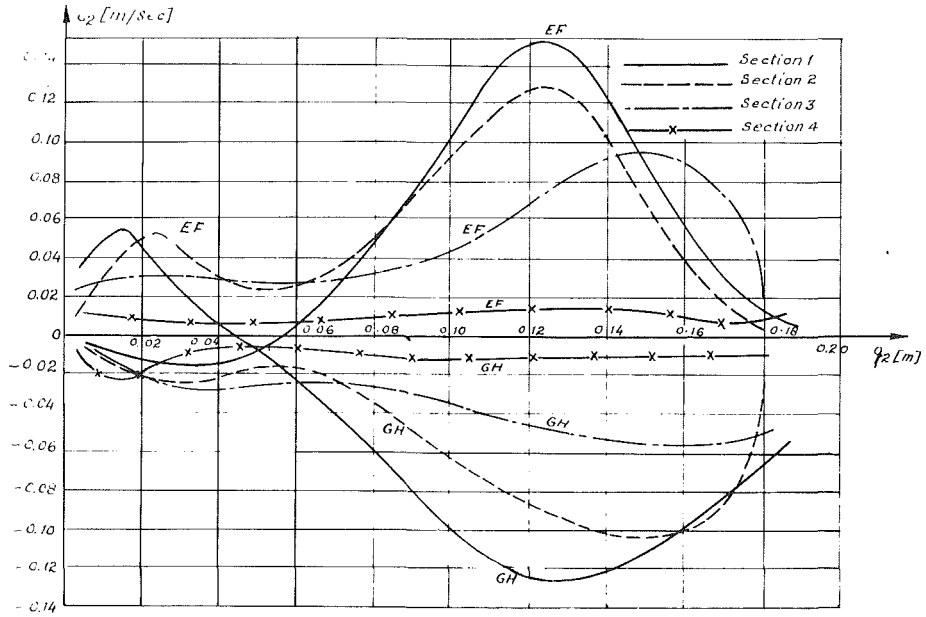


**Fig. 13 Distribution of velocity components $c_2$ ($q_2$) on the blade contours under potential flow: Diagonal Turbine runner (D-60)**

**Table 2 Francis turbine**

| Streamline | | 2 | | 3 | | 4 | | 5 | |
|---|---|---|---|---|---|---|---|---|---|
| Velocity m/s | | $<c_1>$ | $c_2$ | $<c_1>$ | $c_2$ | $<c_1>$ | $c_2$ | $<c_1>$ | $c_2$ |
| Section 1 | EF | 1.175 | −0.42 | 1.593 | −0.56 | 1.95 | −0.60 | 2.38 | −0.47 |
| | GH | | 0.55 | | 0.56 | | 0.40 | | 0.18 |
| 2 | EF | | | 1.47 | −0.38 | 1.735 | −0.36 | 1.925 | −0.38 |
| | GH | | | | 0.30 | | 0.24 | | 0.18 |
| 3 | EF | | | | | 1.561 | −0.37 | 1.61 | −0.22 |
| | GH | | | | | | 0.30 | | 0.14 |
| Vortex flow | | | | | | | | | |
| 1 | EF | 1.175 | 0.02 | 1.593 | −0.13 | 1.95 | −0.34 | 2.38 | −0.53 |
| | GH | | 1.00 | | 0.95 | | 0.75 | | 0.56 |
| 2 | EF | | | 1.47 | −0.38 | 1.735 | −0.28 | 1.925 | −0.30 |
| | GH | | | | 0.43 | | 0.26 | | 0.24 |
| 3 | EF | | | | | 1.561 | −0.43 | 1.61 | −0.375 |
| | GH | | | | | | 0.38 | | 0.10 |

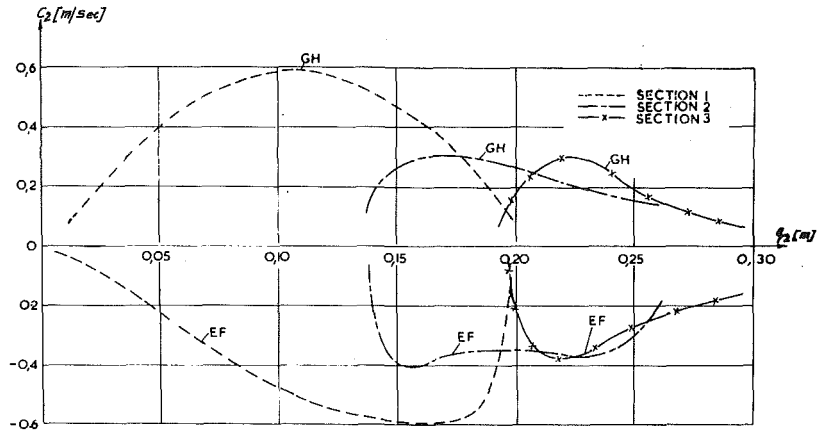


Fig. 14 Distribution of velocity component $c_2$ on the blade contours under potential flow: Francis Turbine runner

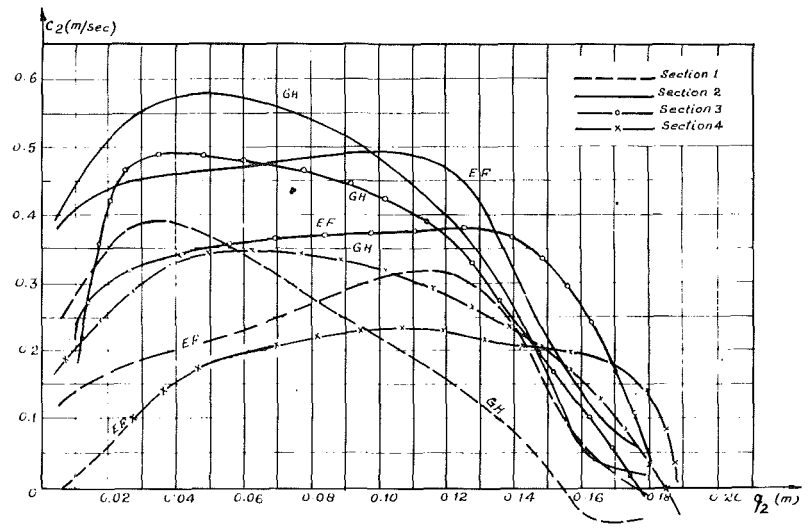


Fig. 15 Distribution of velocity components $c_2$ ($q_2$) on the blade contours under vortex flow: Diagonal Turbine runner (D-60)

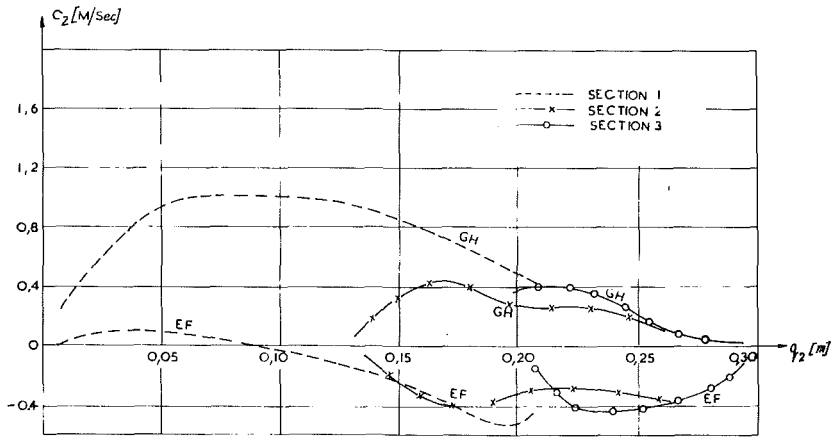


Fig. 16 Distribution of velocity component $c_2$ on the blade contours under vortex flow: Francis Turbine runner

from a quasi three-dimensional solution. For the case of the chosen Francis Turbine the quasi three-dimensional solution gives at certain sections substantial errors when vortex flow is present.

## Conclusions

1. The direct flow problem on the surfaces of rotation $q_1$ = const has been solved giving, on the whole, the solution of

**Table 3 Diagonal turbine (D-60)**

| Streamline | | 2 | | 3 | | 4 | | 5 | |
|---|---|---|---|---|---|---|---|---|---|
| Velocity m/s | | $<c_1>$ | $c_2$ | $<c_1>$ | $c_2$ | $<c_1>$ | $c_2$ | $<c_1>$ | $c_2$ |
| Section 1 | EF | 1.464 | −0.019 | 1.453 | 0.0 | 1.475 | 0.06 | 1.458 | 0.118 |
| | GH | | 0.02 | | −0.02 | | −0.066 | | −0.108 |
| 2 | EF | 1.496 | 0.04 | 1.50 | 0.025 | 1.507 | 0.058 | 1.507 | 0.104 |
| | GH | | −0.026 | | −0.018 | | −0.040 | | −0.072 |
| 3 | EF | 1.491 | 0.03 | 1.48 | 0.026 | 1.48 | 0.035 | 1.513 | 0.056 |
| | GH | | −0.03 | | −0.025 | | −0.030 | | −0.042 |
| 4 | EF | 1.41 | 0.005 | 1.40 | 0.008 | 1.41 | 0.012 | 1.485 | 0.015 |
| | GH | | −0.009 | | −0.10 | | −0.012 | | −0.012 |
| Vortex flow | | | | | | | | | |
| 1 | EF | 1.464 | 0.195 | 1.453 | 0.23 | 1.475 | 0.275 | 1.458 | 0.315 |
| | GH | | 0.390 | | 0.34 | | 0.265 | | 0.205 |
| 2 | EF | 1.496 | 0.450 | 1.50 | 0.47 | 1.507 | 0.485 | 1.507 | 0.490 |
| | GH | | 0.560 | | 0.575 | | 0.530 | | 0.455 |
| 3 | EF | 1.491 | 0.33 | 1.48 | 0.360 | 1.48 | 0.370 | 1.513 | 0.378 |
| | GH | | 0.48 | | 0.475 | | 0.450 | | 0.396 |
| 4 | EF | 1.41 | 0.145 | 1.40 | 0.21 | 1.41 | 0.230 | 1.485 | 0.230 |
| | GH | | 0.320 | | 0.34 | | 0.320 | | 0.275 |

| 6 | | 7 | | 8 | |
|---|---|---|---|---|---|
| $<c_1>$ | $c_2$ | $<c_1>$ | $c_2$ | $<c_1>$ | $c_2$ |
| 1.448 | 0.152 | 1.475 | 0.10 | 1.442 | 0.04 |
| | −0.126 | | −0.114 | | −0.084 |
| 1.496 | 0.128 | 1.516 | 0.078 | 1.491 | 0.026 |
| | −0.094 | | −0.10 | | −0.094 |
| 1.529 | 0.083 | 1.545 | 0.096 | 1.529 | 0.074 |
| | −0.05 | | −0.058 | | −0.074 |
| 1.529 | 0.014 | 1.534 | 0.01 | 1.556 | 0.01 |
| | −0.012 | | −0.008 | | −0.006 |
| 1.448 | 0.300 | 1.475 | 0.180 | 1.442 | 0.035 |
| | 0.130 | | 0.045 | | −0.050 |
| 1.496 | 0.430 | 1.516 | 0.245 | 1.491 | 0.092 |
| | 0.350 | | 0.190 | | 0.033 |
| 1.529 | 0.380 | 1.545 | 0.317 | 1.529 | 0.150 |
| | 0.300 | | 0.160 | | 0.040 |
| 1.529 | 0.208 | 1.534 | 0.195 | 1.556 | 0.115 |
| | 0.226 | | 0.140 | | 0.015 |

the three-dimensional flow problem in the blade systems of hydraulic machines.

2. The solution of the problem has been obtained on the auxiliary plane, conformally connected with the surface $q_1$ = const. Making use of generalized analytic functions, integral equations for velocity and velocity potential function have been found on the basis of a general expression for the complex flow velocity.

3. For the first time during an investigation of flow in the blade systems of arbitrary-type hydraulic machines, the third two-dimensional problem has been formulated and its solution given. This way an approximate solution of the complete three-dimensional flow problem of three-dimensional blade systems is achieved.

4. An algorithm to solve the problem has been worked out and the computer programm developed. It has been

established that the degree of accuracy of the proposed solution is satisfactory, at least for the cases considered.

5. The method has been applied for blade systems pertaining to Diagonal Pumps and Turbines, as well as Francis Turbines. It has been noticed that for potential flow $c_2$ does not go beyond 17 percent; 11 and 38 percent of $< c_1 >$ for the case of Diagonal Pump, Diagonal Turbine, and Francis Turbine, respectively. At certain sections near the runner inlet for vortex flow $c_2$ increases by 37 and 85 percent of $< c_1 >$ for Diagonal and Francis Turbines, respectively.

6. The results demonstrate the allowable accuracy of a quasi three-dimensional solution for the observed Diagonal runners. Because the values of $c_2$ are relatively large for vortex flow in a Francis runner, the results indicate insufficient accuracy of the quasi three-dimensional solution and stress the need for a new more, precise flow model.

## References


1 Raabe, J., "The Relative Vortex as Loss Factor and the Deviation of Stream Surfaces from the Planes of Symmetry in case of an Axial Turbomachine," *Machine Trade*, Vol. 64, No. 3, 1958, pp. 7-13 (German).

2 Korn, G.A., and Korn, T.M., *Mathematical Handbook for Scientists and Engineers*, 2nd Ed., McGraw-Hill, New York, 1968.

3 Lukashevich, V.P., and Samsanov, V.G., "Computer Aided Solution of Rotating Plane Circular Cascade with Arbitrary Profiles," *Trudi VINI Gidromash*, Moscow, No. 37, 1968, pp. 135-140 (Russian).

4 Agarwal, P.K., "The Third Two-Dimensional Problem of Three-Dimensional Blade Systems of Hydraulic Machines," Ph.D. thesis, Moscow Power Institute, Moscow, 1976 (Russian).

# Universal Similarity in the Wakes of Stationary and Vibrating Bluff Structures

**Owen M. Griffin**
Marine Technology Division,
Naval Research Laboratory,
Washington, D.C. 20375

*A universal wake Strouhal number, $St^* = f_s d'/U_b$, has been proposed and is based upon the Strouhal frequency $f_s$ of the incident flow, the measured wake width $d'$ at the end of the vortex formation region, and the mean velocity $U_b$ at the edge of the separated boundary layer. This universal parameter collapses these characteristic parameters for bluff bodies onto a single curve for wake Reynolds numbers between $Re^* = 100$ and $10^7$. The pressure drag, vortex shedding frequency and base pressure are related through an inverse dependence between $St^*$ and a wake drag coefficient $C_D^* = C_D/(d'/d)\,K^2$, where $K = (1-C_{pb})^{1/2}$. The product $St^*\,C_D^*$ is equal to a constant value of $0.073 \pm 0.005$ for $Re^*$ in this same range of Reynolds numbers.*

## Introduction

It is often found that bluff, or unstreamlined, structures display damaging oscillatory instabilities when air and water flow past them. A common cause of these resonant oscillations is the organized and periodic shedding of vortices as the flow separates alternately from the structure. The flow field exhibits a dominant periodicity and the body is acted upon by time-dependent pressure loads which result in steady and unsteady drag forces in-line with the flow and unsteady lift or side forces in the cross flow direction. If the structure is flexible and lightly damped, then resonant oscillations can be excited normal or parallel to the incident flow. For the more common cross flow oscillations the body and the wake have the same frequency near one of the characteristic frequencies of the structure. The shedding then is shifted away from the natural, or Strouhal, frequency at which pairs of vortices would be shed if the structure were stationary.

Bluff body wakes have been the subject of constant study since the 1870's because of the intrinsic complexities and the practical importance of these flows. Just recently McCroskey [1] wryly noted that the problem of a bluff cylinder in a cross flow may have been invented "to insure a perpetual livelihood for fluid dynamicists and flow-visualization photographers."

This paper investigates the question of fluid dynamic similarity in the wakes of bluff bodies. Griffin [2] and Simmons [3] recently have introduced a universal Strouhal number which characterizes the wakes of stationary two-dimensional bluff bodies with fixed and free separation points, vibrating bluff structures, and cylinders in confined flow and at large yaw angles to the incident flow. This Strouhal number $St^* = f_s d'/U_b$ is based upon the natural Strouhal frequency of the wake, $f_s$; the wake width $d'$ at the end of the vortex formation region; and the mean velocity $U_b$ at the edge of the boundary layer. The pressure drag, vortex shedding frequency, and base pressure are also related by means of an inverse dependence between $St^*$ and a wake drag coefficient $C_D^* = C_D/(d'/d)\,K^2$, where $K = (1 - C_{pb})^{1/2}$.

## Related Investigations

Some years ago Roshko [4] proposed a universal Strouhal number to scale the flow separation and vortex formation which take place in the near wakes of stationary bluff bodies of various cross sections. More recently Bearman [5] expanded on Roshko's original ideas and proposed a somewhat different semi-empirical model for unifying the various parameters which affect the vortex formation and the wake dynamics. Both formulations were similar in that the wake width – the principal length scale in the two models – was determined analytically. In Roshko's model the wake width was determined from a "notched hodograph" theory, while in Bearman's formulation the Kronauer stability criterion was used as a basis for computing the wake width. The vortex shedding frequency and the base presure or, equivalently, the mean velocity on the free streamline at separation were obtained from experimental measurements in both cases.

Calvert [6] introduced a universal Strouhal number in his measurements of the wake formation behind cones with different vertex angles, and defined $d'$ to be the *measured* transverse distance between the peaks of the velocity fluctuations, at the point of minimum mean pressure on the downstream axis of the wake. The Strouhal number $St^*$

Contributed by the Fluids Engineering Division and presented at the Winter Annual Meeting, Chicago, Ill., November 16-21, 1980, of THE AMERICAN SOCIETY OF MECHANICAL ENGINEERS. Manuscript received by the Fluids Engineering Division, October, 1979. Paper No. 80-WA/FE-4.

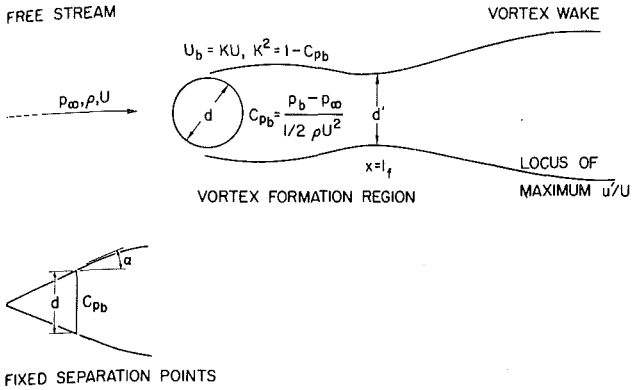


**Fig. 1 Characteristic length, velocity, and pressure scales for the wakes of two-dimensional bluff bodies**

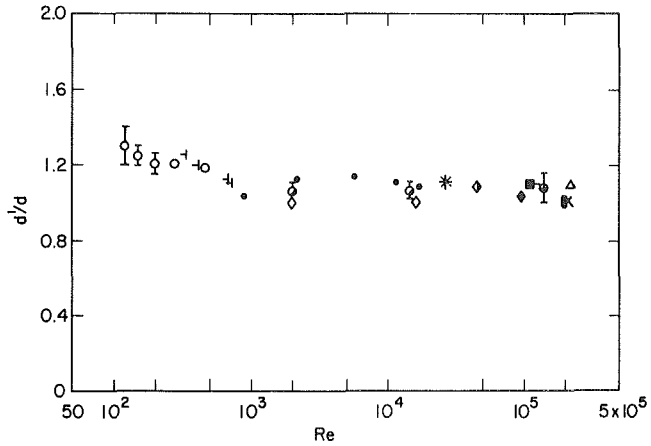


**Fig. 2 Wake width $d'/d$ for circular cylinders plotted against the Reynolds number Re; legend as in Table 1, except for the data (⊕) of Bailou [10]**

obtained in this way was found to be constant at about St* = 0.19 for cone angles between $\alpha = 0$ and 90 deg.

The measured wake width $d'$ concept remained dormant until Simmons [3] and Griffin [2] proposed the use of such a length scale for the vortex formation processes in the wakes of two-dimensional bluff bodies. Physically $d'$ is the wake width at the end of the vortex formation region, where a vortex is fully formed, is shed and then moves away from the base region.

Simmons introduced a universal Strouhal number St*, based on the measured wake width $d'$, for the wakes of two-dimensional bluff bodies with fixed separation angles between $\alpha = 0$ and 90 deg and found a constant value of about St* = 0.163. Griffin at the same time introduced the same St* as part of an investigation of similarity in the wakes of circular cylinders vibrating in the regime of locking-on between the vortex and vibration frequencies. An average St* = 0.178 was found for wake Reynolds numbers between 700 to $5(10^4)$ for vibrating cylinders.

Ramberg [7] has shown that the concept of universal wake similarity is valid for circular cylinders at yawed incidence. Measurements of the vortex shedding frequency $f_s$, the wake width $d'$ and the base pressure coefficient $C_{pb}$ were made at yaw angles up to 60 deg away from normal incidence.

## The "Universal" Strouhal Number

Roshko [4] showed that a characteristic nondimensional group of parameters for scaling of the wakes of bluff bodies could be derived by applying relatively simple physical arguments. The result, after several improvements and refinements [2,3,5,6], is a universal wake Strouhal number St* for vortex shedding from bluff bodies based upon measured parameters of the wake.

If one considers two shear layers a distance $d'$ apart with the velocity just outside the layers equal to $U_b$, the mean velocity at separation, then a wake Strouhal number can be defined as

$$\mathrm{St}^* = \frac{f_s d'}{U_b} = \mathrm{St}\left(\frac{U}{U_b}\right)\left(\frac{d'}{d}\right). \tag{1}$$

The characteristic frequency $f_s$ associated with the configuration is assumed to be proportional to the ratio $U_b/d'$, as sketched in Fig. 1. Here the usual Strouhal number of the cylinder is

$$\mathrm{St} = \frac{f_s d}{U} \tag{2}$$

where $d$ is the cylinder diameter and $U$ is the incident flow speed. When Bernoulli's equation is applied to the flow just outside the boundary layer at separation, the base pressure coefficient is

$$C_{pb} = \frac{2(p_b - p_\infty)}{\rho U^2} = 1 - \left(\frac{U_b}{U}\right)^2. \tag{3}$$

If the base pressure parameter $K = U_b/U$ is introduced, then

$$K^2 = 1 - C_{pb} \tag{4}$$

and

$$\mathrm{St}^* = \frac{\mathrm{St}}{K}\left(\frac{d'}{d}\right). \tag{1a}$$

A wake Reynolds number Re* is defined in a corresponding way as

$$\mathrm{Re}^* = \frac{U_b d'}{\nu} = \mathrm{Re}\ K\left(\frac{d'}{d}\right), \tag{5}$$

where $\mathrm{Re} = Ud/\nu$ is the usual free-stream Reynolds number.

## The Wake Width for Bluff Body Flows

**Stationary Circular Cylinders.** The wake width is an important scaling parameter for the wakes of all bluff bodies with both free (a circular cylinder) and fixed (a flat plate, $D$-section, etc.) separation points. The width $d'$ of the wake behind a stationary circular cylinder is plotted as a function of the Reynolds number in Fig. 2, and the results encompass the entire range of subcritical Reynolds numbers over which regular vortex shedding takes place. The legend for the data points is given in Table 1. With the exception of Reynolds numbers below Re = 500, there is very little dependence of the wake width upon the Reynolds number. This is true for both smooth circular cylinders in very low turbulence level flows [8,9] and moderate, or more typical, wind tunnel turbulence level flows [10,11,12].

Several of the points plotted in the figure have been calculated from the simple equation

$$\frac{d'}{d} = \frac{C_D}{-C_{pb}}, \tag{6}$$

which can be derived from free streamline theory when the base pressure is constant [13,14]. Roshko's notched hodograph free-streamline theory, to which this equation is closely related, allows $C_D$ and $d'$ to be calculated as functions of $K$. The solution then is closed by measuring $C_{pb}$ (and thus $K$). When $C_D$ and $C_{pb}$ are measured, the wake width then follows from equation (6). The approximation given by equation (6) holds for stationary circular cylinders with no separation bubbles, roughness effects on transition, etc. as in the critical Re range. Roshko [4] derived free streamline equations for not only a circular cylinder but also for other

**Table 1 Universal wake similarity for two-dimensional bluff bodies. Legend for experimental data employed in the St* versus Re and $C_D$ versus correlations**

| Symbol | Bluff body type | Medium | Investigators |
|---|---|---|---|
| ○ | Smooth circular cylinder (stationary and vibrating) | Air and water | Griffin (1978)[+] |
| ⊣ | Smooth circular cylinder at yawed incidence | Air | Ramberg (1978)[+] |
| + | Fixed separation angles between $\alpha = 0°$ (D-shaped) and $\theta = 90°$ (Flat Plate) | Air | Simmons (1977)[+] |
| ◥ | Blunt-based hydrofoil models | Air and water | Blake (1977)[+] |
| ◆x | Flat Plate, half cylinder | Air | M.E. Davies (1977 private communication)[+]; Bearman & Davies (1975) |
| ◆ | Smooth circular cylinder in confined flow | Air | Modi & El-Sherbiny (1977)[++] |
| ⊛ | Smooth circular cylinder | Air | Cantwell (1976)[+, ++] |
| △ | Smooth circular cylinder | Air | Brüun & Davies (1975)[++] |
| * | Smooth circular cylinder with and without splitter plate; flat plate | Air and water | Apelt & West (1975); Apelt, West & Szewczyk (1973)[+, ++] |
| ■ | Smooth circular cylinder | Air | Batham (1973)[++] |
| ◁ | Triangular cylinder ($\alpha = 30°$) | Air | Twigge-Molecey & Baines (1973); reference (31) |
| ◆ | Smooth circular cylinder in turbulent flow | Air | Surry (1972) |
| ⊖ | Rectangular cylinders | Air | Bearman & Trueman (1972) |
| ⊛< | Smooth circular cylinder | Air | Bearman (1969)[++] |
| ◇ | Smooth circular | Air | Gerrard (1965, 1966)[++] |
| ▽-▽ | D-shaped cylinder with and w/o splitter plates | Air | Bearman (1964)[+] |
| ⊛ | Smooth circular cylinder | Air | Roshko (1961)[++] |
| ● | Smooth circular cylinder | Air | Roshko (1954, 1955)[++] |

[+]Wake width $d'$ measured at the end of the vortex formation region.
[++]Wake width $d'$ from equation (6).

stationary bluff shapes with separation angles up to $\alpha = 90$ deg (a flat plate).

There is good agreement between equation (6) and the wake width $d'$ measured directly from wake velocity traverses by Cantwell [12]. The vortex formation length $l_F$, the wake width $d'$ from hot-wire traverses of the wake, the drag coefficient $C_D$ and the base pressure $C_{pb}$ were measured at a Reynolds number of Re = 1.4 ($10^5$). The wake widths deduced from equation (6) and from rms profiles of the coherent vortex structure of the turbulent wake are virtually identical and are plotted as a single point in Fig. 2. Apelt, West and Szewczyk [15] also measured $d'$, $C_{pb}$, and $C_D$, and their results at Re = 2.5 ($10^4$) also are in good agreement with equation (6).

The results for $d'$ obtained with equation (6) from the experiments of Bruun and Davies [11], Surry [16] and Batham [17] are in excellent agreement with the wake widths measured directly by Ballou [10], Bloor and Gerrard [9], and Ramberg [7] over the Reynolds number range from Re = 700 to 2 ($10^4$). The wake width behind a circular cylinder increases somewhat at the lowest Reynolds numbers in Fig. 2, but there is only a slight Reynolds number dependence from Re = 700 to 2 ($10^5$) for smooth cylinders in uniform flow.

**Vibrating Circular Cylinders.** When a bluff structure is self-excited by vortex shedding or is forced to vibrate laterally relative to an incident flow in the regime of locking-on or wake capture, there is a complex nonlinear interaction between the wake and the body. The vortex circulation and the base suction are strongly enhanced, as are the unsteady lift and the steady drag forces. The response of the wake is dependent upon both the displacement amplitude and the frequency of the oscillation as shown, for example, by Griffin and Ramberg [2,18,19], Bearman and Davies [20] and Stansby [21].

The wake width measured downstream from a vibrating circular cylinder (both self-excited and forced) is plotted in Fig. 3 against the vibration frequency (normalized by the corresponding Strouhal frequency $f_s$) for a typical lateral displacement of 30 percent of a diameter. Also plotted in the figure are measurements of the base pressure coefficient $C_{pb}$ for a forced vibrating cylinder [21]. The similarities of the wake response to the vibrations in terms of the wake width $d'$ at formation and the base pressure coefficient $C_{pb}$ are evident

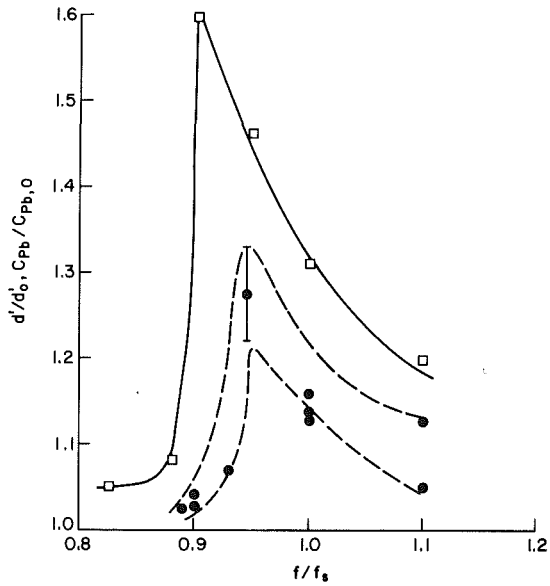


**Fig. 3 Wake width $d'$ and base pressure coefficient $C_{pb}$ measured in the wake of a vibrating circular cylinder, in the regime of locking-on between the wake and cylinder frequencies. Subscripts "O" denote corresponding measurements in the wake of a stationary cylinder. Cylinder displacement amplitude (peak-to-peak) = 0.30 diameter. Present wake width measurements, ●, Reynolds number = 150–700; base pressure measurements, Stansby [21], □, Reynolds number = 8600.**

for this case of locking-on between the vortex and vibration frequencies. All of the data in the figure are divided by corresponding stationary cylinder measurements in order to minimize any Reynolds number effects. Only the frequency dependence of the wake is shown in Fig. 3; both the wake width and base suction increase monotonically with the cylinder displacement at a constant frequency in the regime of locking-on, as shown by the results of Griffin [2] and Stansby [21].

**Other Two-Dimensional Bluff Bodies.** The wake widths

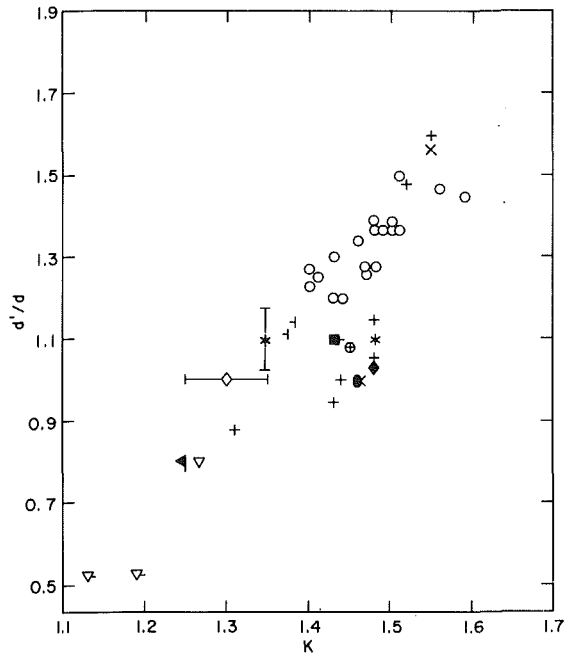


**Fig. 4 Wake width $d'/d$ plotted against the base pressure parameter $K$; legend as in Table 1**

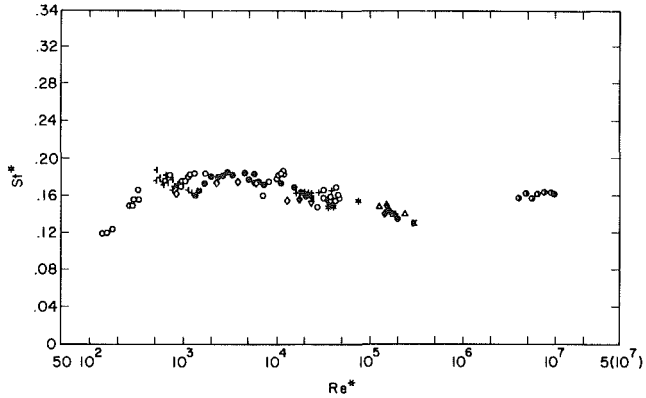


**Fig. 5 Universal Strouhal number St* plotted against the wake Reynolds number Re*; legend as in Table 1.**

measured at the end of the vortex formation region for these and other bluff bodies are plotted against the base pressure parameter $K$ in Fig. 4. The body shapes for which results are included in the figure range from stationary, blunt-based $D$-shaped cylinders of 6:1 aspect ratio with turbulent boundary layers [22] and of 1.5:1 aspect ratio with laminar boundary layers [3]; to stationary circular cylinders at Reynolds numbers between Re = 120 and 2 ($10^5$); and to wedges, flat plates and half-cylinders normal to the incident flow. Also included in the plot are results for vibrating circular cylinders in the regime of locking-on between the vortex and vibration frequencies [2].

The smallest measured wake widths at formation, for $K$ = 1.1 to 1.2, were obtained by Bearman [22] when the vortex formation was delayed by wake splitter plates. The data in Figure 4 correspond to splitter plate lengths of up to one base height, since under these conditions a regular vortex street was formed. The largest wake widths are those measured downstream from a flat plate, from a half-cylinder and in the wakes of vibrating cylinders.

The results in Fig. 4 demonstrate in general the relationship between bluffness (as denoted by $d'$) and base suction or drag (as denoted by $K$). An overall dependence between $d'$ and the separation angle $\alpha$ is also evident. Simmons [3] employed seven models with separation angles between $\alpha$ = 0 deg ($D$-section cylinder) and $\alpha$ = 90 deg (flat plate); see the sketch in Fig. 1. Both $D$-section cylinders have the highest base pressures (lowest drag) and the narrowest wakes of the bodies without wake interference; as the separation angle increases, the wake becomes wider as the bluffness of the body increases.

The vibrating cylinder measurements in Fig. 4 demonstrate the increased bluffness that accompanies the lateral vibrations in the regime of locking-on between the vortex and vibration frequencies. There is a decrease in base pressure as the cylinder vibrates (see Fig. 3) and a corresponding increase in the mean separation velocity $U_b$ as the wake width increases.

## Experimental Measurements of St*

The Strouhal number St* is plotted against the wake Reynolds number Re* in Fig. 5 and the legend for the data again is given in Table 1. The results span five decades of the Reynolds number, from Re* = $10^2$ to $10^7$, except for the critical regime[1] near Re* = $10^6$. The data for St* encompass both stationary and vibrating bluff cylinders and bodies with blunt trailing edges, yawed and normal to the incident flow. There is some Reynolds number dependence at the lowest Reynolds numbers, as is the case for the classical St versus Re relationship, but only a slight dependence of St* upon Re* over the remainder of the subcritical range.

A number of results for yawed cylinders are included in the correlation [7]. The yaw angle $\theta$ of a stationary circular cylinder was increased to as much as 60 deg from normal incidence and simultaneous measurements were made of the wake structure, including the base pressure coefficient $C_{pb}$, the wake width $d'$ at formation and the shedding frequency $f_s$. The flow deviated substantially from the so-called Independence Principle, or Cosine Law, where the wake flow and fluid forces are assumed to be governed by the normal component of the incident velocity to the cylinder, but the wake parameters $C_{pb}$, $d'$, and $f_s$ varied in such way as to maintain a nearly constant value of St*. The base suction $C_{pb}$ at yaw angles of $\theta$ = 40 to 60 deg was 20 and 30 percent higher than would be predicted by the Independence Principle.

Data for St* derived from nominally smooth circular cylinders in uniform flow reach a limiting range of St* = 0.14 to 0.15 as the critical Reynolds number, Re* = 2 to 3 ($10^5$), is approached. All of the St* values obtained in this range from the results of Batham [17] Bearman [8], Bruun & Davies [11] and Cantwell [12] are in good agreement. The flow was subcritical in all cases, at Reynolds numbers just below the critical value. For bodies with fixed separation points the Reynolds number dependence just discussed will not occur, but the Strouhal number likely will remain near St* = 0.16.

The measurements of St* made at transcritical Reynolds numbers by Roshko [14] are also plotted in Fig. 5. These results were based upon measurements of the shedding frequency, base pressure, and drag and confirm the universality principle not only at Reynolds numbers less than $10^5$ but also at higher Reynolds numbers at least to Re* = $10^7$.

There is considerable diversity in the results for St* over the Reynolds number range from Re* = $10^4$ to $10^5$. The body

[1] In this and the sections that follow, reference is made to the subcritical, critical and supercritical ranges of Reynolds number. This terminology applies rigorously only to the circular cylinder where the drag crisis occurs at Re* ≈ $10^5$. These various ranges do not apply directly to bluff bodies with fixed separation points, where the wake formation is relatively uninfluenced by Reynolds number.

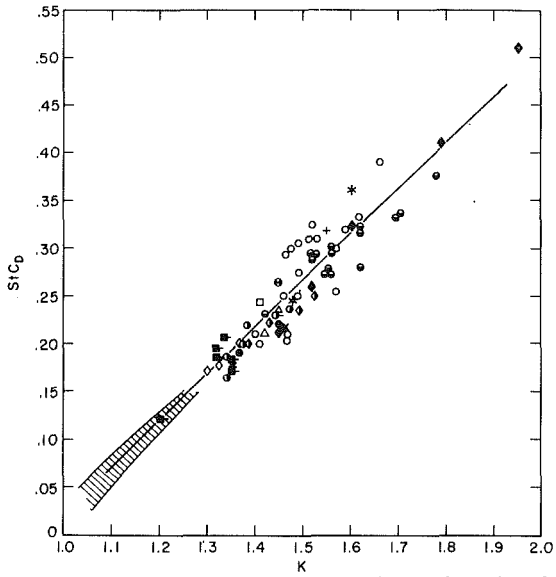


**Fig. 6 The product of drag coefficient and Strouhal number, St $C_D$, plotted against the base pressure parameter $K$; legend as in Table 1. A least-squares fit to the data is given by the solid line, equation (7).**

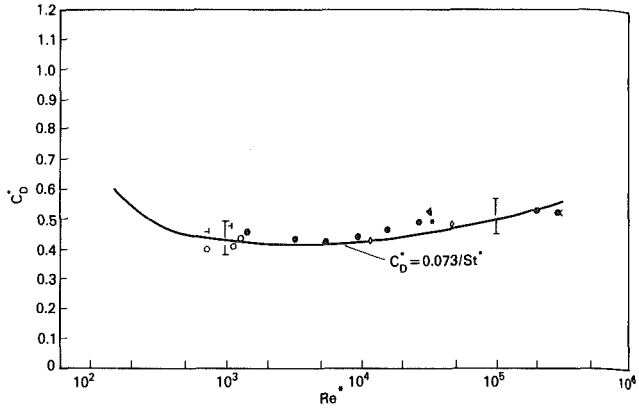


**Fig. 7 Wake drag coefficient $C_D{}^*$ plotted against the Reynolds number Re*. Legend as in Table 1. The solid line is equation (9), $C_D{}^* = 0.073/St^*$.**

cross-sections included there (see Table 1) consist of stationary and vibrating circular cylinders, and a variety of bluff bodies with fixed separation angles between $\alpha = 0$ deg ($D$-section cylinder) and 90 deg (flat plate). Several of the models [22,23] also include wake interference with splitter plates; Bearman's experiments with a blunt-based, $D$-section cylinder included direct measurement of the wake width $d'$ at formation in addition to the shedding frequency $f_s$ and the base pressure coefficient $C_{pb}$. The experiments reported by Blake [24], Apelt, West, and Szewczyk [15] and Simmons [3] also included the simultaneous measurements of the parameters that comprise the universal Strouhal number St*.

The values of St* for stationary circular cylinders obtained from Roshko's and Gerrard's experiments [9,23,25,26], and based on the wake width $d'$ as shown in Fig. 2, are plotted in Fig. 5. There is a slight Reynolds number dependence over the range Re* = $10^3$ to $10^4$, but in general these results for St* also are in good agreement with the concept of universal wake similarity.

Measurements of $C_{pb}$, $C_D$ and St were made for circular cylinders in a confined air flow by Modi and El-Sherbiny [27] at subcritical Reynolds numbers near Re = $10^5$ and for area blockage ratios up to $d/H = 0.36$. The results for St* obtained from equations (1) and (6)[2] are plotted in Fig. 5, for blockage ratios up to 20 percent of the wind tunnel area. The results are in excellent agreement with the other values of St* plotted in the figure near Re* = $10^5$. For blockage ratios greater than 20 percent the pressure distribution on the rear face of the cylinder is increasingly non-uniform and a free-streamline approximation no longer is valid.

Measurements of St* for circular cylinders vibrating in the regime of locking-on between the vortex and vibration frequencies at wake Reynolds numbers Re* between 140 and 5($10^4$) are plotted in Fig. 5. The various experiments upon which the vibrating-cylinder data for St* and Re* were based are described in detail elsewhere [2]; the cylinder displacement amplitudes in the experiments extended up to a full cylinder diameter (peak-to-peak), and the locked-on wake frequencies were between 70 and 120 percent of $f_s$. The drag and base pressure on the vibrating cylinders were increased by as much as 80% from the corresponding measurements made for stationary cylinders at Reynolds numbers below $10^5$ [21,28].

The plot of St* versus Re* in Fig. 5 demonstrates the universal similarity of bluff body wakes over a Reynolds number range from $10^2$ to $10^7$, for two-dimensional smooth cylinders in uniform flow. These results generalize further the original hypotheses of Roshko [4] when St* and Re* are based upon the measured wake width as characterized by Calvert [6], Griffin [2], and Simmons [3].

## Wake Momentum, Base Pressure, and Drag

Bearman [5], in his formulation of a universal Strouhal number based upon the Kronauer stability criterion, showed that St* was dependent only upon the pressure drag coefficient $C_D$, the base pressure coefficient $C_{pb}$ (or $K$) and the Strouhal number St. Simmons [29] reconsidered Bearman's approach and found that the Kronauer criterion was not applicable for $K$ greater than 1.5. For this reason the criterion is no longer considered to be universally applicable, since its validity extends only to $K = 1.5$ whereas the ranges of $C_{pb}$ and $K$ over which regular vortex takes place from bluff cylinders extend at least to $K = 2$. However, as Bearman recently noted (private communication, 1978), the breakdown of Kronauer's hypothesis does not invalidate the basic argument that a universal correlation exists between St, $C_D$ and $K$. This point is now considered.

The product St $C_D$ is plotted against the base pressure parameter $K$ in Fig. 6, and the data encompass the entire range of conditions over which vortex shedding takes place from bluff bodies. The legend for the data points in the figure is given once again by Table 1. The shaded area at low values of $K$ refers to experiments reported by Bearman [5] for vortex shedding from blunt-based, $D$-section cylinders. These experiments included interference with the vortex formation by means of base bleeding of low velocity air and by wake splitter plates. A single point from the experiments conducted by Batham [17] with circular cylinders in the critical range of Reynolds numbers falls within this range of the correlation.

At the higher values of $K$ the results encompass a wide range of conditions that includes smooth circular cylinders in

[2] Equation (6) is a limiting case of the more general free-streamline wake width, base pressure and drag relation. For confined flow

$$C_D = \left\{ K^2 - \frac{1}{\left(1 - \frac{d'}{d}\left(\frac{d}{H}\right)\right)} \right\} \frac{d'}{d} \tag{6a}$$

where $H$ is the height of the channel. When $d/H \to 0$, this reduces to equation (6).

uniform flow at subcritical, critical and supercritical Reynolds numbers, and smooth circular cylinders in highly turbulent incident flows [16] at subcritical Reynolds numbers. Rough circular cylinders in uniform and turbulent flows in the critical range of Re* [17] also fit nicely into the correlation.

The results obtained for vortex shedding from flat plates cover the same range of wake momentum or bluffness as vibrating circular cylinders [2] and circular cylinders in confined flow [27] at the largest values of $K$. The base pressure parameter is a measure of the bluffness of a cylindrical body, and the data in Fig. 6 confirm once again that flow confinement, rectangular cylinders and vibration in the locking-on regime result in the most extreme conditions of wake momentum and bluffness. In fact, the measurement by Modi and El-Sherbiny of vortex shedding from a circular cylinder at a blockage of 36 percent resulted in the largest value of the base pressure parameter, $K = 1.95$, observed by any of the host of investigators listed in Table 1. Previous measurements of $C_D$, St, and $K$ for a rectangular cylinder with a critical aspect ratio (depth/width) of $t/d = 0.6$ [30] was thought to be the limiting bluffness condition.

The drag and base pressure measurements made by Bearman and Trueman [30] showed a slight dependence on the cylinder aspect ratio $t/d$; this is considered by them to be an effect of increasing diffusion length or shear layer thickness, on the vortex formation, as the afterbody length is increased from the case of a flat plate ($t/d = 0$) to a square cylinder ($t/d = 1$). Near the critical aspect ratio the shear layers never became parallel and the pressure coefficient $C_{pb}$ was very non-uniform over the downstream face of the cylinder.

To give a quantitative idea of the correlation between drag, base pressure and shedding frequency, a least-squares fit to the St $C_D$ versus $K$ correlation is plotted in Fig. 6. A linear fit to the data

$$\text{St } C_D = a + bK \qquad \begin{matrix} a = -0.48 \pm 0.03 \\ b = +0.50 \pm 0.02 \end{matrix} \tag{7}$$

yielded the minimum mean-square deviation for all polynominal functions up to order $n = 10$, though the mean-square deviations for $n = 1$, 2, and 3 were virtually indistinguishable.

The dependence between St $C_D$ and $K$ was originally suggested from considerations of universal wake similarity [5] and all of the data that are plotted on the St* versus Re* curve in Fig. 5 are included in the correlation. It is possible on the basis of this dependence to introduce a wake drag coefficient $C_D{}^*$ and consequently to introduce a universal wake drag-Strouhal number-Reynolds number relationship. Let

$$C_D{}^* = \frac{C_D}{K^2 (d'/d)} = \frac{\text{(Force)}}{\tfrac{1}{2}\rho U_b^2 d'} \tag{8}$$

and then introduce both St* and $C_D{}^*$ into equation (7). The result is

$$\text{St}^* C_D{}^* = f(K) = \frac{a + bK}{K^3} \tag{9}$$

and some straightforward calculations show that $f(K) = 0.073 \pm 0.005$ is virtually constant, i.e. $0.067 < \text{f(K)} < 0.078$, between the limits of $K = 1.2$ and 2. On the basis of equation (9) there is an inverse dependence between the Strouhal number St* and the drag coefficient $C_D{}^*$ and the result is plotted in Fig. 7. The solid line in the figure corresponds to a faired line through the data for St* versus Re* in Fig. 5 and the bounds represented by equation (9) are shown at Re* = $10^3$ and $10^5$. There is excellent agreement of equation (9) with a representative distribution of data points from experiments conducted by several of the investigators listed in Table 1. There is correlation not only between the Strouhal number St* and the Reynolds number Re* as shown in Fig. 5, but also a universal correlation between the drag coefficient $C_D{}^*$ and the Reynolds number when the inverse dependence between St* and $C_D{}^*$ is derived from equation (9).

## Summary and Concluding Remarks

A universal wake Strouhal number, St* = $f_s d'/U_b$, has been proposed and is based upon the natural Strouhal frequency $f_s$ of the incident flow to a bluff cylindrical structure, the *measured* wake width $d'$ at the end of the vortex formation region, and the velocity $U_b$ at the edge of the separated boundary layer.

The wake width $d'$ for stationary and vibrating circular cylinders and other two-dimensional bluff bodies is correlated with the base pressure parameter $K = U_b/U$, where $K = (1 - C_{pb})^{1/2}$ and $C_{pb}$ is the cylinder's base pressure coefficient.

St* collapses these characteristic wake scales onto a single curve for Reynolds numbers between 100 and $10^7$. For Re* less than 500, St* increases with Re* as is usually the case. For Re* between 500 to $10^4$ the data for St* are distributed about a value of 0.17, with some Reynolds number dependence. The data for St* are distributed about a mean value of about 0.16 for Re* between $10^4$ and $10^5$, and a range of St* = 0.14 to 0.15 is approached at the critical Reynolds number for a circular cylinder of $2(10^5)$ to $3(10^5)$.

The pressure drag, vortex shedding frequency and base pressure for bluff body wake flows are related through an inverse dependence between St* and a wake drag coefficient $C_D{}^* = C_D/(d'/d)K^2$. The product St* $C^*{}_D$ is equal to a constant value of $0.073 \pm 0.005$.

This paper has been prepared at part of the research program of the Naval Research Laboratory. The author is grateful to A. Roshko and P.W. Bearman for several helpful discussions on the subject of wake similarity.

## Statement of Experimental Uncertainty

All of the nondimensional parameters in this paper, such as St*, Re*, $C^*{}_D$ are estimated to be correct within ±10 percent, unless otherwise noted specifically, i.e. equations (7) and (9).

## References

1 McCroskey, W.J., "Some Current Research in Fluid Dynamics," ASME JOURNAL OF FLUIDS ENGINEERING, Vol. 99, 1977, pp. 8-39; ASME Freeman Scholar Lecture.

2 Griffin, O.M., "A Universal Strouhal Number for the 'Locking-On' of Vortex Shedding to the Vibrations of Bluff Cylinders," *J. Fluid Mech.*, Vol. 85, 1978, pp. 591-606.

3 Simmons, J.E.L., "Similarities Between Two-Dimensional and Axisymmetric Vortex Wakes," *Aero. Quarterly*, Vol. 26, 1977, pp. 15-20.

4 Roshko, A., "On the Wake and Drag of Bluff Bodies," *J. Aero, Sci*, Vol. 22, 1955, pp. 124-132.

5 Bearman, P.W., "On Vortex Street Wakes," *J. Fluid Mech.*, Vol. 28, 1967, pp. 625-641.

6 Calvert, J.R., "Experiments on Low Speed Flow Past Cones," *J. Fluid Mech.*, Vol. 27, 1967, pp. 273-279.

7 Ramberg, S.E., "The Influence of Yaw Angle Upon the Vortex Wakes of Stationary and Vibrating Cylinders," Naval Research Laboratory, Washington, D.C., Memorandum Report 3822, 1978.

8 Bearman, P.W., "On Vortex Shedding From a Circular Cylinder in the Critical Reynolds Number Regime," *J. Fluid Mech.*, Vol. 37, 1969, pp. 577-586.

9 Bloor, M.S. and Gerrard, J.H., "Measurements on Turbulent Vortices in a Cylinder Wake," *Proc. Royal Soc. London*, Series A, Vol. 294, 1966, pp. 319-342.

10 Ballou, C.L., "Investigation of the Wake Behind A Cylinder at Coincidence of a Natural Shedding Frequency of Vibration of the Cylinder and the Vortex Shedding Frequency," Massachusetts Institute of Technology, Cambridge, MA, Report 76028-2, 1967.

11 Bruun, H.H., and Davies, P.O.A.L., "An Experimental Investigation of the Unsteady Pressure Forces on a Circular Cylinder in a Turbulent Cross Flow," *J. Sound Vib.*, Vol. 40, 1975, pp. 535-560.

12 Cantwell, B.J., "A Flying Hot-Wire Study of the Wake of a Circular

Cylinder," California Institute of Technology, Pasadena, CA, Ph.D. thesis, 1976.

13 Eppler, H., "Beiträge zu Theorie und Anwendung der unstetigen Strömungen," *J. Rational Tech. Anal.*, Vol. 3, 1954, pp. 591–644.

14 Roshko, A., "Experiments on the Flow Past a Circular Cylinder at Very High Reynolds Numbers," *J. Fluid Mech.*, Vol. 10, 1961, pp. 345–356.

15 Apelt, C.J., West, G.S., and Szewczyk, A.A., "The Effects of Wake Splitter Plates on the Flow Past a Circular Cylinder in the Range $10^4 < R < 5 \times 10^4$," *J. Fluid Mech.*, Vol. 61, 1973, pp. 187–198.

16 Surry, D., "Some Effects of Intense Turbulence on the Aerodynamics of a Circular Cylinder at Subcritical Reynolds Number," *J. Fluid Mech.*, Vol. 52, 1972, pp. 543–564.

17 Batham, J.P., "Pressure Distributions on Circular Cylinders at Critical Reynolds Numbers," *J. Fluid Mech.*, Vol. 57, 1973, pp. 209, 228.

18 Griffin, O.M. and Ramberg, S.E., "The Vortex Street Wakes of Vibrating Cylinders," *J. Fluid Mech.*, Vol. 66, 1974, pp. 553–576.

19 Griffin, O.M. and Ramberg, S.E., "On Vortex Strength and Drag in Bluff Body Wakes," *J. Fluid Mech.*, Vol. 69, 1975, pp. 721–728.

20 Bearman, P.W., and Davies, M.E., "The Flow About Oscillating Bluff Structures," *Proceedings of the Fourth International Conference on Wind Effects on Buildings and Structures,* Cambridge University Press, 1975, pp. 285–296.

21 Stansby, P.K., "Base Pressure of Oscillating Circular Cylinders," *Proc. ASCE, J. Eng. Mech.*, Vol. 104, 1976, pp. 591–600.

22 Bearman, P.W., "Investigation of the Flow Behind a Two Dimensional Model with a Blunt Trailing Edge and Fitted With Splitter Plates," *J. Fluid Mech.*, Vol. 21, 1965, pp. 241–255.

23 Roshko, A., "On the Drag and Shedding Frequency of Two-Dimensional Bluff Bodies," National Advisory Committee for Aeronautics, Washington, D.C. Technical Note 3169, 1954.

24 Blake, W.K., "Hydroelastic Variables Influencing Propellor and Hydrofoil Singing," *Noise and Fluids Engineering,* ASME: New York, 1977, pp. 191–199.

25 Gerrard, J.H., "The Mechanics of the Formation Region of Vortices Behind Bluff Bodies," *J. Fluid Mech.*, Vol. 25, 1966, pp. 401–413.

26 Gerrard, J.H., "A Disturbance-Sensitive Reynolds Number Range for the Flow Past a Circular Cylinder," *J. Fluid Mech.*, Vol. 22, 1965, pp. 187–196.

27 Modi, V.J., and El-Sherbiny, S., "A Free Streamline Model for Bluff Bodies in Confined Flow," ASME JOURNAL OF FLUIDS ENGINEERING, Vol. 99, 1977, pp. 585–592.

28 Griffin, O.M., Skop, R.A., and Koopmann, G.H., "The Vortex-Excited Resonant Vibrations of Circular Cylinders," *J. Sound Vib.*, Vol. 31, 1973, pp. 235–249.

29 Simmons, J.E.L., "Effect of Separation Angle on Vortex Streets," *Proc. ASCE J. Eng. Mech.*, Vol. 101, 1975, pp. 649–661.

30 Bearman, P.W., and Trueman, D.M., "An Investigation of the Flow Around Rectangular Cylinders," *Aero. Quarterly,* Vol. 23, 1972, pp. 229–237.

31 Twigge-Molecey, C., and Baines, W.D., "Aerodynamic Forces on a Triangular Cylinder," *Proc. ASCE J. Eng. Mech.*, Vol. 99, 1973, pp. 803–818.

# Wake Induced Time-Variant Aerodynamics Including Rotor-Stator Axial Spacing Effects

**S. Fleeter**
School of Mechanical Engineering,
Purdue University,
West Lafayette, Ind.

**R. L. Jay**

**W. A. Bennett**
Detroit Diesel Allison,
Division of General Motors,
Indianapolis, Ind.

*The overall objective of this experimental program was to quantify the effects of rotor-stator axial spacing on the fundamental time-variant aerodynamics relevant to forced response in turbomachinery. This was accomplished in a large-scale, low-speed, single-stage research compressor which permitted two rotor-stator axial spacing ratios representative of those found in advanced design compressors to be investigated. At each value of the axial spacing ratio, the aerodynamically induced fluctuating surface pressure distributions on the downstream vane row, with the primary source of excitation being the upstream rotor wakes, were measured over a wide range of compressor operating conditions. The velocity fluctuations created by the passage of the rotor blades were measured in the nonrotating coordinate system. Data obtained described the variation of the rotor wake with both loading and axial distance from the rotor as parameters. These data also served as a reference in the analysis of the resulting time-variant pressure signals on the vane surfaces.*

## Introduction

The failure of rotor and stator airfoils as a result of aerodynamic excitations has been and yet remains a serious design consideration throughout the gas turbine industry. As early as 1955 the need to develop a fundamental understanding of these "forced response" problems was recognized by Whitmore, Lull, and Adams [1]. In the ensuing time period significant advancements have been made in solution techniques, aerodynamic theory, and computing capability. However, today forced response still ranks as a significant problem area for gas turbine engines.

The ability to accurately predict the structural resonances of blading has been greatly enhanced through the development and application of finite element techniques. Thus, prior to rig or engine operation, the designer is provided detailed information regarding the location of the critical resonant response regions of operation for a given blade row. However, the severity of these response regions to the various upstream or downstream excitations is not known until complete engine evelope conditions have been tested.

The identification of a highly stressed resonance of an airfoil during testing necessitates modifications to reduce the stress. For a component test, the stress can be reduced by simply avoiding the resonance. For an engine in the development phase, one primary method which has been successful involves increasing the axial spacing between the excitation source and the responding airfoils. This method has generally been applied when an upstream airfoil row is the excitation source. In this case the wakes can be the mechanism which creates the time-variant pressures along the chord of the downstream airfoil row, thereby driving the airfoil response. An increase in the axial spacing is then regarded as a reduction in the wake velocity deficit and, correspondingly, as a decreased level of unsteady pressure loading on the responding airfoil.

The time-variant aerodynamic response on an airfoil surface is comprised of two parts. One is due to the upstream disturbance being swept past the non-responding fixed airfoils. The second arises when the airfoil responds to the disturbance. The unsteady pressure distribution on the airfoil surfaces, i.e. the driving force for the airfoil response, is the sum of these two effects. Analytically these effects are modeled by means of two analyses. A gust analysis is used to predict the time-variant aerodynamics of the fixed, nonresponding airfoils to each harmonic of the disturbance. An analysis wherein the airfoil cascade is assumed to be harmonically oscillating is then used to predict the additional aerodynamic effect due to the blades responding.

The aerodynamic gust analysis, as well as the case of harmonic airfoil oscillations, are areas of fundamental research interest [2, 3, 4]. There are many mathematical and physical assumptions inherent in these models, yet only a limited quantitiy of appropriate fundamental data exists with which to assess the range of validity of the models or to indicate refinements necessary to develop a valid predictive design model [5-9].

The overall objective of the experimental research program described herein is to obtain fundamental unsteady forced response aerodynamic data necessary to quantify the effect of rotor-stator axial spacing. This is accomplished by measuring the aerodynamically induced fluctuating pressure distribution

Contributed by the Fluids Engineering Division for publication in the JOURNAL OF FLUIDS ENGINEERING. Manuscript received by the Fluids Engineering Division, February 12, 1979.

**Table 1 Airfoil mean section characteristics and compressor design point conditions**

| | Rotor | Stator |
|---|---|---|
| Type of airfoil | 65 Series | 65 Series |
| Number | 42 | 40 |
| Chord, C-in. (cm) | 4.589 (11.66) | 5.089(12.93) |
| Solidity, $\sigma = C/S$ | 1.435 | 1.516 |
| Camber, $\phi$ - deg | 20.42 | 48.57 |
| Aspect ratio, AR = $S/C$ | 1.046 | 0.943 |
| Leading edge radius/C | 0.0044 | 0.0049 |
| Trailing edge radius/C | 0.0028 | 0.0030 |
| Inlet angle, $\beta_1$ - deg | 59.38 | 37.84 |
| Exit angle, $\beta_2$ - deg | 42.41 | 0.00 |
| Loss coefficient | 0.043 | 0.056 |
| Diffusion factor | 0.449 | 0.410 |
| Rotor-stator axial spacing-in. (cm) | 1.485(3.772) | |
| Flow rate | 31.02 lb/s | (14.07 kg/s) |
| Tip speed | 183.5 ft/s | (5593.1 cm/s) |
| Rotational speed | 876.3 rpm | |
| Stage pressure ratio | 1.0125 | |
| Inlet tip diameter | 48.01 in (121.95 cm) | |
| Hup/tip radius ratio | 0.80 | |
| Stage efficiency, percent | 88.1 | |

in a downstream vane row, with the primary source of excitation being the wakes from the upstream rotor blading. Two rotor-stator axial spacing ratios, representative of those found in advanced design compressors, are investigated over a wide range of reduced frequency values and compressor steady-state operating conditions. This research effort furnishes data not only for the designer, but also for the analyst whose requirements include a detailed breakdown of the unsteady pressures on both the suction and pressure surfaces of the vane.

## Single Stage Research Compressor

The Detroit Diesel Allison large-scale, low-speed, single-stage research compressor facility was used in this investigation. This compressor features blading (42 rotor blades and 40 stator vanes, NACA 65 Series) aerodynamically loaded to levels that are typical of advanced multi-stage compressors and also physically large enough to provide for substantial quantities of instrumentation. Table 1 presents the airfoil mean section properties as well as the design point operating conditions.

An analysis of four advanced design compressors in which excitations created by an upstream blade row caused serious concern for the life of a particular airfoil determined that the ratio of the rotor-stator axial spacing to the upstream axial chord varied from 0.15 to 0.49. The nominal and decreased value for this ratio in the research compressor are 0.2374 and 0.4305. Hence they span the range of interest of design experience.

## Instrumentation

The time-variant quantities of fundamental interest in this experimental investigation include the fluctuating aerodynamic forcing function - the rotor wakes, and the resulting chordwise distributions of the complex time-variant pressure distribution on the downstream stator vane surfaces.

The blade surface dynamic pressure measurements were accomplished by instrumenting a pair of the vanes with flush mounted Kulite thin-line dynamic pressure transducers. The suction and pressure surface transducers are located on the vane meanline at the identical percent vane chord locations: 2.94, 10.0, 20.0, 30.0, 40.0, 50.0, 60.0, 70.0, 80.0, 90.0, 97.0. These vanes are positioned such that one flow passage is instrumented.

The time-variant wake measurements were obtained by means of a cross-wire probe calibrated and linearized to 200 fps (61 mps) and ± 25 deg angular variation. The mean absolute exit flow angle from the rotor is determined by rotating the crosswire probe until a zero voltage difference is obtained between the two linearized hot-wire signals. This mean angle is then used as a reference for calculating the instantaneous absolute and relative flow angles. The output from each channel is corrected for tangential cooling effects and the individual fluctuating velocity components parallel and normal to the mean flow angle calculated from the corrected quantities.

## Data Acquisition and Analysis

In this investigation, both steady-state and time-variant data were acquired. The steady-state data define the points of compressor operation, in terms of overall pressure ratio and corrected mass flow rate, at which the unsteady velocity and surface pressure measurements were obtained.

The time-variant data acquisition and analysis technique used is based on a data averaging or signal enhancement

## Nomenclature

$b$ = airfoil semichord ($C/2$)
$C$ = airfoil chord
$C_p$ = dynamic pressure coefficient $P/\left(\rho \cdot V^2 \cdot \frac{v}{V}\right)$
$P$ = magnitude of unsteady pressure
$R_c$ = compressor pressure ratio
$V$ = absolute velocity
$W\sqrt{\theta}/\delta$ = corrected mass flow
$k$ = reduced frequency ($k = \omega b/V$)
$u$ = longitudinal perturbation velocity
$v$ = transverse perturbation velocity
$\beta$ = inlet angle
$\rho$ = inlet air density
$\omega$ = blade passing angular frequency

Subscripts
1 = first harmonic
2 = second harmonic
ABS = absolute
Rel = relative

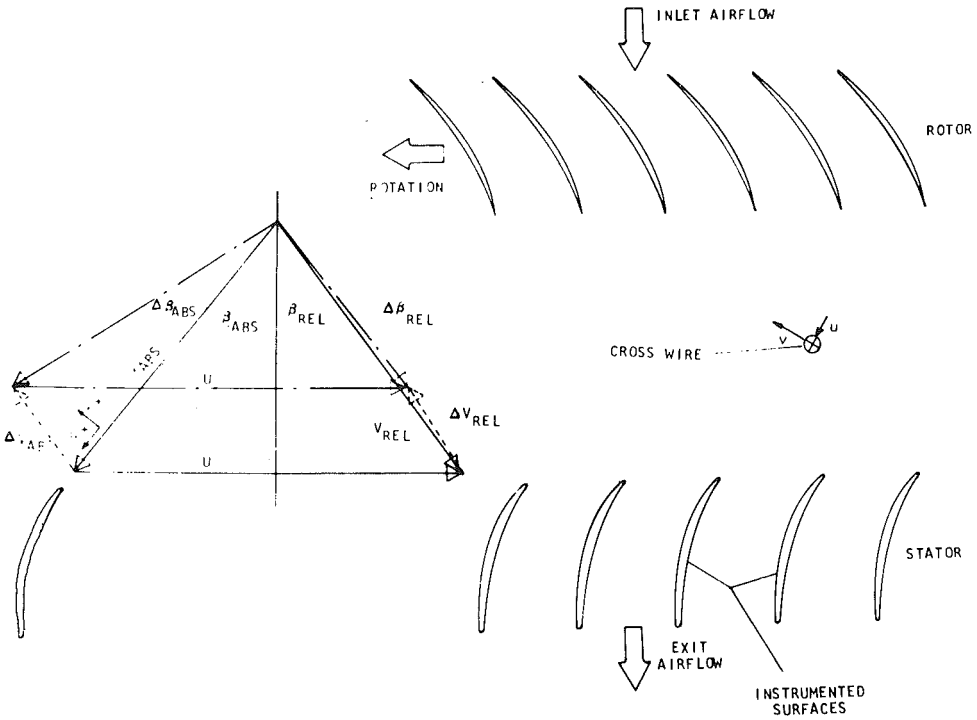


**Fig. 1 Schematic of flow field**

concept. The key to such a technique is the ability to sample data at a preset time. For this investigation the signal of interest is generated at the blade passing frequency. Hence, an optical encoder which delivers a square wave voltage signal having a duration of 1.5 microseconds was mounted on the rotor shaft. The on-line computer analog-to-digital-converter is triggered from the positive voltage at the leading edge of the pulse, thereby initiating the acquisition of the time unsteady data at a rate of up to 100,000 points per second. The data are sampled for $N$ blade passages and over $M$ rotor revolutions. These rotor revolutions are not consecutive because a finite time is required to operate on the N blade passage data before the computer returns to the pulse acceptance mode which initiated the gathering of the data. For this experimental program, 80 to 100 digitized data points are obtained for each of three blade passages averaged over 400 rotor revolutions ($N = 3, M = 400$).

At each steady operating point an averaged time-variant data set, consisting of the two hot-wire and the 22 Kulite signals, are obtained. Each of these signals is digitized and Fourier decomposed into its harmonics. From this Fourier analysis both the magnitude and phase angles referenced to the data initiation pulse are obtained. To then relate the wake generated velocity profiles with the surface dynamic pressures on the instrumented vanes, the rotor exit velocity triangles are examined. Figure 1 shows the change in the rotor relative exit velocity which occurs as a result of the presence of the blade. A deficit in the velocity in this relative frame creates a change in the absolute velocity vector as indicated. This velocity change is measured via the crossed hot-wires. From this instantaneous absolute angle and velocity, the rotor exit relative angle and velocity as well as the magnitude and phase of the perturbation quantities are determined.

The hot-wire probe is positioned in the plane of the leading edge of the stator row. To relate the time based events as measured by this hot-wire probe to the pressures on the vane surfaces, the assumptions are made that: (1) the wakes are identical at the hot-wire and the stator leading edge planes; (2) the wakes are fixed in the relative frame. Figure 1 also presents a schematic of the rotor wakes, the instrumented vanes, and the hot-wire probe. The rotor blade spacing, the vane spacing, and the axial spacing between the vane leading edge plane and the probe holder center line are known quantities. At a steady operating point the hot-wire data are analyzed to determine the absolute flow angle and the rotor exit relative flow angle. Using the two assumptions noted, the wake is located relative to the hot-wires and the leading edges of the instrumented vane suction and pressure surfaces. From this, the times at which the wake is present at various locations is determined. The increment times between occurrences at the hot-wire and the vane leading edge plane are then related to phase differences between the perturbation velocities and the vane surface. To simplify the experiment-theory correlation process, the data are then adjusted in phase such that the transverse perturbation is at zero degrees at the vane suction surface leading edge, thereby corresponding to a sinusoidal disturbance at the vane leading edge per the transverse gust analysis.

Following this procedure the equivalent complex pressure difference across a single airfoil at each transducer location is calculated. The magnitude of the pressure difference is then normalized with respect to the inlet flow parameter ($\rho \cdot V^2 \cdot v/V$) where $\rho$ is the inlet air density, $V$ is the stator inlet absolute velocity, and v is the transverse perturbation velocity measured by the cross-wire probe.

Thus, the final form of the unsteady pressure data describes the chordwise variation of the pressure difference across an airfoil and is presented in terms of an aerodynamic phase lag, $\phi$, referenced to a transverse gust at the airfoil leading edge and a dynamic pressure coefficient, $C_p = P/(\rho \cdot V^2 \cdot v/V)$.

**Experimental Uncertainty**. The above described data averaging or signal enhancement concept for the time-variant data followed that of references [7, 9 and 10]. The fixed errors which contribute to the uncertainty band for the data center on the accurate positioning of the cross-wire. For example, a

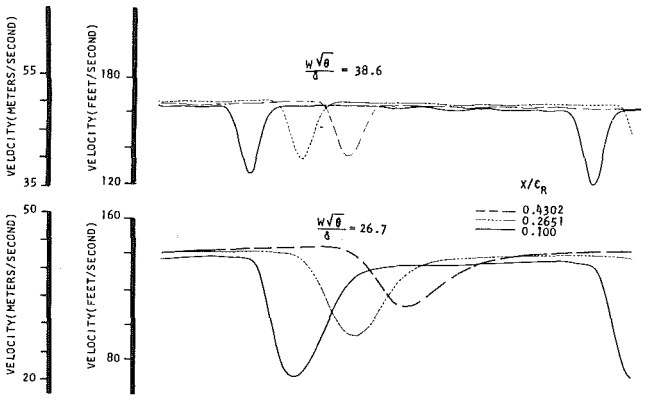


Fig. 2 Variation of the rotor wake profile and axial distance for two levels of loading

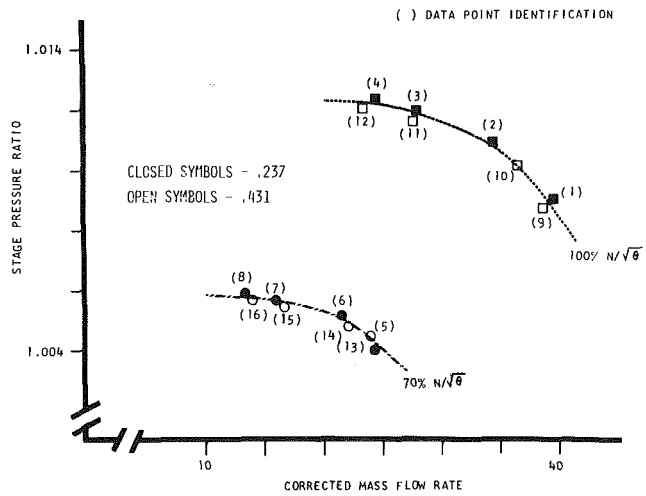


Fig. 3 Data point identification in terms of pressure ratio and mass flow rate

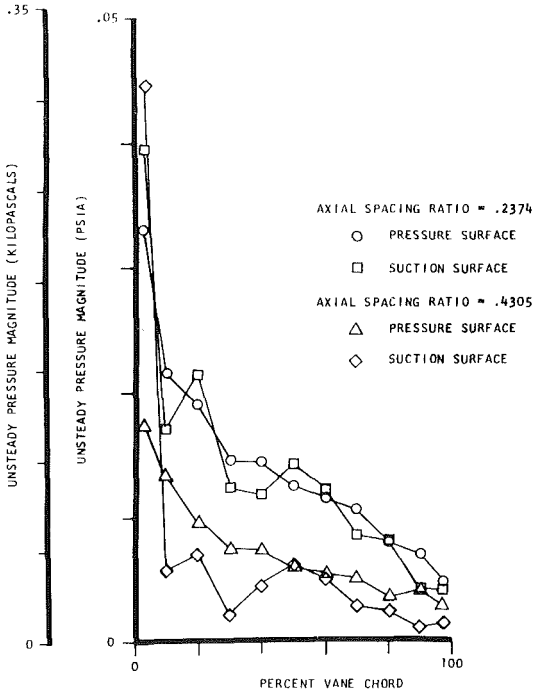


Fig. 4 Unsteady pressure magnitude on the vane surfaces for data points 4 and 12

0.25 cm radial or axial uncertainty in its position results in a 1 or 10 deg error in the aerodynamic phase lag, respectively. Based on the data acquisition and the fixed errors, the uncertainty in the output data is ±25 deg for the aerodynamic phase lag and ±0.1 for the dynamic pressure coefficient.

## Results

Two studies were undertaken: (1) a qualitative study of the rotor wake velocity profile as a function of both compressor loading and downstream axial distance; (2) a quantitative investigation of the time-variant pressures induced on the vanes by these rotor wakes as they are convected downstream. The objective of the qualitative wake study was to obtain a physical understanding of the variations of this aerodynamic forcing function and thereby aid in the analysis of the resulting measured vane surface unsteady pressure distributions. The individual unsteady vane surface pressure data were used to determine the unsteady pressure difference across a single vane and this difference data then correlated with appropriate predictions from a cascade transverse gust analysis.

## Wake Investigation

The velocity is the fundamental quantity used to define the wake and was measured with the cross-wire probe. This measurement, made in the absolute or nonrotating reference frame, together with the absolute flow angle and rotor speed were used to calculate the velocities in the relative or rotating frame of reference.

Figure 2 shows the variation in the rotor wake profile as a function of axial distance as measured from the rotor trailing edge for two values of loading along the 100 percent speed line. At a constant axial distance from the rotor, an increase in the pressure ratio (a decrease in the mass flow rate) can be seen to result in an increase in both the width and velocity deficit of the wake. As the axial distance from the rotor is increased, the wake decays and the difference between the wake centerline velocity and the freestream velocity decreases. At the high level of loading this trend is very pronounced, but is much less significant at the lower level of loading.

## Unsteady Surface Pressures

The primary goal of this investigation was to measure the time-variant pressures on the downstream stator vane surfaces due to the aerodynamic excitation created by the wakes from the upstream rotor blades for two rotor-stator axial spacings over a range of steady-state compressor operating conditions. To accomplish this goal dynamic data were obtained at seventeen steady-state operating points. Figure 3 presents the locations of the steady-state operating points along the 70 and 100 percent corrected speed lines in terms of overall pressure ratio and corrected mass flow rate for both axial spacings. Data points 1 through 8 were obtained for a value of 0.2374 for the ratio of the rotor-stator axial spacing to the upstream axial chord, and data points 9 through 17 for a value of 0.4305 for this parameter.

**Individual Vane Surface Unsteady Pressures.** The magnitude of the measured unsteady pressures on the individual vane surfaces obtained at the design point of the compressor are presented in Fig. 4. The overall level of the unsteady pressure magnitude on both surfaces of the vane increases with loading at approximately the same rate for each value of the axial spacing ratio. This increase is particularly pronounced for the small value of the rotor-stator axial spacing ratio (0.2374), being less significant for the large spacing ratio (0.4305). Along the 70% speed line, the overall

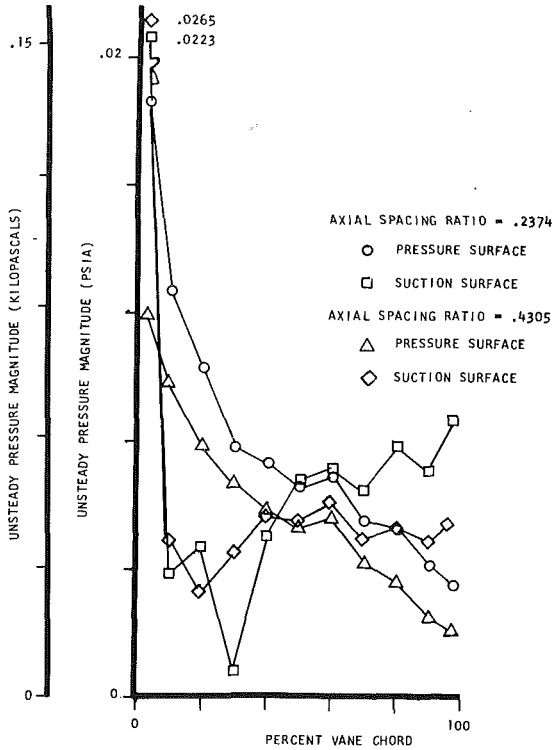


Fig. 5 Unsteady pressure magnitude on the vane surfaces for data points 8 and 16

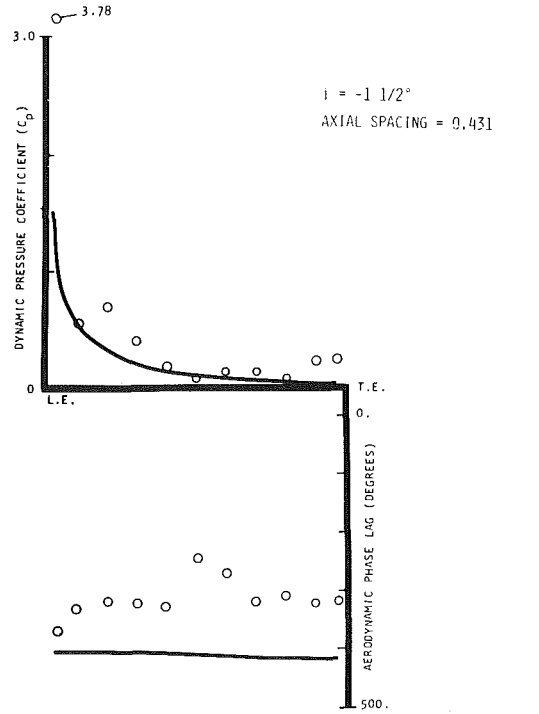


Fig. 6 Chordwise data for first harmonic unsteady pressure difference across the vane and prediction from reference [3] for point 12

**Table 2 Steady-state data identification and description of time-variant parameters**

| Data point | Axial spacing ratio | % speed | $\beta_{ABS}$ | $k_{1\,AX}$ | $k_{2\,AX}$ | $v/V)_1$ | $u/V)_1$ | $v/V)_2$ | $u/V)_2$ |
|---|---|---|---|---|---|---|---|---|---|
| 1 | 0.2374 | 100 | 25 | 6.80 | 13.60 | .02911 | .02113 | .03232 | .01835 |
| 2 | 0.2374 | 100 | 28 | 7.56 | 15.12 | .0300 | .01912 | .03294 | .01692 |
| 3 | 0.2374 | 100 | 33 | 8.88 | 17.76 | .1117 | .07526 | .09862 | .04184 |
| 4 | 0.2374 | 100 | 36 | 9.86 | 19.72 | .03316 | .0239 | .03566 | .01976 |
| 5 | 0.2374 | 70 | 25 | 6.90 | 13.80 | .03358 | .02299 | .03523 | 0.1760 |
| 6 | 0.2374 | 70 | 28 | 7.54 | 15.08 | .1156 | .080 | .0999 | .04368 |
| 7 | 0.2374 | 70 | 33 | 9.12 | 18.24 | .06788 | .0381 | .06720 | .02108 |
| 8 | 0.2374 | 70 | 38 | 10.1 | 20.2 | .06830 | .03049 | .06941 | .01907 |
| 9 | 0.4305 | 100 | 25 | 6.95 | 13.90 | .03148 | .01973 | .03203 | .01583 |
| 10 | 0.4305 | 100 | 28 | 7.27 | 14.54 | .03306 | .01845 | .03452 | .01556 |
| 11 | 0.4305 | 100 | 33 | 8.96 | 17.92 | .07811 | .02499 | .06258 | .01813 |
| 12 | 0.4305 | 100 | 36 | 10.05 | 20.10 | .10798 | .01652 | .07397 | .00754 |
| 13 | 0.4305 | 70 | 25 | 6.95 | 13.90 | .03388 | .02602 | .03622 | .01863 |
| 14 | 0.4305 | 70 | 28 | 7.40 | 14.80 | .03630 | .02360 | .03826 | .01891 |
| 15 | 0.4305 | 70 | 33 | 8.91 | 17.82 | .07803 | .03156 | .06462 | .02419 |
| 16 | 0.4305 | 70 | 36 | 9.82 | 19.64 | .12118 | .02614 | .08612 | .01381 |
| 17 | 0.4305 | 70 | 22 | 5.13 | 10.26 | .0510 | .0350 | .0450 | .0310 |

levels of the unsteady pressure magnitude on both surface also increase with loading at about the same rate. However no noticable difference with loading is apparent between the data for the two rotor-stator spacings, as seen in Fig. 5.

**Unsteady Pressure Differential Data-Theory Correlation.** Figures 6 through 9 present the dynamic pressure coefficient and aerodynamic phase lag data for the first harmonic of the unsteady pressure difference across the vane as a function of percent vane chord. Also included in these figures are the incompressible predictions obtained from the cascade transverse gust analysis of reference [3] for the flow conditions specified in Table 2.

The objective of this section is to discuss the correlation of the unsteady pressure differential data with the predictions from the transverse gust analysis. Thus the difference data have been nondimensionalized by the parameter $\rho \cdot V^2 \cdot v/V$ evaluated at the stator inlet as previously noted. The differences associated with the changes in the rotor-stator axial spacing ratio are thus inherent in this normalizing parameter. Hence the dimensionless time-variant pressure differential data for the two axial spacing ratios should, and indeed do, superimpose upon one another, as seen in Figs. 7 through 9. It should be noted that significant variations in the nondimensionalizing parameter with axial spacing begin to become significant only at the highest pressure ratios attainable in this research compressor.

The low incidence angle dynamic pressure coefficient data generally exhibit very good correlation with the predictions over the entire vane chord, as seen in Figs. 6 and 7. The dynamic pressure coefficient data and theory decrease in the chordwise direction, although the data attain a finite, albeit nonzero, value at the vane trailing edge transducer location (97.0 percent of the chord). It should be noted that the

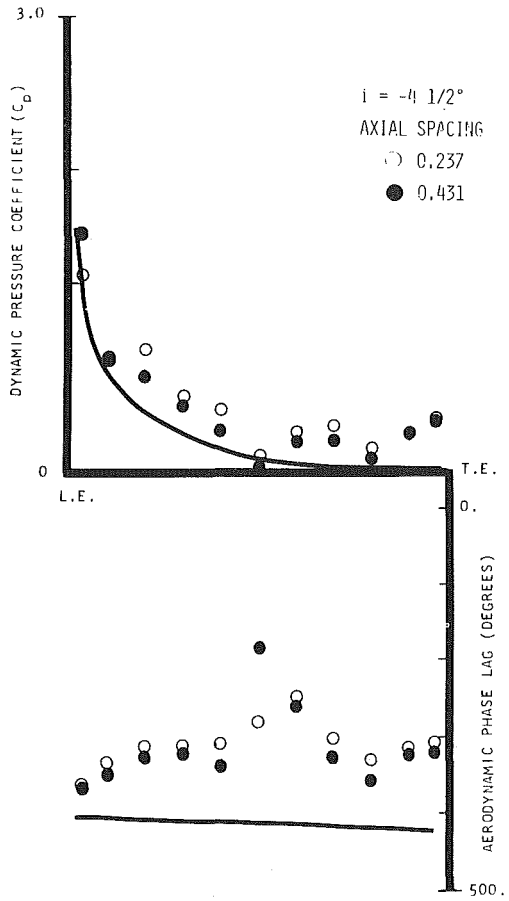


**Fig. 7 Chordwise data for first harmonic unsteady pressure difference across the vane and prediction from reference [3] for points 3 and 11**

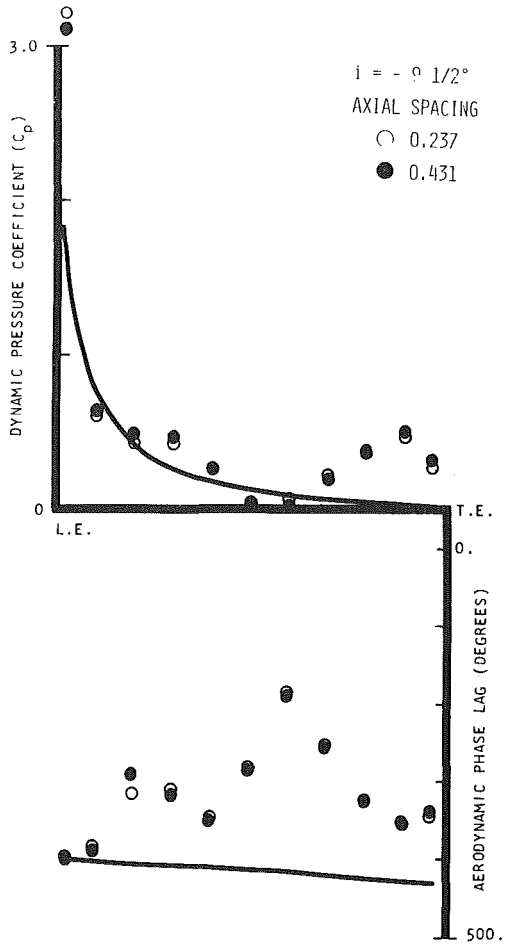


**Fig. 8 Chordwise data for first harmonic unsteady pressure difference across the vane and prediction from reference [3] for points 2 and 10**

finiteness of the trailing edge dynamic pressure coefficient data and also its value reflect upon the validity and the application of the Kutta condition for unsteady flows at these high reduced frequency values ($5.1 < k_1 < 10.1$). It should be emphasized that this data was normalized with respect to a vane inlet velocity and density parameter. Hence, an increase or decrease in $C_p$ implies a corresponding change in the magnitude of the measured unsteady pressure.

The aerodynamic phase lag data for the low incidence angles generally correlate with the prediction, although they appear to be offset in level on the order of 60 deg as compared to the prediction. The phase lag data are smooth over the front half of the vane, correlating with the predictions, but almost always demonstrate a significant negative jump in value at the 50 percent vane chord transducer location. Aft of this location, these data sometimes increase to the general level attained over the front half of the vane and other times remain at the decreased level, as seen in Figs. 6 and 7. Examination of the individual vane surface data reveals that the first harmonic differential data is generally dominated by the pressure surface over the front 40 percent of the vane, and by either the pressure surface or the suction surface data over the aft portion of the vane. At the 50 percent chord location, where the negative jump in phase of the differential pressure is noted, the pressure and suction surface fluctuating pressures are often equal. Whether the phase jump is maintained over the aft portion of the vane appears to correlate with the cases when the suction surface data is dominant. Analogously, the cases where the phase lag jump increases over the aft portion of the vane correlates with the pressure surface data being dominant. It should be noted that the variation along the chord of the individual pressure and suction surface data is smooth.

The intermediate negative incidence angle results are presented in Fig. 8. Deviation between the prediction and the dynamic pressure coefficient and aerodynamic phase lag data increases significantly herein.

The dynamic pressure coefficient data-theory correlation is good over the front 60 percent of the vane surface, with both decreasing in value in the chordwise direction. Over the aft 40 percent of the vane chord, the prediction continues to decrease whereas the data generally begin to increase in value.

For these intermediate negative incidence angles, the aerodynamic phase lag data generally correlate with the predictions over the front 50 percent of the vane, although offset in level on the order of 35 deg. Over the aft portion of the vane, and sometimes over some of the front portion as well, the aerodynamic phase lag data are seen to vary in a linear fashion. Such a linear phase lag variation means that an event occuring at one location on the vane occurs at a later time at a downstream location.

The large negative incidence angle results are presented in Figure 9. The dynamic pressure coefficient data-prediction correlation for these points is similar to that for the intermediate negative incidence angle points. The data and prediction generally decrease in value over the front half of the vane, with the prediction continuing to decrease to the vane trailing edge. The data, however, increase in value over the rear half of the chord. Also, the value of the 10 percent chord dynamic pressure coefficient data is substantially

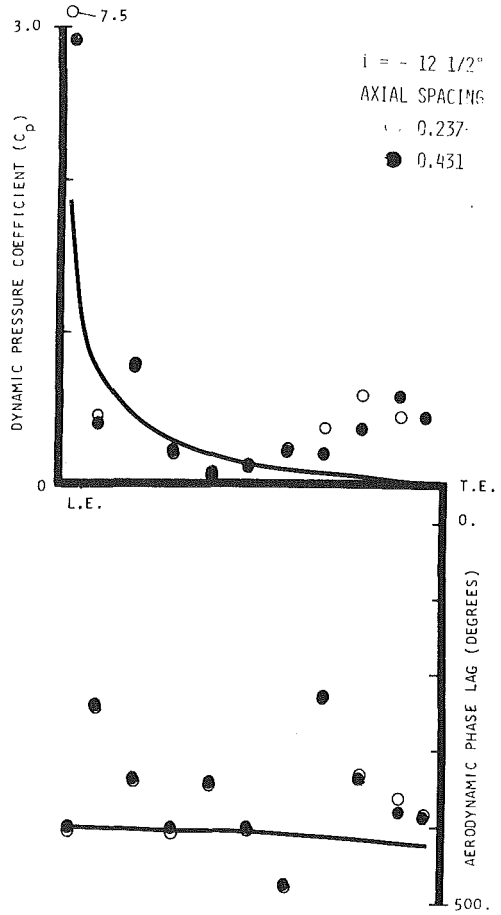


**Fig. 9 Chordwise data for first harmonic unsteady pressure difference across the vane and prediction from reference [3] for points 1 and 9**

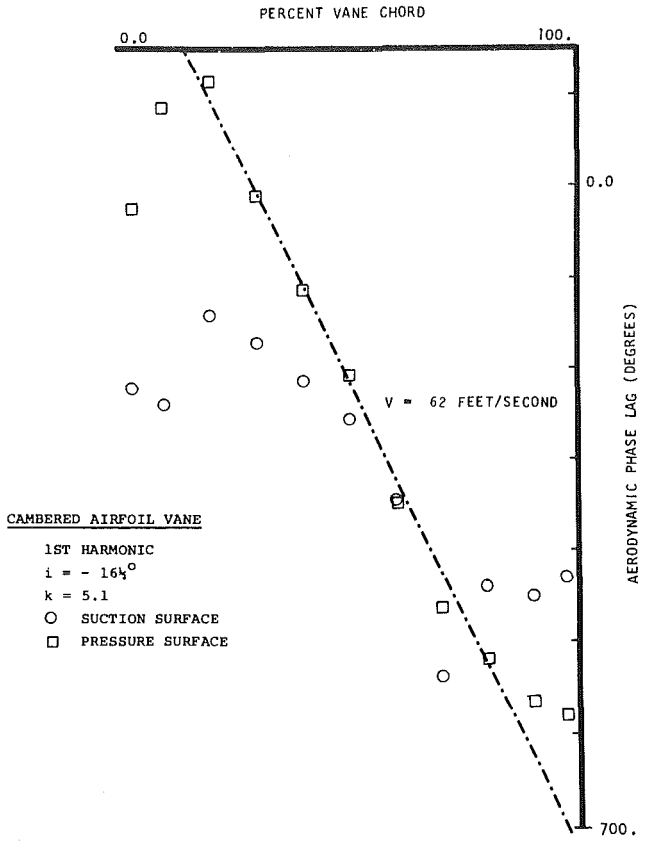


**Fig. 10 Chordwise variation of the first harmonic pressure and suction surface aerodynamic phase lag for point 17**

reduced in value as compared to both the neighboring data points.

The aerodynamic phase lag data at the vane leading edge transducer location correlate extremely well with the prediction. However, a wave related phenomena, as evidenced by the linear increase in phase along the chord and discussed in detail in reference [9], is now generally present over the entire vane chord for these large negative incidence angles.

To examine these wave phenomena, the first and second harmonic of the aerodynamic phase lag data on the individual vane surfaces for the −16 1/2 deg incidence angle value are presented in Figs. 10 and 11. As indicated, the first harmonic phase lag data demonstrate that a convected wave traveling at 62 ft/s (18.90 meters/second) dominates nearly the entire pressure surface, but not the suction surface. The second harmonic phase lag data, show that a convected wave traveling at approximately 112 feet/second (34.14 meters/second) dominates the entire suction surface, but not the pressure surface. Thus, not only does a convected wave phenomena exist at large negative incidence angles, but these waves are convected at different velocities on each surface.

## Summary and Conclusions

The fundamental time-variant aerodynamics relevant to forced response of a downstream vane of realistic geometry, with the primary source of excitation being the wakes from upstream rotor blades, were experimentally determined for two representative values of the rotor-stator axial spacing ratio. The vane incidence angle ranged from −1 1/2 to −16

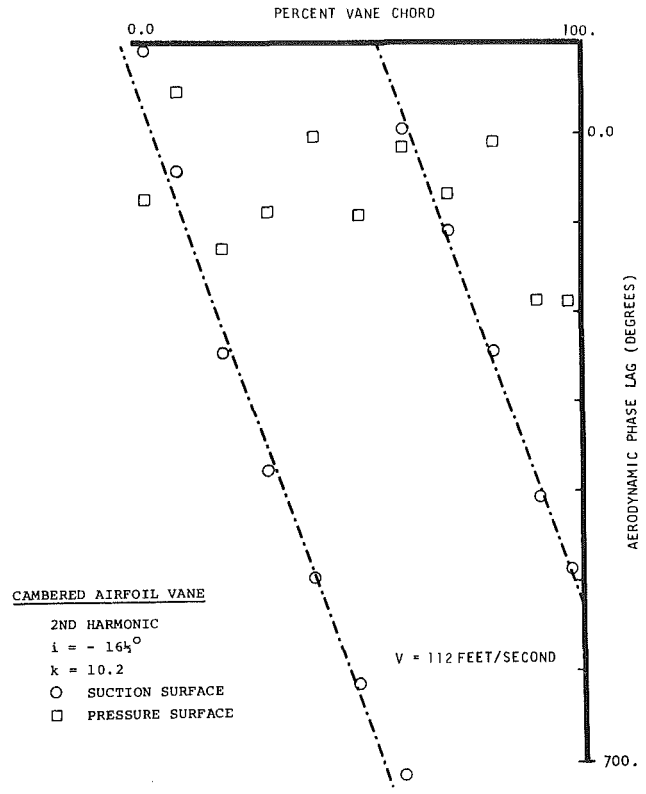


**Fig. 11 Chordwise variation of the second harmonic pressure and suction surface aerodynamic phase lag for point 17**

1/2 deg and the reduced frequency from 5.13 at 10.10. The dynamic data provided qualitative information describing the rotor wake velocity as a function of both compressor loading and downstream axial distance as well as a quantitative description of the resulting time-variant pressures induced by these wakes on the surfaces of the downstream stator vanes. These vane pressure and suction surface unsteady data were used to determine the unsteady pressure difference across a single vane and these difference data correlated with appropriate predictions from a cascade transverse gust analysis.

The overall levels of the time-variant pressure on the vane pressure and suction surfaces were found to increase with loading at approximately the same rate for each value of the rotor-stator axial spacing ratio. On the 100 percent speed line, this increase in overall level was particularly pronounced for the small value of the spacing ratio. No overall differences with spacing ratio were apparent on the 70 percent speed line. Thus, from these data it would appear that increasing the rotor-stator axial spacing is not a universal method to be used to alleviate forced response problems, a result in agreement with experience as discussed in reference [11].

The correlation of the dynamic data describing the unsteady pressure difference across the vane with the flat plate cascade transverse gust analysis was generally good for low incidence angles, becoming less acceptable as the incidence became increasingly negative. This decreased correlation was seen to be due to the appearance of a wave related phenomena not modeled by the analysis becoming dominant. This wave phenomena was seen to exhibit different velocities on the vane suction and pressure surfaces. This demonstrates the necessity for acquiring individual surface unsteady data and then calculating pressure differences as opposed to measuring this pressure differential directly.

## Acknowledgment

This research was sponsored, in part, by the Air Force Office of Scientific Research (AFSC), United States Air Force.

## References

1 Whitmore, J.M., Lull, W.R., and Adams, M.D., "How Sound Affects Vibration in Modern Aircraft Engines," *General Motors Engineering Journal*, Nov.-Dec. 1955.

2 Whitehead, D.S., "Force and Moment Coefficients for Vibrating Airfoils in Cascade," *Aeronautical Research Council R and M* 3254, Feb. 1960.

3 Fleeter, S., "Fluctuating Lift and Moment Coefficients for Cascaded Airfoils in a Nonuniform Compressible Flow," *AIAA Journal of Aircraft*, Vol. 10, No. 2, Feb. 1973.

4 Smith, S.N., "Discrete Frequency Sound Generation in Axial Flow Turbomachines," University of Cambridge, Department of Engineering *Report CUED/A-Turbo/TR 29*, 1971.

5 Fleeter, S., Novick, A.S., and Riffel, R.E., "The Unsteady Aerodynamic Response of an Airfoil Cascade to a Time-Variant Supersonic Inlet Flow Field," AGARD-CP-177, *Unsteady Phenomena in Turbomachinery*, 1975.

6 Commerford, G.L., and Carta, F.O., "Unsteady Aerodynamic Response of a Two-Dimensional Airfoil at High Reduced Frequency," *AIAA Journal*, Vol. 12, No. 1, 1974.

7 Ostdiek, F.R., "A Cascade in Unsteady Flow," Ph.D. thesis, The Ohio State University, 1975.

8 Bruce, E.P., and Henderson, R.E., "Axial Flow Rotor Unsteady Response to Circumferential Inflow Distortions," Project SQUID Technical Report PSU-13-P, Sept. 1975.

9 Fleeter, S., Jay, R.L., and Bennett, W.A., "Rotor Wake Generated Unsteady Aerodynamic Response of a Compressor Stator," ASME *Journal of Engineering for Power*, Vol. 100, No. 4, Oct. 1978.

10 Gostelow, J.P., "A New Approach to the Experimental Study of Turbomachinery Flow Phenomena," ASME Paper 76-GT-47, 1976.

11 "Flow Induced Vibrations," Short Course, University of Tennessee Space Institute, Tullahoma, Tenn., Sept. 1979.

**H. Itō**
Professor.

**Y. Watanabe**
Research Assistant.

The Institute of High Speed Mechanics,
Tōhoku University,
Sendai, Japan

**H. Ishimaru**
Engineer,
Sagamihara Machinery Works,
Mitsubishi Heavy Industries, Ltd.,
Sagamihara, Japan

**Y. Abe**
Engineer,
Odawara Factory,
Fuji Photo Film Co., Ltd.,
Odawara, Japan

# An Investigation Into the Performance of Two Inlet Nozzles for Flow Measurement

*The discharge coefficients for two inlet nozzles with different contraction shapes were studied experimentally together with the behavior of the boundary layer on the nozzle wall. For the inlet nozzle which has the same contraction shape as the ISA 1932 nozzle, it was found that boundary-layer transition with an intermediary separation bubble is responsible for the occurrence of a large hump in the discharge coefficients. The well-rounded inlet nozzle showed a satisfactory performance. The effect of pressure tap size and that of the proximity of a wall to the inlet on discharge coefficients were quantified experimentally.*

## Introduction

An inlet nozzle which is fitted at the suction pipe intake is a kind of fluid meter, the pressure differential between the stagnant fluid at infinity and the nozzle throat being measured to determine the rate of flow in the pipe. Besides its laboratory use [1, 2], the inlet nozzle is used in Japan even to measure roughly the flowrate of pumps [3], blowers [4], and compressors [5]. Because of its small energy losses and ease of use, the inlet nozzle will become one of the useful fluid meters, provided its high accuracy is guaranteed.

So far, a number of studies have been published on the discharge coefficients for nozzles of zero area ratio [6–9]. Recently, a study on Borda inlet air flowmeters was reported by Kinghorn and McHugh [10]. However, so far as the authors are aware, no studies have been published about inlet nozzles with a bellmouth entry, except the work of Itaya and Takenaka [11] who proposed an inlet nozzle, the geometry of which has been standardized since then in the Japanese industrial standards [3-5].

In this paper, the performance characteristics of two inlet nozzles of different shapes were investigated together with some installation effects which should be considered in practical applications. It is hoped that the results given here will help to clear up some peculiarities which may occur in nozzle calibrations, and further, will furnish useful information about the design of inlet nozzles for flow measurement.

Contributed by the Fluids Engineering Division for publication in the JOURNAL OF FLUIDS ENGINEERING. Manuscript received by the Fluids Engineering Division, September 7, 1979.

## Experimental Apparatus

The two inlet nozzles used are identified in Fig. 1 as A and B. Nozzle A was manufactured according to the specification of the Japanese industrial standards, the contraction shape being the same as that of the ISA 1932 nozzle. Nozzle B was a well-rounded inlet nozzle, the contraction shape being determined according to Rouse and Hassan [12] and Rao [13]. The coordinates of the contraction boundary for nozzle B are given by the following equations.

For

$$0 \leqq z/D \leqq 0.0726$$

$$(z/D - 0.2)^2 + (R/D - 0.8614)^2 = 0.04 \tag{1}$$

For

$$0.0726 \leqq z/D \leqq 0.3195$$

$$(z/D - 1)^2 + 9(R/D - 0.8319)^2 = 1 \tag{2}$$

For

$$0.3195 \leqq z/D \leqq 1.2$$

$$(z/D - 1.2)^2 + 36(R/D - 0.6667)^2 = 1 \tag{3}$$

The dimensions of the inlet nozzles tested are given in Table 1. The nozzles were made of brass, each having four pressure taps drilled at 90-deg circumferential intervals. Sufficient care was exercised in scraping off the burrs so that the inside edge of each hole was flush with the surface.

The experimental apparatus using water is illustrated in Fig. 2 (a). Both a large underground reservoir and a small one on the floor were used. When the latter was used, it was

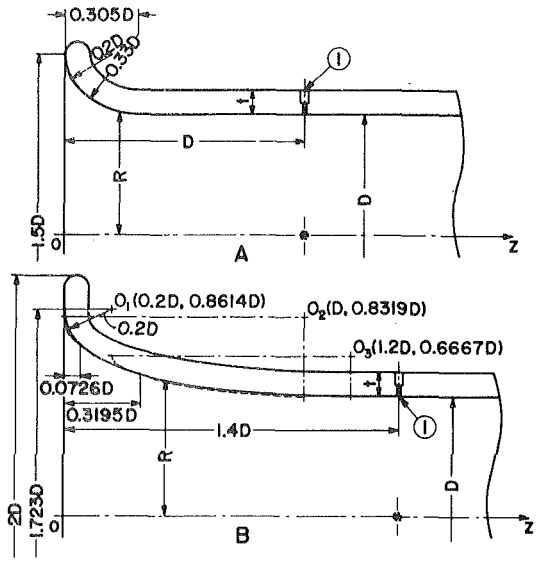


Fig. 1 Details of inlet nozzles: 1 Pressure tap

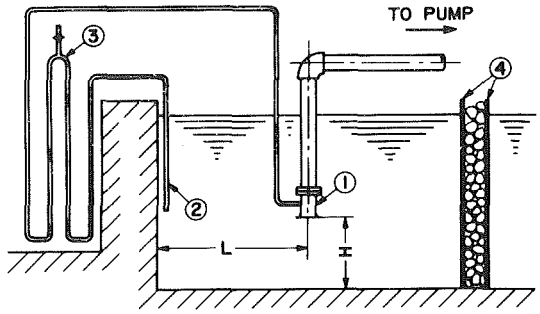


Fig. 2(a) Experimental apparatus using water: 1 Inlet nozzle, 2 piezometer tube, 3 differential manometer, 4 perforated plate

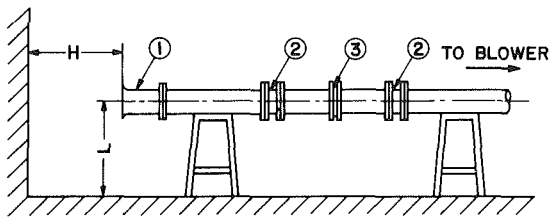


Fig. 2(b) Experimental apparatus using air: 1 Inlet nozzle, 2 honeycomb flow straightener, 3 ISA nozzle in pipe

necessary to supply water from another pump into the reservoir and to provide a simple overflow device in order to keep a constant water-level. Two perforated plates with coke between them were placed in the reservoir to ensure a quiescent flow. The inlet nozzles tested were submerged deep into the water so as to avoid air entrainment. The flowrate was measured using a weighing tank for low flows, and a volumetric tank with a graduated scale for higher flows. The latter had been calibrated accurately before the experiments.

The experimental apparatus using air is illustrated in Fig. 2 (b). The inlet nozzle was installed at a distance from both the wall and the floor. The flowrate was measured by ISA nozzles in the suction pipe.

## Experimental Results

**Discharge Coefficients.** For liquids, the discharge coefficient for the inlet nozzle is defined by the equation

$$q = CA[2(p_\infty - p_h)/\rho]^{1/2}. \tag{4}$$

The Reynolds number based on the differential pressure is given by

$$R_h = [2(p_\infty - p_h)/\rho]^{1/2} D/\nu, \tag{5}$$

which gives

$$R_D = CR_h. \tag{6}$$

For compressible fluids, the equation for the mass flow rate is

$$m = CYA[2\rho_\infty (p_\infty - p_h)]^{1/2}, \tag{7}$$

where

$$Y = \left[\left(\frac{\gamma}{\gamma-1}\right)\left(\frac{p_h}{p_\infty}\right)^{2/\gamma}\left(\frac{1-(p_h/p_\infty)^{(\gamma-1)/\gamma}}{1-(p_h/p_\infty)}\right)\right]^{1/2} \tag{8}$$

For compressible fluids, $R_h$ is given by

$$R_h = Y[2(p_\infty - p_h)/\rho_\infty]^{1/2} D/\nu_\infty, \tag{9}$$

the relation between the Reynolds number based on the fluid properties at infinity, $R_D$ ( $= mD/\rho_\infty \nu_\infty A$), and $R_h$ being given by equation (6).

The experimental values of the discharge coefficients are shown plotted against $R_h$ in Fig. 3, where it is seen that the discharge coefficients for nozzle A are divided into three regions:

Laminar region – the Reynolds number is low, and the boundary layer at the pressure tap is laminar.

Transition region – the region where the discharge coefficients depart from the laminar region values suddenly and gradually approach the turbulent region values.

## Nomenclature

$A$ = cross-sectional area of pipe
$C$ = coefficient of discharge
$D$ = internal dia of pipe (= dia of nozzle throat)
$\bar{f}_{app}$ = mean apparent friction factor
$H$ = distance from floor/or wall
$l$ = length of straight cylindrical throat section
$l_{eq}$ = equivalent length of contraction section
$l'$ = effective length of nozzle, $l + l_{eq}$
$L$ = distance from wall/or floor
$m$ = mass flow rate
$p$ = pressure
$q$ = volume flow rate
$R$ = Cartesian coordinate in radial direction
$R_D$ = Reynolds number based on mean velocity, $mD/\rho_\infty \nu_\infty A$
$R_h$ = Reynolds number based on differential pressure, $R_D/C$
$t$ = wall thickness
$V_h$ = velocity based on differential pressure, $[2(p_\infty - p_h)/\rho_\infty]^{1/2}$
$x$ = coordinate along nozzle wall
$Y$ = expansion factor
$z$ = Cartesian coordinate in axial direction
$\gamma$ = ratio of specific heats of an ideal gas
$\delta$ = pressure tap diameter
$\delta^*$ = boundary-layer displacement thickness
$\nu$ = kinematic viscosity
$\rho$ = density of fluid

Subscripts

$h$ = location of pressure tap
$\infty$ = infinite upstream

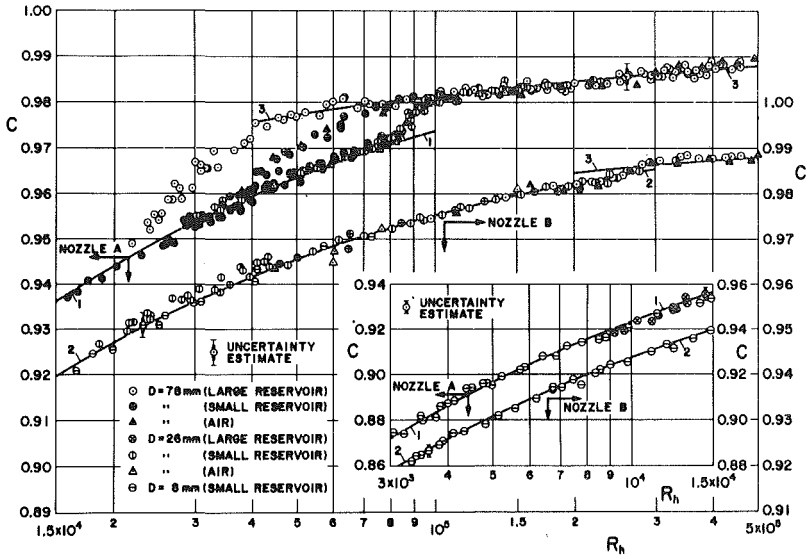


**Fig. 3 Discharge coefficients for inlet nozzles: Left hand scale – nozzle A, right hand scale – nozzle B, 1 equation (10), 2 equation (11), 3 equation (12) (The limited-sample uncertainty propagation means of Kline and McClintock (1953) were employed with 20 : 1 odds. Uncertainties of $C$ and $R_h$ are ±0.3 and ±0.4 percent, respectively)**

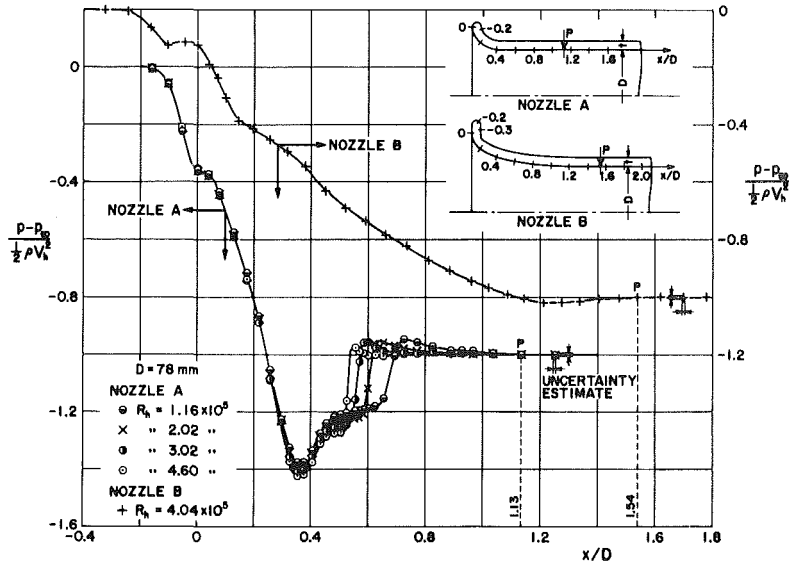


**Fig. 4 Pressure distributions on the nozzle wall: Left hand scale – nozzle A, right hand scale – nozzle B (Uncertainties of $(p-p_\infty)/(\rho V_h^2/2)$ and $x/D$ are ±0.7 and ±0.2 percent, respectively)**

Turbulent region – the Reynolds number is high, and the boundary layer at the pressure tap is turbulent.

The critical Reynolds number at which the observed curve in Fig. 3 leaves the laminar region, depends on the nozzle size and initial quiescence of the fluid. The lowest critical Reynolds number, $2 \times 10^4$, was obtained for the 78 mm dia. nozzle in the large underground reservoir. When the small reservoir was used, the critical Reynolds number for the same nozzle increased to $3.9 \times 10^4$. The highest critical Reynolds number, $8 \times 10^4$, was obtained for the 26 mm dia. nozzle independently of the reservoirs used. When the above nozzles were tested in air, the critical Reynolds number for each nozzle was the same as that obtained in the small reservoir.

The measured discharge coefficients for nozzle B are also shown in the same figure. Although the experiments were carried out using both water and air, and in the former case using the same reservoirs as for nozzle A, it can be seen that all the experimental results conform to a single curve within the test range. The boundary of each region discussed above is indistinct, and the performance of the nozzle appears to be satisfactory. According to the results of surface flow-visualization, the laminar region extends to a $R_h$ of about $2.2 \times 10^5$.

**Pressure Distributions.** The measured pressure distributions on the nozzle wall are shown in Fig. 4, as functions of the developed distance downstream from the nozzle inlet edge. The curves for nozzle A show the characteristic changes which are indicative of the existence of a separation bubble [14–16] on the straight cylindrical wall just downstream from the contraction. As for nozzle B, since the nondimensional pressure distribution is almost independent

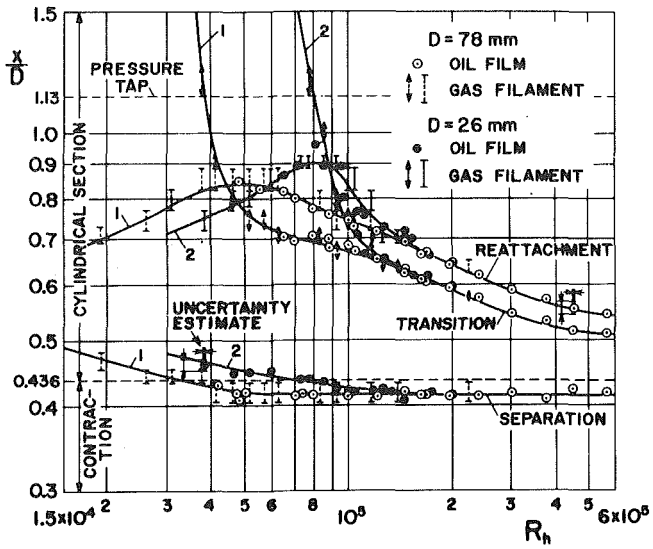


Fig. 5 Variation of the positions of separation, transition and reattachment with Reynolds number for nozzle A: 1 78 mm dia. nozzle, 2 26 mm dia. nozzle (Uncertainties of $x/D$ and $R_h$ and ± 2 and ± 0.4 percent, respectively)

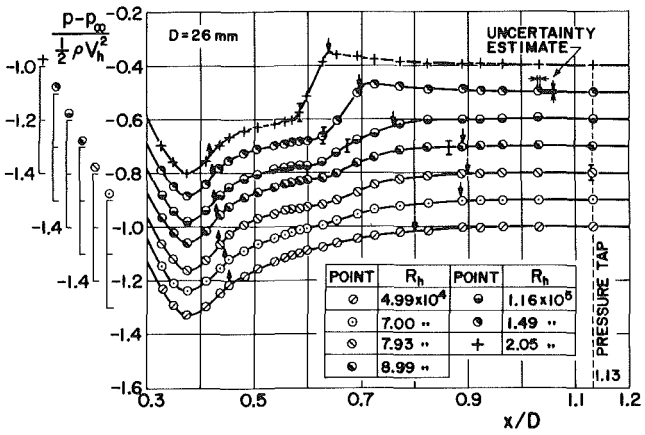


Fig. 6 Pressure distributions for 26 mm dia. nozzle A (pressure recovery region): Upward arrow – laminar separation, vertical mark – transition, downward arrow – reattachment (Uncertainties of $(p-p_\infty)/(\rho V_h^2/2)$ and $x/D$ are ± 0.7 and ± 0.2 percent, respectively)

of Reynolds number, only a typical example is shown in the figure. It is seen that the pressure on the contraction boundary decreases continuously in the downstream direction; it has only a very slight adverse gradient at the end of the contraction.

**Results of Surface Flow-Visualization.** In order to reveal the state of the boundary layer on the nozzle wall, methods of surface flow-visualization were used in the airflow. The results of visualization experiments for two different sizes of nozzle A are shown in Fig. 5. In the oil-film technique [15, 17], a mixture of paraffin oil, oleic acid and titanium white was brushed onto the nozzle wall, and the behavior of this liquid film was observed during airflow. In the gas-filament technique [15], ammonia vapor was emitted from a small hole in the nozzle wall coated with a solution of phenol red in ethyl alcohol, the chemical reaction around the hole and downstream from it being observed carefully during the experiments. The results obtained using this technique are shown by a line connecting the positions of two adjacent

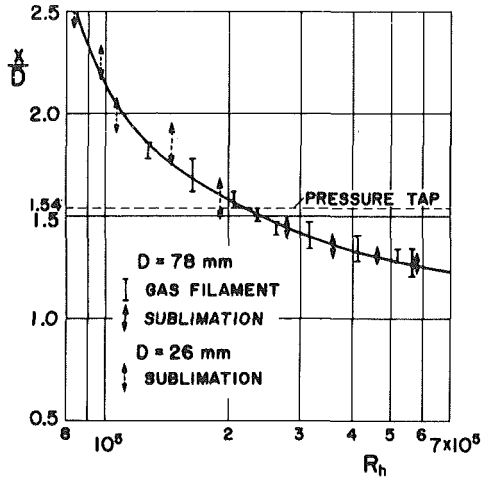


Fig. 7 Variation of the position of transition with Reynolds number for nozzle B (Uncertainties of $x/D$ and $R_h$ are ±2 and ±0.4 percent, respectively)

holes. As shown in the figure, the transition point advances upstream with increasing Reynolds number, and reaches the position of the pressure tap at a $R_h$ of $3.9 \times 10^4$ for the 78 mm dia. nozzle, and $8 \times 10^4$ for the 26 mm dia. nozzle. These are exactly the critical Reynolds numbers shown in Fig. 3. From the flow visualization a laminar bubble [18] was observed on the straight cylindrical wall for the lower Reynolds numbers, and the bubble increases in length (the distance between the separation point and the reattachment point) with an increase in Reynolds number. However, after the transitional bubble [18] size is reached, the length of the bubble decreases with an increase in Reynolds number. The effect of nozzle size is not noticeable for values of $R_h$ higher than $1.5 \times 10^5$.

The pressure distributions in the range $0.3 < x/D < 1.2$ for the 26 mm dia. nozzle A are shown in Fig. 6. The positions of separation, transition and reattachment as determined by the surface flow-visualization are shown by upward arrows, vertical marks and downward arrows respectively. It can be seen that with the increase in Reynolds number, a point of inflection occurs between the positions of separation and reattachment, and after a transitional bubble is formed, the degree of inflection becomes more and more pronounced. Finally, there appears a region of constant pressure in the middle of the bubble, and the transition takes place at the beginning of the marked pressure rise.

Fig. 7 shows the results of visualization experiments for nozzle B, where in addition to the gas-filament technique, the sublimation technique [15, 17] was used to find the start of the transition region. In the latter, a solution of p-dichlorobenzene in petroleum benzine was sprayed onto the nozzle wall. As shown in the figure, the transition point advances steadily upstream with increasing Reynolds number, and reaches the position of the pressure tap at a $R_h$ of about $2.2 \times 10^5$. No discernible effect of nozzle size on the transition point was observed over the entire test range.

**Empirical Equations for Discharge Coefficients.** The empirical equations for the discharge coefficients deduced from the experimental results are summarized in Table 2, where the range of $R_h$ in which the equations can be used is also shown together with the two-sigma uncertainty of the respective equations. The derivation of the equations is given in the Appendix. In the turbulent region, equation (12) can be used coincidentally for both nozzles, because their mean experimental curves coincide with each other within the scatter of their experimental data.

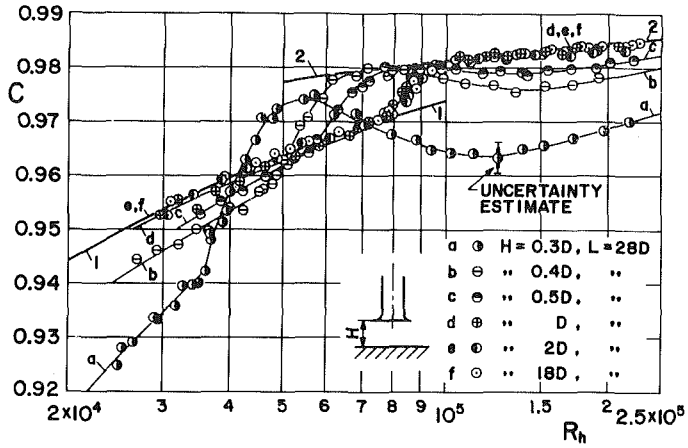


Fig. 8 Effect of the proximity of a floor on discharge coefficients for nozzle A: 1 equation (10), 2 equation (12) (Uncertainties of $C$ and $R_h$ are ± 0.3 and ± 0.4 percent, respectively)

Table 1 Dimensions of inlet nozzles which were tested

| Nozzle | Internal dia of pipe (= dia of nozzle throat), $D$, mm | Wall thickness, $t$, mm | Pressure tap diameter, $\delta$, mm |
|---|---|---|---|
| A and B | 78.00±0.005* | 8.0±0.02 | 0.7±0.02 |
| | 26.00±0.005 | 3.0±0.02 | 0.5±0.02 |
| | 8.00±0.005 | 0.998±0.002 | 0.4±0.02 |

*20 : 1 odds

Note : Possible fixed errors are included within the uncertainty bands stated.

Table 2 Empirical equations for discharge coefficients

| Region | Nozzles | Empirical equations | Range of $R_h$ | Two-sigma uncertainties |
|---|---|---|---|---|
| Laminar Region | A | $C = (1+17.2\,R_h^{-1/2})^{-1/2}$ (10) | $3\times10^3 \leq R_h \leq 8\times10^4$ | ±0.0029 |
| | B | $C = (1+16.2\,R_h^{-1/2})^{-1/2}$ (11) | $3\times10^3 \leq R_h \leq 2.8\times10^5$ | ±0.0029 |
| Turbulent Region | A | $C = 1-0.144\,R_h^{-1/5}(1+ +28.0\,R_h^{-3/8})^{4/5}$ (12) | $4\times10^4 \leq R_h \leq 5\times10^5$ | ±0.0020 |
| | B | | $2.8\times10^5 \leq R_h \leq 5\times10^5$ | ±0.0017 |

## Installation Effects

**Effect of Proximity of a Floor or a Wall to the Inlet.** The effect of the proximity of a floor or a wall on discharge coefficients was studied with the nozzle A (26 mm dia.) using the small reservoir shown in Fig. 2(*a*). The effect of the proximity of a floor on the discharge coefficients is shown in Fig. 8, where the results of measurements for various nozzle heights above the floor are plotted against the Reynolds number. It can be seen that the critical Reynolds number decreases with a decrease in distance between the floor and the nozzle inlet edge. On the whole, the change in the discharge coefficient relative to the basic value obtained from a normal calibration becomes less than about 0.1 percent if the height of the nozzle inlet edge above the floor is greater than one pipe diameter.

The effect of the proximity of a wall parallel to the nozzle axis on the discharge coefficients is shown in Fig. 9. It is seen that the effect is completely negligible if the distance between the wall and the nozzle axis is greater than two pipe diameters.

**Effect of Pressure Tap Size.** The effect of pressure tap size on the discharge coefficients was examined with the nozzle B (26 mm dia.) using the small reservoir. The nozzle used was provided with two pressure taps spaced 180 deg apart circumferentially in the same plane. The hole diameter ratio, $\delta/D$, was varied between 0.019 and 0.20, the depth of the hole being always kept more than twice the hole diameter so that further increase of the depth ceases to have any effect on the pressure reading [19]. The experimental results are shown in Fig. 10, in which it is seen that at a $\delta/D$ of 0.20, the measured results deviate systematically from equation (11) for the higher Reynolds numbers. Thus it may be concluded that the

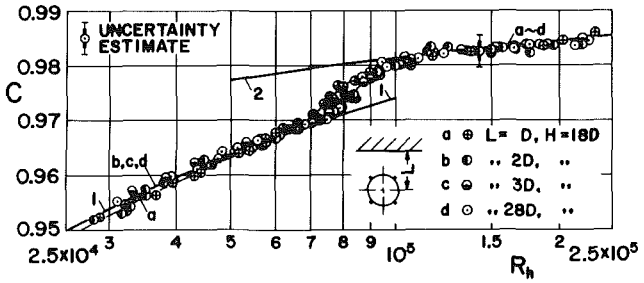


Fig. 9 Effect of the proximity of a wall parallel to the nozzle axis on discharge coefficients for nozzle A: 1 equation (10), 2 equation (12) (Uncertainties of $C$ and $R_h$ are ±0.3 and ±0.4 percent, respectively)

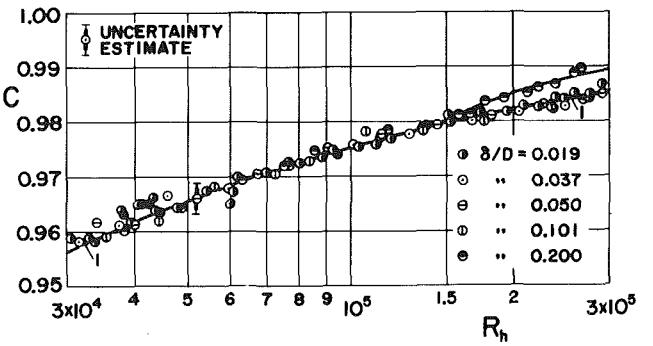


Fig. 10 Effect of pressure tap size on discharge coefficients for nozzle B: 1 equation (11) (Uncertainties of $C$ and $R_h$ are ± 0.3 and ± 0.4 percent, respectively)

effect of the pressure tap size on the discharge coefficients is negligibly small if the hole diameter is less than about $0.1D$.


## Acknowledgments

The authors wish to acknowledge the valuable assistance provided by Messrs. S. Hasegawa and Y. Shōji, technicians, during the experiments, and also the help by Messrs. T. Ishidō, Y. Sue and Y. Sasaki, students of Tōhoku University. The authors are indebted to Professor M. Inoue, Kyushu University, Japan, who suggested us the expression (15) for discharge coefficients.


## References


1 Sato, Y., "Experimental Study on Energy Loss Due to Branching and Confluence in Rectangular Duct Flow," *Transactions of the Japan Society of Mechanical Engineers* (in Japanese), Vol. 28, No. 192, 1962, pp. 881–890.

2 Sprenger, H., "Druckverluste in 90°-Krümmern für Rechteckrohre," *Schweizerische Bauzeitung*, Vol. 87, No. 13, 1969, pp. 223–231.

3 Japanese Industrial Standards Committee, "Measurement Methods of Pump Discharge," (in Japanese), Japanese Standards Association, Tokyo, Japan, 1976, p. 19.

4 Japanese Industrial Standards Committee, "Testing Methods for Turbo-Fans and Blowers," (in Japanese), Japanese Standards Association, Tokyo, Japan, 1976, p. 15.

5 Japanese Industrial Standards Committee, "Testing Methods for Turbo-Blowers and Compressors," (in Japanese), Japanese Standards Association, Tokyo, Japan, 1976, p. 8.

6 Voss, L. R., and Hollyer, R. N., Jr., "Nozzles for Air Flow Measurement," *Review of Scientific Instruments*, Vol. 34, No. 1, 1963, pp. 70–74.

7 Leutheusser, H. J., "Flow Nozzles With Zero Beta Ratio," ASME *Journal of Basic Engineering*, Vol. 86, No. 3, 1964, pp. 538–542.

8 Soundranayagam, S., "An Investigation Into the Performance of Two ISA Metering Nozzles of Finite and Zero Area Ratio," ASME *Journal of Basic Engineering*, Vol. 87, No. 2, 1965, pp. 525–532.

9 Benedict, R. P., and Wyler, J. S., "Analytical and Experimental Studies of ASME Flow Nozzles," ASME JOURNAL OF FLUIDS ENGINEERING, Vol. 100, No. 3, 1978, pp. 265–275.

10 Kinghorn, F. C., and McHugh, A., "The Performance Characteristics of Borda Inlet Air Flowmeters," *Scientific Instruments, Journal of Physics*, Series E, Vol. 11, No. 1, 1978, pp. 87–93.

11 Itaya, S., and Takenaka, T., "Flow Measurement by Means of Inlet Nozzles," *Transactions of the Japan Society of Mechanical Engineers*, (in Japanese), Vol. 23, No. 129, 1957, pp. 319–322.

12 Rouse, H., and Hassan, M. M., "Cavitation-Free Inlets and Contractions," *Mechanical Engineering*, Vol. 71, No. 3, 1949, pp. 213–216.

13 Rao, P. V., "Boundary-Layer Development at Curved Conduit Entrances," *Journal of the Hydraulics Division, Proceedings of the ASCE*, Vol. 94, No. HY 1, 1968, pp. 195–217.

14 Tani, I., "Low-Speed Flows Involving Bubble Separations," *Progress in Aeronautical Sciences*, Vol. 5, 1964, Pergamon Press, Oxford, pp. 70–103.

15 Erlich, É, "Méthodes de Visualisation du Bulbe de Décollement de Bord d'Attaque et Analyse des Résultats," *La Recherche Aérospatiale*, No. 4, 1973, pp. 219–223.

16 Young, A. D., "Some Special Boundary Layer Problems," *Zeitschrift für Flugwissenschaften und Weltraumforschung*, Vol. 1, No. 6, 1977, pp. 401–414.

17 Rosenhead, L., *Laminar Boundary Layers*, Clarendon Press, Oxford, 1963, p. 611.

18 Briley, W. R., and McDonald, H., "Numerical Prediction of Incompressible Separation Bubbles," *Journal of Fluid Mechanics*, Vol. 69, Part 4, 1975, pp. 631–656.

19 Shaw, R., "The Influence of Hole Dimensions on Static Pressure Measurements," *Journal of Fluid Mechanics*, Vol. 7, Part 4, 1960, pp. 550–564.

20 Rivas, M. A., Jr., and Shapiro, A. H., "On the Theory of Discharge Coefficients for Rounded-Entrance Flowmeters and Venturis," *Trans. ASME*, Vol. 78, No. 3, 1956, pp. 489–497.

21 Kline, S. J., and Shapiro, A. H., "Experimental Investigation of the Effects of Cooling on Friction and on Boundary-Layer Transition for Low-Speed Gas Flow at the Entry of a Tube," *NACA Technical Note* 3048, Nov. 1953.

22 Hall, G. W., "Application of Boundary Layer Theory to Explain Some Nozzle and Venturi Flow Peculiarities," *Proceedings of the Institution of Mechanical Engineers*, Vol. 173, No. 36, 1959, pp. 837–870.

23 Truckenbrodt, E., "Ein Quadraturverfahren zur Berechnung der laminaren und turbulenten Reibungsschicht bei ebener und rotationssymmetrischer Strömung," *Ingenieur-Archiv*, Vol. 20, No. 4, 1952, pp. 211–228.

24 Rotta, J. C., "FORTRAN IV-Rechenprogramm für Grenzschichten bei kompressiblen ebenen und achsensymmetrischen Strömungen," *Deutsche Luft- und Raumfahrt, Forschungsbericht* 71–51, 1971.


## APPENDIX

### Derivation of the Empirical Equations for Discharge Coefficients

**Empirical Equations for Discharge Coefficients in Laminar Region.** Rivas and Shapiro [20] derived the following equation of discharge coefficients for rounded-entrance flowmeters considering a developing laminar boundary layer along the nozzle wall:

$$C=(1+\bar{f}_{app}l'/D)^{-1/2}, \tag{13}$$

where $l'$ $(=l+l_{eq})$ is the effective length of the nozzle. The mean apparent friction factor, $\bar{f}_{app}$, over the length $l'$ is given by [21]

$$\bar{f}_{app}=13.74\ \mathrm{R}_D{}^{-1/2}(l'/D)^{-1/2}, \tag{14}$$

Substituting (14) into (13) together with (6), we get

$$C=(1+K\mathrm{R}_h{}^{-1/2})^{-1/2}, \tag{15}$$

where

$$K=13.74\,C^{-1/2}(l'/D)^{1/2}. \tag{16}$$

Based on the test results in the laminar region, $K$ may be assumed to be a constant over the test range. The value of $K$ is determined so as to give the best fit with the experimental results, and we thus obtain equations (10) and (11) for the respective nozzles.

**An Empirical Equation for Discharge Coefficients in Turbulent Region.** Hall [22] derived the following expression for discharge coefficients based on the boundary-layer displacement thickness, $\delta_h{}^*$, at the location of the pressure tap:

$$C=1-4\delta_h{}^*/D. \tag{17}$$

If the Reynolds number is not too high and the power law is assumed for the friction coefficient, $\delta_h{}^*$ may be expressed in the form [23]:

$$\delta_h{}^*/D=\alpha\mathrm{R}_h{}^{-1/5}(1+\beta\mathrm{R}_h{}^{-3/8})^{4/5}, \tag{18}$$

where $\alpha$ and $\beta$ are coefficients which depend on the position of the transition point. To determine $\alpha$ and $\beta$, the growth of the axially symmetrical boundary layer was calculated by the method of Rotta [24] based on the measured pressure distributions on the nozzle wall shown in Fig. 4. The laminar boundary layer was assumed to develop from the nozzle inlet edge. In the case of nozzle A, the transition point was assumed to coincide with the laminar separation point, the existence of the separation bubble being neglected. In the case of nozzle B, the transition point shown in Fig. 7 was used in the calculations. However, the results showed that the predicted discharge coefficients were lower than the experimental values by about 0.2 percent for nozzle A and higher by about 0.5 percent for nozzle B. To obtain an empirical equation for discharge coefficients, it was assumed that both $\alpha$ and $\beta$ are constants over the test range. They were determined so as to give the best fit with experimental results, and the values thus obtained were used in equation (12).

## DISCUSSION

### R. P. Benedict[1]

The authors are to be congratulated for making available to the profession the very useful experimental data concerning plenum inlet nozzle installations. Their $R_h$ is interesting in that it is based on the ideal flow rate rather than the usual actual flow rate.

Several recent references on plenum inlet nozzles could be mentioned in connection with this paper. They are [25] and [26], and concern a theoretical C and an experimental evaluation of the same for ASME throat tap nozzles.

The authors' statement that their results are relatively unaffected by tap size whenever $\delta/D \leq 0.1$ bears some discussion. From equations given in the referenced papers, we calculate an effect based on the minimum $\delta/D$ of 0.019 of $+0.003$ over the zero tap size $C$ at $R_D = 5 \times 10^5$, and an effect of $+0.006$ at $R_D = 3 \times 10^6$. These would be noticeable, and the reason they do not show up in Fig. 10 is that the zero tap size $C$ is not given, but rather a measured $C$.

It is interesting to note that the authors' equation (12), for a turbulent boundary layer at the throat tap, yields an empirical $C$ of 0.988 at $R_h = 5 \times 10^5$, and 0.992 at $R_h = 3 \times 10^6$. At these same $R_h$, the theoretical boundary layer equations of [25] and [26] yield 0.991 and 0.993 respectively. Since these values are within the authors' claim of $\pm 0.3$ percent on $C$, we can conclude that the theoretical equation adequately predicts the authors' experimental work in the turbulent boundary layer regime.

Again, let me thank the authors for providing the excellent data on inlet flow nozzles.

### Additional References


25 Benedict, R. P., "Generalized Fluid Meter Discharge Coefficient Based Solely on Boundary Layer Parameters," ASME *Journal of Engineering for Power*, Vol. 101, Oct. 1979, p. 572.

26 Benedict, R. P., "The Plenum Inlet Discharge Coefficient of an ASME Nozzle," to be presented at the Second International Symposium on Flow, St. Louis, Mi., Mar. 1981.


### J. S. Wyler[2]

The authors are to be congratulated on the extensive data that they have presented. The data from Nozzle B is most interesting in that it apparently has no boundary layer separation, thus offering the possibility of analytical prediction of the boundary layer. The experimental data presented could serve as a check on the analytical prediction techniques. In this regard, it is peculiar that the authors' predictions for Nozzle B using the method of Rotta were higher than the experimental values by 0.5 percent. This would make the predicted values greater than unity, a physical impossibility if pressure tap errors are neglected.

Concerning the authors' study of pressure tap effects, their results do not seem to agree with previous work due to Benedict and Wyler (reference [9]). The magnitudes of the errors expected using the work presented in that reference are much greater than those presented herein. Only if the boundary layer remained laminar would the predicted errors more closely resemble those experimentally determined. The reason for this discrepancy is not clear to the writer.

The final comment is directed towards the authors' use of a Reynolds number based on the potential core velocity at the pressure tap instead of the usual representation in terms of the average velocity at the pressure tap. This is rather unfortunate in that it makes comparison with previous work more difficult, even though the two values are reasonably close over the range of test results presented.

The authors are encouraged to continue the experimental program to define the various boundary layer parameters such as displacement thickness and shape factor. This information would be most useful in further analytical studies.

### Authors' Closure

The authors wish to thank Messrs. Benedict and Wyler for their pertinent comments. Concerning the effects of pressure tap size, the last sentence should had been written as follows; "the effect of the pressure tap size on the discharge coefficients is negligibly small within the test range if the hole diameter is less than about $0.1D$." It can be seen from Fig. 7 that the boundary layer at the pressure tap is laminar for Reynolds numbers smaller than $2.2 \times 10^5$, and turbulent for the higher Reynolds numbers. However, since the experimental curve in the figure shows the beginning of transition, the boundary layer at the tap in the range $2.2 \times 10^5 < R_h < 3 \times 10^5$ is supposed to be still in a state of transition. The authors regret that the experiments on the effect of pressure tap size had not been carried out in the fully turbulent region.

The relation between a zero tap size discharge coefficient, $C_0$, and a measured discharge coefficient, $C$, is given by

$$C = C_0(1 - e/q)^{-1/2}, \tag{19}$$

where

$$e/q = (e/\tau)c_f \tag{20}$$

Here, $e$ is the error in static pressure measurement, $q$ $(=\rho V_h^2/2)$ the dynamic pressure, $\tau$ the wall shear stress, $c_f$ $(=\tau/q)$ the local shear-stress coefficient, and $e/\tau$ is specified in reference [9]. The discharge coefficients in turbulent region for nozzle B were obtained from the 78 mm dia nozzle ($\delta$ = 0.7 mm), which has relatively small hole diameter ratio ($\delta/D$ = 0.009). The values of $c_f$ calculated by the method of Rotta based on the measured pressure distributions for nozzle B are shown in Table 3 together with $e/q$, C and $C_0$. In the turbulent region it is seen that the discharge coefficients, $C$, obtained form equation (12) are in substantial agreement with the zero tap size discharge coefficients. In the laminar region, since equation (11) is based on the experimental results obtained from the 26 mm dia nozzle ($\delta/D$ = 0.019), the agreement between $C$ and $C_0$ is satisfactory. For other hole diameter ratios shown in Fig. 10, the difference between $C$

**Table 3 Summary of data in connection with the effect of pressure tap size for nozzle B**

| $R_h$ | $c_f$ | $e/q$ | $C$ | $C_0$ |
|---|---|---|---|---|
| $2.98 \times 10^5$ (Turbulent) | 0.00443 | 0.00162 | 0.986 | 0.985 |
| $4.04 \times 10^5$ (Turbulent) | 0.00460 | 0.00283 | 0.987 | 0.986 |
| $1.99 \times 10^5$ (Laminar) | 0.00132 | 0.000326 | 0.982 | 0.982 |


[1] Westinghouse Electric Corp., Power Generation Group, Philadelphia, Pa. 19113. Fellow ASME.

[2] Manager, Fuel Management Engineering, General Electric Co., Wilmington, Mass. 01887.

and $C_0$ in laminar region deduced from equation (19) is always less than 0.3 percent. Consequently, no discernible effect of pressure tap size on the discharge coefficients is observed in the laminar region.

The use of a Reynolds number, $R_h$, based on the differential pressure is very convenient in actual practice, because the discharge coefficients depend on the Reynolds number. the relation between $R_D$ and $R_h$ is given by equaiton (6).

Finally, concerning Dr. Wyler's first query, the authors would like to add that the predicted values of the discharge coefficients using the method of Rotta are 0.991 at $R_h = 2.98 \times 10^5$ and 0.992 at $R_h = 4.04 \times 10^5$, which are higher than the experimental values by about 0.5 percent, but less than unity.

# Computation of the Turbulent Flow in an Internal Combustion Engine During Compression

**P. S. Bernard**
Assistant Professor,
Department of Mechanical Engineering,
University of Maryland,
College Park, Md. 20742

*A set of closed dynamical equations for the mean and variance of the turbulent vorticity field are used to study the piston driven flow in a two-dimensional model of an internal combustion engine cyclinder during the compression stroke. A dominant feature of the flow is observed to be the development of large corner vortices. In their vicinity intense production of turbulence occurs which locally greatly exceeds that resulting from the compression of intake generated turbulence. A comparison of the flow field at two strokes to bore ratios is made.*

## 1 Introduction

Knowledge of the detailed flow and combustion processes in the cylinder of an IC engine can aid in the design of fuel efficient and nonpolluting engines. For example, the degree and distribution of mixture turbulence at the time of ignition significantly effects the subsequent flame propagation, see [1-6]. In the present study the turbulent flow generated by the movement of a piston from BDC (bottom dead center) to TDC (top dead center) during the compression stroke is computed by numerically solving a set of closed equations for two-dimensional turbulence developed by the author, see [7-9]. Solutions are obtained for flow in a two-dimensional model of a cylinder. Future work will extend the computations to three-dimensions as well as into the remaining strokes of the engine cycle.

Several different approaches have been taken in computing the flow and combustion processes in engines. Sirignano [10] treated a one-dimensional model of the piston-cylinder problem. In this approach the turbulence generated during the compression stroke was represented by several parameters which entered into equations for the development of the combustion wave. Using a simple turbulence model, Boni, et al. [11] simulated the combustion process in a stratified charge engine. Griffin, et al. [12] computed two-dimensional laminar flow in a cylinder at low Reynolds numbers. Simulations of the laminar axisymmetric flow in a cylinder were reported by Gosman, et al. [13]. In [14, 15] inviscid two and three-dimensional flow in cylinders was calculated using a finite difference scheme of MacCormack. In [16] a new numerical method for computing viscous compressible flow at relatively large Reynolds numbers was applied to the cylinder flow. In this method a vortex sheet technique was used to model the boundary layers while a random choice method was used in computing the interior flow. Gosman and Johns [17] applied the $k$-$\epsilon$ turbulence closure, see [18], to computing the piston driven turbulent flow in cylinders. They computed asisymmetric flow for the compression and expansion strokes without combustion. The effects of different piston bowls and initial swirl levels on piston and squish generated turbulence at TDC was studied in detail.

The present computations of the development and distribution of mixture turbulence during the compression stroke show significant qualitative agreement with the experimental investigations of Witze [3, 19] and Ishikawa and Daily [6]. A comparison of the computed solutions at two strokes to bore ratios is made. The present study also provides some insight as to the relative importance to the generation of mixture turbulence of the compression of residual turbulence created during the intake stroke and the corner-vortex phenomenon. These factors are known to be of special importance to the development of turbulence in cylinders [3, 6, 19].

In the next section a description of the piston cylinder problem is given. In section 3 the dynamical equations to be solved are presented. Next the numerical method used to solve the set of closed equations is described and in section 5 computed results are given. In the final section a brief statement of conclusions is presented.

## 2 Description of the Cylinder-Piston Problem

The flow configuration is shown in Fig. 1. $x$ is the axial coordinate while $y$ spans the width of the cylinder. The origin of the coordinate system is in the lower left hand corner of the cylinder. Lengths are scaled by the bore $B$, i.e. the "diameter" of the cylinder, so in nondimensional coordinates the flow domain is of unit width. $X_p(t)$ is the nondimensional distance of the piston face from the cylinder head. $t$ is a nondimensional time defined using the scaling factor $2\omega$ where $\omega$ is the angular speed of the crankshaft in revolutions per second. For small values of $(r/L)^2$, such as are found in practice, $X_p(t) = \sigma(1/\chi - 1) + (1 + \cos(\pi t))/2$ where $r$ is the length of the crankshaft journal, $L$ is the length of the connecting rod, $\chi$ is the compression ratio and $\sigma$ is the stoke to bore ratio. At $t = 0$ the piston is at BDC and $t = 1$ it is at TDC. The piston velocity $U_p(t) = \dot{X}_p(t) = -\sigma\pi \sin(\pi t)/2$.

For the problem considered here it will be assumed that the Mach number is sufficiently small so that the flow field

Contributed by the Fluids Engineering Division for publication in the JOURNAL OF FLUIDS ENGINEERING. Manuscript received by the Fluids Engineering Division, January 16, 1980.

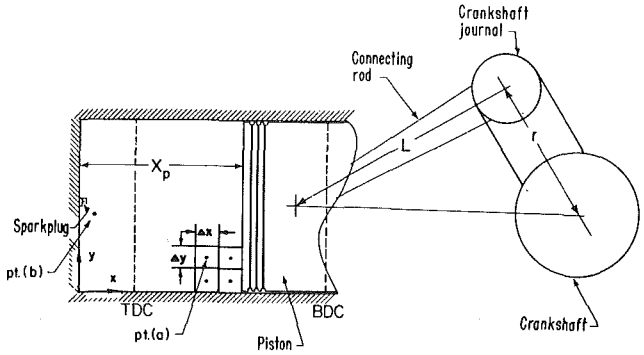


**Fig 1 Description of flow field**

compresses uniformly in space. Consequently the fluid density $\rho$ depends only on $t$, and $\nabla \rho = 0$. This assumption is not unreasonable in view of the conditions found in practice. However, if a combustion process were to be included then a more general accounting of compressibility of the fluid would have to be made. In light of this assumption the velocity field is set equal to $\mathbf{U}_c + \mathbf{u}$ where $\mathbf{U}_c = (U_c, V_c)$ is an irrotational compressible part such that $\nabla \cdot \mathbf{U}_c = \theta$ and $\theta$ is the dilitation. $\mathbf{u} = (u,v)$ is an incompressible rotational velocity field which is the sum of mean and fluctuating parts $\mathbf{U} = (U, V)$ and $\mathbf{u}' = (u', v')$, respectively.

Assuming that the valves shut at $t = 0$ it can be shown using the conservation of mass that $\rho(t) = \rho(0)X_p(0)/X_p(t)$. The continuity equation then gives $-(\partial\rho/\partial t)/\rho = \theta$, so $\theta(t) = U_p(t)/X_p(t)$. From $\nabla \cdot \mathbf{U}_c = \theta$ it is found that $U_c = \theta x$ and $V_c = 0$. $\mathbf{U}_c$ satisfies all of the normal boundary conditions.

## 3 Closed Equations

The dynamical equations to be solved for the cylinder flow are for the mean and variance of the vorticity field. The vorticity, which for planar flows is perpendicular to the plane of motion, is $\xi = \bar{\xi} + \xi'$ where the overbar refers to an ensemble average over all the realizations of the flow field. The variance of the vorticity field is denoted by $\zeta = \overline{\xi'^2}$. The closed equations for the quantities $\bar{\xi}$ and $\zeta$ are, respectively:

$$\frac{\partial \bar{\xi}}{\partial t} = -(U_c + U)\frac{\partial \bar{\xi}}{\partial x} - V\frac{\partial \bar{\xi}}{\partial y} + \frac{\partial}{\partial x}\left(\frac{1}{R} + T_{11}\overline{u'^2}\right)\frac{\partial \bar{\xi}}{\partial x} + \frac{\partial}{\partial y}\left(\frac{1}{R} + T_{22}\overline{v'^2}\right)\frac{\partial \bar{\xi}}{\partial y} - \bar{\xi}\theta \tag{1}$$

$$\frac{\partial \zeta}{\partial t} = -(U_c + U)\frac{\partial \zeta}{\partial x} - V\frac{\partial \zeta}{\partial y} + \frac{\partial}{\partial x}\left(\frac{1}{R} + T_{11}\overline{u'^2}\right)\frac{\partial \zeta}{\partial x} + \frac{\partial}{\partial y}\left(\frac{1}{R} + T_{22}\overline{v'^2}\right)\frac{\partial \zeta}{\partial y} - 2\zeta\theta + 2\,T_{11}\overline{u'^2}\left(\frac{\partial \bar{\xi}}{\partial x}\right)^2 + 2\,T_{22}\overline{v'^2}\left(\frac{\partial \bar{\xi}}{\partial y}\right)^2 - \frac{2\zeta}{\lambda_d^2 R} \tag{2}$$

where $\overline{u'^2}$ and $\overline{v'^2}$ are the velocity variances, $R = 2\omega\rho B^2/\mu$, $\mu$ is the viscosity, $\lambda_d$ is a vorticity microscale and $T_{11}$ and $T_{22}$ are Lagrangian integral time scales. $\lambda_d$, $T_{11}$, and $T_{22}$ will be defined below. A detailed derivation of (1) and (2) may be found in [7-9].

The first two terms on the right of (1) represent convection of $\bar{\xi}$ by the mean velocity field while the third and fourth give the effect of molecular and turbulent diffusion. The final term accounts for the increase in mean vorticity due to compression. On the right of (2) the first two terms represent convection of $\zeta$ while the third and fourth, diffusion. The fifth term accounts for an increase in turbulence intensity due to compression. The sixth and seventh terms give the production of turbulence by the mean shear while the last term in (2) represents its loss due to viscous dissipation.

$U$ amd $V$ maybe computed by defining a stream function $\bar{\psi}$ such that $U = \partial\bar{\psi}/\partial y$ and $V = -\partial\bar{\psi}/\partial x$. $\bar{\psi}$ is determined as the solution of Poisson's equation

$$\nabla^2 \bar{\psi} = -\bar{\xi} \tag{3}$$

## Nomenclature

$B$ = bore
$D$ = flow domain
$D_{+i}, D_{-i}$ = difference operators
$D(\mathbf{z})$ = values of $\mathbf{r}$ such that $R(\mathbf{z}:\mathbf{r}) \neq 0$
$f_i^n, g_j^n$ = discrete functions
$G(\mathbf{x}:\mathbf{z})$ = stream function induced by vortex at $\mathbf{z}$
$G_{ij}^{km}$ = approximation to $G(\mathbf{x}:\mathbf{z})$
$L$ = length of connecting rod
$L_A$ = integral area scale
$M$ = number of mesh points in $y$ dir.
$N$ = number of mesh points in $x$ dir.
$r$ = length of crankshaft journal
$\mathbf{r}$ = a pt. in $D(\mathbf{z})$
$R$ = Reynolds number
$R(\mathbf{z}:\mathbf{r})$ = vorticity auto-correlation function
$R_{ii}(s)$ = Lagrangian velocity auto-correlation function
$t, t_0, s$ = time
$T_{ii}$ = Lagrangian integral time scale
$\mathbf{u} = (u,v)$ = incompressible part of velocity field
$\mathbf{U} = (U,V)$ = mean part of $\mathbf{u}$
$U_c = (U_c, V_c)$ = compressible part of velocity field
$U_p$ = velocity of piston
$\overline{u'^2}, \overline{v'^2}$ = velocity variances
$x$ = axial coordinate
$X_p$ = piston position
$y$ = transverse coordinate
$\delta_{+i}, \delta_{-i}$ = difference operators
$\Delta t$ = integration time step
$\Delta x$ = grid spacing in x dir.
$\Delta y$ = grid spacing in y dir.
$\zeta$ = vorticity variance
$\theta$ = dilitation
$\lambda_d$ = composite vorticity microscale
$\lambda_1, \lambda_2$ = vorticity microscale in $x$, $y$ dir.
$\mu$ = viscosity
$\nu$ = kinematic viscosity
$\xi$ = vorticity
$\rho$ = density
$\sigma$ = stroke to bore ratio
$\chi$ = compression ratio
$\bar{\psi}$ = stream function
$\omega$ = angular velocity of crankshaft
$\nabla$ = gradient
$\nabla^2$ = Laplacian

Superscripts

$(\bar{\ })$ = mean value
$(\ )'$ = fluctuating part
$(\ )^n$ = time step

Subscripts

$(\ )_{ij}$ = $i$th grid pt. in $x$ dir., $j$th in $y$ dir.

for given $\bar{\xi}$, and satisfying Dirichlet boundary conditions.

The final step in closing (1) and (2) consists of computing $\overline{u'^2}$ and $\overline{v'^2}$ from the global distribution of $\zeta$. A relationship between these quantities may be obtained in the form:

$$\overline{u'^2}(\mathbf{x}) = \int_D d\mathbf{z}\; G_i(\mathbf{x}:\mathbf{z})\zeta(\mathbf{z}) \int_{D(\mathbf{z})} d\mathbf{r}\; G_i(\mathbf{x}:\mathbf{z}+\mathbf{r})R(\mathbf{z},\mathbf{r}) \qquad (4)$$

$i = 1,2$ where $D$ is the flow domain, $\mathbf{z}$ is an integration variable covering $D$, $R(\mathbf{z},\mathbf{r})$ is the vorticity auto correlation function

$$R(z,r) = \frac{\overline{\xi'(\mathbf{z})\xi'(\mathbf{z}+\mathbf{r})}}{\zeta(\mathbf{z})}, \qquad (5)$$

$D(\mathbf{z})$ is the region over which $R(\mathbf{z},\mathbf{r}) \neq 0$, $\mathbf{r} = (r_1, r_2)$ is an integration variable covering $D(\mathbf{z})$ and $G_i(\mathbf{x}:\mathbf{z})$ is the velocity field (satisfying normal boundary conditions) generated at the point $\mathbf{x}$ by a unit vortex at $\mathbf{z}$. Letting $G(\mathbf{x}:\mathbf{z})$ be the stream function generated by such a vortex, then $G_1 = \partial G/\partial y$ and $G_2 = -\partial G/\partial x$. In computations (4) is approximated by a suitable quadrature in which the only appearance of $R(\mathbf{z},\mathbf{r})$ is in an integral area scale $L_A = \int_{D(\mathbf{z})} R(\mathbf{z},\mathbf{r})\, d\mathbf{r}$.

The microscale $\lambda_d$ is defined from $1/\lambda_d^2 = 2/\lambda_1^2 + 2/\lambda_2^2$ where $\lambda_i$, $i = 1, 2$ are vorticity microscales defined as the points of intersection with the $r_1$ and $r_2$ axes, respectively, of a parabolic approximation to $R(\mathbf{z}:\mathbf{r})$, see [20]. Thus $\lambda_i^2 = -2/(\partial^2 R/\partial r_i^2)$. For a given point $\mathbf{x}$ at time $t, T_{ii} \equiv \int_0^\infty R_{ii}(s)\, ds$ $i = 1,2$ where $R_{ii}(s)$ is the Lagrangian velocity auto-correlation function $R_{ii}(s) = \overline{u_i'(t)u_i'(t+s)}/\overline{u_i'^2(t)}$. $u_i'(t_0) = u_i'(\mathbf{X}(t_0), t_0)$ where $\mathbf{X}(t_0)$ is the path of a fluid particle satisfying $\mathbf{X}(t) = \mathbf{x}$.

## 4 The Numerical Algorithm

At $t = 0$ the flow domain is divided into $N \cdot M$ cells of equal size with $M$ cells spanning the width of the cylinder and $N$ cells its length. Once constituted, the grid cells are considered to move with the linear velocity field $\mathbf{U}_c$ and thus remain uniform in size. The grid spacing in the $y$ direction $\Delta y = 1/M$, is constant, while in the $x$ direction, $\Delta x(t) = X_p(t)/N$ varies with the motion of the piston. The collection of the centers of the cells at any time $\{(i-\tfrac{1}{2})\Delta x, (j-\tfrac{1}{2})\Delta y, i = 1, \ldots, N, j = 1, \ldots, M)\}$ form a grid (see Fig. 1) which collapses as $t$ varies from 0 to 1. On this grid is defined discrete approximations $\bar{\xi}_{ij}^n$, $\zeta_{ij}^n$ and $\bar{\psi}_{ij}^n$ to $\bar{\xi}, \zeta$, and $\bar{\psi}$, respectively. The superscript refers to the discretized time step so that for example $\bar{\xi}_{ij}^n$ approximates $\bar{\xi}((i-\tfrac{1}{2})\Delta x_n, (j-\tfrac{1}{2})\Delta y, n\Delta t)$ where $\Delta x_n = \Delta x(n\Delta t)$.

The computed results were obtained by solving discrete approximations to (1-4). Corresponding to (1) and (2) are, respectively:

$$\begin{aligned}
\frac{\bar{\xi}_{ij}^{n+1} - \bar{\xi}_{ij}^n}{\Delta t} &= -(U_{ij}^n \delta_{+i}\bar{\xi}^n - U_{i-1j}^n \delta_{-i}\bar{\xi}^n)/\Delta x_n \\
&\quad -(V_{ij}^n \delta_{+j}\bar{\xi}^n - V_{i-1j}^n \delta_{-j}\bar{\xi}^n)/\Delta y \\
&\quad +(f_i^n D_{+i}\bar{\xi}^n - f_{i-1} D_{-i}\bar{\xi}^n) \\
&\quad +(g_j^n D_{+j}\bar{\xi}^n - g_{j-1}^n D_{-j}\bar{\xi}^n) - \bar{\xi}_{ij}^n \theta_n \qquad (6) \\
\frac{\bar{\zeta}_{ij}^{n+1} - \bar{\zeta}_{ij}^n}{\Delta t} &= -(U_{ij}^n \delta_{+i}\zeta^n - U_{i-1j}^n \delta_{-i}\zeta^n)/\Delta x_n \\
&\quad -(V_{ij}\delta_{+j}\zeta^n - V_{i-1j}^n \delta_{-j}\zeta^n)/\Delta y \\
&\quad +(f_i^n D_{+i}\zeta^n - f_{i-1}^n D_{-i}\zeta^n) + (g_j^n D_{+j}\zeta^n - g_{j-1}^n D_{-j}\bar{\zeta}^n) \\
&\quad -2\zeta_{ij}^n\theta_n + T_{11}\,\overline{u_{ij}'^2}^n (D_{+i}\bar{\xi}^n)^2 + T_{11}\,\overline{u_{i-1j}'^2}(D_{-i}\bar{\xi}^n)^2 \\
&\quad + T_{22}\,\overline{v_{ij}'^2}^n (D_{+j}\bar{\xi}^n)^2 + T_{22}\,\overline{v_{ij-1}'^2}_{-1}(D_{-j}\bar{\xi}^n)^2 \frac{-2\zeta_{ij}^n}{R\lambda_d^2} \qquad (7)
\end{aligned}$$

where: $f_i^n \equiv (1/R + T_{11}\,\overline{u_{ij}'^2}^n)/\Delta x_n, g_j^n \equiv (1/R + T_{22}\,\overline{v_{ij}'^2}^n)/\Delta y$, $D_{+i}\phi^n = (\phi_{i+1j}^n - \phi_{ij}^n)/\Delta x_n$, $D_{-i}\phi^n = (\phi_{ij}^n - \phi_{i-1j}^n)/\Delta x_n$, $\delta_{+i}\phi^n = (\phi_{ij}^n + \phi_{i-1j}^n)/2$ and so on. $U_{ij}^n$ and $\overline{u_{ij}'^2}^n$ approximate $U$ and $\overline{u'^2}$ at $(i\Delta x_n, (j-\tfrac{1}{2})\Delta y)$ while $V_{ij}^n$ and $\overline{v_{ij}'^2}^n$ refer to $V$ and $\overline{v'^2}$ at $((i-\tfrac{1}{2})\Delta x_n, j\Delta y)$. Also $\theta_n = \theta(n\Delta t)$. $U_c$ does not appear explicitly in (6) and (7) since it is accounted for identically by the collapsing grid.

$U_{ij}^n$ and $V_{ij}^n$ were obtained from $\bar{\psi}_{ij}^n$ after solution of the standard five point discrete approximation to (3) using a fast direct method, see [21]. $\overline{u_{ij}'^2}^n$ and $\overline{v_{ij}'^2}^n$ were computed from an approximation to (4). The most time consuming part of the numerical algorithm was in evaluating the function $G_i(\mathbf{x}:\mathbf{z})$. This was done efficiently by first using a fast direct method to obtain $G(\mathbf{x}:\mathbf{z})$ and then evaluating $G_i(\mathbf{x}:\mathbf{z})$ by finite differences. The details of these and all other aspects of the numerical scheme may be found in [7].

The solution algorithm for the system of difference equations consisted of using the values $\bar{\xi}_{ij}^n$, $\zeta_{ij}^n$, $\psi_{ij}^n$, $U_{ij}^n$, $V_{ij}^n$, $\overline{u_{ij}'^2}^n$, $\overline{v_{ij}'^2}^n$ to compute $\bar{\xi}_{ij}^{n+1}$ and $\zeta_{ij}^{n+1}$ using (6) and (7). $\bar{\psi}_{ij}^{n+1}$ was then found from $\bar{\xi}_{ij}^{n+1}$ using an approximation to (3) while simultaneously $\overline{u_{ij}'^2}^{n+1}$ and $\overline{v_{ij}'^2}^{n+1}$ were computed from $\zeta_{ij}^{n+1}$ using a discrete form of (4). Then using $\bar{\psi}_{ij}^{n+1}$, the quantities $U_{ij}^{n+1}$ and $V_{ij}^{n+1}$ were computed and the next integration step could begin.

To obtain stability of the numerical computations the integration time step was kept small enough to satisfy the conditions appropriate to a finite difference approximation to the convective heat equation of a form equivalent to (6) and (7), see [22]. This restriction provided no hardship in obtaining practical values of $\Delta t$.

## 5 Computed Results

Solutions for the flow during the compression stroke were computed for $\sigma = 1$ and 2. Uniform initial conditions $\bar{\xi}_{ij}^0 = 0$ and $\zeta_{ij}^0 = .1$ were chosen. These correspond to a homogeneous turbulent field of low intensity and lacking any mean currents. The plausibility of these initial conditions is supported by previous studies. Experimental measurements of Witze [3, 19] have shown rapid decay of intake generated turbulence preceding the compression stroke. Ishikawa and Daily [6] have observed that the intake generated turbulence is well diffused throughout the cylinder by the initial part of the compression stroke and is of fairly low intensity. Gosman and Johns [17] have observed numerically that mean currents held over from a previous stroke rapidly decay during the initial stages of compression. Thus apparently the main influence of the intake generated turbulence is in establishing the magnitude of $\zeta_{ij}^0$. The low value of 0.1 was used here so as to more clearly explore the importance of the piston in generating turbulence during compression.

For all computations $\chi = 8$ and $R = 5000$. In principle, values for the scales $T_{11}$, $T_{22}$, $\lambda_d$, and $L_A$ must be provided by an independent means either experimental or analytical. Until such procedures are developed their magnitude can only be estimated. Witze [19] has measured an Eulerian integral time scale during the engine cycle. It was found to be nearly constant during the compression stroke providing some justification for assigning constant values to $T_{11}$ and $T_{22}$. For the calculations reported here $T_{11} = T_{22} = 0.4$. The scale $L_A$ was set equal to $\Delta x_n \Delta y$ which decreases along with the shrinking flow domain. Lancaster [5] has made measurements of a spatial microscale which varies only slowly during the

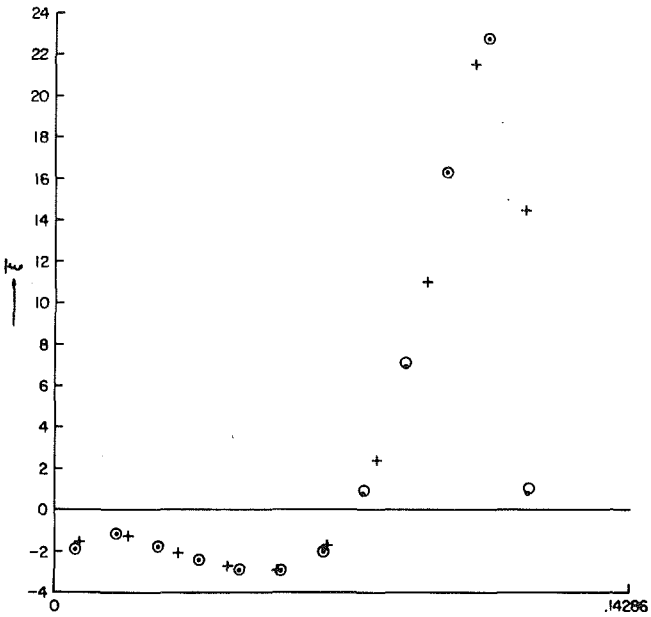


Fig. 2 Computed mean vorticity on axial line $y = 3/2\Delta y$. 0 = run(*a*), + = run(*b*), • = run(*c*)

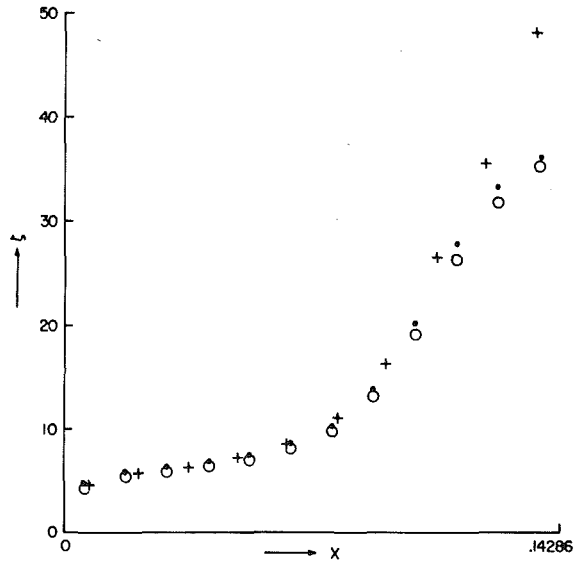


Fig. 3 Computed vorticity variance on axial line $y = 3/2\Delta y$. 0 = run(*a*), + = run(*b*), • = run(*c*)

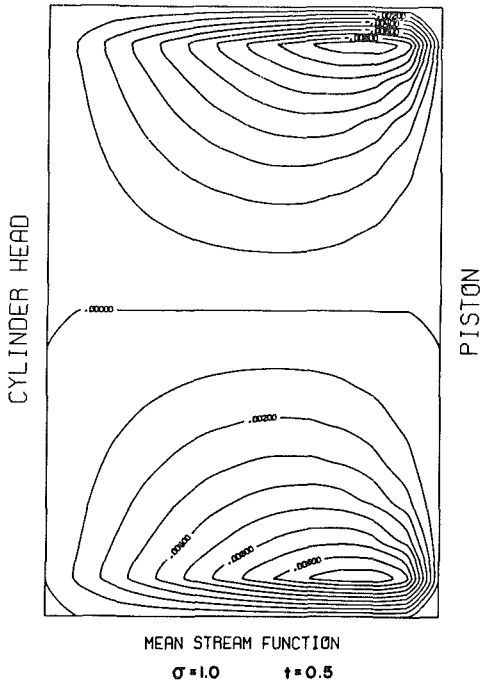


Fig. 4 Mean stream function at $t = 0.5$, $\sigma = 1.0$

compression stroke. However it is defined using Taylor's hypothesis and thus is of questionable validity. In the present study, for simplicity, $\lambda_d$ was assumed to be constant. The values $\lambda_d = 0.083$ for $\sigma = 1$ and 0.094 for $\sigma = 2$ were used.

The solution for $\sigma = 1$ was tested to see if it depended on the particular grid size and time step used in the computations. In Figs. 2 and 3 are shown plots of $\bar{\xi}$ and $\zeta$, respectively, for three different grid size and time step combinations. They give values of $\bar{\xi}$ and $\zeta$ at TDC along the axial line $y = 3/2\ \Delta y$ running from the cylinder head at $x = 0$ to the piston face at $x = 0.14286$. In Run (a) $N = 12$, $M = 16$, and $\Delta t = 0.01$. Run (*b*) differed from (*a*) by having $N = 10$ and run (*c*) differed from (*a*) in having $\Delta t = 0.0075$. These figures show that the computed solutions were largely grid independent. The departure of run (*b*) from (*a*) and (*c*) near the piston in Fig. 2 resulted from the extreme coarseness of the mesh which made it difficult to resolve the large gradients of the mean vorticity field. Since gradients of $\bar{\xi}$ strongly influence the production of $\zeta$, as seen in equation (2), these differences in $\bar{\xi}$ cause the more significant differences in $\zeta$ which are visible in Fig. 3.

In Figs. 4 and 5 are shown contour plots of $\bar{\psi}$ for $\sigma = 1$ at times $t = 0.5$ and 1, respectively. Figure 6 shows the distribution of $\bar{\xi}$ at $t = 1$ and Fig. 7, $\zeta$. It is clear from these figures that a large corner vortex has been created by the movement of the piston. The generation of such vortices by a moving piston has been observed experimentally during the exhaust stroke [23-25] and compression stroke [5, 19, 26]. As is seen from Figs. 2, 5, and 6 the computed vortex occupies only a small part of the cylinder area at TDC. It is at the center of a region of great turbulent intensity which has been produced by the strong shear layer in the corner.

In Fig. 8 is shown the time record of $\zeta$ for two different grid points. Point (*a*) is located where the corner vortex forms and point (*b*) is near the spark plug, see Fig. 1. At the latter point any change in $\zeta$ is due almost entirely to enhancement of the initial turbulence level by compression. As seen in Fig. 8, while the turbulence level at (*b*) has grown from 0.1 to 5.36, that at (*a*) has gone from 0.1 to 33.24. Thus the piston induces a significantly greater level of turbulence intensity, in the region of the corner vortex, than does simple compression of intake generated turbulence. Witze [3, 19] also observed a very similar increase in turbulence intensity during the compression stroke. Significant inhomogeneities of the turbulence at TDC have also been reported in [3, 6, 19]. Gosman and Johns [17] also noted sizable spatial variations of turbulence intensity at TDC, though their computations were made in a more complex geometry than is considered here. In contrast to these results, it has been suggested [2, 5] that the turbulence field at TDC is homogeneous. Lancaster [5] has also observed a decay in turbulence during the compression stroke.

Figures 9 and 10 show contours of $\bar{\psi}$ and $\zeta$, respectively at TDC for $\sigma = 2$. In this case considerably larger vortices and very much higher levels of turbulence have been generated than with $\sigma = 1$. This is a result of the larger stroke of the piston during which higher piston velocities are attained. Qualitatively these results are in agreement with the photographic study of Oppenheim, [26], in which a value of $\sigma$

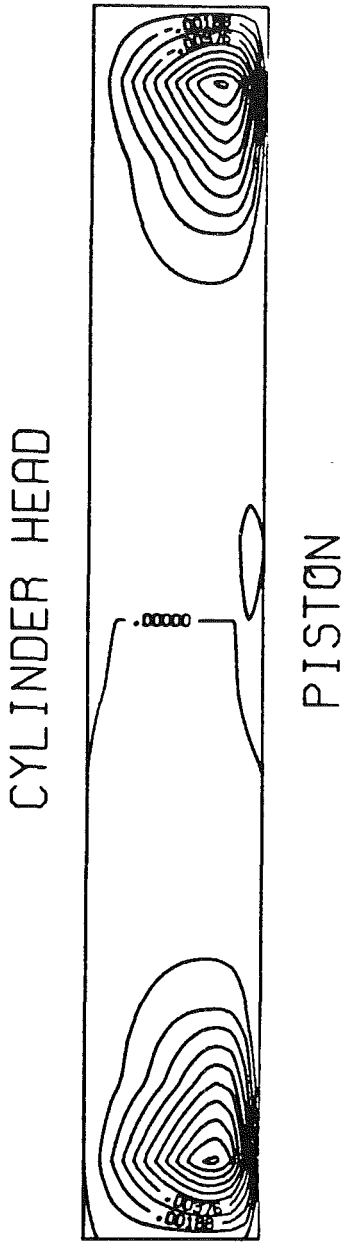


Fig. 5 Mean stream function at TDC, $\sigma = 1.0$

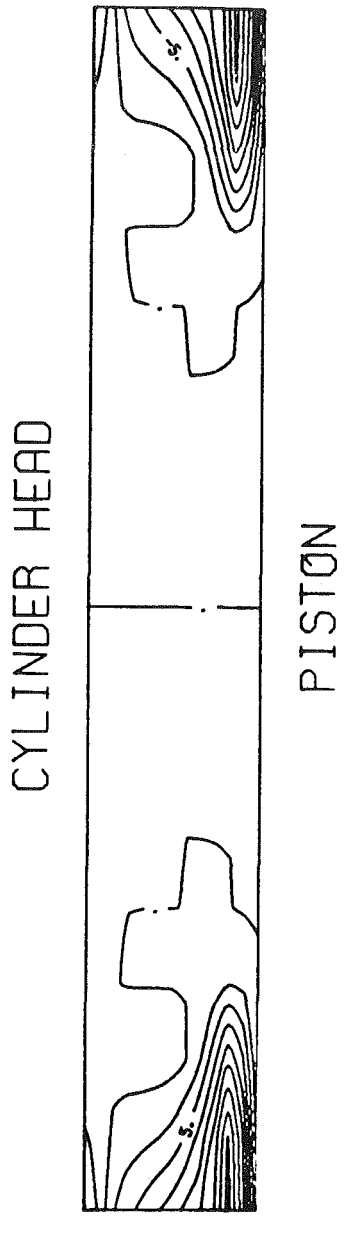


Fig. 6 Mean vorticity at TDC, $\sigma = 1.0$

= 3.5 was used. There, very large macroscopic vortices filling most of the chamber were observed at TDC.

In both cases $\sigma = 1$ and 2 the corner vortices began to expand in size and be convected toward the center of the piston as TDC was approached. Similarly, the intensely turbulent fluid near the corner began to spread and slide across the face of the piston, carried by the vortex. Such effects have been seen before, e.g. [17, 19]. The quantity $A/X^2$ where $A$ is the area of the corner vortex and $X$ is the piston travel has been determined for the experiments of Ishikawa and Daily, [6] in which $\sigma \approx 3.1$. They found that $A/x^2 \approx 0.00504$ when TDC is first reached. It then rises shortly thereafter to $\approx 0.00943$. For the present study, with $\sigma = 1$, $A/x^2 \approx 0.0067 \pm 0.0015$, and for $\sigma = 2$, $A/x^2 \approx 0.0114 \pm 0.0009$. The uncertainty of these estimates reflects the ambiguities in defining vortex size from a discrete set of data. The above results suggest that $A$ increases more rapidly than $X^2$ as $\sigma$ is varied from 1 to 2. Above 2, $X^2$ increases faster than $A$ possibly due to the presence of an upperbound on how large A can become. Thus the quantity $A/x^2$ measured at TDC as a function of $\sigma$ achieves a maximum somewhere in the interval $1 \leq \sigma \leq 3$.

## Conclusions

The present computations suggest that piston generated corner vortices play a major role in the fluid dynamics of the compression stroke for a flat-topped piston. Accompanying the vortices is intense turbulence production which locally may greatly exceed that resulting from the compression of

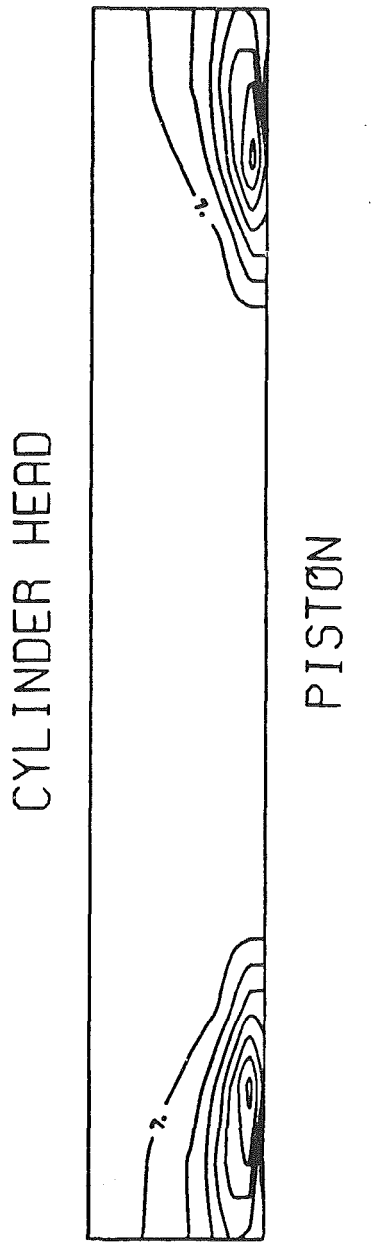


Fig. 7 Vorticity variance at TDC, $\sigma = 1.0$

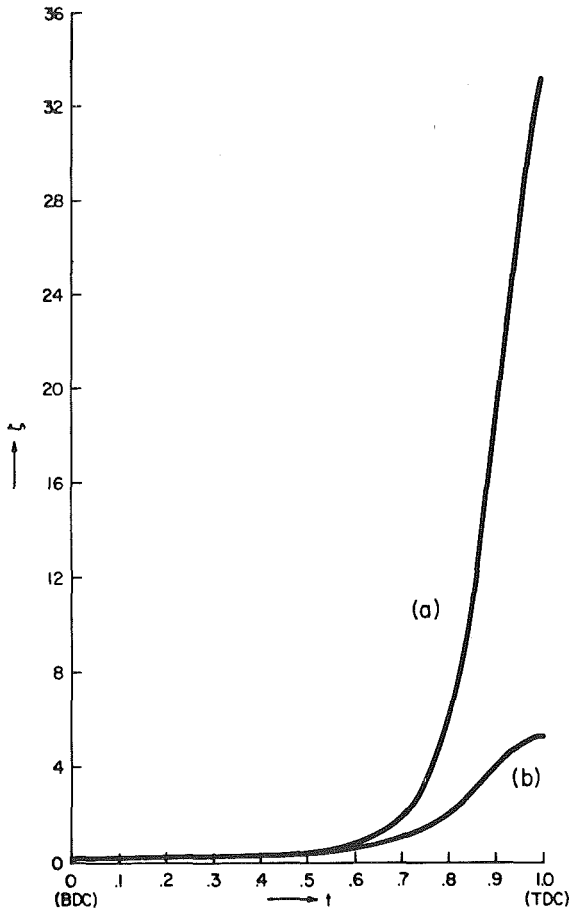


Fig. 8 Vorticity variance as a function of time. Curves (*a*) and (*b*) correspond to points (*a*) and (*b*) in Fig. 1.

intake generated turbulence. According to the present simulations, the size and turbulent intensity of corner vortices increases greatly with stroke to bore ratio.

## Acknowledgment

This work was supported in part by the Engineering, Mathematical and Geosciences Division of the U. S. Dept. of Energy through Lawrence Berkeley Laboratory under contract W-7405-ENG-48.

## References

1 Barton, R.K., Lestz, S.S., and Meyer, W.E., "An Empirical Model for Correlating Cycle-by-Cycle Cylinder Gas Motion and Combustion Variations of a Spark Ignition Engine," SAE Paper No. 710163, 1971.

2 Winsor, R.E., and Patterson, D.J., "Mixture Turbulence, A Key to Cyclic Variation," SAE Paper No. 730086, 1973.

3 Witze, P.O., "Hot-Wire Turbulence Measurements in a Motored Internal Combustion Engine," Sandia Laboratories Energy Report SAND75-8641, 1975.

4 Dent, J.C., and Salama, N.S., "The Measurement of Turbulence Characteristics in an Internal Combustion Engine Cylinder," SAE Paper No. 750886, 1975.

5 Lancaster, D.R., "Effects of Engine Variables on Turbulence in a Spark-Ignition Engine," SAE Paper No. 760159, 1976.

6 Ishikawa, N., and Daily, J.W., "Observation of Flow Characteristics in a Model I. C. Engine Cylinder," SAE Paper No. 780230, 1978.

7 Bernard, P.S., "A Numerical Investigation of Confined Turbulent Shear Flows," Ph.D. thesis, University of California, Berkeley, Dec. 1976. (Also Available as Lawrence Berkeley Laboratory Report LBL-5582).

8 Bernard, P.S., "The Computation of the Mean Properties of Turbulent Flows by the Method of Coarse Graining," Lawrence Berkeley Laboratory Report LBL-6455, 1977.

9 Bernard, P.S., "A Method for Computing Two-Dimensional Turbulent Flows," *SIAM Journal on Applied Mathematics*, Vol. 38, No. 1, 1980, pp. 81–92.

10 Sirignano, W.A., "One-Dimensional Analysis of Combustion in a Spark Ignition Engine," *Combustion Science and Technology*, Vol. 7, 1973, pp. 99–108.

11 Boni, A.A., Chapman, M., Cook, J.L., and Schneyer, G.P., "Computer Simulation of Combustion in a Stratified Charge Engine," *Proc. Sixteenth International Symposium on Combustion*, 1976.

12 Griffin, M.D., Anderson, J.D., Jr., and Diwaker, R., "Navier-Stokes Solutions of the Flowfield in an Internal Combustion Engine," AIAA Paper 76-403, also, *AIAA Journal*, Vol. 14, 1976, pp. 1665–1666.

13 Gosman, A.D., Melling, A., Whitelaw, J.H., Watkins, P., "Axisymmetric Flow in a Motored Reciprocating Engine," *I. Mech. Eng. Proc.*, Vol. 192, 1978, pp. 213–223.

14 Diwakar, R., Anderson, J.D., Jr., Griffin, M.D., and Jones, E., "Invisicid Solutions of the Flowfield in an Internal Combustion Engine," *AIAA Journal*, Vol. 14, 1976, pp. 1667–1668.

15 Griffin, M.D., Anderson, J.D., Jr., and Jones, E., "Computational Fluid Dynamics Applied to Three-Dimensional Nonreacting Inviscid Flows in an Internal Combustion Engine," ASME JOURNAL OF FLUIDS ENGINEERING, Vol. 101, No. 3, 1979, pp. 367–372.

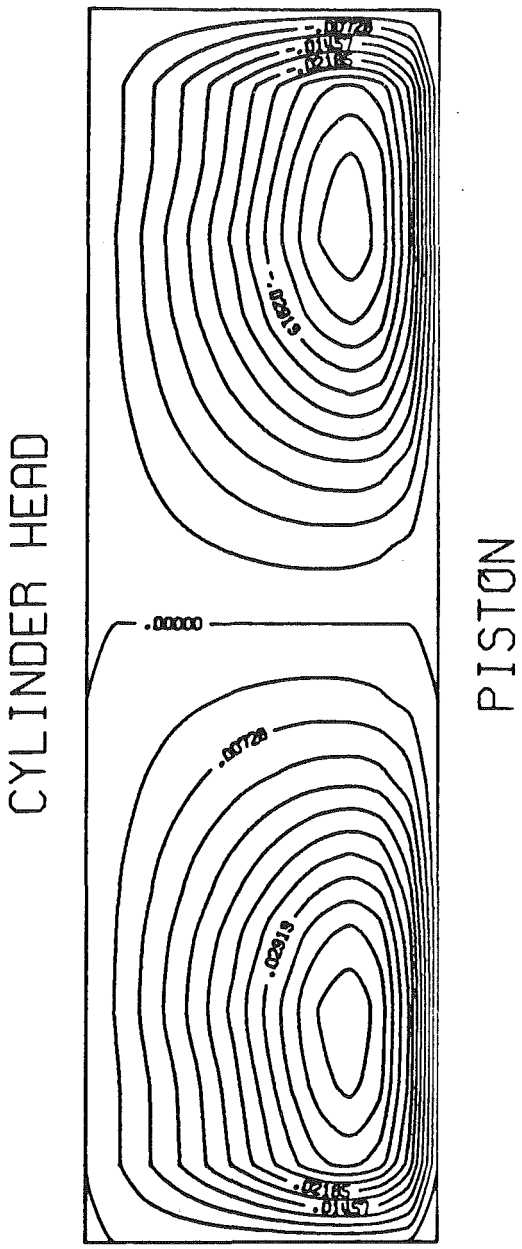


Fig. 9 Mean stream function at TDC, $\sigma = 2.0$

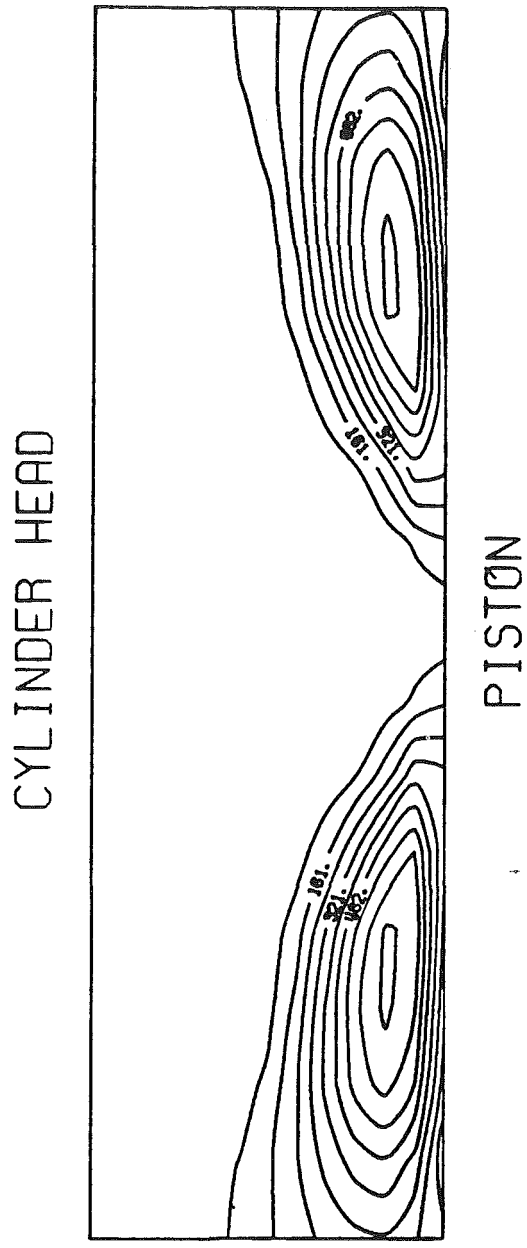


Fig. 10 Vorticity variance at TDC, $\sigma = 2.0$

16 Chorin, A.J., "Vortex Sheet Approximation of Boundary Layers," *Journal of Computational Physics*, Vol. 27, 1978, pp. 428–442.

17 Gosman, A.D. and Johns, R., Jr., "Development of a Predictive Tool for In-Cylinder Gas Motion in Engines," SAE Paper No. 780315, 1978.

18 Reynolds, W.C., "Computation of Turbulent Flows," *Ann. Rev. Fluid Mech.*, Vol. 8, 1976, pp. 183–208.

19 Witze, P.O., "Measurements of the Spatial Distribution and Engine Speed Dependence of Turbulent Air Motion in an I. C. Engine," SAE Paper No. 770220, 1977.

20 Taylor, G.I., "Statistical Theory of Turbulence I," *Proceedings of the Royal Society*, Vol. 151A, 1935, pp. 421–444.

21 Buzbee, B.L., Golub, G.H., and Nielson, C.N., "On Direct Methods for Solving Poisson's Equation," *SIAM Journal on Numerical Analysis*, Vol. 7, 1970, pp. 627–655.

22 Richtmeyer, R.D., and Morton, K.W., *Difference Methods for Initial Value Problems*, Interscience, New York, 1967.

23 Tabaczynski, R.J., Hoult, D.P., and Keck, J.C., "High Reynolds Number Flow in a Moving Corner," *J. Fluid Mechanics*, Vol. 42, 1970, pp. 249–255.

24 Tabaczynski, R.J., Heywood, J.B., and Keck, J.C., "Time-Resolved Measurements of Hydrocarbon Mass Flow Rate in the Exhaust of a Spark-Ignition Engine," SAE Paper No. 720112, 1972.

25 Daneshyar, H., Fuller, D.F., and Deckker, B.E.L., "Vortex Motion Induced by the Piston of an Internal Combustion Engine," *Int. J. Mech. Sci*, Vol. 15, 1973, pp. 381–390.

26 Oppenheim, A.K. et al., "A Cinematographic Study of Combustion in an Enclosure Fitted with a Reciprocating Piston," *Proc. Conf. on Stratified Charge Engines*, Institution of Mechanical Engineers, London, 11/23/25, 1976.

**P. Bar-Yoseph**[1]
Graduate Instructor.

**A. Solan**
Professor.
Mem. ASME

**J.J. Blech**
Associate Professor.

Faculty of Mechanical Engineering,
Technion, Haifa, Israel

# The Effect of Inertia on Flow Between Misaligned Rotating Disks[2]

*The effect of inertia on flow between a rotating and a stationary disk is studied for the case when the stationary disk is tilted with respect to the rotation axis. Based on the three-dimensional Navier-Stokes equations, an analytical solution is developed, with three perturbation parameters: aspect ratio, Reynolds number and tilt parameter. The noninertial hydrodynamic effect is to produce a moment which acts on the rotor and is perpendicular to both rotation and tilt axes. The effect of the inertia terms is to contribute another moment which acts on the rotor along the tilt axis. This analytical prediction explains qualitatively experimental and numerical results obtained at finite Reynolds numbers.*

## Introduction

Many configurations of rotating machinery can be analyzed by a system of two disks, including a rotating rotor against a stationary disk. Often an axis misalignment occurs during manufacture the effect of which is to produce a resultant moment on the rotor. In practical gyroscope systems the experimental results show that this resultant moment is perpendicular to the rotation axis and has components along the tilt axis and perpendicular to the tilt axis. The output of such gyroscope systems is measured through the perpendicular moments which are applied on the rotating rotor. Therefore, in such high precision machinery it is of cardinal importance to reduce the undesirable misalignment effect to an allowable value. The practical technique is to reduce the tilt angle by an empirical trial and error method. However, even this technique, which consumes much working time of a skilled worker, can yield a divergent process.

It seems that an analytical explanation of the misalignment effect is missing. A classical work dealing with the same configuration is that of Taylor and Saffman [1], who examined the effect of compressibility through the solution of the Reynolds equations. However, in most of the practical cases the compressibility effect is negligible. The effect of inertia on leakage flow, torque and separating force was examined in the case of a misaligned radial face seal through the narrow seal approximation by Sneck [2]. In the present research, a consistent perturbation approximation based on the full three-dimensional Navier-Stokes equations is developed.

In general, the flow between a rotating and a stationary disk can be either laminar or turbulent, and either of boundary layer type or fully merged. The four different regimes were described by Daily and Nece, Ketola and McGrew, and Cooper and Reshotko [3]. Here we limit our analysis to what these authors have called Regime I (merged laminar flow) which exists for $\mathrm{Re} = \bar{\omega}\,\bar{H}_0^2/\bar{\nu} < 4$ and $\bar{\omega}\,\bar{R}^2/\bar{\nu} < 10^5$, approximately. In fact, we shall consider a perturbation analysis for $\bar{\omega}\,\bar{H}_0^2/\bar{\nu} < 1$ and $\bar{H}_0/\bar{R} < 1$, which is well inside that regime.

## Basic Equations

Consider the laminar flow of a Newtonian incompressible fluid confined between a stationary misaligned disk and a rotating disk (Fig. 1). The flow is described by the Navier-Stokes equations in cylindrical coordinates, which are, in dimensionless form:

$$\mathrm{Re}\left(Du - \frac{v^2}{r}\right) = -\frac{\partial p}{\partial r} + \left(\frac{\partial^2 u}{\partial r^2} + \frac{1}{r}\frac{\partial u}{\partial r} + \frac{1}{r^2}\frac{\partial^2 u}{\partial \phi^2} - \frac{u}{r^2} - \frac{2}{r^2}\frac{\partial v}{\partial \phi}\right)S^2 + \frac{\partial^2 u}{\partial z^2} \tag{1}$$

$$\mathrm{Re}\left(Dv + \frac{uv}{r}\right) = -\frac{1}{r}\frac{\partial p}{\partial \phi} + \left(\frac{\partial^2 v}{\partial r^2} + \frac{1}{r}\frac{\partial v}{\partial r} + \frac{1}{r^2}\frac{\partial^2 v}{\partial \phi^2} - \frac{v}{r^2} + \frac{2}{r^2}\frac{\partial u}{\partial \phi}\right)S^2 + \frac{\partial^2 v}{\partial z^2} \tag{2}$$

[1] Present address: Room 41-317, Department of Aeronautics and Astronautics, Massachusetts Institute of Technology, Cambridge, Mass. 02139

[2] This research was partially supported by the Technion Fund for the Encouragement of Research (Grant 030-278).

Contributed by the Fluids Engineering Division and presented at the Winter Annual Meeting, Chicago, Ill., November 16-21, 1980, of THE AMERICAN SOCIETY OF MECHANICAL ENGINEERS. Manuscript received by the Fluids Engineering Division, October, 1979. Paper No. 80-WA/FE-2.

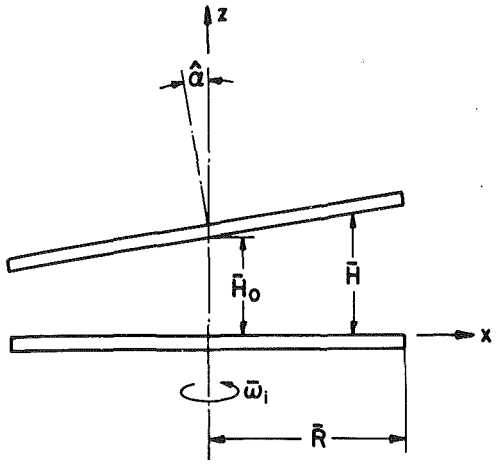


**Fig. 1 A misaligned rotating disk system.**

$$\mathrm{Re}\,Dw = -\frac{1}{S^2}\frac{\partial p}{\partial z} + \left(\frac{\partial^2 w}{\partial r^2} + \frac{1}{r}\frac{\partial w}{\partial r} + \frac{1}{r^2}\frac{\partial^2 w}{\partial \phi^2}\right)S^2 + \frac{\partial^2 w}{\partial z^2} \tag{3}$$

$$\frac{1}{r}\frac{\partial}{\partial r}(ru) + \frac{1}{r}\frac{\partial v}{\partial \phi} + \frac{\partial w}{\partial z} = 0 \tag{4}$$

where

$$D = u\frac{\partial}{\partial r} + \frac{v}{r}\frac{\partial}{\partial \phi} + w\frac{\partial}{\partial z}$$

Here, $\mathrm{Re} = \bar{\omega}\bar{H}_0^2/\bar{\nu}$ is the Reynolds number, $S = \bar{H}_0/\bar{R}$ is the aspect ratio, and the dimensionless variables are defined by the following equations:

$$u = \frac{\bar{u}}{\bar{\omega}\bar{R}}, v = \frac{\bar{v}}{\bar{\omega}\bar{R}}, w = \frac{\bar{w}}{\bar{\omega}\bar{H}_0}, p = \frac{\bar{p}S^2}{\bar{\mu}\bar{\omega}}, r = \frac{\bar{r}}{\bar{R}}, z = \frac{\bar{z}}{\bar{H}_0} \tag{5}$$

The $x$ axis is chosen so that it always passes through points of maximum clearance. This axis is the reference line for the azimuthal coordinate $\phi$. The velocity components and pressure are approximated by an asymptotic series in powers of $S^2$. Substitution of this approximation into equations (1) to (4) yields to *zeroth order in* $S^2$:

$$\mathrm{Re}\left(Du - \frac{v^2}{r}\right) = -\frac{\partial p}{\partial r} + \frac{\partial^2 u}{\partial z^2} \tag{6}$$

$$\mathrm{Re}\left(\mathrm{Dv} + \frac{uv}{r}\right) = -\frac{1}{r}\frac{\partial p}{\partial \phi} + \frac{\partial^2 v}{\partial z^2} \tag{7}$$

$$0 = \frac{\partial p}{\partial z} \tag{8}$$

$$\frac{1}{r}\frac{\partial}{\partial r}(ru) + \frac{1}{r}\frac{\partial v}{\partial \phi} + \frac{\partial w}{\partial z} = 0 \tag{9}$$

with the boundary conditions:

$$\begin{aligned} &0 \le r \le 1, \quad z = 0: \quad u, w = 0, v = r \\ &0 \le r \le 1, \quad z = h: \quad u, v, w = 0 \\ &\qquad\qquad r = 1: \quad p = p_a \end{aligned} \tag{10}$$

Here, $u$, $v$, $w$, and $p$ have finite values on the axis of rotation and are periodic in $\phi$. The foregoing asymptotic expansion is of singular behavior, since the contribution of the high derivatives in the radial direction is neglected. This approximation is equivalent to neglecting the edge effect.

We now assume a power series expansion in Re:

$$u \sim u_i \mathrm{Re}^i, v \sim v_i \mathrm{Re}^i, w \sim w_i \mathrm{Re}^i, p \sim p_i \mathrm{Re}^i \tag{11}$$

(here we used the summation convention), which substituted in equations (6)-(9) leads to a sequence of differential equations, the first two of which are:

*Order* $Re^0$

$$\frac{\partial^2 u_0}{\partial z^2} = \frac{\partial p_0}{\partial r} \tag{12}$$

$$\frac{\partial^2 v_0}{\partial z^2} = \frac{1}{r}\frac{\partial p_0}{\partial \phi} \tag{13}$$

*Order* $Re^1$

$$\frac{\partial^2 u_1}{\partial z^2} = \frac{\partial p_1}{\partial r} + u_0\frac{\partial u_0}{\partial r} + \frac{v_0}{r}\frac{\partial u_0}{\partial \phi} + w_0\frac{\partial u_0}{\partial z} - \frac{(v_0)^2}{r} \tag{14}$$

$$\frac{\partial^2 v_1}{\partial z^2} = \frac{1}{r}\frac{\partial p_1}{\partial \phi} + u_0\frac{\partial v_0}{\partial r} + \frac{v_0}{r}\frac{\partial v_0}{\partial \phi} + w_0\frac{\partial v_0}{\partial z} + \frac{u_0 v_0}{r} \tag{15}$$

and for both $i = 0$ and $i = 1$:

$$\frac{\partial p_i}{\partial z} = 0 \tag{16}$$

$$\frac{1}{r}\frac{\partial}{\partial r}(ru_i) + \frac{1}{r}\frac{\partial v_i}{\partial \phi} + \frac{\partial w_i}{\partial z} = 0 \tag{17}$$

Boundary conditions (10) are transformed to

$$0 \le r \le, z = 0: u_i, w_i = 0; v_i = \begin{cases} r & i = 0 \\ 0 & i > 0 \end{cases}$$

## Nomenclature

$D$ = operator
$\bar{H}$ = local clearance
$\bar{H}_0$ = local clearance at axis of rotation
$h$ = dimensionless clearance $h = \bar{H}/\bar{H}_0$
$h_0$ = dimensionless axisymmetric clearance
$M$ = dimensionless moment, $M = \bar{M}S^2/\bar{\mu}\bar{\omega}\bar{R}^3$
$M_x, M_y$ = dimensionless moment components along $x$ and $y$ directions, respectively.
$M_x^i, M_y^i$ = the contribution of the $i$th order in Re to the moment components.
$p$ = dimensionless pressure, $p = \bar{p}S^2/\bar{\mu}\bar{\omega}$
$p_a$ = ambient pressure
Re = Reynolds number, $\mathrm{Re} = \bar{\omega}\bar{H}_0^2/\bar{\nu}$
$r$ = dimensionless radial coordinate, $r = \bar{r}/\bar{R}$
$S$ = aspect ratio, $S = \bar{H}_0/\bar{R}$
$u$ = dimensionless radial velocity, $u = \dfrac{\bar{u}}{\bar{\omega}\bar{R}}$
$v$ = dimensionless azimuthal velocity, $v = \bar{v}/\bar{\omega}\bar{R}$
$w$ = dimensionless axial velocity, $w = \dfrac{\bar{W}}{\bar{\omega}\bar{H}_0}$
$x, y$ = planar coordinates on the rotor surface
$z$ = dimensionless axial coordinate, $z = \dfrac{\bar{z}}{\bar{H}_0}$
$\hat{\alpha}$ = angle of tilt
$\alpha$ = tilt parameter, $\alpha = \dfrac{\hat{\alpha}}{S}$
$\bar{\mu}$ = absolute viscosity
$\bar{\nu}$ = kinematic viscosity
$\phi$ = azimuthal coordinate
$\bar{\omega}$ = rotor angular velocity
$(\bar{\ })$ = dimensional quantity
$(\ )_i^j$ = $i$th order in Re and $j$th order in $\alpha$

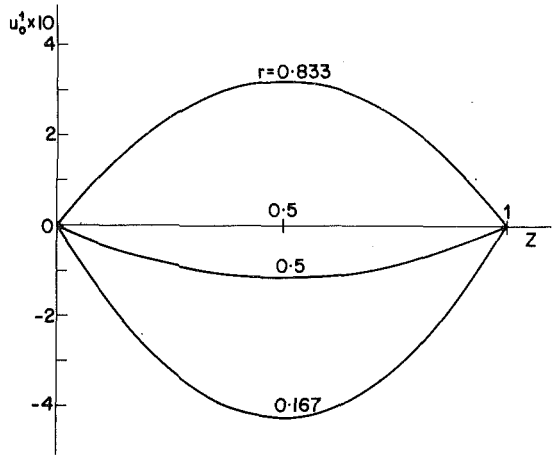


Fig. 2(a)

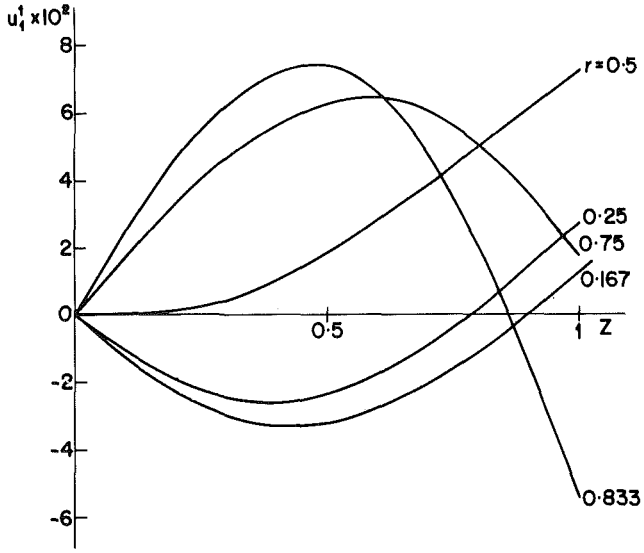


Fig. 2(b)

Fig. 2 Radial velocity $u_0^1, u_1^1$

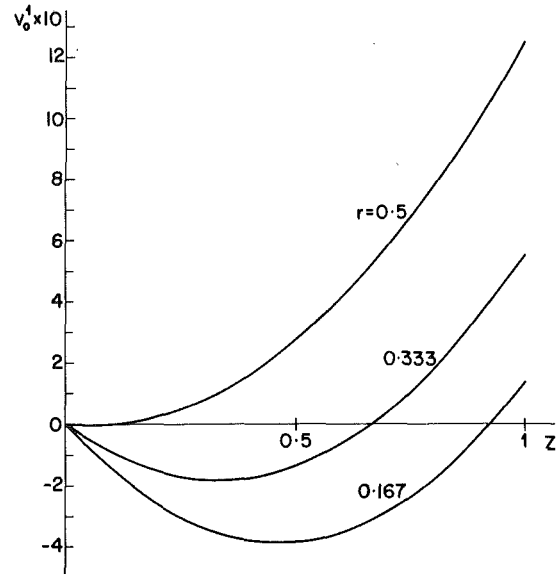


Fig. 3(a)

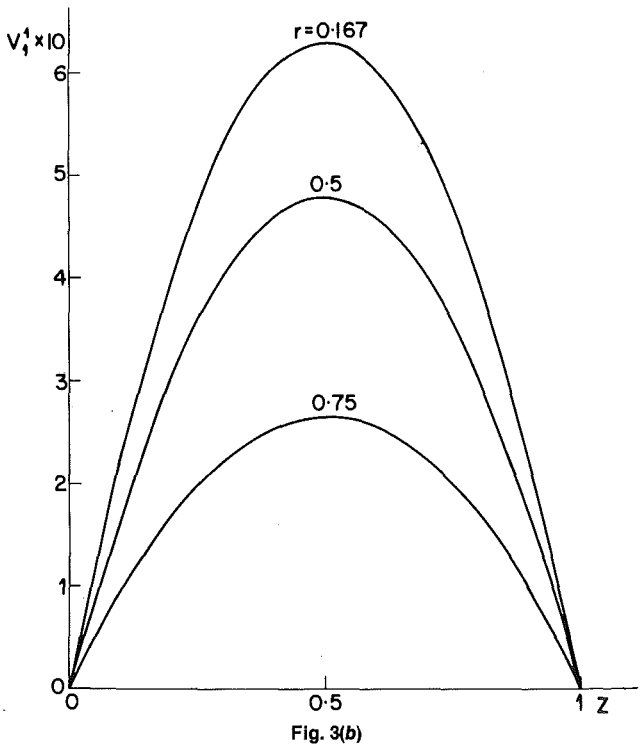


Fig. 3(b)

Fig. 3 Azimuthal velocity $v_0^1, v_1^1$

$$0 \le r \le 1,\ z = h:\ u_i,\ v_i,\ w_i = 0$$

$$r = 1:\ p_i = \begin{cases} P_a & i = 0 \\ 0 & i > 0 \end{cases} \tag{18}$$

Here, $u_i$, $v_i$, $w_i$, and $p_i$ are periodic in $\phi$ and have finite values on the axis of rotation.

Finally, we expand the velocity components and pressure in series in $\alpha$:

$$u_i \sim u_i^j \alpha^j,\ v_i \sim v_i^j \alpha^j,\ w_i \sim w_i^j \alpha^j,\ p_i \sim p_i^j \alpha^j \tag{19}$$

where $\alpha$ is the tilt parameter $\alpha = \hat{\alpha}/S$, and $\hat{\alpha}$ is the tilt angle. Substitution of equation (19) into equations (14) to (17) gives the following set of linear differential equations corresponding to the *first order of Re:*

*Order* $\alpha^0$

$$\frac{\partial^2 u_1^0}{\partial z^2} = \frac{\partial p_1^0}{\partial r} - \frac{(v_0^0)^2}{r} \tag{20}$$

$$\frac{\partial^2 v_1^0}{\partial z^2} = \frac{1}{r}\frac{\partial p_1^0}{\partial \phi} \tag{21}$$

Order $\alpha^1$

$$\frac{\partial^2 u_1^1}{\partial z^2} = \frac{\partial p_1^1}{\partial r} + \frac{v_0^0}{r}\frac{\partial u_0^1}{\partial \phi} - \frac{2v_0^0}{r} v_0^1 \tag{22}$$

$$\frac{\partial^2 v_1^1}{\partial z^2} = \frac{1}{r}\frac{\partial p_1^1}{\partial \phi} + \frac{1}{r}\frac{\partial}{\partial r}(r v_0^0) u_0^1 + \frac{v_0^0}{r}\frac{\partial v_0^1}{\partial \phi} + \frac{\partial v_0^0}{\partial z} w_0^1 \tag{23}$$

Order $\alpha^2$

$$\frac{\partial^2 u_1^2}{\partial z^2} = \frac{\partial p_1^2}{\partial r} + u_0^1 \frac{\partial u_0^1}{\partial r} + \frac{v_0^0}{r}\frac{\partial u_0^2}{\partial \phi} + \frac{v_0^1}{r}\frac{\partial u_0^1}{\partial \phi} + w_0^1 \frac{\partial u_0^1}{\partial z} - 2\frac{v_0^0}{r} v_0^2 - \frac{(v_0^1)^2}{r} \tag{24}$$

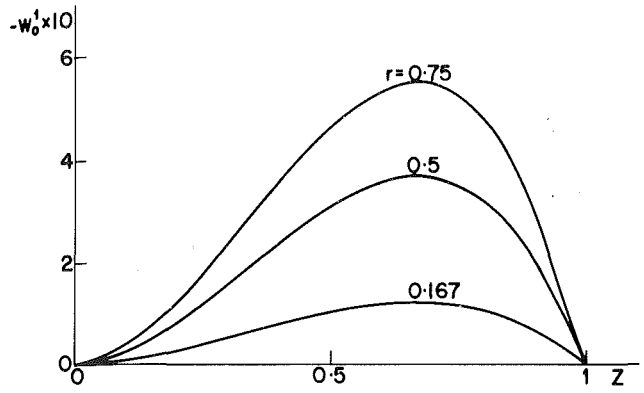


Fig. 4(a)

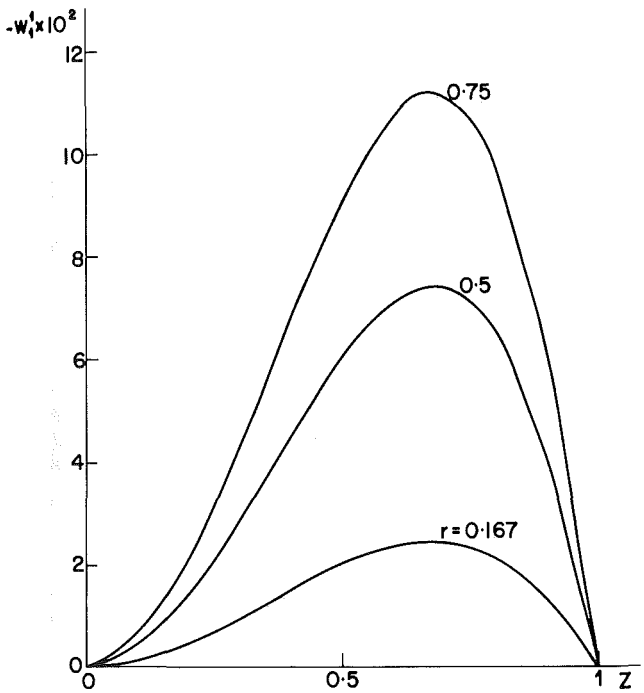


Fig. 4(b)

Fig. 4 Axial velocity $w_0^1$, $w_1^1$

$$\frac{\partial^2 v_1^2}{\partial z^2} = \frac{1}{r}\frac{\partial p_1^2}{\partial \phi} + u_0^1\frac{\partial v_0^1}{\partial r} + u_0^2\frac{\partial v_0^0}{\partial r} + \frac{v_0^0}{r}\frac{\partial v_0^2}{\partial \phi} + \frac{v_0^1}{r}\frac{\partial v_0^1}{\partial \phi} + w_0^1\frac{\partial v_0^1}{\partial z} + w_0^2\frac{\partial v_0^0}{\partial z} + \frac{u_0^1}{r}v_0^1 + \frac{u_0^2}{r}v_0^0 \tag{25}$$

and for all orders of $\alpha$:

$$\frac{\partial p_1^j}{\partial z} = 0 \tag{26}$$

$$\frac{1}{r}\frac{\partial}{\partial r}(ru_1^j) + \frac{1}{r}\frac{\partial v_1^j}{\partial \phi} + \frac{\partial w_1^j}{\partial z} = 0 \tag{27}$$

For the *zeroth order in Re*, the solution of equations (12), (13), (16), and (17), yields the Reynolds equation for the pressure distribution, to which we shall apply asymptotic expansion (19) directly.

The boundary conditions are:

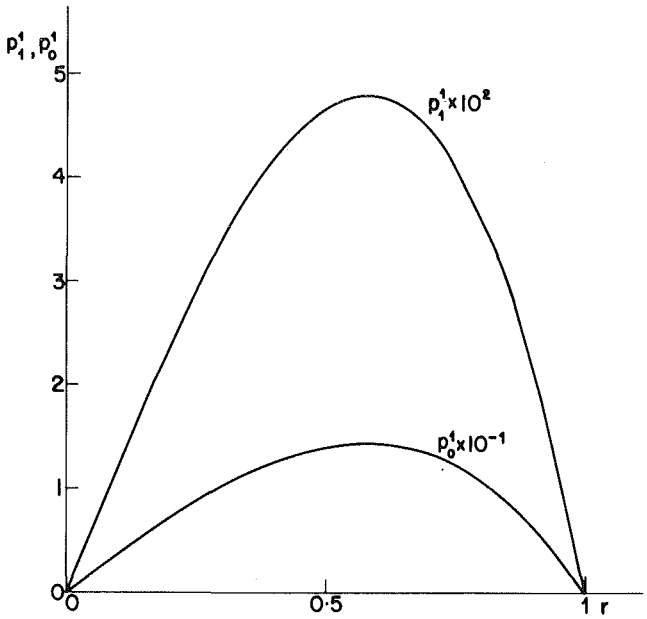


Fig. 5 Pressure $p_0^1$, $p_1^1$

$$0 \le r \le 1,\ z = 0:\ u_i^j,\ w_i^j = 0;\ v_i^j = \begin{cases} r & i \text{ and } j = 0 \\ 0 & \text{otherwise} \end{cases} \tag{28a}$$

$0 \le r \le 1,\ z = h$:

$$u_i \sim u_i^j \alpha^j = 0,\ v_i \sim v_i^j \alpha^j = 0,\ w_i \sim w_i^j \alpha^j = 0 \tag{28b}$$

$$r = 1:\quad p_i^j = \begin{cases} p_a & i \text{ and } j = 0 \\ 0 & \text{otherwise} \end{cases} \tag{28c}$$

Here, $u_i^j$, $v_i^j$, $w_i^j$, $p_i^j$ are periodic in $\phi$and have finite values on the axis of rotation.

For a flat tilted disk the local clearance $h$ can be written in the form

$$h = 1 + \alpha\, r\cos\phi + 0(\alpha^3 S^2) \tag{29}$$

(Later, we shall also discuss a tilted axisymmetrically distorted disk.)

In boundary condition (28*b*) $\alpha$ appears explicitly as well as implicitly, since the local clearance is dependent on $\alpha$ through equation (29). Therefore, it is not possible directly to equate like powers of $\alpha$ to zero [4]. We must first transfer this boundary condition to $z = 1$. If we assume that the velocity components are analytical functions in $z$ at $z = 1$, we can expand in Taylor series to obtain the modified boundary conditions

$0 \le r \le 1,\ z = 1$:

$$V_i^j = \begin{cases} 0, & j = 0 \\ -\sum_{n=1}^{j} \frac{1}{n!} r^n \cos^n\phi \frac{\partial^n V_i^{j-n}}{\partial^n v_i^{j-n}}, & \text{otherwise} \end{cases} \tag{30}$$

where $V = u, v, w$.

The moment components perpendicular to the axis of rotation can be written as

$$\begin{Bmatrix} M_x \\ M_y \end{Bmatrix} = \int_0^1 \int_0^{2\pi} p \begin{Bmatrix} -\sin\phi \\ \cos\phi \end{Bmatrix} r^2\, d\phi\, dr \tag{31}$$

## Solution Procedure

**Zeroth Order in Re.** Equations (12) - (13) are integrated twice with respect to z, taking account of boundary conditions (18), to yield

$$u_0 = \frac{1}{2}\frac{\partial p_0}{\partial r}(z^2\text{-}hz) \tag{32}$$

$$v_0 = \frac{1}{2r}\frac{\partial p_0}{\partial \phi}(z^2\text{-}hz) + r\left(1-\frac{z}{h}\right) \tag{33}$$

Substitution of these expressions into the continuity equation (17) and integration with respect to $z$ gives

$$w_0 = -\frac{1}{12}\frac{1}{r}\frac{\partial}{\partial r}\left[r\frac{\partial p_0}{\partial r}(2z^3-3hz^2)\right] - \frac{1}{12}\frac{1}{r^2}\frac{\partial}{\partial \phi}\left[\frac{\partial p_0}{\partial \phi}(2z^3\text{-}3hz^2)\right] - \frac{1}{2}\frac{\partial h}{\partial \phi}\frac{z^2}{h^2} \tag{34}$$

Similarly, integration across the clearance yields the Reynolds equations for the pressure distribution

$$\nabla \cdot (h^3 \nabla p_0) = 6r\frac{\partial h}{\partial \phi} \tag{35}$$

Equations (32) - (35) are in accordance with the classical lubrication theory [5].

Equation (35) is quite general for h but, since in general it cannot be solved analytically we shall restrict our further discussion to clearance which is described by equation (29). The use of expansion (19) in equation (35) leads to a sequence of differential equations:

*Order* $\alpha^0$:

$$\frac{d}{dr}\left(r\frac{dp_0^0}{dr}\right) = 0 \tag{36}$$

*Order* $\alpha^1$:

$$\nabla^2 p_0^1 = -6r^2\sin\phi \tag{37}$$

*Order* $\alpha^j$:

$$\nabla^2 p_0^j = -\frac{\partial}{\partial r}\left(3r^2\cos\phi\frac{\partial p_0^{j-1}}{\partial r} + 3r^3\cos^2\phi\frac{\partial p_0^{j-2}}{\partial r} + r^4\cos^3\phi\frac{\partial p_0^{j-3}}{\partial r}\right) - \frac{\partial}{\partial \phi}\left(3\cos\phi\frac{\partial p_0^{j-1}}{\partial \phi} + 3r\cos^2\phi\frac{\partial p_0^{j-2}}{\partial \phi} + r^2\cos^3\phi\frac{\partial p_0^{j-3}}{\partial \phi}\right) \tag{38}$$

For $j = 2$, terms with negative superscript are taken as equal to zero. The solution of these equations which satisfies the boundary conditions (28*c*) is

$$p_0 \sim p_a + \left[\frac{3}{4}(r-r^3)\sin\phi\right]\alpha + \left[\frac{15}{16}(r^4-r^2)\sin 2\phi\right]\alpha^2 + \left[\frac{9}{128}(-11r^5+10r^3+r)\sin\phi + \frac{207}{256}(r^3-r^5)\sin 3\phi\right]\alpha^3 \tag{39}$$

Substitution of this pressure distribution into equations (32) - (34) yields

$$u_0 \sim \left[\frac{3}{8}(z^2-z)(1-3r^2)\sin\phi\right]\alpha + \left\{\frac{3}{16}[5z^2(2r^3-r) - z(7r^3-4r)]\sin 2\phi\right\}\alpha^2 + \left\{\frac{3}{256}[3z^2(-55r^4+30r^2+1) - z(-85r^4+50r^2+3)]\sin\phi + \frac{3}{512}[69z^2(3r^2-5r^4) + z(185r^4-127r^2)]\sin 3\phi\right\}\alpha^3 \tag{40}$$

$$v_0 \sim r(1-z) + \left\{\left[r^2 z + \frac{3}{8}(z^2-z)(1-r^2)\right]\cos\phi\right\}\alpha + \frac{1}{16}\{[15(z^2-z)(r^3-r) - z(5r^3+3r)]\cos 2\phi - (5r^3+3r)z\}\alpha^2 + \frac{1}{512}\{[18(z^2-z)(-11r^4+10r^2+1) + 16z(9r^4+15r^2)]\cos\phi + [621(z^2-z)(r^2-r^4) + 16z(-7r^4+15r^2)]\cos 3\phi\}\alpha^3 \tag{41}$$

$$w_0 \sim [r(z^3-z^2)\sin\phi]\alpha + \left[\frac{r^2}{8}(-15z^3+11z^2)\sin 2\phi\right]\alpha^2 + \frac{1}{512}\{[6z^3(264r^3-80r) + z^2(-1104r^3+480r)]\sin\phi + [r^3(1104z^3-624z^2)]\sin 3\phi\}\alpha^3 \tag{42}$$

In this solution, boundary conditions (30) are automatically satisfied. By substitution of equation (39) into equation (31), the contribution of the *zeroth order in Re* to the moment components is obtained

$$M_x^0 = -\frac{\pi}{16}\left(\alpha + \frac{39}{64}\alpha^3\right) + 0(\alpha^4), M_y^0 = 0(\alpha^4) \tag{43}$$

**First Order in Re.** *Solutions of Orders* $\alpha^0$ *and* $\alpha^1$. Using equations (20)-(23), (26)-(28), (30) and (40)-(42) and applying the same procedure as in the solution of order $Re^0$, the following governing equations for the pressure distribution are obtained:

*Order* $\alpha^0$

$$\frac{d}{dr}\left(r\frac{dp_1^0}{dr}\right) = \frac{3}{5}r \tag{44}$$

*Order* $\alpha^1$

$$\nabla^2 p_1^1 = -\frac{1}{5}r^2\cos\phi \tag{45}$$

The combined solution of these equations is

$$p_1 \sim p_1^0 + p_1^1\alpha = \frac{3}{20}(r^2-1) + \left[\frac{1}{40}(r-r^3)\cos\phi\right]\alpha \tag{46}$$

Substitution of equation (46) into the appropriate expressions describing the velocity components gives

$$u_1 \sim u_1^0 + u_1^1\alpha = -\frac{r}{60}(1-z)(-5z^3+15z^2-6z) + \left\{\frac{1}{160}[3(1+r^2)z^5 + 10\left(\frac{5}{3}r^2-1\right)z^4 + 10(1-\frac{13}{3}r^2)z^3 + 2(1-3r^2)z^2 + (19r^2-5)z]\cos\phi\right\}\alpha \tag{47}$$

$$v_1 \sim v_1^0 + v_1^1\alpha = \left\{\frac{1}{480}[(3-7r^2)(-3z^5+10z^4-10z^3) - 6(1-r^2)z^2 + 3(5-9r^2)z]\sin\phi\right\}\alpha \tag{48}$$

$$w_1 \sim w_1^0 + w_1^1\alpha = -\frac{1}{20}\left[2z^3-3z^2+1+\frac{2}{3}(1-z)^5 - \frac{5}{3}(1-z)^2\right] + \left[\frac{r}{60}(-z^6-2z^5+10z^4+2z^3-9z^2)\cos\phi\right]\alpha \tag{49}$$

The contribution of the first order in both Re and $\alpha$ to the pressure and velocity components is shown in Figs. 2-5.

*Solution of Order* $\alpha^2$. Substituting equations (40) - (42) into equations (24) - (28), and (30) yields differential equations and boundary conditions in which the dependence on $\phi$ includes only the second harmonic components. Therefore, the second order solution in $\alpha$ has no contribution to the perpendicular moments. Thus, the contribution of the first order solution in Re to the moment components is

$$M_x^1 = 0(\alpha^3)\ ,\ M_y^1 = \frac{\pi}{480}\,\mathrm{Re}\,\alpha + 0(\alpha^3) \tag{50}$$

At this point we combine equations (43) and (50) to obtain the final result, accurate through $0(\alpha^2)$

$$M_x \sim -\frac{\pi}{16}\alpha\ ,\ M_y \sim \frac{\pi}{480}\,\mathrm{Re}\,\alpha \tag{51}$$

Thus, with increasing Reynolds number the "second" transverse moment $M_y$ will increase and will eventually become of the same order as $M_x$. Though the results in (51) are strictly correct only for Re $<$ 1, by extrapolating these to larger Reynolds numbers we find that the two moments become equal at Re $\simeq$ 30, which is in qualitative agreement with experimental results.

The flow in a "sliced cylinder" was also solved numerically by the authors using the finite element method [6,7], for Re = 0.4 and 12, and $S$ = 0.2. At such aspect ratio, end effects are significant over the outer half of the radius, but can be neglected over the inner half ($r \lesssim 0.5$). Comparing these numerical results for the inner region with the present analysis, shows that the present analysis is a good approximation even for Re $\simeq$ 12, S = 0.2. This fortuitous result is in agreement with similar results obtained by Sneck [2] and Reshotko and Rosenthal [8].

## The Effect of an Axisymmetrically Distorted Disk

In the general case, the misaligned disk is not flat. When in its untilted position the disk is axisymmetrically distorted, we denote by $h_0 = h_0(r)$ the variation in surface flatness (due to manufacturing errors or to thermal distortion), e.g., conical distortion would be $h_0 = 1 + \beta$r. In this case the clearance can be described by

$$h \sim h_0 + \alpha r\cos\phi + A\alpha^2 \tag{52}$$

The second order contribution of $h_0$ due to the deviation from the case of a flat disk ($h_0 = 1$), is represented by $A = A(r,\phi)$. For this case, the non-interial hydrodynamic pressure can be obtained from a modified set of differential equations:

*Order* $\alpha^0$

$$\frac{d}{dr}\left(rh_0^3\frac{dp_0^0}{dr}\right) = 0 \tag{53}$$

*Order* $\alpha^1$

$$\nabla \cdot (h_0^3\ \nabla p_0^1) = -6r^2\ \sin\phi \tag{54}$$

Order $\alpha^2$

$$\nabla \cdot (h_0^3\ \nabla p_0^2) = -\frac{\partial}{\partial r}\left(3r^2h_0^2\frac{\partial p_0^1}{\partial r}\right)\cos\phi + 6r\frac{\partial A}{\partial\phi} - 3h_0^2\frac{\partial}{\partial\phi}\left(\frac{\partial p_0^1}{\partial\phi}\cos\phi\right) \tag{55}$$

Equation (53) has the trivial solution $p = p_a$.

The solution of equation (54) according to boundary conditions (28*c*) yields a pressure distribution with a dependence on $\phi$ of the same type as in the previous case ($h_0 = 1$). Therefore, the $\phi$ dependence of the first order solution in both Re and $\alpha$ is not altered. The solution of equation (55) can yield a contribution to $M_x^1$ and $M_y^0$. Usually, the above distortion is a small quantity. Thus, the axisymmetric distortion has only second order effect on the perpendicular moment components.

## Conclusions

The present solution yields moment components which are accurate through $0(\alpha^2)$, 0(Re), and zeroth order in $S^2$. Although the solution is restricted by these limitations, it correctly accounts for the inertia terms, providing an explanation to the experimental results. Therefore, the present first order solution in both Reynolds number and tilt parameter represents a good approximation to the physical phenomenon.

## References


1 Taylor, G., and Saffman, P.G., "Effects of Compressibility at Low Reynolds Number," *Journal of Aeronautical Sciences*, Vol. 24, 1957, pp. 553-562.

2 Sneck, H.J., "The Effect of Geometry and Inertia on Face Seal Performance-Laminar Flow," ASME *Journal of Lubrication Technology*, Vol. 90, 1968, pp. 331-341.

3 Cooper, P. and Reshotko, E., "Turbulent Flow Between a Rotating Disk and a Parallel Wall," *AIAA J.*, Vol. 13, 1975, pp. 573-578.

4 Van Dyke, M., *Perturbation Methods in Fluid Mechanics*, Parabolic Press, Stanford, Calif., 1975.

5 Pinkus, O. and Sternlicht, B., *Theory of Hydrodynamic Lubrication*, McGraw-Hill, 1961.

6 Bar-Yoseph, P., "Finite Element Solution of Navier-Stokes Equations in Rotating Flow," (in Hebrew), D.Sc. thesis, Technion, Haifa, Israel, 1978.

7 Bar-Yoseph, P., Blech, J.J., and Solan, A., "Finite Element Analysis of Rotating Flow in a Skewed Shrouded Rotor Geometry," Report TME-376, Faculty of Mech. Engng., Technion, Haifa, 1980. Submitted to Int. J. Num. Meth. Engng.

8 Reshotko, E., and Rosenthal, R.L., "Fluid Dynamic Considerations in the Design of Slinger Seals," *J. Am. Lub. Eng.*, Vol. 24, 1968, pp. 303-314.

# Pressure and Vortex Shedding Patterns Around a Low Aspect Ratio Cylinder in a Sheared Flow at Transitional Reynolds Numbers

**D. M. Rooney**
Assistant Professor.

**R. D. Peltzer**
Research Assistant.

Aerospace and Ocean Engineering Department,
Virginia Polytechnic Institute and State University,
Blacksburg, Va. 24061

*Model tests were performed in a wind tunnel to determine vortex shedding patterns induced around a circular cylinder by spanwise shear in transitional Reynolds number flow. In addition, mean and fluctuating pressure measurements were obtained. The introduction of shear in the upstream flow generated two distinct cells of vortex frequencies behind the cylinder in the transcritical regime, thereby documenting for the first time that the re-established high Reynolds number shedding closely parallels patterns already observed in subcritical flow. The two cell pattern did not permit any correlation between shear level and cell length to be found.*

## Introduction

Recent attempts to explore new methods of generating energy have once again drawn attention to ocean thermal energy conversion (OTEC) plants. Work is rapidly proceeding toward deployment of a full-scale plant in the early 1980's. Still to be resolved, however, are some important hydrodynamic effects generated by the interaction of a 1000 meter long, 10 to 15 meter diameter cold water pipe (CWP) and impinging ocean currents. Chief among these effects is the loading induced by vortex shedding around the pipe.

One structurally undesirable effect of major importance caused by vortex shedding occurs when the eddy shedding frequency (Strouhal frequency) of the Karman vortex street is at or near the natural frequency of the CWP. Amplification of the pipe motions to near resonant levels may then occur. This is due to a shifting of or "locking-on" of the pipe vibrational response to the Strouhal frequency. During lock-on, CWP vibrational stresses are magnified and the possibility of structural damage is increased.

The existence of vertical shear in ocean currents complicates the effects of vortex shedding along the CWP. It leads to the presence of discrete cells, distributed along the pipe. The relative frequencies and phasing of these vortex cells can significantly affect the dynamics of the pipe. Therefore knowledge of the effects of shear on vortex shedding is desirable for the optimum design configuration.

The literature pertaining to the subject of vortex shedding from pipes is rapidly increasing. An excellent, up-to-date review of work in the field is presented in a paper by Griffin [1]. Of particular relevance to the present report are studies of interactions of a sheared flow with stationary and vibrating bluff bodies.

Shaw and Starr [2] showed that a synchronized pattern of spanwise shedding frequencies existed, the length of which was a function of the upstream velocity gradient. Further studies performed by Maull and Young [3] verified the existence of distinct shedding cells of constant Strouhal frequency. This was demonstrated by measuring the power spectral density of the eddy-shedding frequency for a bluff body model in shear flow. They stated that "the coherence of the shed vortices requires a constant frequency over the lengths." They also investigated the boundaries between these cells and found "longitudinal vortices lying in the freestream direction" which they hypothesized were "due to a rolling up of the original distributed vorticity into concentrated trailing vortices at the base."

Davies [4] measured cell structures in a highly sheared flow field for Reynolds numbers up to supercritical, at which point the eddies became indistinct. The effect of endplates and the spanwise distribution of vortices were considered in experiments by Mair and Stansby [5]. They found that long endplates produced sharper spectral density peaks of the eddy-shedding frequency and more well-defined cells of vortices than did short endplates. Through further experiments they discovered that elimination of endplates altogether reduced the number of cells present and that for fixed endplates the number and length of cells were insensitive to variations in shear and body aspect ratio.

Stansby [6] investigated the "lock-on" characteristics of cylinders in both uniform and shear flow for mechanically vibrated (at a specified frequency and amplitude) and stationary cylinders in a wind tunnel. He noted that, in general, the Strouhal number for eddy shedding in vibrating

Contributed by the Fluids Engineering Department for publication in the JOURNAL OF FLUIDS ENGINEERING. Manuscript received by the Fluids Engineering Division, March 17, 1980.

cylinders is a function of Reynolds number, shear, aspect ratio, cylinder vibration Strouhal number, and relative amplitude of vibration. Additionally, he observed that the spanwise cell length increased as the relative amplitude of vibration increased, that only one of the cells locked on to the vibrating frequency, and that peaks in the power spectra of adjoining cells became more clearly defined. With stationary cylinders in shear flow he found that for most cases, only two end cells were produced such that "at any given time each cell has a finite length and a single frequency and cells do not overlap."

The Reynolds number for flows in Stansby's studies were all below $1 \times 10^4$, definitely subcritical. For this regime, he computed the range of frequencies for primary lock-on in shear flow and developed an empirical relationship for determining the spanwise length of lock-on cells.

Numerous studies have been made of pressure distributions around circular cylinders, and the relevant ones will be cited during the analysis of the pressure data obtained in the present test program. Special mention must be made, however, of one particularly significant study. Batham [7] measured the mean and fluctuating pressures and vortex shedding strengths around smooth and rough cylinders at two Reynolds numbers ($Re = 1.1 \times 10^5$ and $2.35 \times 10^5$) in two uniform flows, one with very low and the other with very high freestream turbulent intensities. His results and conclusions will be detailed in parallel with the present set of results.

The purpose of the present study is to further illuminate the effects of shear flow on pressure and vortex shedding patterns for both smooth and rough circular cylinders in the transitional Reynolds number regime. Specifically, the primary goal is to isolate the effects of shear on the spanwise distribution of vortex cells in this regime and to determine the magnitudes of the unsteady pressures generated around stationary cylinders.

## Experimental Equipment

Experiments were conducted in the 6 ft by 6 ft (1.8m × 1.8m) cross section Stability Wind Tunnel Facility located in the Aerospace and Ocean Engineering Department at VPI&SU. A sheared cross-stream flow was achieved in the tunnel by means of a series of wire screens of nonuniform cross-stream distribution, placed upstream of the model.

The OTEC cold water pipe was represented by a 56-in. (140 cm) long, 6-in. (15 cm) diameter aluminum cylinder, fixed midway between the floor and ceiling of the test section. The cylinder had 1/16 in. (0.15 cm) thick, 10 in. (25 cm) diameter steel plates attached to both ends to reduce tip vortex interference with the Karman vortex street along the cylinder span.

The ends of the cylinder were 8 in. (20 cm) from the tunnel wall, thereby insuring that the wall boundary layer did not affect the free-stream flow around the model.

To obtain a rough pipe, the surface of the cylinder was knurled to a roughness $K/D \sim 10^{-3}$, where $K$ is the depth of a roughness element and $D$ is the diameter of the cylinder. The roughening was accomplished with a diamond knurl in a machine shop, and its uniformity established with a dial indicator. The purpose of this roughening was two fold. First, the maximum Reynolds number attainable with the smooth 6-in. dia cylinder in the wind tunnel was approximately $5 \times 10^5$. In that range, the flow regime behind the cylinder was expected to display supercritical characteristics, with a highly turbulent wake and incoherent vortex shedding. It is well known [8] that roughening a cylinder can change the flow pattern to achieve premature onset of transcritical characteristics, one of which is a well-defined eddy shedding pattern. Secondly, as Hove, et al. [9] have observed in reference to the cold water pipe, surface roughnesses of the order of $10^{-3}$ caused by plate welds and biofouling appear reasonable. Therefore, as a first approximation to actual conditions, the effect of a uniform surface roughness of $K/D = 10^{-3}$ was sought.

The cylinder itself was hollow, permitting tubing from the pressure-sensing equipment to be fed through the inside and out the endplates to recording instruments outside the tunnel. Mean surface pressure values were measured through a series of three rows of 28 ports of 1/16 in. (0.15 cm) diameter. The ports were spaced at 2 in. (5 cm) intervals along the span of the pipe, with each row 15 deg apart circumferentially. Attached to the ports were 1/16 in. (0.15 cm) diameter scanivalve tubes (84 in all) fitted to a scanivalve pressure transducer switching unit.

In addition, four Kulite pressure transducers (Model CQH 125-5) of 1/4 in. (0.64 cm) diameter (including their plexiglas casings) were flush mounted in the cylinder. They were located 10, 22, 34, and 46 in. (25, 56, 86, 116 cm) from the high velocity end of the cylinder. They were connected to a Tektronix TM 503 Amplifier, so that the output from the transducer could be differentially amplified, as well as filtered to eliminate very high frequency ($>$ 300 Hz) noise. Output from the amplifiers was channeled into a Tektronix Type 561A oscilloscope for visual inspection of instantaneous pressure readings. Simultaneously, the signal was fed into an rms voltmeter which yielded the rms value of the pressure fluctuations. Finally the signal could be sent to an FFT processor (discussed below) which produced a power spectrum plot of the pressure fluctuations.

Free-stream turbulence measurements were determined from a single hot wire probe connected to a constant temperature linearized TSI Model 1051-6 anemometer.

To examine the spectral characteristics of the flow behind the cylinder (in particular, to determine the eddy shedding frequency), the linearized, filtered anemometer signal was processed through a Zonic Technical Laboratories, Inc. Multichannel FFT Processor. To allow for immediate visual inspection of the signal, it was simultaneously monitored on an oscilloscope. The output, in the form of a power density spectrum (log amplitude versus frequency), was plotted on a graphics display terminal. A hard copy of the results was obtained by photographing the terminal screen with a camera mounted on a tripod.

## Test Procedures

Before the effects of transitional Re shear flow on vortex shedding patterns could be investigated, the wind tunnel flow characteristics had to be established. Specifically, measurements were undertaken to determine the upstream velocity profiles corresponding to a given number of shear generating screens, and to verify that free-stream turbulence levels were acceptably low and constant throughout the test section.

Figures 1($a$), 1($b$), and 1($c$) give a typical upstream velocity profile for a high velocity tunnel speed and three sets of screens employed in the tests. In these figures, the left-hand vertical axis shows the normalized velocity ($U/U_c$) based on the center-line flow values ($U_c$), and the horizontal axis is nondimensionalized using the ratio of the spanwise distance ($y$) from the center of the model to the cylinder diameter ($D$). These velocity profiles were obtained by measuring the stagnation pressure at the 0 deg pressure ports along the length of the cylinder. The cylinder was positioned carefully, insuring that the desired pressure port was within ± 0.25 deg of the direction of oncoming flow.

A series of upstream screens was employed to generate both free-stream turbulence and shear. In order to produce turbulence in all the test configurations, it was necessary to

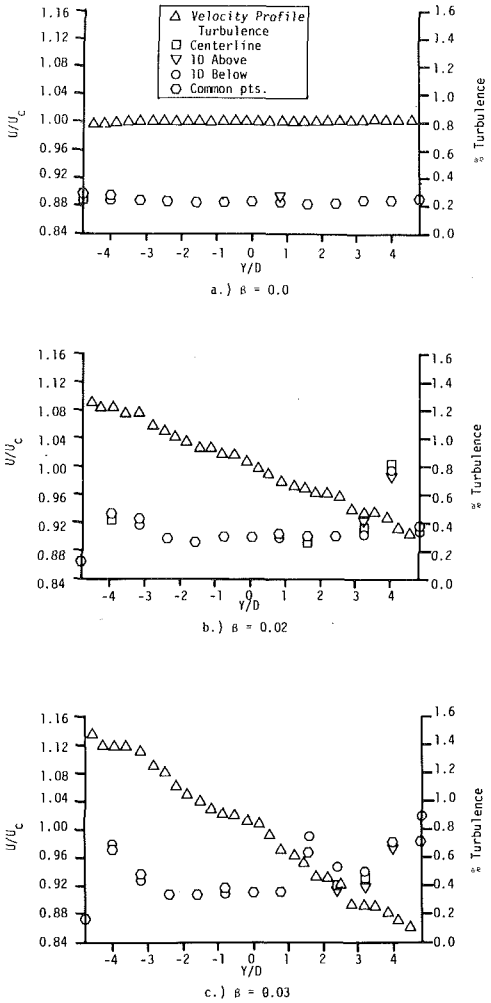


**Fig. 1 Spanwise velocity and turbulence profiles**

employ at least one wire screen. With one screen in place, with wires of uniform density, no velocity shear was generated. With two screens of uneven wire distribution, the shear produced was characterized by a value of $\beta = 0.02$ and with three such screens $\beta$ took on a value of 0.03. The shear parameter $\beta$ is defined as $(D/U_c)dU/dy$ where $D$ is the test cylinder diameter, $U_c$ is the inflow center-line velocity, $U$ is inflow velocity at any longitudinal location, and $y$ is the longitudinal distance from the cylinder center. The values of $\beta$ chosen were selected to represent typical ocean shears. However, as can be seen from Fig. 1, the velocity profiles corresponding to $\beta = 0.02$ and $\beta = 0.03$ are not markedly different and the greatest velocity variation over the length of the cylinder is approximately ± 15 percent of the center-line velocity.

Once the free-stream flow velocities were determined, the free-stream turbulence profiles were measured. To insure that spanwise variations were the result of shear and not of three dimensional turbulence effects, it was desired to have a constant level of turbulence (less than 1 percent) for all experimental configurations employed. Turbulent intensities along the length of the cylinder as well as vertically above and beneath it were obtained. Three shear conditions with free-stream center-line velocities corresponding to Re = $2.5 \times 10^5$, $3.5 \times 10^5$, and $3.9 \times 10^5$ were investigated. A typical profile which is also displayed in Figures 1(*a*), 1(*b*), and 1(*c*), was determined to be independent of Reynolds number. The measurements one cylinder diameter (6 in. or 15 cm) above and below the center line of the cylinder at Re = $3.5 \times 10^5$ for all three shear conditions indicated that the free-stream turbulence was independent of elevation inside the tunnel.

The turbulence level for unsheared flow was found to be virtually constant over the length of the cylinder at approximately 0.25 percent. The addition of shear-generating screens raised the turbulent intensities to about 0.30 percent for $\beta = 0.02$ and 0.35 percent for $\beta = 0.03$ in the range of $-3.0 \leq y/D \leq 3.0$. Beyond these points turbulence readings increased greatly to 0.7 percent and even more. On the high velocity side of the cylinder the turbulent intensity attained a maximum near $y/D = +4.0$. This was a result of the abrupt mixing of the flow near the wall and the shear flow partially obstructed by the wires. The high turbulence levels on the low velocity side of the tunnel were caused by the greater density of shear-producing wires at that end. Neither of these high values was attributable to the tunnel wall boundary layer.

In general, the levels registered were close enough to one another over the major portion of the cylinder to guarantee that the flow regimes experienced by the cylinder were only minimally distorted by differences in intensities from one case to the next.

Before rough pipe investigations commenced, experiments were performed on a smooth pipe model, but physical limitations of the wind tunnel facility presented a severe problem. The highest Re obtainable placed the flow behind the cylinder in the supercritical regime, where vortex shedding patterns are incoherent. Therefore, for the Reynolds numbers tested, only the surface pressure distributions offered significant information to compare with the results obtained by previous investigators. With a roughened pipe, however, the downstream wake pattern was altered enough to place the flow behind the cylinder in the transcritical range, where the vortices were clearly defined and could be measured.

Tests were then performed to describe the mean surface pressure distribution (which yields information characterizing the flow regime as well) and to correlate pressure fluctuations with vortex shedding activity. The surface pressure distribution was obtained by taking mean pressure readings from the pressure ports previously described and by measuring the rms, peak-to-peak, and, for a limited number of configurations, the power spectra of the pressure fluctuations employing the Kulite pressure transducers. (Rotating the model permitted sampling of the mean pressure distribution over the entire surface by the scanivalve unit.) The transducer signal was fed into an rms voltmeter to determine the rms value, in addition to being monitored on an oscilloscope where the peak-to-peak distances were visually estimated. Measurements were taken at cylinder orientations of 0, 45, 90, 135, 225, 270, and 315 deg relative to the upstream flow. These readings were taken for the center-line Reynolds numbers Re = $2.5 \times 10^5$, $3.5 \times 10^5$ and $3.9 \times 10^5$ at lateral locations $y/D = +3, -1, -3$ for the three shear profiles. (Another transducer was installed at $y/D = +1$, but was irreparably damaged early in the test program.) Measurements were also taken of the pressure fluctuations for a center-line flow velocity with Re = $5.2 \times 10^5$. For these readings the transducer signal was sent through an FFT processor to obtain the power spectra of the turbulent pressure, which was then compared to spectra from the hot-wire probe.

The eddy shedding frequency was measured using a hot wire probe mounted on a traverse located four diameters (24 in. or 61 cm) downstream from the cylinder. Readings were taken every 4.7 in. (12 cm). Vertically, the hot wire probe position was varied to measure the frequency of shedding where the strength of the vortices was greatest. The signal from the probe was transmitted to the FFT processor, which was programmed to sample the signal every 5 msec and to

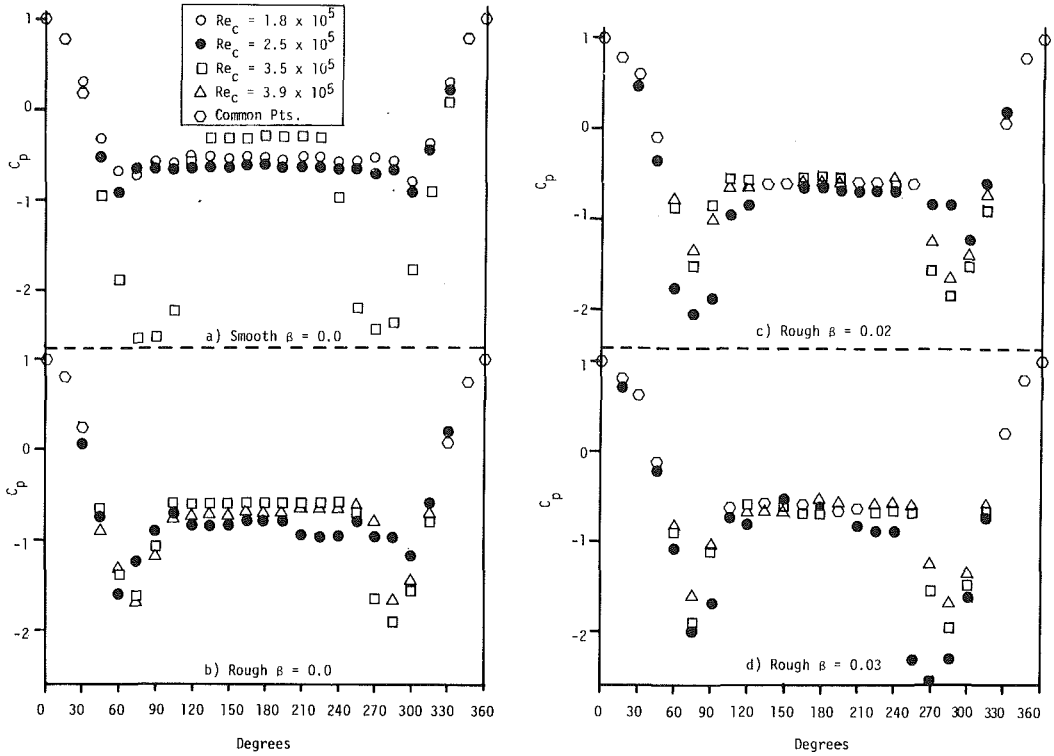


Fig. 2(*a*) Fig. 2(*b*)

**Fig. 2 Mean circumferential pressure distributions around test cylinders**

average 25 spectra before generating the final power spectrum.

## Discussion of Results

**(*a*) Surface Mean Pressure Characteristics.** The surface pressure patterns are presented as a plot of the actual pressure (nondimensionalized by the local stagnation pressure) as a function of circumferential position $\theta$ (where $\theta = 0$ deg is the stagnation point). Each plot corresponds to the position $y/D = -1.2$, slightly toward the low velocity end of the cylinder. The smooth cylinder pressure plots were obtained in the low turbulence (0.03 percent) flow, while the rough cylinder was tested in the 0.25 percent turbulence flow.

Figure 2(*a*) shows the progression of the smooth cylinder pressure distribution from subcritical flow conditions up to the onset of supercritical flow. The two lower Reynolds number plots, although subcritical, exhibit slightly higher than normal base pressures, as a result of the interference generated by insufficiently large endplates. These higher than normal values were also noticed by Davies [4]. At the highest Reynolds number (Re = $3.5 \times 10^5$), the symmetric separation bubble has formed, characterized by the large negative section ($C_p = -2.5$) around $\theta = 90$ and 270 deg. This marks the start of supercritical flow conditions. Achenbach [10] first noticed symmetric separation bubbles at Re = $3.0 \times 10^5$, but he was working with a higher free-stream turbulence (about 0.7 percent) level, which acted to trigger an earlier transition on his cylinder. Bearman [11] found the symmetric bubbles at Re = $3.8 \times 10^5$, but his smooth cylinder had been highly polished, and therefore delayed transition.

The asymmetric separation bubble, characteristic of flow near the end of the critical regime, was present at Re = $2.5 \times 10^5$ on the rough cylinder (Fig. 2(*b*)), although not as clearly as in the sheared cases presented later. Bearman observed the appearance of this phenomenon in the range Re = $3.4 \times 10^5$ to $3.8 \times 10^5$ on his smooth cylinder. At Re = $3.5 \times 10^5$, the rough cylinder was in the supercritical regime, an observation verified (as will be seen) by a lack of coherent vortex shedding. The cylinder entered the transcritical regime, accompanied by an increase in negative base pressure coefficient, $C_{pb}$, and the resumption of vortex shedding, at Re = $3.9 \times 10^5$.

It is therefore evident that roughening the cylinder lowered the Reynolds number associated with transition from Bearman's smooth cylinder value of $3.4 \times 10^5$ to $3.8 \times 10^5$, down to a value of $2.5 \times 10^5$. At the same time, the roughness substantially narrowed the range of the transition regime, triggering an early appearance of transcritical characteristics. Whereas Achenbach obtained a transcritical flow at Re = $1.2 \times 10^6$, and Roshko [12] at Re = $1.5 \times 10^6$, it occurred at Re = $3.9 \times 10^5$ on the rough cylinder. The same observation was made by Batham, when he concluded that the Reynolds number at the start of transition is only slightly reduced, while the Reynolds number marking the end of transition is greatly reduced by roughening a cylinder.

When a shear of $\beta = 0.02$ was introduced, (Fig. 2(*c*)), a highly asymmetric pressure distribution, indicative of the single separation bubble first noted by Bearman, emerged at Re = $2.5 \times 10^5$. The peak suction value near $\theta = 90$ deg was $C_p = -2.1$, while at $\theta = 270$ deg, $C_p = -1.2$. At Re = $3.5 \times 10^5$, the magnitude of the peak suction had decreased, indicating that again the cylinder was in the supercritical regime. With a further increase to Re = $3.9 \times 10^5$, the negative base pressure had increased and the magnitude of the peak suction had decreased further. As in the unsheared case, the cylinder was now in the transcritical regime.

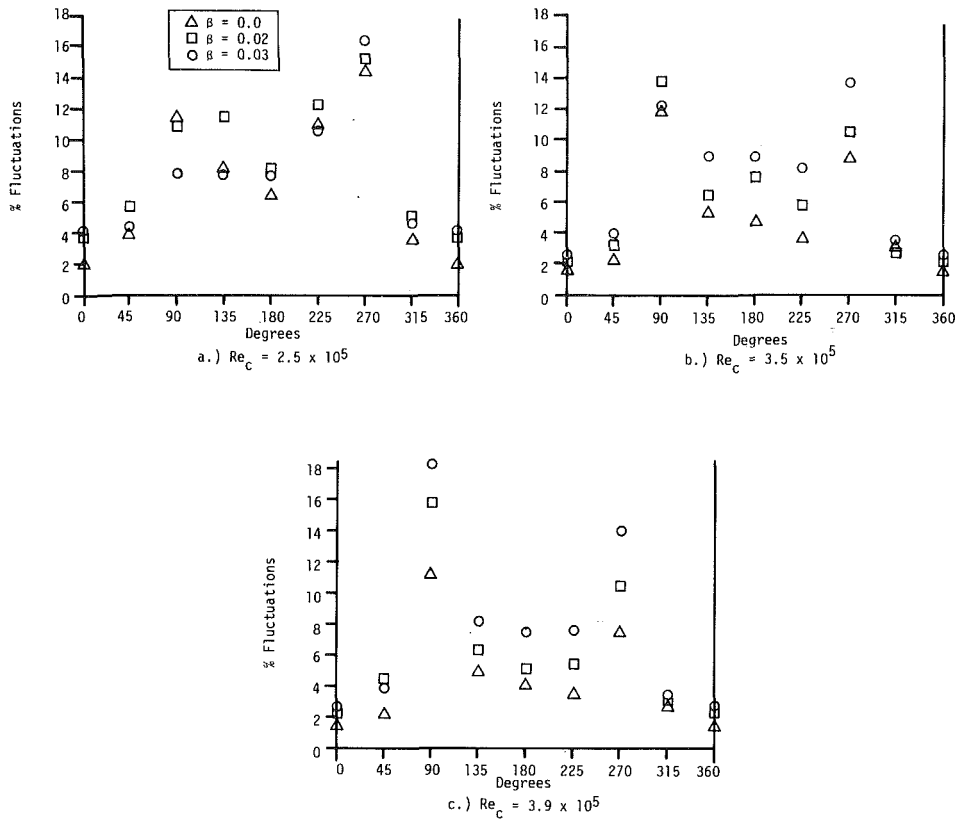


**Fig. 3 RMS pressure fluctuations around rough cylinder**

Figure 2(*d*) reproduces the pressure plots with a shear level $\beta = 0.03$. The same flow patterns emerge as before, except that at $Re_c = 2.5 \times 10^5$, the cylinder is just approaching the fully developed two bubble regime, since at $\theta = 270$ deg, $C_p = -2.5$ and on the other side, $C_p = -2.0$. The familiar decrease in peak suction and increase in negative base pressure noted by Roshko and Achenbach throughout the supercritical regime on smooth cylinders is again repeated for this rough cylinder case.

It is evident, however, that the first bubble has developed on opposite sides for the two shear cases. This is in apparent disagreement with Bearman's observation that it always occurred on the same side on his smooth cylinder. However, the discrepancy can be attributed to a difference in test methodology. In the present setup, as previously described, the cylinder was repeatedly rotated to provide complete coverage of all surface points. The triggering of the initial bubble is the result of microscopic dissimilarities on the opposing sizes of the cylinder. A minuscule adjustment (less than ± 0.25 deg) could easily shift it from one side to the other. In addition, the resetting of the tunnel flow after each 45 deg scanning of spanwise surface pressures is likely responsible for the disparity in left and right-hand lobes in Fig. 2(*c*). The growth and decay of the separation bubbles are restricted to a small Reynolds number range on the rough cylinder, particularly at higher shear and turbulence levels. Therefore the sensitivity to slight differences in freestream flow properties is manifest on these plots.

Yet the pressure plots serve primarily as indicators of the flow regime being experienced by the cylinder, particularly to demonstrate that the flow has undergone transition, and that any reemergent vortex shedding at even higher Reynolds numbers must be transcritical in nature. The above plots definitely verify that the rough cylinder has passed through the transitional regimes and was emerging at $Re_c = 3.9 \times 10^5$ into a transcritical flow regime.

It is not possible to extract significant trends from a comparison of the 6 in. (15 cm) smooth cylinder results with the smooth cylinder drag coefficient data of Bearman and Batham because of the dissimilarity in cylinder geometries. Humphreys [13] has shown that end effects dominate the circumferential flow pattern for Reynolds numbers up to $3 \times 10^5$, at which point three dimensional turbulent effects overshadowed endplate influence.

To demonstrate this point, Batham's results for $Re \leq 2.6 \times 10^5$ are cited alongside the present results. At $Re = 1.11 \times 10^5$, he obtained a typical subcritical drag coefficient. The 6 in. cylinder exhibited a very low $C_D = 0.74$ at $Re = 1.8 \times 10^5$ followed by Batham's $C_D = 0.77$ at $Re = 2.4 \times 10^5$, and the 6 in. cylinder value $C_D = 0.74$ at $Re = 2.5 \times 10^5$. Clearly, the small aspect ratios of both cylinders and the endplate effects make any conclusions hazardous. The 6 in. cylinder drag coefficient at $Re = 3.5 \times 10^5$ was 0.24. Bearman recorded the exact same value only when $Re = 3.8 \times 10^5$. The difference in these critical range values is the result of the slightly coarser finish (as well as the different end geometry) on the 6 in. cylinder.

**(*b*) Fluctuating Surface Pressure Distributions.** The rms pressure fluctuations, measured at 45 deg intervals around the circumference of the 6 in. rough cylinder, are displayed in Figs. 3(*a*), 3(*b*), and 3(*c*) as a function of shear parameter, for each of the three Reynolds number cases. They are plotted as a dimensionless rms value (rms fluctuation as a percent of local stagnation pressure) versus the circumferential angle $\theta$.

It is evident that the maximum fluctuations occurred near separation ($\theta = 90$ and 270 deg). A general trend toward increased fluctuations with increased tunnel shear was noticeable, particularly at higher Reynolds numbers. At Re =

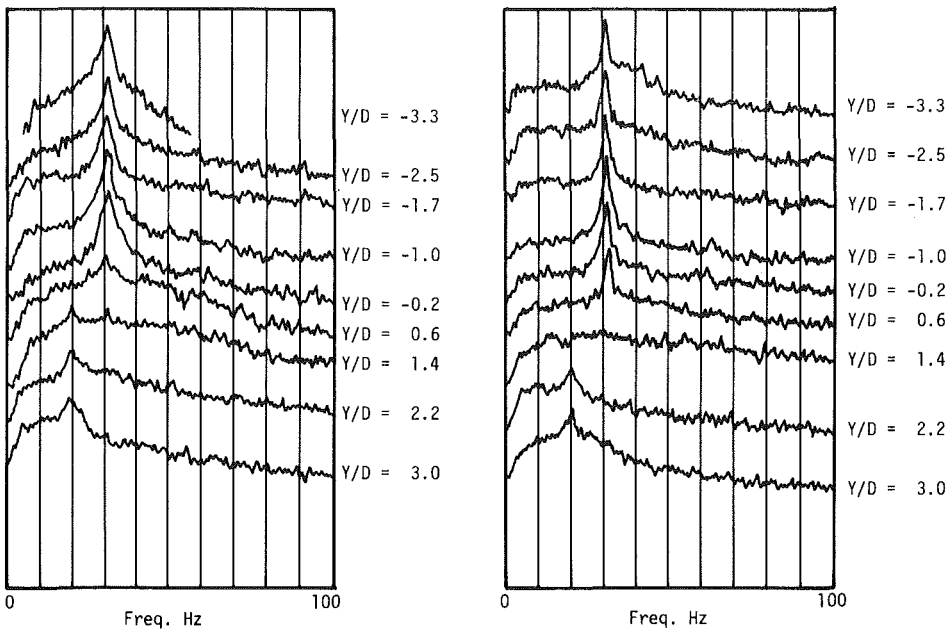


**Fig. 4 Power spectral density of eddy shedding frequency for sheared flow, $Re_c = 2.5 \times 10^5$, rough cylinder**

$3.9 \times 10^5$, there was a 40 percent increase in turbulent pressures from the unsheared flow values to those for $\beta = 0.03$. The characteristic shape of the curves and the magnitude of the fluctuations were in general agreement with Batham's results for pressure fluctuations around his roughened cylinder (with $K/D = 2.2 \times 10^{-3}$) in low turbulence flow.

**(c) Vortex Shedding Characteristics.** The vortex shedding frequencies were measured only in the wake of the rough cylinder. In an unsheared upstream flow, the rough cylinder exhibited uniform sharply defined vortex shedding at 25 Hz at $Re = 2.5 \times 10^5$. Increasing the Reynolds number to $3.5 \times 10^5$ eliminated all coherent shedding, indicating supercritical flow conditions. The reemergence of broadbanded shedding at 45 Hz signified that transcritical flow had just been achieved at $Re = 3.9 \times 10^5$. A stronger peak at 67 Hz at $Re = 5.2 \times 10^5$ represented fully established transcritical shedding. The Strouhal number varied from 0.165 in subcritical and critical flow to 0.215 in transcritical flow. This range agrees with that found by Szechenyi [8] in tests performed on cylinders (one with an aspect ratio of 9.33 and equivalent roughness as on the 6 in. cylinder) in one of his wind tunnels. However, it conflicts with results he obtained in another tunnel, which yielded a range between St = 0.22 and St = 0.26. Tunnel blockage, aspect ratio and wall boundary layer effects were all dismissed by Szechenyi as explanations of this discrepancy, which he was unable to explain.

The power spectra of the spanwise shedding frequency for $Re_c = 2.5 \times 10^5$, with shear levels $\beta = 0.02$ and $\beta = 0.03$ (Figs. 4(*a*) and 4(*b*)) were virtually identical. They reveal two cells of constant frequency: a strongly defined high frequency cell at 30 Hz and a weak low frequency cell at 19 Hz. The ratio between the lengths of the cells (5 to 3) is consistent with that found by Mair and Stansby [5] in their tests on a similar model with $L/D = 8$. They determined that this structure was independent of shear level, which is confirmed by the present results.

Measurements indicated that the spanwise shedding variations for the two shear levels at $Re = 3.9 \times 10^5$ were even more strongly influenced by end effects. A single broadbanded peak centered around 45 Hz existed along the central span of the cylinder at $\beta = 0.02$. Three-dimensional disturbances masked any cellular structure. At $\beta = 0.03$, two broad peaks reemerged, although end effects again obscured the structure near the plates. The low velocity side of the cyinder registered a 45 Hz peak, while on the high velocity side, a 49 Hz peak existed.

Very clear transcritical spanwise cellular structures were present for the two sheared cases at $Re_c = 5.2 \times 10^5$. With $\beta = 0.02$, (Fig. 5(*a*)), a two cell structure with a high frequency cell at 66 Hz and a low frequency cell at 60 Hz emerged. In the central portion of the cylinder, the transition region between the cells was marked by a very broad spectrum in which the two peaks appeared simultaneously. Maull and Young [3] observed the same phenomenon and attributed it to the unsteady boundaries between the cells, each of which was averaged into the power spectrum obtained from the hotwire probe at a fixed position. At the highest shear (Fig. 5(*b*)), the relative cell lengths remained unchanged, except that the high frequency peak shifted slightly upward to 67 Hz and the low frequency peak downward to 59 Hz. In the central span the averaged spectra appear to indicate a gradual downward frequency shift, but again this was the result of the unsteady cell boundaries.

A power spectrum of the pressure fluctuations measured by the Kulite transducers permitted a check of the hotwire results shown in Figs. 4 and 5. The spectra were taken with the transducers at $\theta = 90$ deg at two shear levels. They agreed very well with the hot wire results, and demonstrate the large contribution of the shedding to the pressure fluctuations on the cylinder. It should also be noted that spectra taken upstream of the test model revealed no high energy levels at any frequency, thereby eliminating tunnel propeller blade frequencies, vibrations, or instrument noise as contributors to the spectra discussed in this section.

It has already been noted that endplate effects are of critical importance to the type of shedding structure existing behind a cylinder. The short end-plates used in the present series of

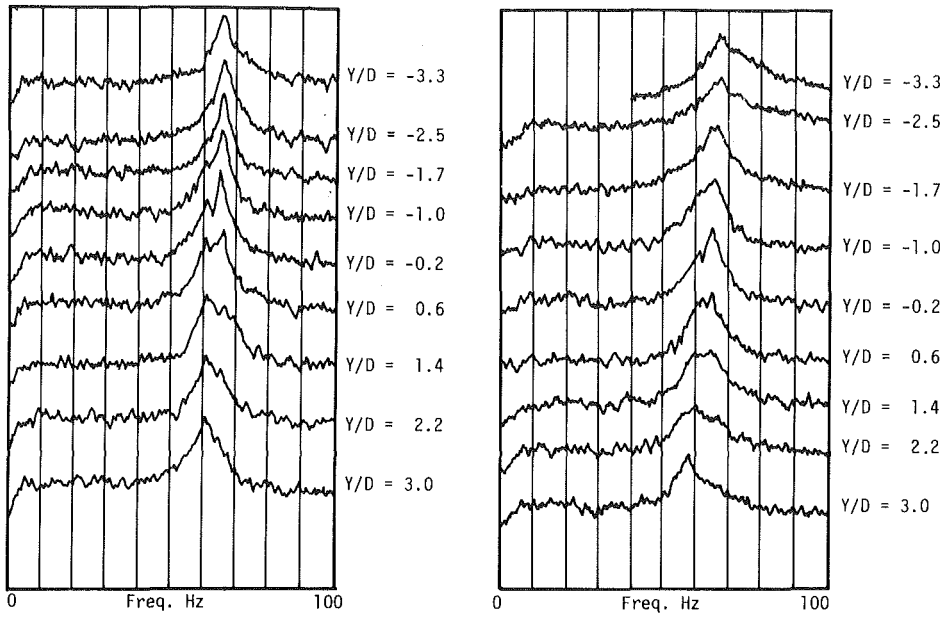


**Fig. 5 Power spectral density of eddy shedding frequency for sheared flow, $Re_c = 5.2 \times 10^5$, rough cylinder**

tests definitely produced broader-peaked cells than would have endplates of the dimensions recommended by Mair and Stansby. Yet for small aspect ratios (of order 10 or less), they have shown that the base pressure coefficient varies significantly all along the cylinder regardless of endplate configuration, so that it is virtually impossible to entirely eliminate three-dimensional effects.

Since the unsheared flow tests revealed a constant spanwise shedding frequency at the three Reynolds numbers tested (despite an end inflow resulting from the small plate size), the sharp division in cells observed in the transcritical shear-flow at $Re_c = 5.2 \times 10^5$ necessarily was the result of the upstream shear.

Accordingly, it may be concluded that reestablished transcritical vortex shedding separates into discrete cells in a manner totally analogous to the previously documented subcritical shedding pattern.

This discovery could be of crucial importance to the behavior of a large ocean structure like the cold water pipe, for which the flow field is definitely transcritical. If such a cellular shedding pattern emerges as a result of prolonged unidirectional currents impinging on the pipe, the interaction between the cells of constant shedding frequency and the natural vibrational modes of the pipe may pose significant structural problems. The remaining issue is to determine how the shedding cell lengths vary as a function of upstream shear, so that the relative lengths of the vortex shedding cells and the natural vibrational modes can be established.

## Conclusions

An experimental investigation into the effects of vertical shear on vortex shedding patterns in transitional Re flow around a circular cylinder has been presented. The flow phenomena were explored through measurements of shedding frequencies, as well as of the pressure distribution around the cylinder. With a roughened cylinder, measurements of shedding patterns were made in the transcritical regime, thus permitting comparisons with low Re tests performed previously elsewhere. The following observations can be made:

1 Discrete cells of eddies are formed in transcritical Re shear flow, but from the data measured, it is impossible to determine a correlation between shear and cell length.

2 For the aspect ratio studied, the eddy shedding pattern for transcritical Re sheared flow was found to be essentially the same as for subcritical Re sheared flow, with two distinct correlated eddies evident.

3 The mean surface pressure distribution on the cylinder indicated (as expected), the narrowing of the critical and supercritical Re ranges with increased roughness, but differing geometries make perfect comparisons with previous results difficult.

4 The fluctuations in pressures on the surface of the cylinder were significantly higher in sheared flow cases than for unsheared flow.

In order to increase the understanding of the effects of shear on vortex shedding, the following investigations are presently under way:

1 The analysis of this study is being extended to include a larger range of shear parameter, particularly for low shears to determine the minimum shear which produces a two cell eddy structure.

2 A smaller cylinder ($H/D \sim 20$) with much larger endplates, similar to models tested by Mair and Stansby [5] is being examined in transitional Reynolds number flows over a wide range of shears so that more cells may be observed.

3 Testing of cylinders at yawed incidence to the upstream flow in a low Reynolds number regime would yield valuable information on vortex shedding patterns around mooring cables.

## Acknowledgments

This work was funded by a grant from NOAA through

ORI, Inc. The help and advice of Dr. Richard Scotti of NOAA and Mr. Jon Buck of ORI, Inc. is deeply appreciated.

## References

1 Griffin, O. M., "Vortex Shedding From Stationary and Vibrating Bluff Bodies in a Shear Flow," *Naval Research Laboratory Memorandum* Report 4287, Aug. 1980.

2 Shaw, T. L., and Starr, M. R., "Shear Flows Past a Circular Cylinder," *Journal of the Hydraulics Division*, ASCE, Vol. 98 Hy 3, 1972, pp. 461-473.

3 Maull, D. J., and Young, R. A., "Vortex Shedding from Bluff Bodies in a Shear Flow," *Journal of Fluid Mechanics*, Vol. 60, 1973, pp. 401-409.

4 Davies, M. E., "The Effects of Turbulent Shear Flow on the Critical Reynolds Number of a Circular Cylinder," National Physical Laboratory (U.K.) NPL Report Mar Sci R 151, Jan. 1976.

5 Mair, W. A., and Stansby, P. K., "Vortex Wakes of Bluff Cylinders in a Shear Flow," *SIAM Journal of Applied Mathematics*, Vol. 28, 1975, pp. 519-540.

6 Stansby, P. K., "The Locking-on of Vortex Shedding Due to the Cross-Stream Vibration of Circular Cylinders in Uniform and Shear Flows," *Journal of Fluid Mechanics*, Vol. 74, 1976, pp. 641-667.

7 Batham, J. P., "Pressure Distributions on Circular Cylinders at Critical Reynolds Numbers," *Journal of Fluid Mechanics*, Vol. 57, 1973, pp. 209-228.

8 Szechenyi, E., "Supercritical Reynolds Number Simulation for Two Dimensional Flow Over Circular Cylinders," *Journal of Fluid Mechanics*, Vol. 70, part 3, 1975, pp. 529-542.

9 Hove, D., Shih, W., and Albano, E., "Hydrodynamic Design Loads for the OTEC Cold Water Pipe," Science Applications, Inc., Report No. SAI-79-559-LA, Sept., 1978.

10 Achenbach, E., "Influence of Surface Roughness on the Cross-Flow Around a Circular Cylinder," *Journal of Fluid Mechanics*, Vol. 46, Part 2, 1971, pp. 321-335.

11 Bearman, P. W., "On Vortex Shedding From a Circular Cylinder in the Critical Reynolds Number Regime," *Journal of Fluid Mechanics*, Vol. 37, Part 3, 1969, pp. 577-585.

12 Roshko, A., "Experiments on the Flow Past a Circular Cylinder at Very High Reynolds Numbers," *Journal of Fluid Mechanics*, Vol. 10, 1961, pp. 345-356.

13 Humphreys, J. S., "On a Circular Cylinder in a Steady Wind at Transition Reynolds Numbers," *Journal of Fluid Mechanics*, Vol. 9, 1960, pp. 603-612.

ORI, Inc. The help and advice of Dr. Richard Scotti of NOAA and Mr. Jon Buck of ORI, Inc. is deeply appreciated.

## References

1 Griffin, O. M., "Vortex Shedding From Stationary and Vibrating Bluff Bodies in a Shear Flow," *Naval Research Laboratory Memorandum* Report 4287, Aug. 1980.

2 Shaw, T. L., and Starr, M. R., "Shear Flows Past a Circular Cylinder," *Journal of the Hydraulics Division*, ASCE, Vol. 98 Hy 3, 1972, pp. 461-473.

3 Maull, D. J., and Young, R. A., "Vortex Shedding from Bluff Bodies in a Shear Flow," *Journal of Fluid Mechanics*, Vol. 60, 1973, pp. 401-409.

4 Davies, M. E., "The Effects of Turbulent Shear Flow on the Critical Reynolds Number of a Circular Cylinder," National Physical Laboratory (U.K.) NPL Report Mar Sci R 151, Jan. 1976.

5 Mair, W. A., and Stansby, P. K., "Vortex Wakes of Bluff Cylinders in a Shear Flow," *SIAM Journal of Applied Mathematics*, Vol. 28, 1975, pp. 519-540.

6 Stansby, P. K., "The Locking-on of Vortex Shedding Due to the Cross-Stream Vibration of Circular Cylinders in Uniform and Shear Flows," *Journal of Fluid Mechanics*, Vol. 74, 1976, pp. 641-667.

7 Batham, J. P., "Pressure Distributions on Circular Cylinders at Critical Reynolds Numbers," *Journal of Fluid Mechanics*, Vol. 57, 1973, pp. 209-228.

8 Szechenyi, E., "Supercritical Reynolds Number Simulation for Two Dimensional Flow Over Circular Cylinders," *Journal of Fluid Mechanics*, Vol. 70, part 3, 1975, pp. 529-542.

9 Hove, D., Shih, W., and Albano, E., "Hydrodynamic Design Loads for the OTEC Cold Water Pipe," Science Applications, Inc., Report No. SAI-79-559-LA, Sept., 1978.

10 Achenbach, E., "Influence of Surface Roughness on the Cross-Flow Around a Circular Cylinder," *Journal of Fluid Mechanics*, Vol. 46, Part 2, 1971, pp. 321-335.

11 Bearman, P. W., "On Vortex Shedding From a Circular Cylinder in the Critical Reynolds Number Regime," *Journal of Fluid Mechanics*, Vol. 37, Part 3, 1969, pp. 577-585.

12 Roshko, A., "Experiments on the Flow Past a Circular Cylinder at Very High Reynolds Numbers," *Journal of Fluid Mechanics*, Vol. 10, 1961, pp. 345-356.

13 Humphreys, J. S., "On a Circular Cylinder in a Steady Wind at Transition Reynolds Numbers," *Journal of Fluid Mechanics*, Vol. 9, 1960, pp. 603-612.

## DISCUSSION

**O. M. Griffin**[1]. Rooney and Peltzer have conducted extensive experiments and they have provided interesting and useful new data for the effects of shear (nonuniform) flow on vortex shedding from circular cylinders. They have clearly shown the re-emergence of the transcritical vortex shedding regime at high Reynolds number by examining the pressure distribution around and the wake flow downstream from a rough circular cylinder. It should be noted that here and in the paper by Rooney and Peltzer the same order of prefixes employed by Roshko [12] is used to characterize the different flow regimes for a circular cylinder, i.e. subcritical → critical → supercritical → transcritical or postcritical. Some authors, including Szechenyi [8], characterize the last two flow regimes in the order transcritical → supercritical.

As observed by the authors, the effects of the surface roughness are to hasten the onset of the critical Reynolds number well before the usual value of $Re = 2 \times 10^5$ for a smooth cylinder and to initiate the re-emergence of regular vortex shedding in the transcritical Reynolds number range at about $4 \times 10^5$. Similar findings have been reported recently by Alemdaroglu, Rebillat, and Goethals [14][2] who employed aeroacoustic coherence measurements in the wake of several roughened cylinders to study the transition from subcritical to critical and to transcritical Reynolds numbers. The results obtained by Rooney and Peltzer are in excellent agreement with those of Alemdaroglu, Rebillat and Goethals, as shown in a recently-published report [1].

When shear was added to the incident flow a typical cellular shedding pattern was obtained at transcritical Reynolds numbers, similar to previous findings at subcritical Reynolds numbers. Although the relatively short length-to-diameter ratios of their cylinders ($L/D = 9$) certainly influenced the cell structure in Rooney and Peltzer's experiments, their results clearly demonstrate for the first time the existence of the cellular vortex structure at very large Reynolds numbers. It would be interesting if the authors could comment upon the effects of larger length-to-diameter ratios ($L/D$) and different shear parameters ($\beta$) on the presence or absence of the cell structure.

The objective of the authors' experiments was to provide data to aid in the design of the cold water intake pipe for an ocean thermal energy conversion (OTEC) power plant. The cold water pipe is thought by many observers to be the critical problem in OTEC development, since the long, slender pipe is particularly vulnerable to problems caused by vortex shedding in steady currents [15] and to other hydrodynamic forces. The problem potentially is made more serious because experiments by Fischer, Jones, and King [16,17] have shown that marine structures undergo large amplitude cross flow vortex-excited oscillations (± 1.5 diameters) even when the incident flow is characterized by shear parameters in the range $\beta = 0.01$ to 0.02, so long as the structural damping of the cylindrical structure is sufficiently small. This range of shear parameters was characteristic of both the model test conditions and field site conditions discussed by Fischer, Jones and King. The experiments conducted by Rooney and Peltzer clearly demonstrate that regular vortex shedding takes place at the large Reynolds numbers, $Re = 10^6$ to $10^7$, and shear parameters, $\beta = 0.01$ to 0.03, that characterize the OTEC cold water pipe.

## Additional References

14 Alemdaroglu, N., Rebillat, J. C., and Goethals, R., "An Aeroacoustic Coherence Function Method Applied to Circular Cylinder Flows," *Journal of Sound and Vibration*, Vol. 69, Part 3, 1980, pp. 427-439.

15 Griffin, O.M., "OTEC Cold Water Pipe Design for Problems Caused by Vortex-Excited Oscillations," Naval Research Laboratory Memorandum Report 4157, Mar. 1980.

16 Fischer, F.J., Jones, W.T., and King, R., "Current-Induced Oscillation of COGNAC Piles During Installation: Prediction and Measurement," in *Proceedings of the Symposium on Practical Experiences with Flow-Induced Vibrations* (Pre-prints), Karlsruhe, Vol. I, 1979, pp. 216-228.

17 King, R., "Model Tests of Vortex-Induced Motion of Cable Suspended and Cantilevered Piles for the COGNAC Platform," BHRA Fluid Engineering Report RR1453, Jan. 1978.

[1] Marine Technology Division, Naval Research Laboratory, Washington, D.C. 20375.

[2] References are numbered sequentially following those of Rooney and Peltzer.

## Authors' Closure

The above paper having documented the existence of a stable cellular shedding structure in transcritical flow, the effects of altering both the aspect ratio and the shear parameter will now be addressed briefly. Assuming that the transcritical cellular structure behaves similarly to that found in subcritical Reynolds number flows (which has just been demonstrated), newly obtained data on shear parameter and aspect ratio effects in subcritical-critical flows can be applied to the high Reynolds number cases.

The authors have, in a more recent investigation, observed that increasing the shear parameter $\beta$ resulted in a decrease in the average cell length along a cylinder of aspect ratio $L/D = 17.3$ in a flow range $1.0 \times 10^5 \leq \mathrm{Re} \leq 3.0 \times 10^5$. A cellular structure existed at virtually all shear values between $\beta = 0.007$ and $\beta = 0.041$, values which represent typically predicted shear levels for the CWP.

Increasing the aspect ratio should generally result in the presence of more cells along the cylinder span. Increasing $\beta$ should also result in a greater spanwise frequency spread, resulting in a very wide range to be encountered in the design of a large aspect ratio CWP subjected to sheared transcritical flow.

# Turbulent Boundary Layer Flow Through a Gap in a Wall Mounted Roughness Element

**W. H. Schofield**
Defense Science and Technology Organization,
Aeronautical Research Laboratories,
Fisherman's Bend, Melbourne, Australia
Mem. ASME

**D. S. Barber**
Department of Mechanics,
United States Military Academy,
West Point, N.Y

**E. Logan**
Department of Mechanical Engineering,
Arizona State University,
Tempe, Arizona,
Mem. ASME

*The center-line development of a turbulent boundary layer flow through a gap in an isolated wall mounted roughness element has been studied experimentally. The centerline flow downstream of the gap can be divided into a distortion region followed by a readjustment region. The nature of the distortion produced by the gap varies with gap size and thus flows downstream of large gaps were found to differ significantly from those through small gaps. After distortion the layer readjusts itself and approaches equilibrium conditions of an undisturbed zero pressure gradient layer. The readjustment starts near the wall with the turbulence adjustment preceding the mean flow adjustment. For flow through all six gap sizes the growth of the centerline internal layer can be described by a single function if internal layer height and distance from the gap are non-dimensionalized with the local wall length scale. Well downstream of the gap it is shown that all six centerline flows are similar and are approaching equilibrium conditions in a similar manner.*

## Introduction

There has been considerable work on the response of turbulent boundary layers to various two-dimensional perturbations. Various studies have considered boundary layer response to changes in wall roughness and pressure gradients, changes in wall suction and injection and to obstacles in the flow. Tani [20] and Schofield [17] have reviewed this work which has both theoretical and practical applications. The theoretical interest comes from Clauser's [6] proposal that these experiments offer the possibility of understanding the internal turbulent exchange mechanisms in the boundary layer by observing the response of a layer to a step or pulse input in one of its boundary conditions. Practical interest in the experiments arises from the need to predict engineering flows involving these perturbations especially in the field of heat transfer, aerodynamics of jet engines, meteorology and wind loads on buildings.

The present work considers the center-line flow of a turbulent boundary layer over and through a gap in a surface mounted roughness element. It is the first stage of a continuing research program that aims to describe the entire three-dimensional flow field. The problem has practical significance in describing the effects of buildings and other obstructions on wind gradients and turbulence levels near V/STOL aircraft landing zones. Data on such flows have not been previously reported. There has however been work on isolated surface roughness elements without gaps. Mueller and Robertson [10] studied a flat plate flow over a wedge shaped element the height of which was of the same order as the boundary layer thickness. Mean and fluctuating velocity profiles were measured up to forty element thicknesses downstream of the element. Reattachment of the flow separation caused by the element occurred at several elements heights downstream of the element. Reattachment was defined as the position where $c_f' = 0$. Downstream from reattachment the skin friction was found to increase rapidly to its undisturbed value. The mean and fluctuating velocity profiles were judged to have returned to their undisturbed forms at a distance of forty element heights downstream of the element. Oka and Kostic [11] performed a similar study using a square roughness element on the floor of a rectangular channel. Reattachment was again located at seven element heights downstream of the element. Turbulence intensity profiles after reattachment showed a large maximum that decreased in magnitude and moved away from the wall with distance downstream. However these maximum values at eighteen element heights downstream of the element, were still considerably larger than values in an undisturbed layer. Similar results were reported by Counihan, Hunt, and Jackson [4] who also used a square cross sectional element. These authors presented an eddy viscosity theory that adequately described the mean flow profiles. Results by Sami and Liu [14] suggest that the distance to reattachment behind an element whose height is the same as the boundary layer, depends on the Reynolds number. However their reattachment lengths were much larger (twelve to fourteen element heights) than those given in other papers. Phataraphruk and Logan [13] found that the reattachment length behind a single roughness element in a smooth pipe depended on the height to width ratio of the roughness element. This may explain the different reattachment lengths reported by authors for flows behind thin two-dimensional fences (Petryk and Brundrett [12] – seventeen fence heights, Good and Joubert [7] – twelve to fourteen fence heights). In the present study, as well as measurements of flows through a

Contributed by the Fluids Engineering Division and presented at the Winter Annual Meeting, Chicago, Ill., November 16-21, 1980, of THE AMERICAN SOCIETY OF MECHANICAL ENGINEERING. Manuscript received by the Fluids Engineering Division, December 3, 1979. Paper No. 80-WA/FE-9.

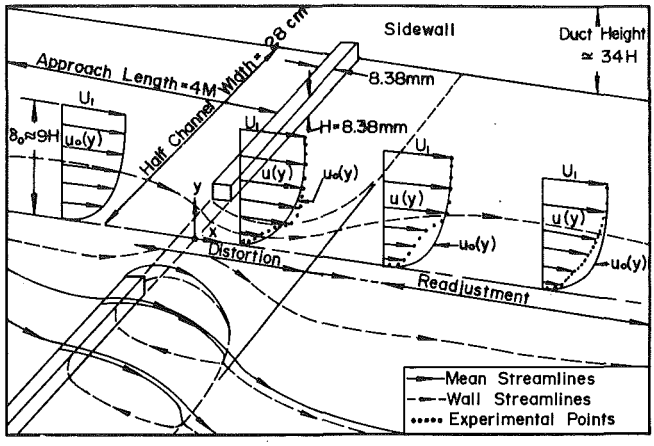


**Fig. 1 Schematic view of experimental flow**

gap, measurements for flows with no gap were taken, as this two-dimensional element case represents a limit for the series of experiments reported here. Comparison with existing data for the no gap case also gave a useful check of experimental method and the agreement obtained with previous data gave confidence in the results for flows through gaps.

Of less relevance to the present study is the considerable work on flow around isolated three-dimensional elements, such as; measurements around a surface mounted cube by Castro and Robins [3], around model buildings by Sharan [18], around a right cylinder by Horning and Joubert [8] and around a surface mounted airfoil by Brown [2]. These flows all generate horse-shoe vortices around the front of the models that shed from both sides of the model into the downstream flow. The results show that this flow disturbance caused by the models decays fairly rapidly with distance downstream of the model. The relevance of these studies to the present work is that in flow through a gap, vortices are most probably shed from each side of the gap and may have an influence on the centerline flow development in the region immediately downstream of the gap.

## Method

A two-dimensional turbulent boundary layer was generated and its center-line development through a gap in a wall mounted roughness element was observed as shown schematically in Figure 1. The element was square in cross section (8.38 mm × 8.38 mm) and the center-line gap was set at six widths over the range 4.19 mm to 83.8 mm (0.5 H to 10.0 H). The experimental flow was generated on the floor of a suction wind tunnel 7.32 m long and 0.56 m wide. The flexible roof of the wind tunnel was adjusted to give a zero pressure gradient flow[1] over the length of the wind tunnel. Air for the tunnel was first filtered and then entered a honeycomb flow straightener. 150 mm downstream of the flow straightener the boundary layer was tripped by a 12.7 mm quarter round rod and then further thickened by 0.6 m of rough sandpaper fixed to the floor. The last 2.4 m of tunnel floor was used to observe the boundary layer's centerline response to the roughness element, which left 4 m before the element for a smooth wall turbulent boundary layer to develop. The Reynolds number based on the development length of the flow at the element was $2.2 \times 10^6$ which was held constant for all tests. The total boundary layer thickness immediately before the element was 77 mm ($\simeq$ 9H).

Pitot tubes and hot wire anemometer probes were mounted on a traversing mechanism above the roof of the tunnel, the probes entering the flow through slots in the roof. The traversing mechanism could only be moved along the tunnel centerline and hence only profiles along the centerline of the flow were recorded.

As a test of the flow and the measuring system, mean velocity and longitudinal turbulence intensity profiles were measured in an empty tunnel. These profiles were compared with zero pressure gradient profiles by Wieghardt and Tillmann [22] and Klebanoff and Diehl [9] and were in satisfactory agreement.

[1] Indicated by static pressure taps in the tunnel walls.

## Results and Discussion

**Flow Description.** This paper presents measurements along the center line of flow through a gap in a wall-mounted roughness element. Research on this flow is continuing, and it is anticipated that full details of the off-centerline flow will be reported at a future date. Thus the flow description, illustrated in Figure 1, is at this stage rather speculative although its major features will be fairly uncontroversial, at least in qualitative terms. Quantitative relations implied by the figure may well have to be recast in the light of subsequent measurements.

Figure 1 shows three flow regions. Well upstream of the roughness element the flow is a standard zero pressure gradient boundary layer. Further downstream the roughness element perturbs or distorts flow through the gap. This distortion is not confined to the gap but extends upstream and downstream of it. The distortion process begins upstream of the gap (as flow off the centerline and near the surface moves toward the centerline and into the gap) and increases continuously up to the gap. Downstream of the gap the centerline flow distortion can increase due to the action of three-dimensional separations generated at each gap edge. The reason for this is that these separations must bow towards the centerline of the tunnel and can further squeeze the centerline flow downstream of the gap. After this the separated regions diverge from the centerline and will most probably join up with the separations caused by flow over the roughness element (see Fig. 1). At this longitudinal position where the separation bubble from the roughness element closes onto the

## Nomenclature

$A$ = constant in logarithmic law of the wall (5.1)
$c_f$ = local skin friction coefficient ($\tau_0/\frac{1}{2}\rho U_1^2$)
$c_{f0}'$ = skin friction coefficient of undisturbed layer
$D$ = gap width
$G$ = Clauser's profile shape factor
$H$ = height of roughness element (8.38 mm)
$u$ = mean velocity in the $x$ direction
$\sqrt{u'^2}$ = longitudinal turbulence intensity
$\sqrt{u_m'^2}$ = maximum value of $\sqrt{u'^2}$
$u_\tau$ = friction velocity ($\sqrt{\tau_0/\rho}$)
$u_{\tau 0}$ = friction velocity of undisturbed layer
$U_1$ = free stream velocity in the $x$ direction
$x$ = distance in the main flow direction
$y$ = vertical distance from wall
$y_m'$ = value of $y$ at $\sqrt{u_m'^2}$
$z$ = local wall length scale
$\delta$ = boundary layer total thickness
$\delta_i$ = height of internal layer
$\kappa$ = von Karman's constant (0.41)
$\nu$ = kinematic viscosity of fluid
$\rho$ = density of fluid
$\tau_0$ = wall shear stress

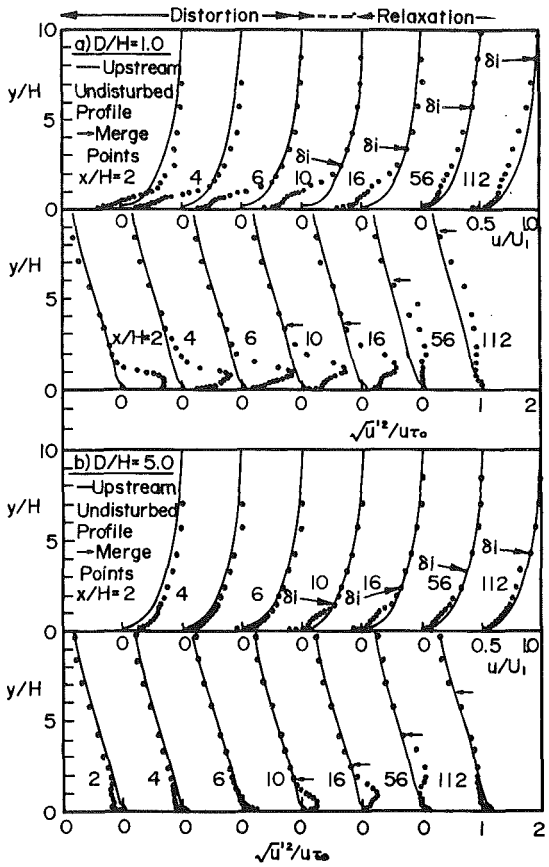


Fig. 2 Selected center-line mean velocity and longitudinal turbulence intensity profiles for a small and large gap flow

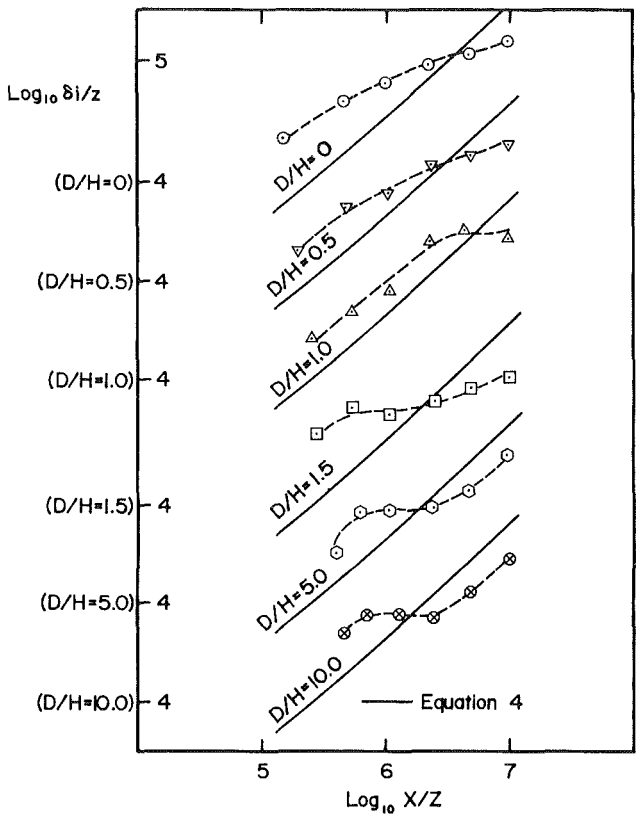


Fig. 3 Internal layer growth of the center-line flow; $\delta_i$ based on mean velocity profiles

wall there is no disturbance (separation or obstacle) left in the flow to cause further distortion, and formally at least, the readjustment region of the flow starts from this point. However the two regions probably merge as the distortion (cross-stream) pressure forces will still be present in the flow downstream of the separation bubble closure. Center-line measurements suggest however that these distortion pressure forces decay fairly rapidly and that the flow moves into a readjustment phase which will eventually return the flow to its original zero pressure gradient form (the final equilibrium condition).

**Flow Distortion.** As discussed above, the distortion of the center-line flow through the gap is caused by flow adjacent to the center-line funnelling through the gap. This combined flow is subsequently squeezed by a reduction in flow area which is partially caused by separated regions flowing from both gap edges which move towards the flow centerline downstream of the gap. The gap edge separations will almost certainly involve counterrotating helical vortices one each side the center-line flow. This flow picture affords an explanation of the different behavior of the center-line flow for large and small gap widths. The center-line flow through large gaps is well removed from the gap edges and is little affected by gap edge separations. Thus the flow funnels through the gap increasing the mean velocity of the centerline flow and decreasing the longitudinal turbulence intensity as in a conventional nozzle. On the other hand, the center-line flow through a small gap is affected by the gap edge separations which in this case occupy a significant proportion of the flow area in the gap. At the smallest gap settings considered here the flow blockage is so severe that the centerline flow is brought nearly to separation and much of the "through gap" flow is diverted up and over the gap, increasing mean flow velocities at distances greater than the element height. The gap edge separations adjacent to the centerline flow increase its turbulence level near the wall.

Data supporting these flow pictures are presented in Fig. 2 where a series of profiles for a small gap ($D/H = 1.0$) and for a large gap ($D/H = 5.0$) are compared with the (upstream) undisturbed boundary layer profiles. In the distortion region ($0 < x/H < 10$ to 16) the small gap center-line profiles show a reduction in mean velocity near the wall, and the corresponding profiles of longitudinal turbulence $\sqrt{u'^2}/u_{\tau 0}$ show a large increase near the wall. Note that both of these series of profiles show maximum distortions at about four to six element heights downstream of the gap due to the bowing out of the separation boundaries downstream of the gap.

The center-line profiles for the large gap show the opposite behavior. In the distortion region the gap edge separations are well removed from the center-line, and thus mean flow velocities are increased (relative to the undisturbed profile) and longitudinal turbulence intensities decreased. Note that in this case maximum distortion occurs in profiles nearest the gap[2] as it is the actual gap not the downstream separation boundaries that are causing most of the centerline distortion.

In both cases the outer portions ($y/H > 2$) of the profiles at the end of distortion ($x/H = 10$ to 16) are again coincident with the undisturbed upstream profiles. This is fortunate as it aids the analysis of the layer's readjustment that is discussed in the next section.

**Flow Readjustment.** As discussed previously, the readjustment of the centerline flow towards velocity distributions of an undisturbed zero pressure gradient layer start

[2] In Fig. 2 this is the profile at $x/H = 2$. Earlier profiles at $x/H = 1$, not shown in Fig. 2, have slightly more distortion.

somewhere in the range, $x/H$ = 10 to 16 for all gap settings. At $x/H$ = 10 distorting forces are apparently small and are decaying rapidly. Downstream of $x/H$ = 10 the dominant feature of the flow is readjustment. Work on two-dimensional flows responding to a perturbation (see Tani [20]) suggest that the readjustment of the present layers will take the form of a slow modification in both the mean and turbulent fields until the entire layer is returned to its original undisturbed zero pressure gradient form. Results for two-dimensional perturbed boundary layers (Tani [20], Schofield [15], Townsend [21]) show that the flow modification process starts from the wall because turbulence near the wall is small scale and short lived and can therefore make rapid adjustments to changing conditions. Further from the wall the flow contains larger turbulent eddies which contain more turbulent energy, have longer lifetimes and travel downstream faster than wall eddies because they exist in regions of higher mean velocity (Townsend [21]). Thus the large eddies take a longer distance to adjust to changing conditions. For these reasons the expected flow modification in a boundary layer after any flow distortion is for adjustment to start immediately at the wall and then proceed ever more slowly through the outer layer. It should be noted that evidence of flow modification at some height in the layer does not mean that the profile has attained its equilibrium distribution but only that the flow at that height has started the re-adjustment process which may initially move the local flow away from its equilibrium form. The attainment of the equilibrium distribution throughout the layer apparently takes a very long development distance. This is a common conclusion of Bradshaw and Wong [1], Townsend [21] and Schofield [15-17] and is further demonstrated in this paper.

To find the depth of modified flow (usually termed the height of the new internal layer) $\delta_i$ the readjusting profile is compared with the profile the layer would have had if the distortion or perturbation had not been applied to the layer (see Schofield [15, 16]). In the present case the unperturbed profile is a zero pressure gradient layer and the comparisons are illustrated in Fig. 2. The rate of adjustment of various flow parameters (such as mean velocity, fluctuating velocities, turbulent shear stress) are not the same (see Siuri and Logan [19]). But as all workers in this field have measured mean velocities, it is usual to determine the depth of modified flow associated with the mean velocity. Thus the height of the internal layer $\delta_i$ is usually defined as the distance from the wall that the actual mean velocity profile merges with the unperturbed profile, as shown in Fig. 2. The merge points for the longitudinal turbulence intensity profiles are also shown in Fig. 2, and it can be seen that modification of the turbulence field slightly precedes modification of the mean velocity for both small and large gap cases. This result applied to all six cases studied in this work. This may be a general result, as in a different type of perturbed flow Siuru and Logan [19] also found that the modification to the turbulence field slightly preceded the mean flow modification.

Many methods have been used by authors to express the variation of the height of the new internal layer as a function of distance from the perturbation. The methods use a variety of length scales to non-dimensionalize the results, but most of these length scales are specific to the particular flow considered (see Schofield [15, 16]). It has been shown by Schofield [16, 17] that for two dimensional flows over step changes in roughness non-dimensionalizing the results with the local wall length scale ($z$) introduced by Townsend [21] collapses data from a very wide variety of flows over a step change in roughness onto a single curve. The wall length scale for smooth wall flow is related to the wall shear and its definition is derived from the logarithmic law of the wall which applies to the inner regions of most two-dimensional turbulent boundary layers. It can be written

$$\frac{u}{u_\tau} = \frac{1}{\kappa}\log_e \frac{yu_\tau}{\nu} + A \tag{1}$$

and the local wall length scale ($z$) is defined by rewriting it as

$$\frac{u}{u_\tau} = \frac{1}{\kappa}\log_e \frac{y}{z} \tag{2}$$

which by comparison gives

$$z = \frac{\nu}{(u_\tau \exp(\kappa A))} \tag{3}$$

Using the local value of $z$ for each profile the variation of the nondimensional internal layer height ($\delta_i$) is compared with the nondimensional distance from the gap ($x/z$) in Fig. 3. It is seen that the data expressed in this form are similar although a systematic variation with gap size can be discerned.

Townsend's analysis [21] considered thick zero pressure gradient flow over a small step change in roughness and gave the following relation for the internal layer height.

$$\frac{\delta_i}{z}\left(\log_e\left(\frac{\delta_i}{z}\right) - 1\right) = 2\kappa^2 \frac{x}{z} \tag{4}$$

Schofield [16, 17] showed that this equation gave quite good descriptions for flow over a wide range of step changes in roughness under all types of flow conditions many of which were very different from those of the Townsend analysis. Equation (4) has been plotted in Fig. 3 and appears to give a useful description of the internal layer growth for the centerline flow for all six gap sizes even though the present perturbation is of a different kind from that analyzed by Townsend.

Figure 4 compares mean velocity and longitudinal turbulence intensity profiles on the centerline at the last measuring station ($x/H$ = 224) for all gap sizes. The mean profiles for all six cases are closely similar while the turbulence intensity profiles are similar to a lesser extent. The two sets of profiles for the previous station ($x/H$ = 112) are also similar, but the degree of similarity is less marked. Thus it appears that during the readjustment process these six center-line flows have forgotten their different distortion histories and tend to common velocity distributions as they approach their final equilibrium form. Figure 4 also shows that both mean and fluctuating flows have, by $x/H$ = 224, returned to their equilibrium distributions in the region immediately adjacent to the wall. However, both profiles still have considerable adjustment to make before they are identical to the undisturbed zero pressure gradient profiles. Thus these results do not agree with the conclusion of Mueller and Robertson [10] that the flow (for the zero gap case) returns to undisturbed conditions at forty element heights downstream of the element. The present results do agree with Bradshaw and Wong's [1] conclusion that full readjustment takes hundreds of boundary layer lengths downstream of an obstacle.

**Mean Flow Parameters.** The skin friction coefficients ($c'_f$) for all profiles were determined by plotting the mean velocity data on axes $u/U_1$ versus $\log_{10} yU_1/\nu$ and comparing the wall region of the profile with the law of the wall (Equation 1) expressed in Clauser's [5] form:

$$\frac{u}{U_1} = 5.76\left(\frac{c'_f}{2}\right)^{1/2}\log_{10}\frac{yU_1}{\nu} + 5.76\left(\frac{c'_f}{2}\right)^{1/2}\log_{10}\left(\frac{c'_f}{2}\right)^{1/2} + 5.1\left(\frac{c'_f}{2}\right)^{1/2} \tag{5}$$

Most of the centerline profiles showed good agreement with

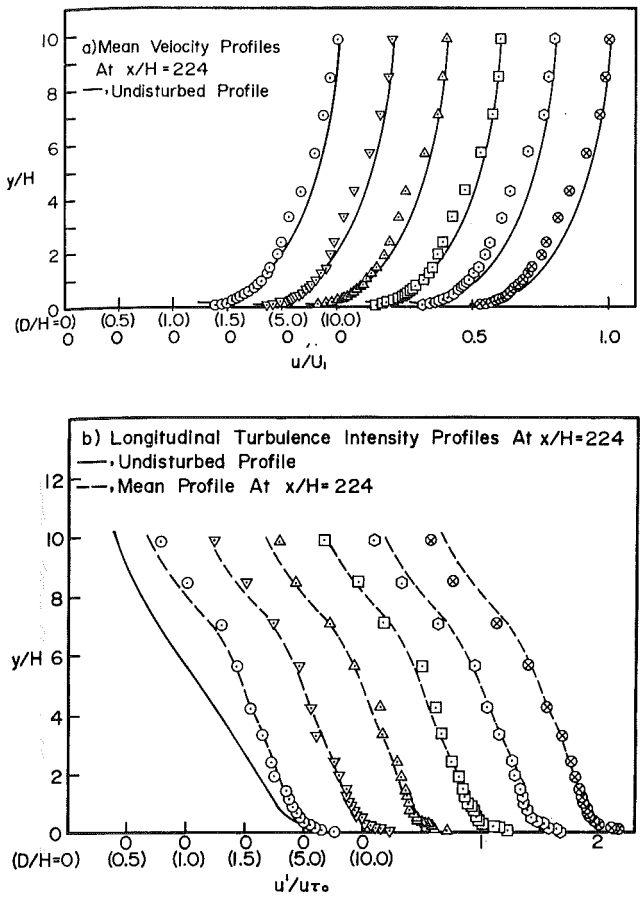


**Fig. 4 Center-line mean velocity and longitudinal turbulence profiles at $x/H = 224$ for all gap sizes.**

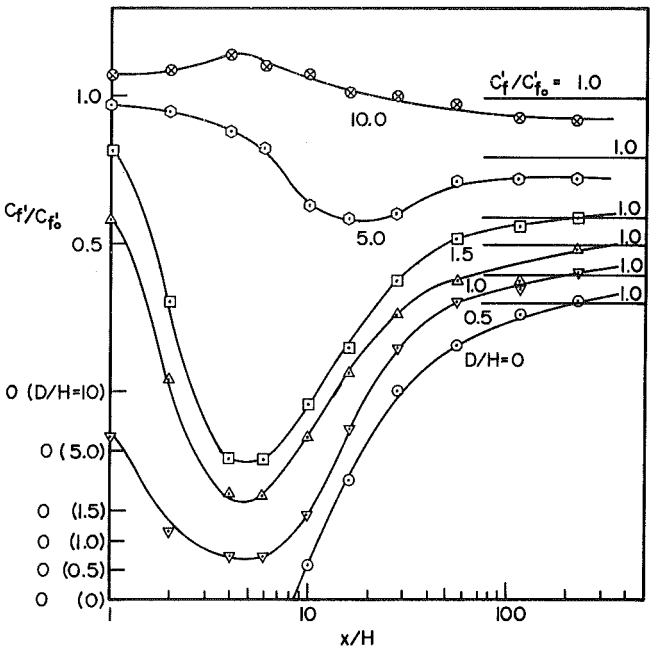


**Fig. 5 Center-line skin friction coefficients**

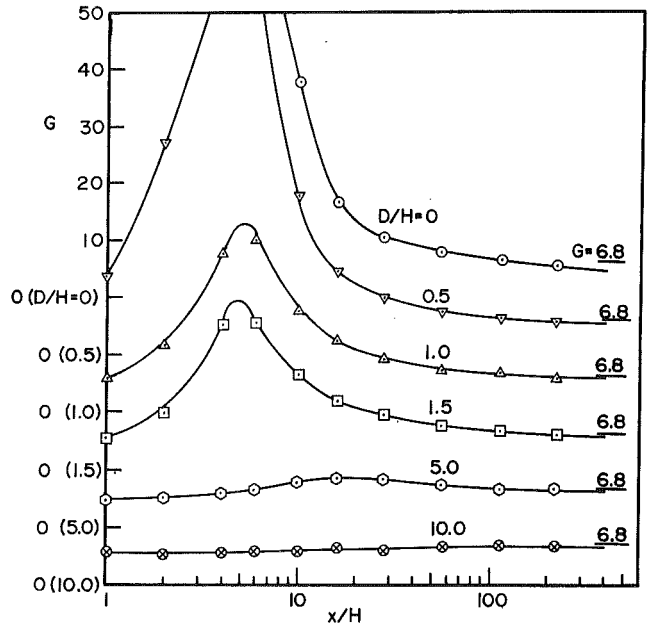


**Fig. 6 Clauser's mean profile shape parameter (center-line flow)**

the Clauser lines and hence reliable values of skin friction coefficient could be inferred.

Ratios of local skin friction coefficient of the centerline flow to the skin friction coefficient of an undisturbed layer are plotted in Fig. 5 for all gap sizes as a function of distance from the gap. During the distortion phase ($0 < x/H < 10-16$) center-line wall shear distributions are different for flows through different gap sizes. For flow through small gaps ($D/H < 5$) the flow restriction caused by gap edge separations block the flow, pushing the center-line profiles towards separation, and hence the skin friction coefficients approach zero. For the smallest gap studied ($D/H = 0.5$) the center-line flow only just remains attached. As gap size increases, the gap edge separations are moved away from the flow centerline, decreasing the flow blockage through the gap, and the minimum skin friction on the centerline increases. At the largest gap size ($D/H = 10.0$) the increased velocity through the gap results in a centerline friction coefficient that actually exceeds the undisturbed value.

During the initial readjustment phase the skin friction distributions depend on the value at the end of the distortion phase. However, all distributions are approaching the final equilibrium value of skin friction from below at the last measuring station. The behavior of the skin friction distributions at $x/H = 224$ is not however uniform. Extrapolated distributions for small gap settings over-shoot the equilibrium value at a short distance downstream of $x/H = 224$, whereas extrapolated distributions for the two largest settings do not.

For the zero gap case Bradshaw and Wong [1] also reported overshooting of the equilibrium skin friction coefficient. Another point of agreement of these results with previous work is the position of reattachment for the zero gap case which, as shown in Fig. 5, occurs at approximately $x/H = 8$. This broadly agrees with previous results by Mueller and Robertson [10] (reattachment at $x/H = 7$), Oka and Kostic [11] (at $x/H = 7$) and Counihan et al., [4] (at $x/H = 6$).

The mean velocity shape factor, $G$, introduced by Clauser [5] is useful in analyzing this type of flow. It is defined as

$$G = \frac{\int_0^\delta \left(\frac{U_1 - u}{u_\tau}\right)^2 dy}{\int_0^\delta \left(\frac{U_1 - u}{u_\tau}\right) dy} \tag{6}$$

For an undisturbed zero pressure gradient layer at high Reynolds number, $G$ has a value of about 6.8. Perturbations

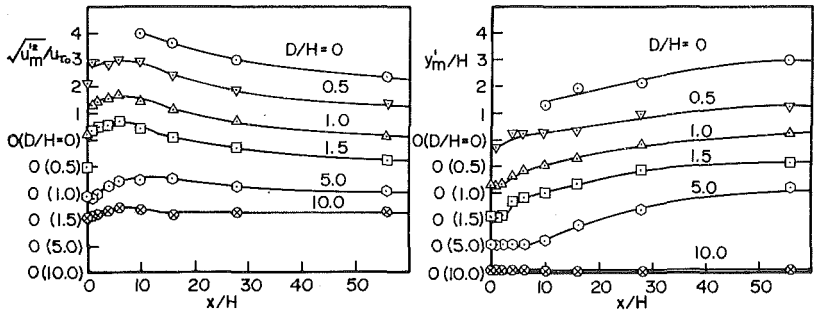


**Fig. 7 Maximum values of center-line longitudinal turbulence intensity and distance from wall of these maximums**

applied to a zero pressure gradient layer, cause $G$ to vary from this equilibrium value. The variation of $G$ after a perturbation is a useful indication of the degree of distortion and subsequent readjustment of the whole layer. Distributions of $G$ for the center-line profiles for all gap sizes have been plotted in Fig. 6. Not surprisingly maximum distortion (i.e., largest $G$ variation) occurs downstream of the smallest gaps. However the profile distortion is remarkably similar for all gap sizes after about $x/H = 60$, which reinforces the previous conclusion that layers forget their distortion history in the readjustment region and follow similar paths back to equilibrium conditions. There are however minor differences in $G$ variation at large distances from the gap. Values of $G$ for small gap flows undershoot the equilibrium value at $x/H = 224$, whereas for the largest gaps $G$ approaches the equilibrium value monotonically. Undershooting for the zero gap case has been previously reported by Bradshaw and Wong [1] who found that the minimum value of $G$ occurred at

$$x/H = 100\sqrt{\delta/H}$$

which for the present experiment gives $x/H = 316$ as the position for minimum $G$ which seems reasonable for the data presented in Fig. 6.

**Turbulent Flow.** Figure 7 plots the maximum nondimensional longitudinal turbulent intensity ($\sqrt{u_m'^2}/u_{\tau 0}$) for each center-line profile and its height from the wall as a function of distance from the gap. There is again different behaviors for flow through small and large gaps. Small gaps produce large maximum values of $\sqrt{u_m'^2}$ which are attained shortly after the gap and are (approximately) maintained throughout the distortion region. $\sqrt{u_m'^2}$ decays exponentially from this maximum value in the readjustment region. The graphs are truncated at $x/H = 56$ because flow readjustment produces profiles, downstream of $x/H = 56$, in which $\sqrt{u_m'^2}$ reverts to a position very near the wall as in the undisturbed upstream profile (see Fig. 2).

The distance from the wall to $\sqrt{u_m'^2}$ varies with distance downstream of the gap. It is initially constant, and then at some distance downstream shows a sudden increase. This sudden increase commences at progressively larger distances as the gap size is increased. For the largest gap ($D/H = 10.0$) an increase in $y_m'$ does not occur within the observation range.

These results are consistent with flow mechanisms previously described. Increasing values of $y_m'$ with distance reflect a flow adjustment that works outwards from the wall. High initial values of $\sqrt{u_m'^2}$ for small gap flows reflect the higher turbulence levels generated by the gap edge separations. For large gap flows, turbulence is generated at the beginning of, and as part of, the readjustment process. These large gap turbulence profiles thus have a small maximum which appears near the end of distortion or at the beginning or readjustment.

## Conclusions

1. Boundary layer flow through a gap in a small isolated roughness element consists of two regions; a flow distortion region followed by a flow readjustment region.

2. Compared with an undisturbed flow, the center-line flow through small gaps has:

- ($a$) an increased longitudinal turbulence intensity near the wall,
- ($b$) a decreased mean velocity near the wall,
- ($c$) a large decrease in wall shear up to $x/H = 50$, and
- ($d$) a large increase in Clauser's profile shape factor $G$ up to $x/H = 50$.

Conversely, the center-line flow through large gaps has:

- ($a$) a decreased longitudinal turbulence intensity near the wall,
- ($b$) an increased mean velocity in the distortion region,
- ($c$) little change in wall shear in the shape factor $G$.

3. The mechanism of flow readjustment downstream of the distortion proceeds by a flow modification that works outwards from the wall. Both the fluctuating and mean flow fields are modified, the modification of the fluctuating flow slightly preceding the mean flow modification for all gap sizes. The growth of this new internal layer as a function of distance from the gap can be described by a single curve if both parameters are nondimensionalized with the local wall length scale.

4. Initial readjustment of centerline flow parameters ($c_f'$ and $G$) depends on their values at the end of distortion. However, later readjustment behavior is similar for all gap sizes with the parameter curves as well as the mean and fluctuating profiles being closely similar after $x/H = 100$.

5. Boundary layer flow over an isolated element without a gap can be regarded as an extreme case of boundary layer flow through a gap. In the zero gap case, profile shapes and parameter variations downstream of reattachment follow the pattern set by centerline flows through small gaps.

## References

1 Bradshaw, P., and Wong, F. Y. F., "The Reattachment and Relaxation of a Turbulent Shear Layer," *J. Fluid Mech.*, Vol. 52, 1972, pp. 113–125.

2 Brown, K. C., "Three Dimensional Turbulent Boundary Layers," Ph.D. thesis, University of Melbourne, 1971.

3 Castro, I. P., and Robins, A. G., "The Flow Around a Surface-Mounted Cube in Uniform and Turbulent Streams," *J. Fluid Mech.*, Vol. 79, 1977, pp. 307–335.

4 Counihan, J., Hunt, J. C. R., and Jackson, P. S., "Wakes Behind Two-Dimensional Surface Obstacles in Turbulent Boundary Layers," *J. Fluid Mech.*, Vol. 64, 1974, pp. 529–563.

5 Clauser, F. H., "Turbulent Boundary Layers in Adverse Pressure Gradients," *J. Aeronautical Sci.*, Vol. 21, 1954, pp. 91–108.

6 Clauser, F. H., "The Turbulent Boundary Layer," *Advances in Applied Mech.*, Vol. IV, 1956, pp. 1–51.

7 Good, M. C., and Joubert, P. N., "The Form Drag of Two-Dimensional Bluff Plates Immersed in Turbulent Boundary Layers," *J. Fluid Mech.*, Vol. 21, 1968, pp. 547–582.

8 Hornung, H. G., and Joubert, P. N., "The Mean Velocity Profile in Three-Dimensional Turbulent Boundary Layers," *J. Fluid Mech.*, Vol. 15, 1963, pp. 368–384.

9 Klebanoff, P. S., and Diehl, Z. W., "Some Features of Artificially Thickened Fully Developed Turbulent Boundary Layers with Zero Pressure Gradient," N.A.C.A., T.N. 2475, 1951.

10 Mueller, T.J., and Robertson, M.R., "A Study of the Mean Motion and Turbulence Downstream of a Roughness Element," *Proc. First Southeastern Conf. on Theoretical and Applied Mechanics,* 1962, pp. 326–340.

11 Oka, S. and Kostic, Z., "Flowfield past a single roughness element in channel of rectangular cross-section," *Heat and Mass Transfer in Boundary Layers*, Vol. 1, Pergamon Press, Ltd., New York, pp. 425–435, 1971.

12 Petryk, S., and Brundrett, E., "Recovery of a Turbulent Boundary Layer Disturbed by a Single Roughness Element," Res. Rep. No. 4, 1967, Dept. of Mech. Engrg., University of Waterloo.

13 Phataraphruk, P., and Logan, E., "Response of a Turbulent Pipe Flow to a Single Roughness Element," *Proc. Ninth Southeastern Conf. on Theoretical and Applied Mechanics,* 1978, pp. 139–149.

14 Sami, S., and Liu, W. H., "Confined Shear Layer Approaching a Stagnation Point," *Proc. Fourteenth Midwestern Mech. Conf. Developments in Mechanics*, Vol. 8, 1975, pp. 497–516.

15 Schofield, W. H., "The Effect of Sudden Discontinuities on Turbulent Boundary Layer Development," Aeronautical Research Laboratories, Mech. Engrg. Rep. 139, (Australian Dept. of Defence) 1973.

16 Schofield, W. H., "The Response of Turbulent Shear Flows to Discontinuous Changes in Surface Roughness," Aeronautical Research Laboratories, Mech. Engrg. Rep. 150, (Australian Dept. of Defence) 1977.

17 Schofield, W. H., "Measurements in Adverse-Pressure-Gradient Turbulent Boundary Layers with a Step Change in Surface-Roughness," *J. Fluid Mech.*, Vol. 70., 1975, pp. 573–593.

18 Sharan, V. K., "On Characteristics of Flow Around Building Models with a View to Simulate the Minimum Fraction of the Natural Boundary Layer," *Intl. J. Mech. Sci.*, Vol. 17, 1975, pp. 557–563.

19 Siuru, W. D., and Logan, E., "Response of a Turbulent Pipe Flow to a Change in Roughness," ASME JOURNAL OF FLUIDS ENGINEERING, Vol. 99, 1977, pp. 548–555.

20 Tani, I., "Review of Some Experimental Results of the Response of a Turbulent Boundary Layer to Sudden Perturbations," AFSOR-IFO-Stanford Conference, Vol. 1, 1969, pp. 483–494.

21 Townsend, A. A., "Structure of Turbulent Shear Flow," 2nd Ed., C.U.P., 1976, pp. 308–313.

22 Wieghardt, K., and Tillmann, W., "On the Turbulent Friction Layer for Rising Pressure," N.A.C.A., T. M. 1314, 1951.

23 Kline, S.J., and McClintock, F.A., "Describing Uncertainties in Single-Sample Experiments," *Mechanical Engineering,* Vol. 75, No. 1, 1953, pp. 3–8.

## APPENDIX

Estimates of uncertainty were obtained using the method of Kline and McClintock [23] with 20:1 odds, and the results are tabulated below. Possible fixed errors are included within the uncertainty bands stated.

Maximum uncertainties are given for each pertinent figure and variable for regions near the wall and at the outer edge of the boundary layer. Calculated uncertainties are based on the uncertainty of each reading estimated as it was taken using the linearized anemometer (digital readout) and the uncertainty of the velocity measurement (pressure probe) used in the calibration procedure.

**Estimates of uncertainty in data**

| Fig. No. | Variable | Uncertainty, percent | |
|---|---|---|---|
| 2 | $u/U_1$ | $\pm 8.0 (y < H)$ | $\pm 0.9 (y \simeq \delta)$ |
| 2 | $\sqrt{u'^2}/u_{\tau o}$ | $\pm 6.8 (y < H)$ | $\pm 5.9 (y \simeq \delta)$ |
| 4 | $u/U_1$ | $\pm 3.3 (y < H)$ | $\pm 0.4 (y \simeq \delta)$ |
| 4 | $\sqrt{u'^2}/u_{\tau o}$ | $\pm 4.3 (y < H)$ | $\pm 4.3 (y \simeq \delta)$ |
| 5 | $c_f'/c_{fo}'$ | $\pm 4.1$ | |
| 7 | $\sqrt{u_m'^2}/u_{\tau o}$ | $\pm 6.8$ | |

J. P. F. Lindhout

G. Moek

E. De Boer

B. Van Den Berg

Nationaal Lucht- en Ruimtevaartlaboratorium, National Aerospace Laboratory NLR, Amsterdam, The Netherlands

# A Method for the Calculation of 3D Boundary Layers on Practical Wing Configurations[1]

*This paper gives a description of a calculation method for 3D turbulent and laminar boundary layers on nondevelopable surfaces. A simple eddy viscosity model is incorporated in the method. Special attention is given to the organization of the computations to circumvent as much as possible stepsize limitations. The method is also able to proceed the computation around separated flow regions. The method has been applied to the laminar boundary layer flow over a flat plate with attached cylinder, and to a turbulent boundary layer flow over an airplane wing.*

## Introduction

Since 1971 a calculation method for 3D incompressible turbulent boundary layers has been available at the National Aerospace Laboratory NLR [1]. This method is based on an extension to three dimensions of Bradshaw's turbulence model for 2D boundary layers and is restricted to simple geometries, i.e. to so-called developable surfaces. The computational results have been compared with the results of 3D turbulent boundary layer experiments carried out at NLR [2]. This comparison showed severe disagreements between calculation and experiment, in particular close to the 3D separation line [3]. Similar disagreements have been reported for methods using a simple turbulence model of the eddy viscosity type as well as for methods using the more complicated $\kappa - \epsilon$ turbulence model [4].

Subsequent turbulence measurements revealed that in all cases the magnitude of the turbulent shear stress was overestimated, in particular in crosswise direction [5].

A large number of 3D boundary layer calculations have been carried out with the NLR method on practical wing configurations. These calculations comprised the 3D boundary layer flow on a simple swept wing [6,7], as well as complicated boundary layer flows with typical 3D separation patterns on various wing root configurations (not published). Notwithstanding the shortcomings in turbulence modelling, the results were not unsatisfactory in these practical cases. This is probably due to the fact that in the cases considered the pressure forces dominate over the turbulent shear stresses, especially in the regions where the boundary layer has a distinctly 3D character.

From the experience so obtained it became evident that the calculation method had certain drawbacks. The required computertime was excessively large and the restriction of the method to developable surfaces appeared to be a severe one. Moreover an orthogonal coordinate system was required and the handling of users input was awkward. In view of these points it was decided to develop a new 3D boundary layer calculation method. The main features of the new method are:

- A simple eddy viscosity turbulence model is incorporated. The deficiencies of the model used are well known, but the more sophisticated models presently available, e.g. Bradshaw's and the $\kappa - \epsilon$ model, do not seem to give significantly better results in 3D turbulent boundary layers.
- A nonorthogonal curvilinear coordinate system, applicable also on nondevelopable surfaces, can be chosen freely by the user.
- To obtain a reasonable computertime hermitian formulations are employed to approximate the tangential derivatives. Normal derivatives are found by standard central difference equations. An organization is adopted which permits to circumvent as much as possible limitations of the stepsize in marching direction, which are imposed by numerical stability criteria.
- The method is able to proceed the computation around regions with small skin friction or large crossflow, where a breakdown of the computation can be expected.

In the following chapters the governing boundary layer equations as well as the numerical method and the flow of the computational process will be discussed. In the last chapter two applications of the new method will be shown.

## Governing Equations

In this section the 3D compressible laminar- and turbulent boundary layer equations will be presented in non-dimensionalized form. After a description of the turbulence model a transformation of the normal coordinate is given and

[1] This investigation has been performed under contract with the Netherlands Agency for Aerospace Programs (NIVR).

Contributed by the Fluids Engineering Division and presented at the Joint ASME/CSME Applied Mechanics, Fluids Engineering, and Bioengineering Conference, Niagara Falls, N.Y., June 18-22, 1979, of THE AMERICAN SOCIETY OF MECHANICAL ENGINEERS. Manuscript received by the Fluids Engineering Division, December 5, 1979.

another scaling of the dependent variables. This chapter ends with a description of the initial conditions.

The equations are given in a coordinate system $(x_1, x_2, z)$ of which $x_1$ and $x_2$ form a general non-orthogonal curvilinear coordinate system over the surface of the body. The coordinate z is normal to $x_1$ and $x_2$.

Continuity:

$$\partial(m\rho u_1/h_1)/\partial x_1 + \partial(m\rho u_2/h_2)/\partial x_2 + m\partial(\rho w)/\partial z = 0 \quad (1)$$

Momentum in $x_\alpha$-direction ($\alpha$ = 1 or 2):

$$u_1/h_1 . \partial u_\alpha/\partial x_1 + u_2/h_2 . \partial u_\alpha/\partial x_2 + w . \partial u_\alpha/\partial z + R^\alpha_{11} u_1^2 + R^\alpha_{12} u_1 u_2 + R^\alpha_{22} u_2^2 - (\partial \tau_\alpha/\partial z)/\rho = \tfrac{1}{2}/\rho . h_1 h_2/m^2 (-h_\beta . \partial C_p/\partial x_\alpha + a_{12}/h_\beta . \partial C_p/\partial x_\beta), \quad (\beta = 3-\alpha) \quad (2)$$

In these equations the lengths are nondimensionalized by a reference length $L$, the velocity components and the density by their free stream values, $u_\infty$ and $\rho_\infty$, and the shear stresses by twice the free stream dynamic head, $\rho_\infty u_\infty^2$. The geometrical quantities are defined in the Appendix. It is assumed that the surface of the body is adiabatic, and the density variation for given $x_1, x_2$, is approximated by the Crocco-relation:

$$\rho_e/\rho = 1 + \tfrac{1}{2} r(\gamma - 1) M_e^2 \{1 - (u/u_e)^2\} \quad (3)$$

For turbulent boundary layers, a simple eddy viscosity model is incorporated in the method. $\tau_1, \tau_2$ can be written as:

$$\tau_\alpha = (\mu + \epsilon\rho)\partial u_\alpha/\partial z \quad (\alpha = 1,2) \quad (4)$$

where

$$\epsilon = F^2 l^2 [(\partial u_1/\partial z)^2 + (\partial u_2/\partial z)^2 + 2\Gamma(\partial u_1/\partial z)(\partial u_2/\partial z)]^{1/2} \quad (5)$$

$$l/\delta_T = \lambda \tanh(\kappa/\lambda . z/\delta_T) \quad (6)$$

$$F = 1 - \exp[-(z^+/b)\{1 + \tfrac{1}{4} a \mu_w/(\rho_w^2 u_\tau^3)\partial C_p/\partial x_w\}] \quad (7)$$

The viscosity $\mu$ and the eddy viscosity ($\rho\epsilon$) are nondimensionalized by $\rho_\infty u_\infty L$. The variation of $\mu$ as a function of the temperature is approximated for computational reasons by a linear relation:

$$(\rho_\infty u_\infty L)\mu = \alpha + \beta T \text{ with} \quad (8)$$

$$\alpha = 3.78_{20}{}^{-6} \text{(kg/m s)}, \quad \beta = 9.8_{10}{}^{-8} \text{(kg/m s K)}$$

This approximation is accurate for air in the temperature range from 180 K to 380 K.

In the formulation of the mixing length, is $\kappa = 0.41$ the Von Karman constant; $\lambda$ gives the value of $l/\delta_T$ in the outer part of the boundary layer. A definition of $\delta_T$ is chosen which is based on a constant velocity defect, 0.05 $u_e$, at $z = \delta_T$:

$$u(x_1, x_2, \delta_T(x_1, x_2)) = 0.95\ u_e \quad (9)$$

The value chosen for $\lambda = 0.11$, is adjusted to this definition.

The function $F$ is a correction function for the mixing length in the viscous sublayer. The term between absolute signs accounts for the effect of the pressure gradient; $\partial C_p/\partial x_w$ has to be taken in the direction of the shear stress vector at the wall. The constants in $F$ are take $a = 20$ and $b = 24.5$. A similarity-type transformation is applied to the dependent variables that vary with $z$:

$$\left.\begin{aligned} &\tilde{u}_\alpha = u_\alpha/u_e \ (\alpha = 1,2), \tilde{w} = w/u_e \\ &\tilde{\rho} = \rho/\rho_e, \tilde{\tau} = \tau/(\rho_e u_e^2) \end{aligned}\right\} \quad (10)$$

A transformation is applied to the coordinate system, to counteract the effect of boundary layer thickness variation:

$$\left.\begin{aligned} &\xi_\alpha = x_\alpha \ (\alpha = 1,2) \\ &\zeta = f(\delta; z) \end{aligned}\right\} \quad (11)$$

where $\delta$ is the outer edge value of $z$. It is taken:

$$\delta = \Pi \int_0^\infty (1 - u/u_e)\, dz, \quad (12)$$

with $\Pi$ a convenient factor; $\Pi = 5$ for laminar flow and $\Pi = 10$ for turbulent flow.

For laminar flow it is appropriate to employ

$$f(\delta; z) = z/\delta \quad \text{(laminar)} \quad (13)$$

For turbulent flow it is desirable that the transformation meets the extra requirement that the normal coordinate near the wall is stretched, in order to have sufficient gridpoints in the viscous sublayer. To effect this the transformation has the following properties:

– Near the wall the transformation is independent of $\delta$ and is constant throughout the complete computation. An appropriate value is assigned to $df\ (\delta;0)\ /\ dz = f_w'$, which depends on the Reynolds number.

## Nomenclature

$a$ = constant in turbulence model, equation (7), $a = 20$; constant in transformation, equation (14)

$a_{\alpha\beta}$ = metric coefficients (appendix)

b = constant in turbulence model, equation (7), $b = 24.5$; constant in transformation, equation (14)

c = local wing chord

$C_f$ = friction coefficient, $C_f = \tau_w/(\tfrac{1}{2}\rho_e u_e^2)$

$C_p$ = pressure coefficient, $C_p = (p - p_\infty)/(\tfrac{1}{2}\rho_\infty u_\infty^2)$

d = computational direction

$F$ = correction function for viscous sublayer, equation (7)

h = $-$sign ($t$)

$h_1, h_2$ = lengths of tangent-vectors to coordinate lines (Appendix)

$l$ = mixing length, equation (6)

$L$ = reference length

$m^2$ = determinant of first fundamental tensor (Appendix)

$M$ = Mach number

$n_1, n_2$ = tangential derivatives

$r$ = recovery factor, $r = 0.89$ (turbulent), $r = 0.85$ (laminar); constant in transformation, equation (14)

$R^\alpha_{\beta\gamma}$ = curvature terms in momentum equations (Appendix)

Re = Reynolds number, $\mathrm{Re} = u_\infty L/\nu_\infty$

$t$ = flow direction, $t = (u_2/h_2)/(u_1/h_1)$

$u_1, u_2$ = velocity components in $x_1$ and $x_2$ direction

$u$ = total velocity, $u^2 = u_1^2 + u_2^2 + 2\Gamma u_1 u_2$

$u_\tau$ = $(\tau_w/\rho_w)^{1/2}$

$w$ = velocity component in $z$-direction

$x_0$ = distance of centre of cylinder from leading edge

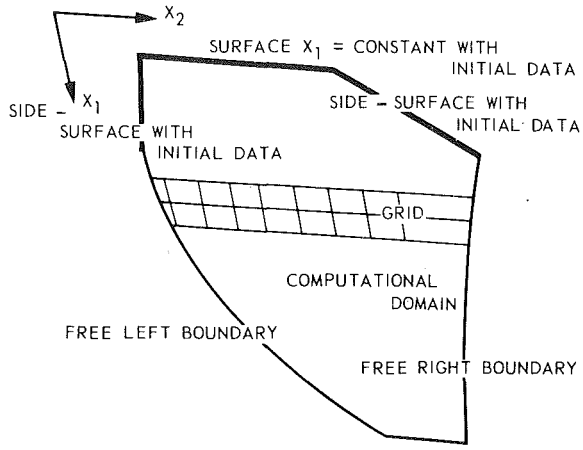


**Fig. 1 Computational domain. The solution at the free boundaries is computed.**

– For large $z$ the transformation tends to be linear. $f'(\delta,\infty)$ is a predetermined fraction of $1/\delta$: $f'(\delta;\infty) = r/\delta$.

A simple rational function in z is able to combine these demands:

$$\zeta = f(\delta;z) = z.(f'_w + a.z/\delta)/(1 + b.z/\delta), \text{ (turbulent)} \tag{14}$$

$$\text{with } a = br/\delta \text{ and } b = (\delta f'_w - 1)/(1 - r)$$

The boundary conditions are as usual:

$$\zeta = 0: \ \tilde{u}_\alpha = \tilde{w} = 0 \tag{15}$$

$$\zeta = 1: \ \tilde{u}_\alpha = \tilde{u}_{\alpha_e} \tag{16}$$

The values of $\tilde{u}_{\alpha_e}$ are obtained in the program by integration of the inviscid flow equations.

Initial conditions are supposed to be given in a plane normal to the surface of the body (Fig. 1). As the computation proceeds in the direction of increasing $\xi_1$ the equations are solved subsequently in planes $\xi_1$ = constant. The method can handle problems that are periodic in the $\xi_2$-direction (typical for fuselage-like bodies) as well as nonperiodic problems (typical for wings). In the periodic case initial data are required only in a plane $\xi_1$ = constant. For the nonperiodic case it is possible that the initial plane includes one or two side planes too. The computational domain consists of the domain of determinacy of all the initial data [8]. The free boundaries of the domain of determinacy, which are not known beforehand, satisfy the differential equation (Fig. 1):

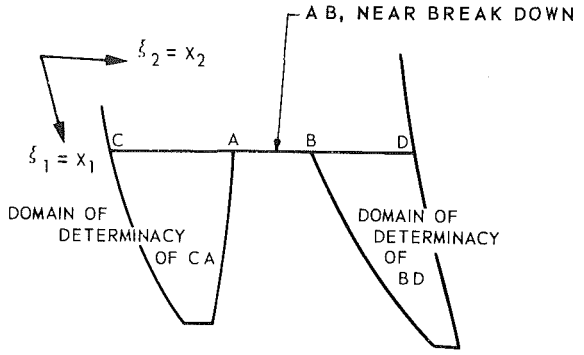


**Fig. 2 Computational domain downstream of a separation region, actually a near breakdown of the calculations**

$$\left(\frac{d\,\xi_2}{d\,\xi_1}\right)^{\text{left}}_{\text{right}} = \min^{\max} t(\xi_1,\xi_2,\zeta) \tag{17}$$

in which $t = (h_1 u_2)/(h_2 u_1)$

At these boundaries the user may not prescribe data. The flow quantities on it are determined by the program itself employing a difference scheme, to be dealt with in the next chapter.

The boundaries do not coincide, in general, with the coordinate lines over the surface of the body.

When an interval $a \le \xi_2 \le b$ occurs, in a plane $\xi_1$ = constant, where the computation is approaching a breakdown of the program (e.g. because the flow is near a singular separation point) then the method circumvents the domain of influence of the interval. The domains of determinacy are computed of the remaining parts of the plane $\xi_1$ = constant. Figure 2 depicts such a situation.

## Numerical Method

In this section a grid is defined and the difference schemes which are applied to the grid functions are given. Because the grid is irregular near the boundaries of the computational domain it is also explained how the difference schemes can be applied near such a boundary.

## Nomenclature (cont.)

$x,y$ = Cartesian coordinates of wing
$x_1,x_2$ = nonorthogonal curvilinear coordinate system over the body surface
$x_w$ = coordinate direction of wall shear stress
$z$ = coordinate normal to the body surface
$z^+$ = $z^+ = (u_\tau \rho_w/\mu_w).z$

**Greek Symbols**

$\alpha,\beta$ = constants in the viscosity function
$\gamma$ = ratio of specific heats
$\Gamma$ = cosine of angle between coordinate lines (appendix)
$\delta$ = value of $z$ at the outer edge, equation (12)
$\delta_T$ = measure for boundary layer thickness, equation (9)
$\Delta_1,\Delta_2,\Delta\zeta$ = stepsizes in, respect, $\xi_1,\xi_2$, and $\zeta$ direction
$\epsilon$ = eddy viscosity
$\mu$ = viscosity
$\lambda$ = ratio of mixing length $l$ and $\delta_T$ at the outer edge, equation (6), $\lambda$ = 0.11
$\tau_1,\tau_2$ = shear stress components in $x_1$ and $x_2$ direction
$\tau$ = $\tau^2 = \tau_1^2 + \tau_2^2 + 2\Gamma\,\tau_1\tau_2$
$\rho$ = density
$\theta_{11}$ = momentum thickness in outer flow direction
$\xi_1,\xi_2,\zeta$ = transformation of $(x_1,x_2,z)$
$\kappa$ = constant in turbulence model, equation (6), $\kappa$ = 0.41
$\phi$ = flow angle with $\xi_1$-axis
$\Pi$ = thickness factor, $\Pi$ = 5 (laminar), $\Pi$ = 10 (turbulent)
$\sigma$ = parameter in difference equations (19)-(21)

**Subscripts**

$\alpha,\beta$ = 1 or 2
$e$ = edge of boundary layer
$w$ = wall, surface of the body
$\infty$ = free stream
$\sim$ = scaled with variables of the boundary layer edge
LE = leading edge of the wing

The boundary layer equations are solved at the knots of a grid of which $\Delta_1$ and $\Delta_2$ are the stepsizes in $\xi_1$- and $\xi_2$-direction and $\Delta\zeta$ is the stepsize in the normal direction. $\Delta\zeta$ is kept constant for the complete computation, whereas $\Delta_2$ is allowed to vary only near the boundaries of the computational region. The stepsize in the marching direction $\Delta_1$, varies with $\xi_1$ and depends on the kind of differencing that is applied (see below). For upstream differencing $\Delta_1$ is limited by the CFL (Courant-Friedrichs-Lewy)-criterion for stability reasons:

$$\Delta_1 \leq \Delta_2 / |t| \tag{18}$$

For downstream differencing there are no stability restrictions on $\Delta_1$.

In earlier computations it turned out that the required computer time to organize the computations (e.g. communication with the disks) was of the same order of magnitude as the time needed to solve the boundary layer equations.

To increase the efficiency of the method it is clearly not sufficient to introduce better approximations of the normal derivatives only, as these would halve the computer time at most. A decrease of organization effort and pure computational time as well can be effected by diminishing the total number of normals that has to be computed. Hence the tangential stepsizes of the grid have to be increased. They are however limited by stability- and truncation error requirements. In the next chapter a method will be described with which it is possible to shift the stability bounds. To diminish the truncation errors of the tangential derivatives, difference schemes are introduced which have a second order truncation error or a small first order one. The control of it is performed by a scalar $\sigma$ which use is explained below. The difference molecules are given in Table 1.

For tangential differencing it is chosen to use derivatives at known gridpoints. This requires extra storage capacity for each point; however the total required storage capacity is not increased because the total number of gridpoints is lowered.

Let $\phi_{ij}^k$ be a grid function at the knots $\xi_1 = i\,\Delta_1$, $\xi_2 = j\,\Delta_2$, $\zeta = k\,\Delta\zeta$ $(i,j,k \in \mathrm{N})$, then the following approximations for the tangential derivatives in $\xi_1$-direction are employed:

$$(n_1)_{i,j}^k = -\sigma(n_1)_{i-1,j}^k + (1+\sigma)/\Delta_1 . (\phi_{i,j}^k - \phi_{i-1,j}^k) \tag{19}$$

where $\phi$ stands for $\tilde{u}$, $\tilde{v}$, and $\delta$; $n_1$ for their derivatives in $\xi_1$-direction and in which $\sigma \in [0,1]$. If at the known level, $i-1$, the tangential derivatives are not available, e.g. at the start of the computations, it is set $\sigma = 0$. For $\sigma = 1$ the approximation is second order accurate else first order accurate. The value of $\sigma$ has influence on the stability properties of the scheme. If $\sigma = 1$ the scheme is weakly dissipative; for $0 \leq \sigma < 1$ it is strongly dissipative. We selected $\sigma = 1$ for laminar flow, and for turbulent flow $\sigma = 0.9$ gave good results.

If neighboring points are available at the newest $\xi_1$-level, $i$, then downstream differencing is used. The $\xi_2$-derivatives are approximated as:

$$(n_2)_{i,j}^k = -\sigma(n_2)_{i,j+h}^k - (1+\sigma)/\Delta_2 . h . (\phi_{i,j}^k - \phi_{i,j+h}^k) \tag{20}$$

where $h = -\operatorname{sign} t$.

If upstream differencing has to be applied then the $\xi_2$-derivatives are approximated by:

$$(n_2)_{i,j}^k = -\sigma(n_2)_{i-j,j+h}^k - h/\Delta_2 . [(1+\sigma) . (\phi_{i-1,j}^k - \phi_{i-1,j+h}^k) + \sigma\Delta_1 \{ (n_1)_{i-1,j}^k - (n_1)_{i-1,j+h}^k \}] \tag{21}$$

Expressions (20) and (21) are second order accurate if $\sigma$ is chosen unity, elsewise they are first order accurate. The choice at a certain point, of a difference scheme from the given alternatives, is discussed in the next chapter.

Near the boundaries of the computational region the grid is disturbed and the approximations described above cannot be used any more. We will show now, as an example, how similar approximation can be derived, second order accurate, on a disturbed grid for the $\xi_2$-derivative in the situation shown in Fig. 3. To estimate the differences in a certain quantity $\phi$ use is made of the expression for a total differential at the given points A and B and at the unknown point C:

$$d\phi = (\partial\phi/\partial\xi_1)\mathrm{d}\xi_1 + (\partial\phi/\partial\xi_2)\mathrm{d}\xi_2$$

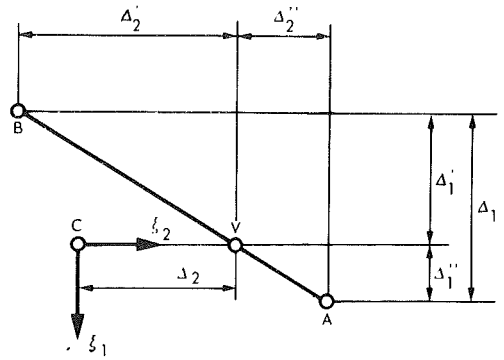


Fig. 3 Approximation of $\xi_2$-derivatives in C from given points A and B, which are part of the computational boundary

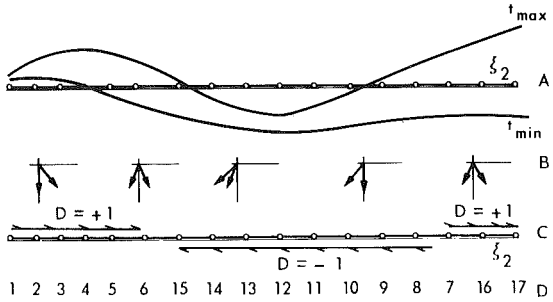


Fig. 4 Steps in the development of a computational sequence

For the total difference between A and C the average values for the partial derivatives at A and C are employed and substituted in the expression above:

$$\phi_C - \phi_A = -\tfrac{1}{2}(n_{1C} + n_{1A}) . \Delta_1'' - \tfrac{1}{2}(n_{2C} + n_{2A}) . (\Delta_2 + \Delta_2'')$$

For the difference in $\phi$ between $C$ and $B$, we use the average values of the derivatives at $B$ and $C$.

$$\phi_C - \phi_B = \tfrac{1}{2}(n_{1C} + n_{1B}) . \Delta_1' + \tfrac{1}{2}(n_{2C} + n_{2B}) . (\Delta_2' - \Delta_2)$$

From the latter two equations the $\xi_2$-derivative in $C$ can be solved:

$$n_{2C} = -(\Delta_1'' . n_{2B} + \Delta_1' . n_{2A})/\Delta_1 + 2/(\Delta_2\Delta_1) . [-\phi_C . \Delta_1 + \phi_B . \Delta_1'' + \phi_A . \Delta_1' + \tfrac{1}{2}\Delta_1'\Delta_1''(n_{1B} - n_{1A}) + \tfrac{1}{2}\Delta_1''\Delta_2'(n_{2B} - n_{2A})] \tag{22}$$

Now we introduce the virtual point $V$ which is defined in terms of the quantities pertaining to $A$ and $B$:

$$n_{2V} = (\Delta_1' . n_{2A} + \Delta_1'' . n_{2B})/\Delta_1 \tag{23}$$

$$\phi_V = (\Delta_1' . \phi_A + \Delta_1'' . \phi_B)/\Delta_1 - \tfrac{1}{2}\Delta_2''/(\Delta_2' + \Delta_2'') . [\Delta_1' . (n_{1A} - n_{1B}) + \Delta_2' . (n_{2A} - n_{2B})] \tag{24}$$

With the aid of this expressions (22) can be written as:

$$n_{2C} = -n_{2V} + 2/\Delta_2 . (\phi_V - \phi_C)$$

which is completely analogous to (20) for $h = +1$ and $\sigma = 1$. For the $\xi_1$-derivatives similar expressions can be derived. So the tangential derivatives near the computational boundaries are obtained by constructing virtual points. Their function

Table 1 Difference-molecules for downstream and upstream-differencing

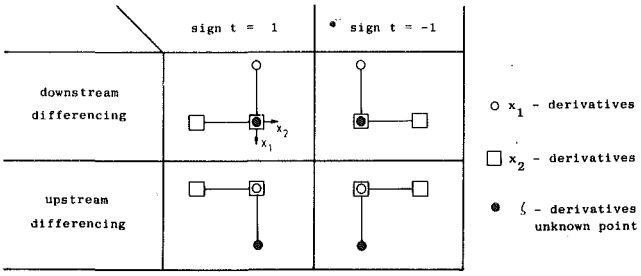


Table 2 Actions to be performed on a normal. $\Delta_1,\Delta_2$ stepsizes in $\xi_1,\xi_2$-direction, $t = (u_2/h_2)/(u_1/h_1)$

| action | t | difference molecules | stability limitations | differencing | purpose |
|---|---|---|---|---|---|
| 1 | $t_{min} \geq 0$ | | $\Delta_1 \leq \Delta_2 / t_{max}$ | upstream | starting normal |
| 2 | $t_{min} < 0$ $t_{max} \geq 0$ | | $\Delta_1 \leq \Delta_2 / \max(t_{max}, -t_{min})$ | | |
| 3 | $t_{max} < 0$ | | $\Delta_1 \leq \Delta_2 / (-t_{min})$ | | |
| 4 | $t_{min} \geq 0$ | | $\Delta_1 < \infty$ | down-stream | continuation normal |
| 5 | $t_{min} < 0$ | | $\Delta_1 \leq \Delta_2 / (-t_{min})$ | both | |
| 6 | $t_{max} \geq 0$ | | $\Delta_1 \leq \Delta_2 / t_{max}$ | | |
| 7 | $t_{max} < 0$ | | $\Delta_1 < \infty$ | down-stream | |
| 8 | | | | | virtual point |

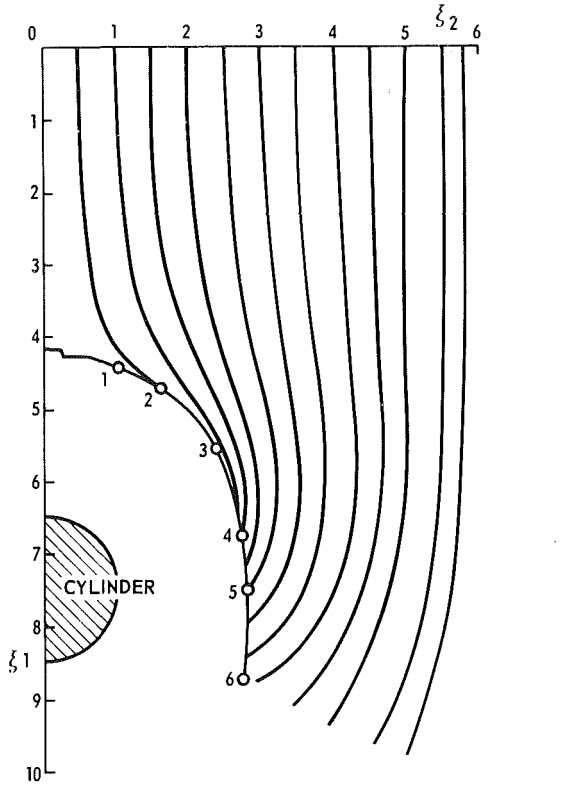


Fig. 5 Laminar boundary layer flow past a flat plate with attached cylinder. Limiting streamlines. Line upstream of station 3 = envelope of limiting streamlines = 3D separation line. Line between station 3 and 5 = envelope of streamlines with maximum flow angle in the boundary layer. Line downstream of station 5 = streamline at the edge of the boundary layer.

values and derivatives are calculated with equations (23) and (24), which can be considered too as a kind of interpolation formulae.

The approximations for the $\xi_1$- and $\xi_2$- derivatives are substituted in the momentum equations. These can be written as:

$$\partial^2 \tilde{u}_\alpha/\partial\zeta^2 + a_\alpha.\partial\tilde{u}_\alpha/\partial\zeta + b_\alpha.\tilde{u}_\alpha = c_\alpha + d_\alpha.\delta(\alpha = 1,2) \quad (25)$$

$a_1$ to $d_2$ are functions of the unknowns. Where the unknown quantities occur in the coefficients their values are taken from the previous iterand. Several methods are available to solve (25) and their appropriate boundary conditions.

We implemented the following standard finite difference approximations:

$$(\partial\phi/\partial\zeta)^k_{i,j} = (\phi^{k+1}_{i,j} - \phi^{k-1}_{i,j})/2\Delta\zeta$$

$$(\partial^2\phi/\partial\zeta^2)^k_{i,j} = (\phi^{k+1}_{i,j} - 2\phi^k_{i,j} + \phi^{k-1}_{i,j})/\Delta^2\zeta$$

## Flow of the Computations

In the previous chapter it is explained how points grouped together along a normal of the body are computed simultaneously. This chapter contains a discussion about the organization of the flow of the computation of normals along a $\xi_2$-coordinate line.

To keep the organization of the program orderly it was decided to control the flow of the computation in each sweep by means of an algorithmic table.

An algorithmic table gives the possibility to break down the problem of solving the boundary layer equations in smaller pieces. It facilitates the development, testing and maintenance of the code.

The table is constructed from the information extracted from the previous known plane $\xi_1$ = constant.

Each line of the table contains the information to compute one normal. It refers to the difference scheme to be used and to the data that has to be fetched and stored. The processing of the table is done by another part of the program that picks out successively the information per normal and calls the appropriate routines.

The actions which can be performed on a normal are comprised in Table 2. An action can be the construction of a virtual point or the solution of the boundary layer equations by a certain difference scheme. Also are given the imposed stepsizelimitations which depend on the kind of differencing and on the extreme values along a normal of t. For each normal the kind of tangential differencing is selected that gives the smallest possible stepsizelimitation. It may be clear from the Table 2 that this selection depends also on the sequence in which the computation is performed. An optimal sequence allows downstream differencing as much as possible. The search for the optimal sequence will be discussed at hand of an example which is depicted in figure 4. A possible distribution of $t_{min}$ and $t_{max}$ is shown in Fig. 4(*a*), and below it the corresponding extreme flow angles are sketched (Fig. 4(*b*)).

Because downstream differencing gives the opportunity to relax the stabilitylimitations this kind of differencing should be preferred. For some normals it is optimal that, at the new $\xi_1$-level, known normals are available at the lefthand side, for the others at the righthand side. For the first kind of normals it is profitable that the computation proceeds in the positive $\xi_2$-direction, for the latter in the opposite direction. Thus it is possible to assign to each normal an optimal computational direction *d*. From Table 2 it can be inferred that d satisfies:

$$d = \text{sign}(t_{min} + t_{max}) \quad (26)$$

Successive normals with the same favourable direction are grouped together in families. A plus-family has a starting normal at the utmost lefthand side and a minus-family at the righthand side. Two families of different sign may have a common starting normal, otherwise the starting normal is situated at the boundaries of the computational domain. At a starting normal upstream differencing is applied (action 1 to 3). At a common starting point the associated stepsize limitation will usually be small, because at a transition from one family to another, $|t|$ is small in general. If a starting point is situated at a free boundary then a virtual point has to be constructed (action 8) followed by upstream differencing. The remaining normals are computed in the sequence dictated by their family. Depending upon the value of t for each point along a normal and the availability of a neighbouring normal upstream or downstream differencing is applied (action 4 to 7). It may be clear that for these points downstream differencing is dominant.

In our example the computational sequence is depicted in Fig. 4(*d*).

## Results

The program described had to undergo appreciable testing. Acceptance tests were performed which comprised 2D and 3D laminar and turbulent boundary layer flows in both Cartesian coordinate systems and nonorthogonal curvilinear coordinate systems. A more detailed discussion of these items can be found in [14]. To show the applicability of the method two examples are given in this section. The first one is the computation of the 3D laminar boundary layer flow over a flat plate with a circular cylinder placed normal to the plate. The second example is the computation of the 3D turbulent boundary layer on a modern airplane wing.

The laminar flow past a flat plate with an attached cylinder was computed earlier by several research workers: Dwyer [9], Fillo and Burbank [10], and Cebeci [11]. The cylinder is assumed to generate the theoretical inviscid pressure distribution on the flat plate:

$$C_p = -[1+2(\xi_2^2 - x^2)]/(\xi_2^2 + x^2)^2 \qquad (27)$$

in which: $x = \xi_1 - x_0$ ($x_0 = 7.4918032$). The distance of the centre of the cylinder from the leading edge is denoted by $x_0$; the radius of the cylinder is scaled to unity. Initial data are given at the leading edge of the flat plate, where a Blasius flow is assumed. No extra information in the plane of symmetry is necessary. The computation proceeds downstream of the leading edge until a point is observed, at the line of symmetry, with a very small $C_f$, It is situated just upstream of the point where singular separation occurs. The last calculated point at the line of symmetry is abandoned from the computation: it is not allowed to produce a downstream successor. The next point at the right is chosen as the start of the lefthand boundary of the computational domain. The computation proceeds downstream until it runs into a region where the limiting stream line angle approaches 90 deg. Points with $\phi_w > 80$ deg are abandoned. Again the next point at the right is taken as a new start of the lefthand boundary. The sharp bends in the boundary line near the line of symmetry are caused by the process of abandoning points from the computation.

Figure 5 shows the wall streamlines. Figure 6 shows the flow-angle profiles of six stations at the lefthand boundary, indicated in Fig. 5. The left-hand boundary is the envelope of the streamlines with maximum flow angle. Up to station 3 the maximum flow angle occurs at $\zeta = 0$. For this reason that part of the boundary coincides almost with the 3D separation line. Downstream of station 3 under influence of the pressure field, the limiting streamline deflects into the direction of the

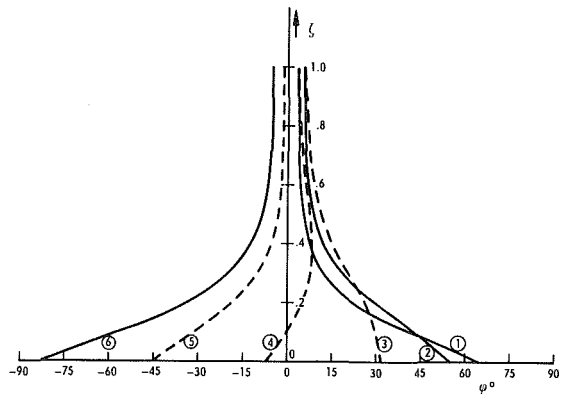


**Fig. 6 Laminar boundary layer flow past a flat plate with attached cylinder. Variation of flow angle through the boundary layer for the stations indicated in figure 5.**

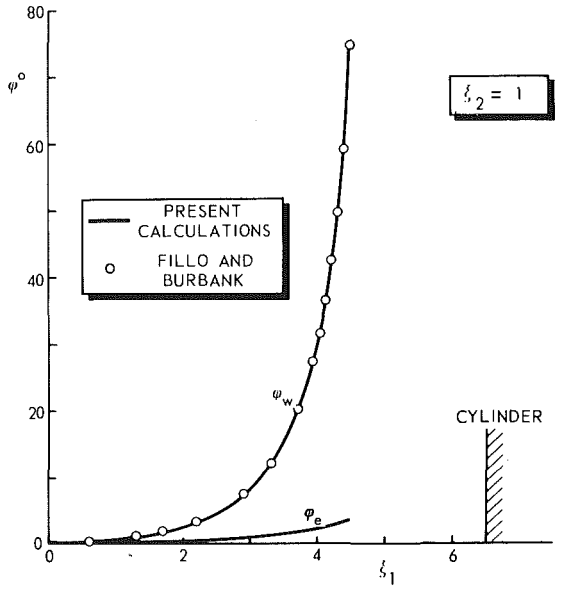


**Fig. 7 Laminar boundary layer flow past a flat plate with attached cylinder. Comparison with the calculation of Fillo and Burbank [10]. Limiting streamline angle variation along $\xi_2 = 1$.**

cylinder. The maximum flow angle between station 3 and 5 occurs somewhere between $\zeta = 0$ and the outer edge of the boundary layer. It may be clear that the separation line can be predicted only when it is situated in the region of determinacy of the initial data. Downstream of station 3 it lies outside this region. Between station 3 and 5 the crossflow changes sign through the boundary layer. A typical crossover profile is shown in Fig. 6 at station 4. Downstream of station 5 the maximum flow angle occurs at the outer edge of the boundary layer. For a small part of the computational region the results can be compared with those published by Fillo and Burbank [10]. In Fig. 7 a comparison of the limiting stream line angles is depicted along a line $\xi_2 = 1$. The agreement is very satisfactory. The complete computation was performed in one run with a Cyber 72 in 90 s; applied stepsizes $\Delta_1 = \Delta_2 = 0.2$.

The second example which we will consider is the 3D turbulent boundary layer flow over an airplane wing. This problem was accepted as a testcase for the 1979-Workshop of the Eurovisc Working Party on 3D shear layes. A detailed description of the testcase and results of the participants can be found in [12]. The pressure distribution and the geometry are shown in Fig. 8.

The same case was computed earlier by Elsenaar with the old NLR program for developable geometries. The present

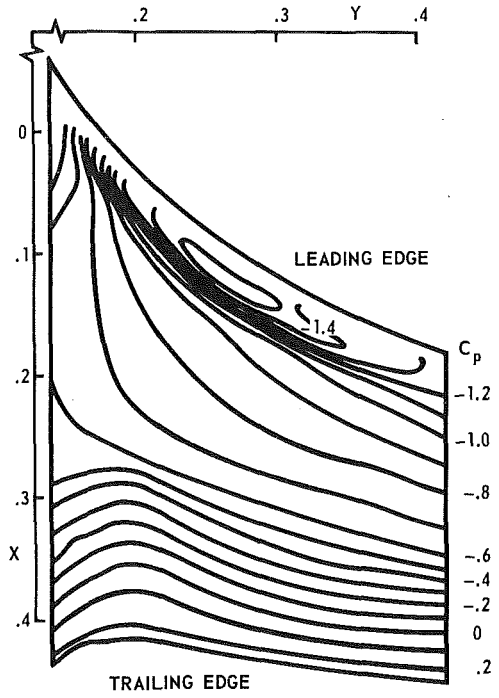


**Fig. 8 Root section of airplane wing. Lines of constant surface static pressure, $C_p$.**

method is able to compute the flow over the actual non-developable wing surface. For reasons of comparison, however, the computation was performed on the developable surface obtained by projection on the chord plane. The following simple coordinate system is employed:

$$\left.\begin{aligned}\xi_1 &= (x - x_{LE})/c \\ \xi_2 &= y\end{aligned}\right\} \tag{28}$$

The reference length L is based on the half span; Re = $u_\infty L/\nu_\infty = 9.08_{10}{}^6$. The computation is performed along lines of constant chord percentages. Initial data for $\theta_{11}$, $\phi_e$ and $C_f$ are given at $\xi_1 = 0.08$, which have been obtained by calculations on the wing leading edge region, assuming a local infinite swept wing flow. It is supposed that at the initial line the collateral velocity profiles can be described by Coles' formula. The sensitivity of the calculation results to changes in the initial data is not large. Doubling the initial $\theta_{11}$ had little effect. The initial streamline angle has a larger influence, although the final flow pattern was qualitatively similar.

In Fig. 9 results for two grids are depicted for $C_f$, $\phi_w$ and $\theta_{11}$ at $\xi_1 = 0.74$. From $C_f$ we can infer that, at $\xi_2 = 0.23$, the flow near the wall is slowed down considerably. Because the inertia forces are almost absent the pressure gradient is able to generate a strong crossflow which causes a convergence of wall streamlines and an increase in boundary layer thickness. The computed wall streamlines are given in Fig. 10(*a*), accompanied by a picture of the actual observed wall streamlines (Fig. 10(*b*)). At A the flow is characterized by a low $C_f$, indicating that a singular separation point is approached; the program abandons this point from further computations and the regions of determinacy of the remaining points are computed. At left there is a region in which the limiting streamlines show flow divergence. The left-hand boundary of the region at the right is situated just upstream of the envelope of the wall streamlines. This envelope may be identified with a 3D separation line emanating from the singular separation point. Cousteix and Houdeville [13] argue that the envelope is a singular solution of the 3D

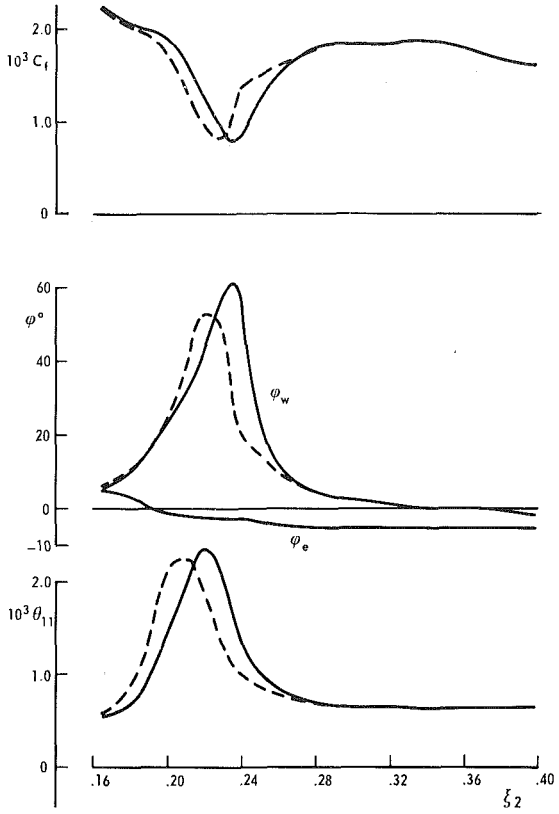


**Fig. 9 Root section of airplane wing. Calculation of results at 74 percent of the local chord, $\xi_1 = 0.74$.**
**$\Delta\zeta = .05$,**
**– –: $\Delta_1 = .04$, $\Delta_2 = .010$; execution time 230 s;**
**——: $\Delta_1 = .02$, $\Delta_2 = .005$; execution time 850 s.**

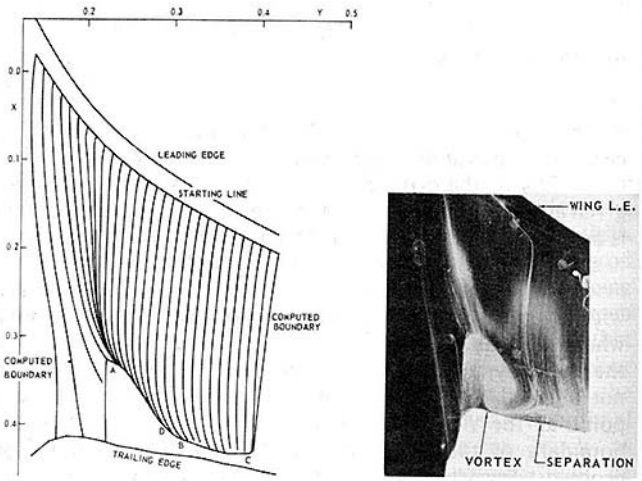


**Fig. 10 Root section of airplane wing. Calculated limiting streamlines and oilflow pattern**
**A = region with large flow angles, BC = region with low $C_f$,**
**AD = approximate 3D separation line. The oilflow pattern visualizes the actual occurring limiting streamlines.**

boundary layer equations. In their opinion this singular behaviour can be resolved by a coupling with the outer flow.

The computation of the right part is halted before the trailing edge is reached because at about 92 percent of the chord a 2D separation region is observed, characterized by a low $C_f < 0.0005$.

Results of Elsenaar's and the present computation are given

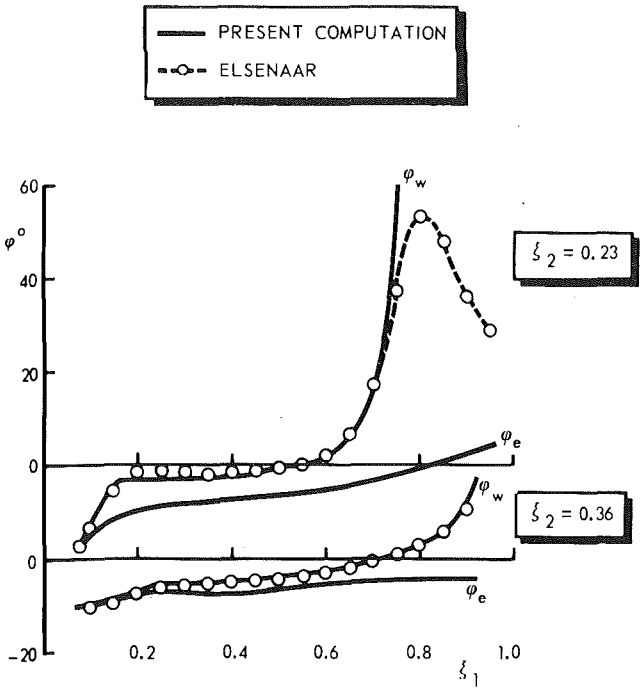


**Fig. 11 Root section of airplane wing. Results in two cross-sections**

in Fig. 11 for two cross sections. Despite the great differences in both calculation methods and their turbulence models the results compare quite favourable in general. The differences in $\phi_w$, near separation, give an exaggerated impression because in Elsenaar's results the onset of separation is shifted over a small distance. The present computations were performed on a Cyber 72 for the crude grid in 230 s and for the fine grid in 850 s. The number of points in normal direction: 21.

## References


1 Wesseling, P., and Lindhout, J.P.F., "A Calculation Method for Three-Dimensional Incompressible Turbulent Boundary Layers," *AGARD Conference Proceedings*, Vol. 93, 1971.

2 Van den Berg, B., and Elsenaar, A., "Measurements in a Three-Dimensional Incompressible Turbulent Boundary Layer Under Infinite Swept Wing Conditions," NLR TR 72092 U, 1972.

3 Van den Berg, B., Elsenaar, A., Lindhout, J.P.F., and Wesseling, P., "Measurements in an Incompressible Three-Dimensional Turbulent Boundary Layer, Under Infinite Swept Wing Conditions and Comparison with Theory," *Journal of Fluid Mechanics*, Vol. 70, 1975, p. 127.

4 East, L.F., "Computation of Three-Dimensional Turbulent Boundary Layers," Euromech 70, Trondheim, F.F.A. TN AE-1211, 1975.

5 Elsenaar, A., Van den Berg, B., and Lindhout, J.P.F., "Three-Dimensional Separation of an Incompressible Turbulent Boundary Layer on an Infinite Swept Wing," *AGARD Conference Proceedings*, Vol. 168, 1975.

6 Piers, W.J., Schipholt, G.J., and Van den Berg, B., "Calculation of the Flow Around a Swept Wing, Taking Into Account the Effect of the Three-Dimensional Boundary Layer, Part 1: Wing With Turbulent Boundary Layer," NLR TR 75076 U, 1975.

7 Van den Berg, B., Piers, W.J., and De Boer, E., "Calculation of the Flow Around a Swept Wing, Taking Into Account the Effect of the Three-Dimensional Boundary Layer, Part 2: Wing With Laminar Boundary Layer on the Lower Surface," NLR TR 77066 U, 1977.

8 Courant, R., and Hilbert, D., Methods of Mathematical Physics," Vol. II: *Partial Differential Equations*, p. 439, Interscience Publishers, 1961.

9 Dwyer, H.A., "Solution of a Three-Dimensional Boundary Layer Flow With Separation," *AIAA Journal*, Vol. 6, No. 7, 1968.

10 Fillo, J.A., and Burbank, R., "Calculation of Three-Dimensional Laminar Boundary Layer Flows," *AIAA Journal*, Vol. 10, No. 3 1972.

11 Cebeci, T., "Calculation of Three-Dimensional Boundary Layers II Three-Dimensional Flows in Cartesian Coordinates," *AIAA Journal*, Vol. 13, No. 8, 1975.

12 Lindhout, J.P.F., Van den Berg, B., and Elsenaar, A., "Comparison of Boundary Layer Calculations for the Rootsection of a Wing: the September 1979 Amsterdam Workshop Testcase," NLR MP 80028, 1980.

13 Cousteix, J., and Houdeville, R., "Analogie des singularités dans les methodes directes de calcul des couches limites tridimensionnelle stationnaire et bidimensionnelle instationnaire - Analyse des modes inverses," AGARD Meeting on The Computation of viscous-inviscid interactions, Colorado Springs, 29 Sept. - 1 Oct. 1980.

14 Lindhout, J.P.F., and de Boer, E., "The NLR Computer Program for Three Dimensional Boundary Layers," NLR report, to be published.


## APPENDIX

**The Metric Coefficients.** The user is free to choose any regular coordinate system. If $\mathbf{X}$ is the position vector in a Cartesian coordinate system the user has to implement in a subroutine the relation:

$$\mathbf{X} = \mathbf{f}(x_1, x_2),$$

$(x_1, x_2)$ is the surface-fitted coordinate system. As part of the program, a library of subroutines exists of coordinate systems for a number of geometries, such as complete wing geometries and cowls. The system $(x_1, x_2)$ generates parameter lines over the surface of the body. Tangent vectors to the parameter lines are denoted by $\mathbf{B}_1$ and $\mathbf{B}_2$. The metric coefficients are defined as the inner products of them:

$$a_{\alpha\beta} = |\mathbf{B}_\alpha . \mathbf{B}_\beta| \; (\alpha, \beta = 1,2)$$

The other geometrical quantities are defined in terms of $a_{\alpha\beta}$ and their derivatives:

$$h_1 = a_{11}^{1/2}, h_2 = a_{22}^{1/2}, \Gamma = a_{12}/(h_1 h_2), m^2 = \det(a_{\alpha\beta}).$$

$$R^1_{11} = \tfrac{1}{2} a_{12}(a_{12}\partial_1 a_{11}/a_{11} + \partial_2 a_{11} - 2\partial_1 a_{12})/(m^2 h_1)$$

$$R^1_{12} = \tfrac{1}{2} h_2 \{(1+\Gamma^2)\partial_2 a_{11} - 2a_{12}\partial_1 a_{22}/a_{22}\}/m^2$$

$$R^1_{22} = \tfrac{1}{2} h_1 (2\partial_2 a_{21} - a_{21}\partial_2 a_{22}/a_{22} - \partial_1 a_{22})/m^2$$

$$R^2_{11} = \tfrac{1}{2} h_2 (-a_{12}\partial_1 a_{11}/a_{11} + 2\partial_1 a_{21} - \partial_2 a_{11})/m^2$$

$$R^2_{12} = \tfrac{1}{2} h_1 \{(1+\Gamma^2)\partial_1 a_{22} - 2a_{12}\partial_2 a_{11}/a_{11}\}/m^2$$

$$R^2_{22} = \tfrac{1}{2} a_{12}(a_{12}\partial_2 a_{22}/a_{22} - 2\partial_2 a_{21} + \partial_1 a_{22})/(m^2 h_2)$$

The arc length along the surface of the body is:

$$ds^2 = a_{11} dx_1^2 + 2a_{12} dx_1 dx_2 + a_{22} dx_2^2.$$

# Evaporation of Small Water Drops Containing Salt in a High Pressure Steam Environment

**G. C. Gardner**
Central Electricity Research Laboratories,
Leatherhead, Surrey, U.K.

*It is important ot be able to calculate the lifetime of drops in central power station boilers so as to determine their penetration into the superheater sections of once-through boilers and as necessary input for the design of spray separators in recirculation boilers. The evaporation rate may be reduced by a large number of factors such as the elevation of the boiling point when the salt concentration in a drop becomes substantial or by the fact that the drop is evaporating in a medium with a density which may be more than a quarter of the water density. All the factors are considered and calculations suitable for deskwork are presented.*

## Introduction

There are chiefly two types of high pressure boiler used in central power stations. In the recirculating boiler a mixture of steam and water, containing about 50 volume percent steam, issues from the boiler tubes and passes to separator equipment. Water mixed with make-up is returned to the boiler and the steam passes forward to superheaters. It is desirable to keep the salt content of the steam as low as possible and, since salt is chiefly waterborne, spray is separated from the steam in passing through stacks of corrugated plates situated after the primary cyclonic steam/water separating devices.

The second type of boiler is called a once-through boiler, since feed water enters a boiler tube at one end and superheated steam leaves at the other end. Therefore all the salt in the feed must pass into the superheater section. It is of interest to know whether the salt is in aqueous solution or not, because this may influence corrosion of the tube material, which is often changed from a ferritic to an austenitic steel within the superheater section. It may be noted that the salt concentration in the water and thus in the drops of a recirculating boiler is typically $10^{-5}$ weight fraction. In a once-through design, the feed typically contains $10^{-8}$ weight fraction of salt and this will also be the concentration in the steam leaving the evaporator section. Now, if there are isolated drops in this steam, they may have a salt concentration approaching the equilibrium value in relation to the steam. The partition coefficient is about $10^{-3}$ at 180 bar and thus isolated drops contain about $10^{-5}$ weight fraction of salt, which is similar to the concentration in drops from the recirculating system.

We are clearly concerned with the evaporation of drops passing into the superheater of once-through boilers. In recirculating systems it is important to note that the steam has about a 5s residence time between the primary separators and the corrugated plate stacks, which, since the vapor pressure is higher over a curved surface, allows smaller drops to evaporate. This may help to set a lower limit to the drop size that has to be separated, which is useful in the design of the plate stacks.

Conservative calculations, which underestimate the rate of evaporation are satisfactory for both the foregoing calculations and therefore it will be assumed that drops are at rest with respect to the steam. This not only implies that there is no motion relative to the bulk steam flow but that relative motion due to turbulence and bouyancy induced currents, due to the heat transfer processes, are absent. Further factors of importance to the heat transfer aspects of the calculations are as follows.

1) There is a steam flow away from the drop surface which reduces the heat transfer rate. It will be seen the dimensionless group of importance is $Q = (c_p \Delta T/L)$, where $c_p$ is the specific heat of steam, $\Delta T$ is the bulk steam superheat and $L$ is the latent heat of evaporation.

2) The drop's surface is receding from the heat source of superheated steam, reducing the heat transfer rate. The dimensionless group of importance is $P = (\rho_s/\rho_w)$, where $\rho_s$ and $\rho_w$ are the densities of steam and water.

3) Increasing the dimensionless group P means that all the heat required to evaporate a drop plunged into superheated steam is available at a short distance from the drop so that conduction paths are shortened. Therefore the role of $P$ is ambiguous.

4) If the drop is subcooled by $\Delta T_w$ some of the heat transferred to the drop surface will not be used for evaporation. This will become important as

$$\frac{\Delta T_w k_w}{\Delta T k}$$

approaches unity, where $k_w$ is the conductivity of water. However, it will be assumed that $\Delta T_w$ is zero for all the calculations given here.

Contributed by the Fluids Engineering Division of THE AMERICAN SOCIETY OF MECHANICAL ENGINEERS and presented at the Winter Annual Meeting, New York, N.Y., December 5-10, 1976. Manuscript received by the Fluids Engineering Division, June 4, 1977. Paper No. 76-WA/FE-35.

5) Salt is relatively involatile so that it will tend to accumulate in the drop, raising the boiling point. It will also tend to collect at the drop's surface and give an even greater increase in the surface temperature. However, Gardner [1] has shown that the surface concentration $c'_l$ is given by

$$\frac{c'_l}{c'_0} = \exp\left(\frac{dv}{4D_w}\right) \tag{1}$$

where $c'_0$ is the concentration at the center of the drop, $d$ is the drop diameter, $D_w$ is the diffusivity of salt within the drop, and $v$ is the velocity of recession of the drop's surface. It can therefore be shown that $c'_l$ does not vary sufficiently from the average concentration for the extra concentration factor to be important in the problems discussed here.

6) The temperature of the drop will be depressed below the saturation value for a plane surface because the curvature increases the vapor pressure, which must then be lowered to that of the system by dropping the drop's temperature.

7) Mass transfer dominates the evaporation process when the salt concentration is raised sufficiently to increase the boiling point to the temperature of the superheated steam. It will be assumed that no salt is lost until the mass transfer process takes over.

All the above factors must be taken into account. The evaporation of a drop of pure water will be considered first, making allowance for the dimensionless groups $Q$ and $P$.

## Evaporation of a Pure Water Drop

It is assumed that a drop at its saturation temperature is plunged into superheated steam. No allowance will be made for depression of the boiling point by surface curvature, since this effect becomes most pronounced towards the end of the lifetime of the drop when the velocity of recession of the surface is greatest.

**Boundary Conditions and Development of an Integral Boundary Layer Equation.** The boundary conditions will be discussed with reference to the differential energy transport equation, which is

$$\frac{\partial T}{\partial t} = \frac{\alpha}{r^2}\frac{\left(r^2\dfrac{\partial T}{\partial r}\right)}{\partial r} - \frac{v_0 r_0{}^2}{r^2}\frac{\partial T}{\partial r} \tag{2}$$

where $T$ is temperature, $t$ is time, $r$ is the radial coordinate, $r = r_0$ is the surface of the drop, $v_0$ is the steam velocity at the surface of the drop, and $\alpha$ is the thermal diffusivity of steam. Boundary conditions are

$$t=0, r<r_0 \text{ then } T=T_0=T_s \tag{3}$$

$$t=0, r>r_0 \text{ then } T=T_\infty \tag{4}$$

$$t>0, r\le r_0 \text{ then } T=T_0=T_s \tag{5}$$

It is to be noted that the steam superheat is assumed constant for the purpose of this section and, since the drop is at its constant saturation temperature, both $T_0$ and $T_\infty$ are constant.

An integral method of solution will be used, which assumes a boundary layer thickness $\delta$. Therefore further boundary conditions are

$$t>0, r>(r_0+\delta) \text{ then } T=T_\infty \tag{6}$$

$$t>0, r=(r_0+\delta) \text{ then } \frac{\partial T}{\partial r}=0 \tag{7}$$

We employ the relation

$$\frac{dT}{dt} = \frac{\partial T}{\partial t} + \frac{\partial T}{\partial r}\frac{dr}{dt} \tag{8}$$

and conditions (6) and (7) in the basic differential equation (2) to determine the further boundary condition

$$t>0, r=(r_0+\delta) \text{ then } \frac{\partial^2 T}{\partial r^2}=0 \tag{9}$$

We require a final boundary condition at the surface of the drop and note first that, because all the heat reaching the drop raises steam,

$$v_0 = \frac{k}{\rho_s L}\left(\frac{\partial T}{\partial r}\right)_0 (1-P) \tag{10}$$

where $k$ is the thermal conductivity of steam.

At the surface of the drop, equation (8) becomes

## Nomenclature

$a$ = defined by equation (50)
$A$ = defined by equation (21)
$B$ = constant of integration
$c'$ = salt concentration in liquid
$c'_l$ = $c'$ at surface of drop
$c'_0$ = $c'$ at center of drop
$c'_w$ = $c'$ at start of water evaporation
$c'_s$ = $c'$ at start of salt evaporation
$c''$ = salt concentration in vapor
$c_p$ = specific heat of steam
$C$ = defined by equation (24)
$d$ = drop diameter
$d_{0/w}$ = $d$ at start of water evaporation
$d_T$ = tube diameter
$D$ = diffusivity in vapor
$D_w$ = diffusivity in liquid
$h$ = heat transfer coefficient
$H$ = total heat required
$k$ = thermal conductivity of steam
$L$ = latent heat of vaporization
$M_s$ = mass of salt in drop
Nu = Nusselt number
$p$ = pressure
$p_0$ = vapor pressure over a plane surface
$P$ = $\rho_s/\rho_w$
$q$ = heat flux
$Q$ = $c_p\Delta T/L$
$r$ = radial coordinate
$r_0$ = radius of drop
$r_{0/w}$ = $r_0$ at start of water evaporation
$r_{0/s}$ = $r_0$ at start of salt evaporation
$R$ = defined by equation (14)
$R_0$ = defined by equation (19)
$t$ = time
$t_H$ = time to evaporate water
$t_M$ = time to evaporate salt
$T$ = temperature
$T_s$ = saturation temperature for a plane surface
$T_\infty$ = temperature far from drop
$\Delta T$ = superheat ($T_\infty$ - $T_s$)
$\Delta T_1$ = superheat at which water is evaporated
$\Delta T_w$ = water subcooling due to surface tension
$v$ = velocity of drop surface
$v_0$ = velocity of steam at drop surface
$\alpha$ = thermal diffusivity of steam
$\beta$ = ebullioscopic constant
$\Gamma$ = partition coefficient
$\delta$ = boundary layer thickness
$\Delta$ = defined by equation (19)
$\theta$ = defined by equation (14)
$\rho_s$ = steam density
$\rho_w$ = water density
$\sigma$ = surface tension
$\sigma_s$ = surface tension of salt solution
$\sigma_w$ = surface tension of pure water
$\Sigma$ = defined by equation (37)
$\tau$ = dimensionless time (equation (25))
$\tau_0$ = $\tau$ for evaporation of drop

$$\left(\frac{\partial T}{\partial t}\right)_0 = -\left(\frac{\partial T}{\partial r}\right)_0 \frac{dr_0}{dt} \tag{11}$$

Also

$$\frac{dr_0}{dt} = -\frac{k}{\rho_w L}\left(\frac{\partial T}{\partial r}\right)_0 \tag{12}$$

Employ equations (10), (11), and (12) in equation (2) to obtain the final boundary condition

$$\left[\frac{\partial\left(R^2\frac{\partial\Theta}{\partial R}\right)}{\partial R}\right]_0 = Q\left(\frac{\partial\Theta}{\partial R}\right)_0^2 \tag{13}$$

where

$$R = \frac{r}{r_0}, \Theta = \frac{T}{\Delta T} \tag{14}$$

The integral condition may be obtained by integration of equation (2) but, because of its simplicity, the following derivation is preferable.

In the initial state there is a drop of radius $r_{0lw}$ containing water which is at the saturation temperature $T_s$. All the steam is at the temperature of $T_\infty$. Consider a fictitious intermediate condition in which the drop size is reduced to $r_0$, its temperature remains at $T_s$ and all steam is, again, at $T_\infty$. The energy $H$ of the system has increased by the heat needed to evaporate water and the heat needed to heat the steam produced to $T_\infty$.

$$H = \frac{4}{3}\pi\rho_w(r_{0lw}^3 - r_0^3)(L + c_p\Delta T) \tag{15}$$

which can be rewritten as

$$H = \frac{4}{3}\pi\rho_w L r_{0lw}^3(1 - R_0^3)(1 + Q) \tag{16}$$

where

$$\Delta T = T_\infty - T_s, R_0 = \frac{r_0}{r_{0lw}} \tag{17}$$

The system is now brought to its final state by reducing the temperature in the boundary layer. Thus the energy in the system becomes equal to the initial quantity. The result is

$$\int_1^{1+\Delta}\left(\frac{T_\infty - T}{\Delta T}\right)R^2 dR = \frac{(1+Q)}{3PQ}\left[\frac{1}{R_0{}^3} - 1\right] \tag{18}$$

which is the required integral equation.

$$\Delta = \frac{\delta}{r_0} \tag{19}$$

**Boundary Layer Temperature Profile and Solutions.** It is well known that solutions to problems associated with flat surfaces using integral equations are insensitive to the form of boundary layer profile chosen. The same is not true with problems associated with cylindrical or spherical surfaces and great care must be taken in choosing an appropriate form. Firstly the profile must agree with boundary conditions (6), (7), and (9). Otherwise we are guided by a known solution when $P \to 0$. Then a quasisteady state exists with $\partial T/\partial t$ in equation (2) equal to zero. This assumption is valid since the rate of change of drop size will be tending to zero. We obtain

$$\frac{T_\infty - T}{\Delta T} = \frac{1 - \exp\left(-\frac{A}{R}\right)}{1 - \exp(-A)} \tag{20}$$

$$A = \frac{v_0 r_0}{\alpha} \tag{21}$$

It is noted that, as $P \to 0$, the boundary layer thickness tends to infinity. Using equation (20) as a guide and taking into account boundary conditions (7) and (9), as well as the finite value of $\delta$ when $P \neq 0$, the following form of boundary layer temperature profile is assumed.

$$\frac{T_\infty - T}{\Delta T} = \left[\frac{1+\Delta}{\Delta}\right]^2\left[\frac{1 - \exp\left[B\left(\frac{1}{1+\Delta} - \frac{1}{R}\right)\right]}{1 - \exp\left[-\frac{B\Delta}{1+\Delta}\right]}\right]\left[1 - \frac{R}{1+\Delta}\right]^2 \tag{22}$$

$\Delta$ and $B$ are constants for any particular value of $R_0$. Evaluation of boundary condition (13) yields

$$\left(\frac{B}{C}\right)^2 C - \frac{4}{\Delta}\left(\frac{B}{C}\right) + \frac{2(2\Delta - 1)}{\Delta^2} = Q\left[\frac{2}{\Delta} + \left(\frac{B}{C}\right)\right]^2 \tag{23}$$

where

$$C = \exp\left(\frac{B\Delta}{1+\Delta}\right) - 1 \tag{24}$$

Equation (23) yields $B$ as a function of $\Delta$ by trial and error. The corresponding value of $R_0$ is determined from the integral equation (18). For this purpose, approximations to the exponential integral given by Abramowitz and Stegun [2] can be used.

Results for a very small value of $P = 6.16\ 10^{-4}$, which is equivalent to 1 bar steam, are given in Fig. 1 and results for $P = 0.531$, which is equivalent to 215.6 bar steam, are given in Fig. 2. Both figures show

$$\left(-\frac{d\tau}{dR_0}\right)$$

plotted against $R_0{}'$, where the dimensionless time is

$$\tau = \frac{k\Delta T t_H}{\rho_w L r^2{}_{0lw}} \tag{25}$$

where $t_H$ is the time for evaporation. This form of plot is chosen because a straight line represents a solution in which the heat transfer coefficient is inversely proportional to the drop diameter. In particular it is noted that the well known steady state solution, using the Nusselt number equal to 2, would be represented by a straight line with a slope of unity in Figs. 1 and 2.

The time $\tau_0$ necessary to evaporate the drop completely is obtained by integration of the results such as in Fig. 1. $\tau_0$ is given versus $Q$, with $P$ as a parameter, in Fig. 3. When $P = 0$, there is an analytical result for the heat transfer coefficient, which can be obtained from equation (20). It is

$$\mathrm{Nu} = \frac{hd}{k} = \frac{2}{Q}\ln(1+Q) \tag{26}$$

This yields the values of $\tau_0$ for $P = 0$ shown in Fig. 3 and in particular it is noted that $\tau_0 = 0.5$, when $Q = 0$ and this is true for all $P$. When $Q = 0$ Nu $= 2$.

The conclusion achieved from Fig. 3 is that the lifetimes of drops for practical values of $Q$ and for high pressure steam will be shorter than estimated by assuming Nu $= 2$. It is therefore conservative to make the very simple assumption that Nu $= 2$, when the overestimate of the lifetime will be less than about 15 percent for 180 bar steam.

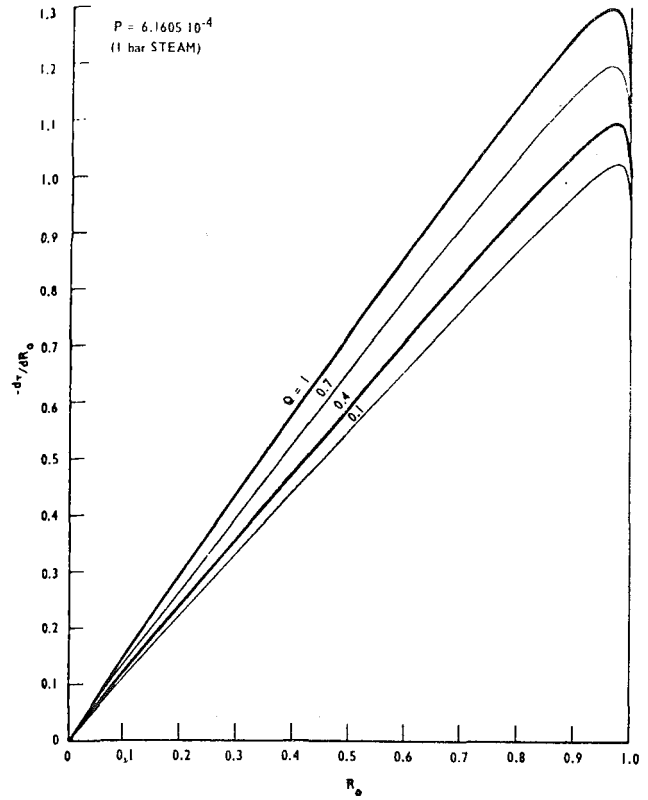


Fig. 1 Evaporation of drops with a small ratio of steam to liquid densities

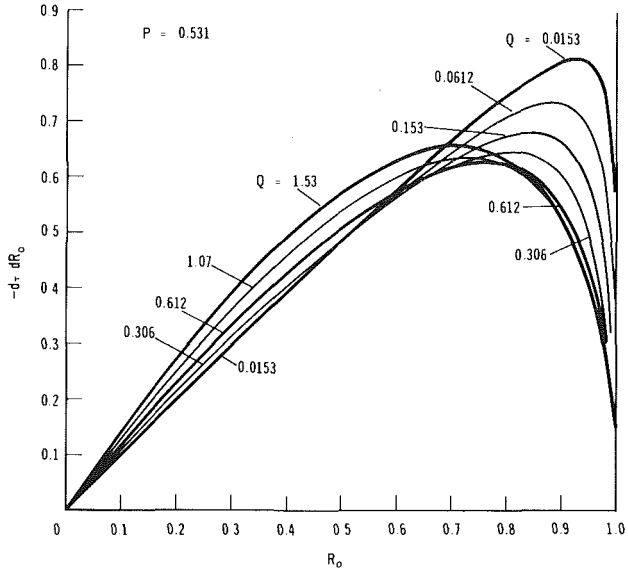


Fig. 2 Evaporation of drops with a large ratio of steam to liquid densities

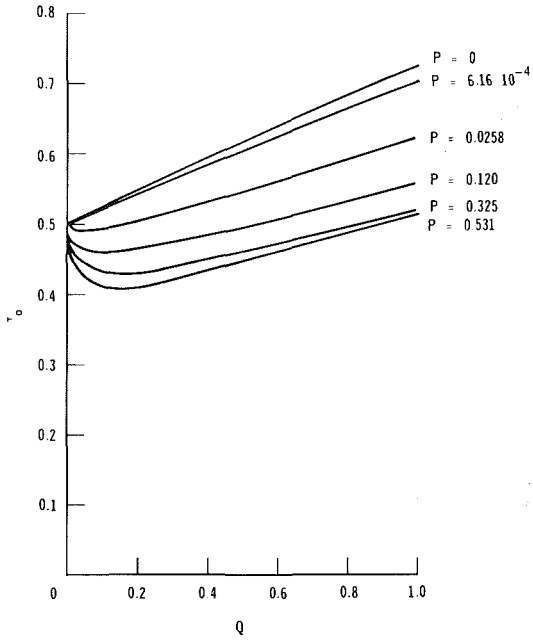


Fig. 3 Time for evaporation of a drop

## Evaporation of a Pure Water Drop in Saturated Steam

The problem of interest is the evaporation of drops in a steam drum where the bulk steam temperature at the pressure under consideration is controlled to the saturation value for a plane surface, since there are large masses of water present. Now the exact form of the Kelvin relationship for the change in vapor pressure due to the surface curvature of a drop of diameter $d$ is

$$\frac{4\sigma}{d} = \int_{p_0}^{p} \left(\frac{1}{p} - 1\right) dp \tag{27}$$

where $\sigma$ is surface tension, $p$ is vapor pressure over the curved surface and $p_0$ is vapor pressure over a plane surface. By assuming that $P$ is constant over the small range of $p$ to be considered and by assuming that the gradient of saturation temperature $T_s$ with respect to pressure is also constant we, find that the drop subcooling is

$$\Delta T_w = \frac{4\sigma}{d\left(\frac{1}{P} - 1\right)} \frac{dT_s}{dp} \tag{28}$$

By assuming that Nu = 2 we can therefore calculate the change in size of the drop with time. The result is that

$$\left(\frac{d_0}{d_{0lw}}\right)^3 = \left(\frac{d_{0l}}{d_{0lw}}\right)^3 - 1 \tag{29}$$

$$d_{0lw}{}^3 = \frac{48k\sigma t_H}{\rho_w L\left(\frac{1}{P} - 1\right)} \frac{dT_s}{dp} \tag{30}$$

$d_{0l}$ is the original drop diameter, $d_0$ is the final drop diameter after time t and $d_{0lw}$ is the value of $d_{0l}$ for which $d_0 = 0$.

We can now consider the design of the corrugated plate stacks. A proper appraisal would require the original drop size distribution at $t = 0$ but this is not available. However, plotting of equation (29), while remembering that the drop mass is proportional to $d^3$, indicates that it is improbable that it is useful to design separators to have a high colleciton efficiency for drops much smaller in size than $d_{0lc}$. Drops that the above calculation indicate would disappear would, in fact, become drops of salt solution in equilibrium with the steam and, since the concentration would change from about $10^{-5}$ to about $10^{-2}$ weight fraction, these salt drops would be about a tenth of the drop size at $t = 0$. It is doubtful that it would be practical to design separators for these rather smaller sizes and, in addition, it should be noted that the salt itself can be evaporated by a mass transfer process, as given in a later section.

An idea of magnitude of $d_{0lc}$ is obtained by examining a 187 bar (360°) boiler with $t = 5$s. $d_{0lc}$ is then 7.0 $\mu$m.

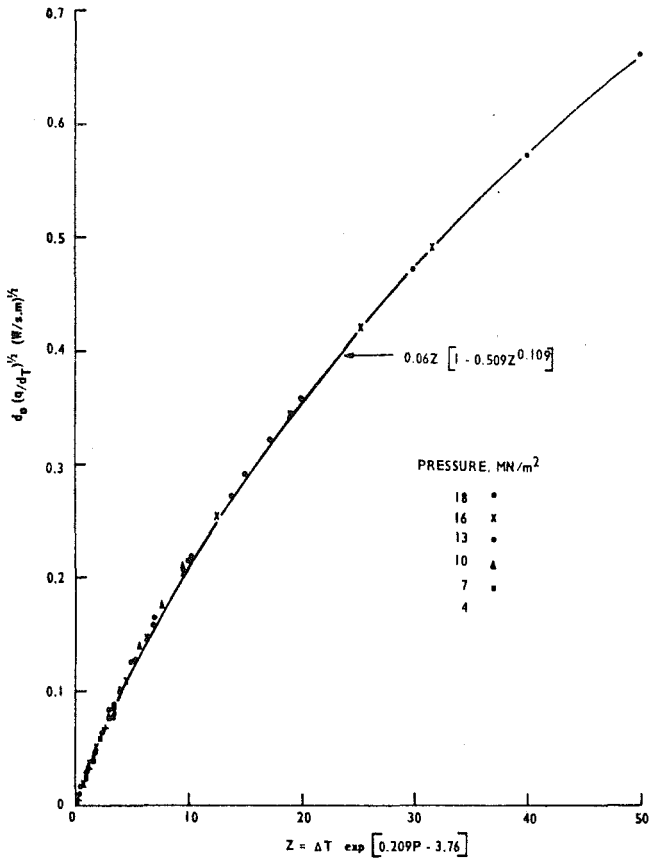


**Fig. 4 Correlation of the evaporation of water drops**

## Evaporation of a Pure Water Drop in Superheated Steam

The problem of concern is the penetration of drops, which are travelling with the steam, into the superheater sections of once-through boilers. To be conservative, the influence of surface tension can be ignored. We assume that the steam is passing along a tube of bore $d_T$ and that there is a uniform heat flux $q$ per unit wall internal surface area. We also assume that Nu = 2 and then

$$d^2_{0lw} = \frac{2d_T}{\rho_w L q} \int_0^{\Delta T_l} k\rho_s c_p \Delta T d(\Delta T) \tag{31}$$

is readily derived, where $\Delta T_l$ is the superheat at which a drop travelling with the steam will completely evaporate. The drop size is $d_{0lw}$ when $\Delta T = 0$.

The integral of equation (31) has been evaluated and, for convenience, the following empirical correlation has been derived

$$d_{0lw}\left(\frac{q}{d_T}\right)^{1/2} = F(z) \tag{32}$$

$$z = \Delta T_l \exp\ (0.209\mathrm{p} - 3.76) \tag{33}$$

where basic S.I. units are employed except that $p$ is in MN/m$^2$. The correlation is valid at least in the range from $p$ = 4 to 18 MN/m$^2$ and for $\Delta T_l$ up to 50K. It is shown in Fig. 4 with a correlating curve of

$$F(z) = 0.06z(1 - 0.509z^{0.109}) \tag{34}$$

As an example, consider a typical system at 180 bar with $d_T$ = 12.8 mm and $q$ = 0.3 MW/m$^2$. It was estimated, by means not given here, that the largest drop to be expected entering the superheater had a size $d_{0lw}$ = 17.7 $\mu$m, which the correlation shows would evaporate at $\Delta T_l$ = 3.3$K$.

## Evaporation of a Salt Drop

A number of assumptions have to be made if a relatively simple analytical expression is to be obtained for the time of evaporation of a salt drop. All the assumptions will be such as to overestimate the lifetime of a drop.

The first assumption is that the time calculated in the previous two sections for pure water drops are added to the times now to be calculated, which are for evaporation by a mass transfer rather than by a heat transfer process. The second assumption is that no salt is lost from the drop until the drop comes to thermal equilibrium with the steam and the mass transfer process begins. These two assumptions introduce little error if the initial salt concentration is small and if the partition coefficient $\Gamma$ between water and steam is small, say $10^{-3}$.

A third assumption is formulated as follows. Consider a drop of pure water of the same size as that of the salt drop but with the surface tension of the salt solution involved. The temperature of the drop below that of the steam will equal $(\Delta T_w + \Delta T)$, where $\Delta T$ is the superheat of the steam relative to a plane water surface. Now the evaporation is assumed to be controlled by mass transfer so that there is thermal equilibrium. To raise the temperature of the drop to equal that of the steam, the salt concentration $c'$ in the drop will be given by

$$\beta c' = \frac{4\sigma}{d_0\left(\frac{1}{P} - 1\right)} \frac{dT_s}{dp} + \Delta T \tag{35}$$

where $\beta$ is the ebullioscopic constant for the elevation of the boiling point.

However, $\sigma$ increases with $c'$ and Gardner [3] has shown that it can be represented for, say, sodium chloride solutions by

$$\sigma = \sigma_w + \Sigma c' \tag{36}$$

$$\Sigma = 4.4\ 10^{-4}(T - 218) J/m^2(\mathrm{kg/kg} \tag{37}$$

where $\sigma_w$ is the surface tension of pure water and $T$ is absoute temperature. If equation (36) were used in equation (35) throughout the following derivations, difficulties would arise since $c'$ would then be found to become infinite before the drop had disappeared. Therefore the fourth assumption is that $\sigma$ is constant throughout the mass transfer process at the value obtaining when the drop first comes to thermal equilibrium. This will not usually produce too large an error, since the evaporation rate is approximately inversely proportional to the drop size. We substitute equation (36) in (35) and solve simultaneously with

$$c'_w r^3_{0lw} = c'_s r^3_{0ls} \tag{38}$$

to obtain $r_{0ls}$. $r_{0lw}$ and $r_{0ls}$ are the drop radius of the initial drop and the drop that first comes to thermal equilibrium and $c'_w$ and $c'_s$ are the corresponding concentrations. We then determine $\sigma$ from equation (36) and employ it as a constant in equation (35) during subsequent events.

The fifth assumption is that the density of the salt solution is constant and equal to the value for water, though salt may increase the density by a factor of as much as two.

The sixth and last assumption is that the superheat of the steam with respect to a plane surface is constant. All the foregoing assumptions can be removed simultaneously but calculations would then be performed numerically by a computer. However, simple analytical results can easily be obtained by the reader for special situations. For example, it

often occurs that the first term on the right of equation (35) can be neglected by comparison with the second, which can be made a function of time. An analytical expression can then be obtained for the time of evaporation. Because such results can be determined, the following must be regarded as guide to the type of derivations possible.

The mass of salt in the drop is

$$M_s = \frac{4}{3}\pi r_0^3 c' \rho_w \tag{39}$$

$$\frac{dM_s}{dt}\frac{dt}{dr_0} = 4\pi r_0^2 c' \rho_w + \frac{4}{3} r_0^3 \rho_w \frac{dc'}{dr_0} \tag{40}$$

Equation (35) is written as

$$c' = \frac{E}{\beta r_0} \tag{41}$$

in which the definition of the constant $E$ is obvious. Differentiation of equation (40) and substitution in equation (41) yields

$$\frac{dm_s}{dt}\frac{dt}{dr_0} = \frac{2}{3} c' \rho_w + \frac{1}{3}\rho_w \frac{\Delta T}{\beta} \tag{42}$$

where $dm_s/dt$ is minus the evaporation rate per unit face area.

Diffusion and convection of salt in the steam phase is given by

$$\frac{d^2 c''}{dr^2} + \frac{2}{r}\frac{dc''}{dr} - \frac{v_0 r_0^2}{Dr^2}\frac{dc''}{dr} = 0 \tag{43}$$

where $c''$ is the salt concentration in the steam and $D$ is the salt diffusivity in the steam.

$$v_0 = -\left[\frac{\rho_w - \rho_s}{\rho_s}\right]\frac{dr_0}{dt} \tag{44}$$

The solution to equation (43) with the boundary conditions that $c'' = 0$ at $r = \infty$ and $c'' = \Gamma c'$ at $r = r_0$ is

$$\frac{c''}{\Gamma c'} = \frac{\exp\left(-\frac{v_0 r_0^2}{Dr}\right) - 1}{\exp\left(-\frac{v_0 r_0}{D}\right) - 1} \tag{45}$$

The evaporation rate is the sum of that due to convection and diffusion from the surface of the drop

$$-\frac{dm_s}{dt} = \rho_s v_0 \Gamma c' - \rho_s D\left(\frac{dc''}{dr}\right)_{r=r_0} = \frac{\rho_s v_0 \Gamma c'}{1 - \exp\left(\frac{-v_0 r_0}{D}\right)} \tag{46}$$

Equation (46) with equations (42) and (44) yields

$$1 - \exp\left(-\frac{v_0 r_0}{D}\right) = \frac{3\left[\frac{\rho_w - \rho_s}{\rho_w}\right]\Gamma}{\left(2 + \frac{\Delta T}{c'\beta}\right)} \tag{47}$$

The right-hand side of equation (47) is smaller than 3/2 Γ. Therefore an adequate approximation is

$$\frac{v_0 r_0}{D} = \frac{3\left[\frac{\rho_w - \rho_s}{\rho_w}\right]\Gamma}{\left(2 + \frac{\Delta T}{c'\beta}\right)} \tag{48}$$

Substituting for $v_0$ and $c'$ yields an equation that can be integrated to give

$$\frac{3P\Gamma D t_M}{a^2} = \frac{3}{2}\left(\frac{r_{0ls}}{a}\right)^2 - \left(\frac{r_{0ls}}{a}\right) + \ln\left(1 + \frac{r_{0ls}}{a}\right) \tag{49}$$

where $t_M$ is time for evaporation during the mass transfer process

$$a = \frac{2\sigma}{\Delta T}\left[\frac{P}{1-P}\right]\frac{dT_s}{dp} \tag{50}$$

The right-hand side of equaiton (49) divided by $(r_{0ls}/a)^2$ only varies form 1 to 1.5. Therefore, when a is large compared with $r_{0ls}$ and thus ΔT can be ignored,

$$t_M = \frac{r_{0ls}^2}{3\Gamma DP} \tag{51}$$

When $r_{0ls}$ is large compared to $a$, so that depression of the boiling point by surface curvature can be ignored,

$$t_M = \frac{r_{0ls}^2}{2\Gamma DP} \tag{52}$$

Let us consider a case where $\Delta T$ is zero. $r_{0ls}$ can be eliminated from equation (51) by using equations (35) and (38). Then equation (30) can be used to obtain

$$\frac{t_M}{t_H} = \frac{\beta c'_w k}{\Gamma D \rho_s L}\left(\frac{\sigma_w}{\sigma_s}\right) \tag{53}$$

where $\sigma_w$ and $\sigma_s$ are the surface tensions of water and salt solution. At 360°C $\beta = 10^2$ °C/kg/kg), $k = 0.16$ W/mK, $\rho_s = 144$ kg/m$^3$, $\Gamma = 1.3\ 10^{-3}$, $L = 0.721$ MJ/kg and $D = 10^{-7}$ m$^2$/s. Let $c'_w$ be $10^{-5}$. Then $t_M/t_H = 0.0035$ and it appears probable that, if the water is evaporated from a drop in the steam space of the drum, the salt will also be evaporated.

Similar calculations can be made for the evaporation of a salt drop for which the superheat ΔT is the dominating factor. It is usually found that the time to evaporate the salt comprises a small part of the time for total evaporation of the original drop.

## Summary

Evaporation of water drops under conditions found in boiler drums and superheaters is examined. The whole process can be divided for the purpose of calculation into two periods in sequence. In the first period the bulk of the water is evaporated and the presence of salt in the drop can be ignored. The first period is dominated by heat transfer. In the second period the drop is assumed to be in thermal equilibrium with the steam. The period starts with a drop containing all the salt present before the start of the whole process of evaporation began and evaporation is by a mass transfer process. It is shown that in practical cases the second period is only a small fraction of the whole evaporation time.

An essential requirement for the calculation of evaporation by heat transfer is a value for the heat transfer coefficient. Account must be taken not only of the radial steam velocity caused by evaporation but also of the high steam density relative to that of the water in a high pressure boiler. The influence of these parameters upon the time of evaporation in steam with a constant superheat is shown in Fig. 3. This shows that the time in high perssure boilers is generally shorter than expected by assuming that the Nusselt number equals 2. A value of 2 is therefore used in all other calculations, since the time for evaporation will then be overestimated, which is conservative for the purpose at hand. The error involved is

not so substantial as to lose the value of the estimates for engineering application.

Equations (29) and (30) provide estimates for the time of evaporation of a pure water drop in saturated steam, taking account of surface tension, which depresses the temperature of the drop. The estimates are useful in deciding upon the smallest drop that has to be removed from the steam by corrugated plate stacks in boiler drums.

Equations (32) and (34) provide estimates of the time of evaporation of a pure water drop travelling with steam which is being superheated.

Equations (51) and (52) provide limiting estimates for the evaporation of the salt in the drop after the bulk of the water has been evaporated. Equation (52) is that usually applicable, since the drop has usually reached a superheat at which the influence of surface tension can be ignored.

## Acknowledgment

This work has been carried out at the Central Electricity Research Laboratories and is published by permission of the Central Electricity Generating Board.

## References

1 Gardner, G.C., "Asymptotic Concentration Distribution of an Involatile Solute in an Evaporating Drop," *International Journal of Heat and Mass Transfer*, Vol. 8, 1965, pp. 667-668.

2 Abramowitz, M., and Stegun, O.A., *Handbook of Mathematical Functions*, 1965, Dover.

3 Gardner, G.C., "Surface Tension Gradients and the Motion of an Evaporating Drop Containing Sale in a Temperature Gradient," *Journal of Aerosol Science*, Vol. 6, 1975, pp. 173-179.

**J. Cervantes de Gortari**
Professor,
School of Engineering,
National University of Mexico,
Mexico, D.F., Mexico

**V. W. Goldschmidt**
Professor,
School of Mechanical Engineering,
Purdue University,
W. Lafayette, Ind.
Mem. ASME

# The Apparent Flapping Motion of a Turbulent Plane Jet—Further Experimental Results

*Measurements of four types of correlations in the self preserving region of a turbulent plane jet are presented. Negative correlations are noted between the two halves of the jet, exhibiting an apparent flapping like motion. That motion is noted to be self-preserving and most likely attributed to the presence of large scale organized structures.*

## Introduction

Turbulent plane jets may exhibit an apparent sideways, flapping type motion. This motion may be attributed either to conservation, along the length of the jet, of the lateral component of momentum due to asymmetric effects at the exit (leading to an overall sideways motion of the flow field) or to the presence of organized coherent structures with oscillations of finite extent. The apparent flapping motion, at one particular downstream station only, was reported in (1).

The apparent flapping, attributed either to a lateral oscillatory-like motion of the entire flow field or to an asymmetric coherent structure within the jet, is hidden in the randomness of the turbulent field and can be found only after long-time statistical averages. It is exhibited by the negative long-time averaged correlation of the longitudinal components of the velocity detected at two points, each one at opposite sides of the jet center line. When the velocity at one point increases, the velocity at the opposite point generally decreases. This could be explained by an overall lateral oscillatory motion of the flow field or by the passage of an organized vortex-street like structure. The time dependent cross correlation, taken with the velocity signal from one point delayed in time with respect to the other, gives further evidence to a flapping like motion by the distinctive negative value at zero time delay as well as by the ensuing quasi-periodic signal.

In the work now reported, standard hot-wire anemometry and on line digital processing instrumentation were used in four types of measurements: (*a*) two normal hot-wires symmetrically positioned with respect to the centerline of the jet; (*b*) two normal hot-wires positioned at opposite sides of the jet but with different lateral coordinates, (*c*) two normal wires, positioned on opposite sides of the jet, with equivalent distances from the centerline but at different $x$ locations ($x$ is measured along the jet axis); and (*d*) a single $x$-wire at the centerline of the jet, sensitive to the lateral component, $v$, in order to determine its autocorrelation. Longitudinal stations ranging from 10 to 100 times the slot width were investigated.

These experiments were planned to:

1) Clearly establish the existence of the flapping-like motion as opposed to a puffing effect, i.e., longitudinal oscillations of the flow field. (A puffing-like motion could be originated by artificial instabilities somewhere upstream of the nozzle exit or by symmetric coherent structures near the mouth of the jet. It would be characterized by periodic cross-correlation functions with positive values at zero time delay.)

2) Look for any dependence of the apparent flapping frequency on the longitudinal and lateral coordinates.

3) Study the characteristics of the apparent flapping behavior in the downstream direction, and

4) Investigate the Reynolds number independence and self-preservation of the apparent flapping motion.

## Experimental Setup

The facility consisted of a vertical rectangular nozzle of 0.635 × 30.48 cm (aspect ratio 48) supplied with air by a 1/4 HP squirrel-cage blower. A flexible duct connector between the blower outlet and the plenum chamber was employed in order to avoid the transmission of vibrations from the blower. The plenum chamber of dimensions 10.25 cm width, 30.48 cm height, and 67.5 cm long, was provided with a series of honeycombs and screens to insure uniform flow. The test section downstream of the nozzle exit was confined between two 90.2 × 122 cm plywood horizontal plates. In this way, a turbulent jet with Reynolds number based on the slot width (0.635 cm) and exit velocity ($2.43 \times 10^3$ cm/s) of approximately $10^4$ was obtained. (No unusual precautions were taken to reduce room draft effects. However, measurements in three different setups, and in different rooms were favorably compared.)

The usual checks for self-preservation, equivalence to other reported data for turbulent plane jets, etc. were made. This particular flow satisfied, for $x/D \geq 20$, the relationships

$$\left(\frac{U_m}{U_0}\right)^{-2} = 0.24\ (x/D - 4.53) \tag{1}$$

$$\frac{b}{D} = 0.083(x/D + 6.62) \tag{2}$$

Contributed by the Fluids Engineering Division of The American Society of Mechanical Engineers and presented at the Winter Annual Meeting, November 16-21, 1980, Chicago, Illinois. Manuscript received by the Fluids Engineering Division, August 3, 1979. Paper No. 80-WA/FE-13.

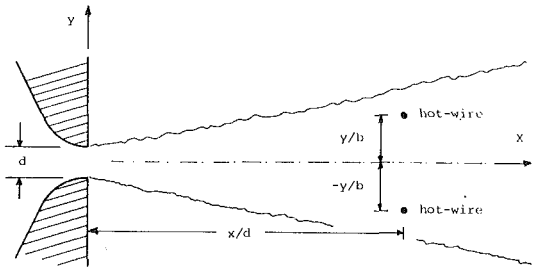


Fig. 1(*a*) Measurements Type I

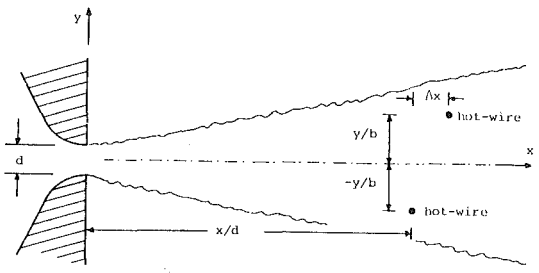


Fig. 1(*c*) Measurements Type III

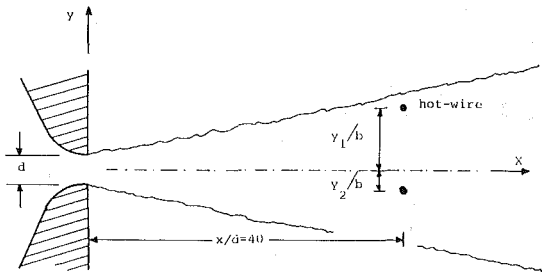


Fig. 1(*b*) Measurements Type II

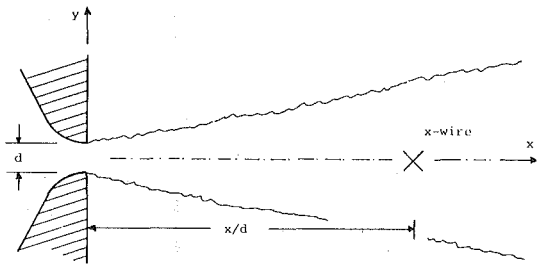


Fig. 1(*d*) Measurement Type IV

Where $U_0$ is the exit velocity, $U_m$ the velocity on the axis, $b$ the half-width of the jet and $D$ the slot width. Details of the mean flow characteristics are given in [2].

Two DISA 55A01 constant-temperature anemometers with DISA 55A22 and DISA 55F11 probe supports and "homemade" plated tungsten sensing elements (0.0002 cm diameter), were used to obtain the velocity signals at any two points in the flow. In computing normalized cross correlations between $u_1$ and $u_2$, calibration of the hot-wires was excluded. It sufficed to measure the correlation using the a.c. voltages themselves.

$$R_{12} = \frac{\overline{u_1 u_2}}{\sqrt{\overline{u_1^2}}\cdot\sqrt{\overline{u_2^2}}} = \frac{\overline{e_1 e_2}}{\sqrt{\overline{e_1^2}}\cdot\sqrt{\overline{e_2^2}}} \tag{3}$$

Preliminary cross correlation function measurements were done using a SAICOR Correlator and Probability Analyzer, model SAI-42. This digital on-line processing instrument provides a correlation computation at 100 incremental lag points simultaneously. By using the "resume" capability of the instrument, an average of various correlation samples can be determined, although the process is slow and tedious. In later measurements a Hewlett-Packard 5452A-2214B Fourier Analyzer System was used instead.

The four probe configurations are shown in Figure 1 while the different probe locations used in the four types of tests are listed in Table 1.

The objective in all the measurements (Types I to IV) was to first determine whether indeed there is an apparent flapping like motion and secondly to diagnose its origin. The first objective was fully met, the second one was not.

## Measurement Results

All measured cross correlation functions between $x$-components of the velocities at two points on opposite sides of the center line of the jet, are persistent and repeatable. They all exhibit a negative value of the correlation function at zero time delay and an alternate succession of positive and negative values as the time delay between the two signals increases. Examples of these correlations are given in Figs. 2(*a*) to 2(*d*).

The magnitude of the correlation at $\tau = 0$ gives a measure of the amplitude of the oscillatory-like flapping motion, whereas the approximate periodicity of the signal gives a measure of the apparent flapping frequency. The times between local maxima or local minima are generally not equal. However, the time to the first maximum is clearly measurable and suggests the definition of a frequency of apparent flapping, $f_1$, as illustrated schematically in Fig. 3. On the other hand, an average time between local maxima and minima, beyond the first local maximum, can be found. With

## Nomenclature

$b$ = jet half-width
$D,d$ = width of the slot of the jet
$e$ = voltage fluctuation
$\epsilon$ = amplitude of apparent flapping motion
$\epsilon_m$ = maximum amplitude of apparent flapping motion
$f_1$ = apparent flapping frequency, see Fig. 3
$f_2$ = apparent flapping frequency, see Fig. 3
$R$ = correlation coefficient (see equation (3)), or correlation function
Re = Reynolds number based on $U_0$ and $D$
$u$ = $X$-component of the velocity fluctuation
$U_c$ = turbulent convective velocity
$U_{cf}$ = convective velocity of apparent flapping motion, equation (7)
$U_m$ = velocity on the axis
$U_0$ = velocity at the mouth of the jet
$x$ = longitudinal coordinate
$y$ = lateral coordinate
$y_1$ = lateral coordinate of Sensor 1
$y_2$ = lateral coordinate of sensor 2
$\tau$ = time delay

**Table 1 Probe configurations**

| Measurements type | $x/D$ | $y_1/b$ | $y_2/b$ | $\Delta x/D$ |
|---|---|---|---|---|
| I | 10,20,30,40,60,80,100 | 0.5 | −0.5 | |
| | √ | 0.75 | −0.75 | |
| | √ | 1.0 | −1.0 | — |
| | √ | 1.25 | −1.25 | |
| II | 40 | 0.25 | −0.5 , −0.75, −1.0 , −1.25 | |
| | √ | 0.5 | −0.25, −0.75, −1.0 , −1.25 | |
| | √ | 0.75 | −0.25, −0.5 , −1.0 , −1.25 | — |
| | √ | 1.0 | −0.25, −0.5 , −0.75, −1.25 | |
| | √ | 1.25 | −0.25, −0.5 , −0.75, −1.0 | |
| III | 20,30,40 | 0.65 | −0.65 | 2,4,6,8,10 |
| | 10,20,30,40 | 1.0 | −1.0 | √ |
| IV | 10,20,30,40,60,80 | 0 | 0 | — |

it a second frequency $f_2$, as also illustrated in Figure 3 can be determined. These two frequencies are not exactly the same in value for reasons not yet fully understood.

**Type I Measurements.** Type I cross correlation functions were determined for the probes equally distant from the axis of the jet and at varying locations. The apparent flapping frequencies measured are plotted as a Strouhal number, $fd/U_0$ on Figs. 4(*a*) and 4(*b*).

The apparent flapping frequency decreases with $x$ but does not strongly depend on the lateral coordinate, $y$, at least for $x/d > 30$ where the jet becomes self-preserving in terms of mean velocity and turbulence intensity [3, 4]. The data points corresponding to $x/d$ values of 10 and 20 show a large amount of scatter. The reason for this could be the lack of self-preservation or simply error in positioning the probes at these small $x/d$ stations.

The decrease of $f_1$ and $f_2$ along $x$ demonstrates a dependence on local scaling properties. The results of Fig. 4(*a*) satisfy, quite closely, a "universal" value

$$\frac{f_1 b}{U_m} = 0.11 \tag{4}$$

The proper scaling parameter can now be applied to normalize the time delay $\tau$. The characterizing time scale is then $b/U_m$, and varies along $x/d$. The measured cross correlations now replotted in terms of $\tau U_m/b$ are plotted in Fig. 5, showing commonality in their shape. The magnitude, particularly the correlation at zero time delay is still dependent on lateral location, as exhibited in Fig. 6. An equation of the form

$$R(0) = (1 - 2.5\ y/b)(\exp\ (-2.9\ y/b) \tag{5}$$

appears to satisfy the data. For small $y/b$ values (within the lateral spatial macroscale) the correlation has to obviously approach the classical lateral correlation functions noted in turbulent flows.

The amplitude of the apparent flapping can be determined from the correlations at zero time delay. If the apparent flapping were locally sinusoidal then its displacement would be given by

$$\epsilon = \epsilon_m \sin 2\pi f t \tag{6}$$

where $\epsilon_m$ is the amplitude to be estimated. As shown in [1], the amplitude of the cross correlation at zero time delay is related to the amplitude of apparent flapping and dependent on the mean velocity gradient and hot-wire response. The amplitudes $\epsilon_m$ are seen to vary from 0.15b to 0.23b as noted in Table 2.

Data were also taken at exit Reynolds numbers of 7900 and 15100 to investigate the dependence on Reynolds number. Figure 7 presents the results. The Reynolds number similarity, at least for the tested range, is confirmed. The apparent flapping behavior characterized by relatively low frequencies should be related to the large-scale components of the flow field, and therefore independent of the viscosity.

**Type II Measurements.** One speculation is that the jet appears to flap while it actually "weaves" through a standing vortex type structure. A train of large scale vortices if present near the edges of the jet would have to give further changes in the sign of the cross correlation function at zero time delay. The type II measurements were performed to diagnose the possible existence of a weaving type motion. The data confirmed (*a*) a constancy of $f_1 b/U_m = 0.11$, (*b*) a correlation at zero time delay, see Fig. 8, always positive whenever $1/2\ (Y_1/b + Y_2/b) \geq 0$ hence not exhibiting, by itself, a vortex street near the edges of the jet capable of inducing a weaving motion. However it does not suffice to dispose the existence of a vortex short like structure smeared across most of the flow field.

**Type III Measurements.** The type III measurements were intended to further investigate the uniformity of the apparent flapping motion. Locating both probes on either side of the jet, but one slightly upstream of the other, gives insight as to the propagation of the apparent flapping type behavior. The cross correlations were measured as one probe was fixed at a certain $x/d$ and the other alternatively moved in steps of 2d downstream. Figure 9 presents one set of the many measured cross correlations. It exhibits a convected pattern where the time delay for a maximum negative correlation shifts by a time $\Delta\tau$ as the probes are $\Delta x$ apart. This indicates that the apparent flapping like behavior as detected at a given longitudinal station can still be sensed with considerable coherence some time later at a downstream location.

A convection velocity for the apparent flapping can be defined by the limit

$$U_{cf} = \frac{\Delta x}{\Delta \tau}\bigg|_{\Delta x \to 0} \tag{7}$$

$\Delta x$ and $\Delta\tau$ can be plotted for each set of curves; an extrapolation to a zero separation distance would permit a measure of $U_{cf}$. Table 3 presents the results and compares them to the data in [5] who, in the same setup, measured the turbulent convective velocity $U_c$ (defining the apparent motion of the turbulent structure). These two velocities are noted to be different, with a lower value for the apparent flapping motion.

**Type IV Measurements.** Autocorrelation functions of the $y$-component of the velocity were determined along the jet centerline at $x/d$ stations of 20, 30, 40, 60, and 80. The data should obviously give the normal autocorrelation function for small delay times, with a maximum (equal to the mean square

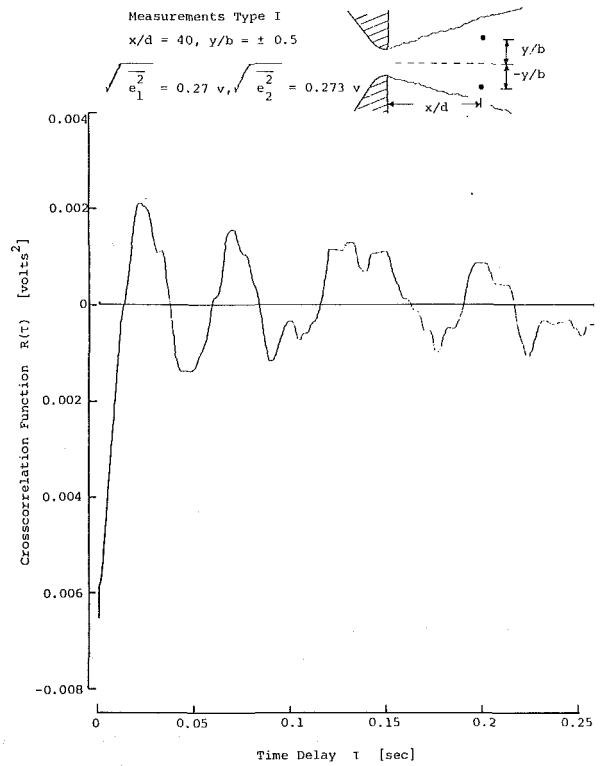


Fig. 2(*a*) Cross correlation function for $x/d = 40, y/b = \pm 0.5$ (Type I)

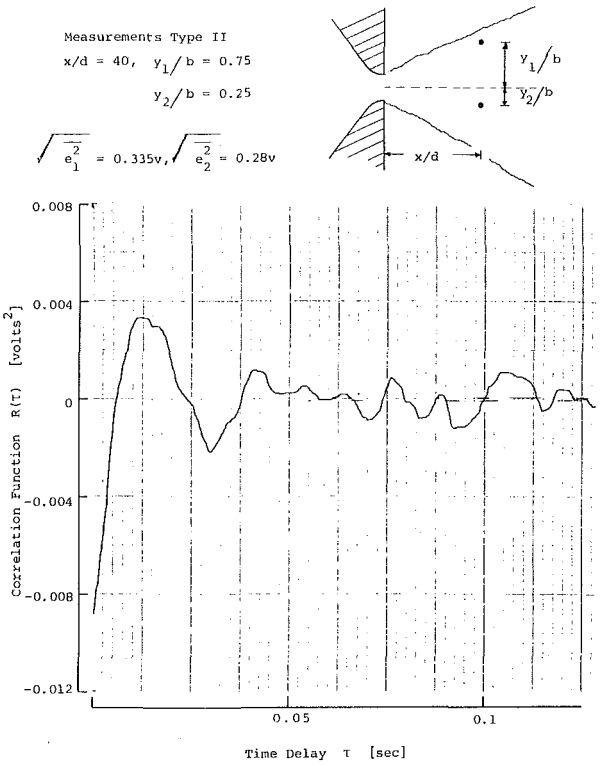


Fig. 2(*c*) Cross correlation function for $x/d = 40, y_1/b = 0.75, y_2/b = -0.25$ (Type II)

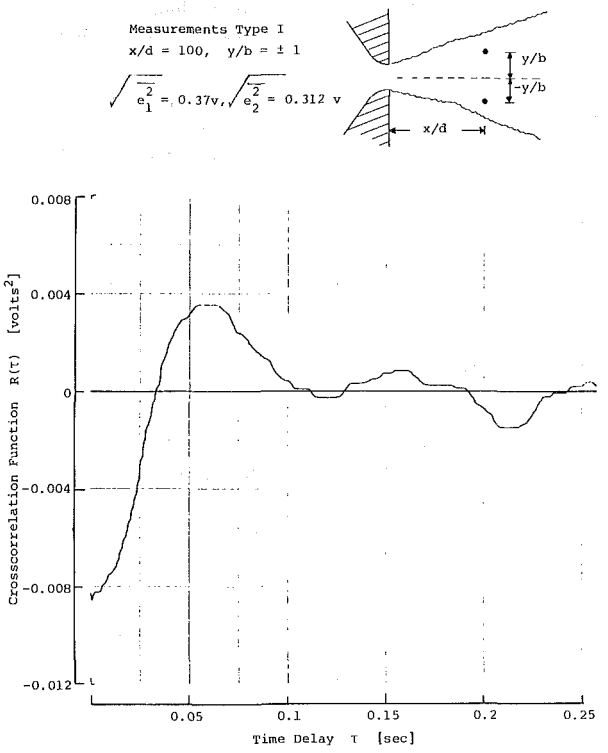


Fig. 2(*b*) Cross correlation function for $x/d = 100, y/b = \pm 1$. (Type I)

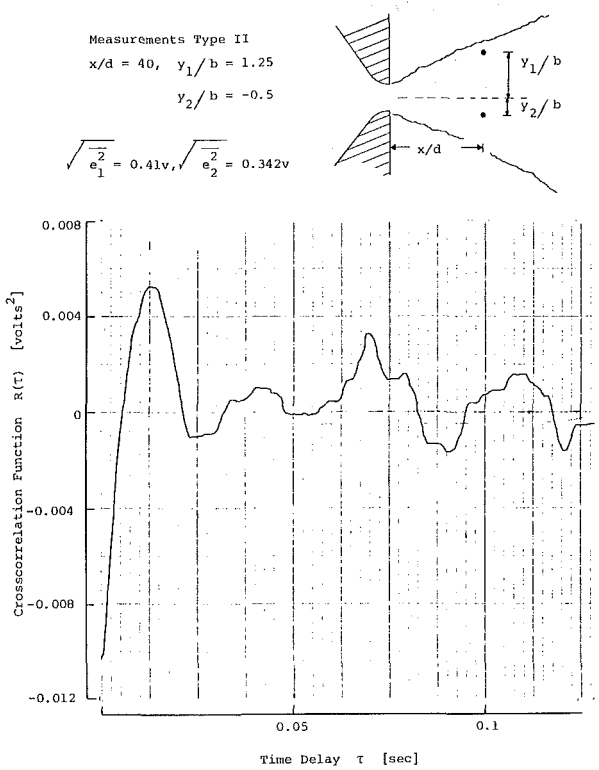


Fig. 2(*d*) Cross correlation function for $x/d = 40, y_1/b = 1.25, y_2/b = -0.5$ (Type II)

value of the signal) at $\tau = 0$. However, for large delay times, the apparent flapping motion (if at all present) should be accompanied by alternatively positive and negative values of the autocorrelation. The results, with a single $x$-wire suffered in signal resolution but did indeed show the expected trends. Figure 10 shows a sample plot at $x/d = 40$. Data were taken at $x/d = 20$ and 80 as well.

The plots are pseudo-oscillatory as the time delay increases, consistent with the previously described cross correlation functions of the x-component of the velocity. The dimen-

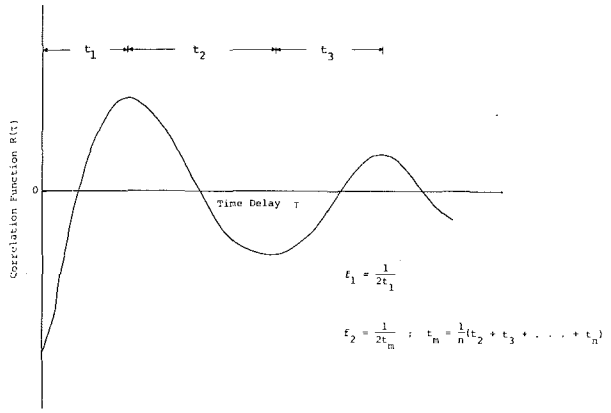


**Fig. 3 Definition of apparent flapping frequency**

sionless apparent flapping frequency can be determined as before and compared with the results of Type I and II data, Fig. 11, favourably confirming the trends noted earlier. (Data of the type I, II or III but based on correlations of the lateral velocity component would have been desirable but was not taken. It would have required four hot wire anemometers.)

## Conclusions and Observations

The following conclusions and observations can be established, based on the experimental results:

1 The apparent flapping motion of a turbulent plane jet is a distinctive and measurable natural phenomenon. This was confirmed by the reported data, spot-checks at two other jet set-ups (not reported herein) and by a previous preliminary investigation, [1].

2 The frequency of the apparent flapping motion decreases in the longitudinal direction and remains unchanged in the lateral direction (within the regions tested).

3 Approximate self-preservation is obtained for the apparent flapping frequency (for $x/d > 30$), if scaled with the centerline mean velocity and the half-width of the jet, giving $fb/U_m \simeq 0.11$.

4 An estimate of the amplitude of apparent flapping gave values in order of 20 percent of the jet half-width.

5 The dimensionless frequency of apparent flapping is independent of the Reynolds number in the range $7900 \leq \mathrm{Re} \leq 15100$.

6 Were the apparent flapping motion to be caused by some overall flapping behavior of the jet then it would be expected to satisfy a travelling wave solution which in turn would not exhibit self-preservation. The fact that the results exhibit self-preservation suggest then that the apparent flapping motion is not due to an overall sideways motion of the jet.

7 Comparing the measured apparent flapping frequencies with the frequency of the structures responsible for intermittency (see for instance ([3,6, and 7]) shows these to be of the same order. This suggests that the apparent flapping motion is attributed to a local large scale motion resulting from an organized coherent structure within the jet's turbulent field.

8 Noting that: (*a*) the apparent flapping frequencies correspond to those of the intermittency (driven by large scale structures), (*b*) the convective velocity of the apparent flapping motion can be seen to correspond to the wave speed of a travelling wave solution, and (*c*) the motions noted are self-preserving, suggests that large scale motions exist which on occasion develop in such a way that the scales are appropriate to a travelling wave solution. However due to the nature of turbulence, this travelling wave would not exist for very long. It could be compared to a suitable large structure occasionally exciting the jet leading to the brief existence of a wave packet exhibited as an oscillation in the correlation curves.

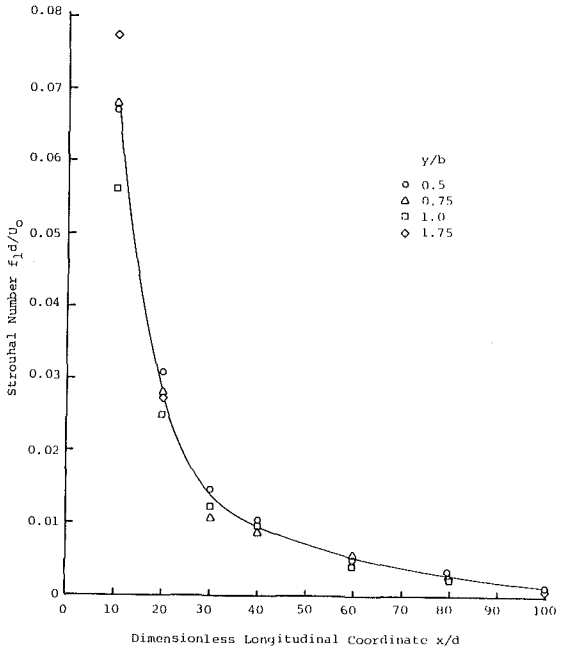


**Fig. 4(*a*) Strouhal number $f_1 d/U_0$ versus $x/d$ (uncertainty in the order of 15 percent)**

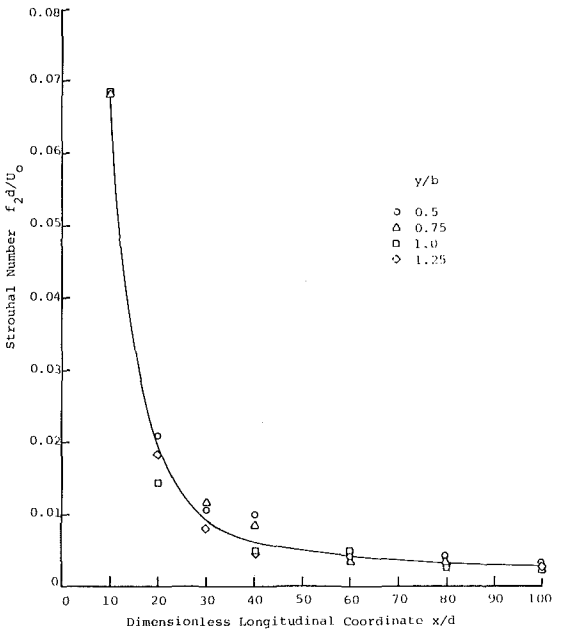


**Fig. 4(*b*) Strouhal number $f_2 d/U_0$ versus $x/d$ (uncertainty in the order of 15 percent)**

## Acknowledgments

The work reported was sponsored in part by the Mexican Government, in a fellowship to the first author through CONACYT. Support from the NSF and ONR in various phases of the research in part reported herein is also gratefully acknowledged. Aspects of the final work were written while the second author was hosted by the Department of Mechanical Engineering (as a Fulbright Scholar) at the University of Queensland. Their assistance, and that of the

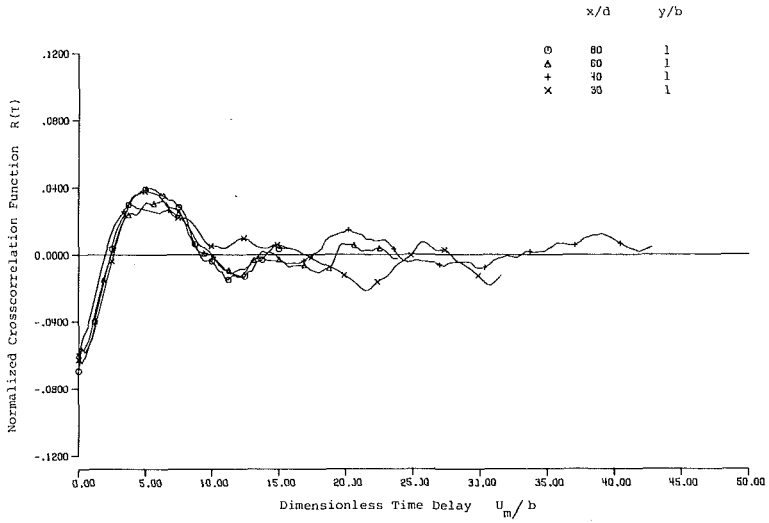


Fig. 5 Normalized cross correlation functions

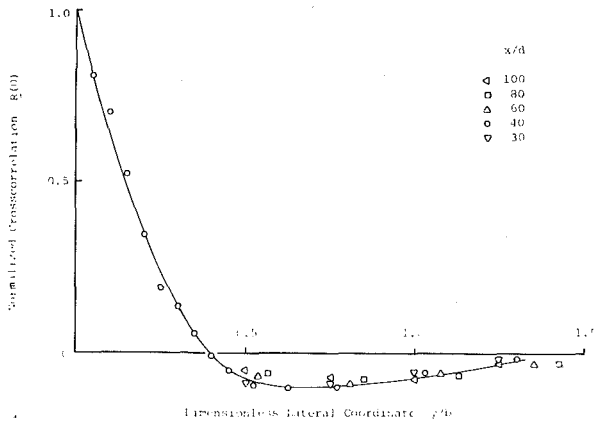


Fig. 6 Normalized cross correlation $R(0)$ versus $y/b$ (uncertainty in the order of 10 percent)

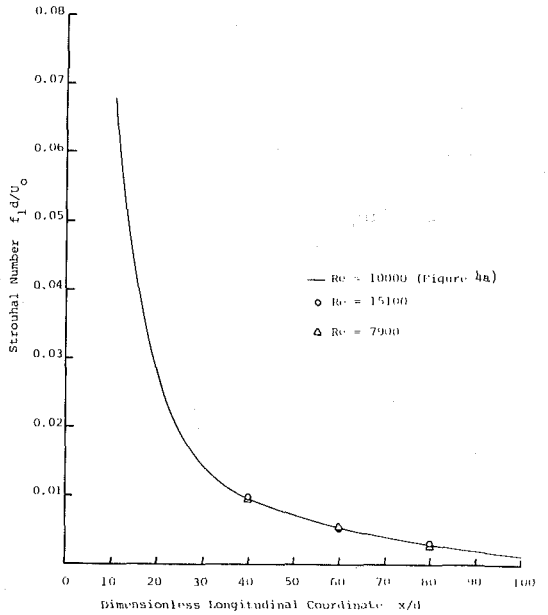


Fig. 7 Strouhal number $f_1 d/U_0$ versus $x/d$ at different Reynolds numbers (uncertainty in the order of 15 percent)

**Table 2 Estimated amplitude of apparent flapping (uncertainty estimated to be in the order of 20 percent)**

| $x/d$ | $y/b$ | $\epsilon_m/b$ |
|---|---|---|
| 80 | 1.13 | 0.18 |
| | 0.85 | 0.21 |
| | 0.56 | 0.18 |
| 60 | 1.07 | 0.17 |
| | 0.80 | 0.19 |
| | 0.53 | 0.23 |
| 40 | 1.03 | 0.15 |
| | 0.77 | 0.16 |

**Table 3 Convective velocities of flapping (with an estimated uncertainty in the order of 20 percent)**

| $x/d$ | $y/b$ | $U_{cf}/U$ | $U_{cf}/U_m$ | $U_c/U^{(a)}$ |
|---|---|---|---|---|
| 10 | 1 | 1.16 | 0.58 | |
| 20 | 1 | 1.28 | 0.64 | 1.68 |
| 30 | 1 | 1.15 | 0.57 | 1.43 |
| 40 | 1 | 1.23 | 0.61 | 1.58 |
| 20 | 0.65 | 0.99 | 0.74 | 1.18 |
| 30 | 0.65 | 0.94 | 0.70 | 1.1 |
| 40 | 0.65 | 1.01 | 0.75 | 1.18 |

(a) Measurements by Young, reference [5].

Australian-American Educational Foundation are ackowledged as well. The authors also acknowledge the perceptive comments and positive criticism of an anonymous reviewer, providing the essence of the last observation listed above.

## References

1 Goldschmidt, V.W. and Bradshaw, P. "Flapping of a Plane Jet," *The Physics of Fluids*, Vol. 16, 1973, pp. 354-355.

2 Cervantes, J.G., "An Experimental Study of the Flapping Motion of a Turbulent Plane Jet," Ph.D. thesis, Purdue University, 1978. (Also available as Herrick Labs Report 78-40).

3 Bradbury, L.J.S., "The Structure of a Self-preserving Turbulent plane Jet," *J. Fluid Mech.*, Vol. 23, 1965, pp. 31-64.

4 Gutmark, E., and Wygnanski, I "The Planar Turbulent Jet.," *J. Fluid Mech.*, Vol. 73, 1976, pp. 465-495.

5 Young, M.F., "A Turbulent Study: Convective Velocities, Energy, Spectra and Turbulent Scales in a Plane Air Jet," M.S.M.E., thesis 1973, Purdue University.

6 Oler, J.W., "Coherent Structures in the Similarity Region of a Two-Dimensional Turbulent Jet: A Vortex Street," Ph.D. thesis, Purdue University.

7 Everitt, K.W., and Robins, A.G., "The Development and Structure of a Turbulent Plane Jet," *JFM*, Vol. 88, No. 3, 1978, pp. 563-568.

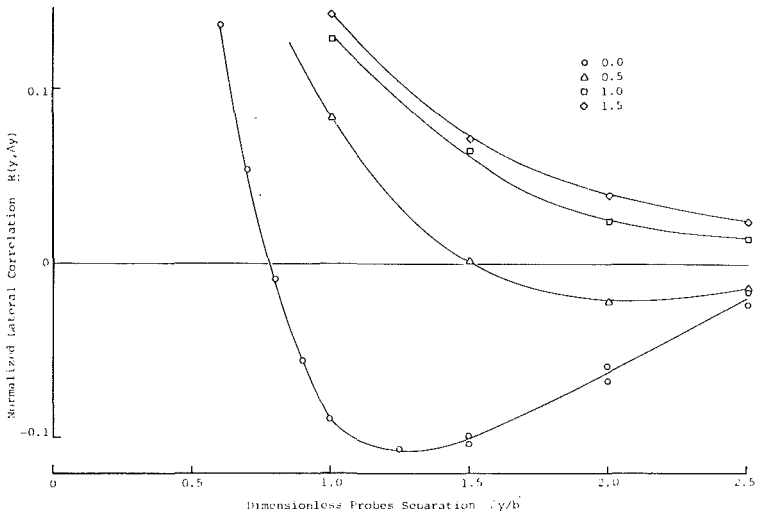


**Fig. 8 Normalized lateral correlation ($y$ now equals $(y_1 + y_2)/2$) (uncertainty in the order of 10 percent)**

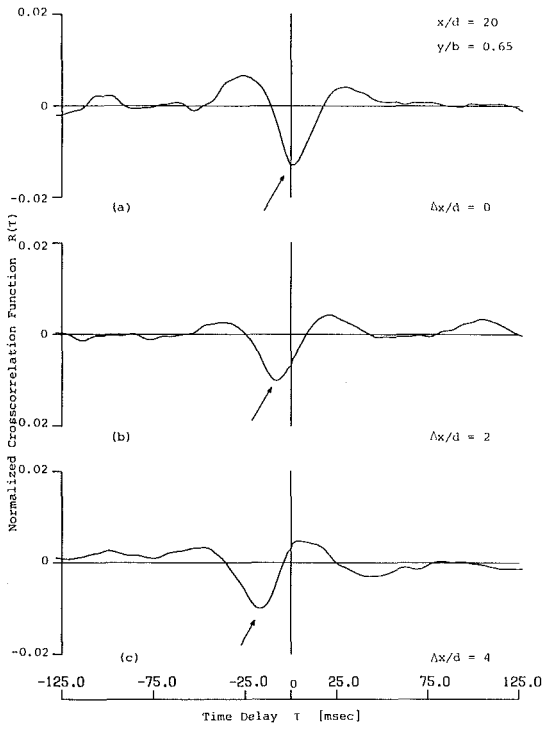


**Fig. 9 Type III Cross correlation functions, $x/d = 20$, $y/b = 0.65$**

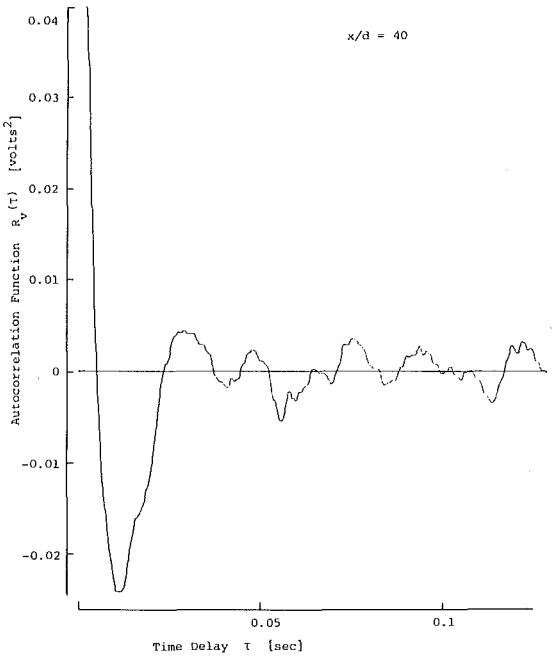


**Fig. 10 Auto correlation of the $v$-component ($x/d = 40$, $y = 0$)**

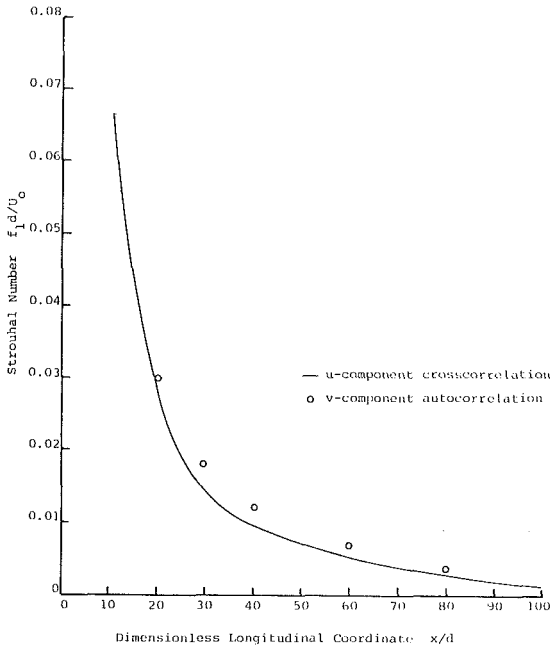


**Fig. 11 Strouhal number $f_1 d/U_0$ versus $x/d$**

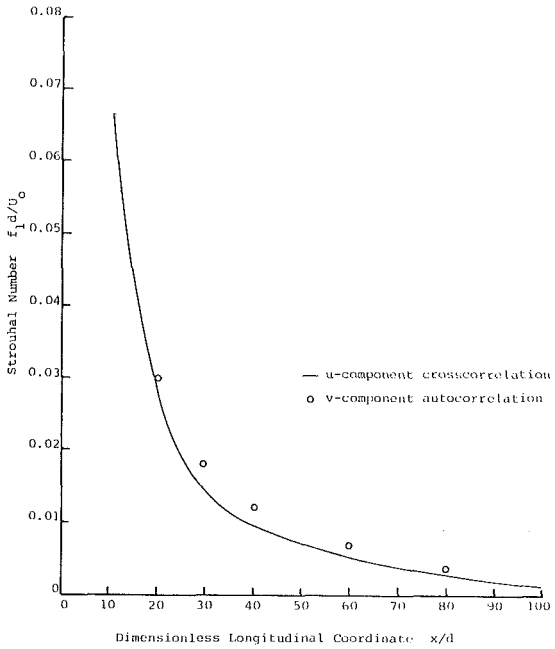


**Fig. 11 Strouhal number $f_1 d/U_0$ versus $x/d$**

## DISCUSSION

### P. Bradshaw[1]

This work seems to be an admirably conclusive demonstration that a distinct "flapping" correlation exits between the two sides of a jet, and that, at least in a jet with uniform exit flow, the flapping is a real part of the turbulence structure rather than an effective disturbed boundary condition. One now asks whether the correlation is entirely the result of pressure fluctuations ("irrotational motion") or whether the large eddies (i.e. vortical motions) extend significantly across the jet center line. In the former case one could still argue that the interaction between the two sides was weak enough to be ignored in turbulence modelling. The point might be settled by pressure-velocity correlations, or, better, by velocity correlations in and near a jet in a slow external stream, so that the irrorational field could be deduced from velocity fluctuations just outside the turbulent zone.

[1] Professor of Experimental Aerodynamics, Imperial College, London, England.

### Authors' Closure

We are grateful for Professor Bradshaw's comments. Only future and further research will authoritatively answer whether or not the correlation is due to pressure fluctuations or to large eddies. Recent photographs taken by K. Moallemi (M.S. thesis, Purdue University, 1980) tend to support the latter. "Smoke wire" visualization in the outer flow shows large scale structures extending well beyond the jet centerline even at positions as far as $X/D = 60$.

**S. E. Elghobashi**
Assistant Professor.
Mem. ASME

**G. S. Samuelsen**
Associate Professor.
Mem. ASME

Mechanical Engineering,
University of California,
Irvine, Calif.

**J. E. Wuerer**
Senior Scientist,
Spectron Development Laboratories, Inc.,
Costa Mesa, Calif.

**J. C. LaRue**
Assistant Research Engineer and Lecturer,
University of California,
San Diego, Calif.

# Prediction and Measurement of Mass, Heat, and Momentum Transport in a Nonreacting Turbulent Flow of a Jet in an Opposing Stream

*The paper addresses the measurement and prediction of heat, mass, and momentum transport in a confined axisymmetric turbulent nonreacting flow of a jet in an opposing stream. The predictions are obtained by solving numerically the conservation equations of the mean flow and the transport equations of the kinetic energy of turbulence and its dissipation rate and the mean square temperature fluctuations. The predicted velocity field is in agreement with the experiment, but the predicted scalar fields point to the need of examining the employed model of a scalar turbulent diffusion.*

## Introduction

The present capabilities of methods available to predict turbulent, reacting flows with recirculation have been demonstrated in studies directed to the evaluation of combustor performance (e.g., [1–3]). The results, though encouraging, suggest that systematic testing is needed to validate the mathematical models employed by such methods. For example, well controlled experiments need to be conducted, and complexities need to be introduced one at a time. A major requirement of such an approach is to first test the performance of the models against the experiment in the absence of reaction and heat release.

In earlier work, tests for the description of mass and momentum transport have been conducted in the absence of reaction and heat release [4, 5]. The present investigation extends the tests to include the transport of heat.

The flow configuration consists of a turbulent pipe flow with an on-axis jet opposing the main flow (Fig. 1). A highly turbulent recirculation zone results from the interaction of the two flows. The flowfield has distinctive features that make it particularly attractive from both experimental and analytical viewpoints. First, the recirculation zone is not attached to solid walls. Secondly, the range of velocity gradients, turbulence levels, and mixing lengths is increased over that offered by bluff bodies. The isolation of the recirculation zone from solid boundaries frees the analysis from complicated questions associated with the boundary condition specifications, while the extension of the range of turbulence

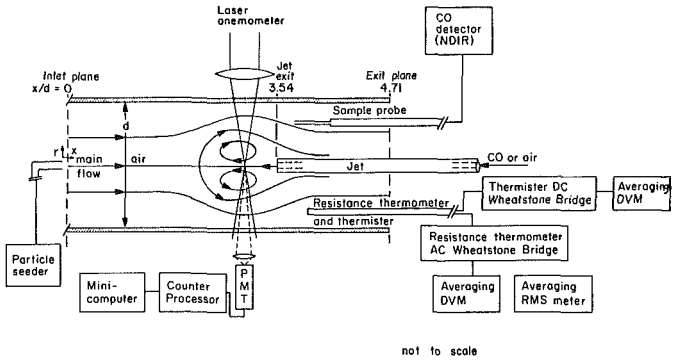


**Fig. 1 Schematic of experimental apparatus**

phenomena provides a broad test of the mathematical models involved in the flowfield predictions.

In the present case, the accuracy of the predicted mass transport was assessed by comparing the predicted and measured axial and radial transport of a tracer species, carbon monoxide, which was introduced through the jet with experimental data. Momentum transport was assessed by comparing predicted values of velocity and turbulence intensity with their measured values. Heat transport was assessed by heating the jet and comparing predicted values of mean and RMS temperature with experimentally measured values.

## Experiment

**Geometry.** The experimental apparatus (Fig. 1) consisted of a 51 mm inside diameter (3 mm wall) by 240 mm long cylindrical Vycor (transparent quartz) tube containing an

Contributed by the Fluids Engineering Division for publication in the JOURNAL OF FLUIDS ENGINEERING. Manuscript received by the Fluids Engineering Division, November 27, 1979.

**Table 1 Operating conditions**

| Variable | Cold flow | | Heated flow | |
|---|---|---|---|---|
| $U_{m,i}$ (m/s) | 7.5 | 15 | 7.5 | 15 |
| Mach No. | 0.025 | 0.05 | 0.025 | 0.05 |
| $Re_i$ | 25000 | 50000 | 25000 | 50000 |
| $U_{m,j}$ (m/s) | 135 | | 153 | |
| Mach, $j$ | 0.4 | | 0.4 | |
| $Re_j$ | 11000 | | 12500 | |
| $T_i$ $(K)$ | 295 | | 295 | |
| $T_j$ $(K)$ | 295 | | 327 | |
| Main flow fluid | air | | air | |
| Jet flow fluid | CO | | air | |

opposing axisymmetric jet. The diameter of the jet was 1.3 mm and the jet exit was located at $x/d = 3.54$ (i.e., 180 mm from the inlet plane). The jet tube was a circular cylinder with an outside diameter of 6.4 mm. The exit plane of the tube was located at $x/d = 4.71$.

**Operating Conditions.** Table 1 summarizes the four experimental operating conditions considered in this study.

**Velocity Measurements.** Velocity measurements were made using a laser anemometer system. One thousand samples of instantaneous velocity were taken at each measurement point within the flowfield. These measurements allowed the subsequent determination of the time-mean and root mean square values of the axial velocity.

The laser anemometer system was operated in a differential doppler mode using forward scattered light collection. Two beams, split from a 15 mw helium-neon laser (Spectra-Physics Model 124B), were focused through a 250 mm lens to form a fringe spacing of 1.69 $\mu$m. A 40 MH frequency shift (TSI Model 915 Bragg Cell) was applied to one beam to resolve ambiguity of velocity direction over the wide dynamic range observed in the highly turbulent flow. Signal validation was obtained using a counter processor (Macrodyne Model 2098). The data were reduced by a minicomputer (DEC Model PDP 11/10). The main flow was seeded with approximately 1 $\mu$m sodium chloride particles. The jet was not seeded in the present experiment. Velocity measurements in the recirculation zone are therefore biased to the main flow within a region bounded by approximately $r/R < 0.3$ and $x/d > 2.5$.

**Concentration Measurements.** The local concentration of the CO tracer species was measured using a continuous probe sampling system in conjunction with a nondispersive infrared analyzer (Beckman Model 915BL). The probe was constructed of capillary tubing (1.25 mm O.D.) to minimize probe perturbation effects. This technique provided local time-averaged concentration measurements. The use of a tracer species having essentially the same molecular mass as that of the main flow avoided biasing errors associated with density fluctuations. Repeated measurements at the same nominal position in the flow indicated that the variation in CO measurement is less that 10%. The repeated measurements included the evaluation of probe perturbation by using independently three probes, each with a unique angle of approach to the sampling point (straight $-0$ deg, angle $-90$ deg, hook $-180$ deg).

**Temperature Measurements.** The temperature signals were obtained by means of 0.125 mm diameter glass coated thermisters and a 1.25 $\mu$m diameter resistance ("cold wire") thermometer. The cold wire were platinum and 0.48 mm in length for $U_{m,i} = 7.5$ m/s, and platinum $-$ 10 percent rhodium and 0.66 mm in length for $U_{m,i} = 15.0$ m/s. The cold wires were operated with a root mean square current of 255 microamperes.

## Nomenclature

$C_\mu, C_1, C_2, C_{T1}, C_{T2}$ = constants in the turbulence model
$d$ = diameter of the large tube
$D$ = molecular diffusivity
$f$ = fluctuation of $F$
$F$ = mass fraction of carbon monoxide
$F_v$ = volume fraction of carbon monoxide
$G$ = production of the turbulence kinetic energy
$h$ = enthalpy fluctuation
$H$ = stagnation enthalpy
$k$ = kinetic energy of turbulence = $\frac{1}{2}\overline{u_i u_i}$
$p$ = mean static pressure
$r$ = radial distance
$R$ = radius of the large tube
$T$ = time-mean temperature
$T'$ = RMS temperature fluctuation
$U_i, u_i$ = mean and fluctuating velocities (tensor notation) in direction $x_i$
$x_i$ = distance coordinate
$\Gamma$ = thermal diffusivity of the fluid
$\delta_{ij}$ = Kronecker delta
$\epsilon$ = rate of dissipation of turbulence kinetic energy, k
$\Theta$ = time-mean temperature difference = $T - T_i$
$\Theta_{max}$ = max time-mean temperature difference = $T_j - T_i$
$\mu_{eff}$ = effective eddy viscosity
$\nu$ = kinematic viscosity of the fluid
$\rho$ = fluid density
$\sigma_k, \sigma_\epsilon, \sigma_H, \sigma_T$ = turbulent Prandtl/Schmidt numbers
$\tau_{ij}$ = stress tensor

Subscripts

C.L. = center line
$i$ = condition at the inlet of the large tube, except when used in tensor notation
$j$ = condition at the jet exit, except when used in tensor notation
$m$ = average axial velocity at a given axial location
max = maximum value

Superscripts

$'$ = fluctuating component
$\overline{\quad}$ = time-averaged value

The measurement of the mean and in particular the root mean square temperature fluctuations requires care and attention in the selection of the geometrical and operating characteristics of the sensor. For example, the sensor length must be much smaller than the length scales associated with the energy containing eddies so as to minimize the effects of spatial averaging [6] but the sensor length must be long enough so that sensor supports have a negligible effect on the sensor response [7-9]. The sensor current must be high enough so that there is a reasonable signal to noise ratio but the current must be low enough so that the sensitivity to velocity is negligible [10]. In addition, the sensor diameter must be small enough so that the corresponding frequency response is higher than that corresponding to the energy containing scales but must be large enough so that the sensor is mechanically robust.

The frequency response at 15 m/s of the thermister and associated d.c. bridge was estimated to be no more than 1Hz, while the frequency response of the cold wires was estimated to be about 1.5kHz [10]. The length scales and frequencies of the energy containing eddies are estimated to be half the radius of the main tube (i.e. 1.25 cm), which at a velocity of 15 m/s corresponds to a frequency of 1.2kHz. Thus the lengths of both sensors are small enough so as to permit the measurement of mean temperature while the length and frequency response of the cold wire permit the measurement of the root mean square temperature. The velocity sensitivity based on the results of reference [10] is estimated to be at most $3.0 \times 10^{-3}$ °C (m/s) − 1. Typical errors in the mean and in the root mean square temperature are respectively 0.01 and 0.02 °C. Thus the error due to velocity sensitivity is negligible compared to the mean temperature which is nominally 1 °C.

The reduction in the measured root mean square temperature relative to the true mean square temperature due to heat conduction to the sensor support is estimated to be less than 12 percent [8].

The accuracy of the measured mean and root mean square is also related to the averaging and data reduction procedure. Both sensors and associated electronics were directly calibrated as a function of temperature so that the output was directly interpretable in terms of temperature, $\Theta(x,y,z,t)$, measured relative to the fluid temperature in the undisturbed pipe flow. The mean temperature from both the thermister and resistance thermometers was obtained by means of an averaging voltmeter, while the root mean square temperature was obtained by means of an averaging root mean square voltmeter. Averaging times of 10-30 seconds were used to obtain the statistical quantities reported herein. These averaging times correspond to averaging of at least 3500 integral time scales which should be adequate so as to insure good statistical reliability. Repeated measurements at the same nominal position in the flow indicate that the variation in relative mean temperature is less that 15 percent and that of the root mean square temperature is less that 5 percent. The primary reason that the variance of the relative mean temperature is greater than that of the root mean square temperature is that the former is determined from the differences of two variables ($T_i$ and $T$), which are the same order of magnitude, while the latter is obtained directly.

Consideration of all the sources of error discussed in the proceeding indicates that the error in the measured and root mean square temperature is less than 15 percent.

## Mathematical Model

**The Mean Flow Equations.** The equations[1] which describe the conservation of mass, momentum, energy and inert species in a turbulent flow are, respectively:

$$\frac{\partial}{\partial x_i}(\rho U_i) = 0 \tag{1}$$

$$\frac{\partial}{\partial x_i}(\rho U_i U_j) = -\frac{\partial p}{\partial x_i} - \frac{\partial \tau_{ij}}{\partial x_i} \tag{2}$$

$$\frac{\partial}{\partial x_i}(\rho U_i H) = \frac{\partial}{\partial x_i}\left(\Gamma \frac{\partial H}{\partial x_i} - \rho \overline{u_i h}\right) \tag{3}$$

$$\frac{\partial}{\partial x_i}(\rho U_i F) = \frac{\partial}{\partial x_i}\left(D \frac{\partial F}{\partial x_i} - \rho \overline{u_i f}\right) \tag{4}$$

In equations (1) to (4), terms involving density fluctuations have been neglected. This is justified in the flows under consideration for the following reasons. In the isothermal case the molecular mass of carbon monoxide and air are almost equal. In the case of the heated jet, the difference between the inlet mean temperatures of the jet and the main flow represents only 10 percent of the main flow temperature.

For the axisymmetric geometry of Fig. 1, two momentum equations (for the axial and radial directions) are required. The five equations (1)-(4) form a closed set when $\tau_{ij}$, $\overline{u_i h}$, and $\overline{u_i f}$, are known. This is discussed in the next section.

**The Turbulence Model.** In order to close the above set of equations the stress tensor $\tau_{ij}$, and turbulent heat flux $\rho \overline{u_i h}$ and the inert species turbulent mass flux $\rho \overline{u_i f}$, are evaluated by means of the standard $k-\epsilon$ turbulence model. In this model, the components of $\tau_{ij}$ are calculated from the following algebraic relation:

$$\rho \overline{u_i u_j} = \frac{2}{3}\rho k \delta_{ij} - \mu_{\text{eff}}\left(\frac{\partial U_i}{\partial x_j} + \frac{\partial U_j}{\partial x_i}\right) \tag{5}$$

where

$$\mu_{\text{eff}} = c_\mu \rho k^2/\epsilon \tag{6}$$

In the foregoing equations $k$ is the kinetic energy of turbulence ($k = 1/2\, u_i u_i$) and $\epsilon$ is the rate of dissipation of that energy ($\epsilon = \nu\ (\partial u_i/\partial x_i)^2$). The spatial distribution of $k$ and $\epsilon$ are obtained from the solution of the following transport equations:

$$\frac{\partial}{\partial x_i}(\rho\, U_i\, k) = \frac{\partial}{\partial x_i}\left(\frac{\mu_{\text{eff}}}{\sigma_k}\frac{\partial k}{\partial x_i}\right) + G - \rho\epsilon \tag{7}$$

$$\frac{\partial}{\partial x_i}(\rho\, U_i\, \epsilon) = \frac{\partial}{\partial x_i}\left(\frac{\mu_{\text{eff}}}{\sigma_\epsilon}\frac{\partial \epsilon}{\partial x_i}\right) + (C_1\, G - C_2\, \rho\epsilon)\frac{\epsilon}{k} \tag{8}$$

$$G = -\rho\, \overline{u_i u_j}\frac{\partial U_i}{\partial x_j} \text{ and} \tag{9}$$

$C_1$ and $C_2$ are constants.

The transport equation for the mean square fluctuation of temperature which is solved simultaneously with the above set of equations is:

$$\frac{\partial}{\partial x_i}(\rho\, U_i\, \overline{T'^2}) = \frac{\partial}{\partial x_i}\left(\frac{\mu_{\text{eff}}}{\sigma_T}\frac{\partial \overline{T'^2}}{\partial x_i}\right) + G_T - C_{T2}\,\rho\,\overline{T'^2}\,\frac{\epsilon}{k} \tag{10}$$

where

$$G_T = C_{T1}\,\mu_{\text{eff}}\left[\frac{\partial T}{\partial x_i}\right]^2 \tag{11}$$

and $C_{T1}$ and $C_{T2}$ are constants.

[1] The equations 1,2,3,4,7,8,10 are quoted here in terms of Cartesian tensors for compactness. Their cylindrical-polar coordinates form is used to obtain the present results.

Table 2

| $C_\mu$ | $C_1$ | $C_2$ | $\sigma_k$ | $\sigma_\epsilon$ | $C_{T1}$ | $C_{T2}$ | $\sigma_T$ |
|---|---|---|---|---|---|---|---|
| 0.09 | 1.43 | 1.92 | 1.0 | 1.09 | 2.8 | 1.4 | 0.9 |

The set of constants used in the turbulence models are given in Table 2.

The values of the first five constants are adopted from Launder and Spalding [11]. The value of $C_{T1}$ was first obtained from comparisons with experimental data of concentration fluctuations in isothermal flows [12]. The value of $C_{T2}$ adopted in [13] was 2; however, the value used here, 1.4, is consistent with the experimental data of the decay of scalar fluctuations in grid turbulence [14], [15].

**The Boundary Conditions.** To complete the mathematical formulation, boundary conditions must be specified along the boundaries of the integration domain. Along the symmetry axis, the radial gradient vanishes for all variables except the radial velocity which equals zero. The inlet velocity profiles for the main flow are specified from the experimental data; for the jet the profile is assumed to be of the plug type. The values of $k$ and $\epsilon$ at the inlet planes are prescribed by specifying the intensity and the scale of turbulence at the inlet.

At the exit plane, it is assumed that the axial gradients for all variables are zero. Along the top cylindrical wall, the axial and radial velocities equal zero. The wall functions [1] are used to calculate the values of the generation and dissipation of k and $\epsilon$ at the near wall node based on the assumption of Couette flow.

**The Numerical Solution Procedure.** The set of equations (1-4), (7), (8), (10) described above, together with their boundary conditions, was solved by an iterative finite difference procedure based on the Simple algorithm of Patankar and Spalding [16], but modified for elliptic flows. The grid refinement tests were carried out using three nonuniform grids: $16\times12$, $25\times12$, and $25\times20$, where the larger number of nodes was in the axial direction. The $25\times20$ grid was employed for the computations presented here.

A typical CPU time required for achieving a converged solution (300 iterations) was 5 minutes on a DEC 10 computer (equivalent to CDC 6400). The convergence criterion employed is that the maximum residual $R_\phi$ is less than $10^{-4}$, where $R_\phi$ = (convection + diffusion + source)/$\phi_{\text{reference}}$, and $\phi$ is the dependent variable solved for.

## Results and Discussions

The experimental and predicted results are presented for the cold and heated flows at 15 m/s and 7.5 m/s inlet velocities in Figs. 2 through 8. These include radial profiles of the time-mean axial velocity, the distribution of kinetic energy of turbulence along the center line of the tube, the radial profiles of the time-mean and the RMS temperature, and radial profiles of CO volume-fraction.

**The Time-Mean Axial Velocity.** Figure 2 shows the radial distributions of $(U/U_{\text{C.L.},i})$ at two axial locations ($x/d$ = 2.95, 3.15) for both the cold and heated flows with $U_{m,i}$ = 15 m/s. At these stations velocity measurements were obtained at radial locations of $r/R$ equal to or greater that 0.2 due to the biasing adjacent to the center line that was caused by the absence of seeding in the jet. At these radial locations, the predicted velocities are in fair agreement with their experimental values.

The two velocity profiles of the cold flow indicate that the stagnation point along the centerline of the jet lies between the two stations of $x/d$ = 2.95 and $x/d$ = 3.15 where the normalized center-line velocity drops from 0.4 to −1.0. The

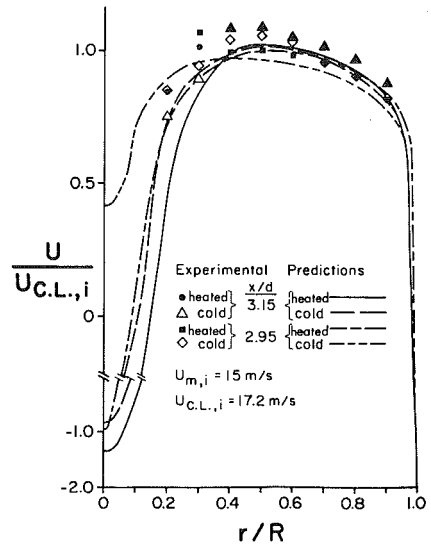


Fig. 2 Radial profiles of time-mean velocity (15 m/s)

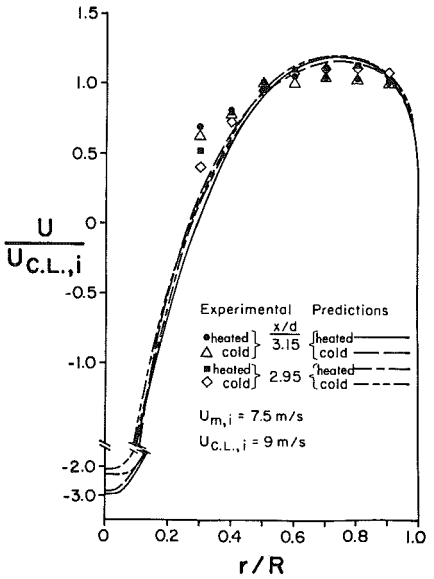


Fig. 3 Radial profiles of time-mean velocity (7.5 m/s)

respective profiles for the heated jet demonstrate that its stagnation point is located upstream the station of $x/d$ = 2.95, i.e. the recirculation zone is longer for the heated than for the cold jet.

The predicted center line velocities for the heated flow attain larger negative values compared to their values in the cold flow. This is because the velocity of the heated jet is approximately 11 percent higher than that of the cold jet. The momentum of the jet is 21 percent and 27 percent, respectively, of that of the main flow for the cold and heated cases.

Figure 3 shows that radial distributions $U/U_{\text{C.L.},i}$ at the same axial stations for $U_{m,i}$ = 7.5m/s. The experiments and predictions depict similar behavior to that of the high velocity case, except that the magnitudes of the negative velocities at the centerline are much larger (almost twice as large) than

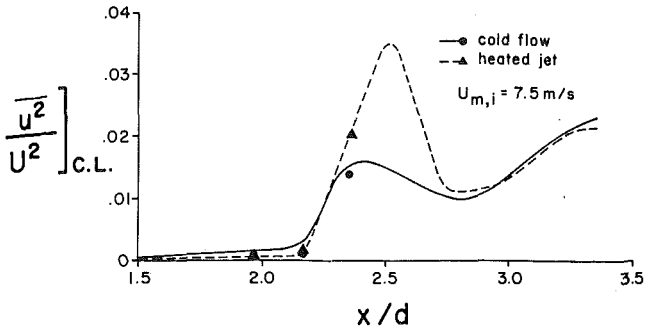


Fig. 4 Axial distribution of turbulence intensity

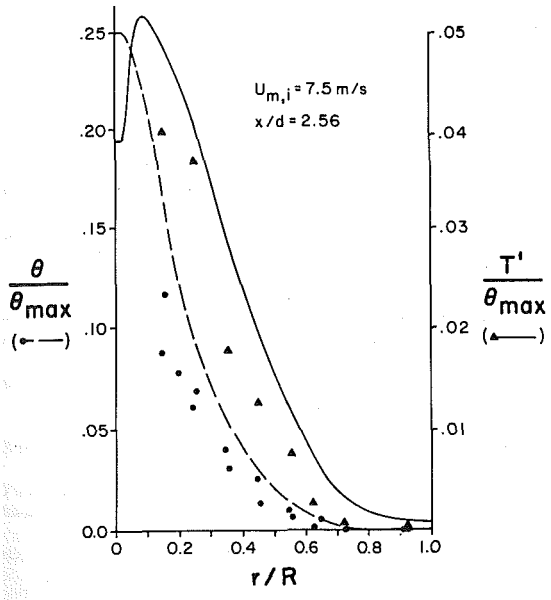


Fig. 5 Radial profiles of time-mean and RMS temperature fluctuation

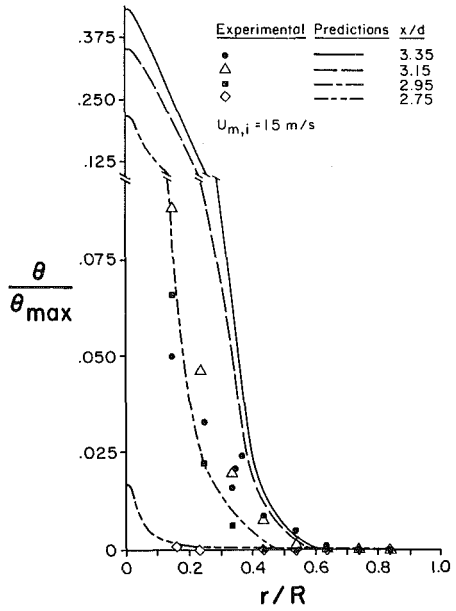


Fig. 6 Radial profiles of time-mean temperature (15 m/s)

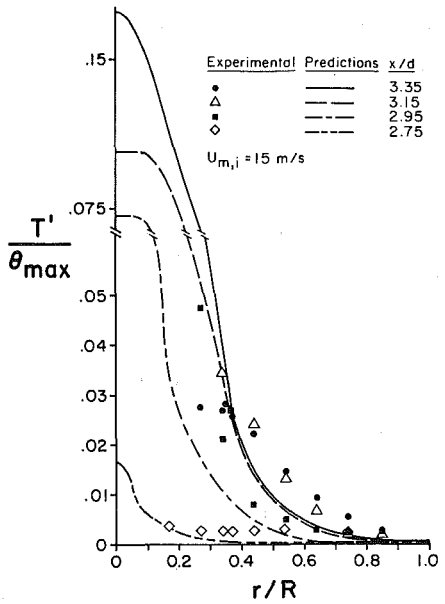


Fig. 7 Radial profiles of RMS temperature fluctuation

before. The reason is that the momentum of the main flow is only 25 percent of that of the high velocity case.

**The Kinetic Energy of Turbulence.** Figure 4 displays the predicted distribution of $(u^2/U^2)_{C.L.}$ for the cold and heated flows of $U_{m,i}$ = 7.5m/s. The value of $u^2$ was approximated as (2/3)k. In the cold flow, the first peak of the turbulence intensity along the centerline is associated with the boundary of the recirculation zone at $x/d \approx 2.5$. The second peak (at $x/d \approx 3.4$) is just upstream of the jet exit ($x/d \approx 3.54$) where the boundary of the small diameter (1.3mm) jet with large negative velocity interacts with the much slower mainstream. At that station, the production of k reaches a maximum at the shear layer between the two flows and is then transported to the axis. It is seen that the first peak in the heated flow is farther from the jet exit than in the cold flow. This is consistent with the discussion of the mean velocity results. The experimental values of $(u^2/U^2)_{C.L.}$ at the three axial locations are shown for both the cold and heated flows. These locations are outside the recirculation zone (i.e., farther from the jet exit). These values are in good agreement with the predictions.

**The Time-Mean and RMS Temperature.** Figure 5 shows the radial profiles of $\Theta/\Theta_{max}$ and $T'/\Theta_{max}$ at $x/d$ = 2.56 for the 7.5 m/s flow. Because of interference between the probe and jet body, measured values were not obtained at radial locations of $r/R$ less than 0.15. The predictions depict a peak at $r/R$ of 0.1 in the $T'/\Theta_{max}$ distribution; this is associated with the steep gradient in $\Theta/\Theta_{max}$ at that radial location. In the outer region, the predictions are in fair agreement with measurements.

Figures 6 and 7 show the radial profiles of $\Theta/\Theta_{max}$ and $T'\Theta_{max}$ at four axial locations for the 15 m/s flow. The axial and radial thermal extent of the heated jet is shown on both figures. It is interesting to note that, as expected, the radial extent of the temperature fluctuations is larger than that of the mean temperature at all the four stations.

The mean temperature is well predicted at stations farther from the jet exit and overpredicted near it. This may be attributed to overpredicted turbulent diffusion coefficients which could be due to low predicted values of $\epsilon$ or due to the use of a constant $\sigma_H$.

At the station $x/d$ = 2.95, the predicted $\Theta/\Theta_{max}$ is in excellent agreement with the experimental data. However, at the same station, the temperature fluctuations are underpredicted. This may suggest a lower value of $C_{T2}$ or a high value of $C_{T1}$ than those employed in the present predictions,

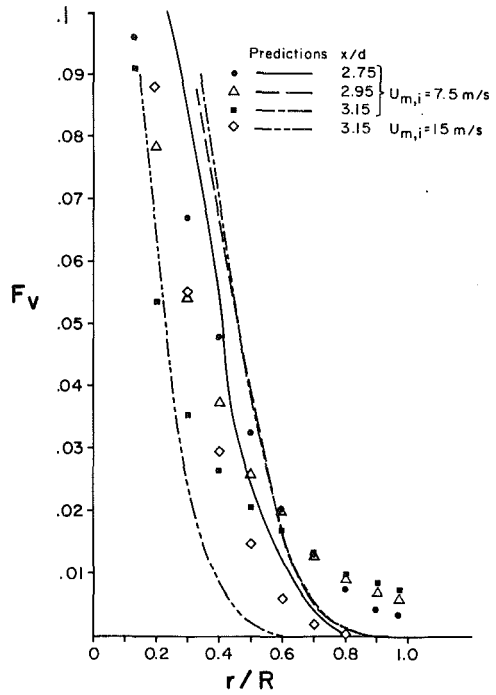


**Fig. 8 Radial profiles of time-mean CO volume fraction**

but an examination of Fig. 5 would run contrary to that suggestion.

It should be mentioned here that the transport equation for the mean square fluctuation of a scalar quantity (10) has been validated for turbulent free jets [17] and for confined turbulent recirculating flows [18]. The same equation (with both the values of $C_{T2}$ of 2. and 1.4) did not predict accurately the measured values of RMS temperature fluctuations under the experimental conditions of this study. This stresses the need to solve a transport equation for the dissipation of the temperature fluctuation.

**The Time-Mean CO Concentration.** Figure 8 exhibits the measured and predicted radial profiles of CO volume-fraction ($F_v$) at three stations for the 7/5 m/s flow and at one station for the 15 m/s flow.

For the 7.5 m/s flow, $F_v$ is overpredicted near the axis and underpredicted in the outer region ($r/R > .5$). However, $F_v$ is underpredicted for the 15 m/s flow. Again, this points out the need for a closer look at the $\epsilon$ equation and for a distribution of $\sigma_F$ instead of the constant value used in the present predictions.

## Conclusions

The present contribution provides detailed measurements of velocity, temperature, and concentration in a turbulent inert recirculating confined flow with the objective of validating current mathematical models of turbulence.

Although fair agreement is obtained between the measured and predicted mean velocity field, discrepancies occur between the experimental data and the predicted time-mean temperature, time-mean concentration and RMS temperature fluctuation.

The need exists for a closer examination of the $\epsilon$ equation and the assumption of the constant turbulent Prandtl and Schmidt numbers. One such example is a recent development of the $k$-$\epsilon$ model [19].

In order to improve the predicted distribution of the temperature fluctuation a transport equation for the dissipation rate of this fluctuation must be solved.

## Acknowledgments

This study was performed at the UCI Combustion Laboratory and sponsored by the Air Force Office of Scientific Research (Grant No. AFOSR-78-3586). The U. S. Government is authorized to reproduce and distribute reprints for government purposes notwithstanding any copyright notation hereon. Support for one of the authors (J. C. LaRue) was obtained from a NSF grant, ENG-78-15712 and NASA grant, L-NSG-3219.

## References

1 Elghobashi, S. C., *Studies in Convection,* Vol. 2, edited by B. E. Launder, Academic Press, 1977, p. 141.

2 Peck, R. E., and G. S. Samuelsen, "Analytical and Experimental Study of Turbulent Methane Fired Backmixed Combustion," *AIAA Journal,* Vol. 15, No. 5, 1977, p. 730.

3 Khalil, E. E., D. B. Spalding, and J. H. Whitelaw, "The Calculation of Local Flow Properties in 2-D Furnaces," *Int. Journal of Heat and Mass Transfer,* Vol. 18, 1975, p. 775.

4 Wuerer, J., and G. S. Samuelsen, "Predictive Modeling of Back-mixed Combustor Flows: Mass and Momentum Transport," AIAA 79-0215, presented at the 17th Aerospace Sciences Meeting, New Orleans, Jan. 1979.

5 Peck, R. E., and G. S. Samuelsen, "Eddy Viscosity Modeling in the Prediction of Turbulent, Backmixed Combustion Performance," Sixteenth Symposium (International) on Combustion, The Combustion Institute, 1977, p. 1675.

6 Wyngaard, J. C., "Spatial Resolution of a Resistance Wire Temperature Sensor," *Phy. Fluids,* Vol. 14, 1971, p. 2052.

7 Bremhorst, K. and D. B. Gilmore, "Influence of End Conduction on the Sensitivity & Stream Temperature Fluctuations of a Hot-Wire Anemometer," *Int. J. Heat Mass Transfer,* Vol. 21, 1978, p. 145.

8 Millon, F., P. Paranthoen, and M. Trinite, "Influence des Echanges Thermiques Endre le Capteur et ses Supports sur la Measure des Fluctuations de Temperatures dans un Ecoulement Turbulent," *Int. J. Heat Mass Transfer,* Vol. 21, 1978, p. 1.

9 Larsen, S. E., and J. Højstrup, "Spatial and Temporal Resolution of a Resistance Wire Sensor," *J. Atmos. Sci,* (submitted for possible publication).

10 LaRue, J. C., T. Deaton, and C. H. Gibson, "Measurements of High Frequency Turbulent Temperature," *Rev. Sci. Instrum.,* Vol. 46, No. 5, 1975, pp. 757–764.

11 Launder, B. E., and D. B. Spalding, "The Numerical Computation of Turbulent Flows," *Computer Methods in Applied Mechanics and Engineering,* Vol. 3, 1974, p. 269.

12 Spalding, D. B., "Concentration Fluctuations in a Round Turbulent Free Jet," *Chem. Eng. Sc.,* Vol. 26, 1971, p. 95.

13 Launder, B. E., and D. B. Spalding, "Turbulence Models and their Experimental Verification," Lectures for Post Experience Course held at Imperial College, Apr. 1973, p. 11.5.

14 Gibson, C. H., and W. H. Schwarz, "The Universal Equilibrium Spectra of Turbulent Velocity and Scalar Fields," *Journal of Fluid Mechanics,* Vol. 16, 1963, p. 365.

15 Launder, B. E., Private Communication, Nov. 1973.

16 Patankar, S. V., and D. B. Spalding, "A Calculation Procedure for Heat, Mass and Momentum Transfer in Three Dimensional Parabolic Flows," *Int. J. Heat Mass Transfer,* Vol. 15, 1972, p. 1787.

17 Lockwood, F. C. and A. S. Naguib, "The Prediction of the Fluctuations in the Properties of Free Round Jet, Turbulent Diffusion Flames, *Combustion and Flame,* Vol. 24, 1975, p. 109.

18 Elghobashi, S. E., W. M. Pun, and D. B. Spalding, "Concentration Fluctuations in Isothermal Turbulent Confined Jets," *Chem. Eng. Sc.,* Vol. 32, 1977, p. 161.

19 Hanjalić, K., B. E. Launder, and R. Schiestel, "Multiple-Time-Scale Concepts in Turbulent Transport Modeling," Proceedings of Second Symposium on Turbulent Shear Flows," July 1979, London.

**H. H. Korst**
Professor of Mechanical Engineering.
Fellow ASME

**R. A. White**
Professor of Mechanical Engineering.

Department of Mechanical and Industrial Engineering, University of Illinois at Urbana-Champaign, Urbana, Ill. 61801

# Evaluation of Vehicle Drag Parameters From Coastdown Experiments Conducted Under Nonideal Environmental Conditions

*Parameter identification by optimization forms the analytical basis for extracting road load information from well controlled coastdown tests. Specific attention is given to the effects of both biased and random errors as may be caused by environmental disturbances, road conditions, inaccurate parameteric input, or signal and instrument noise. As a consequence, experimental conditions can be identified and quantitative criteria established for either avoiding or correcting such errors. Test results are presented which support the methodology and conclusions.*

## Introduction

Fuel economy and emission testing as required by federal agencies specify the use of chassis dynamometers but allow to determine road load power settings by "procedures requested by the manufacturer and approved in advance by the administrator" [1]. Thus, efforts have been made to identify, document, and seek approval for methods of realistically assessing road load power.

Coastdown testing with full scale vehicles on level and inclined roads affords such opportunities, provided that experimental methods, procedures, and data processing can be devised which produce acceptable (i.e., accurate) information. While coastdown testing is not a new experimental approach for determining vehicle drag, introduction of control theory related data processing methods, based on parameter identification by optimizing techniques, has improved the accuracy with which drag components can be separated and quantitatively extracted.

Earlier work by the authors has directed attention to the potential of this method [2,3] which, in its original version of a two-parameter drag component formulation, forms the basis for EPA approved procedures now used routinely by the large car manufacturers. Closer examination of the restrictions imposed [3,4,5] and possible errors in component evaluation caused by the use of only two performance parameters led to the present investigation.

The overall objective is to give a critical appraisal of drag component evaluation by coastdown experiments with full attention given to all significant variables and parameters in such tests, including study of the effects of biased and random disturbances. It is significant that capabilities can be developed for correcting effects of environmental disturbances during coastdown experiments. This holds the promise of sizable cost reductions in fleet testing.

However, the study shows that even while accounting fully for the overall energy dissipation due to aerodynamic drag and road-tire-suspension interactions, coastdown tests cannot cleanly separate these individual component losses without some laboratory testing of the tires. Efforts to improve the overall fuel economy of road vehicles must, therefore, depend on close cooperation and exchange of information between car and tire manufacturers.

## Analysis

**Equation of Motion for Coastdown.** The analysis proceeds from the equation of motion for the vehicle under coasting conditions [3] with the drag contributions distinguishing between "correct performance coefficients," $a_i$, and "disturbance coefficients," $c_i$, in the form of the polynomial

$$-dV/dt[(m_{,0}+\Delta m_{,0})/g_0]=\Sigma_{i=0}^{i=2}\ (a_i+c_i)\,v^i \qquad (1)$$

where the limitation to $i = 2$ is imposed by our chosen form of parameter identification procedure and must be complemented by certain restrictions in experimental conditions.

We identify $a_i$ as the correct performance coefficients

$$a_0=r_{0,0};\ a_1=r_{1,0};\ a_2=r_{2,0}+(\rho_{,0}/2g_0)\,A\,C_D \qquad (2a,b,c)$$

where $r_{0,0}$, $r_{1,0}$, and $r_{2,0}$ relate to the tire rolling resistance parameters

$$F_{0,0} = [(r_{0,0}\ 1000\ g_0)/m_{,0}g)] \qquad (3a)$$

$$S_{1,0} = [(F_{0,0}r_{1,0})/r_{0,0}] \qquad (3b)$$

$$S_{2,0} = (r_{2,0}/r_{0,0})F_{0,0} \qquad (3c)$$

and the aerodynamic drag is accounted for by the parameter

Contributed by the Fluids Engineering Division of THE AMERICAN SOCIETY OF MECHANICAL ENGINEERS and presented at the Joint ASME/CSME Applied Mechanics, Fluids Engineering, and Bioengineering, Niagara Falls, N. Y., June 18-20, 1979. Manuscript received by the Fluids Engineering Division, September 17, 1979.

$$B_{0,0} = A\, C_D\, (\rho_{,0}/2g_0)[(V_{0,0})^2/r_{0,0}] \tag{4}$$

The disturbance terms, due to wind and road slope effects can be identified as follows: An instantaneous vector diagram (Fig. 1 (*a*)) relates the relative flow past the vehicle $V'(t)$ to the vehicle velocity $V(t)$ and the wind speed and direction $(U,\alpha)$ in the form

$$V'(t) = [(V + U\cos\alpha)^2 + (U\sin\alpha)^2]^{1/2} \tag{5}$$

Introducing $C_D'$, the effective drag coefficient in the direction of the car trajectory, the aerodynamic drag can be written as

$$D_{,D} = [(V + U\cos\alpha)^2 + U^2\sin^2\alpha]\,(\rho_{,0}/2g_0)\,A\,C_D'$$

$$= V^2(\rho_{,0}/2g_0)\,A\,C_D' + 2VU\cos\alpha \cdot$$

$$(\rho_{,0}/2g_0)\,A\,C_D' + U^2\rho_{,0}A\,C_D'/2g_0 \tag{6}$$

The contribution due to road slope will be

$$(m_{,0}\,g/g_0)\sin\theta \cong (m_{,0}\,g/g_0)\,H\%/100. \tag{7}$$

Accordingly, the disturbance terms are now[3]

$$c_0 = U^2\,A\,C_D'[(\rho_{,0}g)/g_0] + (m_{,0g}/g_0)\,H\%/100 \tag{8a}$$

$$c_1 = 2U\cos\alpha(\rho_{,0}/2g_0)\,A\,C_D'; \quad c_2 = 0. \tag{8b,c}$$

[3] Discussion of road roughness effects on tire and suspension losses have been treated in reference [8].

The force terms in equation (3) are now identified according to their causes

$$-dV/dt[(m_{,0} + \Delta m_{,0})/g_0] = r_{0,0}$$

$$+ [(m_{,0}g)/g_0)]\,(H\%/100)$$

$$+ U^2\,A\,C_D'(\rho_{,0}/2g_0) + [r_{1,0}$$

$$+ 2U\cos\alpha(\rho_0/2g_0)\,A\,C_D']\,V$$

$$+ [r_{2,0} + (\rho_{,0}/2g_0)\,A\,C_D']\,V^2. \tag{9}$$

Using the initial velocity $V_{0,0}$ as reference, we introduce a dimensionless velocity

$$\nu = V/V_{0,0} \tag{10}$$

and define a dimensionless time

$$\tau = t/T_{,D} \tag{11}$$

where $T_{,D}$ is a characteristic time

$$T_{,D} = [(m_{,0} + \Delta m_{,0})\,V_{0,0}]/\{g_0\,r_{0,0}[1$$

$$+ (U/V_{0,0})^2\,A\,C_D'\,\rho_{,0}\,V_{0.0}^2$$

$$+ (m_{,0}g\,H\%)/(g_0 r_{0,0}100)]\} \tag{12}$$

Contracting the terms according to powers of $\nu$, one arrives, after separation of variables, at

$$-d\tau = d\nu/(1 + 2F\nu + B\nu^2) \tag{13}$$

## Nomenclature

Dimensional Variables[1]

$a_0, c_0$; $a_1, c_1$; $a_2, c_2$ = coefficients in equations (1), (8) [N] [N s m$^{-1}$] [N s$^2$ m$^{-2}$]

A = frontal area of test car

$A[I,1] = v_i$ coastdown matrix $A[I,2] = t_i$ = [–] [s]

$D$ = aerodynamic drag force [N]

$g$ = local gravitational acceleration [m s$^{-2}$]

$g_0$ = gravitational constant = 1 [kg m s$^{-2}$ N$^{-1}$]

$H$ = road slope [%]

$m$ = mass of vehicle [kg]

$\Delta m$ = additive mass accounting for rotational inertia [kg]

$\rho$ = air density [kg m$^{-3}$]

$p$ = tire pressure [N m$^{-2}$] [psig]

$r_0, r_1, r_2$ = tire rolling resistance coefficients [N], [N s m$^{-1}$], and [N s$^2$ m$^{-2}$], respectively

$R$ = tire rolling resistance [N/1000 N]

$S_{1,0}; S_{2,0}; F_{0,0}$ = tire rolling resistance parameters. [N s/1000 Nm], [N s$^2$/1000 Nm$^2$], and [N/1000 N] respectively.

$t$ = time [s]

$T_{,D}$ = reference time [s], see equation (12)

$U$ = wind velocity [m s$^{-1}$]; [ft s$^{-1}$]

$V$ = vehicle velocity [m s$^{-1}$]; [ft s$^{-1}$]; [mph]

$V_0$ = initial vehicle velocity at $t$ = 0 [m s$^{-1}$]; [ft s$^{-1}$]

$\theta$ = road slope [rad]

$\alpha$ = wind direction [rad]

$\Lambda$ = yaw angle [rad]

Dimensionless Parameters

$B$ = see equations (4) and (15)

$C_D$ = aerodynamic drag coefficient at zero yaw angle

$C_D'$ = aerodynamic drag coefficient at yaw angle

$F$ = see equations (3*a*) and (14)

Dimensionless Variables

$\nu$ = $V/V_0$ dimensionless velocity [–]

$\tau$ = $t/T_{,D}$ dimensionless time [–]

Subscripts

,0 = smooth road and undisturbed conditions[2]

,$D$ = disturbed (biased) conditions

$i$ = index for test points

[1] Utilization of some English units is necessitated by the present specifications of the Environmental Protection Agency for vehicle chasis dynamometer testing.

[2] Use of this subscript reflects the need for distinguishing rough road conditions as treated in reference [8].

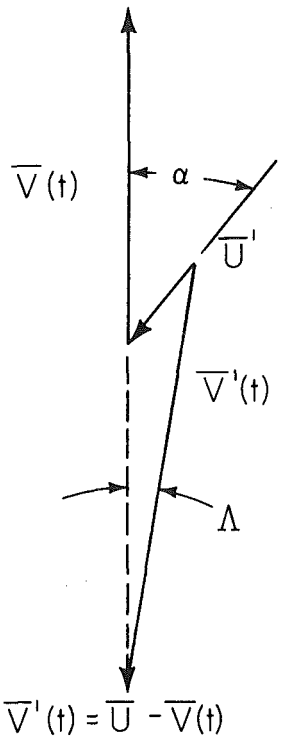


Fig. 1*(a)* Vector diagram of wind-car speed relation

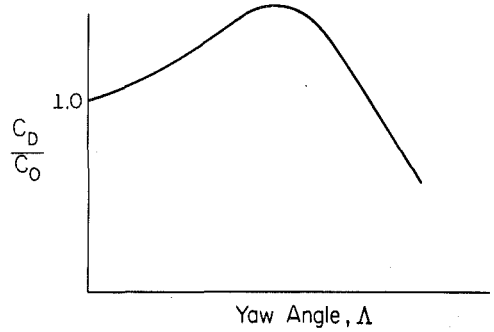


Fig. 1*(b)* Typical normalized wind tunnel data on drag yaw dependence

Fig. 1 Vector diagram of instantaneous wind-car speed relation and normalized drag coefficient yaw dependence

where

$$F = F_{,D} = [(S_{1,0}\ V_{0,0})/2F_{0,0}] + (U/V_{0,0})\cos\alpha\, B_{0,0}]/[1 + (U/V_{0,0})^2 B_{0,0} + (10\, H\%/F_{0,0})] \quad (14)$$

and

$$B = B_{,D} = [B_{0,0} + S_{2,0}(V_{0,0})/F_{0,0}]/[1 + (U/V_{0,0})^2 B_{0,0} + (10\, H\%/F_{0,0})] \quad (15)$$

will ultimately have to be determined by parameter identification through optimization in comparing to experimental coastdown data.

**Theoretical Coastdown Function.** Integrals of equation (13) can be obtained in three distinctively different forms depending on the discriminant

$$B - F^2 \gtrless 0. \quad (16)$$

For our investigations, it is significant that

$$B - F^2 > 0 \quad (17)$$

results in a finite coastdown time while

$$B - F^2 < 0 \quad (18)$$

corresponds to an asymptotic (terminal) coastdown velocity as can be obtained in downhill coasting. The special cases $B - F^2 = 0$ is of no practical significance for our objectives.

**Coastdown on "Level" Roads.** A finite total coastdown time is presumed to exist for properly selected experimental conditions which will be reflected by the determinant $B - F^2 > 0$. (For level coastdown, this imposes physical limits on tailwind strength and road slope so that their combined effects do not lead to a finite terminal coastdown speed.) Upon integration, one obtains for $\tau = 0$ as $\nu = 1$

$$\tau = [1/(B-F^2)^{1/2}]\,\{\tan^{-1}[(B+F)/(B-F^2)^{1/2} - \tan^{-1}[(B\nu+F)/(B-F^2)^{1/2}]\} \quad (19)$$

and a finite dimensionless coastdown time results for $\nu = 0$

$$\tau_F = [1/(B-F^2)^{1/2}]\,\{\tan^{-1}[(B+F)/(B-F^2)^{1/2}] - \tan^{-1}[F/(B-F^2)^{1/2}]\} \quad (20)$$

Inspection of equations (2*a*,*b*,*c*) and (3*a*,*b*,*c*), together with equation (4) shows that four performance parameters are of interest. Obviously, separation of $S_{2,0}$ and $B_{0,0}$ is not possible so that $S_{2,0}$ must be extracted from tire testing or its effects excluded either by proper tire selection or by an appropriate (linear) approximation of tire speed dependency. This leaves three parameters to be determined; however, separation of even three parameters under generally noisy experimental conditions is not possible[4] so that it is deemed necessary to introduce some experimental information on the tire speed dependency, e.g. in the form of values of $S_{1,0}$ or both $S_{1,0}$ and $S_{2,0}$. We shall assume that such data are either available from tire laboratory tests or can be reduced to insignificance (at least for the purpose of establishing aerodynamic drag coefficients) by proper selection of tires, high inflation pressure, and coastdown speed ranges. The remaining two performance parameters are determined by the optimization requirements

$$(\partial/\partial T_{,D})\ \Sigma_N[T_{,D}\tau(\nu_i) - t_i]^2 = 0 \quad (21)$$

$$(\partial/\partial B_{,B})\ \Sigma_N[T_{,D}\tau(\nu_i) - t_i]^2 = 0 \quad (22)$$

with the errors summed for $N$ experimental point pairs, $V_i$ and $T_i$.

We now introduce the following abbreviations with $A(I,1) = \nu_i$ and $A(I,2) = t_i$:

$$A_1 = 1 + (B+F)^2/A_3^2; \quad A_2 = \tan^{-1}(B + F/A_3); \quad (23a,b)$$

$$A_3 = (B-F^2)^{1/2}; \quad A_4 = [1 - (B+F)/(2A_3^2)][A_3/A_1]. \quad (23c,d)$$

$$C_0 = B \cdot A(1,1) + F; \quad C_1 = 1 + C_0^2/A_3; \quad (24a,b)$$

$$C_2 = \tan^{-1}(C_0\, A_3); \quad C_3 = A(I,1) - C_0/(2A_3^2); \quad (24c,d)$$

[4] This is borne out in Fig. 5 where the dependency for the $S_{1,0}$ residual is shown to be submerged in the rms data scatter.

and

$$S_0 = \Sigma_1^N C_2; \quad S_1 = \Sigma_1^N C_2^2; \quad S_2 = \Sigma_1^N A(I,2)\, C_2; \quad (25a,b,c)$$

$$S_3 = \Sigma_1^N A(I,2) \quad S_4 = \Sigma_1^N 1/C_1; \quad S_5 = \Sigma_1^N C_3/C_1; \quad (25d,e,f)$$

$$S_6 = \Sigma_1^N (C_3^2/C_1; \quad S_7 = \Sigma_1^N A(I,2)(C_3/C_1); \quad (25g,h)$$

The optimizing condition, equation (21), yields

$$T_{,D_I} = [A_3(A_2\, S_3 - S_2)]/(N A_2^2 - 2\, A_2\, S_0 + S_1). \quad (26)$$

and equation (22) produces

$$T_{,D_{II}} = \{A_3[(A_4 - A_2/2)S_3 + S_2/2 - A_3\, S_7]\}/$$

$$\{N[A_4 A_2 - A_2^2/2] + (A_2 - A_4)S_0 - A_2 A_3 S_5$$

$$- S_1/2 + A_3\, S_6\}. \quad (27)$$

Using $F_{,D}$ as a variable and expressing $T_D = T_D(F_{,D})$ and $B_{,D} = B_{,d}(F_{,D})$, a numerical iteration can be carried out with the help of digital computers to determine, for $N$ point pairs $\nu_i$, $\tau_i$, a solution for which

$$T_{D,I} = T_{D,II} \quad (28)$$

thus determining the optimized values for $F_{,D}$, $B_{,D}$, and $T_{,D}$. Since

$$B_{0,0} = \{B_{,D}[1 + (10\, H\%/F_{0,0})]$$

$$- S_{2,0}[(V_{0,0})^2/F_{0,0}]\}/[1 - (U/V_{0,0})^2 B_{,D}] \quad (29)$$

and

$$F_{0,0} = [(m_{,0} + \Delta m_{,0}/g\, m_{,0})\, 1000\, V_{0,0} - T_{,D}\, 10\, H\%]/$$

$$\{T_{,D}[1 + (U/V_{0,0})^2 B_{0,0}]\} \quad (30)$$

a unique solution will be obtained for $B_{0,0}$ and $F_{0,0}$. Subsequently, one finds from equation (4)

$$A\, C_D' = (B_{0,0} F_{0,0} m_{,0}\, g)/[\rho_{,0}(V_{0,0})^2 500] \quad (31)$$

One recalls that $C_D'$ is the drag coefficient experienced by the vehicle under varying conditions of yaw angle due to the cross wind component. While yaw angle dependency will vary for different vehicle configurations, the increase in $C_D$ for small yaw angles can be approximated by

$$C_D'/C_D = C_D(\theta)/\left[C_D\Big|_{\theta=0}\right] = 1 + C\,\Lambda^2$$

where $C$ is of the order of 2.53 or less (for $\Lambda$ in rads) [6,7], see Fig. 1(*b*).

During a typical coastdown run as the car speed decreases from about 110 to 55 kmh, yaw angle effects will generally be small in the higher speed range where the present test evaluation procedure puts emphasis on the aerodynamic drag contribution; hence, $C_D = C_D'$. Crosswinds can, however, exhibit more noticeable influence on the rolling resistance if coastdown records are processed to extend the lower end speed range.

**Hill Coasting or Rolling.** Starting again from equation (13), i.e.,

$$-d\tau = d\nu/(B\,\nu^2 + 2\,F\,\nu + 1) \quad (32)$$

with

$$F = F_{,D} \text{ and } B = B_{,D} \quad (33,34)$$

as before but

$$B - F^2 = \Delta < 0 \quad (35)$$

(hence $= \Delta$ is positive) so that the integral of equation (32) is

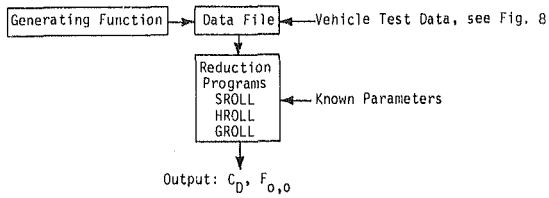


**Fig. 2 Schematic showing use of generating function**

**Table 1**

| | |
|---|---|
| Mass, $m_{,0}$ | 1,814 kg [4,000 $lb_m$] |
| Effective mass ratio | $(m_{,0} + \Delta m_{,0})/m_{,0} = 1.035$ |
| Frontal area $A$ | 2.09 $m^{2(a)}$ |
| Drag coefficient $C_D$ | 0.5 |
| *Tire Rolling Resistance* | |
| $G_{0,0}$ | 12 [N/1,000 N] |
| $S_{1,0}$ | 0.164 N s/1,000 NM |
| $S_{2,0}$ | 0 N $s^2$/1,000 N $m^2$ |
| *Atmospheric Conditions* | |
| Air density, $\rho_{,0}$ | 1.2 kg/$m^3$ |
| Wind speed, $\bar{U}$ | variable, m/s |
| Wind direction, $\alpha$ | degrees, variable |
| Yaw angle coefficient, $C$ | 2.53, dimensionless |

[(a)] Note that only the product $A\, C_D$ is of real significance for drag evaluation and dynamometer setting.

$$\tau = 1/[2(-\Delta)^{1/2}]\{\ln[(-\Delta)^{1/2} + F + B\nu]/[(-\Delta)^{1/2} - F - B\nu]$$

$$- \ln[(-\Delta)^{1/2} + F + B]/[(-\Delta)^{1/2} - F - B]\} \quad (36)$$

A terminal velocity is reached as $\tau \to \infty$

$$\nu_T = [(-\Delta)^{1/2} - F]/B \quad (37)$$

This terminal velocity can be approached in both accelerating runs ($\nu|_{\tau=0} < \nu_\tau$) or decelerating runs ($\nu|_{\tau=0} > \nu_\tau$). Low velocity experiments, starting with $\nu(t = 0) = 0$ will be referred to as hill rolling. Optimization procedures and extraction of the correct performance parameters follow the scheme outlined for level roads.

**Generating Functions.** Parameter identification by optimization has to be carried out in the presence of disturbances which are either random or biased. To study parameter observability, separability, and resulting errors for performance coefficients, it is convenient and instructive to construct generating functions with well defined noise inputs.

Random disturbances such as scatter of data points may result from noisy signals (analog), truncated signals (digital) as received or recorded, or from random processing errors (digitizer). Such disturbances can be modeled and subsequently studied by (i) first establishing a theoretical (smooth) generating function and (ii) subsequently subjecting it to digital randomization (this can easily be achieved by rounding the $V(t)$ curve to any prescribed number of $G$ "decimals"). It is noteworthy that, in this context "decimals" can also be assigned fractional values so that a continuous relation between G and rms is accomplished. This facilitates the discussion of random noise influences on parameter observability and on parameter accuracy.

For biased disturbances, one may consider the following cases as representative: (i) changes in road slope as a function

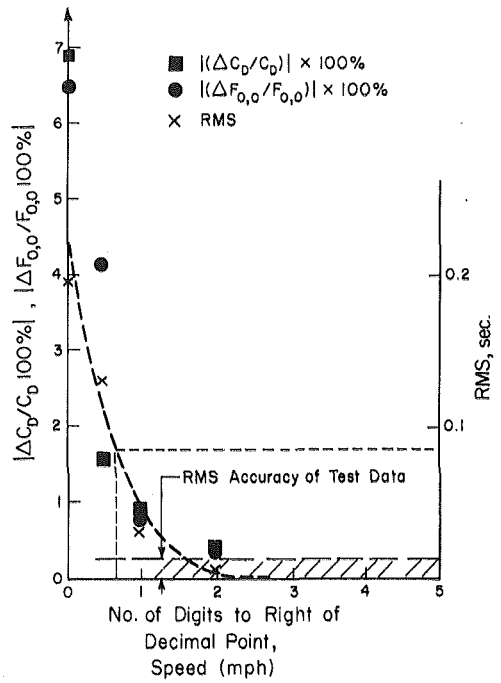


**Fig. 3 Illustration of effect (for "typical test car") of random errors: (1) Percent errors for drag coefficient and zero velocity intercept for rolling resistance; (2) Relation between digital speed accuracy and RMS**

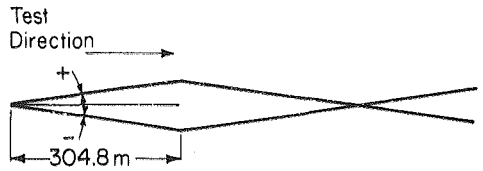


**Fig. 4(a) Road slope assumed to demonstrate effect on $C_D$ and $F_{0,0}$**

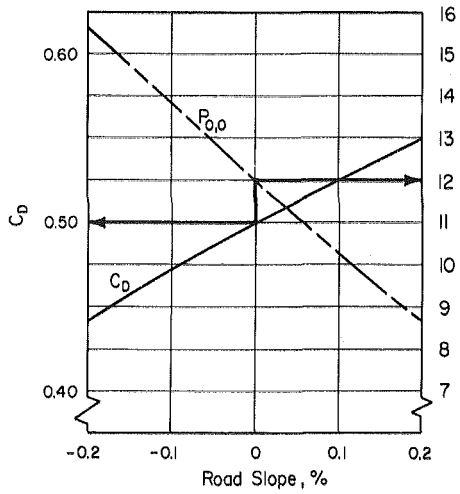


**Fig. 4(b) Apparent values of $C_D$ and $F_{0,0}$ as effected by road slope change for the combination shown in Fig. 4(a)**

of location, (ii) changes of wind vector (depending upon time or traveled distance), (iii) errors in tire rolling resistance coefficients such as $S_{1,0}$ and $S_{2,0}$, and (iv) road roughness effects (depending upon location).

The generating function is used as shown in Fig. 2. This figure emphasizes the computer oriented data processing and illustrates the role of computer generated, simulated coastdown runs in establishing confidence levels for the parameter identification and performance coefficient evaluation by control theory related optimization methods.

Numerical experiments will only produce information which is directly applicable to the selected conditions. It is, therefore, recommended to utilize input data which are closely matched by the test vehicle. Calculations have thus been carried out with the vehicle parameters shown in Table 1. Table 1 also includes the specified atmospheric test conditions.

**Influence of Random Disturbances.** Shown in Fig. 3 are results of numerical experiments which illustrate the effect of random errors on the peformance parameters $C_D$ and $F_0$. On the basis of these, and many additional computer runs, one can draw the conclusion that reliable results for $C_D$ (within ~ 2 percent error) require standard deviations of less than 0.1 second for coastdown runs conducted between 30 and 15 m/s.

**Influence of Biased Disturbances.** Constant road slope can be accounted for in single direction runs, and its effects on tire rolling resistance intercepts $F_{0,0}$ compensated by averaging over runs in opposite direction. By contrast avoiding changes in slope within the full coastdown range is of utmost importance. This is illustrated, for the test car of Table 1 in Fig. 4. It must be noted that "change in slope" does not refer to short wavelength disturbances but rather to distinct breaks (here one located at 304.8 m from the start of the run). Runs in opposite directions obviously do not lend themselves to averaging. "Concave roads" (H percent negative) tend to decrease $C_D$ while producing increased $F_{0,0}$ values. Input of a "correct" $F_{0,0}$ value would result in reasonable values for $C_D$.

Performance parameter determination from wind disturbed

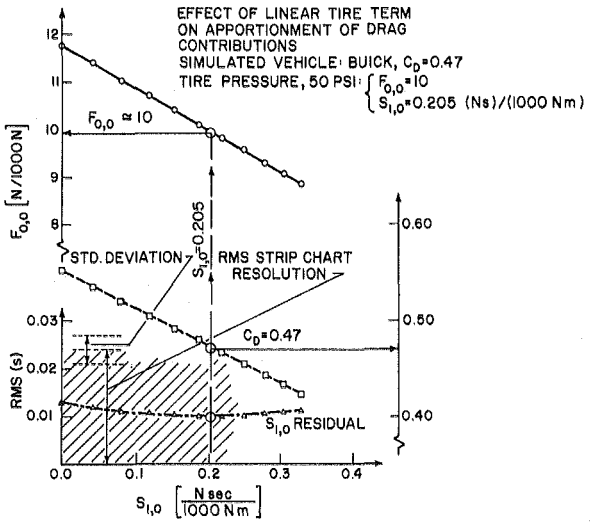


**Fig. 5 Effect of linear tire term on appointment of drag contributions**

runs is greatly enhanced by single direction run evaluations. This technique reduces the requirements for wind vector invariance to a rather small time and travel distance window corresponding to a vehicle velocity range of 30 to 20 m/s (65 to 45 mph). However, as crosswind components become more significant for the lower coastdown range, runs in windy environments will have to exclude the low-velocity portion from the data to be processed. Runs in opposite directions do not eliminate crosswind effects and will not lend themselves to averaging if the rolling resistance has a speed dependent contribution.

Sensitivity studies can be conducted which evaluate the influence on $F_{0,0}$ and $C_D$ by errors introduced due to

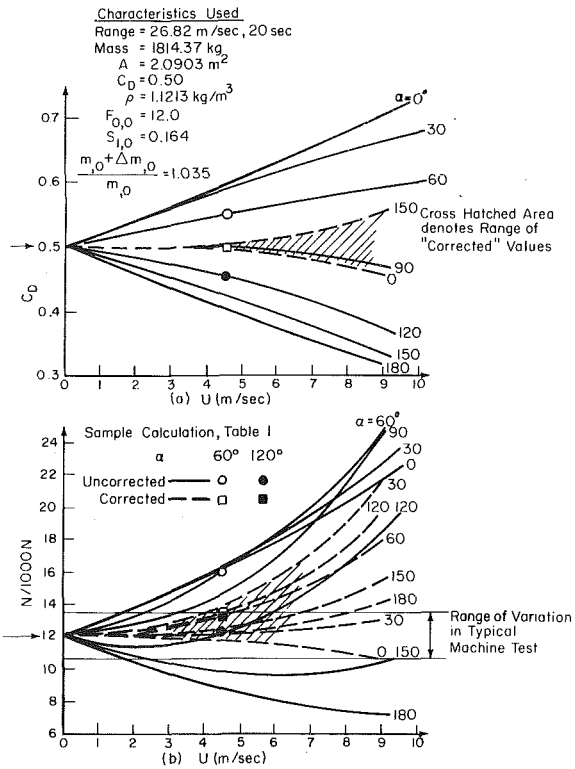


**Fig. 6 Individually corrected versus averaged paired runs – comparison of results obtained for "typical test car"**

deviations in $S_{1,0}$ and or $S_{2,0}$ values. The important influence of tire speed dependence is illustrated in Fig. 5.

**Advantage of Individually Corrected Over Averaged Paired Runs in Opposite Directions.** Earlier analytical concepts in which the linear term in the ideal coastdown function was neglected led to the practice of averaging road load settings obtained for "paired runs." This approach will cancel out (small, constant) slope deviations from level, and also accounts for head or tailwind effects (if wind conditions remained constant over the duration of both runs). Crosswind components would, in principle, be accounted for by an appropriate correction of the (constant) rolling resistance term. Consideration of speed dependency of rolling resistance, however, introduces a linear velocity term which does not change sign in opposite runs. In addition to the need for identical wind conditions during paired runs, there is also the requirement of low wind velocities.

Individually corrected single direction runs, when analyzed and evaluated properly by the present method, remove much of the shortcomings of the earlier method. Simulated test conditions have been selected as $U = 4.47$ m/s (10 mph), $\alpha =$ 60 and 120 degrees, with zero road slope. Performance parameters have been evaluated for the test car and the environmental conditions specified in Table 1. The following three conditions were investigated:

1. Neglecting both the linear tire term and the wind,
2. Using the linear tire term but neglecting the wind,
3. Using the linear tire term and correcting for wind-speed and direction.

Illustrative examples for each of the three cases are given in reference [9].

Shown in Fig. 6 is a summary of wind effect corrections for this car with the wind velocity $0 < U < 8.94$ m/s (20 mph) as abscissa and the wind vector angle as parameter. As can be seen, fully corrected car performance parameters (condition 3) suggest that individual runs can be used to extract very accurate $C_D$ values for wind velocities up to 4.472 m/s (10 mph) while the absolute terms for the tire rolling resistance exhibit the tendency of some overestimation. The nonsymmetrical behavior of $F_{0,0}$ for runs in opposite direction, together with the increasing sensitivity of averaged values for opposite (paired) runs in case of wind variation points to severe difficulties in obtaining properly matched cases. It is this diagram, Fig. 6, which gives weight to the conclusions that properly corrected single direction runs should be considered a more attractive procedure than "paired runs" averaging.

## Computer Programs

Computer programs have been developed for both minicomputer systems (HP 9830) and large scale computing facilities (CYBER 175). Program listing and example printouts which give detail input-output information can be found in reference [9].

## Experimental Program

The development of computer programs to simulate and subsequently analyze coastdown runs provided a firm basis for determining experimental requirements and confidence levels. In particular, quantitative criteria could be established for the following;

1. Road site selection (slope restrictions, surface smoothness, wind exposure);
2. Environmental conditions (wind magnitude, direction, and steadiness, road surface temperature);
3. Vehicle and tire parameter accuracy; and
4. Required accuracy for data acquisition, processing, and analysis.

Accordingly, appropriate site selections were made for both smooth level and a smooth constant slope (3 percent) section [9].

Since the main research objective was the critical evaluation of coastdown testing for determining vehicle drag components, vehicles were chosen to be representative for production model lines of the major car manufacturers.

A 1970 Buick Skylark was selected as the main test vehicle due to a number of factors such as:

1. Its total mass of less than 1814.37 kg (4000 lb) is representative of the on-the-road vehicle population
2. It is owned by the University of Illinois which allowed more extensive and not necessarily reversible internal modifications to accommodate various instrumentation packages.

Since the Buick, as the primary test vehicle, is equipped with an automatic transmission, it was fitted with a specially designed quick disconnect drive shaft arrangement patterned after that used by JPL [10]. This allowed to remove questions regarding the possible contributions of the torque converter on coastdown results.

The instrumentation carried with the vehicle varied depending on the vehicle and the speed measuring as well as data accumulating methodology (continuous analog as compared to high density digital sampling) being used. The salient features of those techniques which were adopted and used as being accurate, practical, readily available, and easily transported are discussed in detail and critically evaluated in reference [9].

A linear d-c generator was mounted on the front wheel grease cap (and restrained by an antirotation strap) which provided excellent low noise analog signals which were input to the data processing system shown in Fig. 7.

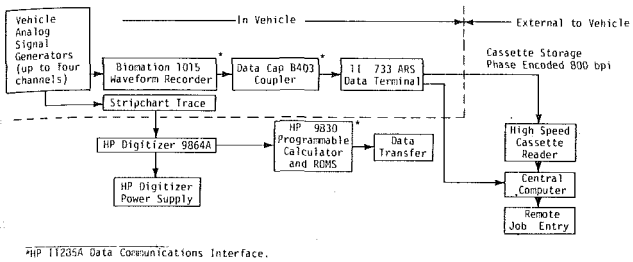


**Fig. 7 Data recording storage and processing systems**

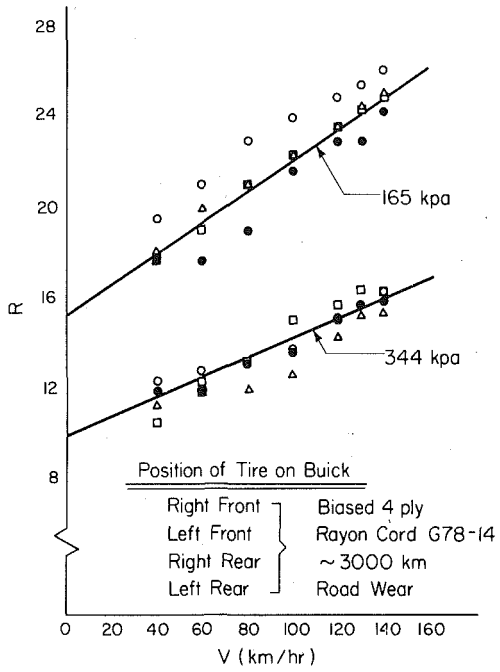


**Fig. 8 Laboratory data on rolling resistance for tires of test vehicle (3.66 m diameter drum corrected to flat road conditions) – test results courtesy of The Firestone Tire and Rubber Company**

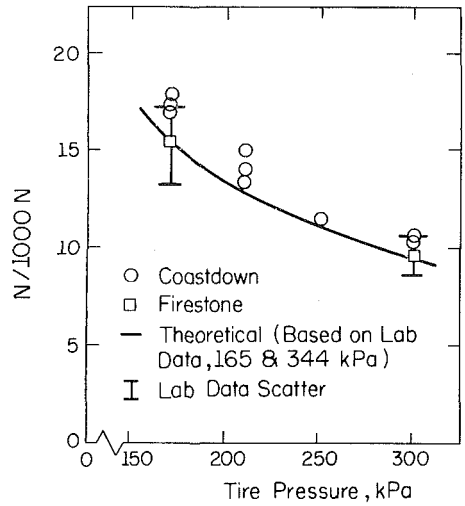


**Fig. 9 Intercepts ($V = 0$) for the linear tire rolling resistance relation, comparison of laboratory and coastdown test results**

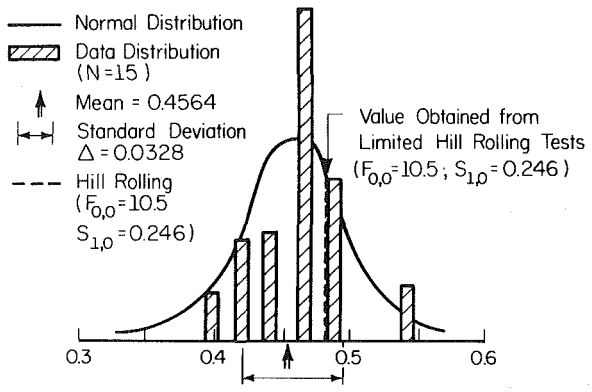


**Fig. 10 Statistical analysis of aerodynamic drag coefficients $C_D$ obtained for 15 coastdown runs with different tire pressures on level "smooth" road**

## Test Results

**Tire Tests.** As discussed earlier, it is essential to have information on tire rolling resistance speed dependence in order to determine the remaining drag components from actual (noisy) test data. This is clearly shown by the results of Fig. 5. It is not crucial, however, in which form the speed dependency is expressed. That is, equally satisfactory results are obtained by using the linear or the square tire rolling coefficients as input parameters. The inclusion of the linear term in the total coastdown equations (equations (18) and (36)) does allow for correction of side wind influences which further supports inclusion, and use, of the first-order velocity terms. Tire test data appear to have less scatter in the linear slope (see Fig. 8) than in the zero speed intercept.

**Vehicle Road Tests.** Extensive tests were carried out using both hill and level road test sites. Emphasis was placed on testing in the late evening hours (dusk) to obtain essentially calm wind conditions, i.e., wind speeds of 3 mph or less. These conditions were sufficient to produce stripchart recordings for different direction runs that were practically identical so that in overlay comparisons, the deviations were within the pen width of the individual records.

The initial tests showed no discernible difference could be found between tests run with the automatic transmission in neutral and those run with the driveshaft disconnected. This lack of a discernible difference was confirmed in back-up tests using another vehicle [9].

Fifteen tests were conducted at four different tire pressures (165, 220, 275, 344 kPa; 24, 32, 40, and 50 psig) and analyzed using the linear tire term as a known quantity and described by the empirical correlation extracted from Fig. 9, i.e.; $S_{1,0} = 0.2139\ (50/P)^{0.564}$. While the exponent used above is based on results for $r_{,0}$, the available data supports the use of the same form and magnitude for the dependence of $S_{1,0}$ on tire pressure, see Fig. 9.

Figure 10 shows a statistical analysis of the drag coefficient obtained for 15 level coastdown tests with varying tire pressures. Also shown for comparison are results of the hill coast experiments.

The multiple test runs discussed above show that even under carefully controlled test conditions, a distribution of drag coefficients (and rolling resistances) can be expected even from data which appear essentially identical. As discussed earlier, these differences may be attributable to biased and unbiased disturbances which, given sufficient information on environmental disturbances, may be corrected utilizing current methods.

Additional studies have been undertaken to explore the effects of road roughness. While the assessment and proper definition of surface roughness and resiliency is, in itself, a

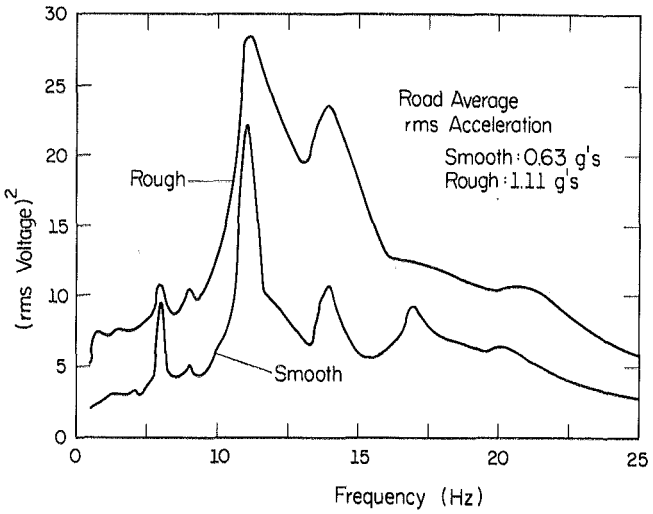


**Fig. 11(*a*) Spectral distribution of RMS values for "smooth" and "rough" roads based on recording by rear axle mounted accelerometer**

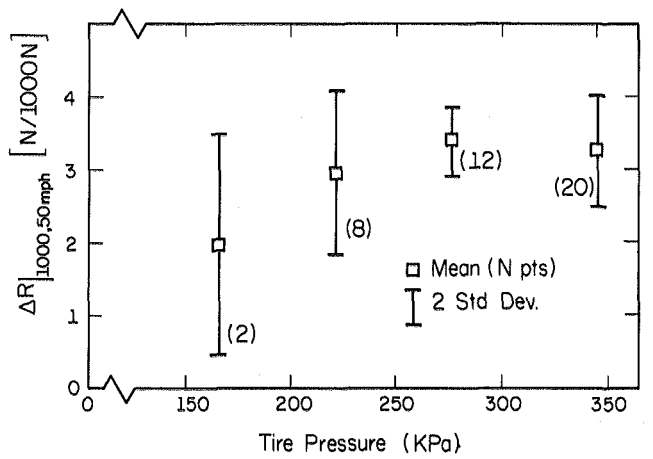


**Fig. 11(*b*) Increase in normalized rolling resistance due to road roughness**

difficult task [11,12] and considerable variations may be expected for a given test site depending upon vehicle placement within a lane width, it was, nevertheless, attractive to correlate road roughness parameters, Fig. 11(*a*), to the changes in rolling resistance, Fig. 11(*b*). For rough roads, an increase in rolling resistance will be due to additional tire rolling resistance contributions (short wavelength disturbances) and to energy dissipation in the vehicle suspension (predominantly in the shock absorbers). A detailed account of the analytical and experimental efforts is given in [13,14] which include the introduction of a dynamic model used to describe the individual dissipative system components responses to well defined roughness elements.

## Conclusion

As a result of the analytical and experimental studies which were strongly linked to, and supported by, computer-oriented efforts, a firm basis for the evaluation of coastdown data has been established. This not only should provide guidance for the government regulating agencies and car manufacturers on how to document road load settings in fuel economy and pollution tests but also allows the assessment of progress made in both vehicle and tire development.

## Acknowledgments

This work was partially supported by the U.S. Department of Transportation under Contract No. DOT-OS-60132.

## References

1 OMSAPC Advisory Circular, U.S. Environmental Protection Agency, Office of Air and Waste Management, A/C No. 55A, 8 Feb. 1978, 15 pp., with Attachments I and II.

2 White, R. A., and Korst, H. H., "The Determination of Vehicle Drag Contributions from Coastdown Tests," *SAE Trans.*, Vol. 81, Section 1, 1972, pp. 354-9.

3 Korst, H. H., and White, R. A., "Aerodynamic and Rolling Resistance of Vehicles as Obtained from Coastdown Experiments," *Proc., 2nd Int. Conf. on Vehicle Mech.*, Paris, France, Swets and Zeitlinger, B. V. Amsterdam, 6-9 Sept. 1971, pp. 146-60.

4 Bez, U., "Messung des Luftwiderstandes von Kraft-fahrzeugen Durch Auslaufversuche," University of Stuttgart, G.E.R., Jan. 1972.

5 Yasin, T. B., "The Analytical Background of Automobile Coastdown Testing," SAE Paper 780334, 1978 SAE Congress and Exposition, 27 Feb. 3 Mar. 1978, Detroit, Mich.

6 Dayman, B., Jr., "Effect of Realistic Winds on the Aerodynamic Resistance of Automobiles," SAE Paper 780337, 1978 SAE Congress and Exposition, 27 Feb. 3 Mar. 1978, Detroit, Mich.

7 Carr, G. W., "Reducing Fuel Consumption by Means of Aerodynamic 'Add-On' Devices," SAE Paper 760187, SAE Congress, 23-27 Feb. 1976, Detroit, Mich.

8 Korst, H. H., and M. A. Funfsinn, "Determination of Effective Rolling Resistance by Coastdown Experiments on Smooth and Rough Roads," *Conf. Proc. P-74,* The Rolling Losses and Fuel Economy, An R and D Planning Workshop, 18-20 October 1977, TSC, Cambridge, Mass.

9 Korst, H. H., and White, R. A., "Full Scale Drag Component Evaluation by Coastdown Testing on Level and Inclined Roads or Tracks," Final Report, Contract DOT-OS-60132, U.S. Department of Transportation, May 1978, DOT/RSPA/DPB/50/78/37.

10 Marte, J., Weaver, R. W., Kurtz, D. W., and Dayman, B., Jr., "A Study of Atuomotive Aerodynamic Drag," Final Report, DOT Contract DOT-TSC-OST-75-28, Sept. 1975.

11 McCauley, M. A., *Measurement of Road Surfaces,* Cranfield Int. Symp. Series, Vol. 4, pp. 93-119, The MacMillan Co., New York, 1963.

12 Tidbury, G. H., *An Introduction to Random Process Theory,* Cranfield Int. Symp. Series, Vol. 7, pp. 3-30, The MacMillian Co., New York, 1963.

13 Funfsinn, M. A., "Experimental and Analytical Study of the Effects of Road Roughness on Vehicle Rolling Resistance (with Emphasis on Coastdown Techniques and Computer Simulation)," M.S. thesis, Dept. of Mech. and Ind. Engr., University of Ill., Urbana-Champaign, Oct. 1977.

14 Velinsky, S., and R. A. White, "Increased Vehicle Energy Dissipation due to Changes in Road Roughness with Emphasis on Rolling Losses," SAE Paper 790653, SAE Passenger Car Meeting, Dearborn, Mich., 11-15 June 1979.

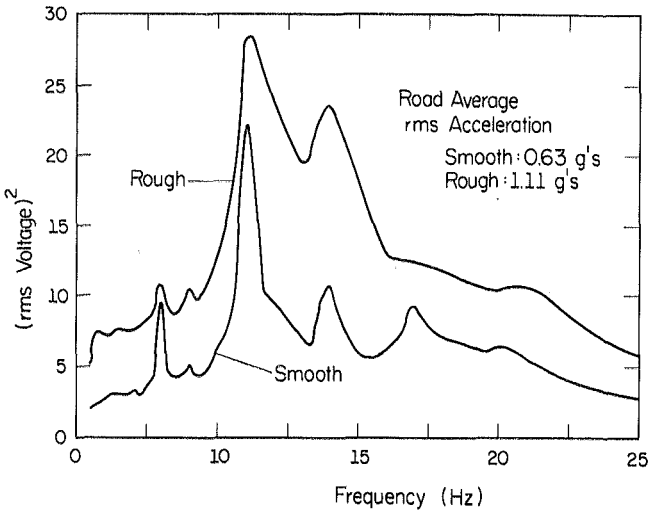


**Fig. 11(*a*) Spectral distribution of RMS values for "smooth" and "rough" roads based on recording by rear axle mounted accelerometer**

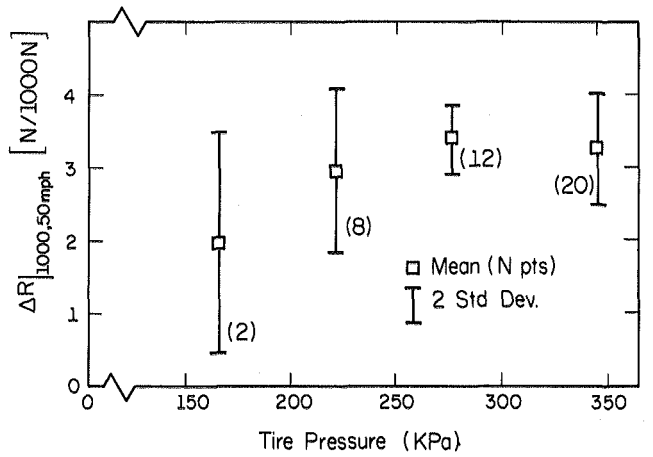


**Fig. 11(*b*) Increase in normalized rolling resistance due to road roughness**

difficult task [11,12] and considerable variations may be expected for a given test site depending upon vehicle placement within a lane width, it was, nevertheless, attractive to correlate road roughness parameters, Fig. 11(*a*), to the changes in rolling resistance, Fig. 11(*b*). For rough roads, an increase in rolling resistance will be due to additional tire rolling resistance contributions (short wavelength disturbances) and to energy dissipation in the vehicle suspension (predominantly in the shock absorbers). A detailed account of the analytical and experimental efforts is given in [13,14] which include the introduction of a dynamic model used to describe the individual dissipative system components responses to well defined roughness elements.

## Conclusion

As a result of the analytical and experimental studies which were strongly linked to, and supported by, computer-oriented efforts, a firm basis for the evaluation of coastdown data has been established. This not only should provide guidance for the government regulating agencies and car manufacturers on how to document road load settings in fuel economy and pollution tests but also allows the assessment of progress made in both vehicle and tire development.

## Acknowledgments

This work was partially supported by the U.S. Department of Transportation under Contract No. DOT-OS-60132.

## References

1 OMSAPC Advisory Circular, U.S. Environmental Protection Agency, Office of Air and Waste Management, A/C No. 55A, 8 Feb. 1978, 15 pp., with Attachments I and II.

2 White, R. A., and Korst, H. H., "The Determination of Vehicle Drag Contributions from Coastdown Tests," *SAE Trans.*, Vol. 81, Section 1, 1972, pp. 354-9.

3 Korst, H. H., and White, R. A., "Aerodynamic and Rolling Resistance of Vehicles as Obtained from Coastdown Experiments," *Proc., 2nd Int. Conf. on Vehicle Mech.*, Paris, France, Swets and Zeitlinger, B. V. Amsterdam, 6-9 Sept. 1971, pp. 146-60.

4 Bez, U., "Messung des Luftwiderstandes von Kraft-fahrzeugen Durch Auslaufversuche," University of Stuttgart, G.E.R., Jan. 1972.

5 Yasin, T. B., "The Analytical Background of Automobile Coastdown Testing," SAE Paper 780334, 1978 SAE Congress and Exposition, 27 Feb. 3 Mar. 1978, Detroit, Mich.

6 Dayman, B., Jr., "Effect of Realistic Winds on the Aerodynamic Resistance of Automobiles," SAE Paper 780337, 1978 SAE Congress and Exposition, 27 Feb. 3 Mar. 1978, Detroit, Mich.

7 Carr, G. W., "Reducing Fuel Consumption by Means of Aerodynamic 'Add-On' Devices," SAE Paper 760187, SAE Congress, 23-27 Feb. 1976, Detroit, Mich.

8 Korst, H. H., and M. A. Funfsinn, "Determination of Effective Rolling Resistance by Coastdown Experiments on Smooth and Rough Roads," *Conf. Proc. P-74,* The Rolling Losses and Fuel Economy, An R and D Planning Workshop, 18-20 October 1977, TSC, Cambridge, Mass.

9 Korst, H. H., and White, R. A., "Full Scale Drag Component Evaluation by Coastdown Testing on Level and Inclined Roads or Tracks," Final Report, Contract DOT-OS-60132, U.S. Department of Transportation, May 1978, DOT/RSPA/DPB/50/78/37.

10 Marte, J., Weaver, R. W., Kurtz, D. W., and Dayman, B., Jr., "A Study of Atuomotive Aerodynamic Drag," Final Report, DOT Contract DOT-TSC-OST-75-28, Sept. 1975.

11 McCauley, M. A., *Measurement of Road Surfaces,* Cranfield Int. Symp. Series, Vol. 4, pp. 93-119, The MacMillan Co., New York, 1963.

12 Tidbury, G. H., *An Introduction to Random Process Theory,* Cranfield Int. Symp. Series, Vol. 7, pp. 3-30, The MacMillian Co., New York, 1963.

13 Funfsinn, M. A., "Experimental and Analytical Study of the Effects of Road Roughness on Vehicle Rolling Resistance (with Emphasis on Coastdown Techniques and Computer Simulation)," M.S. thesis, Dept. of Mech. and Ind. Engr., University of Ill., Urbana-Champaign, Oct. 1977.

14 Velinsky, S., and R. A. White, "Increased Vehicle Energy Dissipation due to Changes in Road Roughness with Emphasis on Rolling Losses," SAE Paper 790653, SAE Passenger Car Meeting, Dearborn, Mich., 11-15 June 1979.

## DISCUSSION

### E. E. Larrabee[1]

Professors Korst and White are to be congratulated on their work in devising accurate parameter identification procedures for the case of an automobile coasting to a stop on a more or less level road. It is certainly a far cry from by own suggestion, in an article on this subject for *Road and Track* magazine in 1961, that the work-up of the data, which might involve an applied mathematician, could be carried out at an hourly rate considerably less than that of a skilled automobile mechanic.

I had hoped then that the instrumentation might be limited to the vehicle's own speedometer and a stopwatch, and that data recording during the coast down might take the form of knee pad notes of the speedometer reading at 5 second intervals. I had supposed that knowledge that the experimental speeds should be an arctangent function of time would allow

[1] Associate Professor of Aeronautics and Astronautics, M.I.T., Cambridge, Mass. 02139.

one to separate noise from the experiment by inexpensive hand plotting as suggested by my survey article, "Road Vehicle Aerodynamics, of Aerodynamics as an Annoyance" in the 2nd AIAA Symposium on the Aerodynamics of Sports and Competition cars, held at Los Angeles in 1974. The procedure outlined there also leads to "parameter identification" of the constants associated with zero speed and square law resistance.

Evidently the financial aspects of vehicle performance and emissions qualification testing require road load resistance determination of the most objective and precise form available. The techniques described in the paper are the best yet published to my knowledge. The detailed experiments described are especially valuable in resolving lingering doubts about validity of the techniques.

## Authors' Closure

The authors appreciate the comments of Dr. Larrabee pointing to the different levels of accuracy required for making assessments of individual road load components and overall vehicle drag. However, the striving for objective methods will remain essentially an academic exercise as long as the EPA and industry do not take full advantage of such improvements. While the EPA and industry continue to publicize euphoric mileage claims appended by fine-print disclaimers, the gap between EPA ratings and on-the-road performance[2] indicates that objective methods will continue to be research tools in the hands of manufacturers attempting to live with, live up to, or get relief from government guidelines and regulations.

[2] McNutt, B. D., McAdams, H. T., and Dulla, R., "Fuel Economy Results for 1974-1978 Automobiles: An Analysis of Trends," SAE Paper 790932, Fuels and Lubricants Meeting, 1-4 Oct. 1979.

# A Round Jet Normal to a Crossflow

**D. Crabb**

**D.F.G. Durão**

**J. H. Whitelaw**

Imperial College of Science and Technology, Department of Mechanical Engineering, Fluids Section, London SW7 2BX, England

*Measurements of the velocity characteristics of a jet in crossflow are reported and encompass the entire mixing region. Laser-Doppler anemometry was used in the upstream region ($x/D \leq 6$) where the turbulence intensities were larger and hot-wire anemometry in the downstream region. The scalar field, stemming from the injection of a trace gas in the jet flow, was also determined. Jet to cross-flow velocities of 2.3 and 1.15 were used. The results confirm and quantify the double-vortex characteristics of the downstream flow and demonstrate that this is associated with fluid emanating from the jet. The velocity maximum observed further from the wall than the double vortex is shown to correspond to freestream fluid accelerated by the pressure field. The mean-velocity profiles in the plane of the jet exit are shown to be far from uniform and the developing jet to be characterised by strong anisotropy associated with the acceleration of the freestream around the jet and into its wake. Probability distributions of velocity together with values of the Reynolds stresses, allow a detailed interpretation of the double vortex in the downstream region and indicate, for example, the larger magnitude of the cross-stream fluctuations. The flow in the downstream region is also characterised by very different magnitudes of the shear stress and the non-coexistence of zero shear stress and zero gradients of mean velocity and turbulence energy.*

## Introduction

With the advent of three dimensional calculation methods it has become more obvious that the amount of available information concerning the mixing of a jet and crossflow is limited. This flow configuration is of direct relevance to studies of chimney plume dispersion, V/STOL aircraft in transition flight and gas turbine combustors and it is the last topic to which this work is most directly related. Combustors use patterns of jets arranged around their circumference, initially to ensure correct combustion in the flame zone and then to dilute the hot gas exiting from the combustor. The present jet and cross-flow, although resulting in a much simpler flow than those in combustors, has been arranged with related flow and geometrical parameters. The results allow fuller understanding of the flow and provide a basis for the improvement of calculation methods, with their embodied turbulence models, which can subsequently be applied to the more complex combustion arrangements.

A guide to previous experimental work is provided in Table 1 which shows that, although the range of parameters covered is large, there is still a lack of detailed information, especially in the initial mixing region. Wall static pressure distributions, for example, have limited value especially when the penetration of the jet into the cross-flow is large. The interference effect on the jet outlet profile due to the cross-flow is also unknown except for some single sensor hot-wire data of Bergeles (21); this profile is a required boundary condition in calculations and the assumption of uniform outlet conditions made, for example, by Patankar, Basu, and Alpay [25] requires quantitative confirmation. Kamotani and Greber [14] and Ramsey and Goldstein [11] have observed that the higher velocity locus for a heated jet is not necessarily jet fluid in origin and further information is necessary to quantify and explain this result. McMahon et al. [10], Chassing, et al. [18] and Mousa, et al. [22] have all measured in the wake region of the jet and observed the double vortex structures similar to those behind a solid body but the velocity measurements presented in this region, which have been obtained by pressure and hot-wire probes, must be considered of uncertain precision due to the inability of this instrumentation to discriminate reverse velocities in the regions of recirculation and high turbulence.

This work is an attempt to provide data covering the whole of the jet cross-flow mixing process. Jet to cross-flow velocities of $V_J/U_\infty = 2.3$ and 1.15 were used. The measurements were recorded using laser Doppler anemometry, hot-wire anemometry and helium trace concentrations. Recent measurements have demonstrated that laser Doppler anemometry can be used to obtain accurate measurements in regions of recirculation and high turbulence intensity without the doubts associated with probe interference effects. Hot-wire measurements are limited to regions of low turbulence because, at turbulence intensities of greater than around 30 percent, there is a probability of reverse flow which the hot-wire cannot determine. The laser Doppler anemometer was used to cover the range from one diameter upstream of the jet center to six diameters downstream and measured the horizontal and vertical mean

Contributed by the Fluids Engineering Division and presented at the Winter Annual Meeting, Chicago, Ill., November 16-21, 1980, of THE AMERICAN SOCIETY OF MECHANICAL ENGINEERS. Manuscript received by the Fluids Engineering Division, November 11, 1979. Paper No. 80-WA/FE-18.

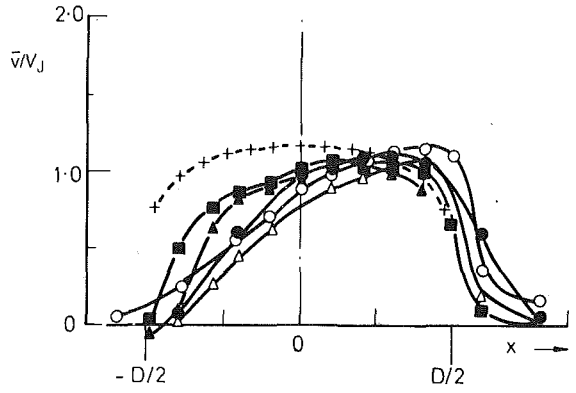


Fig. 1(*a*)

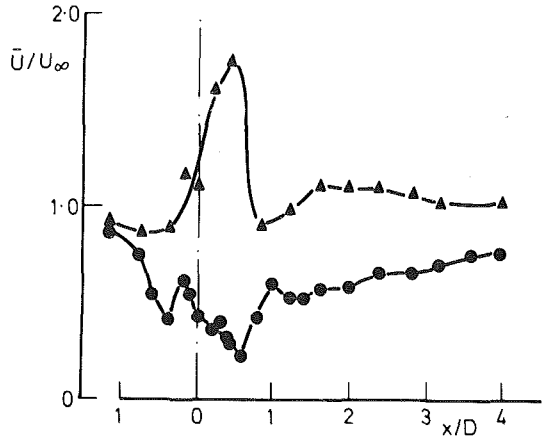


Fig. 1(*c*)

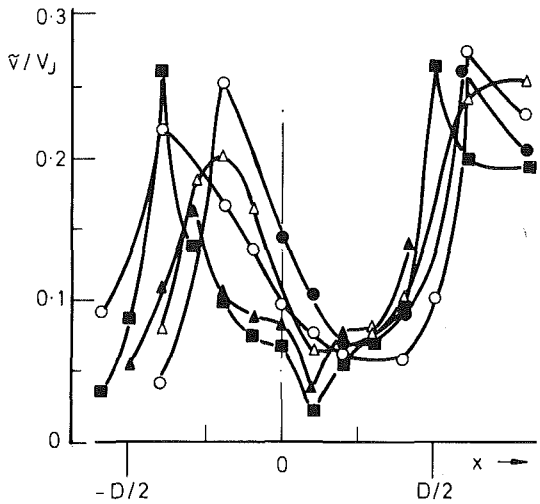


Fig. 1(*b*)

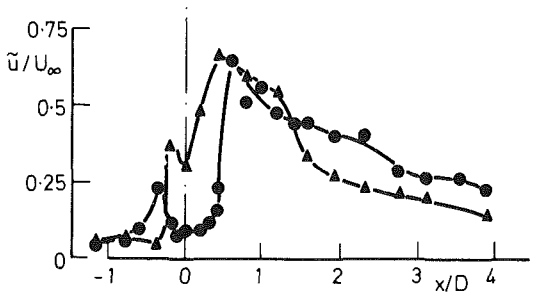


Fig. 1(*d*)

Fig. 1(*a,b,c,d*) Mean velocity and normal stress profiles

| | $\frac{Y}{D}$ | $\frac{Z}{D}$ | $V_J/U_\infty$ |
|---|---|---|---|
| ■ | 0.25 | 0 | 2.3 |
| ▲ | 0.25 | 0.25 | 2.3 |
| ◆ | 0.25 | 0.50 | 2.3 |
| ● | 0.75 | 0 | 2.3 |
| ○ | 0.25 | 0 | 1.15 |
| △ | 0.25 | 0.25 | 1.15 |
| + | 0 | 0 | – |

velocities and normal stresses. Beyond the region the turbulence levels fell to a sufficient level to allow the use of a hot-wire anemometer to record mean velocities and turbulence characteristics. Helium trace measurements were recorded for $x/D \geq 4$ and provided profiles of concentration flux which allowed the identification of jet fluid.

This paper continues in four further sections concerning apparatus, measurement systems, results, and a concluding discussion respectively.

## Experimental Apparatus

The open circuit wind tunnel used for these experiments was

## Nomenclature

$D$ = diameter
$E$ = voltage of hot-wire anemometer signal
$U,V,W$ = instantaneous velocities in $X,Y$, and $Z$ directions
$\bar{U},\bar{V},\bar{W}$ = time-average velocity in $X,Y$, and $Z$ directions
$U_\infty$ = freestream time-average velocity
$u,v,w$ = fluctuating component of velocity in $X,Y$, and Z directions ($U \equiv \bar{U}+u$ etc.)
$\tilde{u}$ = rms of velocity fluctuations ($\equiv\sqrt{u^2}$)
$V_J$ = jet velocity, averaged across $D$
$X$ = coordinate measured from hole center-line in downstream direction
$Y$ = coordinate measured from floor of wind tunnel
$Z$ = coordinate measured from line of hole centre-line across wind tunnel
$\theta$ = mean concentration
$\sigma$ = standard deviation

**Table 1 Previous experimental investigations of round jets in crossflow**

| ref. | jet diameter (mm) | incident angle | jet velocity profile | cross-flow velocity (m/s) | velocity ratio | measured |
|---|---|---|---|---|---|---|
| 1 | 6.35, 9.5 12.7, 15.9 | 90 | orifice | – | – | penetration parameters |
| 2 | 6.35, 9.5 12.7, 15.9 | 30, 45 60, 90 | orifice | 72 122 | 2-8 | correlation between parameters |
| 3 | 12.7 25.4 | 90 | orifice | – | 4, 6, 8 | total pressures, flow directions |
| 4 | 9.5 | 90 | pipe | 1.5 | 4,.6, 8 | velocity, turbulence intensity, entrainment |
| 5 | 25.4 | 90 | pipe | 18.3, 36.6 | 2, 4, 8, 11.3 | static pressure distributions |
| 6 | 6.35 | ±15, ±30, ±45, ±90, | pipe | 1.6 | 4, 6, 8 | jet trajectory, entrainment |
| 7 | 25.4 | −180, 30, 60, 90, 120, 150, 180 | nozzle | – | 1.18-10 | trajectory by photographs |
| 8 | 50.8 | 90 | pipe | 7.6 15.2 | 4.12 | wall static pressures |
| 9 | 8.4 | 90 | nozzle | MACH 0.1, 0.2 0.4, 0.6 | 1.4 | wall static pressures |
| 10 | 50.8 | 90 | nozzle | 15.2 | 8, 12 | turbulence measurements in wake region |
| 11 | 23.5 | 35, 90 | pipe | 30.5 61 | 0.1-2 | temperature, velocity, turbulence intensity contours |
| 12 | 25.4 | 90 | nozzle | 12.2 | 2, 4, 8, 12, 16, 20 | wall static pressures, turbulence intensity vorticity |

| ref. | jet diameter (mn) | incident angle | jet velocity profile | cross-flow velocity (m/s) | velocity ratio | measured |
|---|---|---|---|---|---|---|
| 13 | 23.5 11.8 | 35, 90 | pipe | 30.5 61 | 0.1-2.18 | adiabatic wall temperature, film cooling effectiveness |
| 14 | 6.35 | 90 | pipe | 6-9 | 2.8-8.5 | velocity and temperature distributions |
| 15 | 23.5 | 35, 90 | pipe | 30.5 61 | 0.1-2.0 | adiabatic wall temperatures, pitot and static pressures |
| 16 | 38.1 76.2 | 90 | orifice | – | 2, 4, 6, 8, 12 | wall static pressure distribution |
| 17 | 8.4 | 90 | nozzle | MACH 0.1, 0.2 0.4, 0.6 | dynamic pressure ratio 0 - 1000 | floor static pressures |
| 18 | 40 | 90 | pipe | 3.4 | 2.37, 3.95 6.35 | velocity distributions |
| 19 | 101.6 | 90 | orifice | 30.4 | 53.3 | velocity and vorticity |
| 20 | 101.6 | 45, 60, 75 90, 105 | nozzle | 30.5 55.3 | 8 | velocity |
| 21 | 19.05 | 90 | pipe | 26 | 0.046-0.1 | static pressure, velocity, film cooling effectiveness |
| 22 | 23.6 | 90 | pipe | 8.5 | 3.48 | velocity, vorticity |
| 23 | | | | pipe flow | 2-5-12.3 | |
| 24 | varied | 90 | orifice | 15 | 2.45-7.75 | temperature profiles |

previously discussed in references [26 and 27]. The carefully established two-dimensional flow is produced through a 7:1 contraction ratio section and the free stream turbulence is less than 0.6 percent in the range 6-20 m/s. A free stream velocity of 12 m/s was used for these experiments. The dimensions of the working section of the wind tunnel are 0.46 m wide, 0.30 m high and 1.8 m long. The wind tunnel, without the jet flow, had a zero static pressure gradient over the working length.

A single tube, 25.4 mm inside diameter and 0.75 m long was used to inject the jet normal to the freestream. The jet was located at a distance 0.15 m downstream of a $25 \times 460$ mm emery paper trip. The resulting boundary layer thickness at the leading edge of the jet was, at the 99 percent value, approximately 6 mm with no jet flow. The jet was supplied from a centrifugal fan through a screened plenum chamber and resulted in a fully developed turbulent pipe flow profile, in the absence of cross-stream flow.

The tunnel floor was made from a high surface quality aluminum block with a flatness tolerance of $\pm 0.05$ mm. The jet tube was stainless steel honed to $\pm 0.05$ mm over the final 0.25 m. The velocity profile at the exit plane of the jet, which was flush with the tunnel floor, was measured on two orthogonal planes, without the cross-flow, and found to be symmetric to better than 1% of the center-line mean velocity. Hot-wire measurements were made laterally across the jet and cross-flow at a downstream plane corresponding to $X/D = 10$ and showed symmetry to within 2 percent of the undisturbed free-stream velocity. The maximum temperature difference between jet and free stream was 1°C.

The LDA optical system was traversed in three orthogonal planes and the measurement location was known to an accuracy of better than $\pm 0.1$ mm. Hot-wires and other probes were traversed with a mechanism located on the roof of the tunnel and providing movement in three orthogonal planes to within $\pm 0.1$ mm. The hot-wire probe holder had three further movements, allowing pitch, yaw and rotation of the sensor. Rotation was limited to eight equi-spaced positions by means of a locating dowel. Positioning of the sensors, both LDA and hot-wire, was achieved with slip gauges, a pointer located within the jet and a grid of 0.3 mm holes arranged across the floor of the tunnel.

## Measurement Systems

**Laser-Doppler Anemometry.** The laser-Doppler anemometer made use of an Argon ion laser (Spectra Physics 164) operating at 488 nm and approximately 800 mW. An acousto-optic water filled cell, based on the arrangement of reference [28], operated with a frequency shift of 21.00 MHz and divided the beam into zero and +1 order beams of approximately equal intensity. The two beams, after separation and parallel alignment, were focussed to an intersection zone and backward scattered light collected through the same lens. The collected light was focused by another lens, via a mirror, onto a pinhole located immediately in front of the cathode of a photomultiplier (EMI 9815B). The resulting control volume had a calculated diameter of approximately 0.12 mm and length 0.85 mm. The distance between consecutive fringes was 2.05 $\mu$m and the zero frequency corresponded to $-43.05$ m/s. The resulting Doppler signal was processed by a spectrum analyzer, Hewlett Packard RF stage (model 8553B) and IF stage (model 8552A) and counter unit similar to that described by Durão, Laker, and Whitelaw [29]. At central linearly spaced frequencies, the number of signals in a predetermined time (usually 30 seconds) and with constant bandwidth (usually 100 kHz), were counted over the range of Doppler signal frequencies and yielded a probability distribution of signal frequencies. Each probability distribution consisted of more than $10^3$ signal counts. The effective control volume dimensions were slightly smaller than the quoted values due to the instrumentation electronic discrimination.

To provide a measurable particle arrival rate, the wind tunnel and jet were seeded with kerosene smoke generated from an evaporation/condensation arrangement. The two flows were seeded from a common reservoir at a rate proportional to the respective volume flow rates causing uniform seeding thus avoiding bias due to different seeding levels. The resulting droplets were smaller than 5 $\mu$m in diameter and allowed construction of a velocity probability distribution in less than 15 minutes.

The average quality of the signals processed corresponded to a signal to noise ratio of approximately 20 dB which allowed easy discrimination and processing. Limitations on the precision of the measurements were imposed by the number of observed signals and the histogram intervals resulting in an estimated accuracy of 2 and 5 percent of the local mean and rms frequency, respectively. In addition, the combination of photomultiplier and particle-velocity correlation bias can contribute to uncertainty but, as shown by Durão, Laker, and Whitelaw [30] the overall effect is likely to be small. The overall uncertainty in measured values of mean velocity is of order 3 percent and of the rms frequency 7 percent.

When measuring the vertical velocity component, close to the wind tunnel floor, the complete optical system was inclined to a maximum 5 deg to avoid the lower beam intersecting the tunnel floor. The maximum possible error associated with this procedure was 0.8 percent assuming $|\tilde{V}| = |\tilde{W}|$; however these profiles were only taken over the jet area where $\bar{V} > W$ and the probable error is less than 0.4%.

**Hot-Wire Anemometry.** The constant temperature anemometers, DISA 55D01 or 55M01, were operated at an overheat ratio of 0.8 and, with a bridge ratio of 20 and cable compensation adjustments, a bandwidth of approximately 40 kHz was obtained. The probe types were DISA 55P11 and 55P12, normal and slanting, respectively, and DISA 55P61 crosswire. The holders, DISA 55H20 and 55H24 were both located within stainless steel tubing to maintain constant sensor position when the probes were rotated.

Static calibration was performed using the potential core of a 50 mm diameter jet with a turbulence intensity of less than 0.3 percent. The reference velocities were from a standard NPL pitot static tube and input to a minicomputer for comparison via a Furness Controls electronic transducer. The probes were calibrated before every run and checked at various stages during the measurements to insure the effect of accumulated dirt and drift were negligible.

Exponential type linearisers, DISA 55D10, were preferred to digital linearisation, transfer function or curve storage, since both digital procedures were found to be lacking in either efficiency (curve storage) or accuracy (transfer function based upon a King's law relationship). The linearisers accurately reproduced the relationship $E = aU + b$ and the incorporation of two external operational amplifiers allowed "$b$" to be removed.

All hot-wire signals, for calibration or measurement, were processed with a DEC PDP 8E minicomputer and peripherals. The minicomputer, with 12k of random access memory, operated with a 1.2 $\mu$s cycle time using 12 bit words. Communication was through an ASR 33 teletype with paper tape reader and punch. The anemometer signals were input to a multiplexer (DEC A124) either directly or through the sample and hold modules (Burr Brown SH40) when the crosswires were sampled. The signal from the multiplexer was then passed, via a programmable gain amplifier and sample and hold module, to an $A/D$ converter. The converter (DEC A862) produced a 10 bit word plus two sign bits thus the total input voltage range was resolved into 2047 divisions. A digital

tape system, RACAL T7000, was used to facilitate data transfer between the PDP 8E and a CDC 6500.

The method of data processing was dependent on the degree of complexity required; for standard hot-wire measurements involving only mean and rms quantities, all the processing was done by the PDP 8E but for more complicated analysis the data was transferred to a CDC 6500. To produce mean and rms quantities at least 150,000 samples were taken depending on the fluctuation magnitude and for probability density distributions 400,000 samples were recorded. Energy spectra were obtained with a General Radio (Model 1564-A) frequency analyzer with a 1/10 octave filter.

The interpretation of the hot-wire signals was based on the evaluation method of Champagne and Sleicher [31].

The accuracy of the signals recorded by the hot-wire was dependent on the accuracy of the calibration and linearisation. A single wire was linearised to within 1% of the velocity recorded on the manometer over the range 3-30 m/s and a pair of cross wires were similarly linearised to within 3 percent. The total system was dependent upon the accuracy of the manometer used for calibration and for these measurements the maximum manometer error was around 0.6 percent which occurred in the low velocity range. It can be anticipated that the precision of the measurements, due to the transform equation, will diminish for values of turbulence intensity above around 0.20. Where negative velocities occur, additional errors will occur; in general the laser-Doppler anemometer was used in these flow regions. The summation of the total errors for the hot-wire system at a turbulence intensity of 15% gave probable uncertainties of $\bar{U}/U_\infty \pm 2$ percent; $\tilde{u}/\bar{U}$, $\tilde{v}/\bar{U}$, $\tilde{w}/\bar{U} \pm 7$ percent; and $\overline{\tilde{u}\tilde{v}}/\bar{U}^2$, $\overline{\tilde{u}\tilde{w}}/\bar{U}^2$, $\overline{\tilde{u}\tilde{w}}/\bar{U}^2 \pm 15$ percent.

Helium trace measurements were recorded using a probe with external and internal diameters of 0.87 mm and 0.26 mm, respectively. The air sample was passed to a Servomex thermal conductivity cell, located in a constant-temperature oven. This allowed the measurement of helium concentration to within ±2 percent of the 1 percent concentration level at the jet exit. In the range of measurements, the calibration indicated that the relationship between the output voltage of the thermal conductivity cell and helium concentration was linear.

A more detailed discussion of this method and analysis of the optimum operating condition is found in reference [32].

## Results

The results are discussed in three sections which relate to the initial mixing region where the measurements were obtained by laser Doppler anemometry, the downstream zone where hot-wire anemometry was used; and finally the helium trace concentration results obtained throughout the flow.

**Initial Region.** The laser Doppler anemometer measurements were extended to cover the range of the flow, $x/D = -1$ to 6, where hot-wire measurements would be subject to imprecision from directional ambiguity for turbulence levels greater than around 30 percent. Figures 1 to 4 present results showing $\bar{V}/V_j$, $\tilde{v}/V_j$, $\bar{U}/U_\infty$ and $\tilde{u}/U_\infty$ for vertical planes corresponding to $Y/D$ of 0.25, 0.75, 1.35, and 2.5.

The jet development in the vicinity of the pipe exit is shown in figure 1a with the profile of the undisturbed jet velocity, which has the characteristics of a fully developed turbulent pipe flow. When subjected to the cross-flow, distortion of the jet potential core has begun even by a height of 0.25D and by 0.75D is well pronounced. The measurements recorded at a lower velocity ratio (1.15) show greater distortion of the outlet profile than in the higher velocity case and suggest that the profile is modified at the outlet plane. For both ratios the front half of the jet has a decreased velocity and the rear half is forced to accelerate, and probably widen, to compensate for the extra flow of jet fluid. This rear-edge acceleration is more noticeable in the lower velocity case.

As indicated on Fig. 1(*c*), the mainstream flow in the symmetry plane and in front of the jet shows a minimum of 0.42 $U_\infty$ but the reduction in the vertical velocity in the upstream part of the jet is accompanied by an increase in the horizontal component up to a value of 0.61 $U_\infty$. At the rear of the jet the minimum value of $\bar{U}$ is 0.23 $U_\infty$ and no recirculation is shown, indicating that the flow is very different from that associated with the wake from a solid body. The region immediately behind the jet is filled with mainstream flow that has mixed with low momentum boundary-layer fluid from the jet which is easily transformed into horizontal momentum.

Figure 2(*a*), at $Y/D = 0.75$, shows two important characteristics of the jet in the initial stages. First, the twin vortex pair starts to develop as indicated by negative values of $\bar{V}$ at $Z/D = 1.0$, $-0.5 < X/D < 0.7$. The loci of the center of the vortex can be traced from $\bar{V}$ profiles on this figure. The vortex commences at $x/D = -0.5$ with its center lying between $Z/D = 0.5$ and 1.0. The center moves outwards to beyond $z/D = 1.0$ at approximately $X/D = 0.5$ but is drawn back into the wake, due to the low pressure zone, at $X/D = 2$. The center remains at $Z/D = 1.0$, as indicated by the zero mean vertical velocity, until $X/D = 3.25$ when it again moves outward. In the wake region behind the jet the centre-plane mean vertical velocity is consistently higher than that at $Z/D = 0.5$ due to the greater distance from the vortex center-line. Secondly, as shown by Fig. 2(*c*), the recirculation region behind the jet is formed at $X/D = 0.75$ in the center-plane and extends for a length of approximately half a diameter. The recirculation is formed as a result of the combined blockage of the jet and vortex structure since no recirculation was found at locations closer to the wall. The jet still has a strong central core at this height but its maximum has been displaced slightly further downstream to $X/D = 0.3$.

By the plane $Y/D = 1.35$, Figs. 3(*a*) and 3(*c*), the vertical jet velocity maximum has been considerably reduced and a large $\bar{U}$ maximum ($1.58U_\infty$) has developed, evidence of the strong streamline curvature in this region. The vortex structure is again clearly indicated by the negative vertical component at $Z/D = 1.5$ and the positive one at both center-plane and $Z/D = 0.5$ with the center-plane having the larger component. The recirculation zone has developed to a width of greater than 1D and length of 1.5D extending to nearly X/D = 3 where the vortex center begins to move outwards again. Due to the vortex structure, the fluid in the recirculation region flows upwards and $\bar{V}$ is always positive in this region.

Figure 4(*a*) shows that by $Y/D = 2.5$ the jet has lost most of its vertical momentum and the maximum velocity is only 40 percent of the average at the outlet plane. Over the next diameter the vertical momentum is destroyed completely and the center-plane profile at $Y/D = 3.5$ shows only a small positive vertical velocity, probably due to the mainstream flowing over the obstruction caused by the jet. Because the jet has turned into crossflow by $Y/D = 2.5$, the profiles of the vertical and horizontal velocities (maximum $1.8U_\infty$) are flatter than those at lower locations and the recirculation zone does not extend to this height. To the side of the jet, $Z/D = 1.5$, the flow accelerates slowly to a horizontal maximum of $1.2U_\infty$ while maintaining a near zero vertical component until $X/D = 3.5$ where it is influenced by the vortex.

The normal stress profiles from $Y/D = 0.25$ to 1.35 are dominated by twin peaks, both for $\tilde{u}/U_\infty$ and $\tilde{v}/V_j$ at the edge of the jet and originate from the boundary layer structure of the pipe flow. The downstream peak of $\tilde{u}$ is

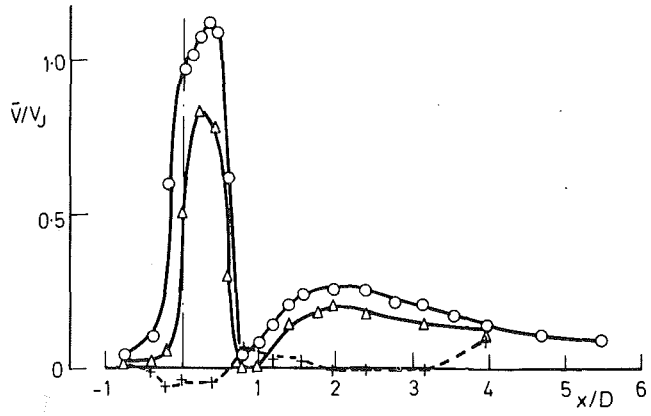


Fig. 2(a)

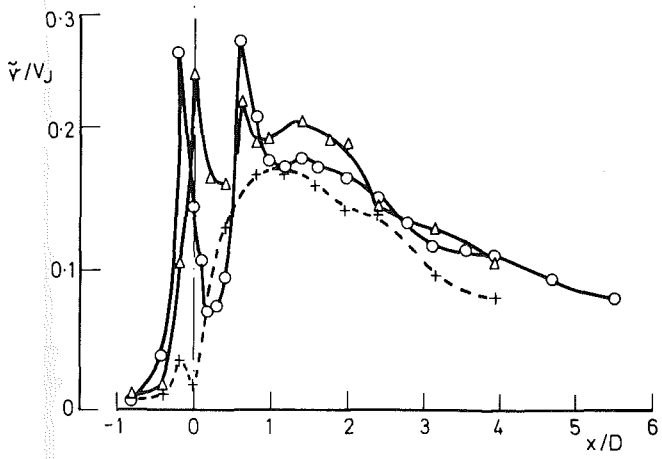


Fig. 2(b)

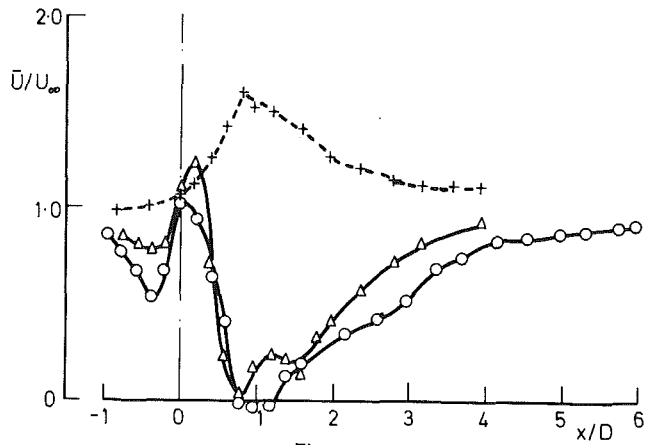


Fig. 2(c)

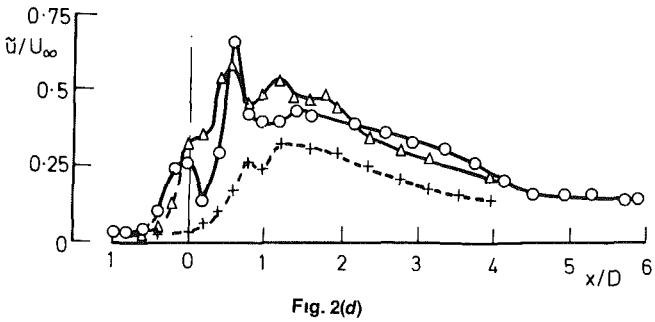


Fig. 2(d)

*Fig. 2(a,b,c,d) Mean velocity and normal stress profiles*

| | $\frac{Y}{D}$ | $\frac{Z}{D}$ |
|---|---|---|
| ○ | 0.75 | 0 |
| △ | 0.75 | 0.5 |
| + | 0.75 | 1.0 |

consistently larger than the upstream while the downstream peak of $\tilde{v}$ tends to disappear with increasing $Y/D$; the structure is largely anisotropic. The normal stresses in the inner core of the jet increase in amplitude with height until $Y/D=1.35$ after which the inner core is destroyed leaving, for $\tilde{v}$, a single maximum in the $Y/D=2.5$ plane which is further halved by $Y/D=3.5$. Immediately downstream of the jet the normal stresses are high, on all planes, and decrease slowly with increasing downstream distance.

Figure 5 presents profiles of $\bar{U}/U_\infty$ and $\tilde{u}/U_\infty$, interpolated from Figs. 1 to 4, for center-plane locations in the region $X/D=-1$ to 4. The mean velocity profiles show a peak beginning at $X/D=0$ and continuing at $X/D=0.5$ and 0.75 with a wake region developing between it and the floor of the tunnel. This peak is the result of jet fluid that has been transformed from vertical to horizontal momentum. The peak is reduced in size at $X/D=0.75$ and is destroyed by $X/D=1.0$ when the recirculation zone commences. The profile at $X/D=1$ shows the end of the high velocity region which stems from the jet. Further downstream, at $X/D=1.5$, there is a strong recirculation zone in the region of the former peak and a new maximum has developed above it composed mainly of cross-flow fluid as is confirmed by the later helium trace concentration measurements. The second peak increases at $X/D=2$, with a small reduction in recirculation strength; by $X/D=4$ the peak has reduced and the gradients can be expected to diminish with further downstream distance. The normal stress profiles between $X/D=0.5$ and 1.0 exhibit a peak in the region under the mean velocity peak but at $X/D=1.5$ and 2, with regions of strong recirculation, the normal stress profile is fairly uniform. At $X/D=4$ a normal stress peak is again developing under the second mean velocity peak.

**Downstream Region.** The results presented on Fig. 6 and appropriate to the downstream region from $X/D=6$ to 20, were obtained by hot-wire anemometry. The results represent a continuation of the centre-line values of figure 5, measured by LDA, although it should be noted that the normalising constant of the rms value is now the local mean velocity since

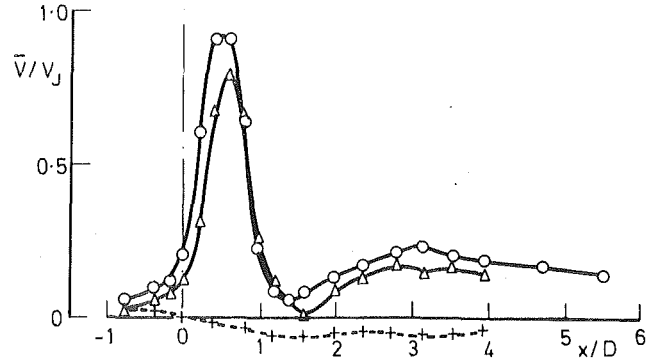


Fig. 3(*a*)

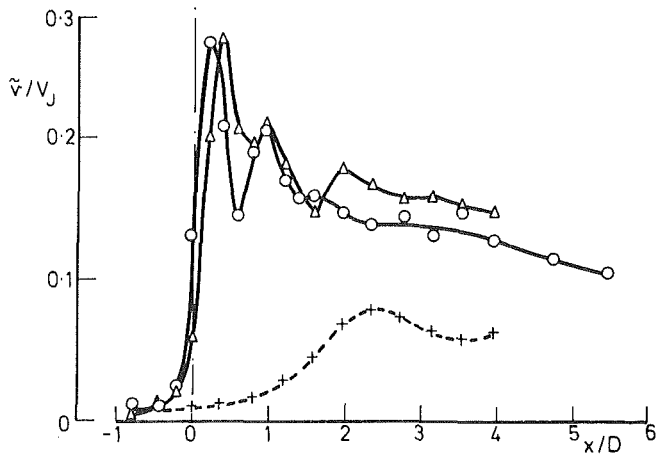


Fig. 3(*b*)

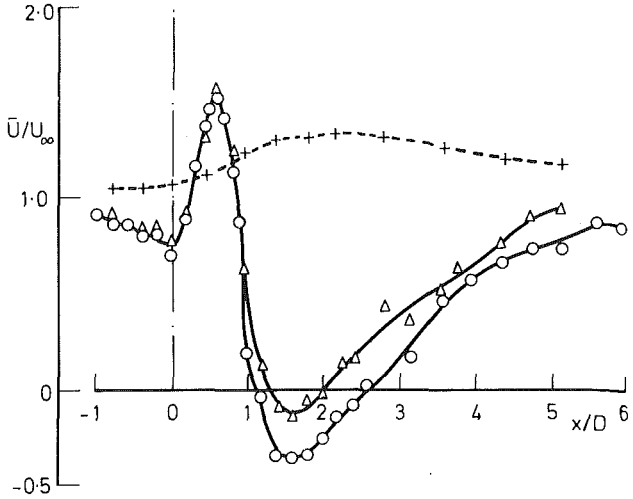


Fig. 3(*c*)

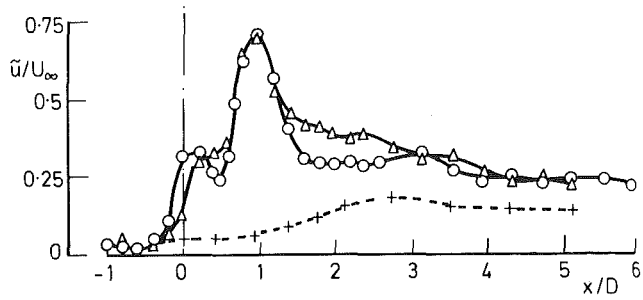


Fig. 3(*d*)

Fig. 3(*a,b,c,d*) Mean velocity and normal stress profiles

| | $\frac{Y}{D}$ | $\frac{Z}{D}$ |
|---|---|---|
| ○ | 1.35 | 0 |
| △ | 1.35 | 0.5 |
| + | 1.35 | 1.5 |

this does not give rise to infinite values. The mean velocity profiles show two peaks; the higher has often been considered as the locus of the jet trajectory, and the lower as fluid flowing into the wake behind the near vertical part of the jet. The turbulence intensity maximum consistently falls in the region of high velocity gradient slightly above the point of inflexion between the two high velocity regions.

Figure 7 presents lateral profiles of $\bar{U}/U_\infty$, $\tilde{u}/\bar{U}$, $\tilde{v}/\bar{U}$, $\tilde{w}/\bar{U}$, $\overline{uv}/\bar{U}^2$ and $\overline{vw}/\bar{U}^2$ for the plane $X/D=8$, and for four values of $Y/D$ including one, $Y/D=4$, above and outside the wake behind the normal part of the jet. Profiles obtained at larger values of $Y/D$ showed that the mean velocities, turbulence intensities and shear stresses diminished rapidly.

The mean velocity values quantify the width of the wake and show, for example, that it is largest in the vicinity of $Y/D$ of 2 and already non-existent at $Y/D$ of 4. The normal stresses in the wake region are not far from isotropy at this downstream region except at the near-wall station when the crossstream component is largest; at $Y/D$ of 4, the component normal to the wall is slightly larger.

The high $\overline{uv}$ and $\overline{uw}$ correlations at $Y/D=2$ and 3 are evidence of the jet forming the characteristic vortex pair and balancing out the wake developed by the free stream around the jet: on the center-line, $\overline{uv}$ is large and negative and $\overline{uw}$ is zero suggesting that the slower moving elements of fluid ($<\bar{U}$) have a high probability of being entrained upward into the underside of the jet. In the vicinity of $Z/D=1$, both $\overline{uv}$ and $\overline{uw}$ are large and negative suggesting that faster moving elements of fluid ($U>\bar{U}$), from regions further from the center-plane are tending to move down ($V<\bar{V}$) and inward ($W<\bar{W}$) into the wake of the jet.

The probability density distributions of Fig. 8 correspond to the plane $X/D=8$ and confirm the interpretation of the $\overline{uv}$, $\overline{uw}$ correlations represented above. At $Y/D=3$, $Z/D=0$, the positively shewed U and negatively shewed $V$ together with the large negative $\overline{uv}$ correlation are the result of slower moving elements being entrained upward into the higher velocity region. At $Y/D=3$, $Z/D=1.18$, the results show negatively skewed $U$ and positively skewed $V$ and $W$. This, in conjunction with the large negative $\overline{uv}$ and $\overline{uw}$ correlations at this point, shows that faster moving fluid elements in this region are probably those moving down and inward to the wake region of the jet.

The W probability distribution at $Y/D=1$, $Z/D=0$, Fig.

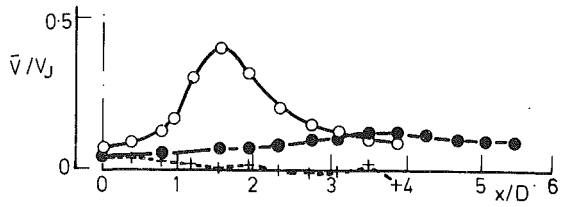


Fig. 4(*a*)

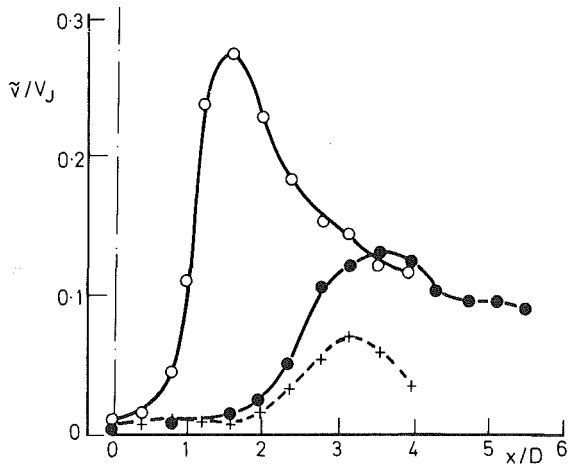


Fig. 4(*b*)

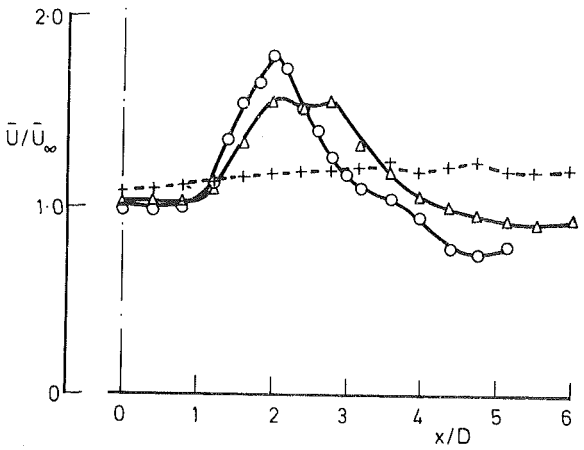


Fig. 4(*c*)

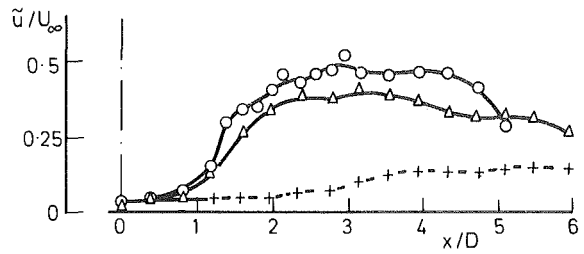


Fig. 4(*d*)

Fig. 4(*a,b,c,d*) Mean velocity and normal stress profiles

| | $\frac{Y}{D}$ | $\frac{Z}{D}$ |
|---|---|---|
| ○ | 2.5 | 0 |
| + | 2.5 | 1.5 |
| ○ | 3.5 | 0 |
| △ | 2.5 | 0.5 |

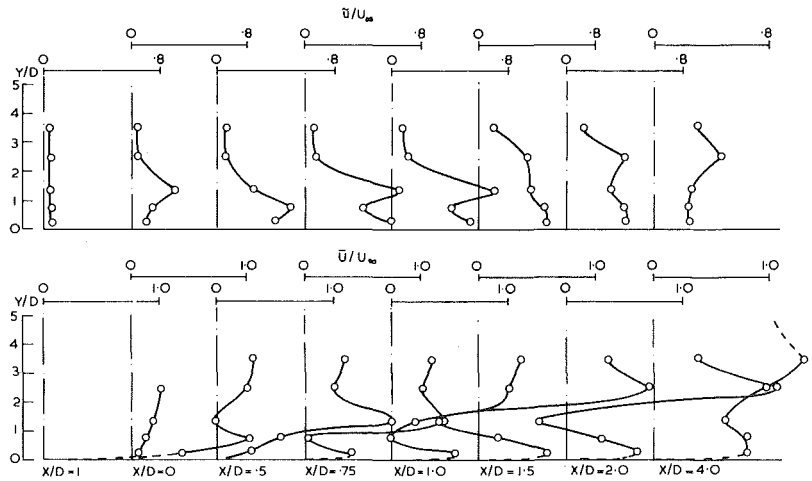


Fig. 5 Centerplane mean velocity and normal stress profiles

8(*c*) shows significant bimodality though both $U$ and $V$ have near Gaussian distributions. The mean velocity profiles of Fig. 6 indicate that the line $Y/D=1$, $Z/D=0$, is the approximate locus of the maximum wake mean velocity, suggesting that the bimodal shape stems from the wake behind the obstacle imposed by the jet. A single hot-wire, sensitive to all three velocity components, was used to measure the corresponding energy spectrum and showed a very small peak at a frequency of 25 Hz, about four times lower than that corresponding to a Strouhal number based on

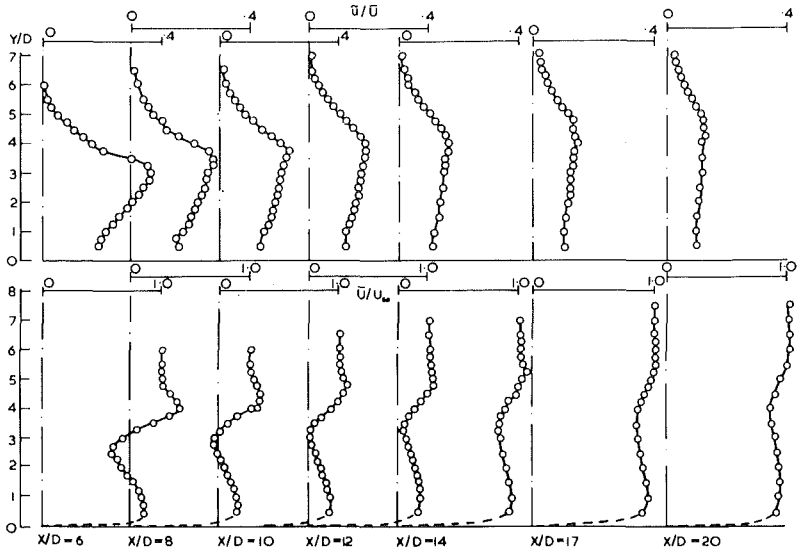


Fig. 6 Centerplane mean velocity and intensity profiles

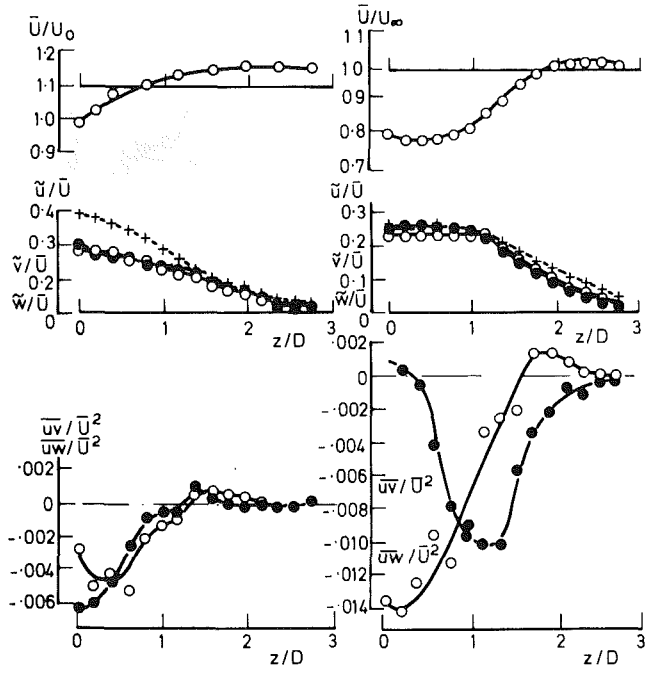


Fig. 7(a,b)

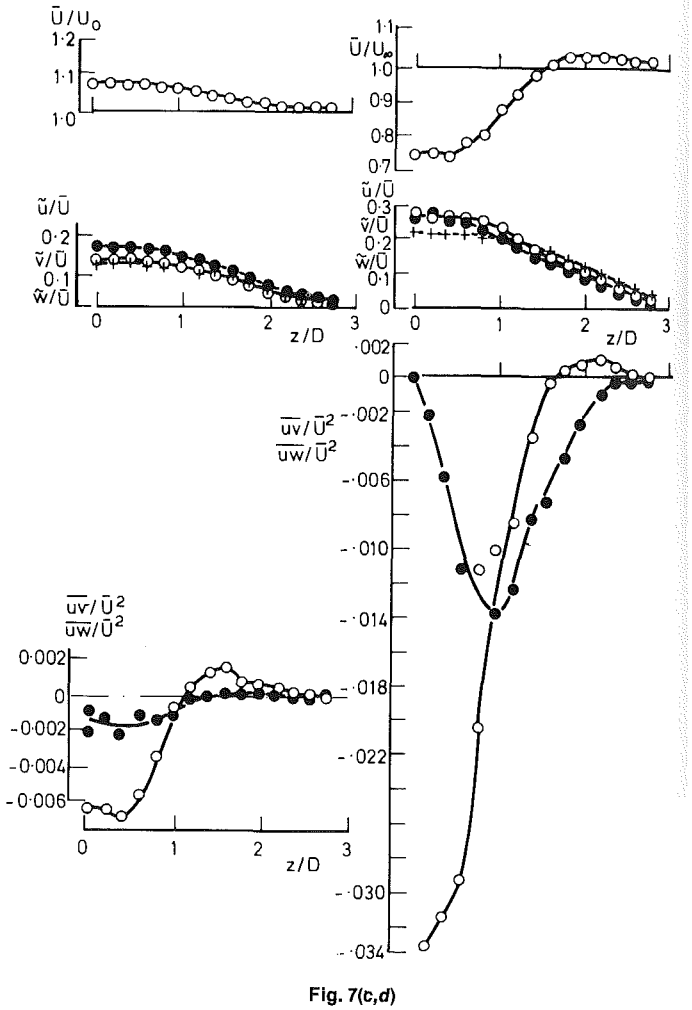


Fig. 7(c,d)

Fig. 7 Mean velocity and Reynolds stress profiles at $X/D = 8$.
*a.* $Y/D = 1$, *b.* $Y/D = 2$, *c.* $Y/D = 3$ *d.* $Y/D = 4$.
○ $\tilde{u}/\bar{U}$ ● $\overline{uv}/\bar{U}^2$
○ $\tilde{v}/\bar{U}$ ● $\overline{uw}/\bar{U}^2$
\+ $\tilde{w}/\bar{U}$

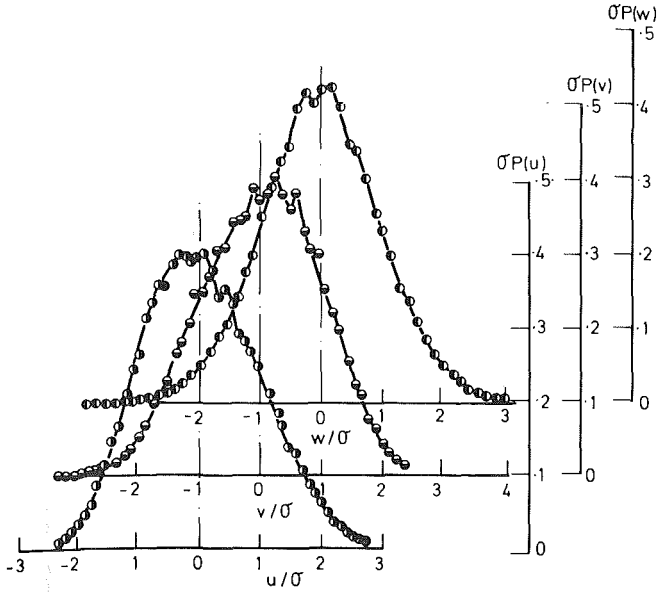


Fig. 8(a)

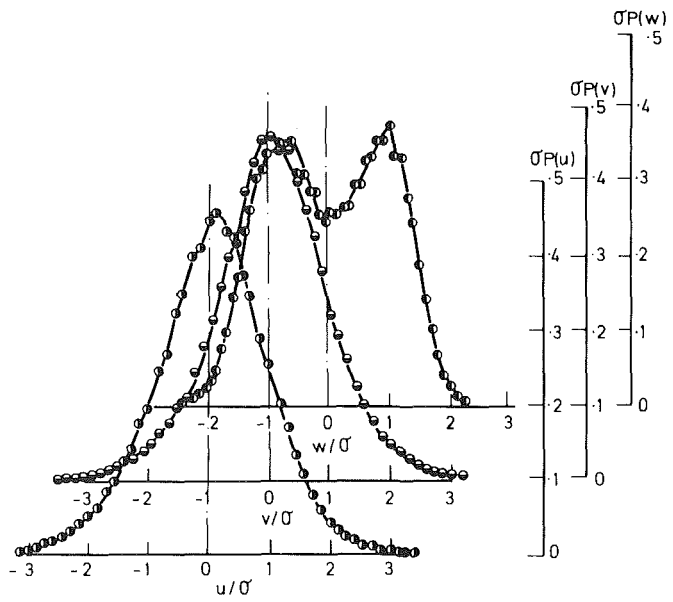


Fig. 8(b)

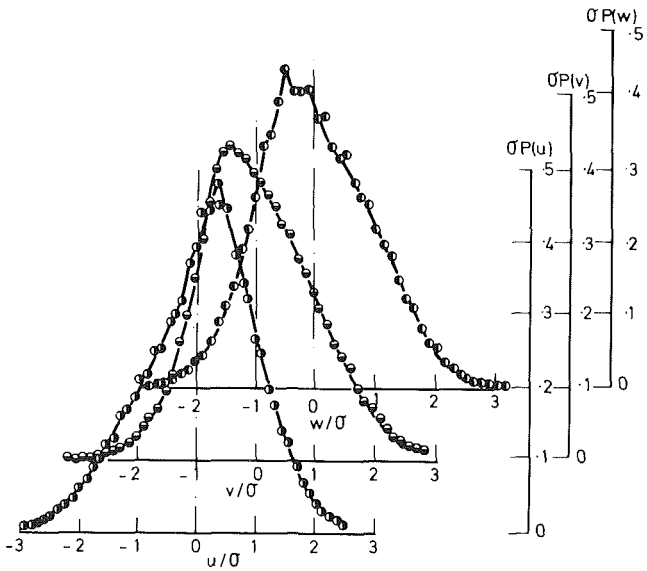


Fig. 8(c)

**Fig. 8 Velocity probability distributions at $X/D$ = 8, *a.* $Y/D$ = 3, $Z/D$ = 0, *b.* $Y/D$ = 3, $Z/D$ = 1.18, *c.* $Y/D$ = 1, $Z/D$ = 0.**

the pipe diameter of 0.2. McMahon, et al. observed a similar frequency energy spectra peak for a jet to cross-flow velocity ratio of 12. The small amplitude of the peak is consistent with the observation of a bimodal probability distribution in only one velocity component.

The center-plane helium trace profiles are presented in Fig. 9 for locations $X/D=4$, 6, 8 and 10; also included at $X/D=6$ are the profiles of $\bar{U}/U_\infty$, $\tilde{u}/\bar{U}$ and $(\bar{U}\cdot\tilde{\theta}/U_\infty\theta_J)$. The profiles of mean velocity and helium concentration do not coincide, in fact the maximum helium concentrations are in the wake region of the flow and coincide more closely with the turbulence intensity profiles. The concentration flux profile has a maximum in the lower region of the velocity peak but is consistantly high across the majority of the wake region. Figure 10 allows a comparison between contours of helium concentration and mean velocity in the plane $X/D=8$ and shows very clearly the non coincidence of $\bar{U}$ and $\bar{\theta}$. The regions of high helium concentration, i.e. containing original jet fluid, are found in the wake region. The excess velocity regions, and low helium concentration, are mostly mainstream fluid forced to flow over the obstruction of the jet and mixing with the higher momentum jet fluid. Kamotani and Greber [14] present a comparison between center-plane trajectories of maximum temperature and velocity for both lightly and strongly heated jets and clearly show a similar difference for velocity ratios between 3.9 and 7.7.

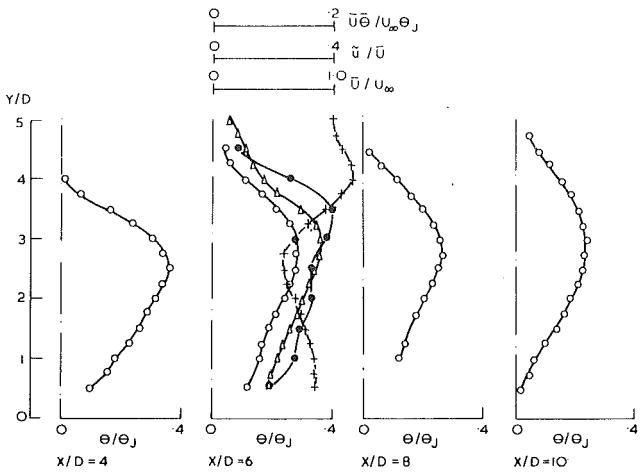


Fig. 9 Centerplane helium trace concentrations
○ $\bar{\theta}/\theta_J$
+ $\bar{U}/U_\infty$
● $\bar{U}/U_\infty \cdot \bar{\theta}/\theta_J$
△ $\tilde{u}/\bar{U}$

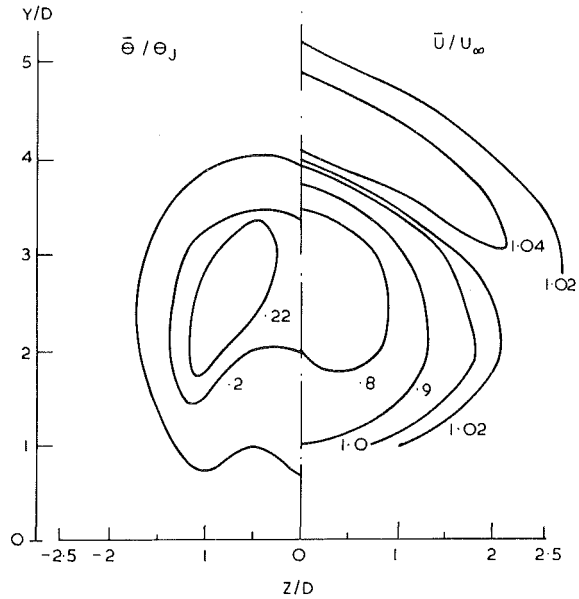


Fig. 10 Contours of helium trace concentration and mean velocity in plane $X/D = 8$

## Concluding Discussion

The present results confirm the general trends of previous investigations and provide further information which adds to knowledge of the flow structure. The double vortex structure of the downstream region, for example, is observed and quantified for the present configurations: the upstream measurements allow its formation to be recognized at $x/D = -0.25$, $Y/D = 0.75$ and between $Z/D = 0.5$ and 1.0. Similarly, the contour plots of mean velocity and helium concentration confirm that the locus of maximum velocity does not correspond to fluid from the jet exit; indeed, the downstream regions of high velocity are shown to be composed mainly of free-stream fluid.

In its mean-flow characteristics, the jet in cross-flow is controlled mainly by pressure forces which cause the bending of the jet and the double-vortex structure. In principle, therefore, and provided the considerable curvature of the flow can be adequately represented, the flow should be readily calculable without detailed knowledge of the structure of turbulence. This is, in part, confirmed by the results of Patankar, et al. [25] and the present observation that the spectral distributions of turbulence energy in the wake region are not greatly different from those associated with a fully turbulent flow. The local existence of coherent structure is consistent with the observations of Ramsey and Goldstein [11]; they do, however, contribute little to the overall fluctuation energy.

The boundary conditions for jets in crossflow are likely to be very important, as indicated by Bergeles [21] particularly in relation to the jet-exit condition. It can also be expected, for example, that the distance between the jet exit and the opposite wall will be very important since it influences the pressure field. The present results in the vicinity of the jet exit show that at $Y/D$ of 0.25, the velocity of the front half of the jet is reduced by more than 30 percent of the mean jet outlet velocity and that the rear half has accelerated and widened to accommodate the extra flow. It is reasonable to presume that, even though the flow characteristics will change between $Y/D$ of zero and 0.25, the corresponding exit profile is similarly distorted. It is likely that this effect will diminish with increasing velocity ratio but, for the two ratios considered here, it cannot be ignored.

The contour plot of Fig. 10 shows large differences between the distributions of velocity and helium concentration and, in particular, the outer velocity maximum corresponds to a region of low helium concentration and to free-stream fluid forced to accelerate around the obstruction caused by the jet. The origin of this outer velocity maximum can be traced, from Figs. 5 and 6, to $X/D$ of 1.5 where it is shown to coincide with the beginning of the wake recirculation. The jet fluid, on the other hand, is pulled into its own wake by free-stream fluid which accelerates around the jet and entrains the lower-momentum jet fluid. It enters the recirculation region, and is entrained into the double vortex where most of the jet fluid exists at $X/D$ of 8. The velocity deficit across the wake is balanced by the momentum of the spiralling vortex pair.

The turbulence structure of the flow is characterised by substantial anisotropy in the upstream region. Further downstream there is a tendency towards a more isotropic flow but significant variations still occur, especially in the wake and at lower values of Y where the W-component, with its more ordered structure, predominates. As might be expected, the shear stresses are more different in magnitude and, where zero values occur, they are not coincident with zero gradients of mean velocity or turbulence energy.

## Acknowledgments

We are glad to acknowledge financial support from the Procurement Executive of the Ministry of Defence and from the Science Research Council.

## References

1 Callaghan, E.E., and Ruggeri, R.S., "Investigation of the Penetration of an Air Jet Directed Perpendicularly to an Air Stream," NACA TN 1615, 1948.

2 Ruggeri, R.S., "General Correlation of Temperature Profiles Downstream of a Heated Air Jet Directed at Various Angles to an Air Stream," NACA TN 2855, 1952.

3 Jordinson, R., "Flow in a Jet Directed Normal to the Wind," A.R.C. R. and M. 3074, 1956.

4 Keffer, J.F., and Baines, W.D., "The Round Turbulent Jet in a Cross Wind," *Journal of Fluid Mechanics*, Vol. 15, 1963, p. 481.

5 Bradbury, L.J.S., and Wood, M.N., "The Static Pressure Distribution around a Circular Jet Exhausting Normally from a Plane Wall into an Airstream," A.R.C. CP 822, 1965.

6 Platten, J.L., and Keffer, J.F., "Entrainment in Deflected Axisymmetric Jets at Various Angles to the Stream," Univ. of Toronto UTME TP 6808, 1968.

7 Margason, R.J., and Fearn, R., "Jet Wake Characteristics and their Induced Aerodynamic Effects on V/STOL aircraft in Transition Flight," NASA SP 218, 1969.

8 McMahon, H.M., and Mosher, D.K., "Experimental Investigation of Pressures Induced on a Flat Plate by a Jet Issuing into a Subsonic Cross Wind," NASA SP 218, 1969.

9 Street, T.A., and Spring, D.J., "Experimental Reaction Jets at Subsonic Speeds," NASA SP 218, 1969.

10 McMahon, H.M., Hester, D.D., and Palfery, J.G., "Vortex Shedding from a Turbulent Jet in a Cross Wind," *Journal of Fluid Mechanics*, Vol. 48, 1971, p. 73.

11 Ramsey, J.W., and Goldstein, R.J., "Interaction of a Heated Jet with a Deflecting Stream," NASA CR 72613, 1972.

12 Thompson, A.M., "The Flow Induced by Jets Exhausting Normally from a Plane Wall into an Air Stream," Ph.D. thesis, Univ. of London, 1971.

13 Eriksen, V.L., "Film Cooling Effectiveness and Heat Transfer with Injection through Holes," NASA CR 72981, 1972.

14 Kamotani, Y., and Greber, I., "Experiments on a Turbulent Jet in Cross-Flow," AIAA Journal, Vol. 10, 1972, p. 1425.

15 Goldstein, R.J., Eckert, E.R.G., and Ramsey, J.W., "Film Cooling with Injection through a Circular Hole," NASA CR 54604, 1973.

16 Mikolowsky, W., and McMahon, H.M., "An Experimental Investigation of a Jet issuing from a Wing in a Cross-Flow," *Journal of Aircraft*, Vol. 18, 1973, p. 546.

17 Shaw, C.S., and Margason, R.J., "An Experimental Investigation of a Highly Underexpanded Sonic Jet Ejecting from a Flat Plate into a Subsonic Cross-Flow," NASA TN D 7314, 1973.

18 Chassaing, P., George, J., Claria, A., and Sananes, F., "Physical Characteristics of Subsonic Jets in a Cross-Stream," *Journal of Fluid Mechanics*, Vol. 62, 1974, p. 41.

19 Fearn, R., and Weston, R.P., "Vorticity Associated with a Jet in a Cross-Flow," *AIAA Journal*, Vol. 12, 1974, p. 1666.

20 Weston, R.P., "A Description of the Vortex Pair Associated with a Jet in a Cross-Flow." Workshop Proc. "Prediction Methods for Jet/V STOL Propulsion Aerodynamics." Inst. for Defence Analyses, Arlington VA, 1975.

21 Bergeles, G., "Three Dimensional Discrete Hole Cooling Processes," Ph.D. thesis, Univ. of London, 1976.

22 Moussa, Z.M., Trischka, J.W., and Eskinazi, S., "The Near Field in the Mixing of a Round Jet with a Cross-Stream," *Journal of Fluid Mechanics*, Vol. 80, 1977, p. 49.

23 Rathgeber, D.E., and Becker, H.A., "Mixing between a Round Jet and a Transverse Pipe Flow," *Proceedings of 1st Symposium on Turbulent Flows*, Penn. State University, 1977.

24 Holdeman, J.D., and Walker, R.E., "Mixing of a Row of Jets with a Confined Cross-Flow," *AIAA Journal*, Vol. 15, 1977, p. 243.

25 Patankar, S.V., Basu, D.K., and Alpay, S.A., "Prediction of the Three Dimensional Velocity Field of a Deflected Turbulent Jet," ASME JOURNAL OF FLUIDS ENGINEERING, Vol. 99, 1977, p. 758.

26 Kacker, S.C., and Whitelaw, J.H., "The Turbulence Properties of Wall Jet and Wall Wake Flows," ASME *Journal of Applied Mechanics*, Vol. 38, 1971, p. 239.

27 Vasilic-Melling, D., "Three-Dimensional Turbulent Flow Passed Rectangular Bluff Bodies," Ph.D. thesis, Univ. of London, 1976.

28 Durão, D.F.G., and Whitelaw, J.H., "The Performance of Acousto-Optic Cells for Laser-Doppler Anemometry," *Journal of Phys. E.* (Sci. Instruments), Vol. 8, 1975, p. 776.

29 Durão, D.F.G., Laker, J., and Whitelaw, J.H., "Digital Processing of Frequency-Analysed Doppler Signals," *Proc. of LDA-75 Symposium Technical University of Denmark*, 1976.

30 Durão, D.F.G., Laker, J., and Whitelaw, J.H., "Bias Effects in Laser-Doppler Anemometry," *Journal of Physics E.* (Sci. Instruments), Vol. 13, 1980, p. 442.

31 Champagne, F.H., and Sleicher, C.A., "Turbulence Measurements with Inclined Hot-Wires. Part 2. Hot-Wire Response Equations," *Journal of Fluid Mechanics*, Vol. 28, 1967, p. 177.

32 Folayan, C.O., "Influence of Flow and Geometric Parameter on Film Cooling," Ph.D. thesis, Univ. of London, 1976.

**J. Hoch**
Engineer,
Pope, Evans and Robbins, Inc.,
New York, N.Y. 10004
Assoc. Mem. ASME

**L. M. Jiji**
Professor,
Department of Mechanical Engineering,
The City College of the
City University of New York,
New York, N.Y. 10031
Mem. ASME

# Two-Dimensional Turbulent Offset Jet-Boundary Interaction

*This paper presents a theoretical and experimental study of two-dimensional, turbulent jet-boundary interaction. The jet is discharged parallel to and offset from a solid wall in the presence of a secondary freestream. An integral approach which makes use of the entrainment concept is used to predict the jet characteristics. The theoretical model departs from previous studies by relaxing the constant base pressure and radius of curvature restrictions and treating both as variables in the preattachment region. In general, good agreement is observed between experimental and theoretical predictions.*

## 1 Introduction

The free jet has long been of major interest in the study of turbulent shear flows. Besides having many engineering applications, the free turbulent jet provided early investigators with a simple geometry upon which to base various speculative models. Most important among these were the different forms of the mixing length theory developed by Prandtl and Taylor. These early studies established the framework for much of the later work on more complex turbulent jet problems.

Although much attention has been focused on the development of theoretical models to predict jet characteristics of unbounded flows, the effects of jet-boundary interaction have not been fully explored. Three types of jet-boundary interaction problems are commonly encountered: (1) wall jets, where the fluid is discharged at the boundary, (2) impinging jets, where the discharge is aimed towards the boundary, and (3) offset jets, where the fluid is discharged at some distance from the boundary and eventually attaches to it due to lateral pressure forces. The wall jet may be considered a limiting case of the offset jet.

Additional factors such as ambient motion, buoyancy, discharge orientation, and three-dimensional effects may further complicate a particular jet-boundary interaction problem. This theoretical and experimental study is concerned with nonbuoyant two-dimensional turbulent jets discharging parallel to and offset from a solid boundary. The effect of ambient motion on the jet is also considered.

The proximity of a solid boundary for a two-dimensional offset jet significantly affects jet characteristics. Reduced entrainment from the boundary side of the jet results in a low pressure between the jet and the boundary causing the jet to bend towards the boundary and eventually be attached to it.

In the flow regime prior to jet attachment, known as the pre-attachment region (see Fig. 1), pressures are generally lower than hydrostatic levels. As the jet approaches the boundary, pressure levels inside the jet increase, causing the jet to decelerate, eventually reaching a maximum as the jet is attached. By attaching to the boundary a recirculation region is set up which is bounded by the discharge plane, the solid boundary and the dividing or reattaching streamline. Fluid entrained by the jet from the recirculation region is returned to it resulting in no net mass exchange.

The fluid above the dividing streamline is accelerated along the boundary following jet reattachment due to the jet's positive pressure. In the second or impingement region, the pressure decreases, eventually reaching hydrostatic levels, and the acceleration ceases. In the third zone the jet undergoes turbulent diffusion analgous to that of a wall jet in what is known as the wall jet region.

**Previous Work and Present Study.** Bourque and Newman [1] were among the first to investigate the velocity and pressure behavior of a two-dimensional jet discharging into a quiescent ambient in the vicinity of a solid boundary. The problem was greatly simplified by assuming that the presence of the boundary has no effect on the velocity distribution of the jet. Thus the velocity field is taken from the solution of the two-dimensional free turbulent jet. This assumption implies a zero pressure gradient along the jet trajectory. This is accomplished by assuming that the radius of curvature of the jet centerline and the pressure inside the recirculation region are constant.

With the velocity known, the introduction of an additional equation is necessary to determine the only remaining unknown: the radius of curvature. This is achieved by applying the horizontal component (the terms horizontal and vertical as used in this paper refer to the $x$ and $y$ coordinates, in Fig. 1, respectively) of momentum locally at the point of reattachment neglecting local pressure variation.

This model, which is limited to the pre-attachment region, gives reasonable predictions of the reattachment point. However, the assumption of constant radius of curvature and base pressure and the use of the free jet velocity distribution are not borne out by their experimental data. The model also

Contributed by the Fluids Engineering Department for publication in the JOURNAL OF FLUIDS ENGINEERING. Manuscript received by the Fluids Engineering Division, December 5, 1979.

fails to account for the rise in pressure and deceleration of the jet as it approaches the point of reattachment.

Bourque [2] relaxed the constant radius of curvature restriction by assuming a sinusoidal shape for the reattachment streamline and jet centerline. Although this approximation was intended to offset the unrealistic assumption of constant base pressure, corresponding changes in the model were not made.

The constant radius of curvature assumption has dominated subsequent jet-boundary interaction models. Sawyer [3], like Bourque and Newman, focused on the preattachment region. Using a control volume approach together with the constant radius of curvature assumption, he obtained a solution for the reattachment point as a function of discharge offset distance employing a single value for the jet spread parameter.

Using a first-order mixing length model, Sawyer [4] showed that the effect of using different entrainment rates does not substantially alter the velocity profiles from their free jet shapes, and that the total entrainment is independent of curvature.

In a study related to jet-boundary interaction, Marsters [5] investigated the interaction of two parallel two-dimensional jets issuing into a quiescent surrounding. This analysis is based on the constant radius of curvature assumption of Bourque and Newman [1]. Although the theory predicts the merging of the jets reasonably well, it does not accurately predict the secondary flow entrained into the unobstructed space between the nozzles.

Rajaratnam and Subramanya [6] experimentally investigated the velocity and pressure fields of a two-dimensional jet initially offset from a parallel surface. In particular, attention was focused on the transition of the jet from the preattachment region to the reattached wall jet region.

In summary, all previous experimental and theoretical studies of two-dimensional offset jets are limited to discharges in quiescent ambient. Most investigators focused on the preattachment region and were concerned with the determination of the point of reattachment. Pressure variation inside the recirculation region is not taken into consideration and the velocity distribution is assumed to be unaffected by the presence of a boundary. Assumptions regarding pressure, velocity and radius of curvature for the preattachment region are unrealistic and generally not borne out by experimental observations. None of the current models is capable of predicting velocity and pressure distribution of a two-dimensional offset jet.

This study theoretically and experimentally investigates the problem of two-dimensional jet-boundary interaction of a submerged turbulent offset jet. It takes into consideration the effects of freestream motion and offset parameter, and deals with the near and far fields of the jet. A theoretical model is presented which elimates the simplifying assumptions made in previous studies and predicts jet pressure variations. The analysis is based on the integral formulation of the basic conservation equations.

The jet entrainment assumption, first introduced by Morton, Taylor, and Turner [9] for free jets has been modified for the offset jet. In addition, the classical jet-integral solution has been extended so as to account for variations of pressure in both the preattachment and impingement regions.

## 2 Formulation

Integral formulation of the conservation equations in the three regions identified in Fig. 1 is presented in dimensionless form. The formulation is based on two-dimensional flow with constant properties:

(*i*) *Preattachment Region.* Using the jet coordinate system shown in Fig. 1, conservation of mass gives

$$\frac{d}{dx_3}\int_{-w}^{w} u dx_1 = \frac{dQ_e}{dx_3} \tag{1}$$

## Nomenclature

$a_0, a_1, a_2$
$a_3, a_4, a_5$ = jet trajectory profile coefficients
$b$ = dimensionless measure of jet spread
$b_R$ = dimensionless distance from the dividing streamline to jet axis, $b^*_R/d^*$
$c_f$ = skin friction coefficient, $\tau_0/1/2\rho u^{*2}_d$
$d^*$ = discharge width
$h$ = dimensionless offset height, $h^*/d^*$
$J$ = jet momentum at reattachment, see Fig. 2
$J_a$ = downstream jet momentum at reattachment
$J_b$ = reversed jet momentum at reattachment
$P$ = dimensionless pressure, $P^* - P^*_\infty/\rho u^{*2}_d$
$P_b$ = dimensionless base pressure
$P_w$ = dimensionless wall pressure
$Q_e$ = dimensionless volumetric mass entrained, $Q^*_e/u^*_d d^*$
$r$ = dimensionless radius of curvature, $r^*/d^*$
$Re_d$ = Reynolds number, $u^*_d d^*/\nu$
$u$ = dimensionless axial velocity, $u/u^*_d$
$u_m$ = dimensionless maximum axial velocity
$u_\infty$ = dimensionless free stream velocity
$w$ = dimensionless jet width, $w^*/d^*$
$x$ = dimensionless horizontal cartesian coordinate, see Fig. 1, $x^*/d^*$
$x_A$ = reattachment point, see Fig. 3
$x_1, x_2, x_3$ = dimensionless jet coordinates in preattachment region, see Fig. 1
$Y_{1/2}$ = jet half-width, value of $y$ at which $(u-u_\infty)/(u_m-u_\infty) = 1/2$
$\alpha$ = entrainment coefficient
$\beta$ = pressure spread parameter
$\gamma_R$ = angle at which the dividing streamline intersects the solid boundary
$\delta$ = dimensionless thickness of inner layer for a wall jet, $\delta^*/d^*$
$\nu$ = kinematic viscosity
$\phi_R$ = angle between jet axis and the horizontal axis near the reattachment point, see Fig. 1
$\tau_0$ = wall shearing stress

Superscripts

$*$ = dimensional quantity

Subscripts

$1/2$ = location where velocity or temperature is one-half the maximum value
$d$ = discharge
$i$ = point of inflection
$m$ = maximum
$0$ = quantity evaluated at end of zone of flow establishment
$R$ = recirculation or reattachment
$w$ = wall
$\infty$ = ambient quantity

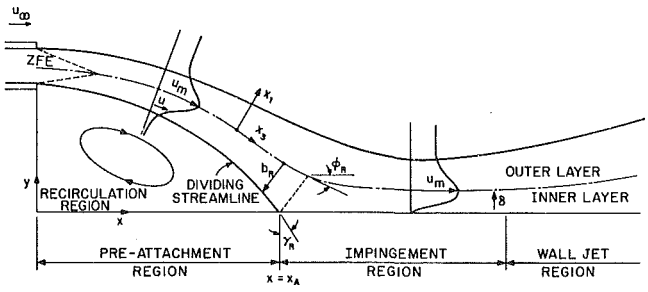


**Fig. 1 Schematic of the two-dimensional offset jet**

Conservation of axial and transverse momentum gives

$$\frac{d}{dx_3}\int_{-w}^{w} u^2 dx_1 = u_\infty \frac{dQ_e}{dx_3} - \frac{d}{dx_3}\int_{-w}^{w} P dx_1, \tag{2}$$

and

$$\frac{1}{r}\int_{-w}^{w} u^2 dx_1 = -P_b(x_3), \tag{3}$$

where $x_1$ and $x_3$ are the transverse and axial directions, respectively, $u$ the axial velocity, $u_\infty$ the freestream velocity, $w$ the jet's outer limit, $Q_e$ the volumetric mass entrained, $r$ the local jet radius of curvature, $P$ the jet pressure, and $P_b$ the base pressure. The base pressure is obtained by evaluating $P$ at $x_1 = -w$. Thus

$$P_b(x_3) = P(-w, x_3).$$

(*ii*) *Impingement Region.* This region begins at the point of reattachment, where the pressure is above hydrostatic level due to impingement, and ends further downstream where the pressure is hydrostatic. Using the rectangular coordinate system shown in Fig. 1 and assuming that the flow is parallel to the solid boundary, conservation of mass yields

$$\frac{d}{dx}\int_0^w u dy = \frac{dQ_e}{dx} \tag{4}$$

where $x$ and $y$ are the horizontal and vertical axes, respectively.

Conservation of momentum is now applied to the two layers defined by the velocity profile in this region: the inner layer, where the flow behaves like a boundary layer, and the outer layer where the flow behaves like a two-dimensional free jet (see Fig. 1). For the inner layer conservation of axial momentum gives

$$\frac{d}{dx}\int_0^\delta u^2 dy - u_m \frac{d}{dx}\int_0^\delta u dy = -\frac{1}{2}u_m^2 c_f - \frac{d}{dx}\int_0^\delta P dy, \tag{5}$$

and for the outer layer we have

$$\frac{d}{dx}\int_\delta^w u^2 dy + u_m \frac{d}{dx}\int_0^\delta u dy = u_\infty \frac{dQ_e}{dx} - \frac{d}{dx}\int_\delta^w P dy, \tag{6}$$

where $u_m$ is the maximum axial velocity, $\delta$ the boundary layer thickness and $c_f$ the skin friction.

(*iii*) *Wall Jet Region.* This region is characterized by a uniform pressure equal to hydrostatic level. Equations (4) - (6) are applicable except that the pressure gradient terms in (5) and (6) vanish.

## 3 Solutions

The solutions to equations (1) - (6) are obtained by assuming appropriate velocity profiles for each region. The preattachment region is considered first.

Following previous studies in assuming that the jet velocity profile is similar to its free jet counterpart, a Gaussian velocity profile is used to give:

$$u = (u_m - u_\infty)e^{-(x_1/b)^2} + u_\infty \quad , \quad x_1 > 0 \tag{7}$$

$$u = u_m e^{-(x_1/b)^2} \quad , \quad x_1 < 0 \tag{8}$$

where $b$ is a measure of jet spread. Implicit in equation (8) is the assumption that the jet velocity within the recirculation region is small compared to the axial velocity $u_m$.

Although the presence of a freestream may degrade jet symmetry, differences in jet spread should not be significant at low values of the free stream velocity ratio and will therefore be neglected.

It should be emphasized here that while previous studies assumed that the functions $b\ (x_3)$ and $u_m\ (x_3)$ are the same as that of a free jet, this model does not. Here only the local velocity profile is assumed to behave like that of a free jet.

Substituting (7) and (8) into the integral equations for the preattachment region (1) - (3), integrating all Gaussian integrals to infinity, and setting $w - \sqrt{2}\,b$ the three conservation equations give:

Conservation of Mass:

$$\left[(2u_m - u_\infty) + 2\sqrt{\frac{2}{\pi}}u_\infty\right]\frac{db}{dx_3} + 2b\frac{du_m}{dx_3} = \frac{2}{\sqrt{\pi}}\frac{dQ_e}{dx_3} \tag{9}$$

Conservation of Axial Momentum:

$$[(u_m - u_\infty)^2 + \sqrt{2}u_\infty(u_m - u_\infty) + u_m^2]\frac{db}{dx_3} + (2u_m + \sqrt{2}u_\infty)b\frac{du_m}{dx_3} = -\frac{2\sqrt{2}}{\pi}\frac{d}{dx_3}\int_{-w}^{w} P dx_1 \tag{10}$$

Conservation of Transverse Momentum:

$$P_b = \frac{\pi}{4}\frac{b}{r}\left[u_m^2 + (u_m - u_\infty)^2 + 2\sqrt{2}u_\infty(u_m - u_\infty) + \frac{4}{\sqrt{\pi}}u_\infty^2\right] \tag{11}$$

where $r$ is the radius of curvature.

To evaluate the pressure integral in (10) $P$ is assumed to vary linearly across the jet according to

$$P(x_1, x_3) = \frac{P_b(x_3)}{2}\left[1 - \frac{x_1}{w(x_3)}\right] \tag{12}$$

As with all integral solutions of free turbulent shear flows, an appropriate closure assumption must be introduced. Sawyer [6] demonstrated that curvature effects on the jet entrainment rate are small and that, on the average, the entrainment is similar to that of a free jet. The entrainment assumption, which has been used in many free jet applications, was first introduced by Morton, et al. [7]. This assumption states that the jet entrainment is proportional to the difference between the local maximum and minimum velocities. For this case, where free stream effects are limited to one side of the jet, one obtains:

$$\frac{dQ_e}{dx_3} = \alpha u_m + \alpha(u_m - u_\infty). \tag{13}$$

where $\alpha$ is the entrainment coefficient. The entrainment coefficient is expected to vary between the free jet value of 0.069 [8] (near the discharge) and the wall jet value of 0.036 [9] (near the point of reattachment). Because pressure effects are predominant in the preattachment region, the solution is

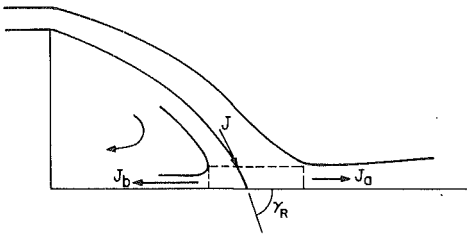


Fig. 2 Horizontal momentum condition

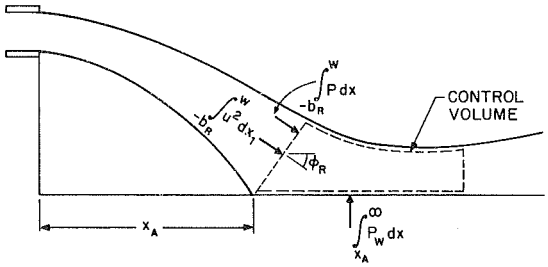


Fig. 3 Vertical momentum condition

not too sensitive to the value of $\alpha$. It is therefore reasonable to use the average value of 0.052.

Using (12) to eliminate $P$ from (10) and substituting (13) into (9) to eliminate $Q_e$, the three conservation equations (9) - (11) will have four unknowns: $b$, $P_b$, $u_m$, and $r$. To complete the solution a fourth equation is introduced by profiling the jet trajectory. Using a fifth degree polynomial, yields:

$$y = a_0 + a_1 x + a_2 x^2 + a_3 x^3 + a_4 x^4 + a_5 x^5. \tag{14}$$

Noting that the jet is discharged in the $x$-direction, neglecting higher order derivatives, (i.e. $P(0) = 0$), and knowing the discharge location we obtain:

$$y = \left(h + \frac{1}{2}\right) + a_4 x^4 + a_5 x^5. \tag{15}$$

Two remaining boundary conditions may be obtained by applying conservation of the $x$ (horizontal) and $y$ (vertical) components of momentum for a reattached jet. Bourque and Newman [1] and Sawyer [3] applied conservation of horizontal momentum locally at the point of reattachment for the control volume shown in Fig. 2 in their constant radius of curvature solution. Their approach is followed here and briefly presented.

Neglecting local pressure variation, conservation of horizontal momentum for the control volume shown in Fig. 2 gives:

$$\cos\gamma_R \int_{-w}^{w} u^2 dx_1 = J_a - J_b. \tag{16}$$

where $\gamma_R$ is the angle at which the dividing streamline attaches to the boundary, $J_a$ the momentum that proceeds downstream along the wall, and $J_b$ the momentum of the jet below the dividing streamline returned into the recirculation region. $J_a$ and $J_b$ are approximated by [1,3]:

$$J_a = \int_{-b_R}^{w} u^2 dx_1. \tag{17a}$$

and

$$J_b = \int_{-w}^{-b_R} u^2 dx_1. \tag{17b}$$

where $b_R$ is the position of the dividing or reattaching streamline relative to the jet trajectory.

The approximations made by Bourque and Newman [1] and Sawyer [3] leading to equations (16) and (17) were examined by Hoch [10] to assess their effect on the solution to the jet trajectory profile. Hoch used an alternate formulation of the horizontal momentum equation (16) and found no perceptible change in the solution.

The variable $b_R$ is determined by observing that the dividing streamline extends from the edge of the discharge to the point of re-attachment. Thus all the mass entrained in the inner part of the jet is eventually returned to the recirculation region at jet impingement. The equation for the dividing streamline is therefore given by:

$$\int_{-b_R}^{0} u dx_1 = \frac{1}{2}. \tag{18}$$

Using an appropriate velocity profile near the point of reattachment [11], equation (21) gives:

$$b_R = \frac{2}{3u_m} \tag{19}$$

The jet is considered reattached when $b_R$ is equal to the distance along $x_1$ between the jet axis and the boundary. Substituting equations (8) and (17) into (16) yields:

$$\cos\gamma_R = \frac{2u^2{}_m \mathrm{erf}(\sqrt{2}b_R/b) + (u_m - u_\infty)^2 - u_m{}^2 + 2\sqrt{2}u_\infty(u_m - u_\infty) + 4u_m^2/\sqrt{\pi}}{u_m^2 + (u_m - u_\infty)^2 + 2\sqrt{2}u_\infty(u_m - u_\infty) + 4u_\infty^2/\sqrt{\pi}} \tag{20}$$

Once $b_R$ is known $\gamma_R$ can be easily determined from geometrical considerations.

The final boundary condition is obtained by applying conservation of momentum in the vertical direction for a control volume enclosing the portion of the jet that continues downstream following reattachment. Using the control volume shown in Fig. 3, we obtain:

$$|\sin\phi_R| \int_{-b_R}^{w} u^2 dx_1 = \int_{x_A}^{\infty} P_w dx_3 - |\sin\phi_R| \int_{-b_R}^{w} P dx_1. \tag{21}$$

where $\phi_R$ is the angle between the jet axis and the horizontal axis near the reattachment point. The first and last integrals in equation (21) are evaluated at the point of reattachment. Assuming the wall pressure in the impingement region, $P_w$, exhibits similarity characteristics [11] yields:

$$P_w = P_w(x_A) e^{-\beta(x - x_A)^2/h^2}. \tag{22}$$

Here $x_A$ is the value of $x$ at reattachment and $\beta$ is a semiempirical pressure spread coefficient which is determined by comparison with experimental data. Using equations (7), (8), (12), and (22) into equation (21) we obtain:

$$\sin\phi_R = \frac{\sqrt{2}h^2 P_w(x_A)/\beta}{[u_m^2 \mathrm{erf}(\sqrt{2}b_R/b) + (u_m - u_\infty)^2 + 2\sqrt{2}(u_m - u_\infty)u_\infty + 4u_\infty^2/\sqrt{\pi}]b + P_b(\sqrt{2}b + b_R)^2/2\sqrt{\pi}b} \tag{23}$$

Equations (20) and (23) represent two independent boundary conditions that should be sufficient to solve for the remaining constants in the trajectory profile, however they cannot be directly applied because of their implicit nature. We therefore introduce two substitute explicit boundary conditions on the independent variable $x$ and $y$ regarding the

trajectory shape, that will be confirmed by equations (20) and (23) in an iterative procedure. We proceed by making use of the fact that there is an inflection point in the trajectory upstream of reattachment. At the point of inflection, the following conditions apply:

$$x=x_i, \quad y=y_i \tag{24}$$

and

$$x=x_i, \quad \frac{d^2y}{dx^2}=0 \tag{25}$$

where $x_i$ and $y_i$ refer to the conditions of the inflection point. Substituting these conditions into equation (15), gives:

$$y=\left(h+\frac{1}{2}\right)+\frac{5}{2}\left(h+\frac{1}{2}-y_i\right)\left[\left(\frac{x}{x_i}\right)^4-\frac{3}{5}\left(\frac{x}{x_i}\right)^5\right] \tag{26}$$

With suitable values of $x_i$ and $y_i$ the radius of curvature of the jet axis can be determined from [12]:

$$r=\frac{[1+(dy/dx)^2]^{3/2}}{d^2y/dx^2} \tag{27}$$

where the derivatives $dy/dx$ and $d^2y/dx^2$ are obtained using equation (26).

The final step in the solution of the preattachment region is the specification of adequate boundary conditions for $u_m$, $b$, and $P_b$. These boundary conditions are obtained from the solution of the zone of flow establishment in which a transition of the relatively uniform discharge conditions to a Gaussian distribution takes place.

To obtain the boundary conditions at the start of the zone of established flow, $x = x_0$, we integrate the continuity and momentum equations (1) and (2) between $x_3 = 0$ and $x_0$, using entrainment relationship (13), noting that $u_m = 1$ and assuming $P_b = 0$ at the discharge. Using equation (3) and rearranging gives:

$$b(x_0)=\frac{r(x_0)}{\sqrt{2}}\left\{\frac{4\sqrt{2}[1+2\alpha u_\infty(1-u_\infty)x_0]+1}{r[(1-u_\infty)^2\sqrt{\pi}/2+2u_\infty(1-u_\infty)\sqrt{\pi}+2\sqrt{2}u_\infty^2}\right\}^{1/2}-1 \tag{28}$$

and

$$x_0=\frac{[(1-u_\infty)\sqrt{\pi}+2\sqrt{2}u_\infty]b(x_0)-1}{2\alpha(1-u_\infty)} \tag{29}$$

The entrainment coefficient $\alpha$ is set at the free jet value of 0.052 [8] in this zone. A numerical solution of equations (28) and (29) gives the values of $b(x_0)$ and $x_0$ for a given jet trajectory, where the radius of curvature is determined using equation (27).

Proceeding now to the impingement and wall jet regions we begin by noting that, except for the excess pressure, the jet behavior in both regions is similar to a velocity profile given by [10]:

$$u+u_m(y/\delta)^{1/7}, \quad 0\le y\le\delta, \tag{30}$$

$$u+(u_m-u_\infty)e^{-\left(\frac{y-\delta}{b}\right)^2}+u_\infty, \quad y\ge\delta \tag{31}$$

As in the preattachment region we will assume that the pressure across the jet varies linearly, with the maximum at any cross-section occuring at the wall. Therefore:

$$P(x,y)=P_w(x)\,[1-y/w] \tag{32}$$

where $P_w$ is the wall pressure.

Substituting equations (22) and (30) - (32) into equations (4) - (6), integrating all Gaussian integrals to infinity, and setting $w = \sqrt{2}\,b + \delta$ yields for the conservation of mass:

$$\left[\frac{7}{8}\delta+\frac{\sqrt{\pi}}{2}b\right]\frac{du_m}{dx}+\left[\frac{\sqrt{\pi}}{2}(u_m-u_\infty)+\sqrt{2}u_\infty\right]\frac{db}{dx_3}+\left[\frac{7}{8}u_m-u_\infty\right]\frac{d\delta}{dx}=\frac{dQ_e}{dx} \tag{33}$$

and for conservation of momentum

$$[\sqrt{\pi}/2(u_m-u_\infty)b+\pi u_\infty b+7/8u_m\delta]\frac{du_m}{dx}+(7/8u_m^2-u_\infty^2)\frac{d\delta}{dx}+\sqrt{\pi/8}(u_m-u_\infty)^2+\pi u_m(u_m-u_\infty)+\sqrt{2}u_\infty^2]\frac{db}{dx}=u_\infty\frac{dQ_e}{dx}-\frac{1}{2}\frac{dP_w}{dx}[\sqrt{2}b+\delta-\delta^2/(\sqrt{2}b+\delta)] \tag{34}$$

and

$$7/72\,u_m^2\frac{d\delta}{dx}-49/72\,u_m\delta\frac{du_m}{dx}=\frac{1}{2}u_m^2c_f+\delta\frac{dP_w}{dx}\left[1-\frac{1}{2(1+\sqrt{2}\,b/\delta)}\right] \tag{35}$$

We again use Morton's [7] entrainment assumption to specify the entrainment rate, which for a wall jet gives

$$\frac{dQ_e}{dx}=\alpha(u_m-u_\infty) \tag{36}$$

where $\alpha = 0.035$ [9].

The skin friction, $c_f$, may be determined using Blasius' law for turbulent flow through pipes and over flat plates as adjusted for a wall jet by Sigalla [13]. In dimensionless quantities $c_f$ is given by:

$$c_f=0.056\,(\mathrm{Re}_d u_m\delta)^{-1/4} \tag{37}$$

The boundary conditions for the impingement region are obtained by matching with the preattachment region at the point of reattachment. The values of $u_m$ and $b$ are taken directly from the velocity profile just prior to the point of impingement, $\delta$ is set equal to the distance between the boundary and the jet axis, and $P_w(x_A)$ is set equal to the value of $P_b$ at jet reattachment.

**Experimental Set-Up.** An experimental investigation of the two-dimensional jet-boundary interaction problem was conducted in the low speed wind tunnel facility of the Mechanical Engineering Laboratory of the City College of New York. The tunnel has a test section measuring 42 in (1.07m) wide by 30 in. (0.75m) high by 90 in. (2.3m) long. The working section is enclosed in a large pressure-tight chamber. Air flow through the wind tunnel, which was used to simulate free stream motion, was produced by a centrifugal blower which exhausts air from the observation chamber. The maximum velocity obtained under this arrangement was approximately 13 ft/s (4m/s). Lower velocities were produced by adjusting the blowers exhaust baffles. A detailed description of the wind tunnel is found in Reference [14].

Observations and measurements on two-dimensional jet-boundary interaction were made in the wind tunnel test section shown in Fig. 4. The free stream velocity through the test section was designed to be steady and uniform with recorded turbulence intensity levels below 0.1 percent. The primary air was supplied to the test section via a variable height vertical inlet duct which was connected to a horizontally oriented rectangular nozzle. Two different nozzles were used, one with a height $d^*$ of 0.26 in. (0.66cm) and another of 0.46 in. (1.17cm). Both nozzles had a width of

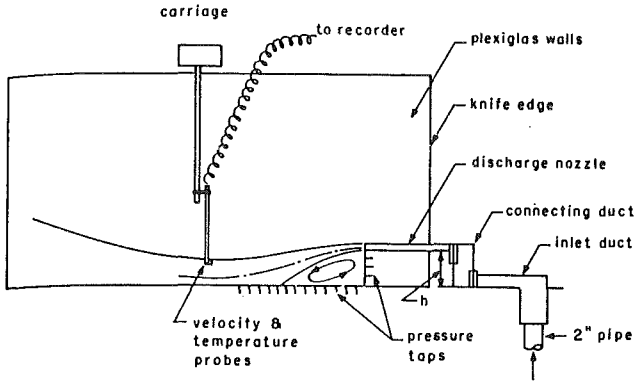


Fig. 4 Test section

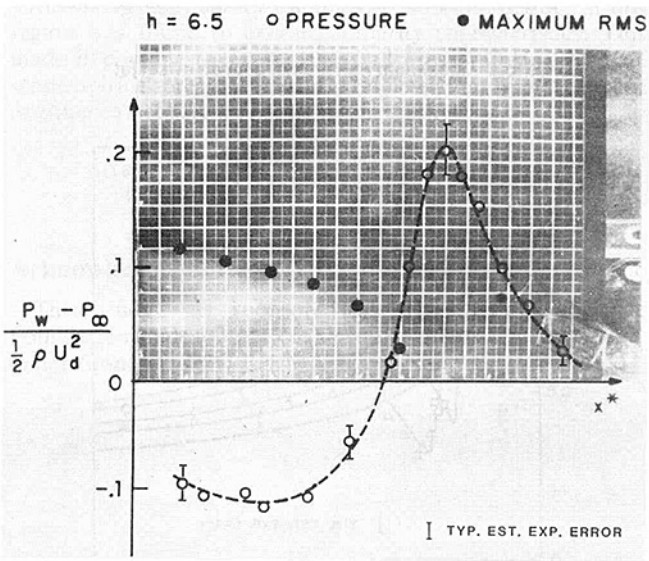


Fig. 5 Smoke photograph, maximum RMS and wall pressure of the preattachment region of an offset jet

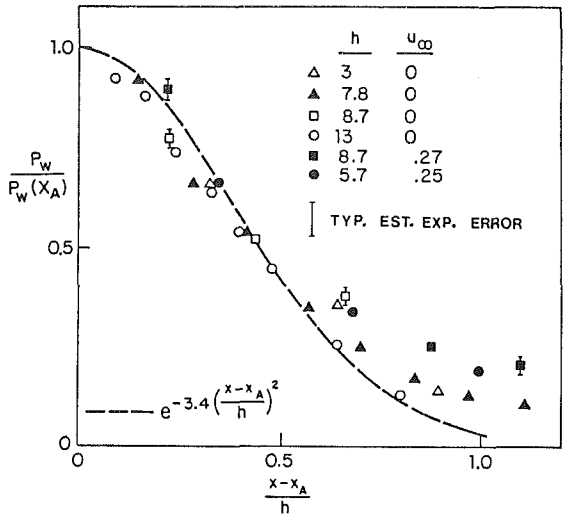


Fig. 6 Normalized wall pressure in the impingement region of an offset jet

approximately 4 7/8 in. (12.4cm). Average jet discharge velocities were varied from approximately 10 to 120 ft/s (3 to 36 m/s), depending on nozzle height. Discharge Reynolds numbers were well within the turbulent range and discharge velocity profiles were observed to be nearly top-hat.

In order to insure that the jet remains two-dimensional, two 24 in. (0.6m) high and 80 in. (2m) long plexiglass plates with tapered leading edges were placed vertically on each side of the jet nozzle, forming a channel with a spacing equal to the nozzle width. Smoke tracer tests revealed that the leading edges were effective in preventing any separation of the free stream. The two-dimensionality of the flow was substantiated through velocity measurements [10]. A horizontal plate was inserted at the bottom of the channel with which jet interaction took place.

Mean velocities were measured using a constant temperature hot wire anemometer system. The wall pressure distribution was determined by the use of pressure taps on the bottom surface. Pressure taps at the step face of the discharge plane were also used to examine the possibility of streamline separation in the recirculation region.

The flow pattern in the pre-attachment region of an offset jet was examined by injecting small quantities of smoke into the recirculation region via ports in the rearward facing step. The dividing streamline can be approximated by the outer boundary of the trapped recirculating smoke. RMS turbulence measurements were also used to locate the position of the dividing streamline, which is characterized by the locus of peak RMS values [14].

**Results.** To check the validity of the theoretical model experimental data was used to examine some of the basic assumptions as well as the accuracy of theoretical predictions of jet characteristics. Possible fixed error is included within the uncertainty bands displayed in Figures 5 through 11, with the experimental data. The uncertainty was estimated using the limited - sample method of Kline and McClintock [15].

Figure 5 is a typical photograph of the flow pattern in the recirculation region showing the position of the dividing streamline. Superimposed on the photograph is the locus of peak measured RMS values which correlate with the position of the dividing streamline. Also shown in Fig. 5 is the measured wall pressure profile. This confirms our assumption that the maximum wall pressure occurs at the end of the preattachment region.

The value of the pressure spread coefficient $\beta$ in the impingement region is determined by matching the wall pressure profile, equation (22), with experimental data. Figure 6 shows that $\beta = 3.4$ correlates well with experimental data for different values of the offset parameter $h$ and freestream velocity $u_\infty$. Deviation between the assumed pressure profile and experimental data at the end of the impingement region will not affect theoretical predictions because of the reduced pressure levels.

Figure 7 compares predicted jet trajectories with experimental data for various combinations of the parameters $h$ and $u_\infty$. The favorable agreement between theory and experiment demonstrates the adequacy of the approximations used in determining the coefficients of the assumed trajectory profile described by equation (14) leading to the theoretical solution given by equation (26).

Theoretical predictions of the re-attachment point, based on the position of maximum wall pressure $x_A$, are compared with experimental data in Fig. 8. Also shown in Fig. 8 are the experimental data of Bourque and Newman [1] and Sawyer [3]. Data on the maximum wall pressure, $P_w(x_A)$, is plotted in Figure 9 and compared with theoretical results. Reasonable agreement is obtained between theory and experiment. Agreement with Sawyer's [3] data for $u_\infty = 0$ is very good.

The variation of the jet maximum velocity $u_m$ with the axial distance $x$ is presented in Fig. 10. Data for $u_\infty = 0$ and various values of the offset parameter $h$ is compared with theoretical

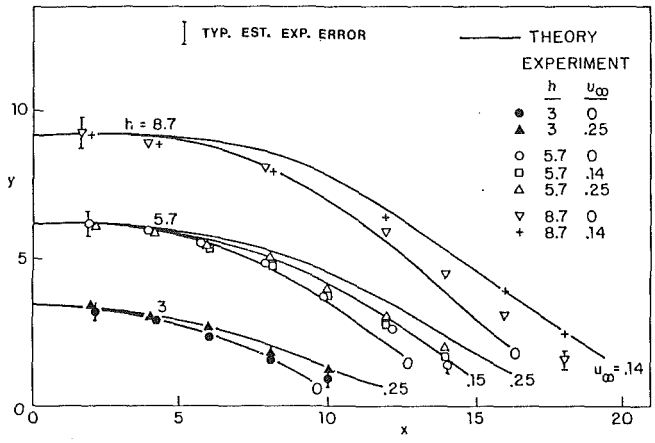


Fig. 7 Jet trajectory in the preattachment region of an offset jet

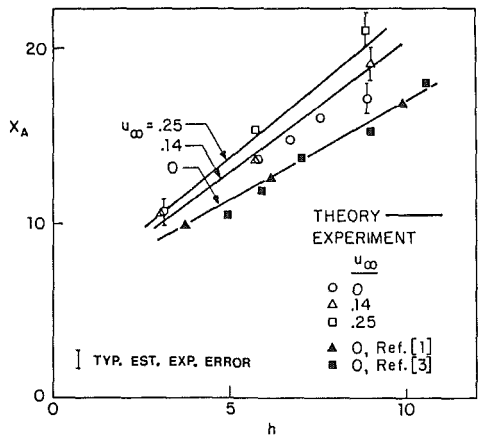


Fig. 8 Variation in the reattachment length of an offset jet

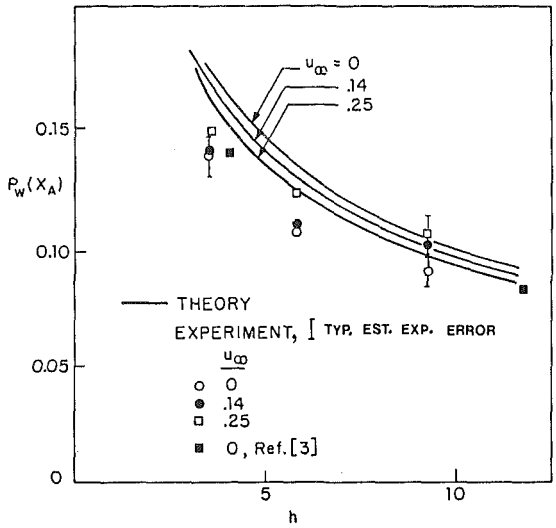


Fig. 9 Maximum wall pressure for an offset jet

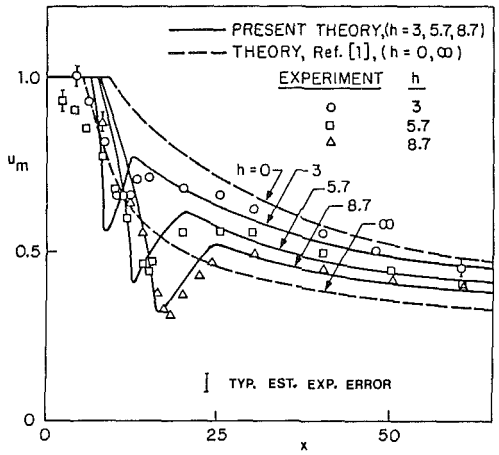


Fig. 10 Maximum axial velocity decay for an offset jet ($u_\infty = 0$)

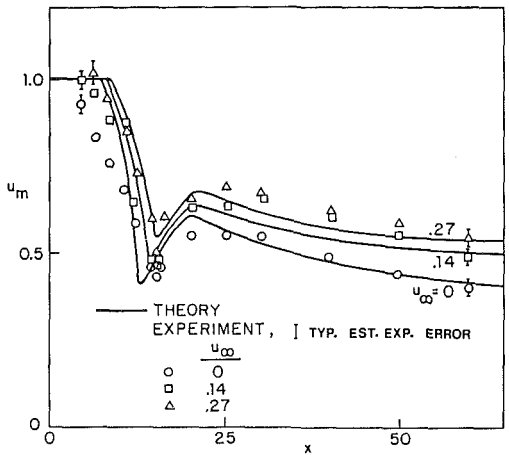


Fig. 11 Maximum axial velocity decay for an offset jet ($h = 5.7$)

solutions. The two points along each curve where the slope changes sign correspond, approximately, to the end of the reattachment and impingement regions. Also shown in Fig. 10 are the theoretical solutions for the two limiting cases of two-dimensional free jet ($h=\infty$) and wall jet ($h=0$) taken from Rajaratnam [9]. As might be expected these two solutions bracket the offset jet data and theory in the wall jet region.

The effect of free stream velocity on the behaviour of the jet maximum velocity $u_m$ is shown in Fig. 11 for a fixed offset parameter value of $h=5.7$. Freestream velocity does not seem to substantially affect the maximum axial velocity in the preattachment and impingement regions. This is probably because there is only a small perturbation in the pressure field for low values of the freestream velocity ration ($u_\infty < 0.3$), and the jet dynamics rather than the turbulent mixing govern the flow in these regions.

## Conclusion

An integral solution coupled with an entrainment assumption was used to predict the velocity and pressure fields of a two-dimensional jet discharging offset from, and parallel to a solid boundary in the presence of a secondary free stream. A new approach is used in which the pressure and the local radius of curvature in the pre-attachment region were considered as variables to be determined by the solution. By allowing the pressure to vary, the model resulted in an axial velocity distribution distinctly different from that of a free jet. The entrainment assumption used was essentially the same as the one advanced by Morton, et al. [7]. The favorable agreement between our theoretical predictions and experimental data supports the hypothesis that the entrainment mechanism in an offset jet is not affected by the pressure field.

Except for the pressure terms, the governing conservation equations are similar to their free jet counterparts. However, because jet pressure and radius of curvature are treated as variables, the conventional jet integral solutions are not applicable. The integral method was thus modified by specifying a polynomial profile for the jet trajectory. The polynomial coefficients were determined by an iterative procedure from boundary conditions, geometric considerations and the two approximate momentum relationships. The resulting jet trajectory, axial velocity distribution and reattachment pressure compare well with experimental data. Caution should be used in applying the model outside the range of our experimental data ($h > 12$, $u_\infty > 0.3$) because of uncertainties involved in some of the model's approximations outside this range [10].

The solution of the impingement region was similar to that of an ordinary wall jet, except for the addition of pressure terms in the momentum equations. The wall pressure in this region was found to exhibit similarity characteristics. This made it possible to profile the wall pressure using a single semiempirical pressure spread parameter that is independent of either offset height or free stream motion.

## Acknowledgment

This study was sponsored by The National Science Foundation under Grant No. ENG 78-10004 and by CUNY under Grant No. PSC-BHE 12312.

## References

1 Bourque, C., and Newman, B.G., "Reattachment of a Two-Dimensional Incompressible Jet to an Adjacent Flat Plate," *Aeronautical Quarterly,* Vol. 11, 1960, pp. 201–232.

2 Bourque, C., "Reattachment of a Two-Dimensional Jet to an Adjacent Flat Plate," *Advances in Fluidics,* Fluidics Symposium, ASME, 1967, pp. 192–204.

3 Sawyer, R.A., "The Flow Due to a Two-Dimensional Jet Issuing Parallel to a Flat Plate," *J. of Fluid Mechanics,* Vol. 9, 1960, pp. 543–560.

4 Sawyer, R.A., "Two-Dimensional Reattaching Jet Flows Including the Effect of Curvature on Entrainment," *J. of Fluid Mechanics,* Vol. 17, 1963, pp. 481–498.

5 Marsters, G.F., "Interaction of Two-Plane Parallel Jets," *AIAA Journal,* Vol. 15, 1977, pp. 1756–1762.

6 Rajaratnam, N., and Subramanya, K., "Plane Turbulent Reattached Wall Jets," *ASCE J. of Hydraulics Div.,* Vol. 94, HYi, 1968, pp. 95–112.

7 Morton, B.R., Taylor, G.I., and Turner, J.S., "Turbulent Gravitational Convection from Maintained and Instantaneous Sources," *Proc. Royal Soc.,* London, Series A234, 1956, pp. 1–23.

8 Jirka, G., and Harleman, D.R.F., "Heat Dissipation from Power Plants," MIT Parsons Laboratory for Water Resources and Hydrodynamics, Technical Report No. 206, 1975.

9 Rajaratnam, N., *Turbulent Jets,* Elsevier Scien. Publishing, Amsterdam, 1976.

10 Hoch, J., "Two Dimensional Jet-Boundary Interaction for Submerged Thermal Discharges," Doctoral Dissertation, The City University of New York, 1979.

11 Hoch, J., and Jiji, L.M., "Two-Dimensional Turbulent Offset Jet-Boundary Interaction," ASME Paper No. 80-WA/FE-12, 1980.

12 Kreyszig, E., *Advanced Engineering Mathematics,* 3rd Ed., J. Wiley, New York, 1972.

13 Sigalla, A., "Measurements of Skin Friction in a Plane Turbulent Wall Jet," *J. Royal Aero. Soc.,* Vol. 62, 1958, pp. 873–877.

14 Tandowski, B., "Near Field Pollution Due to Emissions from Short Stacks on Buildings," Doctoral dissertation, Mechanical Eng'g. Department, The City University of New York, 1977.

15 Kline, S.J., and McClintock, F., "Describing Uncertainties in Single Sample Experiments," *Mechanical Eng.,* 1953.

# Wake Structure of Typical Automobile Shapes

**S.R. Ahmed**
Institut für Entwurfsaerodynamik, DFVLR,
Braunschweig, West Germany

*The time averaged wake structure of three characteristic vehicle shapes viz. Estate, Fastback and Notchback was studied on the basis of flow visualization and wake surveys behind smooth quarter scale models in a wind tunnel. The models differed through their upper rear-end shape. Flow in the separation bubble at vehicle base and the subsequent formation of a pair of longitudinal vortices aft of this region is analysed. The kinetic energy of the rotational motion in the wake is evaluated to give a "vortex drag" rating for the vehicle shapes investigated. Effect of body details was assessed by a parallel set of experiments with detail models of same principal dimensions. Force measurements supplemented the investigations.*

## Introduction

Considerable interest in the aerodynamic drag characteristics of bluff vehicle type bodies moving in ground vicinity has been evoked by the present energy situation. A significant amount of the total energy consumed during the movement of a ground vehicle is expended in overcoming the aerodynamic drag. In view of the large number of vehicles moving on roads and tracks, saving in fuel and energy through reductions in aerodynamic drag can have a large impact on ground transportation requirements.

The amount of drag experienced by a body is related to the structure of wake it creates. A characteristic of a low drag body is the weak transverse flow in its wake. For a better understanding of the drag creating mechanisms, detailed information about this part of the flow is needed. This knowledge can be put to practical use in generating aerodynamically favorable vehicle shapes having low drag, good road handling qualities and in reducing adverse interference effects among vehicles moving in close proximity.

Various flow visualization techniques are employed by automobile manufacturers during the course of body optimisation in wind tunnels to study the flow around the vehicle and in wake. Hypothetical qualitative models of flow in wake, derived on the basis of extensive flow visualisation and measurement of forces and base pressure are proposed in the work of Potthoff [1], Carr [2], Hucho [3], Mason and Beebe [4], and Morel [5]. Quantitative information about flow quantities in wake of vehicle type bodies is scarce in the literature. Howell [6] presents total pressure and velocity distribution data in wakes of some vehicle models. A correlation of drag with corresponding wake structure was not attempted.

Due to this apparent need, a comprehensive experimental investigation was carried out. Wake surveys were done at a number of downstream locations enabling the quantitative determination of pressure and velocity fields in planes perpendicular to the main flow. Wake visualization and force measurements supplemented the wake structure analysis experiments.

## Experimental Arrangement and Test Procedure

**Wind Tunnel.** The tests were conducted in the DFVLR low speed wind tunnel. This facility described in [7], is an open test section closed-return wind tunnel with a square nozzle of 9 $m^2$ cross section area and a working section length of 5.86 m, Fig. 1.

Maximum continuous wind speed attained is 60 m/s and turbulence intensity in the empty test section lies below 0.5 percent. All tests were conducted at the maximum speed corresponding to a model length based Reynolds number of 4.29 million.

**Models.** The basic smooth configuration, Fig. 2(*a*), was a quarter scale 1.044 m long automobile model with a length: width: height ratio of 3.02 : 1.16 : 1. The upper rear-end was interchangeable. Ground clearance at lowest point of model undersurface was 0.05 m. All upper- and under-surface details were smoothed out, edges and hood front were rounded.

Main dimensions of the three interchangeable rear-ends are given in Fig. 2(*b*). Frontal area of model including wheels was 0.1122 $m^2$, which is 1.25 percent of wind tunnel nozzle area.

The detail model, Fig. 3, had the same principal dimensions and body geometry as the smooth model, but was provided with upper- and undersurface details, realistic wheels and wheel houses. Engine compartment features and cooling air flow path were not simulated. Also this model had three interchangeable detail rear-ends.

**Test Arrangement And Flow Field Probe.** For flow field exploration, the model was fixed upside down via wheels directly on to a ground plane 3 m wide, Fig. 1. The model was positioned so that the distance between ground plane trailing edge and model base was about 2.5 times model length. This was deemed necessary (see [8]) to avoid interference effects between model wake and flow at ground plane trailing edge. Wake surveys were done for zero model yaw only.

Contributed by the Fluids Engineering Division for publication in the JOURNAL OF FLUIDS ENGINEERING. Manuscript received by the Fluids Engineering Division, August 22, 1979.

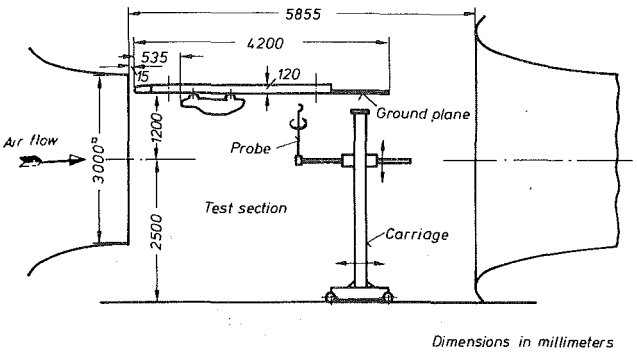


**Fig. 1 Model setup in wind tunnel**

A nine-hole conical-tip yawmeter probe Fig. 4, was used for the wake survey. The arrangement of the four orifices on the conical tip is such as to make the pressure difference between one opposing pair sensitive primarily to flow yaw, and the other to flow incidence. The instrument is used as a null yaw-reading device, in the sense that yaw rotations are imposed until the pressure in the opposing pair of orifices is equalised. In this condition, the tip axis is pointing nominally along the direction of local yaw. The pressure in the central tip orifice and the mean of the pressures in the four orifices on cylindrical tip sleeve is a function of the local total and static pressures respectively. Values of total and static pressure are evaluated from these data using calibration curves. Thus magnitude and direction of the local velocity vector and local total head are determined, given the yaw angle displacement of the probe in the balanced state together with the pressures in the rest seven orifices.

The probe was mounted on a carriage, Fig. 1, which provides rectangular cartesian translations along the full length, width and height of the working section. All translational motions are effected by remotely controlled electric motors, and measured by electronic counters. Probe was moved continuously with a speed of 3.6 mm/s during surveys in the $z$-direction with $x$- and $y$-position kept fixed. The $z$-traverse was repeated for a new value of y which was increased in steps of 20 mm (or 40 mm) till a traverse half-plane from $y=0$ mm to 400 mm and $z=5$ mm to 600 mm was scanned.

**Data Acquisition and Estimated Accuracy.** A completely computerised acquisition and data reduction system in which

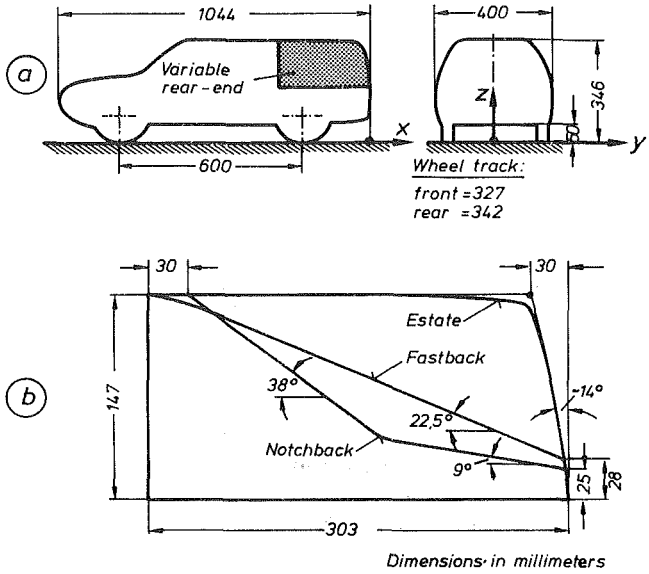


**Fig. 2 Wind tunnel model**
**(a) overall dimensions**
**(b) rear-end shapes**

various corrections and calibrations were taken into account enabled a rapid flow field exploration. Measured quantities could be displayed on a graphic unit to monitor the experiments.

The data acquisition system was developed and calibrated for steady flow. Flow visualisation of the wake indicated unsteady regions at separation bubble edge and at closure. To evaluate the performance of the system in unsteady flow, progressively higher frequency harmonic fluctuations were imposed on the calibration flow. This analysis, together with oscilliscope traces of pressure, led to the choice of 0.2 s as the suitable data integration time. The continuously acquired data was integrated over this time interval to arrive at the average value recorded. The pressure fluctuations of the empty tunnel flow were below 5 Hz. Choice of the above said integration time thus avoided the inclusion of wind tunnel flow fluctuations in the averaging process. Estimated accuracy of the incidence angle measured is ± 0.3°. Errors of upto 1 percent of the value of free stream dynamic pressure are estimated to be present in the pressures measured.

## Nomenclature

$b$ = model width
$c_D = D/(q_\infty F)$ = drag coefficient
$c_g = (g-p_\infty)/q_\infty$ = total pressure coefficient
$c_L = L/(q_\infty F)$ = lift coefficient
$c_p = (p-p_\infty)/q_\infty$ = static pressure coefficient
$c_V$ = vortex drag coefficient (equation (3))
$D$ = drag force
$F$ = projected frontal area of model
$g, g_\infty$ = local and free stream total pressure
$h$ = model height above ground
$k(y)$ = local kinetic energy factor (equation (2))
$\bar{k}(y) = k(y)/(V_\infty{}^2 h)$ = dimensionless value of $k(y)$
$l$ = model length
$L$ = lift force
$p, p_\infty$ = local and free stream static pressure
$q_\infty = (\rho/2)V_\infty{}^2$ = free stream dynamic pressure
$\mathrm{Re} = V_\infty 1/\nu$ = Reynolds number based on model length
$V_x, V_y, V_z$ = velocity components in $x$-, $y$-, and $z$-directions
$V_{xz}, V_{yz}$ = resultant of $V_x$, $V_z$ and $V_y$, $V_z$ velocity components
$V_\infty$ = free stream velocity (= vehicle velocity)
$x, y, z$ = rectangular road fixed coordinate system as defined in Fig. 2(*a*)
$y_1, y_2, z_1, z_2$ = coordinates of traverse plane edge
$\Gamma(x) = \oint (V_y dy + V_z dz)$ = local vortex strength (equation (1))
$\nu$ = kinematic viscosity
$\rho$ = density

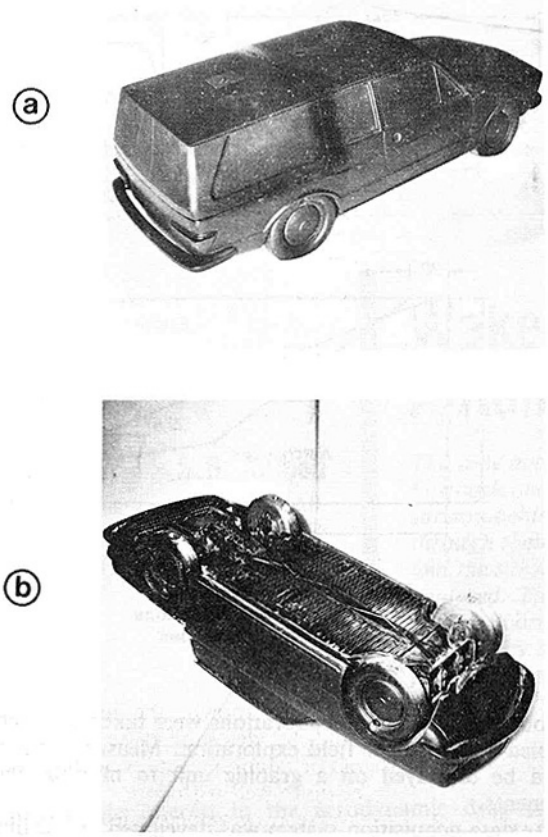

Fig. 3 Detailed model
ⓐ surface details (Estate model)
ⓑ underbody details

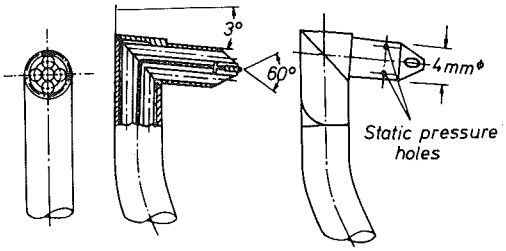


Fig. 4 Probe-head details

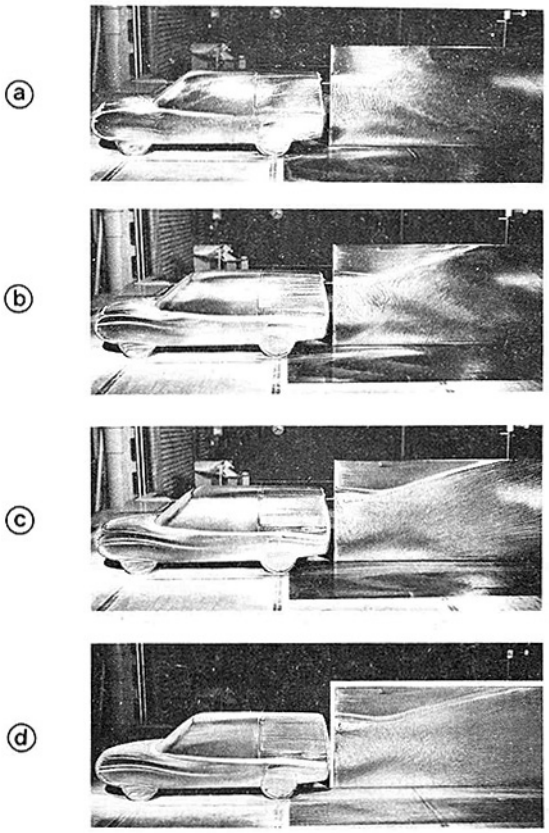

Fig. 5 Development of surface and wake flow
ⓐ initial,
ⓑ and ⓒ intermediate, and
ⓓ final stage

**Force Measurements.** Six component force measurements were made with the model in normal position and ground plane arranged 1.2 m below tunnel center line. The model was fixed by four studs on to a strain gauge balance mounted below the ground plane. The cylindrical studs, projecting through oversize holes in the ground plane, fitted into holes provided for in the wheels. Wheel bottom was flattened to leave an air gap of about 1.5 mm between it and ground plane to avoid grounding of the balance. Balance assembly was screened from tunnel air flow by a casing.

**Flow Visualization.** A 2 mm thick plate, 1.5 m long and 0.5 m high was fixed vertically in the central plane on the ground board with its well rounded upstream edge leaving a gap of about 25 mm behind the model base. An emulsion of aluminum oxide and kerosene was sprayed uniformly over the plate surface and the wind turned on. To facilitate the interpretation of the developing wake pattern, pictures were taken at short time intervals.

## Results

**Nature Of Flow In Wake Central Plane.** The development of flow on model surface and wake central plane is shown in the picture series of Fig. 5 for the model with Estate rear-end. Flow near the vehicle base is characterized by an oval separation bubble. Flow inside the separation bubble consists mainly of a recirculatory motion directed up from road and down along model base (see also Fig. 6). A similar flow at the base of a tractor-trailer model was observed by Mason and Beebe [4]. Embedded between this and the flow coming over the roof is a narrow recirculation region with an opposite sense of rotation. The velocity in this region appears to be small. The accumulated emulsion is carried away into the upper flow thereby marking the boundary between the "potential flow" and the wake.

The "contraction" and subsequent "expansion" of the wake is caused by the different near- and far wake structures. The oval separation bubble at vehicle base induces a downward tilt to the flow over the roof. Downstream of bubble closure, a pair of contrarotating longitudinal vortices are formed (see next section). In the case of Estate model these generate an upwash which lifts the main flow up from the ground.

Streamlines derived from oil flow pictures for Fastback and Estate models are sketched in Fig. 6. It is interesting to note that the sense of rotation in the lower and upper regions of the separation bubble is same in both cases. The central plane flow in separation bubble behind Notchback model is split up into two nearly equal halves housing circulatory motions of opposite sense (see [9], Fig. 6). Flow visualisation data of present study is insufficient to confirm a ring vortex type of structure inside the separation bubble.

**Transverse Flow Velocity Field In Wake.** The pressure difference between the model upper- and undersurface in-

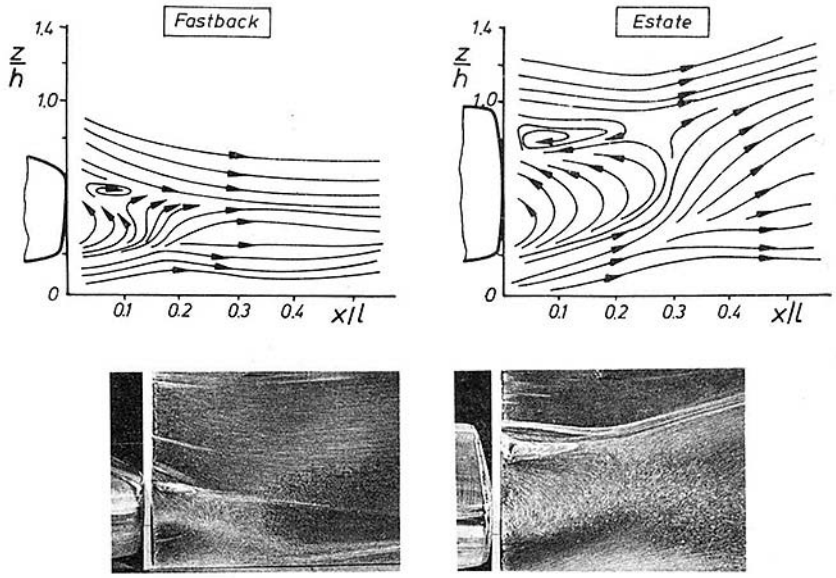


Fig. 6 Stream line pattern in near-wake

duces, as in the case of a finite airfoil, a transverse flow. For a finite airfoil with a sharp trailing edge, the induced flow leads to the formation of a pair of contrarotating longitudinal "trailing vortices."

The situation at the bluff base of a road vehicle is complicated by the presence of a separation bubble emanating from the trailing perimeter of the base. The main flow interacts after leaving the body with the separation bubble. Transverse flow field generated behind the separation bubble depends in its strength and disposition on the outcome of this interaction.

An indication of the development of the transverse flow velocity field behind smooth models with Estate, Fastback, and Notchback rear-ends is presented in Figs. 7(*a*), 8, and 9. Length and orientation of the pointers represents the magnitude and direction of the transverse flow velocity vector $V_{yz}/V_\infty$ at pointer base. Results for only the main part of the 400 mm × 600 mm traverse planes are reproduced. Blank area represents the separation bubble domain.

The strong transverse flow induced toward separation bubble boundary, diminishing extent and closure of the bubble downstream and subsequent formation of a pair of contrarotating longitudinal vortices is clearly visible for all three rear-end shapes. A relatively short and narrow separation bubble forms behind the Fastback model and a sharply defined pair of longitudinal vortices with a considerable rotational kinetic energy content is created after bubble closure.

Considering the Estate rear-end as one with a base slant angle of 0 deg, decreasing the base slant angle from 22.5 deg (Fastback) to 0 deg changes the downwash into an upwash (see Figs. 7(*a*) and 8). An important conclusion which follows is that in between these values, a base slant angle should exist for which no rotational motion is present in the wake. Recent investigations with a systematic variation of base slant angle have substantiated this conjecture. These results, which are to be published in a forthcoming paper by the author, show that the total aerodynamic drag also reaches a minimum for this value of base slant angle.

As hypothesized later in the present paper, the kinetic energy of the rotational motion in the wake contributes significantly to the total aerodynamic drag.

**Spatial Location Of The Longitudinal Vortices.** With the transverse flow velocity field known, the location of the vortex core center could be determined as the point of maximum total head loss or minimum total velocity. Maxima of total head loss agree quite well with core center locations determined from transverse flow velocity field. Results obtained for the three models are plotted in Fig. 10.

The upwash creating vortices of the Estate model move away from ground downstream. Presence of ground slows down the sinking of the downwash creating vortices behind Fastback and Notchback models so that a strong sideward deflection is the result. Tendency of the vortices to move toward each other behind the Estate model is damped by the ensuing increase in upwash between them and the resulting dissipation of vortex strength in the real flow.

Relative to the base edges (①, ②, ③, and ④) indicated in Fig. 10, the vortices of the Estate and Notchback models originate slightly above, and for the Fastback below the model mid-height. For all three models, the vortex origin lies about 0.2 times model width away from center plane.

Qualitatively similar trends are exhibited by the detailed models. Body details have however opposite effects on the spatial location of the vortices behind Estate and other two models. Most significant effect of body details is a decrease in the lateral distance between the vortices for the Estate and an increase for the Fastback model. One reason for this is the increased flow velocity along the sides and roof and decreased flow velocity between body underside and ground due to underbody protuberances.

Spatial location of the vortices and their sense of rotation is of importance for the traffic safety during wet or dusty conditions. Flow field induced in the wake can cause obscured vision and unexpected side forces on overtaking and passing vehicles, especially in presence of side winds.

**Strength Of The Longitudinal Vortices.** The strength of the longitudinal vortices was determined by evaluating the line integral of velocity along perimeter of *yz*-traverse (half-) planes (see e.g. Sketch in Fig. 7):

$$\Gamma(x) = \oint (V_y dy + V_z dz) \tag{1}$$

Effect of vortex-axis curvature was ignored. From the results of Fig. 10 it follows that the values of $\Gamma$ $(x)$ obtained are

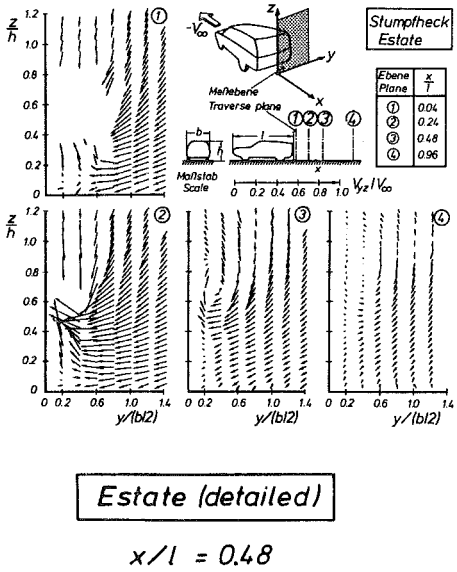


Fig. 7 Transverse velocity field behind Estate model
(a) smooth, and
(b) detailed model

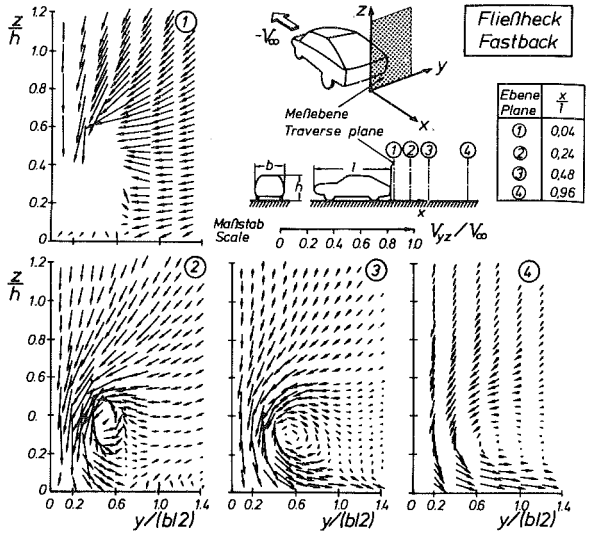


Fig. 8 Transverse velocity field behind Fastback model

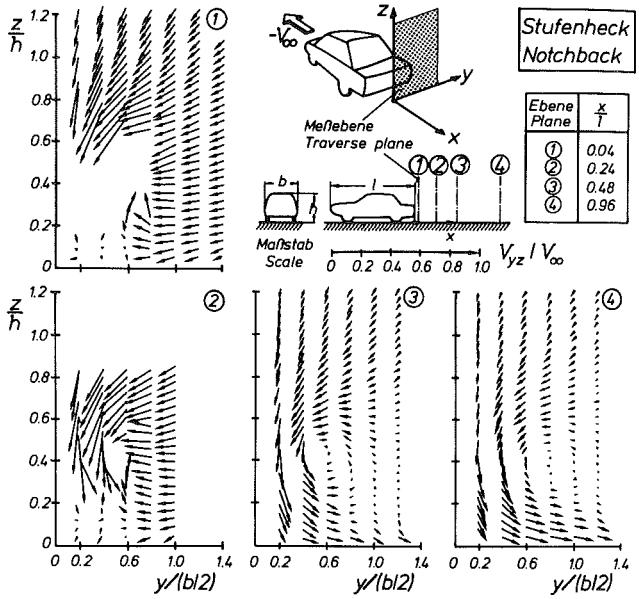


Fig. 9 Transverse velocity field behind Notchback model

smaller than if the axis curvature were taken into consideration. The path of integration above the ground was chosen to lie above the edge of ground plane boundary layer.

Fig. 11 shows the downstream variation of the vortex strength for the smooth models. At $x/1 = 0.48$, the absolute value of the vortex strength behind the Fastback model is 1.76 times that for the Estate model, indicating the associated large kinetic energy content of the vortex motion in the wake.

**Kinetic Energy Distribution and "Vortex Drag."** The distribution of kinetic energy across the wake of the three smooth models at a downstream station $x/1 = 0.48$ is shown in Fig. 12. At various lateral positions ($y$ = const), the kinetic energy factor $k(y)$ was evaluated as

$$k(y) = \int_{z_1}^{z_2} V_{yz}^2 dz \qquad (2)$$

Limits of integration were given by the ordinates of the traverse plane viz. $z_1 = 5$ mm and $z_2 = 600$ mm. Separation of the ground boundary layer from the region of integration was not attempted.

Similarity of the wake flow characteristics of Fastback and Notchback models is apparent. In contrast to the energy rich inner portion in the wake of the Fastback model, the Estate wake exhibits energy concentration in the laterally outer region of the wake.

As discussed earlier the effect of surface and underbody details is visible in an increase of kinetic energy content in the wake, which is borne out by the results of Fig. 13. The velocity increase over the roof and sides leads to a considerable increase in the kinetic energy content of the Fastback wake.

The dissipation of the rotational kinetic energy downstream

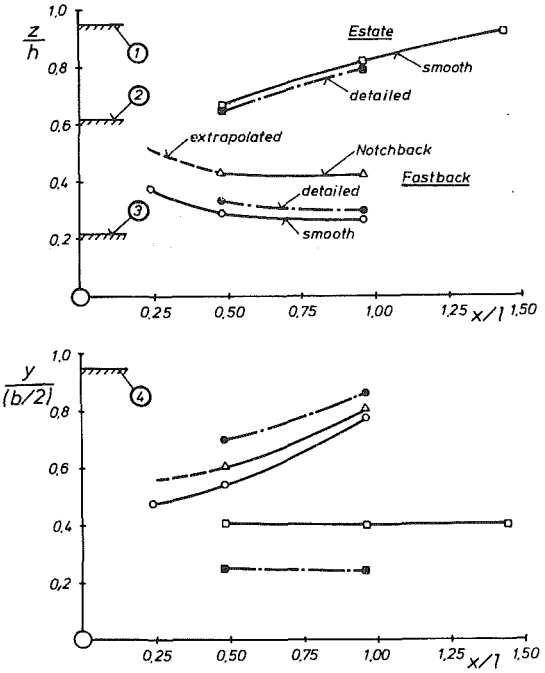


Fig. 10 Vortex-core location; top: above ground, and bottom: away from central plane.

Location of base trailing upper edge:
① Estate model
② Fastback and Notchback model
③ Location of base trailing lower edge (all models)
④ Location of base trailing side edge (all models)

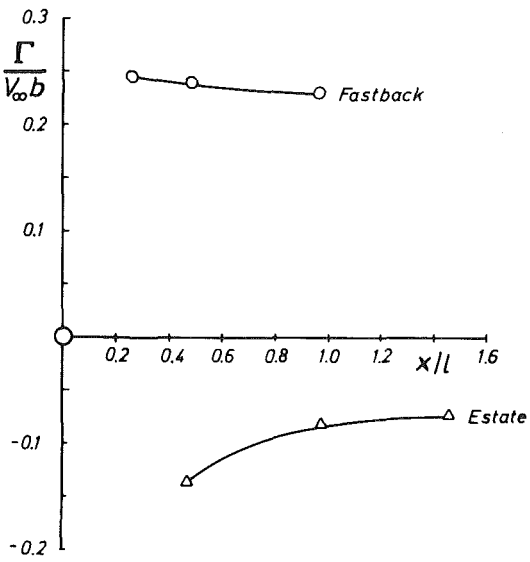


Fig. 11 Variation of vortex strength downstream

is demonstrated in Fig. 14 for the Fastback model. The sharply defined vortex core as indicated by the peak in $k$-distribution is no more visible at $x/1 = 0.96$.

As a final results of the wake surveys, a quasi vortex drag defined as

$$c_V(x) = \frac{2\int_{y_1}^{y_2} k(y)\,dy}{V_\infty{}^2 F} \tag{3}$$

was evaluated at different downstream stations and plotted as

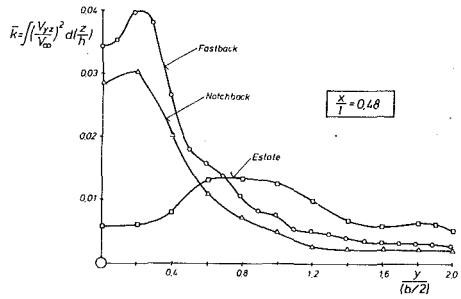


Fig. 12 Distribution of kinetic energy across wake

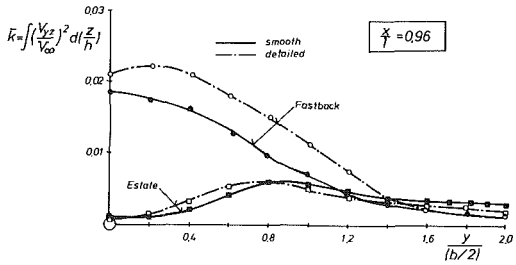


Fig. 13 Influence of body details on kinetic energy distribution

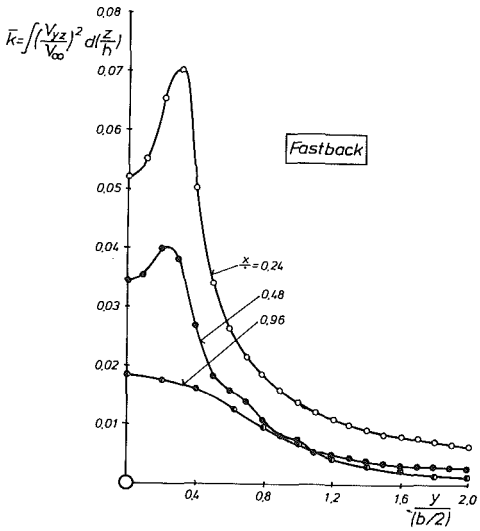


Fig. 14 Dissipation of kinetic energy downstream

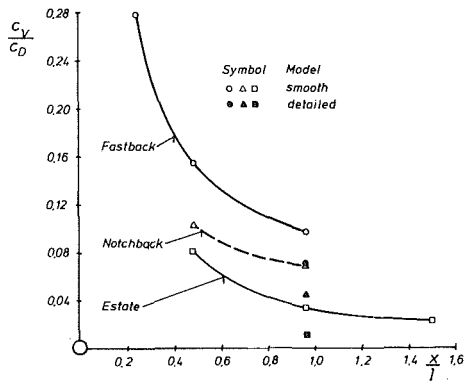


Fig. 15 "Vortex drag" of Estate, Fastback, and Notchback models

fraction of the total aerodynamic drag $c_D$ in Fig. 15. Limits of integration in the $y$ direction are: $y_1 = 0$ mm, $y_2 = 400$ mm. The choice of the lateral and vertical limits of integration, which were dictated by the dimensions of the wake survey plane, implies some arbitrariness in the absolute value of the vortex drag obtained. Choosing still bigger survey plane dimensions leads to inclusion of large areas of unaffected flow with very low values of transverse velocity (bordering on the acquisition accuracy of the system) in the kinetic energy evaluation. As this is a source of error, the choice was made for a survey plane size beyond which the vortex drag value changed insignificantly with increase in survey plane dimensions.

It is assumed that the rotational kinetic energy content of a survey plane is a measure of the body vortex drag. Highest value of the vortex drag is obtained at a downstream station just aft of the separation bubble closure. Taking this value to be the characteristic value of the vortex drag the body is capable of creating, it follows from Fig. 15 that the smooth Fastback model possesses a vortex drag component amounting to almost 28 percent of the total aerodynamic drag. Corresponding value for the smooth Estate model is about 8 percent.

Influence of surface details is also to be seen in Fig. 15 for a downstream distance $x/l = 0.98$. The details increase the vortex drag but much more so the total aerodynamic drag $c_D$ (see Table 1), so that the value of $c_V/c_D$ for the detailed models is lower than that of corresponding smooth models.

**Aerodynamic Forces.** Values of drag and lift for zero yaw are given in Table 1. for all models investigated.

**Table 1 Force measurement results. Values for detail models are in brackets.**

| Rear-end shape | $c_D$ | $c_L$ |
|---|---|---|
| Estate | 0.272 (0.437) | −0.148 (0.129) |
| Fastback | 0.215 (0.415) | 0.210 (0.422) |
| Notchback | 0.236 (0.444) | 0.155 (0.365) |

Even though the Fastback model had the lowest drag value among the three rear-end shapes, it is not to be generalised as an inherent characteristic of this vehicle configuration.

The relative increase in the value of drag coefficient with addition of surface details is 93 percent for Fastback, 88 percent for Notchback and 61 percent for the Estate model. Since surface details provided on the major part of model surface (except those on rear-end) of the three models did not change, the different drag increments can not be attributed to changes in friction drag. Main reason for the increment differences of 32 percent between Estate and Fastback vehicles is apparently the enhanced vortex drag component of the latter.

The value of lift coefficient $c_L$ of Estate model reveals in Table 1 a change of sign from negative for the smooth model to positive for the detail model. Protuberances on undersurface of detail model strongly decelerate the flow between it and the ground (see [9], Fig. 15). The mass of air which would otherwise have passed below the vehicle is now diverted along model side and upper surface. As the Estate model exhibits relatively weak transverse flow on model surface (see [9], Figs. 5, 12, and 14), this "extra" mass is evenly distributed over vehicle cross-section, leading to a small increase in surface flow velocity. Lift forces on the upper surface thus vary little. Change of sign of the total lift is primarily due to prevention of negative lift on model underside. Another interesting feature of the Estate model results is that inspite of a change of sign of lift, the sense of rotation of wake vortices does not change by addition of surface details, Fig. 7(*b*).

As explained above, the reason for this appears to be the small difference between the velocity distribution around upper and side edges of the base of smooth and detailed Estate models. This velocity distribution seems in this case to govern the structure of the wake created behind the vehicle. A conclusion which follows is that a change of sign of the lift experienced by the body does not necessarily imply a change in the sense of rotation of wake vortices. Thus the concept of a correlation between body lift and the "trailing vortices," known from wing theory, is inapplicable to bluff vehicle type of configurations.

## Conclusions

1 The near wake of Estate, Fastback, and Notchback vehicles is characterized by a separation bubble emanating from trailing perimeter of the base.

2 Flow in the separation bubble central plane consists of an upper and lower recirculation region. Sense of rotation in the lower region is up from ground and down along vehicle base; and vice versa in the upper region. Separation bubble central plane flow of Notchback vehicle is split up in almost equal halves and for Fastback and Estate vehicles it is divided into a major lower and a minor upper half.

3 After closure of the separation bubble, a pair of contrarotating longitudinal vortices are formed in the wake. These vortices induce an upwash behind Estate and downwash in the wake of Fastback and Notchback vehicles.

4 Between the base slant angles of 0 deg (Estate) and 22.5 deg (Fastback), there should exist a base slant angle for which there is no rotational motion in wake and consequently no vortex drag.

5 Behind the Estate vehicle, the vortices move up and towards each other. The vortices of Fastback and Notchback vehicles move down and apart downstream.

6 The vortices in wake of Estate vehicle are dissipated faster downstream as they are carried up and into the main flow by their induced motion. Higher vortex strength and slower dissipation downstream is characteristic of the vortices behind Fastback vehicle.

7 Kinetic energy distribution across the wake exhibits a region of concentration in the laterally outer region of the Estate and in the inner region of Fastback and Notchback wake. Significant increase in the kinetic energy content of Fastback wake is effected by the surface and body details.

8 Evaluating vortex drag on the basis of the kinetic energy of vortex motion just aft of separation bubble closure, the vortex drag of the smooth Fastback vehicle amounts to about 28 percent of the total aerodynamic drag. Corresponding value for the Estate vehicle is 8 percent.

9 Surface details significantly increase the vortex drag of Fastback and Notchback models.

10 The negative lift of Estate model is changed into positive through addition of surface details. The sense of rotation of wake vortices remains however unchanged. This means that a correlation between lift and trailing vortices is inapplicable to bluff vehicle type bodies.

11 Surface details do not influence the sense of rotation of wake vortices of Fastback and Notchback models.

## References

1 Potthoff, J., "Luftwiderstand und Auftrieb moderner Kraftfahrzeuge," *First Symposium on Road Vehicle Aerodynamics*, City University, London, England, 1970, Paper 12.

2 Carr, G.W., "Influence of Rear Body Shape on the Aerodynamic Characteristics of Saloon Cars," Report No. 1974/2. 1974, MIRA, U.K.

3 Hucho, W.-H., "The Aerodynamic Drag of Cars. Current Understanding, Unresloved Problems and Future prospects," *Proceedings of Symposium on Aerodynamic Drag Mechanisms of Bluff Bodies and Road Vehicles*, (Editors G. Sovran et al), Plenum Press, New York, 1978, pp. 7–40.

4 Mason, W.T., and Beebe, P.S., "The Drag Related Flow Field Characteristics of Trucks and Buses," *Symposium Proceedings*, reference [3], pp. 45–93.

5 Morel, T., "The Effect of Base Slant on the Flow Pattern and Drag of Three-Dimensional Bodies with Blunt Ends," *Symposium Proceedings*, reference [3], pp. 191–226.

6 Howell, J.P., "Wake Properties of Typical Road Vehicles," *Procedings of the second AIAA Symposium on Aerodynamics of Sports and Competition Automobiles*, Los Angeles, U.S.A., 1975, pp. 99–109.

7 Riegels, F.W., and Wuest, W., "Der 3-m-Windkanal der Aerodynamischen Versuchsanstalt Göttingen," *Zeitschrift für Flugwissenschaften*, Nr. 9, 1961, pp. 222–228.

8 Ahmed, S.R., and Hucho, W.-H., "The Calculation of the Flow Field Past a Van With the Aid of a Panel Method," Paper No. 770390, 1977, Society of Automotive Engineers, Inc.

9 Ahmed, S.R., and Baumert, W., "The Structure of Wake Flow Behind Road Vehicles," *Symposium on Aerodynamics of Transportation*, (Editors T. Morel et al.), ASME New York, 1979, pp. 93–103.

# The Effect of Cross-Winds on Trains

**R. K. Cooper**
Research & Development Division,
British Railways Board,
United Kingdom

*Low mass, high speed trains may be in danger of being overturned by strong cross-winds. This paper examines the aerodynamic data required to estimate overturning wind speeds. The results of wind tunnel tests and a moving model experiment, including the effect of the turbulent wind, are described.*

## Introduction

Railway operations have a high tolerance of adverse weather conditions, but there have been some serious accidents caused by vehicles overturning in strong winds. Overturning incidents on narrow gauge track (1.067 m) in New Zealand and Japan were discussed by Garrod [1] and Fukuchi [2], respectively. The Japanese National Railways use extensive anemometry to give warning of strong winds so that operations can be stopped. The only known overturning incident in Britain (1.435 m gauge) occurred in 1904, when all the carriages of a train, which was stopped on an embankment, were blown over.

## 1 Overturning Wind Speed

The estimation of overturning wind speed for a particular vehicle is usually based on simple statics and steady aerodynamic force data. The aerodynamic overturning moment is assumed to be balanced by the gravity restoring moment minus the centrifugal overturning moment due to curving and track cant. Fukuchi [2] also includes a term due to the dynamical effect of rough track. Neglecting this effect we may obtain the approximate result valid for small values of cant deficiency,

$$\tfrac{1}{2}\ \rho\ V_R{}^2 Ah\ C_R(\psi) = mg(s - h_c\theta_d)$$

where cant deficiency angle is

$$\theta_d = \tan^{-1}\frac{V_T{}^2}{r_c g} - \theta_c \simeq \frac{V_T{}^2}{r_c g} - \theta_c$$

Assume that the critical wind speed, $V_c$, is normal to the direction of travel, so

$$V_c = V_R \sin\psi$$

then we obtain

$$V_c = \left[\frac{mg(s - h_c\theta_d)}{\tfrac{1}{2}\ \rho\ Ah}\right]^{1/2} \frac{\sin\psi}{C_R(\psi)^{1/2}}$$

Unfortunately, the critical speed does not give much useful information about the safety of the train. The probability of overturning for operation over a particular route is really what is required [3]. Probability calculations have been performed but the results will not be considered here.

Garrod [1] estimated critical overturning wind speeds for several empty freight vehicles on the New Zealand Railways; values varied from 36 m/s to 53 m/s. A gust would have to persist at 10 percent above the critical value for about three seconds to overturn a vehicle completely. Obviously this is a function of gust shape and vehicle inertia as well as aerodynamic characteristics.

The effect of embankment is important. On an 8 m high embankment, the wind speed, which is practically uniform over the height of the train, is about 25 percent higher than the reference value 10 m above open ground on the approach [4]. Thus the forces experienced on exposed embankments are significantly larger than on equivalent flat sites.

To obtain reliable estimates of critical overturning wind speed and hence probabilities of overturning, we require accurate aerodynamic data, in particular, for the coefficient of rolling moment about the lee rail.

## 2 Steady Flow Wind Tunnel Tests

The British Railways Advanced Passenger Train is a low mass, high speed train with a tilting body to allow higher speeds on curves without discomfort to passengers. We will consider some wind tunnel experiments which attempted to model the effect of cross-winds on APT.

**2.1 High Reynolds Number Tests.** Using the Compressed Air Tunnel at the National Maritime Institute, Teddington, Gould [5] tested a model of APT at 90° yaw over a range of Reynolds numbers ($R_h = \bar{V}_R h/\nu$, $h$ is body height) from $10^5$ to $5 \times 10^6$. The maximum value corresponds to a wind speed of about 22 m/s at full scale. With bogies and rails represented, the coefficients of sideforce, lift and rolling moment about the lee rail were almost constant for Reynolds number above $2 \times 10^5$ (Fig. 1). However, between $10^5$ and $2 \times 10^5$ there was a large effect, mainly due to movement of the top surface separation point from the windward corner (laminar separation) to the lee corner (turbulent separation). The flow on the lower body surface was thought to be similar for Reynolds number above $10^5$.

When the rails and bogies were removed and the body faired, there was very little change in the coefficients of side

Contributed by the Fluids Engineering Division for publication in the JOURNAL OF FLUIDS ENGINEERING. Manuscript received by the Fluids Engineering Division, March 27, 1980.

force and rolling moment, but there was a substantial decrease in lift coefficient, which was also a function of Reynolds number. This was due to unblocking of the flow between body and ground. A small increase in ground clearance gave a significant increase in lift coefficient, but virtually no change in the other coefficients, at least for $R_h > 2 \times 10^5$.

The pressure coefficient distribution around the body (no bogies or rails) for a super-critical Reynolds number (Fig. 2) showed a suction peak over the top windward corner and an almost uniform base suction. The suction region between body and ground was the only area significantly altered by adding rails or changing the ground clearance.

**2.2 APT Model at Low Yaw Angles.** A 1/24th scale 3 car model of an early APT design was tested up to yaw angle of 30 deg [6]. The sideforce coefficient on car 1 was significantly larger than that on car 2. This was due to a combination of inviscid flow effects on the nose of the model and the strong lee side vortex growing from the separation line on the top lee corner.

Pressure coefficient distributions at 20 deg yaw and Reynolds number $5.5 \times 10^5$ are shown in Fig. 3. The pressure patterns were generally similar to those at 90 deg yaw, although the three dimensional flow around the nose had strong local effects. There was a suction peak on the top windward corner and a fairly uniform base suction which caused most of the sideforce and rolling moment. With body faired and no rails, there was a strong suction on the lower surface. However with bogies and rails on, the flow between model and ground was partly blocked and strong local pressure fields were generated, especially on the lee side. Thus the forces and moments were significantly increased. The pressure distributions were integrated to give local force and moment coefficients (based on normal velocity) which varied significantly with distance from the nose (Fig. 4). The random error is about $0.02/\sin^2\psi$, so the results at 5 deg yaw must be regarded with some caution.

**2.3 Long Slender Bodies in Ground Effect.** Simmonds and Stewart [7], under British Railways sponsorship, examined the flow around long cylindrical bodies in ground effect. An extensive programme of pressure plotting on a circular cylinder with a semi-ellipsoidal nose at yaw angles from 15 to 30 deg, showed the very complex nature of the flow, which exhibited significant Reynolds number effects. Due to the absence of sharp corners, there were no fixed transition or separation lines on the body. A strong lee side vortex flow was set up, with vortices forming alternately from the lower surface and then the upper surface. Each vortex grew to a certain point and was then detached to be convected downstream. This behaviour caused a longitudinal variation of lift and side force on the body.

A cylinder with a cross-section which was square with rounded corners was also tested. The primary separation lines were then located either near the windward corner (laminar separation) or the lee corner (turbulent separation). In the latter case a laminar separation bubble with turbulent reattachment was present near the windward corner. The transition occurred at a Reynolds number of about $2 \times 10^5$ and resulted in a rapid change in pressure distribution, but there was little change with increasing Reynolds number above the transition value. This behavior was similar to that observed on train models.

In an attempt to simulate high Reynolds numbers ($> 10^6$) a sand roughened surface ($k/\text{dia} = 0.65 \times 10^{-3}$) was used. The effect on the noncircular cylinder at low angles of yaw was simply to move the transition Reynolds number to a lower value, with little effect on the pressure distribution. This is of particular significance when testing long models of 4 or 5 vehicles up to yaw angles of, say, 60 deg.

## 3 Moving Model Experiment

There are several aspects of the cross-wind problem that cannot be modelled satisfactorily using stationary models in conventional wind tunnels. The main cause of the difficulty is

## Nomenclature

$A$ = side area of vehicle in a train
$C_L$ = coefficient of lift (side force similar), $L/qA$
$C_{L_n}$ = coefficient of lift based on normal velocity component, $C_L/\sin^2\psi$
$C_p$ = coefficient of pressure, $(p\text{-}p_0)/q$
$C_R$ = coefficient of rolling moment about lee rail, $R/qAh$
$g$ = gravitational acceleration
$h$ = height of train body cross-section
$h_c$ = height of center of mass above rail level
$l_1$ = length of leading vehicle
$L$ = lift force
${}^xL_u$ = scale length of u-component of wind turbulence in mean wind direction
$n$ = frequency (Hz)
$q$ = dynamic pressure, $\frac{1}{2}\rho \bar{V}_R^2$
$r_c$ = radius of curvature of track
$R$ = rolling moment about lee rail
$R_h$ = Reynolds number, $\bar{V}_R h/\nu$
$s$ = distance from track center line to lee rail reference point (0.75 m full scale)
$S$ = side force
$S_u(n)$ = power spectral density function of $u$-component of wind (for example)
$u$ = component of wind velocity in the mean wind direction
$V_n$ = component of wind normal to track, $V_R \sin\psi$
$V_R$ = resultant wind speed with respect to train
$V_T$ = train speed
$\bar{V}$ = mean wind speed
$|X_s(n)|^2$ = aerodynamic admittance function of side force
$\theta_c$ = cant angle of track (angle between line joining rail-wheel contact points and horizontal in track cross-section)
$\theta_d$ = cant deficiency angle
$\nu$ = kinematic viscosity of air
$\rho$ = density of air
$\sigma$ = standard deviation
$\tau$ = time delay (auto and cross-correlations)
$\phi$ = angle between mean wind direction and track (0 deg for head wind)
$\psi$ = yaw angle between resultant wind direction and train

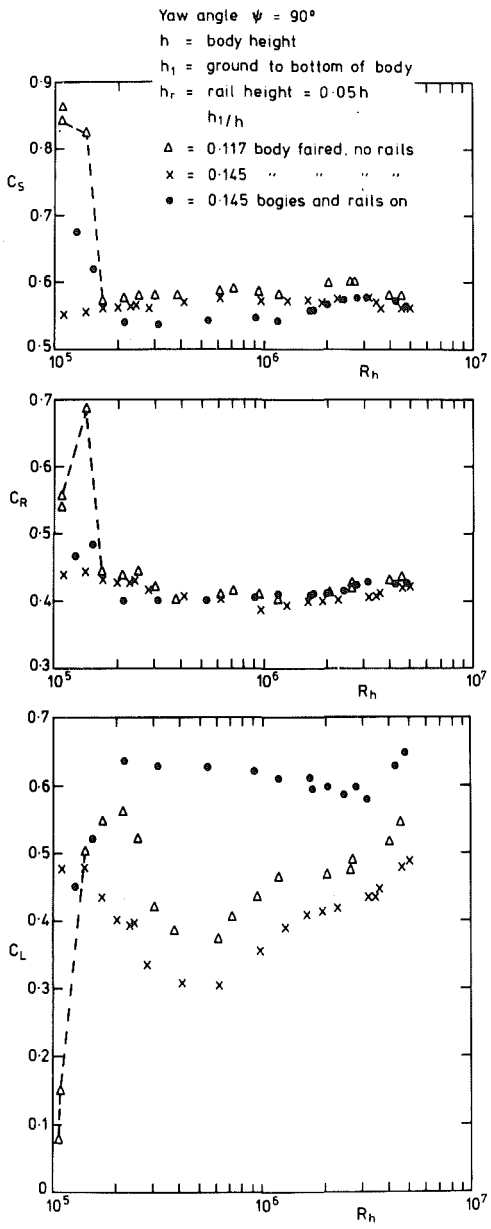


Fig. 1 Coefficients $C_S$, $C_R$, $C_L$ versus Reynolds number at 90 deg yaw

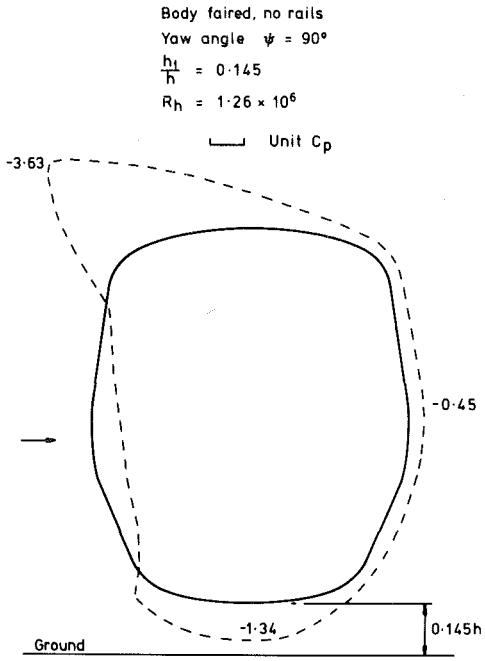


Fig. 2 Pressure coefficient distribution on APT cross-section

the lack of relative motion between the model and ground. The logical solution is to propel the model through a turbulent wind simulation, thus achieving:

1) The correct relative motions between the model, ground and wind

2) The correct representation of the wind, including shear and turbulence and, if necessary, the effect of embankments, viaducts and wind fences.

A suitable track for a moving model experiment existed at the Proof and Experimental Establishment, Pendine, Wales. The track was about 950 m long and consisted of two rails mounted via steel sleepers on to a concrete plinth (Fig. 5). The track level was about 1 m above ground level. The fetch in the direction of the prevailing wind consisted of low sand dunes.

A preliminary experiment showed that winds of between 5 and 10 m/s at track level could be expected on several days each month during the winter. The turbulence intensity $\sigma_u/\bar{V}$ was about 0.25. The power spectral density function of the wind speed fitted the von Karman model, (see Section 3.5) and had a length scale of about 7 m. Comparing the result to data provided by the Engineering Sciences Data Unit [8], the wind was judged to have reasonable properties for a 1/5th scale model test.

**3.1 Design of 1/5th Scale Model APT-P.** The 1/5th scale model APT-P consisted of two vehicles; the leading vehicle carrying a load measuring body shell and a rear vehicle (about half the length of a scaled intermediate car) acting as an aerodynamic fairing (Fig. 5). The low mass body shell of the leading car was constructed of reinforced plastic with a mesh of carbon fibre roving. The body was suspended via 5 load cells and a drag link on to a steel space frame, which was mounted on 2 wheelsets. The model bogies were of wooden construction and were mounted directly to the wheelsets.

The load cells (semiconductor strain gauge type) were positioned to enable lift, sideforce, rolling moment, yawing moment and pitching moment to be resolved. The axial force was not measured, but wind tunnel results showed it to be much less than the other forces for yaw angles above 10 deg. A total pressure probe insensitive to yaw (Kiel tube) and a direction vane were mounted on a probe through the nose of the model. Static pressure was obtained from sealed, insulated containers within the model. The signal conditioning and recording equipment was housed in a Fort Transit Van, which also propelled the test train along the track via an outrigger and push rod (Fig. 6). Zero windload (necessary for zeroing and electrical calibration) was obtained by driving the model into a makeshift shelter over the track.

One of the most difficult aspects of the experiment was the measurement of dynamic pressure of less than 100 Pa. The strong winds made it difficult to obtain a reliable static pressure, and the sealed system was subject to drift. This was kept to a minimum by venting the system at the beginning of each run.

**3.2 Steady Flow Test.** Subsequently, the 1/5th scale model was tested in the full scale wind tunnel at the Motor Industry Research Association, Nuneaton. The model was mounted on a ground board to avoid the thick boundary layer on the floor

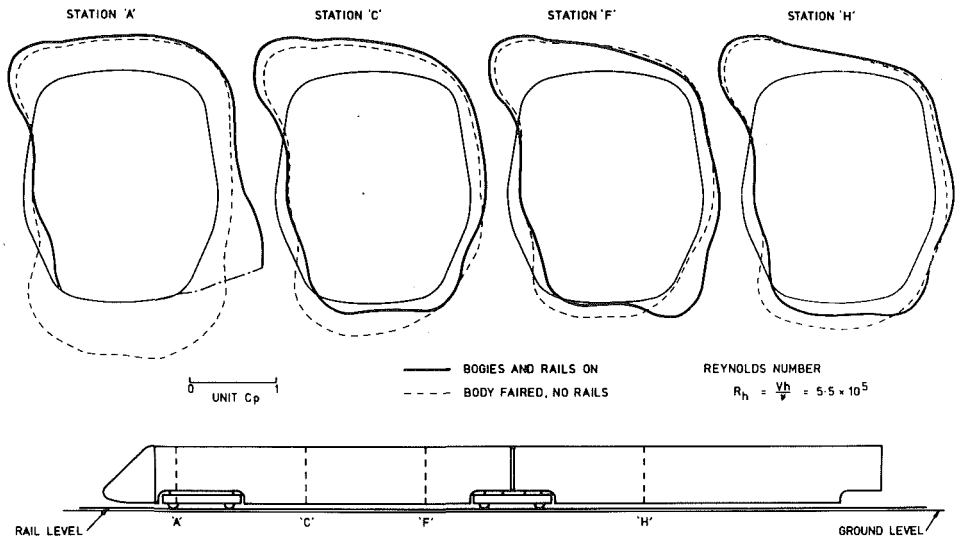


**Fig. 3 Pressure distribution on model APT at 20 deg yaw**

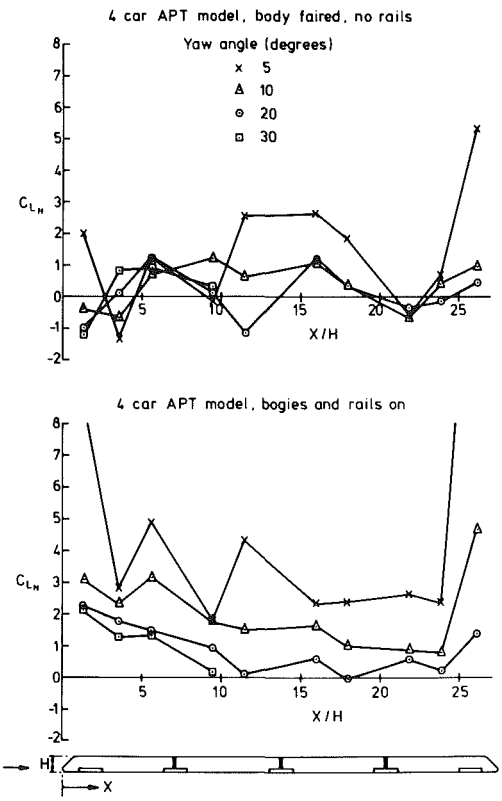


**Fig. 4(*a*) Local lift coefficient based on normal velocity versus *X/H***

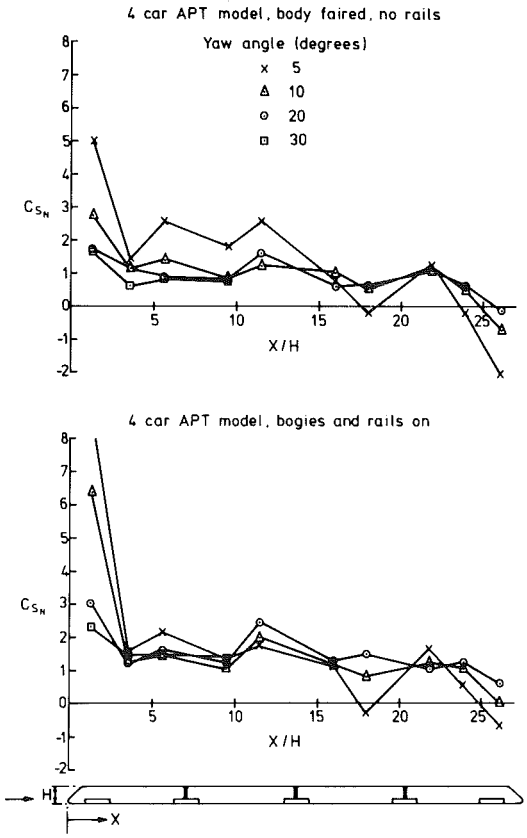


**Fig. 4(*b*) Local side force coefficient based on normal velocity versus *X/H***

of the wind tunnel (Fig. 7). The Reynolds number was about $1 \times 10^6$.

The model interfered with the reference dynamic pressure at higher yaw angles, so there was some doubt about the blockage corrections. Maskell's method as modified by Cowdrey [9] was applied, assuming a ratio of drag coefficient to base pressure coefficient of $-1.2$ obtained from wind tunnel tests. The systematic error in the coefficients due to inadequate corrections may be 5 percent at yaw angles above 40 deg. The random error is estimated to be 3 percent at 95 percent confidence.

**3.3 Results.** Typical records from the Pendine experiment show the nonsteady behavior of the forces and moments (Fig. 8). Due to the track roughness and the flexible tyres on the moving model, there was a dominant sway mode, with a frequency of about 8.5 Hz. The records were filtered at 4 Hz to remove the roughness component, leaving only the aerodynamic component. The load cell forces were resolved into body axis forces and moments, means were computed over short averaging times defined by $t_{av} = 3l_1/\bar{V}_R$, and the values converted to coefficient form using a similarly averaged dynamic pressure.

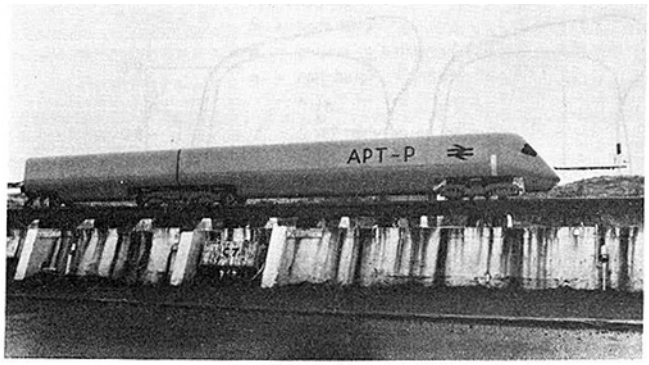


Fig. 5 1/5th scale model APT on test track

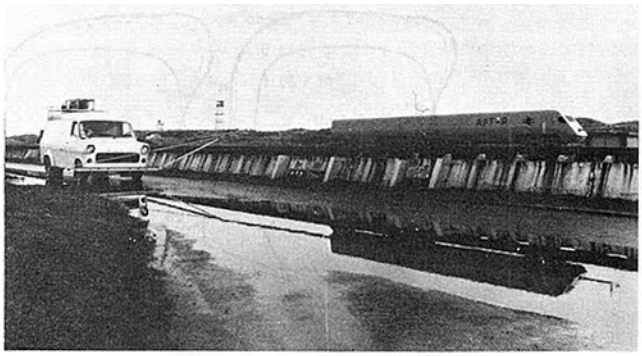

Fig. 6 1/5th scale model APT and propelling vehicle

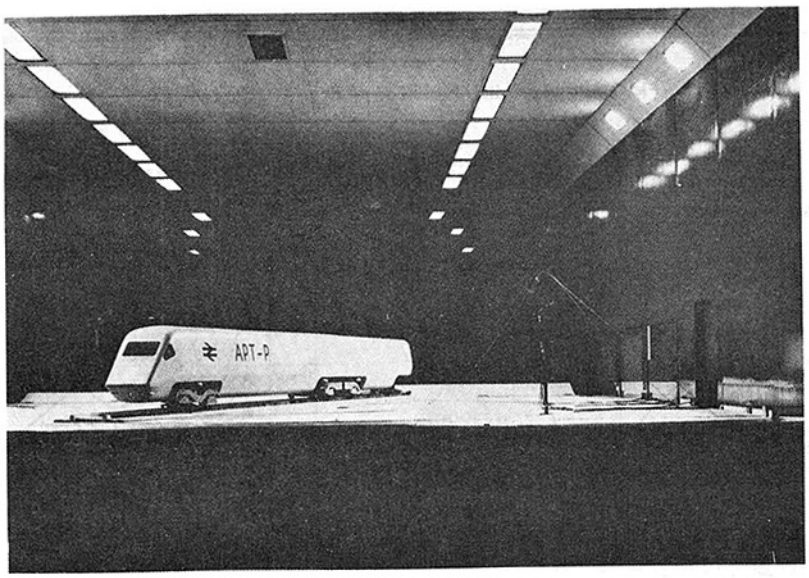


Fig. 7 Model on ground board in wind tunnel

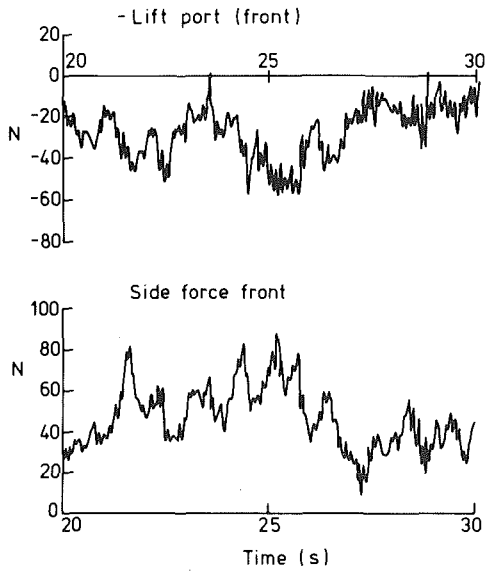


Fig. 8 Typical records for moving model experiment

The yaw was found to have an unexpectedly large position error. I am indebted to Dr. K.R. Cooper of the National Aeronautical Establishment, Ottawa, for informing me of the work of Walston, et al. [10] on a full size truck. They found a position error of about 25 percent up to 15 deg yaw, for a yaw vane in front of the truck. In our case, a wind tunnel test showed that the relative error in the yaw angle was about 32 percent at 20 deg yaw, reducing to 21 percent at 40 deg yaw. (Angles greater than 60 deg have not been corrected).

Basic data for the moving model experiment are given in Table 1, and results for moving model and wind tunnel tests are plotted in Fig. 9. The mean of the moving model results lies slightly below the steady flow wind tunnel curve. The scatter about the mean is due to the unsteady cross-wind, although the imperfect response of the dynamic pressure and yaw instruments may contribute. Possible differences due to (*a*) the relative motion between the model and ground, (*b*) modification of the mean flow field by the turbulence, (*c*) imperfect modelling of the track and embankment at Pendine, appear to be of secondary importance. Previously these effects were thought to be more significant [15].

Random errors at the 95 percent confidence level for means over the short averaging time, $t_{av} = 3l_1/\bar{V}_R$, are estimated to be 10 percent for the coefficients and yaw angle. Systematic errors in the coefficients are about 5 percent for yaw angles above 40 deg, due to the low dynamic pressure.

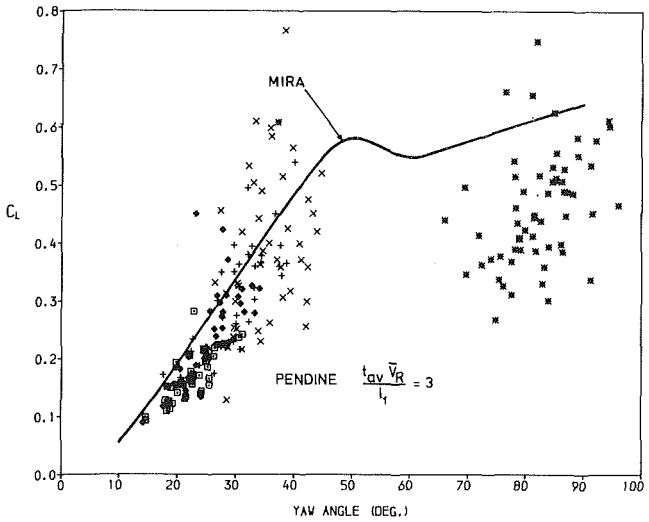


Fig. 9(a)

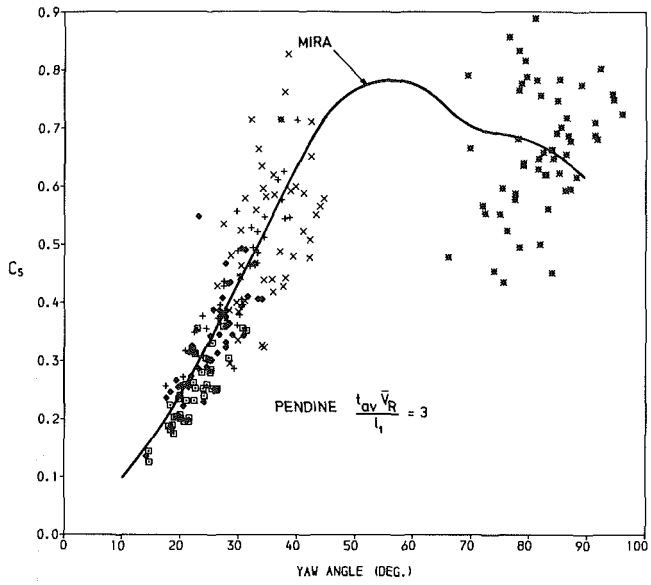


Fig. 9(b)

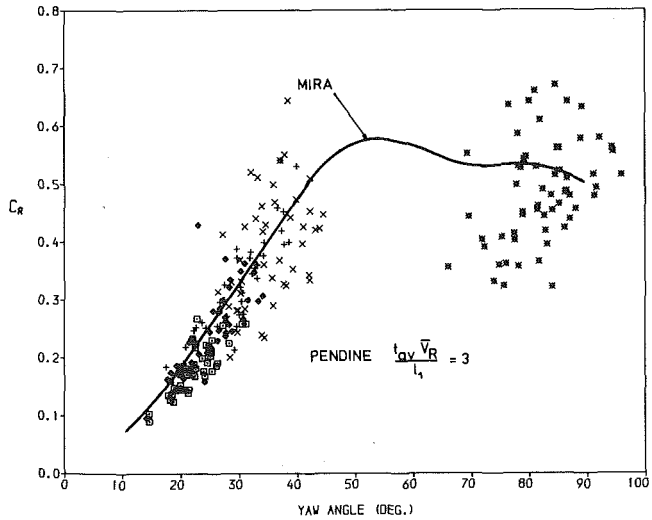


Fig. 9 Coefficients of lift, side force, and rolling moment versus yaw angle

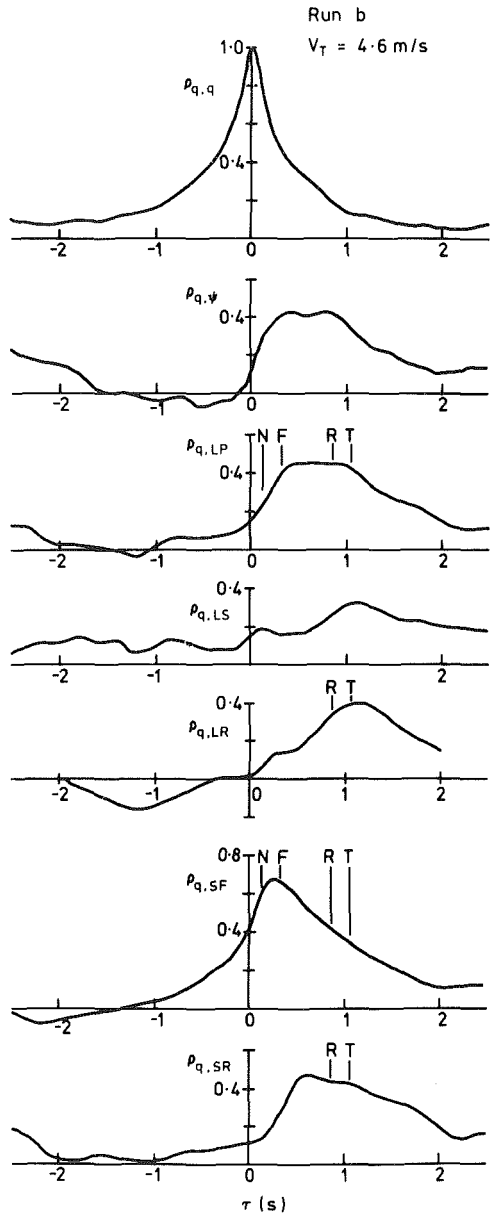


Fig. 10 Correlation functions

**3.4 Cross-Correlation Functions.** The auto-correlation function of dynamic pressure, $q$, and the cross-correlation functions of q with yaw angle ($\psi$), port lift (LP), starboard lift (LS), lift rear (LR), side force front (SF), and side force rear (SR), respectively, are shown in Fig. 10 for a typical run. The dynamic pressure is sensed on the probe in front of the nose of the model, so the response of the load cells is delayed. The times at which various points on the body pass a fixed point on the track, after the end of the probe, are labeled as N, F, R, T, (nose, front load cells, rear load cells, tail), respectively.

The time delay to the peak of $\rho_{q,SF}$ is just less than the time $F$. This may be caused by a combination of the rapid response due to inviscid effects near the nose and the slower response of the vortex system. The port lift load cell (LP) is on the windward side and it shows a significantly greater correlation with q than does LS This may be due to the suction peak over the top windward corner. The correlation of yaw angle $\psi$ with $q$ is delayed, probably due to the response time of the vane.

**3.5 Power Spectral Density Functions.** To facilitate analysis of the unsteady data it was necessary to assume that

**Table 1 Data for moving model experiment**

| Run | Period (s) | $V_T$ (m/s) | $\bar{q}$ (Pa) | $\bar{V}_R$ (m/s) | $\bar{\psi}$ (deg) | $\bar{V}_n$ (m/s) | $R_h$ $10^5$ |
|---|---|---|---|---|---|---|---|
| *a* | 150 | 0.0 | 23 | 6.2 | 83 | 6.1 | 2.7 |
| *b* | 59 | 4.6 | 54 | 9.4 | 36 | 5.5 | 4.1 |
| *c* | 45 | 6.7 | 69 | 10.6 | 30 | 5.3 | 4.7 |
| *d* | 40 | 8.9 | 91 | 12.2 | 26 | 5.2 | 5.4 |
| *e* | 37 | 11.0 | 136 | 14.9 | 22 | 5.7 | 6.6 |

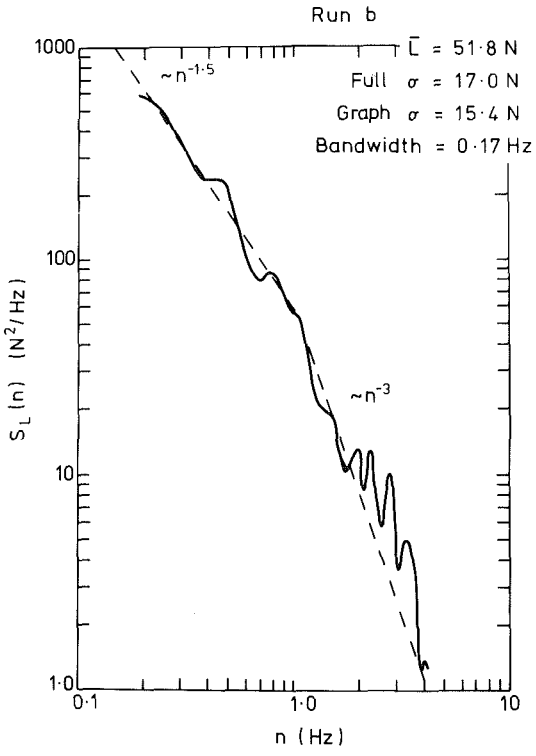


Fig. 11(*a*) Power spectrum of lift

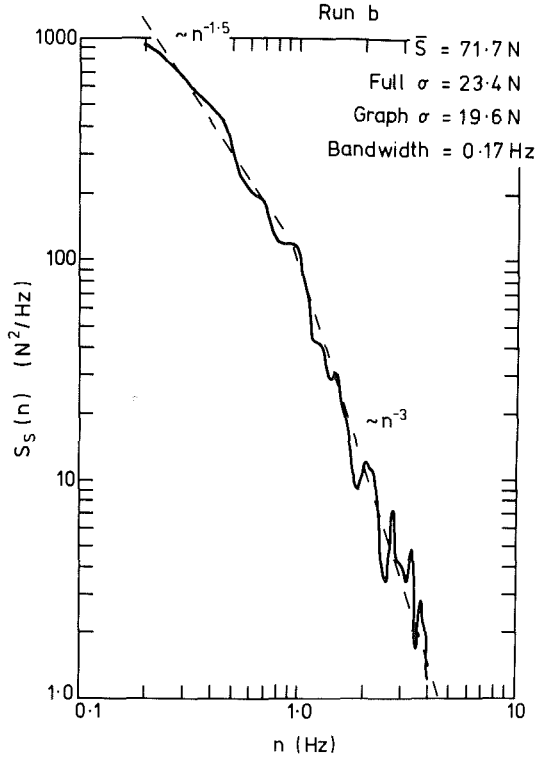


Fig. 11(*b*) Power spectrum of side force

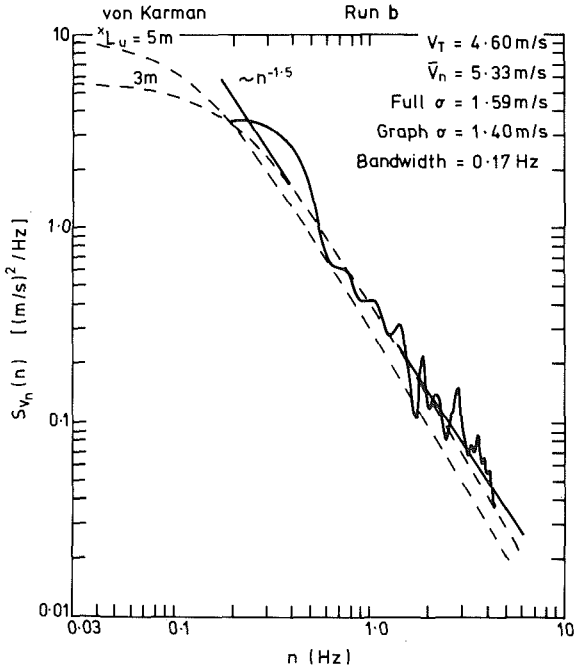


Fig. 11(*c*) Power spectrum of normal component of wind velocity

the wind speed and the resultant forces on the model were stationary random processes. Power spectral density functions were computed using the method of Welch [11] based on the fast Fourier transform. Spectra for a typical run are shown in Fig. 11, where logarithmic axes are used.

The normal component of wind velocity, $V_n = V_R \sin \psi$, is used as a reference velocity. Consideration of steady flow data showed that this was a reasonably independent variable over a significant range of wind speed $V_w$ and angle $\phi$ for a fixed train speed $V_T$. The spectrum of $V_n$ has a slope of about $-1.5$ and so has the form

$$S_{V_n}(n) \sim n^{-1.5}$$

This is compared with the theoretical von Karman spectrum for the $u$-component of velocity, obtained from ESDU data [8], as follows

$$S_u(n) = \frac{4\sigma_u{}^2 {}^xL_u}{\bar{V}\left[1+70.8\left(\frac{{}^xL_u n}{\bar{V}}\right)^2\right]^{5/6}}$$

$$= 0.115\sigma_u{}^2\left(\frac{\bar{V}}{{}^xL_u}\right)^{2/3} n^{-5/3} \text{for} \frac{{}^xL_u n}{\bar{V}} > 0.4 \text{ say.}$$

A reasonable fit was obtained with a length scale of ${}^xL_u = 3$ m rather than 7 m as indicated by the trackside anemometers.

The spectra of lift force, L, side force S, and rolling moment R, have a slope of $-1.5$ at lower frequencies, but for frequencies greater than about 1 Hz, the slope decreases to about $-3$. The higher frequency components of turbulence are less effective in producing resultant force since the turbulent eddys are correlated over smaller distances with increasing frequency. The standard normalized error of the spectrum (standard deviation/mean) is 27 percent. Estimated random errors in the mean values are, 3 percent for the forces $\bar{L}$, $\bar{S}$, and 15 percent for the normal velocity $\bar{V}_n$, due to the combined effect of errors in dynamic pressure and yaw angle.

**3.6 Aerodynamic Admittance Functions.** In relating the spectrum of an output (force) to the spectrum of the input (velocity) the concept of aerodynamic admittance defined by Davenport [12] is useful. Let $D$ be the drag force on a stationary object in the turbulent wind of velocity $U$, then the aerodynamic admittance of the drag force is defined

$$|X_D(n)|^2 = \frac{S_D(n)\bar{U}^2}{4S_u(n)\bar{D}^2}$$

where $S_D(n)$, $S_u(n)$ are power spectral density functions and $\bar{D}$, $\bar{U}$ are the mean values of drag and wind speed respectively. Bearman [13] obtained experimental values of the aerodynamic admittance functions for square plates in a turbulent flow. Following the work of Vickery [14], Bearman developed the theoretical result for rectangular plates of length $B$, height $H$

$$|X_D(n)|^2 = \frac{4}{B^2H^2}\int_0^H\int_0^B (B-x)(H-y)F(u_1,u_2)(r,n)\,dx\,dy$$

where $F(u_1,u_2)(r,n)$ is the normalized cospectral density function for the $u$-component of turbulence at points separated laterally by a distance $r$. Using a normalized cospectral density function $F(u_1,u_2)(r,n) = \exp(-8nr/\bar{U})$ the theoretical curve shown in Fig. 12 was obtained. This result is a reasonable fit to experimental data for square plates in the range $0.375 < {}^xL_u/\sqrt{A} < 1.5$, where $A$ is the plate area,

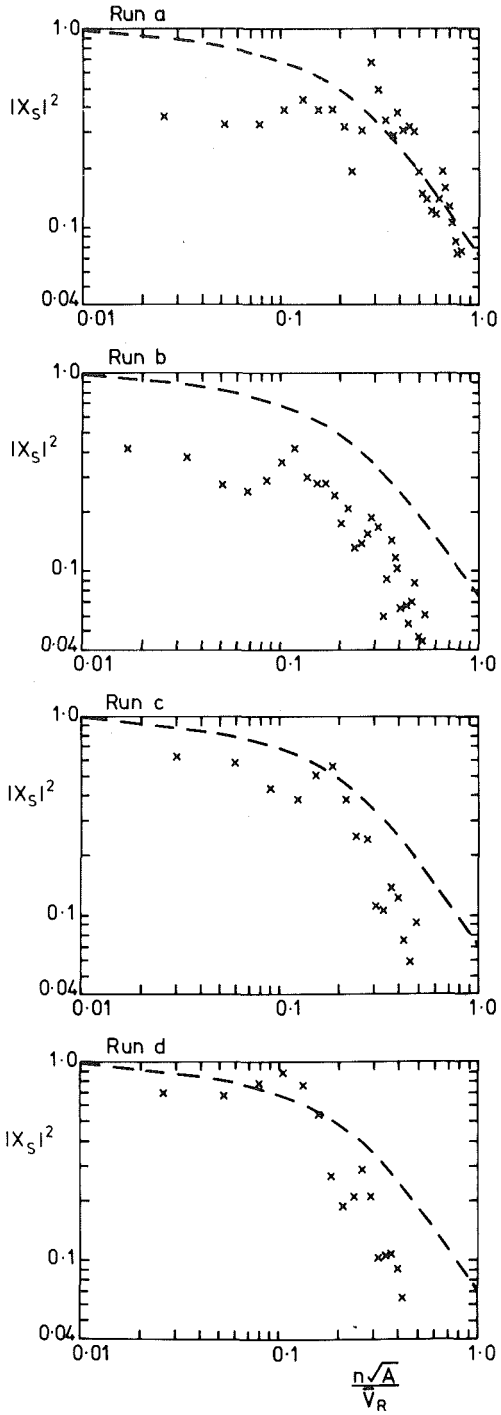


**Fig. 12 Aerodynamic admittance of side force**

Using the normal component of wind velocity $V_n$, as the reference quantity, the aerodynamic admittance of side force (for example) is defined as

$$|X_S(n)|^2 = \frac{S_S(n)\bar{V}_n{}^2}{4S_{V_n}(n)\bar{S}^2}$$

Aerodynamic admittance functions of side force for several runs are plotted against reduced frequency $n\sqrt{A}/\bar{V}_R$ in Fig. 12. The model speeds, mean resultant wind speeds, yaw angles etc. for the runs analysed are given in Table 1. The standard error of the aerodynamic admittance, due to random errors in the spectra, is about 38 percent. This accounts for the variability about the mean curve. However there is an ad-

ditional error of about 36 percent due to the large random error in $\bar{V}_n$ as discussed above.

The general form of the aerodynamic admittance is similar to the theoretical function for a square plate derived by Bearman [13]. The aerodynamic admittance reduces rapidly for $n\sqrt{A}/\bar{V}_R > 0.2$ which is in agreement with the expected behaviour, due to the reducing correlation of gusts over the side area of the vehicle as frequency increases. The aerodynamic admittance of rolling moment was almost identical to that of side force, since rolling moment was due to the same pressure components on the body. Aerodynamic admittance of lift showed more scatter than that for side force but again appeared to be similar to the flat plate function.

## 4 Conclusions

Wind tunnel tests over a wide range of Reynolds numbers showed that satisfactory results for the forces on trains due to cross-winds could be obtained at a Reynolds number of $2 \times 10^5$, based on body height.

A moving model experiment in the open air was performed to examine a realistic simulation of the effect of cross-winds on a train. The mean values for force and moment coefficients were slightly lower than those obtained from a steady flow wind tunnel test on the same model. Although most of the scatter was due to turbulence, the difference in the means could be due to experimental error. The effects of moving model and embankment simulation were secondary.

The unsteady effects due to the turbulent wind were examined via power spectral density functions of various force components. The aerodynamic admittance of side force was found to be similar to that for the drag of a square plate in a turbulent flow.

It is necessary to perform experiments with moving models through a wind tunnel simulation of the terestrial boundary layer, to obtain data on the effect of cross-winds on moving trains. This work could show conventional wind tunnels to be adequate for most purposes. However, the effect of embankments and wind fences can only be correctly simulated by a moving model technique.

## Acknowledgment

The author wishes to thank the Director of Research, British Railways Board, for permission to publish this paper.

## References

1 Garrod, S.D., "Wind Gusts on Rolling Stock," New Zealand Government Railways Research Report No 136, Aug. 1967.

2 Fukuchi, G., "Statical Considerations for Railway Vehicle Overturning Due to Lateral Winds," Japanese National Railways, Quarterly Reports, Vol. 16, No 2, 1975, pp. 49–53.

3 Cooper, R.K., "The Probability of Trains Overturning in High Winds," *Proceedings of the 5th International Conference on Wind Engineering*, Fort Collins, Colorado, July 1979.

4 Cooper, R.K., "Edwalton Embankment Wind Experiment," British Railways Board, Research and Development Division, Technical Memorandum TM AERO 27, Aug. 1978.

5 Gould, R.W.F., "Wind-Loading Scale Effects on an Advanced Passenger Train Coach in Direct Side Winds," National Maritime Institute, Report Proj No 89/0294, 1976.

6 Ellicott, S.P., "Pressure Plotting Tests on a 1/24th Scale Model of the British Railways Advanced Passenger Train," British Aerospace (Brough), Note Nos. YWT 1571LS (1974) and YWT 1580 LS (1975).

7 Stewart, A.J., "Flow Around Slender Bodies at Yaw," Ph.D. dissertation, Department of Engineering, University of Cambridge, Sept. 1977.

8 "Characteristics of Atmospheric Turbulence Near the Ground. Part II: Single Point Data for Strong Winds (Neutral Atmosphere)," Engineering Sciences Data Unit, Item No 74031, Oct. 1974.

9 Cowdrey, C.F., "The Application of Maskell's Theory of Wind-Tunnel Blockage to Very Large Solids Models," NPL Aero Report 1247, Oct. 1967.

10 Walston, W.H., Buckley, F.T., Marks, C.H., "Test Procedures for the Evaluation of Aerodynamic Drag on Full Scale Vehicles in Windy Environments," SAE Paper 760106.

11 Welch, Peter D., "The Use of Fast Fourier Transform for the Estimation of Power Spectra: A Method Based on Time Averaging Over Short, Modified Periodograms," *IEEE Trans. Audio and Electroacoustics*, Vol. AU-15, No. 2, June 1967.

12 Davenport, A.G., "The Application of Statistical Concepts to the Wind Loading of Structures," *Proc. Inst. Civil Engineering*, Vol. 19, 1961, pp. 449–472.

13 Bearman, P.W., "An Investigation of the Forces on Flat Plates Normal to a Turbulent Flow," *J. Fluid Mech*, Vol. 46, 1971, pp. 177–198. (Nat Phys Lab Aero Rep No 1296, 1969).

14 Vickery, B.J., "On the Flow Behind a Coarse Grid and Its Use as a Model of Atmospheric Turbulence in Studies Related to Wind Loads on Buildings," Nat Phys Lab Aero Report 1143, 1965.

15 Cooper, R.K., "The Effect of Cross-winds on Trains," ASME Symposium on the Aerodynamics of Transportation, Niagara Falls, New York, June 1979.

Journal of Fluids Engineering

# Discussion

## The Linear Instability Due to the Compressible Crossflow on a Swept Wing[1]

**K. Stewartson.**[2] In this paper the author presents a number of interesting studies on the application of some recent ideas about the growth of small disturbances to the important case of transonic flow past swept wings. He does not appear to differentiate between the merits of spatial and temporal theories and I would like to take this opportunity of explaining why I think the former has the greater physical significance.

The primary goal of stability theories such as these is to predict the onset of transition and clearly a linear theory cannot be used on its own for this purpose. This point may be emphasized by noting the wide range of values for $N$ in the $e^N$ rule reported for Blasius boundary layers ranging from 2.6 (Mach reference [3]) when the free stream turbulence level is 1 percent to 13 (reference [15]) when it is 0.013 percent. At best the theory can be regarded as a basis on which to build nonlinear theory and to that end a physical foundation for it must be formulated. This can be done if the disturbance is supposed generated at a fixed point of the boundary layer and propagates downstream. Since the disturbance is assumed to be small each Fourier component may then be analyzed separately and we are led at once to the spatial theory since $\omega$ must be kept real. Further allowance for the slow growth of the boundary layer achieved by the replacement of $\alpha x + \beta z$ in (equation 1) by $\int (\alpha dx + \beta dz)$ where now $\alpha$, $\beta$ are slowly varying functions of position. This line of argument is discussed in references [11, 12]. It is now conceivable that nonlinear terms might eventually modify the growth rate and lead to a prediction of $N$, possibly determined in part by the amplitude of the disturbance at the absolute neutral curve or zarf (reference [12]).

A temporal theory must assume that $\alpha$, $\beta$ are real, $\omega$ to be computed and $\omega_i$ related in some way to the spatial growth. As such it is formally irrelevant to the evolution process described above, being strictly concerned with the growth of the disturbance at a fixed point.

Notwithstanding the differences between the two procedures (in which either $\omega$ is real and $\alpha$, $\beta$ complex or $\alpha$, $\beta$ are real, and $\omega$ complex) the tests in reference [6] suggest that for Blasius flow, taking $\beta = 0$, the values of $N$ predicted by the two methods might be close. A possible explanation is that the values of $\alpha_i$, $\omega_i$ computed are small at the chosen value of $R$ and the difference in the growth rates according to the two methods is only $0(\alpha_i^2)$. How far can this principle be extended to three dimensions, one extra complication being that the direction of the group and phase velocities may be quite different even when both are real? Even for Blasius flow (references [16, 17]) the two dimensional neutral curve and the zarf are quite different the latter having typically $\beta \simeq \alpha \simeq 0.2$. The author does not present estimates for $N$ using the two approaches but there are grounds for believing that, as in Blasius flow (reference [16]), they will be nearly the same. For, although the variation of $\omega_i$ with $\alpha$, $\beta$ is quite rapid (e.g. Fig. 4), once the restriction $\partial\alpha/\partial\beta$ real is applied the corresponding variation of $\sigma$ is very slow. The author proves the important result that this condition applies in the temporal study at the extremum of $\omega_i$. Hence the difference between the value of $\sigma$ computed from this number and that computed according to spatial theory is likely to be small even though the corresponding values of $\alpha$, $\beta$ may be quite different. Another useful conclusion which can be inferred from Fig. 7 is that when calculating $N$ by spatial modes any convenient value of $\bar{\psi}$ will do, for example that at the zarf (reference [12]).

[1] By S. G. Lekoudis, published in the December, 1980 issue of the ASME JOURNAL OF FLUIDS ENGINEERING, Vol. 102, No. 4, pp. 502–509.

[2] Department of Mathematics, University College London, London, England.

### Additional References

15 Winter, K.S., and Maskell, E.G., "The Reynolds Number for Transition on a Flat Plate in the RAE 4 ft. × 3 ft. Low Turbulent Wind Tunnel," RAE Tech. Memo 1854, May 1980.

16 Cebeci, T., and Stewartson, K., "On the Prediction of Transition in Three Dimensional Flows," Laminar-Turbulent Transition IUTAM Symposium, Stuttgart, 1979, Springer 1980, p. 243–252.

17 Cebeci, T., and Stewartson, K., "Asymptotic Properties of the Zarf," Submitted to *AIAA Journal*.

## Authors' Closure

I agree with Professor Stewartson about the physical significance of the spatial stability theory. However the purpose of the work was to compare the spatial and the temporal theories because the later was, and still is, used in design work. The reason the temporal theory was developed first is that it offers certain computational advantages, for example with spectral methods. I agree only partially with the last statement because I have not seen what the growth rates do when the $\bar{\psi}$ is about 90 deg away from the direction of the group velocity.

## The Influence of Swirl on the Flow Characteristics of a Reciprocating Piston-Cylinder Assembly[1]

**W. C. Reynolds.**[2] It would be helpful to have the authors' estimates of the experimental uncertainty in some key results, for example the location of the center of the vortices, the angles of the jet-exit streamlines, and the strength of the recirculations.

**L. D. Cloutman.**[3] Recent interest by automobile manufacturers in more fuel-efficient engines that produce less pollution has resulted in attempts to model the detailed reacting flows that occur in internal combustion engine cylinders (for example, references [1-3] and the work referenced by the authors). One goal of this effort is to provide engine designers with a tool that can supplement their expensive and time-consuming experiments. It is necessary to validate these complex numerical fluid dynamics programs by comparing computed results with analytic solutions and carefully performed and documented experiments.

In the present paper and its reference [1], the authors have made a significant contribution to the validation process. These experiments are attractive for code validation because of their simplicity. One especially useful aspect of this experiment is its axisymmetric nature. Most of the present detailed engine programs are limited to two dimensions. In addition, it is a relatively simple turbulent fluid flow without complicating features such as combustion. A reliable engine model must be able to simulate such an experiment accurately before it makes sense to worry about chemistry, fuel sprays, etc.

To be useful to numerical modelers, the documentation of an experiment must include enough information to allow the computations to be done without guessing at any parameters: geometry of the experiment, thermodynamic state and composition of the fluid(s), initial conditions, and boundary conditions (including possible time dependence). The report by Dyer [4] on a constant volume bomb experiment is a good example of a sufficiently well-documented study. However, authors almost invariably leave out some critical piece of information or include some complication that makes it impossible to simulate the experiment numerically. The present paper is marginal in this regard, as the thermodynamic state and composition of the working fluid are not specified. In general, this omission would render the results useless for numerical simulations. However, in this particular case, the omission is not serious as the flow is basically isothermal and incompressible, and therefore probably insensitive to these details. Gosman, et al. [5] have attempted to simulate some of these experiments, and their discussion elaborates on some of the problems encountered in trying to compare even these relatively simple experiments with calculations. Additional simple, well-documented experiments, perhaps each emphasizing one physical process such as combustion or fuel sprays, would be most welcome.

[1] By A. A. Morse, J. H. Whitelaw, and M. Yiameskis, published in the Dec. 1980 issue of the ASME JOURNAL OF FLUIDS ENGINEERING, Vol. 102, No. 4, pp. 478-480.

[2] Stanford University, Stanford, Calif.

[3] Theoretical Division, University of California, Los Alamos Scientific Laboratory, Los Alamos, N. Mex. 87545.

### Additional References


1 Butler, T. D., Cloutman, L. D., Dukowicz, J. K., and Ramshaw, J. D., "CONCHAS: An Arbitrary Lagrangian-Eulerian Computer Code for Multicomponent Chemically Reactive Fluid Flow at All Speeds," Los Alamos Scientific Laboratory report LA-8129-MS, 1979.

2 Butler, T. D., Cloutman, L. D., Dukowicz, J. K., Ramshaw, J. D., and Krieger, R. B., "Toward a Comprehensive Model for Combustion in a Direct-Injection Stratified-Charge Engine," in *Combustion Modeling in Reciprocating Engines,* ed. J. N. Mattavi and C. A. Amann, General Motors Research Laboratories, New York, Plenum Press, 1980.

3 Cloutman, L. D., Dukowicz, J. K., and Ramshaw, J. D., "Numerical Simulation of Reactive Flow in Internal Combustion Engines," *Proc. of the Seventh Intern. Conf. on Numerical Methods in Fluid Dynamics,* in press, 1980.

4 Dyer, T. M., "Characterization of One- and Two-Dimensional Homogeneous Combustion Phenomena in a Constant Volume Bomb," Sandia Laboratories report SAND78-8704, 1978.

5 Gosman, A. D., Johns, R. J. R., and Watkins, A. P., "Assessment of a Prediction Method for In-Cylinder Processes in Reciprocating Engines," in *Combustion Modeling in Reciprocating Engines,* ed. J. N. Mattavi and C. A. Amann, General Motors Research Laboratories, New York, Plenum Press, 1980.


### Authors' Closure

**Reply to W.C. Reynolds, Stanford University**

The enquiry requests estimates of the experimental uncertainty on three topics - (i) the location of the centers of the vortices, (ii) the strength of the recirculations, and (iii) the angles of the jet-exit streamlines. These are considered in turn.

(i) The primary vortices occupy the bulk of the flow space, are stronger and are much more accurately defined than the secondary vortices which form in the corners near the cylinder head and piston face and in the near-axis region behind the head. The vortices were plotted by joining up contours of the stream function $\psi$, obtained by integration of the mean axial velocity values, and adding or subtracting small amounts of mass (typically up to $\pm 10$ percent of the net mass flux) to correct for departures of the measurements from continuity requirements.

The vortex centers can however be located since the value of the stream function is either a maximum or a minimum at these points. Thus, for the centers.,

$$\text{at constant } x, \frac{d\psi}{dr} = 0, \text{ i.e. } \bar{U} = 0,$$

$$\text{and at constant } r, \frac{d\psi}{dx} = 0, \text{ i.e. } \bar{V} - 0.$$

Hence, the vortex centers may be determined by plotting the loci of points (at constant $x$) where $\bar{U} = 0$ and (at constant $r$) where $\bar{V} = 0$. The point of intersection gives the vortex center. Interpolation is necessary in the latter case due to the relative coarseness of the axial spacing. An example is shown on Fig. A for the profiles at 90 deg ATDC and S = 1.20 (see Figs. 2(*a*) and 3(*c*) of the paper). The location of the center of the primary vortex is almost exactly as shown in the paper, while that of the vortex in the corner between the cylinder head and wall is in the correct radial position but slightly further from the wall than shown in Fig. 2(*c*). No information can be obtained for the center of the third vortex since there is no region near the axis in Fig. 3(*c*) where $\bar{V} = 0$ (except at the axis itself). This confirms that the center of this vortex must be nearer to the wall (i.e. as shown) than $z = 10$ mm. For the primary vortex, therefore, the contours presented in the paper are consistent with the mean values of the radial velocity. The

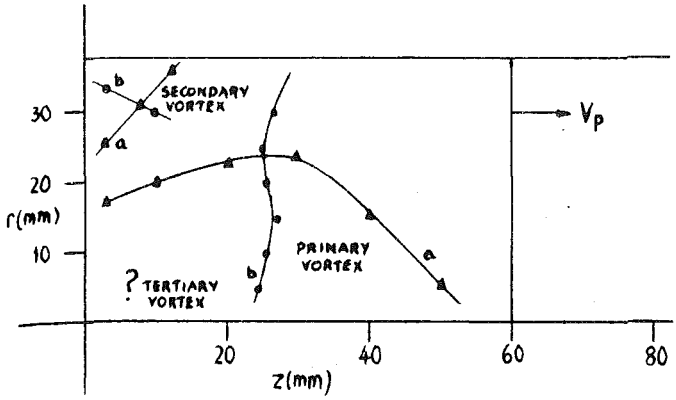


**Fig. A Determination of vortex centers ($S$ = 1.20, 90 deg ATDC). (*a*) Loci of points at constant $x$ where $\bar{U}$ = 0, (*b*) loci of points at constant $r$ where $\bar{V}$ = 0. Location of vortex centers. Primary vortex—from above: $z$ = 25.1 mm, $r$ = 23.8 mm. From 80-WA/FE-8: $z$ = 23.5 mm, $r$ = 22.7 mm. Secondary vortex—from above: $z$ = 7.6 mm, $r$ = 31.2 mm. From 80-WA/FE-8: $z$ = 5.5 mm $r$ = 31.3 mm**

same confirmation of the location of the centers cannot however be drawn for the secondary vortices since there are not enough data points in the volumes occupied by the vortices for clear definition. In general, the estimated location of the vortex centers is accurate to within ±2 mm in both the axial and radial directions so that, as a rough guide, the innermost contour for each vortex may be considered as representing the area of uncertainty for the true center of rotation.

(ii) The quoted values for the mass flux recirculated by each vortex are probably more accurate for the secondary vortices than for the primary vortex since corrections to the mass balances to satisfy continuity were always made in the regions of large velocity, i.e. in the primary vortex and the indrawn jet. The quoted strengths of the primary vortices are accurate, therefore, to the same order as the extent of the corrections required to adjust the mass balances (i.e. an upper limit of ± 10 percent). The secondary vortices were drawn on the basis of integration from the nearest boundary at which the stream-function values was known, i.e. from the wall or the axis as appropriate, and *no corrections to the measured velocity values were made*. Thus, the accuracy of the quoted vortex strengths is that of the measurements themselves, i.e. ±3 percent.

(iii) The angles of the jet-exit streamlines are subject to appreciable uncertainty in the zero swirl case (Figs. 1(*a*), 2(*a*), and 4(*a*)) since the nearest station of measurement to the cylinder head was at $z$ = 10mm. Interpolation across the initial 10mm of flow space is difficult in view of the steep gradients of axial velocity (and hence of the stream function) which prevail. The situation is improved for the cases with swirl since the profiles at z = 3mm were also measured.

**Reply to L. D. Cloutman, Los Alamos Scientific Laboratory**

Dr. Cloutman's remarks about our paper (80-WA/FE-8) indicate a philosophy which is essentially the same as we have adopted at Imperial College in the alliance of measurements in simple "engine-like" configurations to the development of computer codes to predict the flow field in reciprocating systems of increasing complexity. Consequently, as he realizes, we have endeavoured in our measurements to provide the computor with sufficient information to simulate the experiments numerically without major uncertainties concerning the initial and boundary conditions or the working state of the fluid. We have provided in the paper, data which show the increasing effect of swirl on the in-cylinder flow processes and should assist in the development of numerical procedures and turbulence models to predict the basic flow field in the absence of complicating effects such as compression and combustion. A more comprehensive statement of the data is available in the report cited in the paper.

Following on from the data presented, we have now made measurements in a similar swirling flow configuration with different clearance volumes and bore-to-stroke ratios. These demonstrate clearly the effects of such parameters on the growth and decay of the vortex structure. The effect of off-setting the inlet valve to produce a three-dimensional flow has also been explored. Both sets of data are available in the form of Imperial College reports. Measurements are currently being performed in similar plexiglass configurations but with the addition of compression ratio − 3.5, and the program has been supported by data obtained in a practical diesel engine of compression ratio 17.5.